Swansea University
Prifysgol Abertawe

Understanding and Development of Glass Film for Grain Oriented Electrical Steel

By: Ashley Spencer Hill

Submitted to Swansea University in fulfilment of the requirement for the Degree of Doctor of Engineering in Materials

Swansea University

2021

i

Abstract

The mechanisms and the development of the surface oxide known as "Forsterite" during the high-temperature annealing process of electrical steel is not fully understood. Research has demonstrated that a uniform Forsterite layer develops at 1200°C and adding certain compounds to the magnesium slurry improves consistency. This thesis investigates the development of Forsterite during the high-temperature coil annealing cycle and the effect of introducing selected compounds to the magnesium slurry on the Forsterite layer.

Based on a literature review on the transition of Fayalite to Forsterite and the influence of high-temperature soak, an experiment was conducted on laboratory coated samples that were then heat-treated using a custom laboratory furnace. The heat treatment that was conducted was interrupted at various points during the heating phase and the high-temperature soak phase. An additional investigation into the effects of TiO_2, V_2O_3 and FeO-Fe_2O_3 when added to the magnesium slurry has on Forsterite was also studied.

The results indicate that magnesium-enriched surface is developed as early as 1050°C, and with the introduction of TiO_2 to the magnesium slurry a Ti enriched region also develops at 1050°C as part of the surface oxide. Further research is needed to identify the compounds of the magnesium and titanium enriched regions.

Declaration

This work has not previously been accepted in substance for any degree and is not being concurrently submitted in candidature for any degree.

Signed.......... ⬛⬛⬛⬛⬛⬛⬛⬛⬛⬛⬛⬛ ....

Date.................... 24/05/2022 ....

This thesis is the result of my own investigations, except where otherwise stated. Other sources are acknowledged by footnotes giving explicit references. A bibliography is appended.
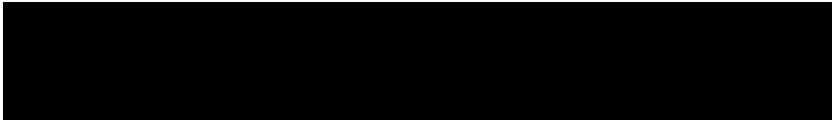
Signed....... ⬛⬛⬛⬛⬛⬛⬛⬛⬛⬛⬛⬛ ....

Date.................... 24/05/2022 ....

I hereby give consent for my thesis, if accepted, to be available for photocopying and for inter-library loan, and for the title and summary to be made available to outside organisations.

Signed........... ⬛⬛⬛⬛⬛⬛⬛⬛⬛⬛⬛⬛

Date.................................... 24/05/2022 ....

The University's ethical procedures have been followed and, where appropriate, that ethical approval has been granted.

Signed................ ⬛⬛⬛⬛⬛⬛⬛⬛⬛⬛⬛⬛

Date.. 24/05/2022 ....

Acknowledgements

Table of Contents

List of Figures

xiv

xviii

List of Tables

List of equations

Abbreviations

BCC	Body Centre Cubic	XRD	X-Ray Diffraction
B-H loop	Flux Density – Magnetizing force Loop	VCI	Volatile Corrosion Inhibitor
CAA	Citric Acid Activity		
CGO	Conventional Grain Oriented		
CSL	Coincidence Site Lattice		
CVD	Chemical Vapor Deposition		
EDS	Energy dispersive x-ray spectroscopy		
FTIR	Fourier Transform infrared Spectroscopy		
GDS	Glow Discharge Spectrometer		
GOES	Grain Oriented Electrical steel		
GOSS	Grains of the {110} <001>		
Hi-B	High Permeability		
HTCA	High Temperature Coil Annealing		
HTS	High Temperature Soak		
LTS	Low Temperature Soak		
NOES	Non-Grain Oriented Electrical Steel		
P_{Anom}	Anomalous losses		
Pbw	Parts By Weight		
P_{Ed}	Eddy Current		
P_{Hyster}	Hysteresis losses		
PVD	Physical Vapor Deposition		
SEM	Scanning Electron Microscope		
TGA	Thermal Gravimetric Analysis		

Chemical abbreviations:

$2NH_3$	Ammonia	H_2O	Water
$3HNX$		HF	Hydrogen Fluoride
Al	Aluminium	K	Potassium
Al_2O_3	Aluminium Oxide	$Mg(OH)_2$	Magnesium Hydroxide
$Al-N$	Aluminium nitride	$Mg_2(OH)_2$	Magnesium hydroxide
B	Boron	Mg_2SiO_4	Forsterite
C	Carbon	$MgAl_2O_2$	Spinel
$Ca(OH)_2$	Calcium Hydroxide	$MgCl_2$	Magnesium Chloride
$CaCl_2$	Calcium Chloride	MgO	Magnesium Oxide
CH_4	Natural gas	$MgO_2Al_4Si_5O_{18}$	Cordierite
Cl	Calcium	Mn	Manganese
Co	Cobalt	MnO_2	Manganese Dioxide
CO	Carbon Monoxide	MnS	Manganese Sulphide
CO_2	Carbon Dioxide	N	Nitrogen
Co_3O_4	Cobalt (III) Oxide	$Na_4P_2O_7$	Sodium Pyrophosphate
CoO	Cobalt(II) Oxide	$Na_4P_2O_7*10H_2O$	Tetrasodium Pyrophosphate
Cr_2O_3	Chromium (III) Oxide	$NaOH$	Sodium Hydroxide
CrN	Chromium Nitride	NH_4Cl	Ammonium Chloride
Cu	Copper	Ni	Nickel
CuO	Copper (II) Oxide	NiO	Nickel Oxide
Fe	Iron	O	Oxygen
Fe_2SiO_4	Fayalite	S	Sulphur
Fe_3O_4	Iron (III) Oxide	Sb	Antimony
FeO	Iron (II) Oxide	$Sb_2(SO_4)_3$	Antimony Sulphate
H_2	Hydrogen	Si	Silicon
SiO_2	Silica		
Sn	Tin		
SnO_2	Tin (IV) Oxide		
Sr	Strontium		
$Sr(NO_3)_2$	Strontium Nitrate		
$Sr(OH)_28H_2O$	Strontium hydroxide Octahydrate		
$SrCO_3$	Strontium Carbonate		
$SrSiO_4$	Strontium		
$SrSO_4$	Strontium Sulphate		

Ti	Titanium		
TiN	Titanium Nitride		
TiO$_2$	Titanium Dioxide		
V$_2$O$_5$	Vanadium (V) Oxide		
ZnO	Zinc Oxide		
Zr	Zirconium		

Mathematical Definitions:

∂	Resistivity cycled to maximum induction	n	Number of laminations
B	Gauss	nm	nanometres
B$_m$	maximum flux density	^{o}C	Degrees Celsius
cm	centimetre	P$_h$	Hysteresis loss
d	Domain wall	t	thickness
E	Free energy	T	tesla
Eλ	Magneto-elastic anisotropy energy	V	Volume
f	frequency	W	Watts
g	Grams	ρ	Density
H'$_e$	Coercive force after ageing	σ	Resistivity
H$_e$	Coercive force before ageing		
Hz	Hertz		
Kg	Kilograms		
K$_h$	constant that depends upon the magnetic material		
m	meter		
M$_s$	magnetic saturation		
n	Steinmetz exponent		

Chapter 1.   Introduction

Electrical steel is a unique, specialist type of steel that does not adhere to the typical properties of traditional steel. The mechanical properties of the electrical steel are not essential - the primary focus is placed on the magnetic properties. The electrical steel industry is set to see an increase in demand and importance in the next five years[1]. Electric cars are beginning to become customary in the automotive industry, which uses electrical steel for motors. Finally, due to increased effort to reduce worldwide pollution, expansion is expected in the demand for electrical steel used for the cores of high-efficiency transformers to supply homes and industries in both developed and developing countries efficiently and reduce pollution [2].

The electrical steel industry is split into two main categories - Non-Grain Oriented Electrical Steel (NOES) and Grain Oriented Electrical Steel (GOES).

NOES have an isotropic microstructure which is characterised by the gauge of the lamination that is in the range of 0.1-0.5mm and a typical silicon content between 1.5-3.4 wt%-Si. NOES properties are best suited for electric motors, which can range widely in size from small motors used in toy cars to large industrial cranes [2].

GOES has an anisotropic microstructure, where the magnetic properties are favourable in the rolling direction rather than perpendicular to the rolling direction[3]. The silicon content of GOES is typically around 3.5wt%-Si and is limited by the complications of brittleness that can arise during cold rolling[4].

This thesis will focus on the GOES, which is routinely used to construct the cores of highly efficient transformers. The GOES and NOES market price is directly dependent on the efficiency properties of the electrical steel. GOES properties directly reflect the amount of energy lost when power stations transmit and distribute the energy through the national grid. Several transformers are required to upscale and downscale the voltage.

These highly efficient transformers are typically around 98% efficient. The inefficiency arises through the generation of heat and has substantial economic and environmental costs. If any improvements in efficiency can be achieved, the value of the steel can increase considerably due to the efficiency saving of the transformer over its lifetime [5].

1.1 Literature review

Laminations of GOES are used to form the core of a transformer, as shown in Figure 1. A transformer aims to reduce the high voltages produced by power stations, typically between 400,000 to 750,000 Volts, to a suitable voltage that can be used to power appliances[6].

The reduction in voltage is performed through magnetism rather than electric conduction, where a primary winding of wire is wrapped around one end of the laminated core. This induces a magnetic flux through the silicon-iron transformer core, and a secondary winding at the opposite side of the transformer core can step up or step down the voltage depending on the configuration of the windings.

The step-down configuration typically used to supply homes has more turns at the primary winding than the secondary winding. The step-up design is the opposite of the step-down configuration, where there are more turns at the secondary winding than the primary. An example of this is in Figure 1.
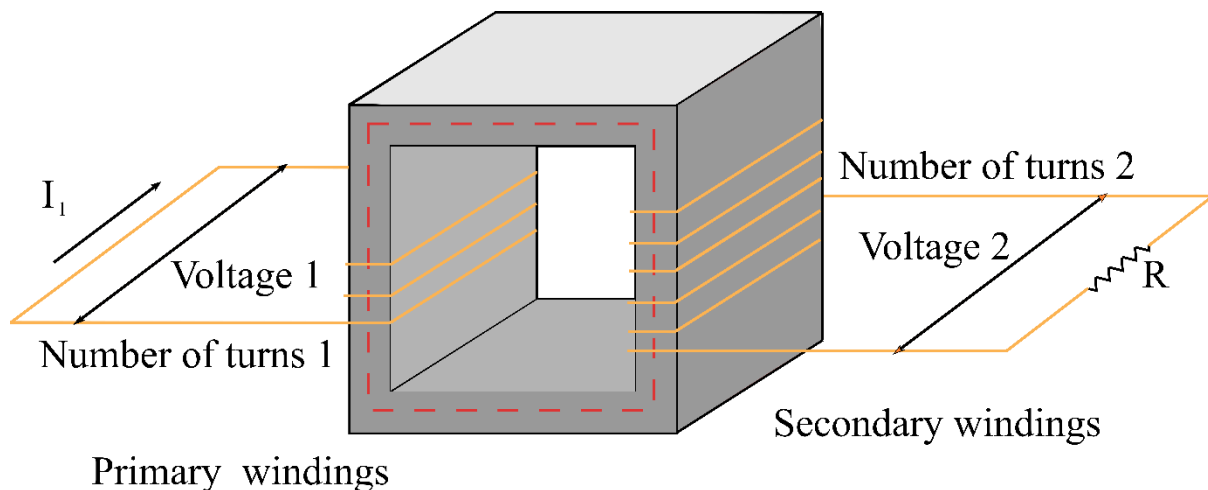
Figure 1. A simplified diagram of a transformer operation.

The material of which the transformer core is made of is critical to its overall efficiency. There is only a small selection of elements that are suitable for this – iron (Fe), cobalt (Co) and nickel (Ni) [7][8]. Each element on the periodic table has a type of magnetism related to the magnetic susceptibility of the bulk of the material. In basic terms susceptibility of the bulk of the material is due to the electrons within an element have a specific charge and a spin[7]. These electrons spinning have an energy-related to them. However, if an equivalent electron is spinning in the opposite direction, the energy is cancelled out, resulting in no magnetic field being created. However, not all electrons are cancelled out, resulting in an imbalance of electron spin. This creates a small magnetic field in an atom. The elements have been categorised into four main groups, and they are: - Ferromagnetic, Antiferromagnetic, Paramagnetic and Diamagnetic, which are displayed below in Figure 2[8].
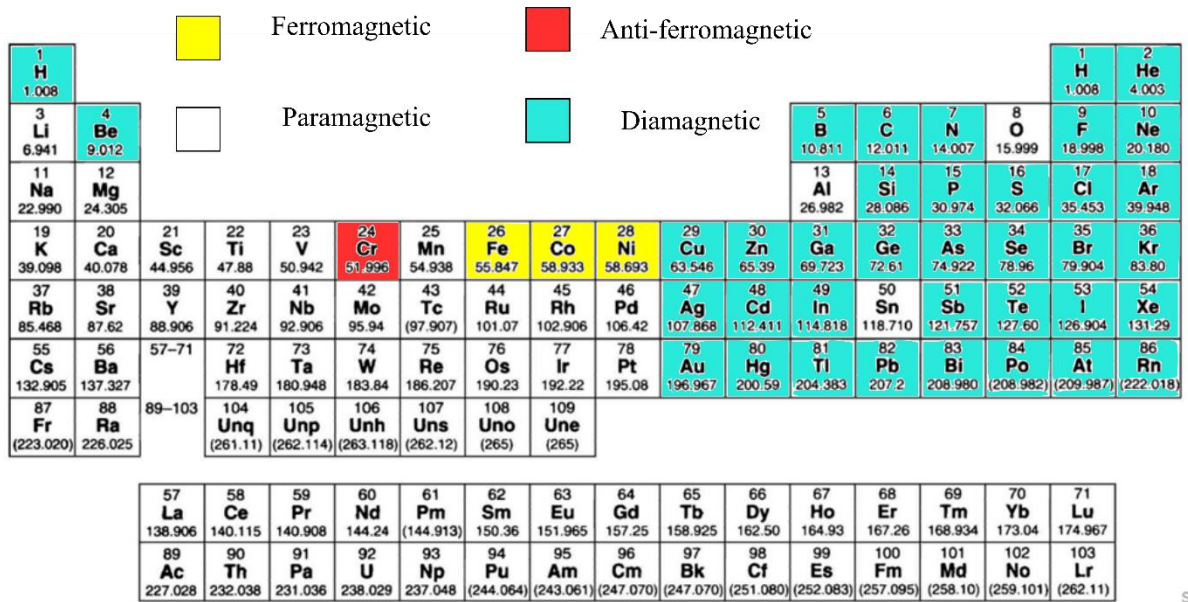
Figure 2. Periodic table displaying the four categories of magnetism where by the ferromagnetic material is displayed in yellow, paramagnetic material in white, anti-ferromagnetic in red and diamagnetic in blue [9].

Ferromagnetic material is a unique feature of spontaneous alignment of the magnetic moments of the individual atoms. The elements which display this characteristic are limited to 3 elements Fe, Ni and Cu (as shown in Figure 2). Under equilibrium conditions, the bulk material does not exhibit an external magnetic field due to the energy of the material being at a minimum due to the arrangement of magnetic domains effectively creating a closed circuit, as shown in Figure 3. Therefore no external magnetic field is emitted[10]. However, when an external magnetic field is applied to the ferromagnetic material, it results in the alignment of domains in the direction of the magnetic field[10]. This will result in the ferromagnetic material that exhibits an external magnetic field. When all the domains are aligned with the magnetic field, this is known as magnetic saturation (M_s). The magnetic saturation can significantly decrease with thermal disruption, in which the ferromagnetic characteristics are entirely removed and the temperature at which this happens is known as the Curie temperature.

N= North pole
S= South pole
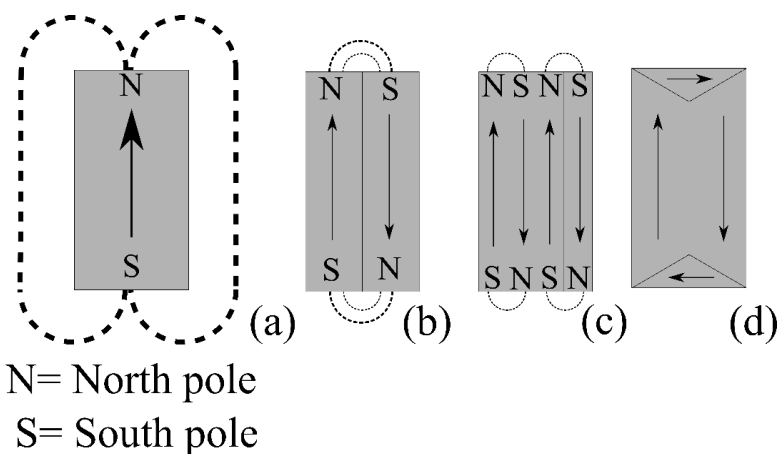
Figure 3. Schematic illustration of domains under magnetisation (a) Single domain under maximum saturation (b) two domains (c) four domains, and (d) closed domains under no applied magnetic field.

1.2　Introduction to Orb Steelworks and Processing Method at Orb Steelworks

Cogent is an umbrella company of multinational companies which consists of Orb Steelworks, Surahammars Bruk and, Cogent Power. Surahammars Bruk is in Sweden and manufactures NOES for the core of electric motors. Cogent Power is based in Canada, where they manufacture transformers. Orb Steelworks manufactures GOES and is based in Newport, Wales. The manufacturing of GOES is a complicated process and the next section will provide details of the process.
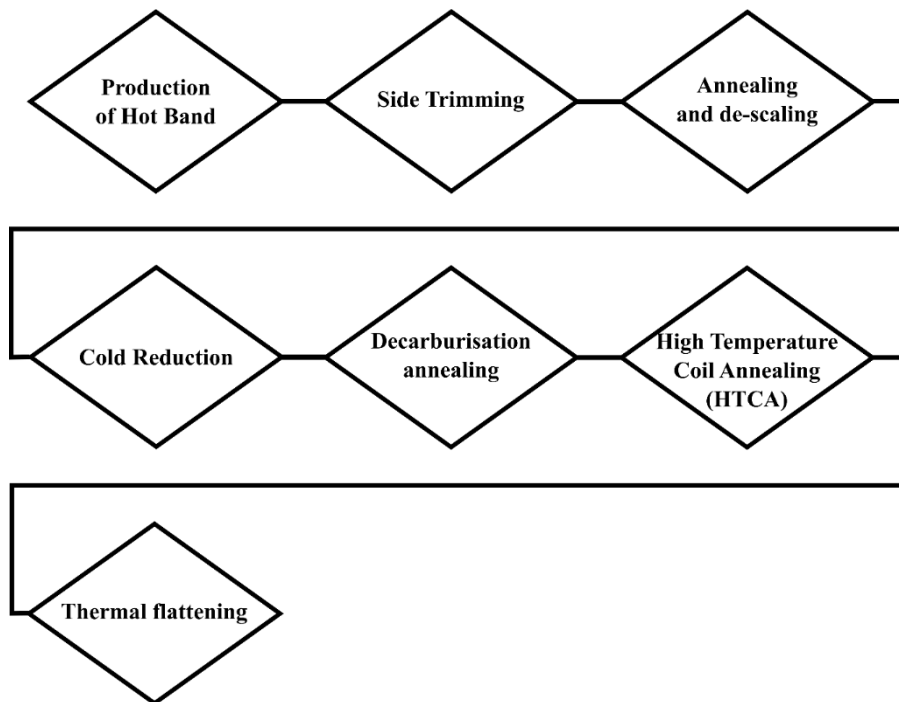
Figure 4. Flow chart of the manufacturing process at Orb Steelworks.

1.2.1 Production of Hot Band

Tata Steel IJmuiden manufacturing site is part of Tata Steel group and produces various products such as hot and cold rolled coils, galvanised and tin-plated strips. In addition, they provide Orb Steelworks with the high silicon hot-rolled coil of a thickness of 2.3mm, weighing approximately 20 tonnes. IJmuiden creates this hot-rolled coil through a continuous casting process following conventional steelmaking. These slabs are cast directly from the ladle before entering a tunnel reheating furnace immediately after leaving the mould and exit the tunnel furnace at 1150°C and are around 70 mm thick[11].

The slab is initially rough, reduced down to 40% and then further reduced to 2.3mm, it is then rolled into a coil, and the coil cools down from 640°C to room temperature. Once the hot band has reached room temperature, it is shipped to Orb steelworks[11]. The steel Ijmuiden produces is not typical of conventional steel works; the steel requires extensive processing to construct steel with suitable magnetic properties for use in the core of transformers.
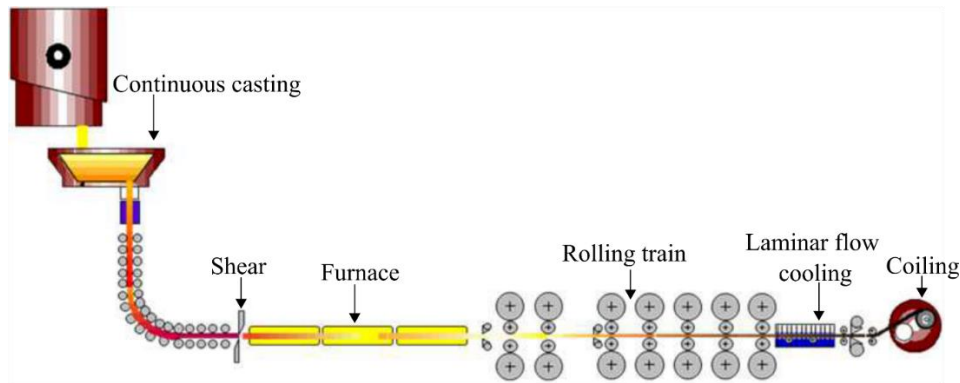
Figure 5. Schematic representation of hot rolling at Ijmuiden [11][12]**.**

1.2.2 Production at Orb Steelworks

The 20-tonne hot band coils arrive at Orb Steelworks with a thickness of 2.3mm with defective edges and a highly oxidised surface, as shown in Figure 6.

Figure 6. (a) Hot band coils arrived at Orb steels from Ijmuiden and (b) the edge defects.

These defects must be dealt with before any progress can be made on producing high-quality electrical steel. The composition of the typical incoming hot band is displayed in Table 1.

Element	C	Si	Mn	S	Al	Cu	Sn	Ti
Wt%	0.05	3.1	0.019	0.005	0.001	0.09	0.09	0.08

1.2.3 Side Trimming

The initial processing of side trimming, in which it is essential to get the correct profile balance since this is a costly process as removal of 1cm edge results in 600 tonnes of scrap a year which can create as much as £1.5 million loss of product. Although this is a costly process, it is nevertheless essential because if side trimming is not carried out, it can cause cracks in the edges. These cracks then become concentration points for stresses, which will lead to cracks propagating through the width of the strip that subsequently cause failure of the strip. Failure of the strip can cause extensive delays in production and cause significant damage to the processing line. To aid the removal of the edges of the hot band, the edges are first heated; this reduces the chances of producing additional cracks by raising the edges above the brittle/ ductile transition temperature. To improve the efficiency of the process, the hot bands are welded together, allowing continuous processing of the hot band.
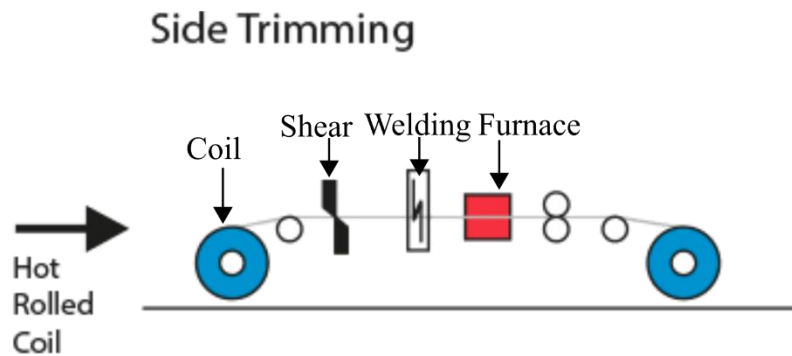
Figure 7. Schematic representation of the side trimming at Cogent[12].

1.2.4 Normalizing Annealing and De-Scaling

Once the side trimming is completed, the strip is subjected to normalizing annealing that heats the strip up to 1080°C. The normalizing heat treatment causes an increase in ductility, allowing straightforward processing of the hot band and burns off any contaminants at the surfaces that may have been picked up during transportation. During the normalization annealing, a dispersion of precipitates develops, which is essential in the later stages of the process. The distribution of precipitates is initially important during cold rolling.

The precipitates prevent dislocation movement between grains and, therefore, recrystallization. Due to dislocations being mis-oriented atoms from the matrix, there is an energy associated with them. This stored energy is then used to drive secondary recrystallization during the high temperature anneal[13]—the distribution of precipitates is also critical during the decarburization stage, where the precipitates prevent primary recrystallization. Therefore, the distribution of precipitates plays a crucial role in providing large secondary grains with the correct orientation.

Immediately after the strip has been heated to 1080ºC, the removal of scale is dealt with by several means. First, the strip is shot blasted with small pellets, which remove most of the scale; this is made easier with the strip held at high temperature. The coils are then dipped in hydrochloric acid (5-6 %) tanks that are heated to the desired temperature, which ensures that all corrosion is removed from the strip, resulting in a shiny surface finish.
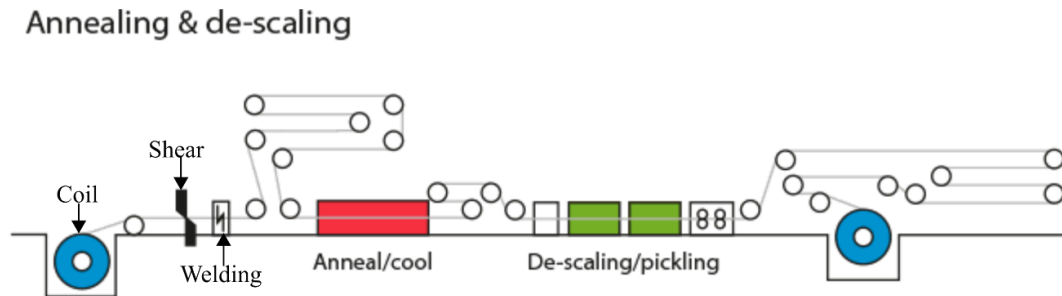
Figure 8. Schematic representation of the annealing and de-scaling[12].

1.2.5 Cold Rolling

The cold rolling at Orb Steelworks is performed by a reversing mill which uses 1500 tonnes of load applied to the strip. The strip is passed through 5 times to reduce the coil down to the desired thickness, typically either 0.35mm, 0.30mm, 0.27mm, or 0.23mm. The material is subjected to an initial three times through the rollers to achieve approximately 65% reduction, for a target thickness of 0.6-0.7mm thickness. This is then cold rolled for a further 60% reduction to the desired final thickness.

There are several purposes of cold rolling; the primary is to distort the microstructure, which will cause dislocations to form and are pinned by precipitates such as C, Mn, and S. The additional distortion of the matrix puts the material in a higher energy state of which is a method of storing energy in the material. This stored energy is then used during secondary recrystallization to form large GOSS grains. The secondary reasoning for cold rolling is to produce thin laminates to reduce the size of transformers and increase the number of laminations within the transformer. The thinner gauge of steel has a beneficial impact on magnetic properties, with thinner gauges increasing the efficiency of the steel. Although this process is described as cold reduction, by the third pass, the strip temperature rises to approximately 200ºC, allowing inter-pass ageing that is also beneficial to the magnetic properties.
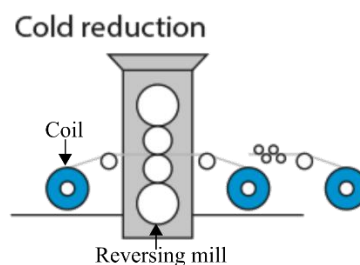
Figure 9. Schematic representation of reversing mill at Cogent[12].

1.2.6 Decarburization of the Steel Substrate

The decarburisation stage, as shown in Figure 8, is a critical part of the production process where several mechanisms are taking place. The conditions in the decarburisation furnace range in temperature between 800ºC – 900ºC in a wet gas 75%H_2 -25% N_2(Volume fraction)[14] atmosphere. The coil initially goes through the burn from section to remove any contaminants off the surface and immediately into the induction section to increase the strip temperature for recovery following deformation of cold reduction and decarburization.

One of the first mechanisms to take place is primary recrystallization, where the elongated grains produced during cold rolling re-crystallize to form grains that have an average grain size of 18-22 μm [15]. This takes place throughout the decarburization when the strip temperature hits 600ºC then at 840ºC. Once the strip is at a temperature around 800ºC, the strip is initially decarburized.

The hydrogen is introduced into the furnace is critical to removing the carbon from the coil since the carbon is no longer required to pin the grain boundaries after cold rolling. Carbon removal is essential to prevent magnetic ageing due to the low solubility and slow diffusion activity energy [16]. The carbon content is reduced from 0.05 to <0.002% by the following chemical reaction[17].

$$C + H_2O \rightarrow CO + H_2$$

$$C + 2H_2O \rightarrow CO_2 + 2H_2$$

$$C + 2H_2 \rightarrow CH_4$$
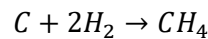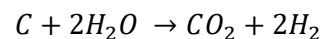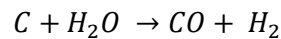
Magnetic ageing is a result of increasing the coercive force which is given by: -

$$K_{age} = \frac{H'_e - H_e}{H_e} 100\%$$

Where H_e is the coercive force before ageing H_e' is the coercive force after ageing [17]

After completing the decarburization, ammonia (2NH3) and natural gas (CH4) are introduced to the furnace. This causes an increase in nitrogen levels from 20 ppm to 220 ppm, which forms nitrides used for pinning the primary grains and delay secondary recrystallization during the high temperature anneal cycle to generate large grains[18][19][20]. The nitrides developed during this stage, such as Al nitrides, Mn inhibitors and two different hexagonal crystal structures that are β-Si_3N_4 and α-Si_3N_4, have been found[21]. Additionally, during the decarburization annealing, an oxide layer develops at the surface known as Fayalite (Fe_2SiO_4), and this will be discussed further in Section Fayalite (Fe_2SiO_4) 1.8.1. Once the decarburization stage has been completed, the coils are coated with MgO slurry, dried before further processing. Further details on the decarburization stage will be explained in 1.8.
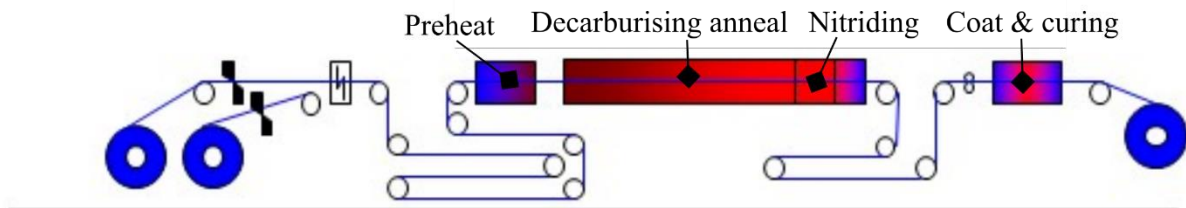
Figure 10. Schematic representation of the Decarburising stage at Cogent [12].

1.2.7 High-temperature coil annealing (HTCA)

The purpose of processing the coils up to this point is to develop the correct microstructure, distribution of inhibitors and stored energy to allow for large Goss grains to nucleate and grow to dominate the microstructure of the strip during the HTCA. The heating cycle takes over seven days to complete, where two coils are stacked on top of each other using stalks, and an inner cover is placed over them. Up to 8 coils can be placed in this arrangement, and the furnace is then placed over these inner covers, as shown in Figure 11.

During this stage, two individual phenomena take place at temperatures between around $950^{\circ}C$ – $1200^{\circ}C$. These two phenomena co-occur where the first phenomenon is developing the insulation oxide layer of the Forsterite layer, and the second phenomenon is secondary recrystallization of GOSS grains[21] [22]. The developing Forsterite layer appears to allow diffusion of some precipitates such as MnS, which improves magnetic properties due to the reduction of domain wall pinning of precipitates[15]. These two processes are discussed in further detail in sections 1.10 and 1.7.
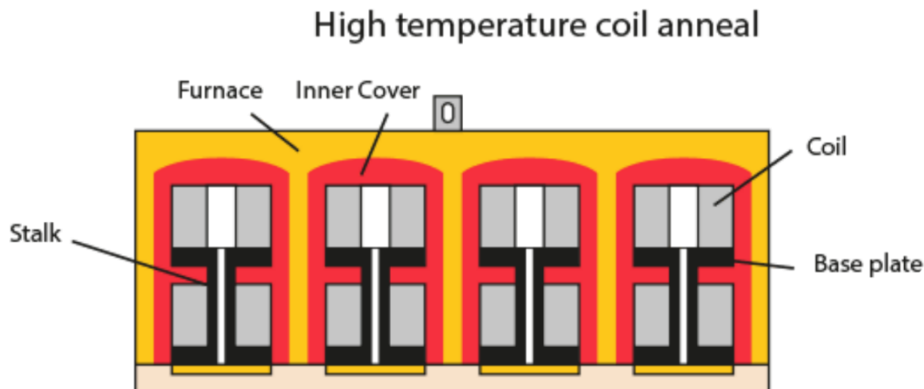
Figure 11. Schematic representation of the HTCA at Orb Steelworks [12].

1.2.8 Thermal Flattening

Once the coils have completed the HTCA cycle, the coils have become distorted in shape and require further processing before they can be sold to customers. The coil is initially cleaned to remove any unreacted MgO at the coil's surface using a washer and brushes. Immediately after cleaning the surface, a phosphate coating is applied and cured with temperatures reaching $850^{\circ}C$. The phosphate coating induces an additional tension onto the substrate, which has been shown to improve magnetic properties further [23]. The strip is annealed whilst either experiencing controlled elongation or hot

tension levelling to flatten the strip to make it suitable for transformer laminations. After controlled deformation, the strip is annealed for a sufficient time at temperature to remove the stresses imposed. The strip goes through a controlled cooling stage to avoid reintroducing stresses and causing thermal shock in the coating. Finally, it is laser scribed to reduce the size of the domains within the strip, which allows an increase in domain movement and subsequently reduces losses. However, any heat treatment applied after laser scribing will reverse the effect [14]. Mechanical scribing is a permanent method of reducing the sizes of the domains and can be heat treated after scribing [23].
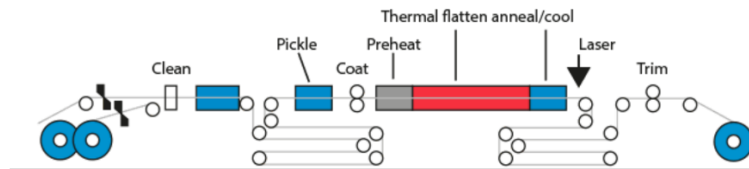
Figure 12. Schematic representation of the Thermal Flattening stage[12]**.**

1.3 Magnetic Properties

The major component of a transformer is the core, where the laminations of GOES are stacked upon one another arranged in a manner where the anisotropic properties are with the direction of flow of the induced field. For this reason, the magnetic properties of the GOES dictate the overall efficiency of the transformers, and the primary aim of GOES is to produce good magnetic properties, which means low losses (W/kg) and high permeability. A reduction of by 0.1 (W/kg) can increase the price by an additional £200- £500 per tonne and save the operator a significant amount of money over the lifetime of its operation.

The power loss is indicative of how much energy is dissipated in the process of cycling the material around its B-H loop. The total losses are separated into three basic vital categories, which make up the area inside the B-H loop created and is given by the following equation[24][25]: -

$$Total\ Power\ Loss\ \left[\frac{W}{Kg}\right] = P\ classic\ eddy\ losses + P\ Anomalous\ losses + P\ Hystersis\ losses$$

Equation 1. The equation to calculate the total losses [25].
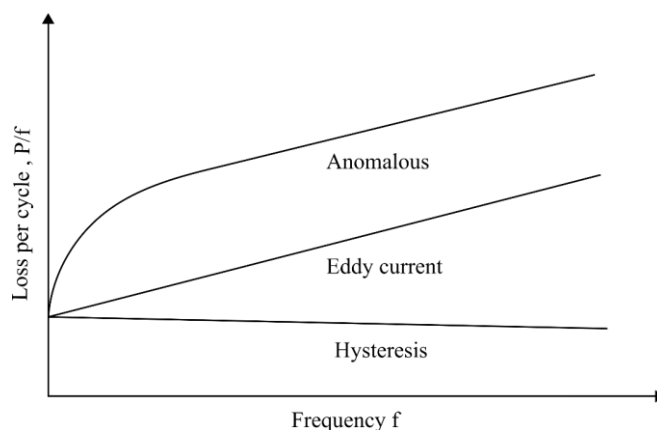
Figure 13. Displaying the portion of each category of losses has against frequency [25].

1.3.1 Eddy Current Losses

Heinrich Lenz law states that when an altering magnetic flux is induced on a Ferro-material, a voltage is created. Faraday's law states, "when voltage is created in Ferro-material that is generated by an altering magnetic flux, the polarity of induced voltage will produce a current with a magnetic field that opposes the change in the flux" [26][27][28]. From Lenz's law, the current produced from the electromagnetic field will cause resistance to the flow within the material, generating Joule heating [27].

The aspects which affect eddy losses can be seen in the classic eddy losses formula below: -

$$Classic\ Eddy\ Current\ Losses = \frac{\pi^2 t^2 B^2 f^2}{6\sigma\rho}$$

Equation 2. A formula to calculate the eddy losses [29][30].

t is the thickness
B is induction
f is frequency
ρ the density in g/cm^3
σ the resistivity in ohm/ cm
The eddy current losses in W/kg

The eddy losses produced are a function of the square of supply frequency[29]. Due to eddy current being a function of frequency, if operating frequency becomes too high, the performance of the transformer will considerably decrease [29]. A standard method of reducing eddy current losses is by reducing the core to thin laminations which are insulated from one another. Because of this the eddy path is distributed which reduces the magnetic core.
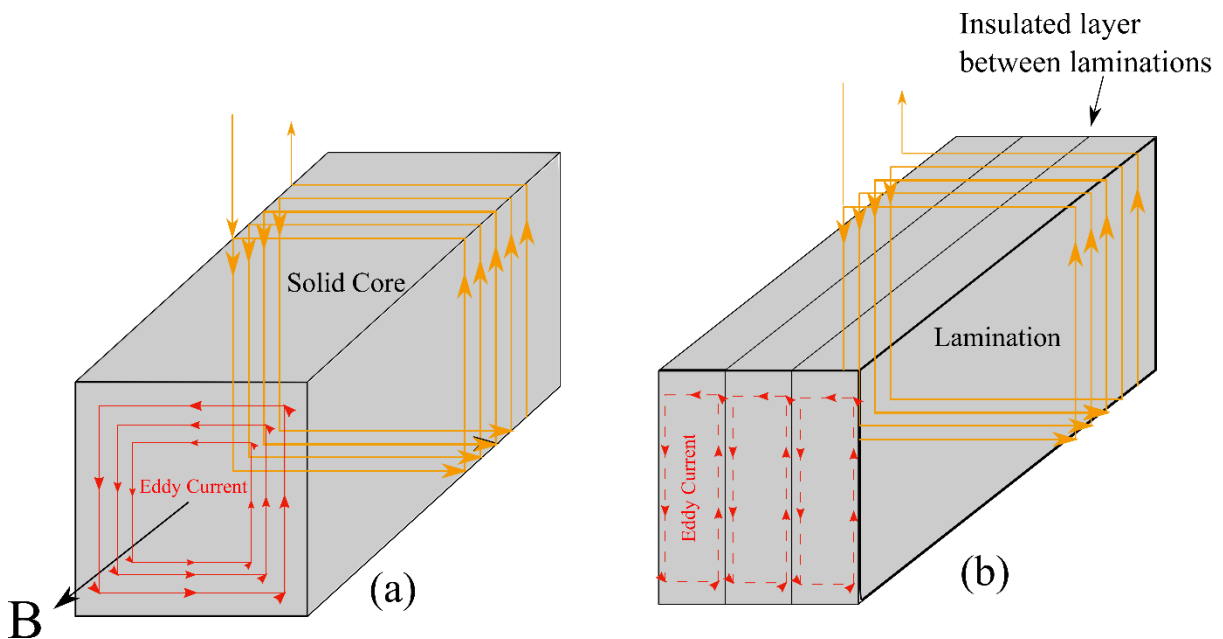
Figure 14. Illustration of the reduction of eddy current through dividing a solid core to lamination core[31].

1.3.2 Hysteresis Losses (P_{hyster})

The operation of a transformer involves continuously alternating flux; power is required for the continuous reversal of the molecular magnets in the core of the transformer[31]. The power required to reverse these molecular magnets is dissipated in the form of heat. From Figure 13, the hysteresis is not a function of frequency and reducing the hysteresis losses is significantly beneficial for all frequencies and is the most controllable. The losses are influenced by factors such as the orientation of domains, purity and stress of the substrate which all play a critical role in the hysteresis losses.

The hysteresis losses can be expressed as:

$$P_h = K_h f B_m^n V$$

Equation 3. Formula to calculate Hysteresis losses [31].

P_h = hysteresis loss (Watts)

K_h = is a constant that depends upon the magnetic material

n = is the Steinmetz exponent

B_m = is the maximum flux density in Tesla (T)

V = is the volume of magnetic material in cubic meters (m^3)

The fundamental methods of reducing the hysteresis losses begin at casting, whereby the chemistry is unique, and the purity of the GOES has a significant effect on the magnetic losses. However, that would be detrimental to the magnetic losses through pinning domains or affecting the development of the oxide layer, which reduces the tension applied to the substrate.

The greatest challenge of developing GOES is creating the correct texture in the rolling direction, and this involves careful distribution and size control of the inhibitors to develop GOSS texture. Traditionally Conventional Grain Oriented (CGO) was used, which produced a mis-orientation 7º away from the GOSS texture, which predominantly uses MnS[32] inhibitor. High Permeability (Hi-B) inhibitors have overtaken the use of these inhibitors, which has reduced the miss orientation to 3º away from the GOSS texture[32], which uses a combination of AlN inhibitors and MnS. The outcome of reducing the miss orientation results in permeability and reduction in total magnetic losses. Development of GOSS texture is the greatest challenge in manufacturing material with the lowest magnetic losses and high permeability properties due to the influences from processes before HTCA where secondary recrystallization occurs. Finally, other aspects that can increase hysteresis losses are the internal stresses caused by thermal deformation or physical damage such as dents and scratches, increasing the hysteresis losses by impeding the domain movement. These aspects can be reduced by carefully processing the coils through the process and controlled heat treatment during the latter stages of thermal flattening.

1.3.3 Anomalous Losses (P$_{Anom}$)

The remaining losses that have not been accounted for by Eddy current (P$_{Ed}$) and Hysteresis losses are accounted for by Anomalous losses. There have been several theories to explain the occurrence of these losses, such as studies investigating micro-eddy currents, non-uniform magnetisations that are due to the domain walls and bowing of domain walls[23][33][34]. The reduction of anomalous losses is achieved by aligning domain walls parallel to one another. As a result, this is a decrease in the distance the walls are required to move during the magnetization cycle. In addition, in GOES, the domain structure can be manipulated through laser or mechanical scribing of the surface of the steel to refine the domain structure[23].

The fundamental explanation for anomalous losses is by the Pry and Bean model[35]: -

$$P_{Anom} = \frac{(4fBmax)^2 dt}{\pi \partial} \sum_{n \, odd} \frac{1}{n^3} \coth\left(\frac{n\pi d}{t}\right)$$

Equation 4. The theoretical equation for calculating the anomalous losses.

B$_{max}$ is the maximum flux density in Tesla (T)

n is the number of laminations

f frequency in Hz

∂ Resistivity ∂ cycled to a maximum induction B$_{max}$

d domain wall (note* ideally should be uniform in grain-oriented electrical steel)

The magnetic losses are complicated mathematically which this thesis will not study in great depth. However, it is critical to the research to understand and appreciate the multiple roles in which various techniques are used to reduce the total losses and what the impact if one of these techniques is used is on the overall performance of the steel.

1.4 Domains

1.4.1 Introduction to Domains

There will be regions where magnetic moments are aligned with one another in a ferromagnetic material due to interactions between the atoms. These regions where magnetic moments of atoms are aligned are called domains [35]. These domains can be considered as vectors, and the net magnetization can be calculated [36]. The modelling of these domains and domain walls has been extensively researched to model and simulate the domain movement and interactions between domains [36][37].

A fundamental concept of visualising an individual domain is that it can be considered a miniature traditional bar magnetic field, where the magnetic field transfers from one magnetic dipole to another

(Figure 15). The typical amount of atoms that make up a domain is around 10^{15} atoms. However, in electrical steel, this is dependent on the grain size produced [38].
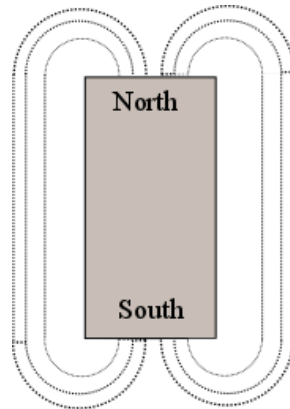
Figure 15. An illustration of a domain as a concept of a bar magnet and the magnetic field created between the magnetic poles.

When opposite dipole domains are next to one another, this creates an interface. This interface is known as a domain wall [39]. The magnetic moments in this region rotate 180° to align with the opposite dipole, and when the domain spacing is thicker than the domain walls, the domain walls must move rapidly to rotate the magnetisation.[39] Therefore, large domains rotating will result in bowing and nucleation of extra walls and, consequently, increased losses. There are two main types of domain walls, and the first one is Bloch walls, whereby the vectors rotate in a screw manner, rotating out of the film plain. These Bloch walls are typically in the order of microns [39][40]. The second domain wall is the Neel wall, where the magnetization rotates in the film plane [40]. The difference can be seen in Figure 16.
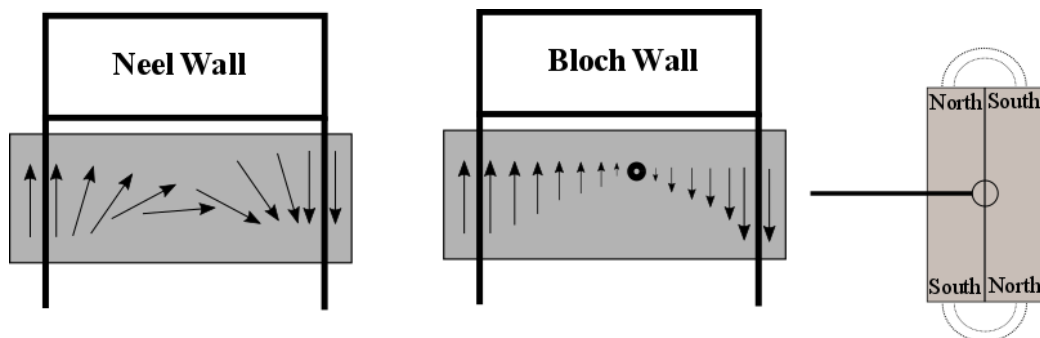
Figure 16. An illustration of the differences of Neel and Bloch wall of the rotations of domains at the domain wall.

1.4.2 Domains in Ferromagnetic Materials

The domains in a ferromagnetic material when no external magnetic field is applied show alignment of some domains. However, there are no distinct directions. When an external magnetic field is applied to the ferromagnetic material, the domains, i.e., the magnetic moment, aligns perpendicular to the magnetic field, and once the magnetic field is removed, the domains organise themselves to equilibrium. When the temperature is increased in ferromagnetic materials, the domains begin to lose

their individual magnetic moments at a specific temperature known as the Curie temperature. The steel becomes paramagnetic [40].

The Curie temperature of iron is around 770ºC, which has consequences during electrical steel production due to the coil being required to be moved from the furnace to the cooling area [39]. The alloying elements added to the silicon steel, especially Si, lower the Curie temperature for electrical steel to 720ºC. Usually, this would be done using a magnetic attachment on the cranes; however, due to the temperature of the coils, the use of clamps to move the coil is required to ensure that the furnace is available. The use of clamps on the coil can result in damage of coils resulting in increased waste.

There have been multiple studies investigating domains in NOES and GOES [41][42]. The domain structure in a ferromagnetic material can be influenced by imposing a magnetic field, which causes the domains to mechanically towards the direction of the applied field. As a result, the domains will change shape and length. This process is influenced by the domain's original orientation with the relevance of the direction of the applied field and the strength of the magnetic field.

When there are domains with no magnetic field applied to the substrate, the domains are arranged to co-exist in the lowest magnetic energy state and these domains have no preferred direction, as seen in Figure 17 at point 0. However, once a magnetic field is applied, the domains transition to a higher energy state and the domains that are closest to parallel to the magnetic field begins to rotate towards the directions of the magnetic field (point 1 and 2). Consequently, the domain walls mechanically begin to move rotating miss-aligned domains towards the direction of the magnetic field, changing the shape and size of the domain.

The additional external magnetic field is required to rotate the highly misaligned domains towards the magnetic field. With a continuously increasing magnetic field, the magnetic field is eventually increased sufficiently, causing maximum saturation, meaning the domains that are misaligned have been rotated towards the domain aligned parallel with the magnetic field. Once the domains align in a single direction, that of the external field, this is known as magnetic saturation (point 4). Any further increase of external field does not affect any increase of polarisation on Figure 17 is point 4.

From the B-H curve, a great deal can be learned about the characteristics of GOES and indicates the alignment and size of the domains within the electrical steel. The parameters that can be collected from the B-H curve are: -

Permeability: - the measurement of the ease in which the material can be magnetized to that induction calculated from the gradient of the curve. For electrical steel, the permeability is high, meaning that only a small amount of magnetic force is necessary to reach maximum saturation [43].

Magnetic Losses: - the amount of energy consumed to complete a B-H loop, the completion of the B-H loop is a rotation of domains to align them parallel with the magnetic field [44][45]. Hence, poor

domain structure, i.e. orientation in relation to the magnetic field and small domains will result in significant magnetic losses displayed with a large area within the B-H loop [44]. The magnetic losses can be divided up into three subcategories: Hysteresis Losses, Eddy current losses and Anomalous losses [45].

Magnetic coercivity: - is a measurement of the amount of magnetic field to reverse the material from maximum saturation to zero [32].
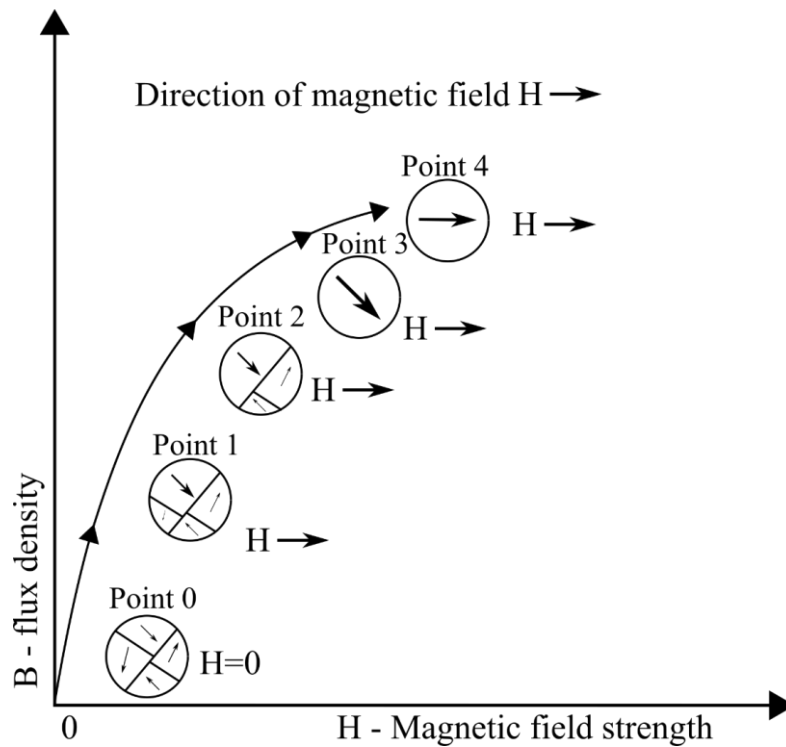
Figure 17. The reorganisation and rotation of domains under an increasing magnetic field [32].

1.5   Domain Colonies

As previously explained in section 1.4.2 a single domain will align with the external magnetic field applied. However, there will be multiple domains within a grain. These domains are organised in the lowest possible energy state; this is achieved by opposing domains next to each other when the magnetic field is applied to the electrical steel. Within a grain, there will be numerous domains and domain walls; these domains can be thought of as "domain colonies" and tend to align in the same direction within the grain, as shown in Figure 18. The domains organize themselves into the lowest energy state when an external field is applied to the substrate. The balancing of these domains is a balancing act between energy systems, explained in section 1.5.1.
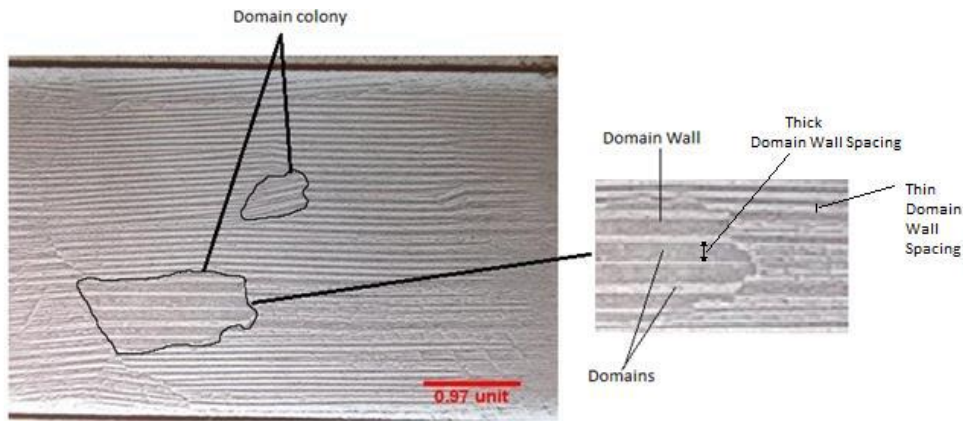
Figure 18. A visual representation of the appearance of domains, domain walls and domain colony.

1.5.1 Landau-Lifshiz Energy Equation

This section will briefly discuss the Landau – Lifshiz domain theory and then explain the impact of this in electrical steel and the difficulties optimising the domains to achieve minimum losses in electrical steel. Landau – Lifshiz developed the theory of magnetic domains to explain the contributions of the different internal factors have on free energy. The free energy equation E is given by:

$$E = Eex + ED + E\lambda + Ek + EH$$

Equation 5. The Landau-Lifshiz energy equation to describing domain theory as an expression of free energy [9] [46]

Magneto-elastic anisotropy energy (Eλ) is the change in dimensions of the crystal when the material is magnetized. Because the change of dimensions' results in elastic strain, the lattice and the direction of magnetization that minimizes these strain energies will be favourable [9].

Magneto-crystalline anisotropy energy (Ek) is magnetic anisotropy where the ease of magnetization is dependent on the crystal orientation of a material. For example, in iron easy directions of magnetization are in the [100], and the hard direction of magnetizations are in [111] [46]. In traditional steel, the orientations of each different grain vary. However, grain-oriented electrical steels take advantage of the easy direction and deliberately produce grains in the [100] direction in the rolling direction [9].

Zeeman Energy (EH) is the interaction between the magnetization field and the magnetization vectors of the domains. Therefore, the domains which are parallel to the magnetic field will have low Zeeman energy. If the domains are perpendicular to the magnetic field, this will increase the Zeeman energy. Applying a magnetic field to a ferromagnetic material would result in domain wall movement if the magnetic field applied is increased adequately. The magnetic vectors opposing the applied field will be consumed and rotated towards the direction of the field [10].

Exchange Energy (Eex) is the movement of domains from one polarization to the opposite polarization. It is possible to reduce this exchange energy to virtually zero by spreading the angular transition over a distance. However, this comes at the cost of an increase in anisotropy energy.

The grain size that is developed during the secondary recrystallization has a fundamental role in magnetic performance, whereby large grains are desired. These large grains are enabled by a combination of cold rolling and inhibitors that prevent nucleation and growth of undesirable orientations of nuclei. This gives an advantage to the desired GOSS orientated grains. This will significantly reduce the number of grain boundaries within the coil, and the orientation will be the required direction needed, increasing the length of domains and high permeability. Within each grain, there are domains, and the larger the grain, the wider the domain spacing, which increases the internal energy [5]. There is a delicate balance between grain sizes and domain size, where grain boundaries act as pinning sites for the domain wall motion. So, if there is an increase in grain boundaries due to a more refined microstructure, it makes it hard for domain wall movement and thus lowers permeability.

If the domain spacing is thicker the domain walls should move more rapidly to rotate with the magnetisation. Because of the larger domains rotating faster, they are prone to bowing and nucleation of extra walls and therefore increased losses [6]. Thus, there must be a balance between large grains and thin domains to produce the supreme magnetic properties required.

1.5.2 Barkhausen Noise

As previously explained in section 1.4.2, when inducing a ferromagnetic material with an external field, the magnetic domains will align parallel to the applied magnetic field, creating a B (flux density)-H (magnetic field) curve. However, under close examination of the curve (seen in Figure 19), there is a discontinuous change of the B-H curve called the Barkhausen effect[39]. The Barkhausen effect is the small magnetization step changes whereby domains suddenly align parallel with the magnetic field. The Barkhausen noise impedes the motion of domain walls, which grain boundaries can cause, second phase particles and domain walls interacting with pinning sites as the domains reorganize. This impedance of the domain wall motion is known as domain wall pinning[47].
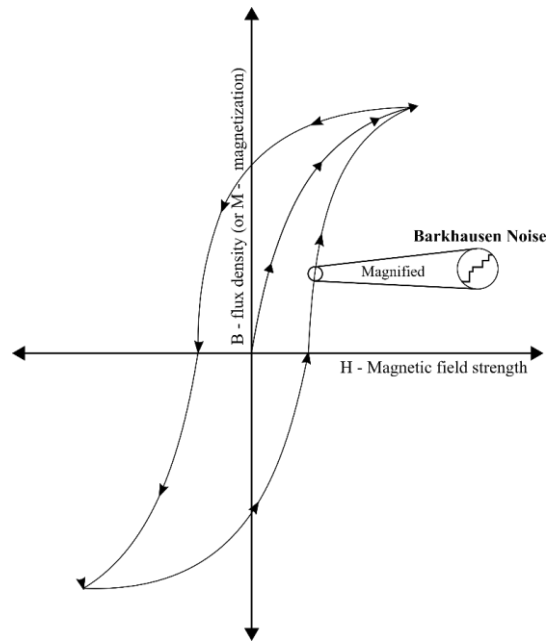
Figure 19. A visual representation of Barkhausen Noise on a B-H loop magnified [39].

1.6   Magneto-Crystalline Anisotropy

The spontaneous magnetization in ferromagnetic materials is not arbitrary. Instead, the magnetisation response depends on the direct exchange of electron spins between neighbouring atoms in a metal[48]. Therefore, the symmetry of the lattice structure of a metal is critical to the exchange process, which is known as magneto-crystalline anisotropy energy.

This variation of rate of magnetization can be explained in a Fe single-crystal where the minimum amount of applied field needed to reach maximum saturation is in the <100> direction in an iron crystal. This is known as the easy axis. Alternatively, if the magnetic field is applied across the <111> direction, the exchange process is not as efficient, requiring additional applied field to achieve the maximum saturation, known as hard axis, and between these two axes is a medium axis displayed below.
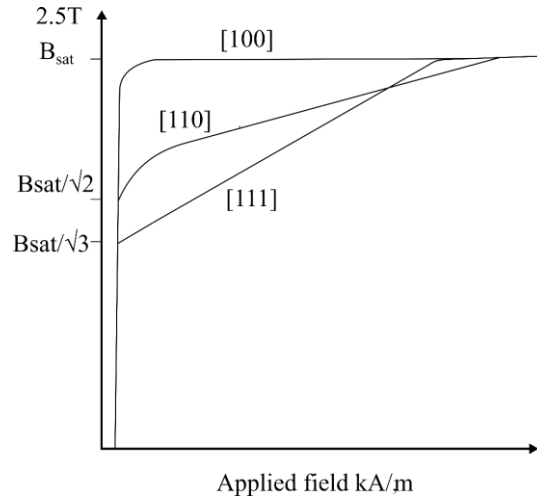
Figure 20. The magnetization for a Fe single-crystal where by magnetic fields were applied along the principal crystalline axes of [111], [110-] and [100][35].

Grain-oriented electrical steel has a body-centred cubic (BCC) structure and exploits the favourable properties in the <100> direction in reference to the rolling direction. The entire manufacturing process is designed to ensure that the favourable <100> microstructure is developed. Because of this, the amount of magnetic field required to reach maximum saturation is at its theoretical minimum. The anisotropy energy can be expressed mathematically and for a Fe, cubic structure is given by: -

$$E_\alpha = K_0 + K_1\,(\alpha_1^2\alpha_2^2 + \alpha_1 2^2\alpha_3^2 + \alpha_1^2\alpha_3^2) + K_2(\alpha_1^2\alpha_2^2\alpha_3^2) \text{ [35]}$$

Equation 6. A basic formula to describe the anisotropy energy density for a cubic crystal [49].

Whereby: - $\boldsymbol{\alpha}_1$, $\boldsymbol{\alpha}_2$ are direction cosines, and K_1 and K_2 are magneto-crystalline anisotropy constants.

$$\boldsymbol{\alpha}_1 = \cos\boldsymbol{\theta}_1 = \cos\boldsymbol{\Phi}\sin\boldsymbol{\theta}$$

$$\boldsymbol{\alpha}_2 = \cos\boldsymbol{\theta}_2 = \sin\boldsymbol{\Phi}\sin\boldsymbol{\theta}$$

$$\boldsymbol{\alpha}_3 = \cos\boldsymbol{\theta}_3 = \cos\boldsymbol{\theta}$$

In the manufacturing of grain-oriented electrical steel, it is hard to achieve the perfect crystal structure throughout a substrate due to its complexity. This leads to slight or complete misorientation resulting in the need for an additional applied magnetic field to reach maximum saturation and, therefore, an increase in the overall magnetic losses (W/kg) and a decrease in the maximum flux density.

1.7   Development of GOSS Grains

To produce the anisotropic magnetic properties required for grain-oriented electrical steels requires careful processing and selection of inhibitors to allow for the desired large Goss grains. In the 1930's Dr Norman P Goss developed a method of manufacturing silicon steel that manipulated nucleation and growth of grains, producing the desired anisotropic microstructure where by, the grains are of orientation {110}, <001> in relation to the rolling direction[50]. The textures developed is now

known as GOSS texture i.e. {110} <001>. This method of producing grain-oriented electrical steel (GOES) opened a new era of transformers, and continuous improvements have been made in the past 90 years to reduce the magnetic losses and improve the permeability of the silicon steel resulting in the market producing 0.75 (W/kg) consistently[50].

The Goss texture is produced through secondary recrystallization that occurs during the HTCA, whereby the grains of {110} <001>, and the GOSS nuclei have an advantage over other orientations allowing them to nucleate and grow, resulting in them dominating the microstructure. To prevent normal grain growth, second phase particles are used, which are present around primary recrystallization and during the HTCA these particles allow for Goss grains to nucleate and grow to dominate the structure.
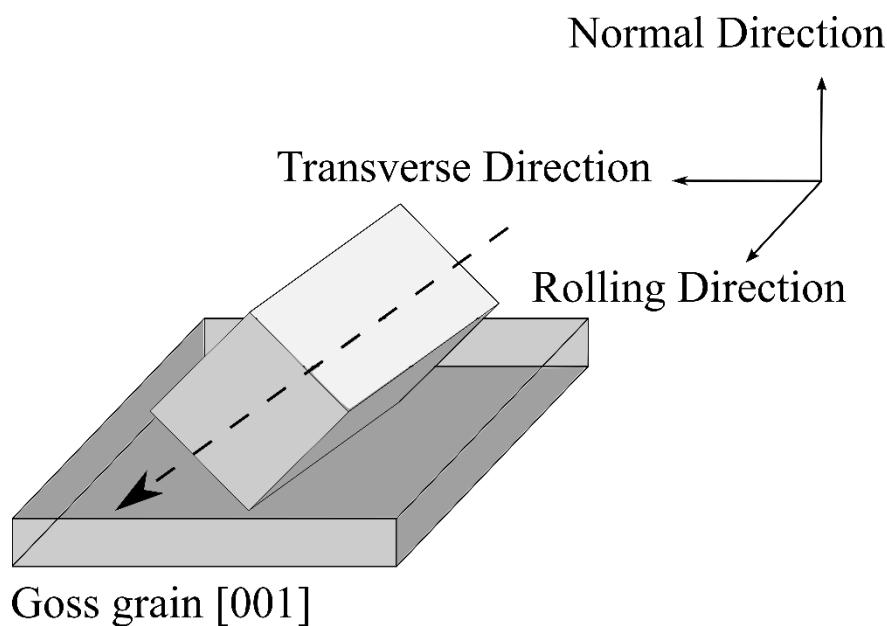
Figure 21. The orientation of GOSS texture in relation to the rolling direction of grain-oriented electrical steel [25].

These second phase particles are known as inhibitors, and in recent years have changed from the main CGO (Conventional Grain Oriented) steel inhibitor being manganese's sulphide (MnS) to aluminium nitride (AlN) in High Permeability (Hi-B). Studies have shown that the size of inhibitors plays a critical role in determining the effectiveness of pinning grain boundaries. Precipitates that are > 100nm have no significant pinning effect during the high temperature anneal, and precipitates <50nm have a pinning effect during the high-temperature annealing[51]. The study identified that most of the inhibitors observed in these studies were approximately a mean particle size of 30nm of aluminium-silicon manganese nitride [51]. The distribution of these inhibitors determines the development of texture and grain size. The size and distribution of these inhibitors are continuously altered through the casting of the silicon slabs conducted at IJmuiden to the HTCA. Each process influences the characteristics of the inhibitors and therefore influences the final product produced.

The development of Goss grains is not entirely understood, and there is a debate in the scientific literature about the mechanism in which the abnormal growth occurs [52][53][54].

One of the theories is oriented growth theory, it is proposed that many orientations of nuclei are formed, and nuclei which have a specific boundary characteristic with respect to the surround matrix will have a faster growth rate and results in a dominant final texture. [49].The second theory-oriented nucleation theory assumes that the selection of orientation is determined at the nucleation stage. This theory claims that nuclei of a specific orientation originate rapidly over other orientations and these nuclei determine the final recrystallization texture of the material [49].

Grain-oriented electrical steel creates these deformations during hot rolling, where the steel slabs are reduced to 2.3mm before phase change occurs ($\gamma \rightarrow \alpha$) during the cooling process[17]. During the hot rolling, significant changes occur in the microstructure, whereby grains become elongated. However, the microstructure is not uniform throughout the cross-section. Studies have shown that recrystallization occurs more easily on the surface, which has a lower deformation temperature and more considerable strain. This allows the surface grains to reduce the stress through recrystallization, although the substrate's centre cannot recrystallize significantly and, therefore, have a higher dislocation density[55]. This further emphasises the importance of the deformation occurring during cold rolling. Therefore, the oriented nucleation theory is based on the premise that nucleation begins with grains with the highest stored energy, then grows into grains with lower stored energy[56].

Another theory is oriented growth theory, which put forward that nuclei are formed with numerous orientations. A particular condition of the nuclei with a specific boundary characteristic with a specific matrix allows for an advantage over other nuclei to grow[52]. This allows for this orientation to dominate the final structure. Coincident Site Lattice (CSL) boundaries particularly $\Sigma 9$, $\Sigma 7$ and $\Sigma 5$ develop the abnormal grain growth. It has been observed that these lattices boundaries have higher mobility than other surrounding boundaries, which can play a vital role in the development of GOSS grains[49]. It has been suggested that impurities/inhibitors are not as effective on the $\Sigma 9$, $\Sigma 7$ and $\Sigma 5$ CLS boundaries. This allows for these nuclei to grow and dominate the final microstructure. Research is continuing looking at both theories. However, there is no current definitive explanation of the phenomena of the development of GOSS texture.

1.8   Grain Oriented Electrical Steel Coatings

The insulation layer known as Forsterite created on the surface of GOES has continuously been modified since the initial invention in the 1930s, where it replaced the traditional clays used to form the insulation layers[57]. The industry currently uses a two-layer coating system to provide enough insulation and corrosion resistance to ensure no electrical conductivity occurs over the lifetime of a transformer. The first coating is known as 'glass film', an oxide layer known as Forsterite (Mg_2SiO_4) and develops during the HTCA where it provides insulation to prevent short circuits between laps in

the core of the transformer. The Forsterite layer also induces a tension to the high silicon substrate, which has been shown to improve magnetic properties [58]. Before the Forsterite layer can be created, a Fayalite (Fe_2SiO_4) layer must be produced to establish the correct silicon oxide content at the surface of the substrate for Forsterite to develop. The thickness and adhesion of the Forsterite layer are vital to producing electrical steel with excellent magnetic properties and good surface properties[59]. The amount of Forsterite developed during the high temperature anneal is dependent on the quality and thickness of Fayalite during the decarburization stage[59]. Once the Forsterite layer has been produced during the HTCA, the excess MgO is removed. Then, a secondary phosphate coating is applied on top of the Forsterite. The phosphate coating is applied during the thermal flattening process to provide additional tension, enhancing the magnetic performance aspect and adding extra corrosion resistance[60].
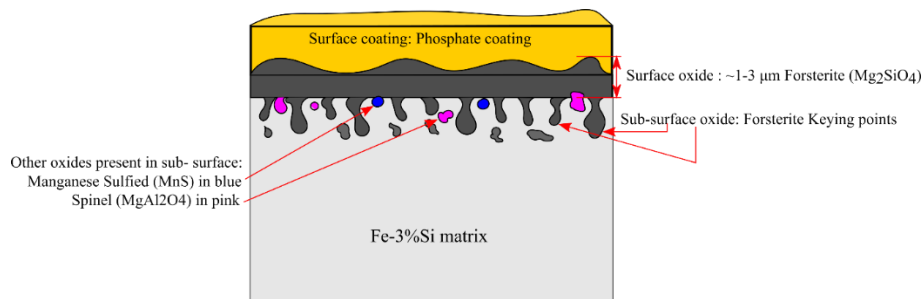
Figure 22. Illustration of the final product with the phosphate coating and Forsterite oxide layer that has developed during the HTCA.

1.8.1 Fayalite (Fe_2SiO_4)

The Fayalite is critical in developing excellent glass film with good adherence and which, in turn, has excellent magnetic properties. Once cold rolling is completed, the steel is processed in the decarburization line, where the goal of the initial section of the line is to remove the carbon. Carbon in the electrical steel is detrimental to the performance of the steel. It causes magnetic ageing, as explained previously in section 1.2.6. The carbon is removed in the decarburization stage, where oxidizing conditions are created to eliminate the carbon content to low levels <30 ppm.

The removal of carbon is critical to prevent a phenomenon named magnetic aging. Magnetic aging is the result of microstructural changes and precipitation of second phase particles such as carbides and nitrides[61]. The presence of carbon can form principates such as $Fe_{2.4}C$ and hexagonal crystal structure and these principates act as pinning sites for the magnetic domain was during the magnetisation[62]. As a result, the coercive force and hysteresis losses increase[61], [62].

After the carbon content is reduced to low levels, the second stage in the decarburization process is to create the correct Fayalite layer to allow diffusion of MgO during the HTCA to create the desired Forsterite (Mg_2SiO_4). This is achieved by creating an environment of 75%H_2/25%N_2 in a wet atmosphere at a temperature of 850°C. This promotes a subscale of oxide layers to be created, which

23

is critical to provide the silicon required for Forsterite. The oxide layer is known as Fayalite (Fe_2SiO_4), as displayed in Figure 23 [63].
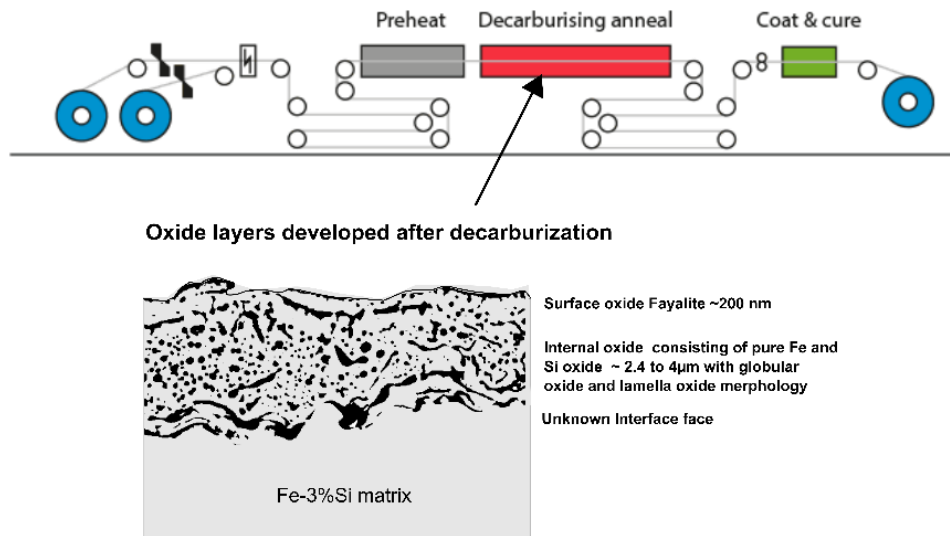
Figure 23. The region in the Decarburization line in which the Fayalite and the morphology of the Fayalite oxide.

The substrate is an iron matrix with a subscale composed of Fayalite (Fe_2SiO_4) situated at the substrate's surface. However, an iron oxides (FeO; Wustite and Fe_3O_4; magnetite) and silica (SiO_2) may develop; this depends on the conditions which are created by the temperature and oxidation potential (pH_2/pH_2O)[64].

The decarburization stage intends to initially form an oxide film bearing iron and silicon on its surface. To achieve this, the decarburization stage creates a potential oxidizing atmosphere, where the partial pressures of steam and hydrogen P_{H2O}/P_{H2} are typically between 0.52 – 0.57[65]. The conditions in the decarburization furnace are then modified, the temperature is increased, and it causes the dew point to drop to 0.45. This modification of the environment in the furnace promotes SiO_2 formation, which subsequently forms an iron oxide known as Fayalite (Fe_2SiO_4). This formation of Fayalite is necessary to produce a high-quality glass film on the steel surface [65].

The quality of the Fayalite is responsible for providing the correct environment/foundation to allow a successful layer of Forsterite to develop. A thin layer of Fayalite results in the amount of oxygen provided by the SiO_2 being insufficient; consequently, the 'glass film' will be thin and result in defects such as bare patches. However, if the layer of Fayalite is too thick, it allows the Forsterite layer to develop an irregular surface, and when the phosphate coating is applied on top of the Forsterite, it protrudes through the phosphate layer. As a consequence, this results in appearance defects and resistance complications [65].

1.9　Current Understanding of the Development of Fayalite

1.9.1　Structure of Fayalite

Extensive research has been carried out on the oxide layers formed during the decarburization stage of GDOES production. The literature agrees that there is a variation of oxides distributed, as shown in Figure 24 [66]. At the surface of the substrate, a 2µm Fayalite (Fe_2SiO_4) develops in which Mn can be present also in the Fayalite layer (($Fe, Mn)_2SiO_4$). The reason why Mn can be present is that the Fayalite and (($Fe, Mn)_2SiO_4$) have an identical crystal structure, whereby the Mn can replace the Fe atom within the structure[67][68]. Below the Fayalite region, around 2 to 4µm, a pure Fe and Si oxide of globular and lamella forms exist.

The four principal possible oxides developed at the surface and subsurface of the substrate during the decarburization are Fayalite (($Fe, Mn)_2SiO_4$) and in-between the surface and matrix there is tridymite (SiO_2) and iron oxides (FeO, Fe_3O_4)[69][70]. The reasoning for the presence of these four oxides will be explained in the later section.
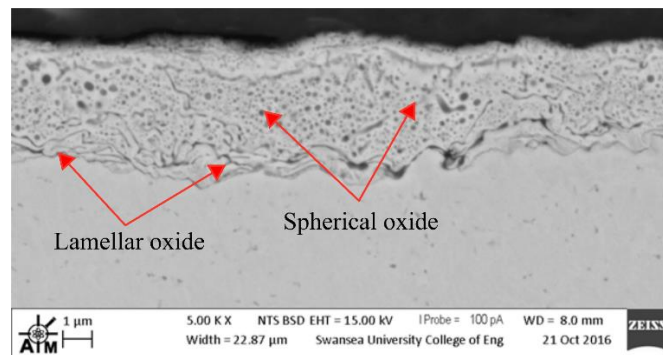
Figure 24. Image of a type of the structure of Fayalite and lamella and spherical silica arrangement after decarburization stage.

Several studies have shown that crystalline Fayalite is found at a thickness of tens of nanometres in the surface region where the Fayalite is in the crystalline orthorhombic phase and amorphous silica is found in the upper and lower region of the subscales, reaching depths a few microns deep. The amorphous silica surrounds the spherically shaped dark regions and acts as an interface between the dark and surrounding areas. The depth of the lamellar silica has been detected consistently to 9µm below the surface[63][71]. The morphology of these oxides is significantly influenced by the atmosphere's oxygen potential, which will be discussed in further detail in the following section [72].

1.9.2　The Effects of Temperature and Dew Point on the Development of Fayalite during the Decarburization Stage

Multiple studies have demonstrated that the effects of temperature and dew point significantly affect the development of the Fayalite and the development of undesired oxides. Predictions of oxides that may occur at alternative furnace conditions are illustrated in Figure 25, where the approximate oxides developed with alternative furnace conditions considering only FeO, Fe_3O_4, CO and Fe_2SiO_4[73].
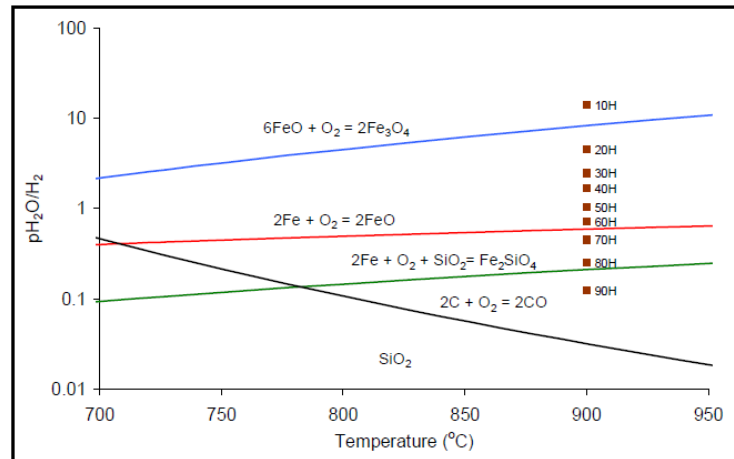
Figure 25. Equilibrium predictions of oxides developed under pH_2O/H_2 at various temperatures[73].

Figure 25 is the approximated oxygen potentials for the experiments displayed in the oxide equilibrium diagram showing the oxidation equilibrium formation lines for FeO, Fe_3O_4, CO and Fe_2SiO_4. The samples were heat treated in a Thermogravimetric Analysers (TGA) furnace. To simulate the decarburisation line at Orb Steelworks at range of partial pressures in a humid atmosphere, the TGA used the indirect water-shift reaction products ($H_2+CO_2 = CO + H_2O$) to produce the range of partial pressures in a humid atmosphere in the study. The percentage of H_2 introduced to the TGA is displayed by the red squares in Figure 27.

Several studies have been conducted to confirm the predictions shown in Figure 25, and as expected, with a 100% hydrogen atmosphere, there are no oxides developed on the steel surface [73]. Increasing H_2O/H_2 ratio results in the increase of water in the atmosphere and the amount of oxidation. Several studies demonstrated when the conditions of the experiment had a dew point of $p(H_2O/pH_2) = 0.34$ and temperature around ~840°C during the decarburization stage produces only metallic silicon, although an increase of dew point results in the development of Fayalite [64][73]. A different intensity in oxidation can be seen when increasing the temperature (900°C), where the Fayalite becomes predominately seen at surface scale and sub-surface. However, as displayed in Figure 25, this increases the probability of iron oxides to develop FeO. The result of an increase of temperature and dew point results in a distinct improvement in a uniform Fayalite oxide layer produced in both visual analysis and Fourier-Transform Infrared (FTIR) spectroscopy [73]. Not only does the uniformity of the Fayalite layer alter when increasing the temperature, but the morphology of the internal oxide developed, with a lamellar structure developed at a lower temperature, i.e. ~850°C and an increased temperature (~900°C) results in internal oxides adopting a spherical morphology[73] as shown in Figure 26. Several partial oxygen levels are essential to control as high levels will cause the formation of FeO [72]

26
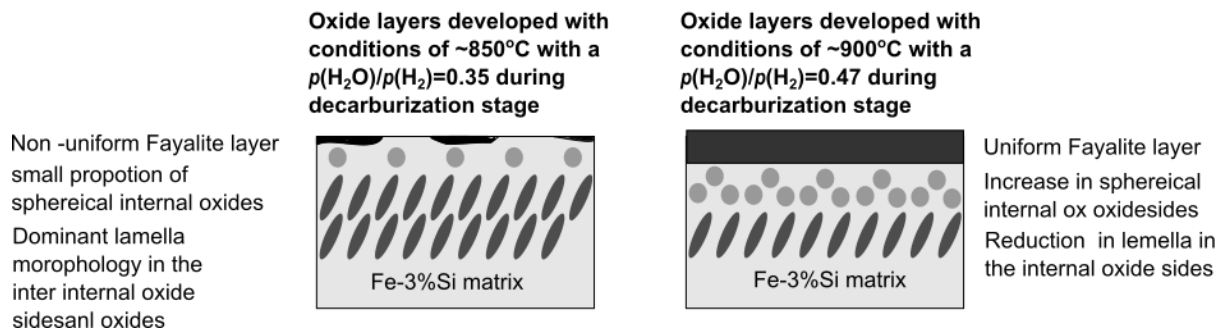
Figure 26. Schematic drawing of the effect on the morphology of oxides with altering decarburization conditions.

Studies looking at the effect of nitriding the substrate, which has been shown to be a 3-stage process, explaining the reasons behind the changing morphology in the Fayalite layer [66]. During the first stage (0-40 seconds), TGA analysis identified a slight weight loss caused by the H_2 atmosphere reducing the oxide layer and therefore removing oxygen. This removal of oxygen results in the lamellar oxide that has been produced is reduced and therefore transformed the lamella structure to spherical morphology and then leading to a more porous layer [66][74]. During this initial stage, little or no nitriding occurs due to the lamellar oxide acting as a barrier layer for the nitrogen diffusing into the substrate [66]. The continuation (40-120 seconds) of reduction caused by the H_2 atmosphere results in further lamellar structure transforming into spherical morphology. The change in morphology to spherical oxide allows the nitrogen diffusion to penetrate further into the steel. Therefore, increasing the nitriding time increases the diffusion rate of nitrogen into the steel. The study displays the influence on the rate of diffusion of nitrogen into the substrate during the decarburization stage. The morphology of Fayalite potentially could influence the development of Forsterite layer and the breaking down of the inhibitors during the HTCA.

1.10 Problems in using MgO for the Development of Forsterite (Mg_2SiO_4)

The development of Forsterite occurs in the HTCA stage of the process. The purpose of the process up to this stage is to process the steel to have the correct microstructure and distribution of inhibitors for GOSS texture to develop and the correct Fayalite oxide layer to develop Forsterite layer. The conditions in which the Forsterite develops is a 75%H / 25% N atmosphere, where the temperature reaches 1200°C and then is held at that temperature for several hours.

This Forsterite layer is critical to both the magnetic properties and the appearance of the coil, which affect the value of the coil. However, due to the high temperature and unique processing, the thin Forsterite layer research has been limited and secretive.

27

1.10.1 Current Understanding of the Forsterite Layer Development

The Forsterite development is relatively well studied in several fields such as geological, blast furnace conditions and biological applications[75][76][77]. However, all these studies have significantly different methods of producing the Forsterite. For example, in the cases of geographical studies, Forsterite production involves significantly higher pressures and temperatures than those used to develop the glass film on GDOES. Although these alternate methods are vastly different from the development of glass film, they can also enhance the understanding of the development of Forsterite. The geological studies demonstrated that under high pressures (~75 Kb) and elevated temperatures it is possible to form Fayalite (Fe_2SiO_4) to Forsterite (Mg_2SiO_4) can develop under solid solution[74].
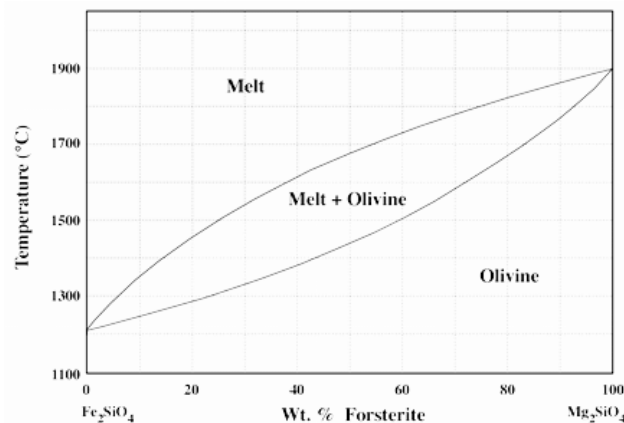
Figure 27. Thermodynamic phase diagram of Fayalite (Fe_2SiO_4) – Forsterite (Mg_2SiO_4) system of olivine[78].

The Fayalite – Forsterite phase diagram display above shows that the lowest temperature that a melting phase is present is 1200°C and with increase in concentration of Forsterite increase the melting point. The high temperature process at Orb Steelwork reaches during High Temperature Coil Annealing (HTCA) is 1195°C which suggest that the mechanism for the development of Forsterite is an alternative mechanism.

The development of the Forsterite layer occurs between the Fayalite (Fe_2SiO_4) and the magnesium oxide layer that is applied to the surface of the substrate, whereby a hydrogen atmosphere applied during HTCA reduces the iron and allows diffusion between the silicon and magnesium to form a Forsterite insulation layer Figure 28 [79][80].
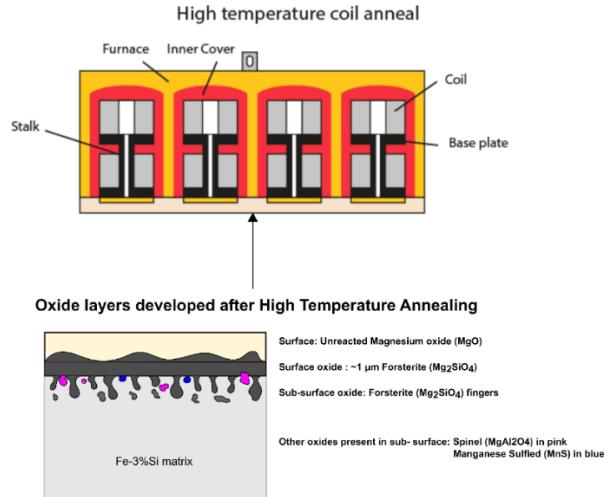
Figure 28. Displaying the process in which the Forsterite layer develops during the HTCA and a schematic drawing of the surface oxide developed after heat treatment in the batch furnaces.

Studies suggested through thermo-gravimetric analysis that the reduction of Fayalite begins to occur at 800ºC[79]. Significant morphology changes in the Fayalite oxide layer are seen when temperatures reach ~900ºC, whereby a non-uniform thin film develops at the surface of the strip, which has a small concentration of Mg, Si and O, which suggest that it is possible to be Forsterite. Although more significant changes occur below this region where a large layer of SiO_2 occurs from the resulting reduction of iron[79] [81]. The limiting factor in which Forsterite develops is the MgO diffusion rate. When temperatures are further increased to 1000ºC, a clear development of Forsterite layer with a predominant SiO_2 phase is still present in both studies. Finally, when the steel reaches the maximum 1200ºC and is soaked for 15 hours, a 1-micron Forsterite continuous layer develops, which has good adhesion to the substrate, although some protruding Forsterite particles are located matrix[79].

1.10.2 The mechanism of development of Forsterite

As previously explained, to enable Forsterite to develop, the correct oxide layer is required, known as Fayalite (Fe_2SiO_4). This is formed during the decarburization stage of production. The conditions to create this oxide are a wet hydrogen/nitrogen atmosphere at temperatures between 700ºC to 850ºC. Since silicon has a higher affinity for oxygen to form SiO_2 than iron, the following reaction can occur[33]:-

$$2Fe + SiO_2 \rightarrow Fe_2SiO_4$$
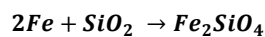
Equation 7. The chemical equation for **Fayalite** [33]**.**

Once the 3-4 µm Fayalite layer has been produced, a magnesium oxide layer is coated directly onto the surface of the Fayalite. Next, the coated coils are placed in the HTCA furnace, within which the coils will be treated in a reducing atmosphere where the heating rate is slow up-to-the HTCA soaking temperature (1200ºC) and held for an extended period. During heat treatment, it is thought that the development of Forsterite can occur at temperatures as low as 700ºC – 800ºC by a substantial reaction of Fe and Mg.

$$Fe_2SiO_4 + MgO \rightarrow Mg_2SiO_4 + 2FeO$$
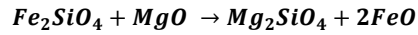
Equation 8. The chemical equation for **Fayalite** to Forsterite [33]

The early development of Forsterite inhibits the oxidation of the substrate during the higher temperatures of the heating cycle [33]. It has been suggested that during the high temperature (>1000°C), the Fayalite acts as a catalyst for the solid-state reaction to further increase the thickness of Forsterite at the surface/subsurface of the substrate.

In addition to this development of Forsterite, research using Glow Discharge Optical Emission Spectrometry (GDOES) has shown an indication that several alternative films may develop during the HTCA[34]. The main is Forsterite (Mg_2SiO_4) and an oxide known as spinel ($MgAl_2O_4$), which contains Al or a combination of Si and Al cordierite ($MgO_2Al_4Si_5O_{18}$) or Sapphirine [34].

Spinel: - $MgAl_2O_4$

The study conducted identified two main steps in developing the glass film; the first is that a primary Forsterite film develops, and then the Spinel is formed. These interrupted heat cycle experiments conducted revealed that the primary Forsterite develops around 900°C with Sb-based addition and B addition to the MgO. These increase to around 950°C using GDOES analysis. When interrupted, annealing conducted at 1000°C the spinel was consistently identified in this region. From this indication, it is believed that the primary inhibitor AlN decomposes, and Al diffuses to the surface of the steel sheet. The diffused Al then reacts with the Forsterite at the steel surface, which forms the spinel[34]. When the formation of Forsterite is delayed and co-occurs with the diffusion of Al to the surface of the steel, there is potentially aluminum developing as a surface oxide known as spinel, which then hinders the development of Forsterite glass film. The formation of spinel deteriorates the surface oxide properties, and problems with spot defects and bare patches occur[34].

If the correct formation of Forsterite is developed on the steel, it will produce a higher amount of tension in the steel due to the thermal expansion coefficients where the silicon steel is typically around 13.6×10^{-6}/K and the Forsterite layer is typically 11.4×10^{-6}/K [82][83]. Therefore, the coefficient of Forsterite and steel substrate has a significant difference, allowing an additional tension applied to the substrate, which reduces the losses by reducing the domain thickness (as explained in 1.4) [84].

Additional detail on the High-Temperature Coil Annealing (HTCA) process at Orb Steelworks in section 1.2.7 introduced the purpose of the HTCA, and this section will elaborate on the current arrangement of Orb Steelwork production furnace and give further details on the heat treatment conducted. The HTCA is a critical stage whereby secondary recrystallization, the development of 'glass' film and purification of the strip will occur. Therefore, all prior processing will heavily influence the quality of the magnetic properties and the resulting glass film. The heat treatment is

carried out in a static batch annealing process. The batch furnaces can heat-treat eight coils in one furnace in which the coils are stacked with the eye of the bore facing vertically upwards, as shown in Figure 29. The coils are arranged in pairs whereby a larger coil in the bottom with a protection plate shaped like a doughnut is placed on the top coil. A smaller coil is placed on top of the larger coil, and then an inner cover is placed over the two coils. This is repeated four times, and the furnace bell is placed over the four inner covers.
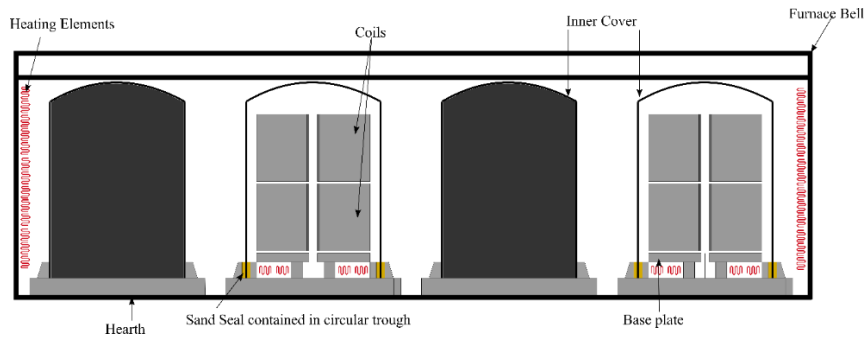
Figure 29. A schematic drawing of a cross-section of an HTCA furnace at Orb Steelworks.

Figure 30 shows the furnace arrangement at Orb Steelworks, and the HTCA is composed of 3 main components: Hearth, Inner Covers, and furnace bell. The following section will give further details of these components.
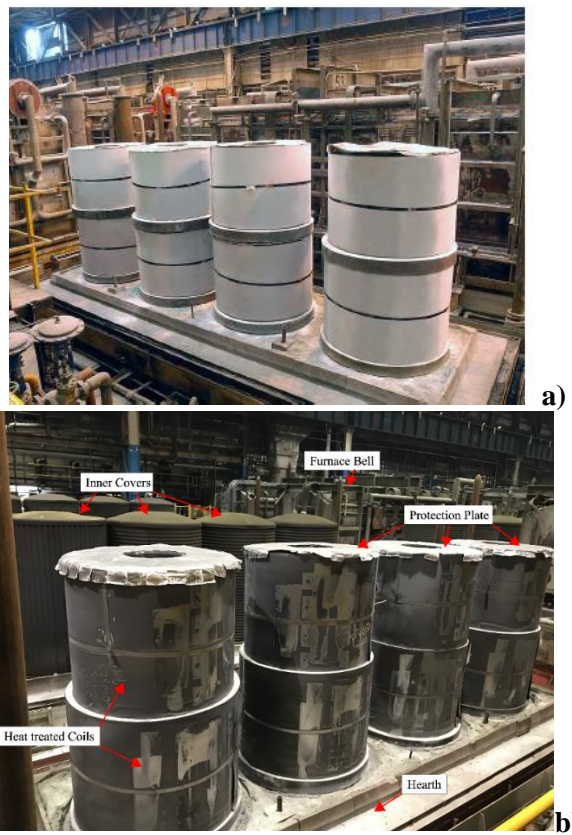
Figure 30. a) Displays the MgO coated coil before heat treatment. **b)** Displays the coil after heat treatment and the various stages of assembly of the HTCA at Orb Steelworks.

1.10.3 The Hearth

The hearth is a rectangular steel structure that is lined with fire bricks. The hearth has a parallel dual steel trough around the edges of the hearth in which one of the troughs is filled with sand, and the other trough is filled with water. Once the bell is placed on top of the hearth, the two skirts that follow the parameter of the bell are submerged in the two troughs in the hearth. This provides a seal that prevents air ingress into the furnace and prevents the gases used in the process from escaping the furnace, preventing an explosion. The hearth has four evenly distributed doughnuts made from fire brick. The trough created is filled with sand in which the inner covers are submerged. The base plate is on the inner walls of the trough and in the inner circle of fire bricks. In the centre of the inner circle, a gas inlet goes through the centre of the base plate and the eye of the bore. Elements are also placed in the inner area between the inner walls of the trough and the inner circle. The base plate is a stainless-steel plate with a hole in the centre where the gas inlet gains access to the inner cover. A layer of MgO is coated onto the base plate to prevent welding the coil to the base plate.

1.10.4 The Furnace

The furnace bell is a cuboid steel structure lined with high-temperature refractory bricks and loose insulation where needed. When the steel structure is placed on the hearth, the furnace becomes gas sealed with the skirting following around the perimeter steel structure placed in the sand and water troughs. Electrical heating elements are placed on the vertical walls of the furnace bell because of the arrangement of the furnace; the two coils in the centre do not get the same exposure to the heating elements as the coils at the end. This results in a higher proportion of energy received by the end coils rather than the middle coils. This is an inherent disadvantage with this design of the furnace.

1.10.5 Inner Cover

The inner covers are stainless steel tubes with a concave top. The purpose of the inner covers is to protect the coils from direct heat from the elements preventing defects on outer laps and create a desired gas environment within the inner cover. Around the base plate, there is a circular trough where sand is retained. The inner cover is submerged in the sand and provides the seal. It is a partial seal, and the resistance to the flow creates a positive pressure in the inner cover and prevents ingress of contaminated gas.
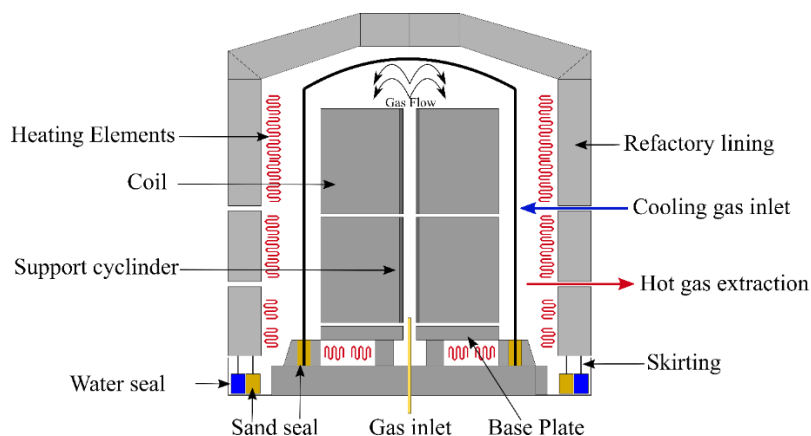
Figure 31. Illustrates schematic drawing of the cross-section of the HTCA highlighting the significant components that construct on the HTCA furnace.

1.11 The Annealing Cycle Conducted by HTCA.

The annealing cycle that Orb Steelworks conducts on electrical Steel during the HTCA is a commercially sensitive, so details on the precise heat treatment cannot be fully disclosed. However, this section will give a general idea of heating rates, soak duration and gas environments. Figure 32 illustrates the evolution of the batch annealing process with the change from CGO to Hi-B technology.

Stage 1 - Heat and purge: Once the inner covers and furnace have been placed over the coils, the furnace is purged with 3HNX to remove air from within the furnace to ensure that combustion does not occur when H_2 is introduced. 3HNX is a gas mixture of 97% nitrogen 3% hydrogen.

Stage 2- Heating: The temperature is increased to the Low-Temperature Soak (LTS) at approximately 200º/C per hour.

Stage 3- LTS: The LTS aims to allow the coils to achieve thermal equilibrium by holding the temperature of the furnace at approximately 750ºC for 15 hours. The magnesium oxide that was applied and dried to the surface of the steel has some retention of chemically bonded water present, and the moisture must be removed from the furnace before a continuation of the annealing cycle. Failure to remove the moisture will result in several defects in the Forsterite layer. The moisture is removed from the furnace through the exhaust pipe, creating a dry atmosphere in the furnace.

Stage 4 -Controlled heating rate: The heating rate between the LTS and HTS is critical to the quality of the electrical steel. As stated previously in section 1.7, secondary recrystallization occurs between 900ºC and 1200ºC, where large GOSS grains develop. Therefore, a controlled heating rate is required between the LTS-HTS to ensure the development of the desired texture. The heating rates for CGO and Hi-B vary with CGO; a consistent heating rate to the maximum temperature of 12ºC per hour is maintained. While Hi-B starts at 12ºC per hour until temperature reaches 1050ºC, further control is required with a heating rate of 6ºC per hour. The different heating rates are due to the

precipitates used where CGO predominately uses MnS, while Hi-B uses Al-N. The additional control of heating rate allows a reduction of temperature gradients created, which maximise the potential of developing GOSS nuclei and grain growth.

Stage 5 -HTS: The coils are held at 1150ºC – 1200ºC for 24 hours to ensure the coils have reached the desired temperature, and the coils have been purified from sulphur, developed a consistent Forsterite layer, and secondary recrystallization has occurred.

Stage 7 –Cooling: Once the coils have soaked for 24 hours, the coils are cooled in a pure hydrogen atmosphere to 650ºC. Caution is taken when transferring to the 3HNX atmosphere due to unintentional nitriding of the steel will occur; as a consequence, 3HNX is introduced to purge the H_2 at 600ºC. At 300ºC, the inner covers are removed and exposed to the atmosphere.
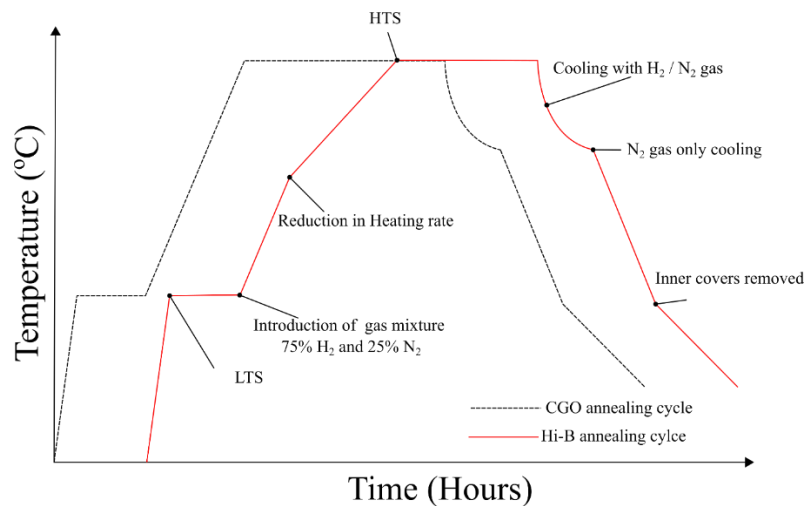
Figure 32. Illustrates the differences between the annealing cycle of CGO material in the black dash lines and the Hi-B annealing in red.

Although the heat treatment is aimed to follow the heat cycle as displayed in Figure 32, the reality is that the coils do not receive uniform heating and regions within a coil will experience different temperatures at different times. The following section will delve into work that has previously investigated this issue.

Previous work has investigated the performance of the batch annealing process, specifically at Orb Steelworks, and whether modifications can improve the efficiency of these furnaces to reduce energy costs using modelling and simulation. However, these investigations predominantly focused on the heat transfer and heat profile of the furnace, with minimal consideration of secondary recrystallisation, the development of the Forsterite layer, and the substrate's purification. The model and simulations have identified the large temperature gradients created during the annealing process, and regions of the furnace did not reach the desired temperature of 1190ºC for several hours. This was confirmed in an investigation conducted by Andrew Buckley, who placed thermal couples at various

locations within a 0.27mm gauge coil as seen in Figure 34, which was then exposed to the CGO heat cycle. [85]
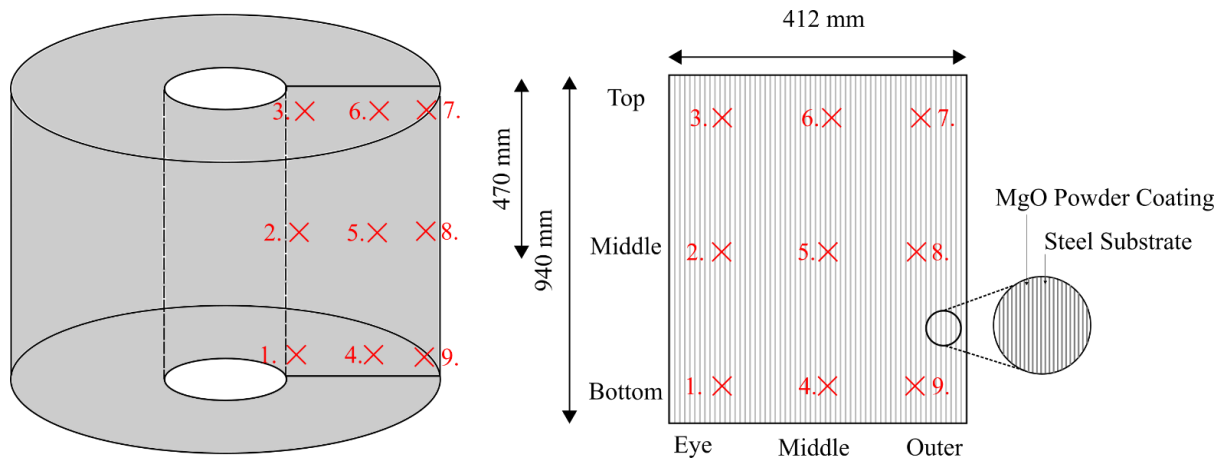
Figure 33. Displays the rough location of thermal couples that were placed between the laps of the coil. (**a**) Is a schematic drawing of a coil with the locations of thermal couples' placement. (**b**) Is a cross section of the coil with vertical lines representing the individual laps.

The temperature at the various points is displayed in Figure 34, demonstrating that the heating is not uniform. The outer top, middle and bottom follow the intentional heating profile showing signs of low-temperature soak and a consistent heating rate between the low and HTS, with a significant time spent at temperature. However, the eye and middle of the coil do not experience the intended heat treatment or reach maximum temperature. The consequence of not achieving the desired heat profile in relationship with magnetic properties, purification of the substrate, and the Forsterite's development was not investigated in this study.
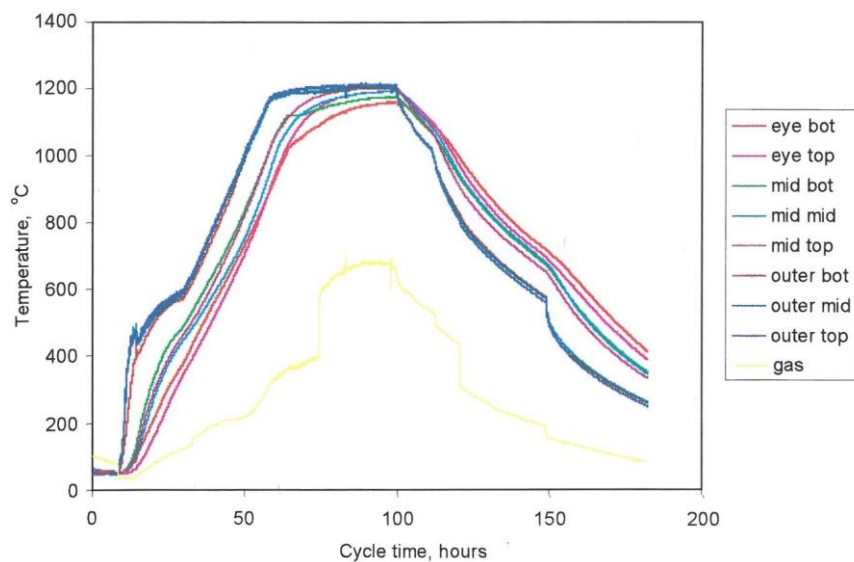
Figure 34. Illustrates the recorded temperatures from thermal couple's place in various positions in 0.27mm coil following CGO heat treatment[85].

Understanding the changes of steel properties and the development of Forsterite is critical for designing an optimum heating cycle to produce high-performance electrical steel with the minimum

time required in batch furnaces. Answering these questions will give a basis for Orb Steelworks in future investments in upgrades to the current furnaces or new furnaces.

1.12 Magnesium Oxide (MgO)

1.12.1 Introduction to MgO

Magnesium oxide (MgO) is used diversely across industries from cement production to superconductors; however, the electrical steel industry uses the MgO in a unique application[86]. The magnesium oxide (MgO) is made into a slurry that is applied and dried at the end of the decarburization stage Figure 35. The MgO is suspended in water; due to MgO being suspended in the water, partial hydration will occur $MgO \rightarrow Mg(OH)_2$[87]. The partial hydration of MgO will create moisture in the furnace. This moisture will alter the dewpoint between the laps of the coils and can causes defects, which will be discussed in more detail in section 1.12.5. Any additions to the MgO are added during the mixing of the MgO slurry, and these additions are thought to reduce the melting point of the MgO, which then, in turn, improve the adhesion of the 'glass film'[88].
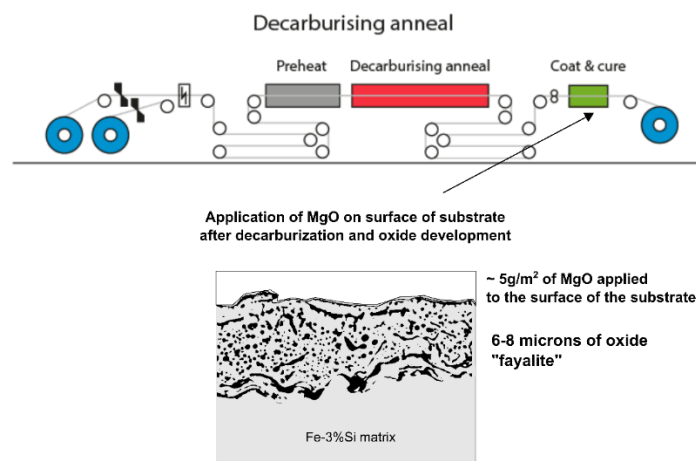
Figure 35. Demonstrates the position of MgO is applied to the surface of the substrate and the morphology of the Fayalite on which the MgO is coated.

The MgO was initially added only to prevent the welding of the laps of the coil during the HTCA, which is commonly known as an annealing separator[89]. However, unintentionally the MgO reacted with the Fayalite (Fe_2SiO_4) and formed a 'Glass Film' which was found to be Forsterite Mg_2SiO_4[90]. The Forsterite created an insulation layer on the surface of the substrate, and when the sheets of electrical steel are stacked to form the core of the transformer, the insulation layer prevents short circuits from occurring during the operation of the transformer[91]. It was later discovered that the formed MgO induces a tension on the strip and results in improvements in the magnetic losses by causing domains to refine[58]. The tension produced results from the difference of thermal expansion coefficient between the Forsterite (Mg_2SiO_4) oxide produced and the Fe-Si substrate[92].
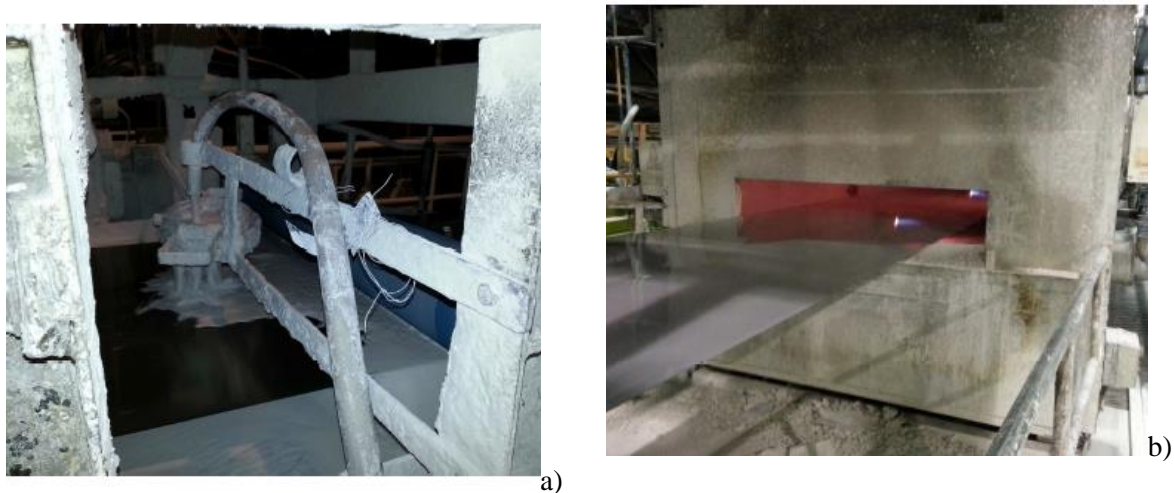
Figure 36. a) Coating of the substrate at Orb Steelworks. **b)** Drying off the MgO slurry[93].

The magnesium oxide used conventionally is produced around 800ºC – 900ºC, and the MgO ideally should have no impurities such as chlorine and sulphur, which may cause deterioration of the steel [94].

The MgO slurry is applied after the decarburization has successfully reduced the carbon content of the strip and developed the critical Fayalite layer. The MgO slurry is rolled on to apply around $6g/m^2$ on the surface of the substrate on each side and immediately dried where the conditions of the furnace range between 200–300ºC to ensure that majority of the water is removed.

As explained previously in section 1.10.1, during the HTCA, a small proportion of the MgO reacts with the 2µm unstable Fayalite (Fe_2SiO_4), due to the hydrogen atmosphere, that causes the iron in the Fayalite to reduce (as shown in the formula below) and leaving silica and metallic iron. This silica can react with the MgO resulting in a Forsterite layer.

$$Reduction\ of\ Fayalite:\ Fe_2SiO_4 + 2H_2 \rightarrow SiO_2 + 2Fe2H_2O$$

$$Formation\ of\ Forsterite:\ SiO_2 + 2MgO \rightarrow Mg_2SiO_4$$
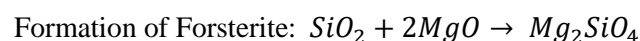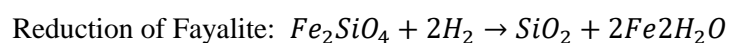
1.12.2 Problems in using MgO.

An intentional excess of MgO is applied to reduce the likelihood of welding the laps during the HTCA. It prevents laps of the coil welding together by some of the MgO not reacting during the HTCA consequently, acting as a spacer between the laps. This unreacted MgO falls off when the laps are unrolled during the thermal flatting, and to ensure there is no residue MgO on the surface of the coil brushes, ensure that the surface is clean to allow excellent adhesion of the phosphate coating.

However, problems occur around the edges of the laps of the coil whereby the edges of the coils are exposed, and fusing can occur, the reason why this occurs is not fully understood, but may be explained by the long exposure and high temperature that the edges of the coil experience during the HTCA or could be due to the retraction of MgO coating or Forsterite layer. This is not helped by the

poor shape of edges caused by cold rolling and the placing of coils on top of one another in HTCA. A large quantity of the MgO does not react during the HTCA process, which is a very costly method to prevent laps from welding together due to the large quantity of MgO brushed off.

The MgO, which has been converted to Forsterite, produces a thin and transparent coating that influences the appearance of the coil. If undeveloped Forsterite occurs on a coil, it leaves a bare patch leaving the area vulnerable to corrosion. The Forsterite must be present as a uniform layer with good adhesion due to the further processing of electrical steel at the customer, such as punching, slitting, and bending. If the adhesion is lacking, the flakes of glass film are removed, resulting in exposed bare metal. This can lead to short circuits in the core and can potentially cause significant damage to the transformer.

It has been identified that moisture caused by the magnesium oxide coating is one of the main reasons for the defects found on the electrical steel—the MgO hydrates forming magnesium hydroxide during the mixing of additives. Once applied to the substrate, the MgO slurry is "dried" off in the drying oven. However, if not all the hydroxide is removed as a consequence, this increases by the dew points between laps and the atmosphere are made non-uniform in the longitudinal and the width direction[95].

The uniformity of the Forsterite layer is also essential to increase the amount of lamination placed within a transformer and prevent non-uniformed stacking due to variation of coating thickness. Therefore, the appearance of a coil has a significant influence on the value of the finished product. The development of Forsterite is essential to ensure insulation between laminations when placed in a transformer, but it also directly influences magnetic properties by altering domain structure explained in section 1.13.6. Failure in the development of Forsterite results in a decrease in the performance in the magnetic properties, which directly reduces the price of a coil significantly. If the Forsterite develops in the Fe matrix, this can have an adverse effect causing disruptions to the domain structure and result in domain wall pinning, which is explained in 1.3.2

1.12.3 Manufacturing of Magnesium Oxide (MgO).

Currently (the year 2019), MgO is supplied by Tateho (Japan), which has supplied Orb Steelworks since the 1970s. The two main components that are used to produce MgO are magnesium chloride and calcium oxide. The exact process which Tateho uses to produce its MgO is patent protected. However, the two basic reactions which occur during the MgO production process are:

$$MgCl_2 + Ca(OH)_2 \rightarrow Mg(OH)_2 \downarrow + CaCl_2$$

$$Mg(OH)_2 \rightarrow MgO + H_2O \uparrow$$
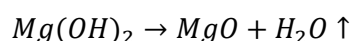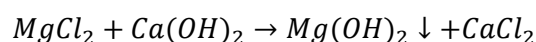
These chemical reactions occur during the rotary kiln process, where the MgO particle size is controlled by firing. The fine particle size produced of MgO requires laser particle size analysis

customarily carried out as part of the pre-dispatch quality assurance protocols. Other analyses conducted by Tateho are: -

- Chloride levels
- Dry Ignition loss
- Hydrated Ignition loss
- Percentage boron
- Percentage calcium oxide
- Percentage sulphur trioxide
- Percentage silica
- Citric acid activity
- Wet viscosity at 15seconds, 5 minutes and 50 minutes

Once the manufacturing of MgO is complete, the MgO is packaged in a polythene bag surrounded by a brown paper bag. The initial concerns are that MgO may be affected by moisture during shipping to Orb Steelworks, which would result in MgO reverting to magnesium hydroxide ($Mg_2(OH)_2$). However, it is monitored by repeating the analysis conducted by Tateho at Orb Steelworks upon receipt of the MgO to confirm that product quality has not been altered during the shipment.

1.12.4 Magnesium Specification

The MgO slurry follows meticulous specifications and procedures to ensure that a consistent Forsterite layer is produced. The significant properties which are monitored are Citric Acid Activity (CAA), viscosity, chemical composition, granulometry, porosity and surface area[88][96].

The CAA measures the hydration rate of magnesium oxide and is determined by the time required for a given weight of magnesia to provide sufficient hydroxyl ions to neutralize a specific amount of citric acid. For example, if the CAA of magnesia is high, the magnesia readily hydrates, resulting in the MgO having a high degree of water retained in the MgO powder. From this acid test, it can be categorized into several classifications[97]: -

Acid neutralization values of <60 seconds are used to define highly reactive (soft burnt)

Medium reactive MgO between 180 – 300 seconds

Low reactivity MgO (hard burn) >600 seconds

Dead burnt >900 seconds.

Studies carried out examining the effects of low CAA (activity for a MgO slurry is high) result in incomplete development of glass film and are not totally formed at the surface of the substrate. Conversely, when the activity of the MgO slurry is low (CAA > 250 seconds), the glass film has inadequate adhesion, and the glass film is thin [98][95].

However, if the CAA is too high, it is believed that it interferes with the precipitates leaving the grains during the secondary recrystallization, and the Forsterite is acting as a barrier layer for the inhibitors.

This causes the inhibitors to remain longer in the substrate removing the advantage of selective grain growth of GOSS oriented grains[98]. Furthermore, in the case of developing "glass film", when the reactivity of the MgO powder <40 seconds CAA, the control of hydration of the MgO becomes difficult during the mixing of MgO [95].

The amount of MgO applied on the surface has an important role, and research directly looking at this has been carried out by Wang Bao-Chuan, Yang Ping and his collaborators[90]. Their research displayed the effects of reducing the MgO coating down; they initially looked at $5g/m^2$ where the Forsterite coating is consistent and compact. When reducing the amount of MgO to $3g/m^2$, defects begin to appear in the form of bare patches and when further reduction of MgO to $1g/m^2$, there was a further increase in defects [90]. Their research indicated that the increase in MgO per g/m^2 resulted in a decrease in elements detected in the Forsterite such as Fe and Al and increased detection of O, Si and S. This indicates increasing the amount of MgO produced a Forsterite layer. This causes increased resistance due to the reduction of Fe and improved substrate purity due to the removal of S increasing into the Forsterite layer that has been proven to affect magnetic performance[90].

1.12.5 Understanding of hydration of MgO

As explained, the MgO is suspended in water, this slurry is applied to the substrate via rollers, and the MgO slurry is then dried rapidly in an oven. The hydration of the MgO can be controlled by several methods: production line conditions such as the temperature of furnace, the temperature at which the slurry is processed[87]. An alternative method of controlling the hydration rate of the MgO is heat-treating the MgO at a high temperature ($>1200^\circ C$). This high-temperature results in the suppressed dehydration reaction, although this has an undesired effect which causes a low reactivity of SiO_2 that is present in the Fayalite layer, which makes the MgO less likely to form Forsterite, therefore creating poor glass film with less adhesion and as a consequence lower magnetic properties[87]. Thus, there must be a balance of the reactivity of MgO to satisfy the reaction rate during the HTCA to allow diffusion to take place between SiO_2 - MgO to form Forsterite (Mg_2SiO_4) and to prevent hydration of MgO during the suspension in water.

To understand the effect of hydration rate and diffusion rate with the silicon, there must be an appreciation of the effect of processing has on the MgO physical and chemical properties. The production of MgO is usually prepared by calcining magnesium carbonate, whereby calcining takes place below the material's melting point, which causes a reduction or oxidation and decomposition of the carbonates and other compounds removal of water. During this process, the escape of CO_2 creates a porous structure made up of agglomerates of many MgO microcrystals [99]. The microcrystals sinter that causes an increase in their average size and a reduction in internal porosity of the material[99]. Hence the duration and temperature of the calcination process have a significant effect

on the reactivity of the MgO formed[100]. The reactivity of MgO is a reference to the rate at which the MgO hydrates ($Mg(OH)_2$) on exposure to water[101].

1.13 Additives Introduced During the MgO Slurry Mixing Process.

This section will review the additives added during the MgO slurry creation; this process is highly variable and protected by various patents. The timing of the degradation of inhibitors is critical to the development of Forsterite. This section will discuss the selection of additives that this research will be focused on in understanding the role of these additives during the development of Forsterite.

1.13.1 Addition of 1% of Strontium ($SrSiO_4$)

Numerous studies have discussed the addition of 1% $SrSiO_4$ to the slurry at the mixing stage, where the temperature of the water used was at 5°C. Once the samples were coated, they were heat-treated for 15 hours at 1200°C in a hydrogen atmosphere. The techniques that were used including EDS, XRD and GDS to characterize the Forsterite layer. The samples with $SrSiO_4$ were then compared to samples with MgO only that had been processed [102].

The results showed a significant improvement in the reduction of Forsterite penetrating the substrate, and an increase in O%, Mg% and Si% in the continuous layer was observed. Furthermore, reducing the penetration of Forsterite particles and improving the continuous layer shows a significant improvement of core losses[102].

Previous studies investigating strontium in MgO slurry that was patented in the 1980s also suggested that the addition of strontium reduces the penetration of Forsterite particles into the substrate[102]. The study was carried at various amounts of Sr addition to the slurry between 0 to 10% by weight. The same study also looked at different compounds of Sr: - $SrSO_4$, $Sr(OH)_2.8H_2O$, $SrCO_3$ and $Sr(NO_3)_2$.

The method of analysis is vague due to the patent restrictions. However, the analysis completed looked at the microstructure using photomicrograph and completed magnetic tests to identify W/kg and B10(T). In addition, the adhesion test was examined, but it was not stated how this test was completed.

The magnetic performance reported with no Sr in magnetics was 1.24 W/kg, a B10(T) 1.86 and adhesion of Ø35mm using a mandrel, the additions which showed the most improvement in magnetic properties was the 1% Sr with B10(T) of 1.87 and 1.16 W/kg. However, there was a decrease in adhesion, dropping to Ø30 mm mandrel. Thus, the addition of Sr only appears to improve the magnetic properties. However, there is a trade-off with adhesion. The two other compounds $Sr(OH)_2$, $SrSO_4$ at weight 1 %, showed similar improvements in magnetic performance.

Although there is a clear improvement with the addition of Sr, the study did not show a clear role or mechanism in which the Sr played in developing Forsterite. Furthermore, the study did not identify

/state any Sr detected in the continuous / particle Forsterite layer. This indicates that Sr is used to provide additional SiO_4 to the upper surface of the substrate and is likely to find the Sr in the unreacted MgO.

One of the significant components of Forsterite (Mg_2SiO_4) is SiO_4, and the addition supplied $SrSiO_4$ would imply additional Forsterite (Mg_2SiO_4) would occur with SiO_4 provided with Sr. This may explain why there are reduced Forsterite particles in the substrate due to the additional availability and more thermodynamically favorable from SiO_4 at the surface supplied by $SrSiO_4$.

There is a lack of definitive analysis on the influence of strontium compounds in the development of the glass film and in loss reduction. In addition, further investigation is required to identify what, if any, role Sr has on the development of Forsterite itself.

1.13.2 Addition of Antimony Sulfate ($Sb_2(SO_4)_3$) and Sb, Sr, Ti and Zr Chlorides

There has been an extensive amount of research conducted looking at various chlorides. In these patents, it is claimed that magnetic properties and Forsterite development have been improved with additions ranging between 5-20wt%. Nippon Steel conducted the initial investigation during the 1980s whereby antimony sulfate ($Sb_2(SO_4)_3$) and a chloride consisting of at least one of the following Sb, Sr, Ti and Zr are added during the slurry mixing process. However, antimony sulfate has a disadvantage due to it being toxic and insoluble in water.

The slurry was applied and dried onto the substrate and heat-treated at 1200°C for 20 hours[103]. They claim that antimony sulfate and chloride of Sb, Sr Ti and or Zr in the glass film decrease the crystallization temperature of the Forsterite and therefore lower the formation temperature of the glass film [103]. This deterioration of the oxide film can occur during the latter stages of the HTCA by reduction or oxidation if the formation temperature of the film is high, as explained in section 1.10.1. and will not achieve the excellent properties needed[103]. They propose two reasons why the prevention of the deterioration of the oxide films is possible.

The first is a dense Sb film developing on the surface of the substrate due to the melting of the antimony sulfate during the drying of the MgO slurry /or the during the HTCA. The Sb layer shields the Fayalite and SiO_2 from the atmosphere applied during the HTCA annealing. If the inhibitors are prematurely removed or gas atmosphere or nitrides during the HTCA, this can remove the advantage of the GOSS grains[103]. Secondly, because Orb Steelworks uses a nitrogen atmosphere at the initial stages of the HTCA, this will likely cause N_2 absorption and S removal[103]. Therefore they conclude that the Sb provides " a sealing function of the films of MgO and SiO_2 and prevents the absorption and removal of inhibitors in the substrate"[103].

Similarly, the chloride melts during the drying stage of the MgO slurry or during the HTCA, which reacts in a molten state with the Fayalite layer, and this increase decreases the FeO content and

increases the SiO_2 present in the Fayalite layer[103]. This is believed to have a considerable contribution to improving the magnetic properties, and the glass film developed. The patent explains the amount of addition of antimony sulfate and the chloride, which is ideally added to the MgO slurry. The optimum range of antimony sulfate based on 100 parts by weight of MgO is applied on the decarburization ranges between 0.05 and 2 wt%. If <0.05, there is no effect on the magnetic properties. However, if greater than two, there is a damaging effect on the appearance of the glass film and reduction of the magnetic properties [103].

The patent states that the optimum amount of a variation of Sb, Sr, Ti and Zr chlorides is added such that chlorine is contained in an amount of from 5-20% by weight based on 100% of the chlorides and antimony sulfate. If the content is <5%, then iron oxide (FeO) is not effectively reduced due to the etching function of the chloride[103]. However, if the content is >20%, the chloride remains present at high temperature during the HTCA that results in colour change and irregular glass film development, and this is enhanced if the gas permeability between the laminations of a coil are poor or water content is high which causes oxidation [103]. Combination and unique additions of the Sr – Ti- Zr chlorides were added to the MgO, which contained five weight parts of TiO_2 and antimony sulfate in the slurry. The slurry was applied in the manner as previously explained. The results showed that all combinations showed improvement in magnetic properties and improvements of appearance of glass film compared with no additions of the three chlorides.

In conclusion, the patent explained the reasoning for using the antimony sulfates and the Sr-Ti-Zr chlorides and displayed the improvements in magnetic performance compared with no additions. However, there is limited information explaining why the combination of the three chlorides has an alternative variation of improvements and as expected are vague about certain aspects such as the characteristics of MgO powder used, which has a significant influence on the development of the glass film. The limited amount of information on some aspects, the fact that Nippon has patented the additives and other studies have been conducted on the back of this patent shows the importance of this research.

1.13.3 Additions of Ammonium Chloride (NH_4Cl or NH_4Ch nH_2O) and Sodium Pyrophosphate ($Na_4P_2O_7$ or $Na_4P_2O_7.nH_2O$)

The study of additions of ammonium chloride and sodium pyrophosphate was to solve the problems in previous studies whereby antimony sulfate ($Sb_2(SO_4)_3$) combined with Sb, Sr, Ti or Zr chlorides; however, these additions are toxic and exhibit poor solubility in water[103][104]. In addition, other additives such as Mg, Ca, Na and/or K chlorides result in solid residues at the surface of the substrate after annealing during the HTCA[103][104].

The patent claims a solution to resolve these problems is the addition of alternative additives. These additives added to the MgO slurry are ammonium chloride and sodium pyrophosphate for which the

amount is calculated from the concentration of chlorine in relation to the proportion of the weight of MgO used ideal range between 0.02% to 0.05%[104]. The addition of ammonium chloride as a chlorine addition is explained that has two advantages in aiding developing the Forsterite. The first advantage is that the heat treatment during the HTCA allows the bonding partner of the chlorine to be conveyed away via the gaseous phase without leaving solid residues on the surface of the substrate. Additionally, the ammonium chloride is thermally separated into NH_3 group during the HTCA, increasing the partial pressure between the windings. It is claimed these conditions act as a precondition for the avoidance of degradation of nitride inhibitors, i.e. Al-N in the steel and is decomposed into harmless N_2 and H_2[104]. The sodium pyrophosphate boosts the property enhancing effect of the addition of chlorine and counteracts any distinct increase in the nitrogen content of the substrate[104].

The method of addition of these additives is not stated, and neither is the heat treatment within the patent. However, the assumption is that they are added during the slurry mixing due to referencing previous patents. There is a 6% TiO_2 addition to the mix with all the experiments. The results presented showed an improvement in magnetic losses with NH_4Cl and $Na_4P_2O_7*10H_2O$ compared with the MgO + 6% TiO_2. The MgO + 6% TiO_2 only has a 200ppm Cl / 20ppm Na within the mixture, that produced a loss at 1.7(T) of 0.93 (W/kg). With additions of 0.042% NH_4Cl to the MgO and TiO_2, the Cl concentrations increase to 475 ppm, and the Na remained 20 ppm. This produced a magnetic loss of 0.91 (W/kg), a decrease of 0.02 (W/kg) compared to the MgO + TiO_2 only. A significant decrease in magnetic properties was observed when the addition of both 0.042% NH_4Cl and 0.13% $Na_4P_2O_7*10H_2O$. The addition of $Na_4P_2O_7*10H_2O$ increased the Na 300 ppm while the Cl remains at 475 ppm, producing a loss of 0.88 (W/kg) and compared with the MgO+TiO_2, there is an improvement of 0.05 (W/kg)[104].

In conclusion, the ammonium chloride and sodium pyrophosphate display a significant reduction in losses. However, a limited amount of information about mixing and heat treatment leaves a lot unexplained. Therefore, it is hard to determine the reasoning for the improvements displayed in the patent.

1.13.4 Addition of Titanium

The addition of 0-30% titanium (Ti) to the MgO slurry is commonly found in both patents and scientific papers, but the reasoning for the titanium addition is rarely explained. For example, a patent explains that due to partial hydration of MgO during the mixing of slurry (as explained in section 1.12), water being discharged during heating and the oxides produces embrittlement of the steel. To combat this problem, the inventors discovered that when additions of Ti compounds (oxides or hydroxides) are made, this provides a stable and strongly adherent glass film while reducing the initial problem of the brittleness of the substrate[105]. The method of reducing the brittleness is suggested to

be that the MgO- TiO_2 reacts with the silicon on the surface, creating a dense glass film reducing the influence of the annealing atmosphere and the Ti compounds additionally acts to purify the impurities the substrate[103] directly. However, true understanding of the mechanisms that TiO_2 and other compounds of Ti are not fully explained by the literature, though the addition of Ti compounds is consistently used in various papers and patents.

1.13.5 Titanium Dioxide in a Hydrogen Atmosphere

Many studies have been conducted looking into titanium dioxide in photovoltaics[106]. In addition, studies looking into the effect of TiO_2 in the hydrogen atmosphere are of interest to this research. Hydrogen (H_2) is commonly used as a reducing agent, and examples of industrial uses are steel manufacturing [107]. The use of hydrogen as a reduction allows for most oxides to be reduced below their melting point.

Titanium dioxide is an example of this, and at 300ºC, the following reduction occurs:

$$4H + TiO_2 + 2H_2O_{(g)} + Ti \qquad \Delta G_f^o = -348kJ$$
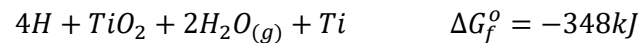
Equation 9 The Gibbs Free energy for TiO_2 in hydrogen at 300ºC [108].

Studies have observed a change in TiO_2 from a white powder to a black powder when under exposure to hydrogen at an elevated temperature(300ºC-1000ºC). These studies were focusing on the performance of the TiO_2 for battery and photovoltaic performance. However, they give an insight into the changes that occur in the TiO_2[109][110][109][111]. The surface of titanium dioxide is covered in hydroxyl groups[112][113]. When the titanium dioxide is heated to high temperatures, the hydroxyl groups are removed as water:

$$2OH \rightarrow H_2O + O$$
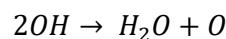
Equation 10. The chemical equation for water [113].

The surface of the titanium dioxide is covered with bridging oxygen atoms, where the oxygen atom is shared by two or more titanium atoms. When a hydrogen molecule encounters the surface, the oxygen will be removed as water resulting in a surface depleted in oxygen, creating a crystal lattice defect[114]. The depletion of oxygen in the crystal lattice results in changes in the appearance of the TiO_2 and can be obtained with the various colours grey, blue, brown, or black colour depending on utilization conditions. The "darker" the TiO_2 powder increases density defects such as Ti^{3+} and oxygen vacancies[115].

The evolution of H_2O from TiO_2 is of interest due to heat treatment conditions during the high-temperature batch annealing process, as explained in section 1.2.7. The environment during the heat treatment is a high temperature (1200ºC) in a concentration of a hydrogen atmosphere of 75% hydrogen 25% nitrogen for an extended period (75 hours). The release of water from the TiO_2 will alter the dew point within the furnace and between the laps of the coil. As explained in section 1.9.2,

the dew point is critical in the development of oxide and could affect the success of Forsterite development.

1.13.6 The Effect of Forsterite on Domain Structure

It has been established in the science community that the domain structure is critical to enhancing the magnetic properties of electrical steel[116]. One of the significant influences in which the domain structure can be influenced is applying tension to the substrate, which reduces the width of domains where the tension is applied. There have been multiple studies looking at single crystal domain structures and the effect of scratching and inducing a tension on the substrate using various methods clamps, tensile machines etc. The domain wall size reduces under tension. This was confirmed by inducing tension in the substrate.

This knowledge development of inducing this tension to material causes a reduction in domain wall spacing, resulting in improvements in magnetic properties. As a result, a method of permanently inducing tension to the substrate of electrical steel was needed to reduce the magnetic losses. Using coatings that have a significant difference in thermal coefficient of expansion from the substrate. This was achieved by using a unique method of developing a Forsterite layer that induces tension on the substrate. Because of this, tension developed on the surface has a similar effect as tension as clamps and causes domain wall size to reduce.

A paper published in 1979 by William G. Morris and Jack W. Shilling carried out a study on the effects of Forsterite on the domain structure, whereby a sample with Forsterite coating had this layer removed by acid pickling and then an area of interest micro-graphed using Scanning Electron Microscope (SEM). The samples were then coated with the MgO slurry and cured; the exact location as previously analyzed was scanned. The region of interest initially displayed with no Forsterite, showed the domains' sheet thickness ratio (2L/d) to be around 6, simply meaning the widths of domains were large. They demonstrated that the Forsterite induced tension on the substrate, therefore reducing domain wall spacing and eliminating of aligned lancet comb structure. However, they reported an increase in domain wall pinning, which produced a net increase in losses, although there was a reduction in domain spacing [58].

1.13.7 Novel Application of Ceramic Films

A study has investigated the effect of applying alternative coatings to the MgO slurry using Physical Vapor Deposition (PVD) and Chemical Vapor Deposition (CVD). This study looks at a wide range of chemical compounds such as TiN, CrN and Al_2O_3. To prepare the substrate, a NaOH solution is used to remove the insulation coating and then chemical polishing takes place using a solution of 3% HF + 97% H_2O_2, which produced a mirror-like finish. As a consequence of removing the film had two beneficial effects, the first is that it removes any impurities from the surface, which reduces the hysteresis losses[87]. Secondly, the presence of impurities, it can cause alternative oxides to develop

on the surface during the development of glass films such as spinel and MnS. The outcome of producing alternative oxides prevents anchoring of the Forsterite and produces less tension in the coating that increases eddy losses[87]. Therefore, there is a natural improvement in losses by eliminating these influences on magnetic performance.

The research conducted observed the effect of applying alternatives to the ceramic alternative via PVD and CVD. The alternative coatings examined of interest were TiN, CrN, TiC SiO_2 and Al_2O_3. Whereby the TiN, CrN displayed the best performance in inducing a tension onto the substrate resulting in a refined domain structure, and the TiN silicon is inducing an 8MPa tension [87]. Comparing these unconventional coating TiN, CrN with the oxide ceramic films SiO_2 and Al_2O_3 displayed significant improvements in reducing losses[87].

The improvements displayed in these studies have shown significant improvement in losses. However, the technique of application of PVD and CVD is currently not suitable for a continuous line due to the requirements of a vacuum and the associated high capital costs. Additional MgO plays a critical role in preventing laps from welding to one another during the HTCA.

1.14 Additives

Kawasaki Steel Corporation published a patient on the effects of various compounds had on the formation of Forsterite when added to the MgO/ silicon pellets or MgO slurry[117]. The patent does not specify the exact compounds used but give the elemental compositions. The investigation explored the following compounds: -

- TiO_2
- SnO_2
- V_2O_5
- Cr_2O_3
- MnO_2
- FeO
- Fe_2O_3

- Fe_2O_4
- CoO
- Co_3O_4
- NiO
- CuO
- ZnO

The initial experiment was on powder samples where MgO and SiO_2 were mixed by the molar ratio of 2:1 and 10 Parts By Weight (pbw) of one compound above and added to the MgO/SiO_2 mix. The mixture was then molded and fired at 950ºC for 1 hour in a hydrogen atmosphere. The fired pellets were then crushed and analyzed with X-Ray Diffraction (XRD). The spectra collected compared the peak intensity of (I_1) caused by Mg_2SiO_4 at the (211) plane to the peak (200) plane caused by MgO (I_2). The ratio of I_1/I_2 was compared with the standard MgO and SiO_2 only sample to establish

whether the additions have promoted Forsterite developments. The results of the effect additives have on promoted Forsterite development is illustrated in Figure 37.
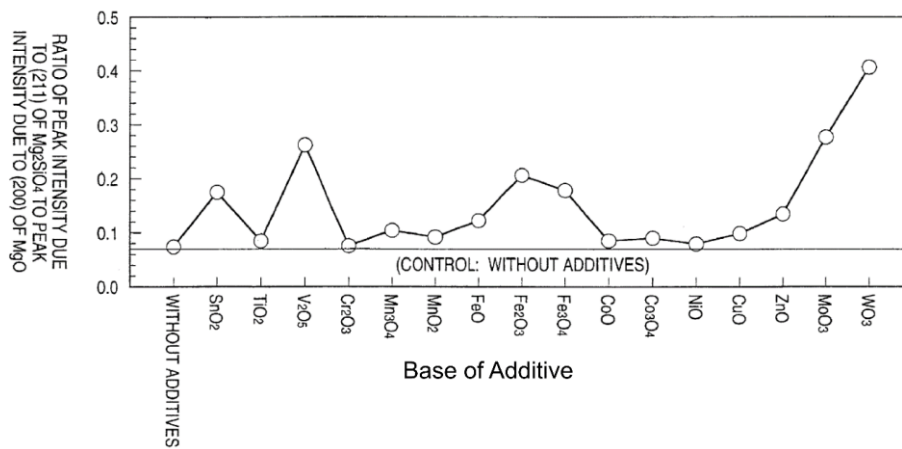
Figure 37. The results of ratio of peak intensity due to (211) of Mg_2SiO_4 to peak intensity due to (200) of MgO[117].

The results from the ratio of I_1/I_2 gathered from XRD are seen in Figure 36, and patent claims that SnO_2, V_2O_5, Fe_2O_3, Fe_3O_4, MoO_3, and WO_3 have shown promotion in the formation of Forsterite during firing at 950°C.

The increase in Forsterite detection in the powder mix suggested that possible benefits may be seen if incorporated into the magnesium slurry and applied to the substrate. Decarburised sheets cut from a coil were coated with a slurry composed of 100 Parts by Weight (pbw) of MgO and 0.5-20 pbw of TiO_2 of any one member or more selected from SnO_2, V_2O_5, Fe_2O_3, Fe_3O_4, MoO_3, and WO_3. The experimental design was based on the Box-Behnken Experimental design resulting in 66 combinations of the various additive/concentration. Once coated with the preferred slurry, samples were dried and annealed at 850°C in a nitrogen atmosphere. After the annealing cycle at 850°C, the samples were heated to 1150°C at a rate of 20°C per hour in a 75% hydrogen 25% nitrogen atmosphere. The samples were finally subjected to purification at 1200°C for 5 hours. The resulting Forsterite layer was assessed by visual inspection assessing the quality of the Forsterite layer produced. The study claims the samples that had slurry composed of 100 pbw of MgO, 1.0-15 pbw TiO_2, and any of one member or more selected from SnO_2, Fe_2O_3, Fe_3O_4, MoO_3 results in a uniform Forsterite layer. It was found that V_2O_5 does not show improvement in coating characteristics on the sheet samples, although it displayed improvements in powder samples.

It must be noted that the electrical steel used in this patent has a different chemical composition incoming material using 0.1-1 wt.% of Cr and Bi between 0.005 - 0.20 wt.%, which is an indication of different techniques used to develop Grain-oriented electrical steel compared with Orb Steelworks. In addition, the heat treatment conducted is different to the annealing process at Orb Steelworks, whereby Orb Steelworks has a slower heating rate to the HTS, while this study has a significantly faster rate of 20°C per hour.

The study conducted by Kawasaki Steel Corporation has identified potential enhancements of Forsterite with powder samples, although the improvements seen in powder samples do not always transfer when applied on the substrate as V_2O_5 displayed in this study [117]. In addition, the study gives limited information on possible improvements of the thickness of the Forsterite layer increased and what effect these improvements have on other properties of the electrical steel. Therefore, further investigation into additives that have shown improvements would benefit Orb Steelwork to understand the benefits claimed in the patient submitted by Kawasaki Steel Corporation.

1.15 Literature Conclusion

Electrical steel is a unique and specialised family of steels that require additional processing after hot rolling in which a significant microstructural and chemical change within the steel and steel surface. The electrical steel industry has seen significant changes in processing since the 1900s, resulting in a reduction in magnetic losses, increased permeability, and efficiency of manufacturing electrical steel. However, the knowledge of the development of "glass film" is not fully understood, and limited information is presented in patents and scientific papers targeted specifically at glass film. The development of the "glass film" during heating phase and soaking phase of the annealing cycle is not known and information gathered from the manufacturing process is difficult and inaccurate to interpret the development of the "glass film". Due to the wide temperature gradients created during the high temperature coiled annealing process. By identifying the changes in occurring throughout the annealing process will allow Orb Steelworks to optimise the annealing process to ensure a consistent "glass film" to be developed.

Furthermore, the claims made with patents are complicated to determine the benefits of additives to magnesium slurry due to the analysis typically based on comparing the magnetic properties of various slurries. Due to the variation of the substrate (such as precipitates), it cannot be guaranteed that the improvements are solely due to improvements in glass film. However, the literature has shown promise in improvements in the glass film and magnetic properties by the inclusion of in additives (V_2O_3, FeO-Fe_2O_3, TiO_2) to the MgO slurry.

Therefore, it is essential to enhance the knowledge of the development of glass film during the high temperature annealing cycle and the consequence of additives to the magnesium slurry on the substrate and the glass film.

Chapter 2.   Methods and Materials

2.1   Introduction to Equipment

Electrical steel has unique properties and characteristics when compared to "traditional" steel. Consequently, specialized equipment unique to electrical steel is needed to evaluate its properties. This chapter will provide information on the apparatus and the function of this equipment.

2.2   Selection of Samples and Pre- Preparation of Samples

The chemical composition of each batch of hot band material is provided by IJmuiden using a spark optical emission spectrometer. The coils that were selected are representative of standard production material used at Orb Steelworks. The chemical composition of these coils is displayed in Table 2.

Table 2. Composition of hot band material that coatings were applied to in the study.

Element	N	C	Mn	P	S	Si	Al	Cu	Sn	Cr	Ni	B	Ti	V	Ca
Composition (%) J15155	0.0072	0.056	0.200	0.008	0.008	3.093	0.034	0.102	0.087	0.020	0.201	0.002	0.002	0.002	0.00023
Composition (%) J19071	0.0067	0.058	0.196	0.008	0.007	3.084	0.036	0.099	0.088	0.014	0.020	0.002	0.002	0.002	0.00025

The steel was high silicon steel (wt-3.10%) that has been cold rolled down to 0.23mm thickness and decarburized, nitrided and coated with MgO during the decarburization stage production line as discussed in section 1.2.6. The coils are intercepted at the exit of the Decarburization line (D-line), where 10-metre-long by 1.04-meter-wide sheets are removed from the process. The samples were tested to identify the decarburization stage had its intended effect using Leco TN400 and Leco CS744 to measure the carbon, sulphur, nitrogen, and oxygen levels. Further details Leco TN400 and Leco CS744 are explained in section 2.10. The content of carbon nitrogen and oxygen after decarburization stage is displayed in Table 3.

Table 3. Content of carbon, oxygen and nitrogen after the decarburization stage has been completed on the substrates using the Leco CS844 and TN 400.

Sample ID	Carbon (% weight)	Oxygen (ppm)	Nitrogen (ppm)
J15155	0.00010	700	257
J19071	0.00012	735	245

The 10-metre samples have been coated in magnesium slurry and cured during the decarburization stage of the production line. The samples were cut using foot shears to 35cm × 10cm × 0.023cm. The 35cm ×10cm × 0.023cm samples had the MgO coating removed with a brush. Once the majority of the MgO is removed, the substrate is then wiped with paper towels doused in white sprits and finally dried with clean paper towels to remove any MgO and grease from the surface of the substrate. Due to the vulnerability of the steel to corrosion occurring at the exit of the decarburization stage, there is only a limited amount of time samples can be stored for using anti-moisture paper to prevent corrosion and extend the time for which samples can be stored.
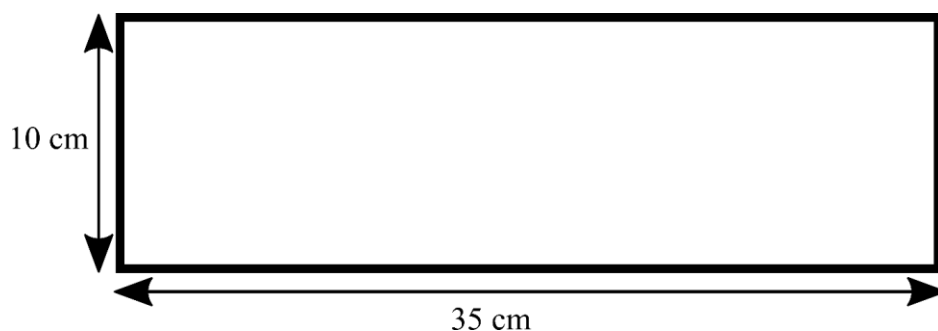
Figure 38. Dimension of the samples that were cut out from production line material.

The flow chart below displays the steps in the sample collection preparation before coating to ensure the quality of the substrate and coating materials.
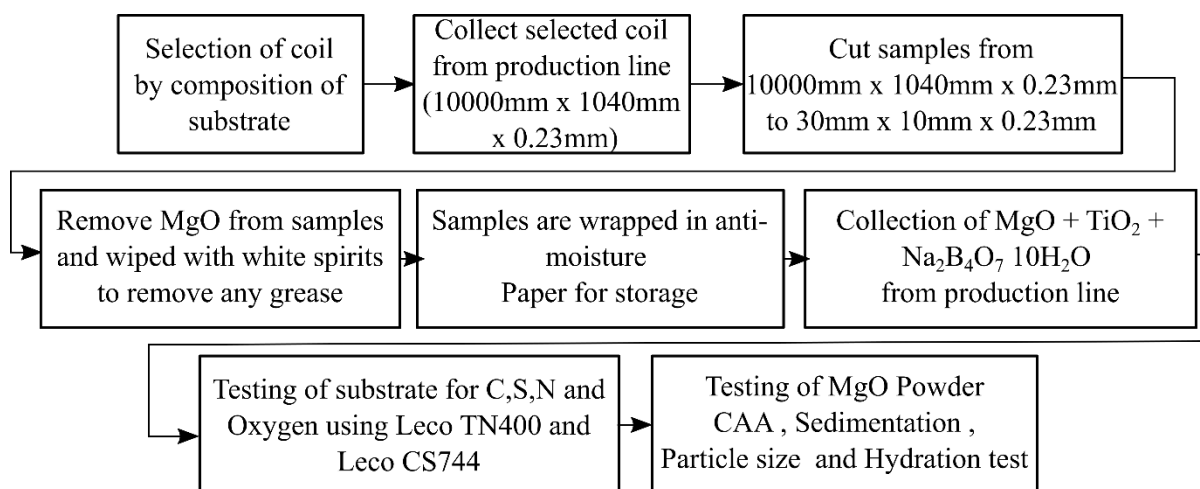
Figure 39. Flow chart for preparation of samples before the coating is applied to the substrate.

2.3 Coating Procedure

The 35cm x 10cm x 0.023cm samples prepared as outlined in section 2.1 were removed from storage, and a visual inspection is carried out on every panel before coating to ensure no corrosion product had developed. Samples with signs of corrosion on the substrates was disposed of.

The powders used in the experiments are displayed in sections 2.4 and 2.5, the quantity of additives added to the MgO slurry.

The magnesium coating was produced by chilling a beaker containing 800 ml distilled water to 10°C in a beaker that is held in a Haake D8 cooling bath. Once the distilled water reaches 10°C, the necessary quantity of MgO and any required additives was added to achieve the mix desired. The various mixes are displayed in sections 2.4 and 2.5. The borax is required to be dissolved in hot water before being added to the mix. This was done whenever borax was used in a mix. Once the MgO and necessary additives was added, the beaker was placed back in the Haake D8 cooling bath. A VWR Power max general-purpose mixer with a tri-blade propeller was placed into the beaker and mixed for one hour before coating. The setup of the mixing process is displayed in Figure 40.

51
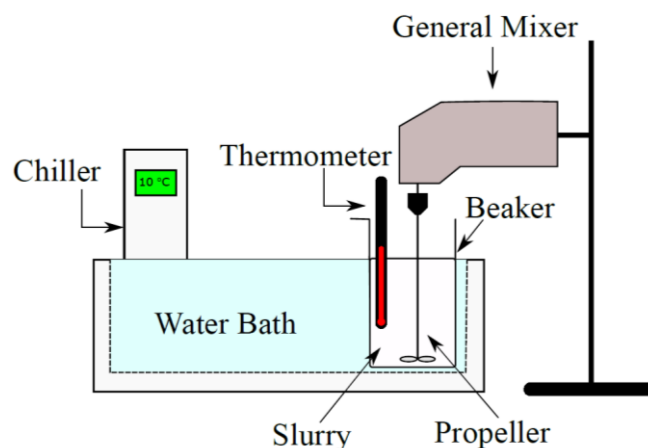
Figure 40. Schematic of the mixing process to produce the slurry for the coating.

Before coating, the substrate was weighed and labelled on the right side in the centre using a precision balance and a permanent pen before being coated. The mixed slurry was tested for pH and viscosity using the Amerall handheld pH meter and Brookfield viscometer. Once tested, the slurry was placed in the tray of the custom roller coater and positioned into position with the bottom roller partially submerged in the slurry. When the rollers are rotating, the grooves in the rolls pick up the slurry, which distributes the slurry to the top roller. The sample was placed between the roller gap, and the slurry transfers from the rollers to the surface of the substrate. The samples were passed five times through the roller to ensure a consistent coating across the sample. The slurry was then dried in the Nabertherm electric oven at 750°C, whereby the MgO slurry turned from a transparent grey to a white appearance and was naturally cooled to room temperature. Further details of drying are explained in section 2.5.6.

To ensure that both sides are coated with a uniform thickness and minimise the gravitation effect on adherence of the MgO during the coating and drying process, the sample were rotated and coated in the same procedure on the opposite side. During the coating of samples, segregation occurs due to the bottom roller only disrupting the top surface of the slurry. To prevent segregation of the slurry, the slurry was removed from the coating tray and placed back in the breaker and mixed for 5 minutes every 15minutes, and the pH and viscosity were tested to ensure there were no changes during mixing. This minimises segregation and temperature changes in slurry during coating. The sample was reweighed after drying and packaged in Volatile Corrosion Inhibitor (VCI) paper. This process of coating is displayed simply in the flow diagram below.
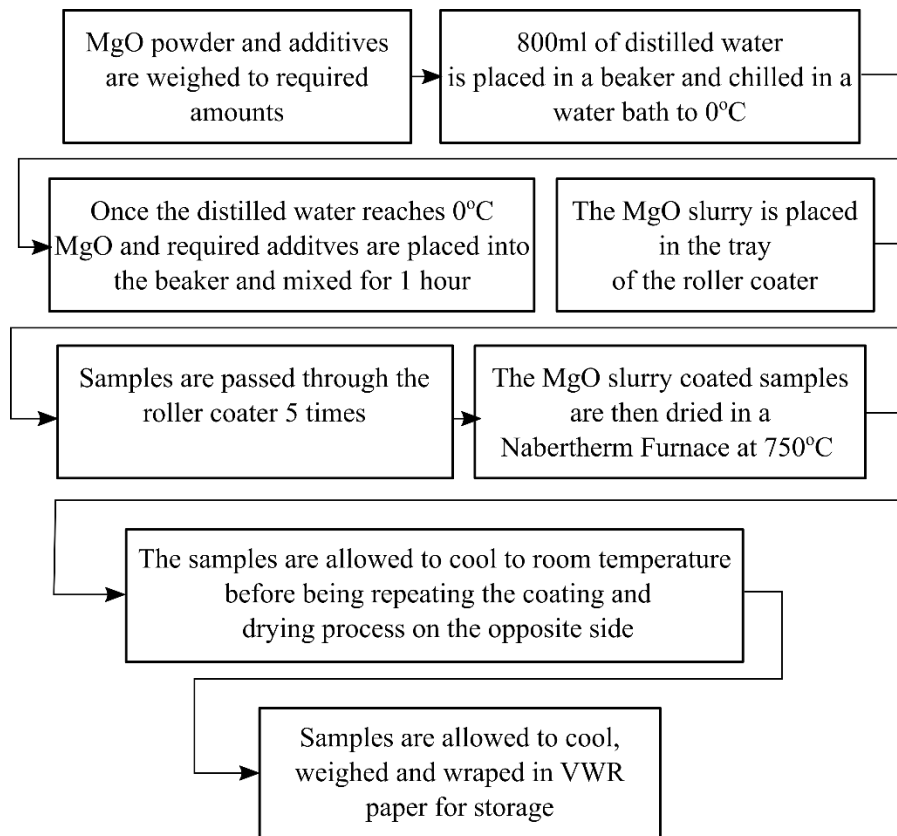
Figure 2.41. Flow diagram displaying the process of coating substrate.

2.4 Mixtures for Interrupted Annealing, the Effect of Duration at High-Temperature Soak and High-Temperature Coil Annealing in Production Furnaces.

Table 4 displays the quantity of each additive (in Wt % of MgO) to form each combination of a mix. These mixtures were used for experiments during the interrupted annealing, the effect of duration at high-temperature soak and high-temperature coil annealing in the production furnaces experiments. The powders that were used for the mixes are as follows –

2.4.1 Magnesium oxide

The magnesium oxide used in the study was supplied by Tateho and was removed from the production line at Orb Steelworks. The product information is Tateho Mag (Batch # 4120, Bag 257 BS 613). The quality of MgO is critical to the development of Forsterite. Therefore, routine quality checks are conducted. The details of the magnesium oxide used can be found in 1.12.

2.4.2 Titanium dioxide

The titanium dioxide used was supplied by Univar solutions. A 5kg bag was removed from the production line and was stored in a glass bottle, in a dry ambient temperature room.

2.4.3 Sodium Tetraborate Decahydrate (Borax)

The sodium tetraborate decahydrate used was supplied by Univar solutions and was obtained from the store available at Orb Steelworks. The borax was stored in a sealed plastic container.

Table 4. Quantities of additives in each mixture for coating the interrupted annealing, the effect of duration at high-temperature soak and high-temperature coil annealing in production furnaces.

Mix	MgO	TiO$_2$	Borax (Na$_2$B$_4$O$_7$)	Distilled water (ml)
MgO Only	112g	-	-	800
MgO + TiO2	112g	4.80g	-	800
MgO + TiO2 + Borax	112g	4.80g	0.092g	800
MgO + Borax	112g	-	0.092g	800

2.5 Mixtures for the Study of the Effects of Additives on the Development of Forsterite Film.

The magnesium and titanium dioxide used were the same as identified in the previous section 2.4. The table below displays the quantity of each additive (in Wt % of MgO) to form each combination of the mix. As explained in the coating procedure section 2.3, the additives were added to chilled distilled water once the distilled water has reached the desired temperature. Once the additives are added to the water, they are mixed for 1 hour. Each percentage increase of additive was created using a new batch of slurry with the relevant quantity of additive. The additives that were used were as follows: -

- Titanium Dioxide
- Vanadium (III) oxide
- Iron (II, III) oxide

Table 5. Displays the ingredients to create the mixtures of slurry.

Wt.% of additive of interest	MgO	The amount of additive to the slurry	Distilled water (ml)
0.5%	112g	0.56g	800
1%	112g	1.12g	800
5%	112g	5.6g	800
10%	112g	11.2g	800
15%	112g	16.8g	800
25%	112g	28g	800

2.5.1 Titanium Dioxide

The titanium dioxide (TiO$_2$) used was the same as Orb Steelworks which is supplied by Univar solutions. A 5kg bag was removed from the production line and was stored in a glass bottle in a dry ambient temperature room.

2.5.2 Vanadium (III) Oxide

The vanadium (III) oxide V$_2$O$_3$ used was supplied by Alfa-Aesar as a blue powder with a purity of 99.7% metal basis. The vanadium (III) oxide was stored in a glass bottle at ambient temperature. Table 5 displays the amount of V$_2$O$_3$ additive required to create the desired slurry.

2.5.3 Iron (II, III) oxide

Iron oxide (II, III) Fe$_3$O$_4$ used in this project was supplied by Sigma-Aldrich as a fine black powder. The purity of the iron oxide was 97% with a trace of metal basis. The particle size of the powder ranged between 50-100nm and was stored in a glass bottle provided by Sigma-Aldrich.

2.5.4 Laboratory mixing

All slurry mixing was completed using a VWR Powermax general-purpose mixer with a 3 cm mixing paddle attachment. The VWR Powermax general-purpose mixer can achieve between 100 – 3400 RPM mixing with a torque of 0.0626 Nm^{-1}. The tri-blade propeller mixes the slurry rather than blends. The slurry was mixed for a minimum of 1 hour to ensure adequate mixing and hydration of MgO to simulate the production line at Orb Steelworks.

Figure 42. Photograph of the VWR Powermax general-purpose mixer with the tri-blade propeller attached.

2.5.5 Laboratory machine coater

The laboratory roller coater used is a custom-built machine that applies the coating via rollers whereby slurry is retained in the tray below the rollers. The rollers are grooved, which allows for a fine layer of coating to be maintained on the roller surface. The rollers are supplied with coating mix by the tray, which retains between 100ml to 500ml of the mix which is adjusted by additions of ceramic blocks into the tray. The lower roller was partially submerged in the tray, which allows for the pickup of the coating. The lower roller supplies the top roller with a coating mixture. The distance between the rollers can be adjusted via bolts, consequently regulating the coating applied to the substrate. The sample size is restricted to the diameter of the upper roller due to the amount of coating retained on the upper roller. The maximum sample size is 0.5cm × 16cm × 35cm, whereby the samples were manually passed through the rollers five times to ensure that a uniform coating is applied to the substrate.

Figure 43. A custom Laboratory Roller Coater was used to coat samples at Orb Steelworks.

2.5.6   Drying of Slurry

After the slurry has been applied to the surface of the substrate by the Laboratory roller coater, the water in the slurry was removed by heating the substrate up to ~100°C, leaving a dry MgO powder on the surface of the substrate. Insufficient water removal from the MgO slurry will fail or lead to difficulty producing the glass film due to a dew point change within the furnace. Uniform coating is difficult to achieve as the slurry progressively moves to the edges of the substrate, and the time taken to form the final pass through the roller coater to the furnace will result in a progressively worse uniformity of coating. Additionally, the amount of MgO applied to the bottom surface was lower than the top surface of the substrate. This is due to gravity causing poor adhesion to the bottom surface and, therefore, lower coating weights at the bottom surface of the substrate. To overcome these issues, coating and drying are done twice with substrate rotation in-between drying and second coating.

The furnace used at this stage is made by Nabertherm, and it can reach temperatures between 30°C to 3000°C with modifications. The Nabertherm at Orb Steelworks is set to be operating at temperatures between 30°C to 1000°C, whereby curing samples is conducted at 750°C. Samples are held using tongs during drying in the furnace with the focus of keeping the sample horizontal and flat to minimize the movement of slurry to the edges. The time the sample remains in the furnace is around 10-20 seconds while the slurry transforms into a powder that adheres to the surface of the substrate. Tests were conducted to measure the water content of the MgO after drying, whereby 1g of MgO was removed from the substrate and placed in a platinum crucible. The crucible with the MgO content was heated at 950°C and held for 3 hours. The samples were then allowed to cool to room temperature in a desiccator, and the change in mass gives the water content of the MgO. These tests were conducted on several samples, and the results were comparable to production material.

Figure 44. Nabertherm furnace was used to remove water from the coated samples.

2.6   Carbolite GPC 1300 Furnace

The Carbolite GPC 1300 furnace 2001 model is a conventional laboratory muffle furnace capable of reaching 1300°C. The furnace has been modified with a stainless-steel retort, gas process unit and a PLC Eurotherm 2408 furnace controller. The stainless-steel retort is secured into the muffle furnace and an insulation skirting to seal the steel retort to the muffle furance. In addition to these modifications, an advanced furnace technology (AF) was added to reduce the gas pressure from

production gas supplies and adjust the flow rates which was supplied by Carbolite. The mixture of the gas can be adjusted with increasing or decreasing the 3HNX content. This AF modification allows for the higher pressure of the gas supply and a gas saturator to simulate the HTCA process accurately. These modifications to the furnace allow for effective simulation of the HTCA whereby the hydrogen nitrogen atmospheres can be created at high temperatures. Additionally, the dew point of the furnace can be adjusted by passing the gas through the moisture controller introducing moisture to the gas mixture. This gas mixture is then transferred to the chamber creating a dew point in the chamber.
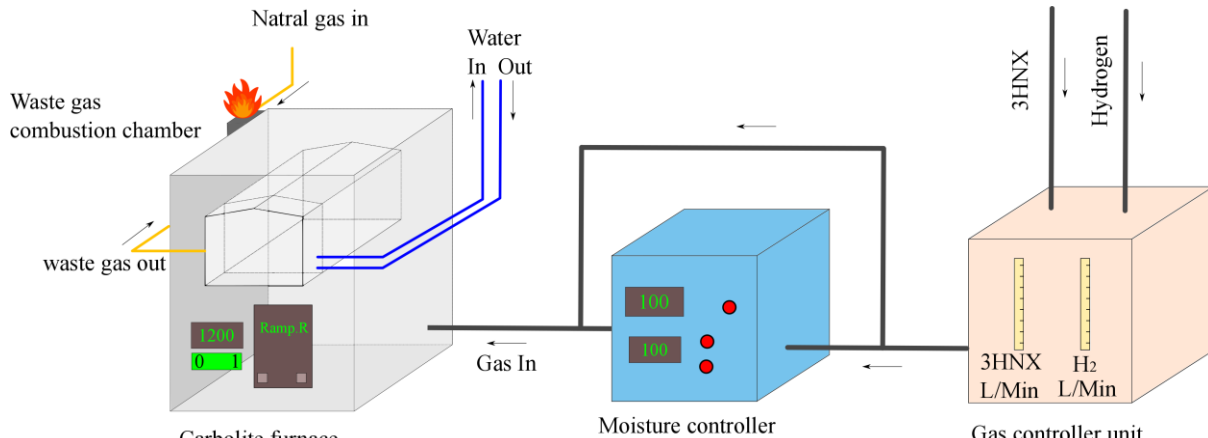
Figure 45. Diagram of the Carbolite furnace that has been adapted with retort, moisture controller and gas control unit.

The stainless-steel retort allows a controlled atmosphere once the door is secured to the retort, which creates an airtight vessel. Nitrogen and hydrogen are introduced at the rear of the retort, and the exhaust is located at the front of the furnace. Slight positive pressure is created in which the gases are forced out through the exhaust pipe.
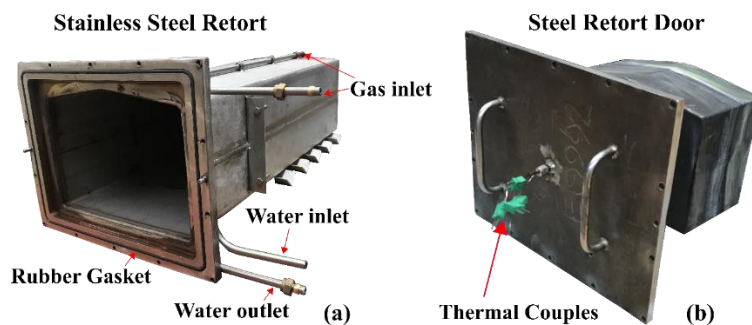
Figure 46. (a) Stainless Steel retort that is fixed within the Carbolite furnace (b) Steel retort door that seals the retort allowing for controlled atmosphere in the furnace.

2.6.1 Sample Size and Sample Organization

All samples were collected from the exit of the D5 production line, whereby the substrate has been coated in MgO slurry and dried. 5 to 10-meter samples has been removed from a coil to ensure enough samples are available, and any defects in samples such as dents or buckles caused by handling can be removed. The dimensions of the samples for the high-temperature soak experiment and additives to MgO slurry are all 0.23mm $\times$ 100mm $\times$ 300mm. The MgO from the production line is

removed before coating with a brush and then wiped with a cloth soaked with industrial spirits to ensure of removal of MgO. Samples are weighed and labelled with a permanent pen on the centre right-hand side. This provides a reference of the sample and the top surface, and the label will be visible due to this being the location in which the tongs are holding the sample.

As previously explained in section 2.3, samples are coated using a laboratory roller coater and dried using the Nabertherm furnace. Samples are coated within 24 hours after removing the MgO coating from the production line to ensure that no corrosion development occurs that may affect the development of Forsterite. Once coated, the samples are stamped on the top surface bottom left-hand side of each sample. This provides a reference to the top surface and the closest edge to the furnace door and, therefore, indicates the substrate's coolest region during the heat treatment. The samples are labelled with a superscript which specifies the location of the sample in the horizontal where 0 is the coolest region, and 8 is the hottest region. The subscript indicates the location of samples vertically axis, as displayed in Figure 47.
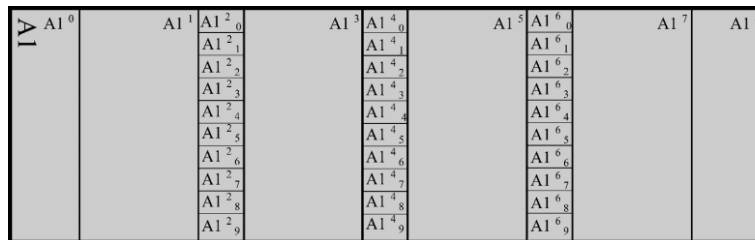
Figure 47. Drawing of the sample labelled and dividing substrate for analysis.

2.6.2 Heat Treatment

During this work, a variety of heat treatments were conducted on samples and are referenced in this section. In addition, the samples that have been laboratory coated and stored in VCI paper were removed from storage, and they were stamped with the identification on the bottom left-hand corner of the sample. The identification stamps give a reference point on position within the furnace, i.e., the stamped region was always placed closest to the furnace door.

For the interrupted annealing and high-temperature varying soak time variation experiments, the samples were stacked upon one another and grouped by mixtures with three sacrificial samples are placed top and bottom of the coated samples, and two base plates are placed on the top and bottom of the sacrificial samples stack. Metal banding was secured in place with pressure applied to simulate the coiled material pressure and hold the samples. The heat treatments for the Interrupted annealing and high temperature with different soak durations experiments used the Carbolite GPC 1300 furnace laboratory furnace. Two furnace bricks were placed at either end of the furnace, and the banded samples are placed on top of these bricks to prevent samples from welding to the retort. The samples were placed flat on the bricks, which results in an up-facing surface (top surface) and a down-facing surface (bottom surface). The up-facing surface will have the stamped labels correctly orientated, and the down-facing surface will have the inverse.
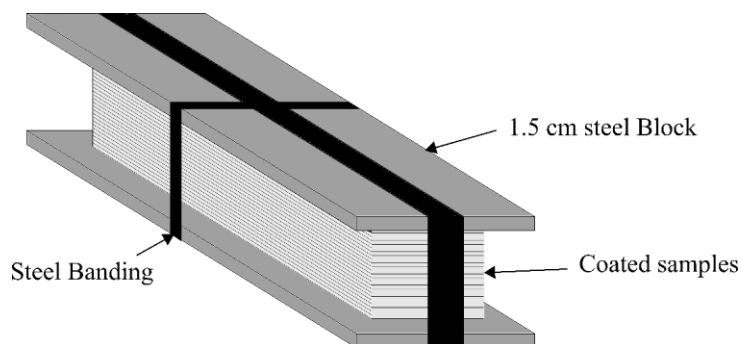
Figure 48. Drawing of the sample's places between steel block with banding holding the samples and steel blocks to gather.

The investigation on the effect of additives in Chapter 5 the samples was placed in the production line in the HTCA. All mixes were placed in the same stack with a sacrificial sample between different mixes. For example, all concentrations of vanadium were grouped separated by a sacrificial sample between the iron oxide mixes. All samples underwent one of the following heat treatment profiles (heat treatment A), B), and C).

2.6.2.1 Annealing cycle, A)

Annealing cycle, A) was conducted on samples investigating the effect of soaking time on the development of Forsterite and the influence on magnetic properties. Annealing cycle, A) follows the following annealing cycle: -

- From temperature room to 750ºC, the heating rate is 250ºC per hour in a 97% nitrogen / 3% hydrogen atmosphere.
- At 750ºC, a 10-hours soak is known as the Low-Temperature Soak (LTS). The purpose of the LTS is to achieve uniform heating and to ensure that the temperature in the retort is suitable for change of atmosphere from a 97% nitrogen / 3% hydrogen atmosphere to a 25% nitrogen 75% hydrogen atmosphere.
- After the 10-hours soak at 750ºC and the change in atmosphere, the temperature increased from 750ºC to 1050ºC at a rate of 12ºC per hour.
- At 1050ºC, the heating rate is reduced to 6ºC per hour. This heating rate is maintained to reach a max temperature of 1195ºC.
- Once at 1195ºC the temperature is held at the temperature for a period as followed 5,10,15,20,25,30,35,40,45, and 50 hours.
- After the soak is completed, the samples are cooled as fast as possible in a controlled manner which the furnace allows. The cooling is a two-stage process where initially the hydrogen atmosphere allows for rapid cooling at ~70ºC per hour. At 660ºC, the change in atmosphere from 75% hydrogen 25% nitrogen atmosphere to 97% nitrogen 3% hydrogen there is a slight slowing of the cooling rate due to thermal conductivity, and the steel samples are at a lower energy potential. The total cooling period takes approximately 11 hours.

2.6.2.2 Annealing cycle B)

Annealing cycle B) was used to investigate the development of the Forsterite oxide layer during the heating phase. Annealing cycle, B) is identical to Annealing cycle A) but the heat treatment was interrupted at 700ºC, 750ºC, 800ºC, 850ºC, 900ºC, 950ºC, 1000ºC, 1050ºC, 1100 ºC, 1150 ºC and

1195ºC. At the desired temperature, a 3-hours soak was applied to ensure that the substrate had reached the desired temperature and minimise thermal gradient.

2.6.2.3 Annealing cycle C)

Annealing cycle C) was used to examine the effects of additives on forming the Forsterite layer. Samples were bound together, as explained in section 2.6.2. The bound samples were then placed into the production furnace on the edge of the end coil.

The production furnace heat treatment altered during this project, where the LTS was removed, and a lower heating rate was used between 750ºC and 1050ºC. The incentive for the removal of the LTS was to increase productivity. Details of the adapted heating cycle cannot be discussed due to the commercial sensitivity. Due to the size of the samples and the location of samples, it is presumed that the samples are uniformly heated and accurately follows the heating cycle applied by Orb Steelworks. The heating cycle applied to the laboratory furnace was held at 750ºC for 10 hours, then a 12ºC per hour was applied. The new HTCA heating cycle did apply the 10 hours LTS at 750ºC, so at 750ºC, the heating of the coils continued at several degrees lower than 12ºC. However, this is more critical for large mass products to minimise temperature gradient.

This is not believed to be important to the laboratory samples placed in the production HTCA furnaces. A small mass of samples and the location of the samples allowed for "ideal" heating rates following the intended heating rates applied by the furnace.
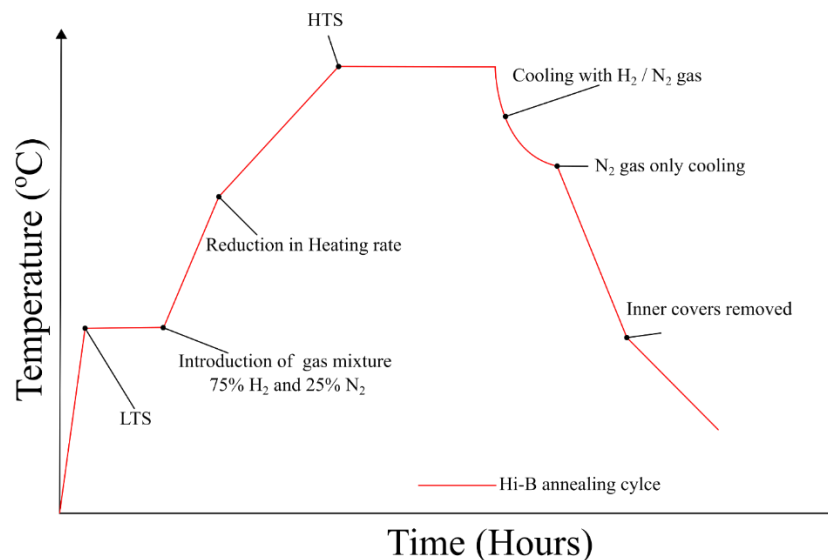
Figure 49. A typical annealing cycle profile conducted by Orb Steelwork (prior changes in 2018)

An experiment was developed to understand the heat transfer through the samples and monitor this heat transfer between the laps. A cylinder with a diameter of ~10 cm and a depth of 12 cm was machined in the centre of the two refractory bricks. Thirty punched disc samples from the D-line production sampling with MgO coating applied were collected. These samples were weighed, and

thickness was recorded using a micrometre to 3 decimal places and a general-purpose weighing scale to 2 decimal places.
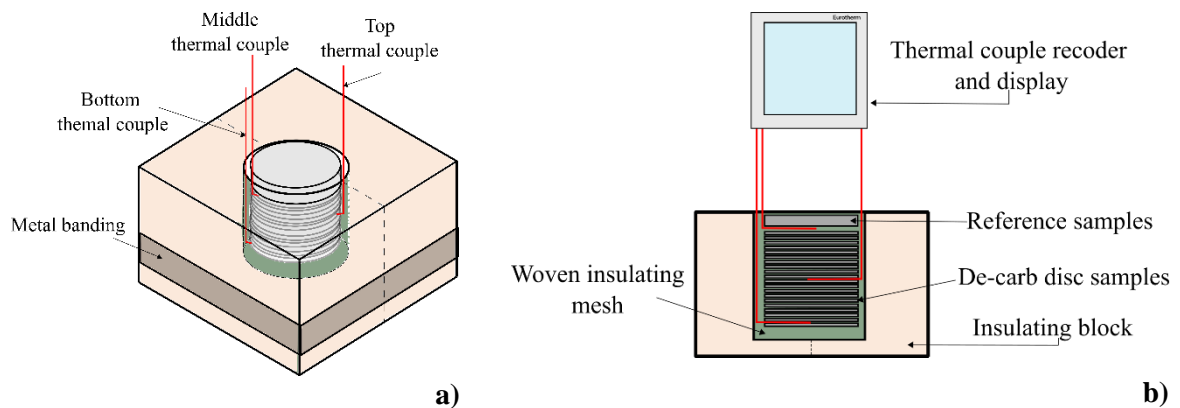
Figure 50. a) Setup of the monitoring the heat transfer **b)** is a front view of a)

The woven insulating mesh was laid flat on the table, and the decarb discs were stacked upon one another. During the stacking of the discs, the thermal couples were punctured through the woven insulating mesh. Once all 30 samples were stacked upon one another, a stainless-steel reference sample was placed on top. The additional mesh was wrapped around the stack. Next, the samples were sandwiched between the two machined refractory blocks, and metal banding was placed to hold the samples secure and the blocks together. The secured block with samples was then placed into the laboratory furnace, and the thermocouples fed through the hole in the door, as Figure 46b) displays. Next, the thermal couples were attached to a thermal couple reader (Eurotherm -Nanotherm), and the door was secured. Finally, an additional thermal couple was placed in the retort to monitor the temperature within the retort.

The heat treatment conducted was as follows: -

- From room to 750ºC, the heating rate is 250ºC per hour in a 97% nitrogen / 3% hydrogen atmosphere.
- At 750ºC, a 10-hours soak is known as the Low Temperature Soak (LTS). The purpose of the LTS is to achieve uniform heating and to ensure that the temperature in the retort is suitable for change of atmosphere from a 97% nitrogen / 3% hydrogen atmosphere to a 25% nitrogen 75% hydrogen atmosphere.
- After the 5-hours soak at 750ºC and the change in atmosphere, the heating rate from 750ºC to 1160ºC at 12ºC per hour.
- Once at 1160ºC, the temperature is held at the temperature for 10 hours.
- After the soak is completed, the samples are cooled as fast as possible in a controlled manner which the furnace allows. The cooling is a two-stage process where initially the hydrogen atmosphere allows for rapid cooling at ~70ºC. At 660ºC, the change in atmosphere from 75% hydrogen 25% nitrogen atmosphere to 97% nitrogen 3% hydrogen there is a slight slowing of the cooling rate due to thermal conductivity, and the steel samples are at a lower energy potential.
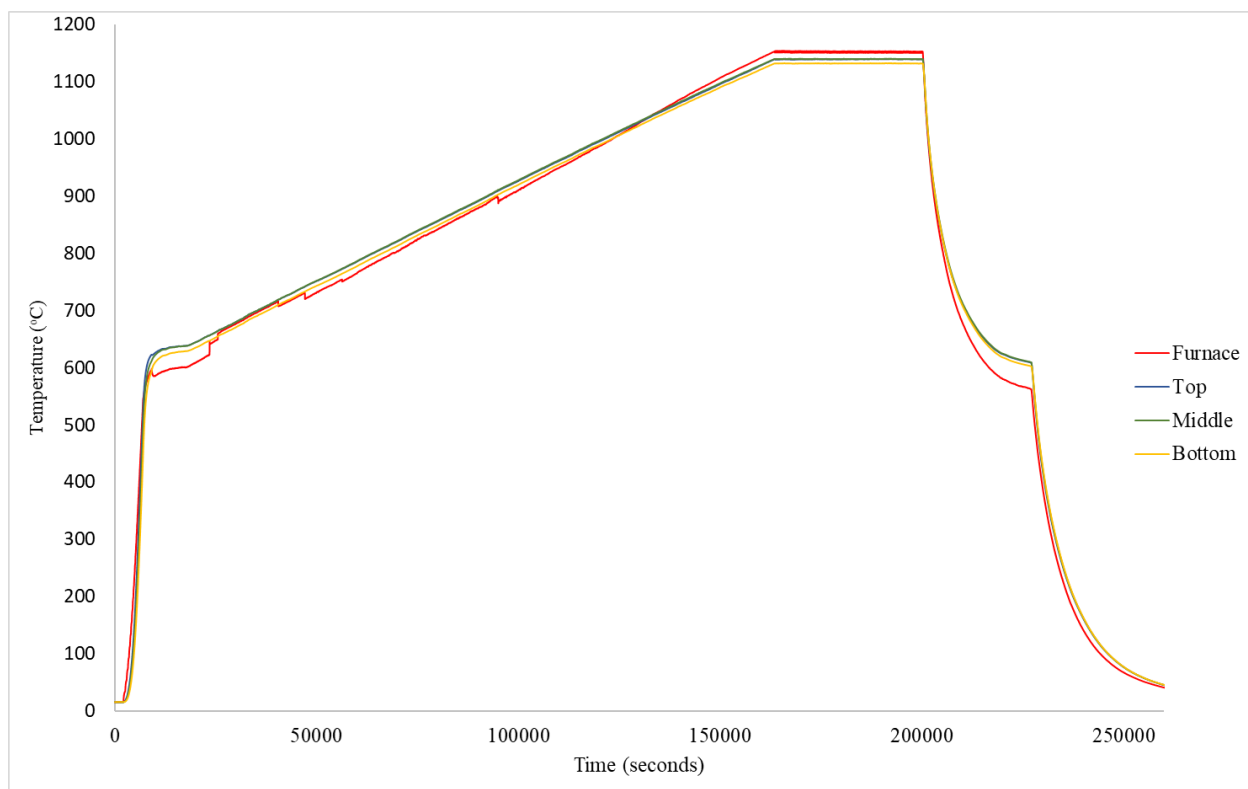
Figure 51. A graph showing the temperature recorded at the top, middle and bottom of the Stack.

The experiment illustrating heat transfer between samples is displayed in Figure 51. The furnace temperature recorded was initially placed too close to the gas inlet location. As a result, the temperature was lower than anticipated, at a temperature around 600ºC – 1000ºC. The lower temperature recorded was due to the location of the control thermocouple, which was placed near the entry point of gases and when the introduction of H_2 resulted in a decrease in temperature. The thermal couple was adjusted during the experiment, which resulted in a more stable temperature measurement.

Even so, the temperature data recorded between top, middle and bottom thermocouples is illustrated, in Table 6 and displays the temperatures at various stages of the heat treatment. The temperature between the top thermal couple and middle measurement remained relatively consistent with one another, with a ±3ºC difference between the two thermal couples. The bottom thermocouple did exhibit a temperature gradient between the top and middle thermal couple, lagging a maximum of 10ºC lower. At maximum temperature, the furnace thermal couple temperature record was 1150.5ºC. However, the top thermal couple temperature remained around 1140ºC, indicating a 10ºC difference. Complete insulation of the samples may not have been achieved to create a single surface to absorb and transfer the heat, but it has provided confidence that temperatures are near the ideal temperature when heat treating samples for experiments in this thesis in a laboratory furnace.

Table 6. The temperature was recorded at various stages of the heat treatment.

Time (hours)	9.8	17.7	25.7	33.6	37.9	41.9	46.7
Furnace Temperature (°C)	697.1	781.3	888.4	990.6	1053.8	1109.7	1150.5
Top Temperature (°C)	700	799.1	899.6	998.2	1050.1	1098.4	1138.5
Middle Temperature (°C)	700	800	900.9	1000	1052	1100	1139.4
Bottom Temperature (°C)	690.9	791.3	892.8	992.3	1044.7	1092.7	1131.4

2.7   Metallurgical analysis

The analysis of the development of Forsterite thickness by optical microscope or scanning electron microscope (SEM) requires specific preparation. The samples were cut with shears to the ideal dimensions of 25mm by 15mm, with the longest edge the one to be examined. Steel spring clips were used to hold samples in place. A SimpliMet 3000 mounting press that is capable of mould pressure between 1200-4400psi in 5 bar increments and a moulding temperature between 50-80ºC was used to mount the samples. Samples are placed in the centre and surrounded using conductor-mount 2 to allow good conductivity to improve imaging quality under SEM. Up to 3 samples were placed in a single mount, but a divider sample was needed to ensure no emergence of the Forsterite layer and prevent buckling of the sample of interest. An L shape sample is used as a reference for the organization of the samples with the top surface facing the L shape samples, and the samples are ascending from the L shape samples.
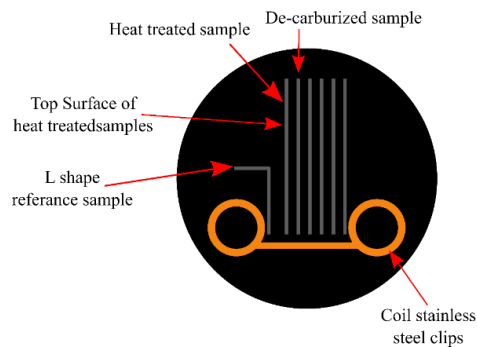
Figure 52. Drawing of the layout of mounted samples for SEM analysis.

Table 7 Illustrates the grinding and polishing procedure used to produce a mirror finish. In between each stage, samples were washed with acetone to minimize carryover of contaminants.

Table 7. Grinding and polishing procedure to produce high-quality surface for imaging SEM.

Grinding / Polishing	Time (minutes)	Pressure	Lubricant
SiC Paper Grit 320	1	25N	water
SiC paper grit 500	1	20N	water
SiC paper grit 1000	1	20N	water
SiC paper grit 1200	1	15N	water
SiC paper grit 2000	1	15N	water
SiC paper grit 4000	0:45	15N	water
Struers Dac	4	15N	DiaPro Dac 3 μm
Struers Nap	1:30	10N	DiaPro Dac 1 μm
Struers Nap	1:30	10N	DiaPro Dac 0.25 μm

All samples were ground and polished with the Struers RotoPol-21 whereby grinding was completed on the left-hand side with water as a lubricant, and the right-hand side is used for polishing using Struers DP lubricant Blue. The Struers RotoPol-21 can rotate at 150 or 300 rpm and a force placed on the samples between 5-50N with 5N increments.

2.7.1   Zeiss EVO WSEM

The EVO SEM was equipped with a large vacuum chamber that can hold samples up to $210 \times$ 300mm. The EVO WSEM was fitted with an oxford Electron Dispersive Spectroscopy (EDS) detectors and Electron Back Scattering Electron (EBSD). The Magnification capability of the EVO SEM is between $7\times$ to $1,000,000\times$ with adjustable acceleration voltages between 0.2kV to 30 Kv.

Figure 53. Zeiss EVO WSEM.

To achieve the maximum potential of quality of images for measurements of the Forsterite and elemental analysis/chemical characterization, two settings were used. For the imaging of the Forsterite layer, the accelerating voltage was kept at 15kV with a 10Pa to achieve a high-resolution image of the Forsterite layer. For EDS analysis, the acceleration voltage remained 15kV and the probe current increased to 250pa to increase the signal to the EDS detector.

2.7.2   Imaging Procedure

After heat treatment has been completed on a mix, a minimum of three samples were selected. These were then cut, mounted, and polished for SEM analysis. Images were captured at $\times$5k magnification and EDS analysis at carried out at $\times$7k for each sample. 5 images of the cross-section were captured for each down facing (bottom surface) and up facing (Top surface) of each sample.

These images were then processed using a custom Matlab procedure developed to measure the thickness, where scale is set by measuring the number of pixels of the known length from the scale bar provided by the SEM images. Once the scale is set, the surface oxide layer was traced in which a binary is created from the traced surface oxide layer. At each X-axis interval, a count of white pixels is counted and converted to a length. This was repeated across the image, and an average thickness is calculated. Three samples were imaged with each top and bottom surface examined with five images of each surface. It was resulting in an average thickness calculation covering 30 images. It must be

noted that further data extraction would have been useful, such as standard deviation. However, this was not realised until after the analysis was conducted.
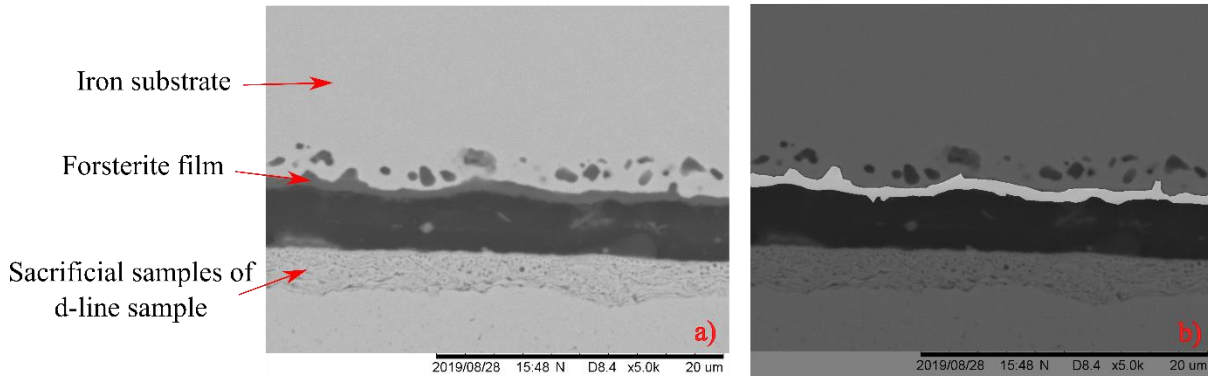
Figure 54. a) An image of a cross-sectional image prior process, b) Is the result of tracing the surface oxide and a binary image created by Matlab.

2.8 Soken DAC–IR-3

The Soken DAC –IR-3 is a magnetic probing device that can measure the local magnetic losses that are created within the steel using a 5.5 cm (diameter) probe consisting of a U-shaped yoke and detecting coil.

The gauge of the sample can be between 0.1 to 1 mm and adjusted with 0.01mm increments. They can be measured at a frequency of 50Hz or 60Hz, and the flux density can be adjusted at 1T, 1.5T or 1.7T. For this experiment, all testing was completed at 50 Hz at 1.7T on 0.23mm samples. Calibration samples are provided to ensure that the Soken tester is operating correctly. These calibration samples were tested before sample testing started.

Samples were tested in four locations, as displayed Figure 56. To ensure that readings were in similar locations, a stencil was used with a 5.5cm diameter circle with a centre line to align the probe. The distance between the circles was 1.8cm to achieve an even spacing. The stencil was aligned with the edges on the opposite side of the punched labels to ensure that the influence of the punched labels had minimal effect on the magnetic results.

Figure 55. The equiment used to gather mangetic properties Soken DAC –IR-3

65

Soken test 1   Soken test 2   Soken test 3   Soken test 4

A1
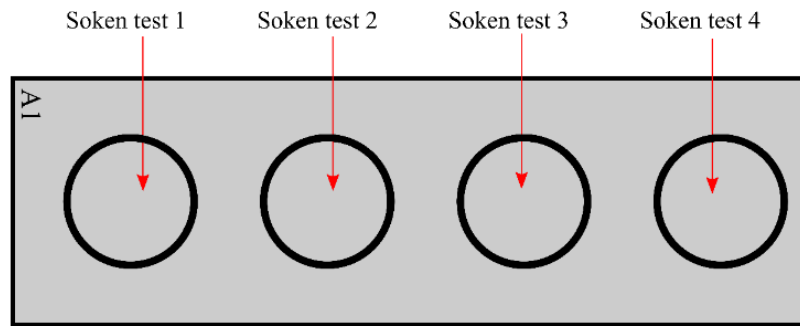
Figure 56. The loaction in which the mangetic properties were collected using the Soken tester.

2.9 Brockhaus Franklin Tester

The Brockhaus Franklin tester is used to measure the total current that flows along with the single side insulation layer and, therefore, the electrical resistance of the coatings. The Franklin Test is used in the GOES industry to measure the electrical resistance of the steel when both Forsterite and Phosphate coatings have been applied. It is essential to prevent conductivity because lamination of the GOES steel is stacked to form the transformer's core. Failure will result in conductivity between the stacked laps, which will cause catastrophic failure of the transformer. To summarise, each lamination is required to be electrically isolated from one another to reduce eddy currents and therefore reduce the total losses produced by the transformer.

Figure 57. Brockhaus Franklin tester to measure current detected through the coating.

The Franklin tester is designed to penetrate the insulating coating on a single surface and apply a defined voltage. If any inconsistencies in the coating allow leakage of current, this will be detected by the probes.

The operation of the Franklin tester uses two drilling screws that penetrate the coatings into the matrix of the substrate of the surface of interest. Between the two drilling screws are 8 steel rods with stainless steel measuring contacts, that are arranged 2 by 4. The total surface that the detectors cover is 6.45 cm^2 +- 0.5%. The electrodes are hydraulically pressed onto the surface of the substrate at 125N, and each detector is pressed onto the surface of the substrate using a force of 2N. The resistance of the coating can be calculated from the induced current through the substrate. The detection of the current can be between 0-1 amps through the coatings. From the current detected and

66

voltage, the resistance can be calculated. The Brockhaus franklin tester follows the international standard IEC 60404-11. A sample is divided into four sections across the substrate, and a test is done.
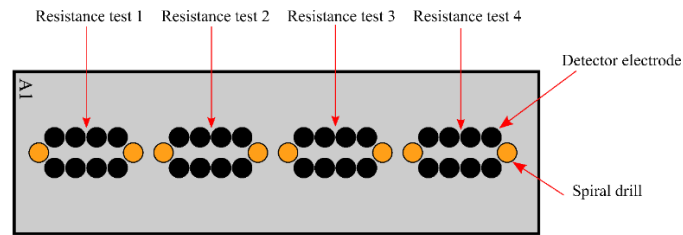
Figure 58. Is a sample in which the location of readings of Franklin tester were conducted.

2.10 TN 400Leco Nitrogen.

The TN400 determines the total nitrogen and oxygen content of steel samples. The determination of nitrogen and oxygen is achieved through the thermal conductivity of gases that are released from the sample when subjected to a high current. The oxygen from the sample combines with the carbon from the graphite crucible and forms carbon monoxide (CO) and (CO_2) carbon dioxide. The carbon dioxide is removed by reacting with a catalyst lecosorb filter (copper oxide), and water vapour is removed through an Anhydrone® filter. The gases of interest are analyzed in the thermal conductivity cell.

The 400Leco is equipped with two filaments that are supplied with a constant gas flow. In this case, helium gas is used as the carrier gas. The oven temperature is held at 50ºC to remove variation that is experienced at room temperature. One of the filaments is only subjected to the carrier gas, which is known as the reference filament. The second filament is subjected to the gases released from the sample and the carrier gas. This filament is known as the measurement filament. If both chambers only consist of helium, then the output is zero. However, if the measurement filament has nitrogen present this will change the output. Since the thermal conductivity of nitrogen is lower than helium, the temperature of the measurement filament will increase, which is dependent on the concentration of nitrogen present. This will result in a change in current in the filament, which creates an output that is transmitted to a preamplifier and is converted to digital reading.

Figure 59. Image of 400Leco used for detecting the content of the Oxygen and Nitrogen levels.

2.11 CS844 Carbon.

The C844 analyzer can determine the carbon and sulfur content of the steel samples. The CS744 combusts 1 gram of sample through radio frequency induction in an oxygen atmosphere. The carbon and sulfur that is released from the sample oxidize to form carbon dioxide (CO_2) and sulfur dioxide (SO_2). The carrier gas oxygen transports the oxides through a drying reagent (Anhydrone® and quartz wool). The sulfur (SO_2) is detected using non-dispersive infrared. The gas then continues to the heated catalyst, where the sulfur dioxide is converted to sulfur trioxide (SO_3), which is then removed by the cellulose filter. The carbon monoxide (CO) is converted to carbon dioxide (CO_2). A second non-dispersive infrared cell is used to detect the CO_2 content. The CO_2 and SO_2 have a unique inferred wavelength, and through concentrations of known standards, the concentration of carbon and sulfur can be calculated.

Figure 60. Image of CS844 Leco analyser used to determine carbon and sulphur content.

2.12 Erichsen Conical Mandrel Bending Tester

The Erichsen conical mandrel bending tester is a method to evaluate the adhesion and flexibility properties of coatings when subjected to a bend stress. Test sample size is 75mm by 150mm which is placed in the sample clamp. The pivoted roller is pulled over the conical mandrel with the use of a lever. Drawing the sample between the pivoted roller and the conical mandrel results in the sample being bent with a tighter radius at one end and a larger radius at the other forming a cone shape. The coating is examined for any delamination or cracking in the Forsterite. Coating or delamination will appear white and possibly display the bare substrate underneath the Forsterite. This is graded between 1 and 7, where 7 is good coating adherence due to this being the region where the substrate is bent over a small radius without delamination or cracking of the coating. The Erichsen conical mandrel bending tester Model 312 follows BS EN ISO 6860:2006 and BS 3900 E11:2006 were the dimension of the smallest diameter 3.1 (±0.1) mm and large diameter 38 (± 0.1mm) and the length is 203 (±3mm).
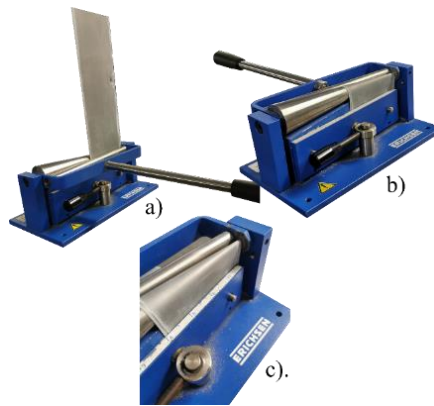
Figure 61. a) Erichsen conical mandrel bend tester with a sample place in clamp **b)** shows the lever press over conical mandrel, **c)** a close-up of the surface of the substrate.

2.13 Brookfield Viscometer

The Brookfield dial reading viscometer, as shown in Figure 62a) is used to measure the viscosity of liquids using a submerged rotating spindle. There is a variety of spindles provided to measure the range of viscosity of liquids. The spindle used to measure the slurry viscosity is an LV-1 spindle (Figure 62b) supplied by Brookfield. The Brookfield viscometer requires a level surface and the slurry to be submerged to the notch on the spindle. The torque measurement accuracy is 1% of the full-scale range and repeatability of 0.2% of the full-scale range. The viscosity of the mixes was measured five times before applying the slurry to the substrate and repeated when the slurry had been removed from the roller coating tray and remixed.

Figure 62. a) Is a Brookfield viscometer **b)** is a LV-1 spindle.

2.14 Data Presentation

Due to the variation in results the data will be represented as box plots. Figure 63 describes the information contained in a box plot.
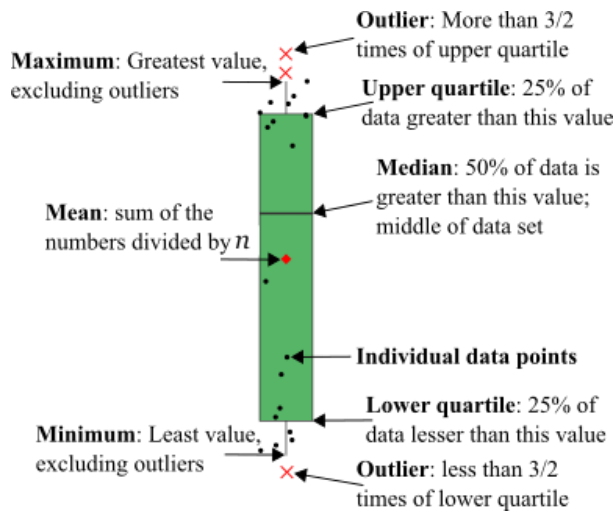
Figure 63. Explanation of box plot.

2.15 Glow Discharge Optical Emission Spectroscopy

The Glow Discharge Optical Emission Spectroscopy (GDOES) is a method for qualitative and quantitative analysis of metallic and non-metallic solid materials. This method is destructive and creates a crater of 3 mm diameter on the sample. The GDOES is capable of bulk analysis or compositional depth profiling. In this thesis, compositional depth profiling was used.

The method of compositional depth profile is explained in detail in the Glow Discharge Optical Emission Spectroscopy: A practical guide. Where it explains that Plasma is ignited, then argon ions bombard the sample surface. The sputtering then removes atoms from the surface of the sample into the plasma [118].
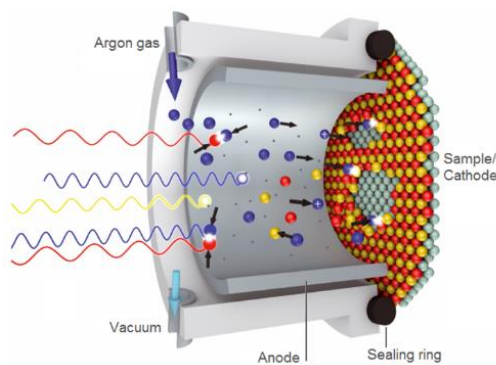
Figure 64. Demonstrating the sputtering at the surface of the sample that is occurring within the chamber[119].

The sample surface is devoid of easily sputtered atoms and enriched with more difficult to sputter atoms, and this is known as preferential sputtering. The rate of atoms being removed from the surface is proportional to their composition in the subsurface. Consequently, this results in the conservation of the mass while the crater bottom surface continues to be removed, causing the crater to get deeper and deeper[118].

The atoms that are removed from the bottom surface through sputtering move by diffusion into the negative glow region of the plasma and the assumption that the diffusion process is in dynamic equilibrium[118]. The negative glow region of the plasma is then characterized by a relatively high density of charged particles and excited argon atoms. Using different processes, such as inelastic collisions and charge transfer, some of the sputtered sample atoms are excited[118]. These exciting excited atoms then relax to a lower energy state resulting in the emission of characteristic photons that can be detected by the spectrometer [118].

2.15.1 Sample preparation

The sample preparation is simple as the technique only requires a surface roughness <20μm that has no contaminants such as grease. The sample size required is around 6mm in diameter to ensure a good seal with the O-ring and ensure a vacuum is produced.

2.15.2 GDOES Assumptions

Due to the large area being analyzed ($7.07mm^2$) and a non-uniform surface oxide thickness has led to an assumption to be made about the end of a uniform coating. The assumption presumes that the Mg oxide layer ends when the line of interception occurs between Fe and Mg. This assumption allows a definitive point to be calculated, and typically after this line of interception, the Mg concentration begins to diminish.

The oxygen levels were detected at very low levels, and typically a correction factor is used to correct the oxygen content detected. However, expertise and understanding in applying this correction factor were not well-known during this time the project was conducted. Therefore, this correction factor was not applied and only applies to the oxygen content.

It must be noted that the assumption of etching rates of elements is presumed uniform due to the limited time available on GDOES and expertise on the GDOES at Tata Steel innovation centre at Swansea Singleton campus. Therefore, if the etching rate of elements is not equal, it will result in peaks and troughs at the surface that is being examined. This will lead to incorrect elements detected, whether that would be above or below the surface of analysis of interest.

2.15.3 Evaluation of GDOES Results with SEM Images and EDS Analysis.

The GDOES technique was a new technique available to Orb Steelworks, and limited information on the technique and data was available for GOES. Therefore, it was essential to evaluate a sample at various times through the surface oxide to understand the distribution of elements across the area that has been analyzed. First, a single heat-treated sample was coated in the laboratory, as explained in section 2.3. The sample was then heat-treated in production furnaces (heat treatment c). The excess MgO powder was removed from the surface, and GDOES analysis was conducted. These areas that have undergone surface GDOES analysis at various durations were then surface imaged using SEM and EDS analysis to map the elements present at these regions. There must be some caution taken

with EDS analysis due to the interaction volume whereby detection of elements below the surface will be detected.
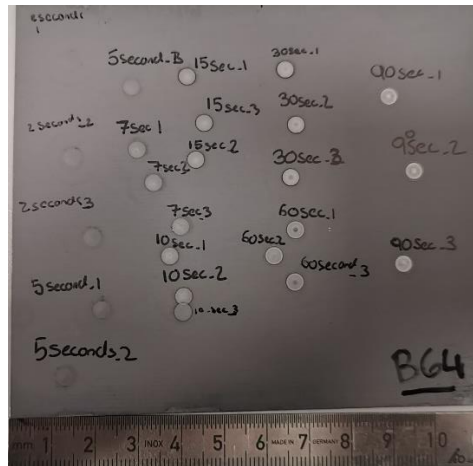
Figure 65. Displays the various duration of analysis conducted on a sample by GDOES method.

The duration of analysis by GDOES was varied between 2 seconds to 90 seconds to understand the composition of that surface at that region. It must be stated that each duration of analysis conducted has its own set of GDOES data, but the work presented will use the 90 seconds plot and assume that the composition change is comparable with all areas analyzed. Although the GDOES analysis is conducted for a set period of time the first ~2 seconds is locating the sample's surface before contact and analysis of the surface begins.
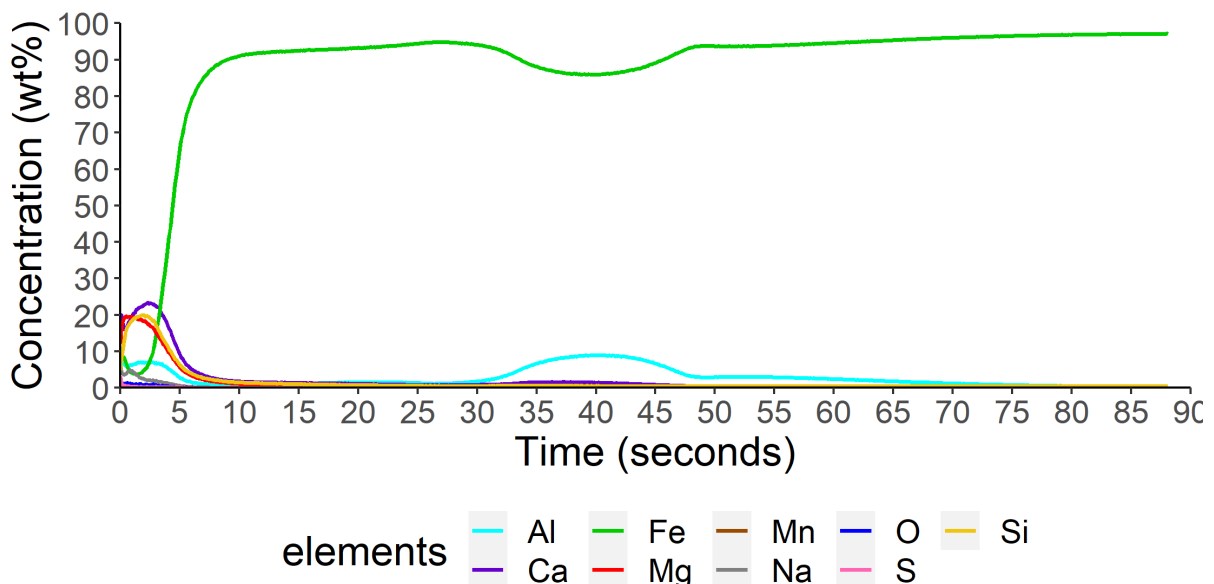
Figure 66. The result of 90 seconds run time of GDOES of a MgO coated sample and heat treated in production furnaces.

The results displayed in Figure 66 shows two regions of interest the first region between 0-10 second and the second region 30-65 seconds. There are multiple elements detected with Mg, Fe, Si, Ca, and Al all being present in the first region. These then reduce, and the second peak of Al is seen in the 30 – 65 seconds of the analysis.
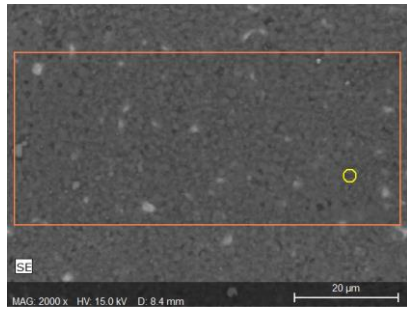
a) original surface
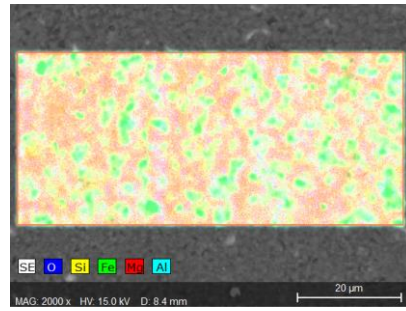
b) original surface
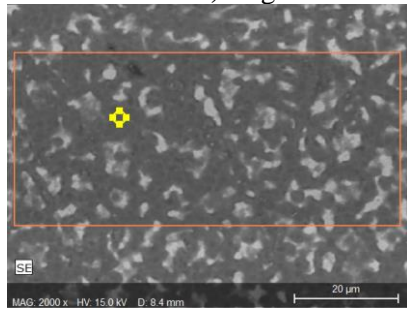
c) 0.1 seconds etch surface
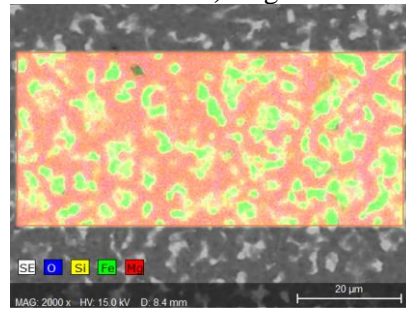
d) 0.1 seconds etch surface
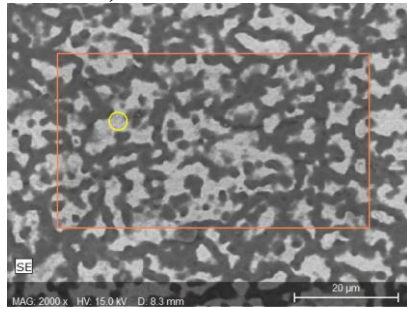
e) 3 seconds etch surface
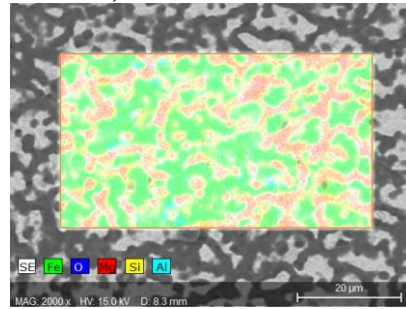
f) 3 seconds etch surface
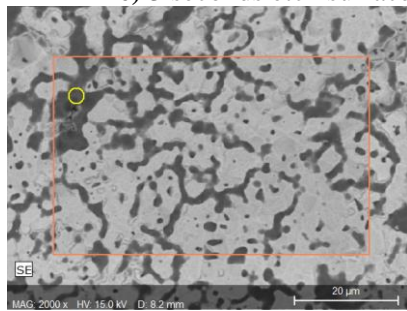
g) 13 seconds etch surface
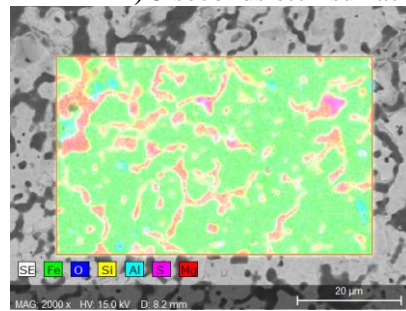
h) 13 seconds etch surface
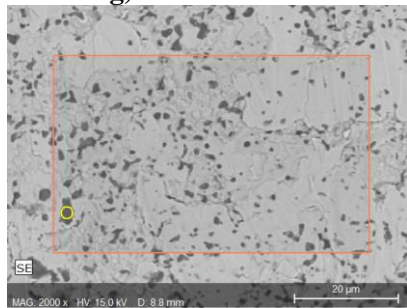
i) 28 seconds etch surface

j) 28 seconds etch surface

73

k) 58 seconds etch surface

l) 58 seconds etch surface

m) 88 seconds etch surface
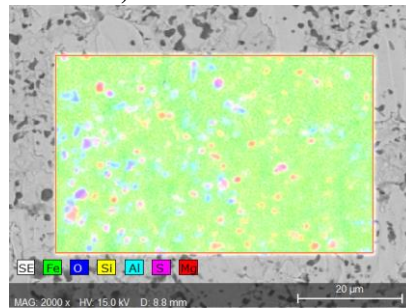
n) 88 seconds etch surface
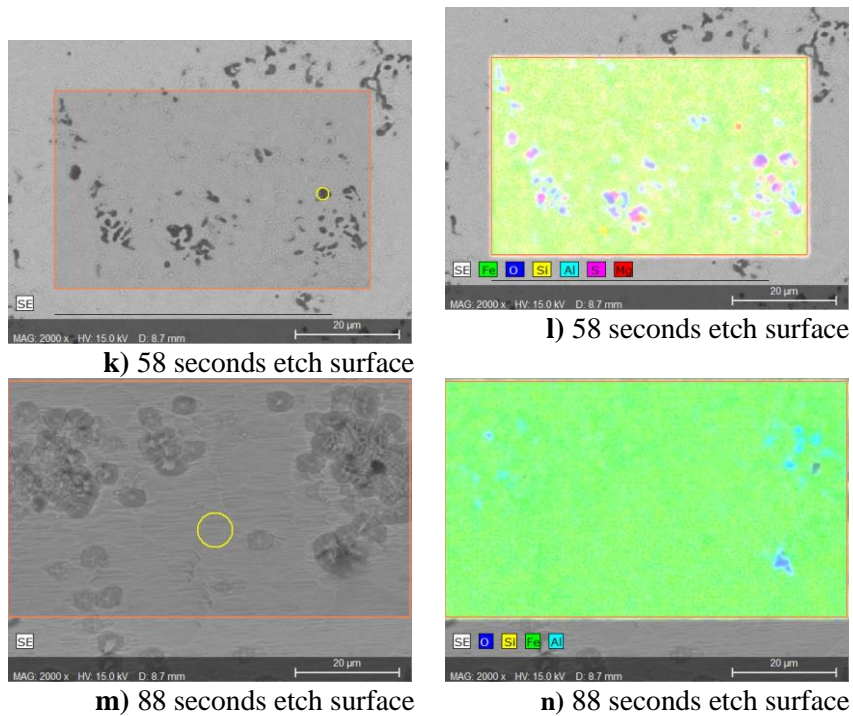
Figure 67. Surface SEM images and EDS analysis of GDOES analysed samples that have been analysed for various durations. a + b) SEM and EDS of surface oxide before GDOES analysis, c + d) SEM and EDS images analysed for 0.1 seconds by GDOES, e + f) SEM and EDS images analysed for 3 seconds by GDOES, g + h) SEM and EDS images analysed for 13 seconds by GDOES, i + j) SEM and EDS images analysed for 28 seconds by GDOES, k + l) SEM and EDS images analysed for 58 seconds by GDOES and m + n) SEM and EDS images analysed for 88 seconds by GDOES.

The surface of the samples before GDOES analysis shows a dark textured surface with a few bright spots present. From EDS point scans, these dark regions predominantly consist of Mg, O and Si, with some Fe detected as seen in Figure 68. One notable difference between GDOES and EDS analysis is the detection for oxygen with very low levels detected in the GDOES data but significant in the EDS analysis. The EDS analysis is supported by the TN 400 Leco analysis, which detects ~ 1000ppm of oxygen detected. Additionally, the Ca levels detected in GDOES are unexpectedly high. Whether this is linked with the error seen in oxygen is unclear, but the EDS found very little Ca detected in the EDS analysis.

a)

74

| Point Scan 1 | Point Scan 2 |
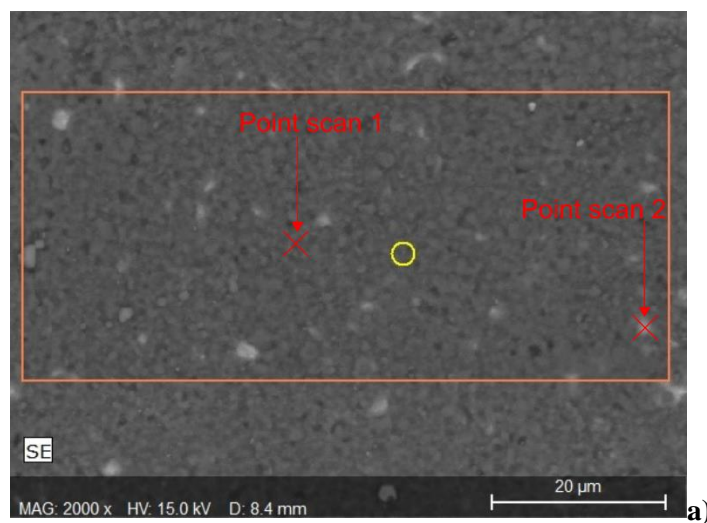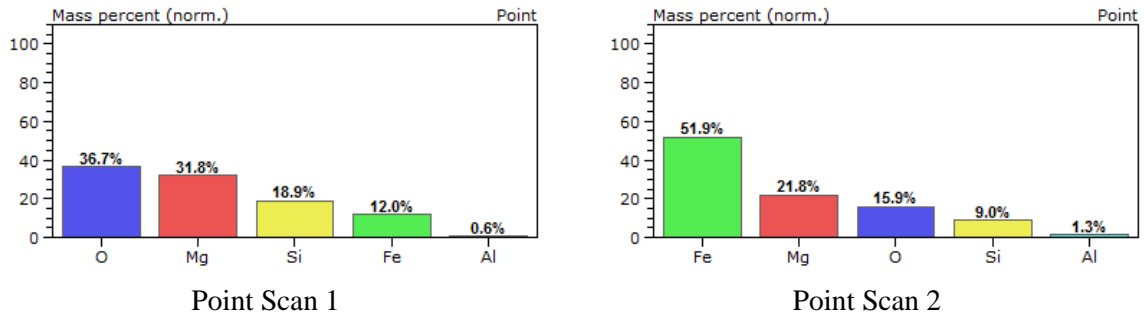
Figure 68. a) SEM image of the surface oxide before GDOES analysis has taken place with regions of point analysis have been taken.

The etch surface after 0.1 has produced an increase in the "bright regions" seen on the SEM image Figure 67 c), which can be seen as iron enriched regions.

After 3 seconds of etching (Figure 67 f), it has resulted in a considerable reduction in Mg enriched regions and an increase in iron concentration which correlates with the GDOES analysis where the Mg concentration is decreasing, and Fe is increasing. Also, there are pockets of enriched Al being detected throughout the EDS image.

At 13 seconds, the Mg has continued to reduce, and the iron concentration has increased, and pockets of S and Al are detected. Figure 67i+j) shows the complete reduction in Mg presence, and the presence of, i.e., Si, Al, and S is detected. At 88 seconds, many elements detected have completely dropped with only signs of Al and O enriched regions and dominated by Fe in the EDS analysis.

Chapter 3.   The Development of Surface Oxide During Heating Phase of the High-Temperature Annealing Process

3.1.1   Introduction

As explained in Section 1.2.6, the development of the Fayalite oxide layer during the decarbonization stage has been studied extensively, and the success of these changes of the Fayalite layer is frequently displayed as the success of the Forsterite thickness [71], [73], [120], [121]. However, there is limited information about the change in oxidation between Fayalite and Forsterite development during the HTCA process. The literature and phase diagrams suggest that the development of Forsterite occurs at 1200ºC, which is the maximum temperature that a coil will experience in production as seen in Figure 27. However, due to the nature of the production process, there are significant temperature gradients which means that the desired temperature is not always achieved [78]. In addition to the complex development of the Forsterite layer, Orb Steelworks adds TiO_2 and Borax to the MgO slurry, which is believed to improve the development of the Forsterite layer. However, the role in which these additives play to improve the oxide layer is unclear, and any data supporting these improvements come from production trials whereby monitoring of magnetic properties, visual inspections, and a small number of wet chemical analyses to determine the Forsterite layer thickness are the primary outputs.

The following chapter describes the change in morphology and chemical composition of the surface oxide through the heating stage of the HTCA process. It develops an understanding of when magnesium begins to develop as a surface oxide and the effects of TiO_2 and Borax using current proportions that Orb Steelwork has on developing the Forsterite layer.

3.1.2   Methods

The following section outlines the details of the substrate selection, the amount of addition, coating method, heat treatment and analysis conducted on the heat-treated samples presented in this chapter. Further details on all described processes can be found in Methods and Materials Chapter 2.

The substrate used for all the samples in this chapter was J15155 collected from the exit of D-line at Orb Steelworks and reduced to $350 \times 100 \times 0.23$mm samples. The morphology of the Fayalite is displayed in Figure 69, a typical example of the sample under SEM.
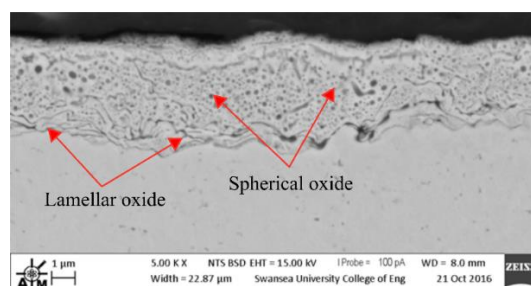
Figure 69. A standard Fayalite oxide layer was developed at Orb Steelworks at the end of the decarburisation stage of the process.

The additives that were added to the magnesium slurry were TiO_2 and Borax. The quantity and combination of these additives are displayed in Table 8, and these quantities are the proportions that Orb Steelworks currently use in production. The MgO and additives were added in distilled water that was chilled at 10ºC and mixed for 1 hour before the coating was applied to the substrate. The viscosity and pH of the slurry were tested for each mix. The heat treatment and experiments were conducted on mixture MgO + Borax samples but showed no significant changes compared to MgO only and MgO + TiO_2+Borax. This will be included in the Chapter 7section.

Table 8. Illustrates the quantity of ingredients used to create the various percentages of additives to create the desired slurry.

Mix	MgO	TiO_2	Borax $(Na_2B_4O_7)$	Distilled water (ml)
MgO Only	112g	-	-	800
MgO + TiO_2	112g	4.80g	-	800
MgO + TiO_2 + Borax	112g	4.80g	0.092g	800
MgO + Borax	112g	-	0.092g	800

The samples were coated at Orb Steelworks using the custom laboratory roller coater. The slurry applied to the substrates was dried in the Nabertherm furnace at 750ºC until the water has been driven out of the MgO slurry. The samples were individually weighed before and after coating.

All mixtures and reference samples were placed in a stack with sacrificial samples between different mixes. The stack of samples was then placed between two steel heat treatment blocks, secured with metal banding in a cross configuration to ensure intimate contact between layers mimicking the environment within a coil.

Heat treatment was carried out within Orb Steelworks bespoke Carbolite GPC 1300 furnace. The stack of banded samples was placed in the furnace and followed the heat treatment cycle carried out by Orb Steelworks and followed annealing cycle b) in which the annealing cycle stopped at the following temperatures 700ºC, 900ºC, 950ºC, 1000ºC, 1050ºC, 1100ºC and 1150º. Once the desired temperature had been achieved, the samples were held at this target temperature for 3 hours to ensure a homogeneous temperature had been achieved. After this soak period the samples were cooled to room temperature within the furnace.

On completion of the heat treatment in the laboratory, furnace samples were removed from the furnaces and banding was removed. Excess magnesium powder was removed from the surface with distilled water and a cloth.

A minimum of 5 samples per additive was analysed. A wide range of analyses was conducted to evaluate the magnetic properties, resistance, bulk composition, coating thickness and chemical composition of developed surface oxide. The following methods were used to evaluate the samples:

- SEM cross-sectional

- GDOES depth profiling surface oxide
- LECO bulk analysis of elements (C, O, N and S)
- Soken testing magnetic performance.

The following chapter presents analyses from the samples examined using these techniques unless stated otherwise.

3.2 The Influence of the Heating Phase of the High-Temperature Annealing Process when Coated with MgO.

3.2.1 Morphology of Surface Oxide Developed

Figure 70 illustrates the morphology of the surface oxide after being heat-treated to 900°C with the MgO coating applied and cooled to room temperature in the laboratory furnace. The subsurface on the top and bottom surface has not shown any noticeable change in the Fayalite oxide layer that was developed during the decarburization processing. There is no noticeable layer developing at the surface of the substrate where the Fayalite and Mg interact.

(a)	**(b)**
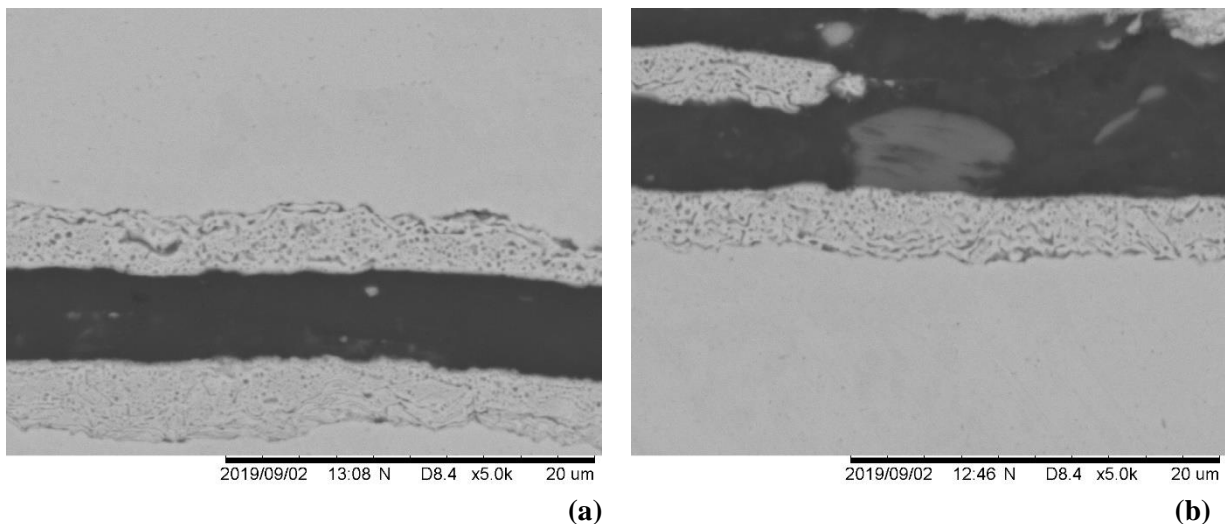
Figure 70. Representative morphology developed when heated to 900°C and coated with MgO only (a) up-facing surface (b) down-facing surface.

The morphology of the surface oxide when the HTCA is interrupted at 950°C is illustrated in Figure 71. The morphology of the top and bottom surface has changed at 950°C, and the morphology of the Fayalite layer has changed its structure compared to 900°C images and the decarburisation Fayalite images. The fine lamella and spherical structure are seen in the decarburization have transformed to a coarse spherical feature.

It appears that there is a difference observed between the top (Figure 71a) and bottom surfaces (Figure 71b), with larger globular structures developed in the bottom surface compared with the fine globular structure developed in the top surface. The spherical features have been identified as SiO_2 using TEM [122]. However, the bottom surface of the substrate (Figure 71b) has developed a uniform dark region

between the Fe matrix and the Fayalite region. The identification of the dark uniform layer has not been made.

(a) **(b)**
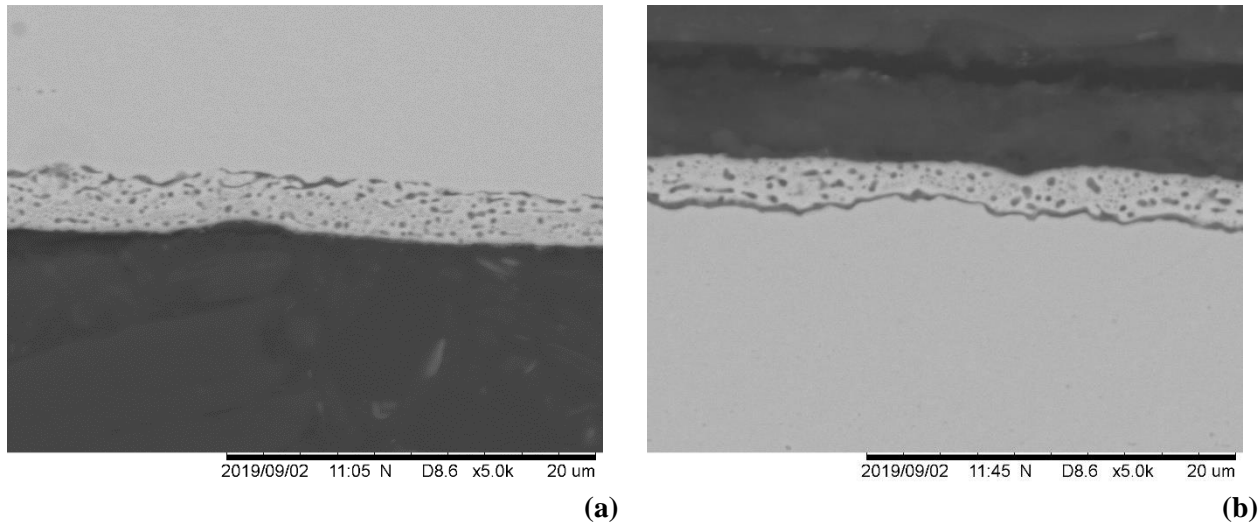
Figure 71. Morphology of the oxide annealed to 950°C and coated with MgO only (a) up-facing surface (b) downwards-facing surface.

The representative morphology of the surface oxide when the HTCA is interrupted at 1050°C is illustrated in Figure 72. The first signs of the desired surface oxide are seen in both top, and bottom images and the surface oxide appears to be a thin layer at the surface with regions of incomplete oxide formation visible. The subsurface oxide continues to coarsen and forms a range of sizes of subsurface oxides.

a) **b)**
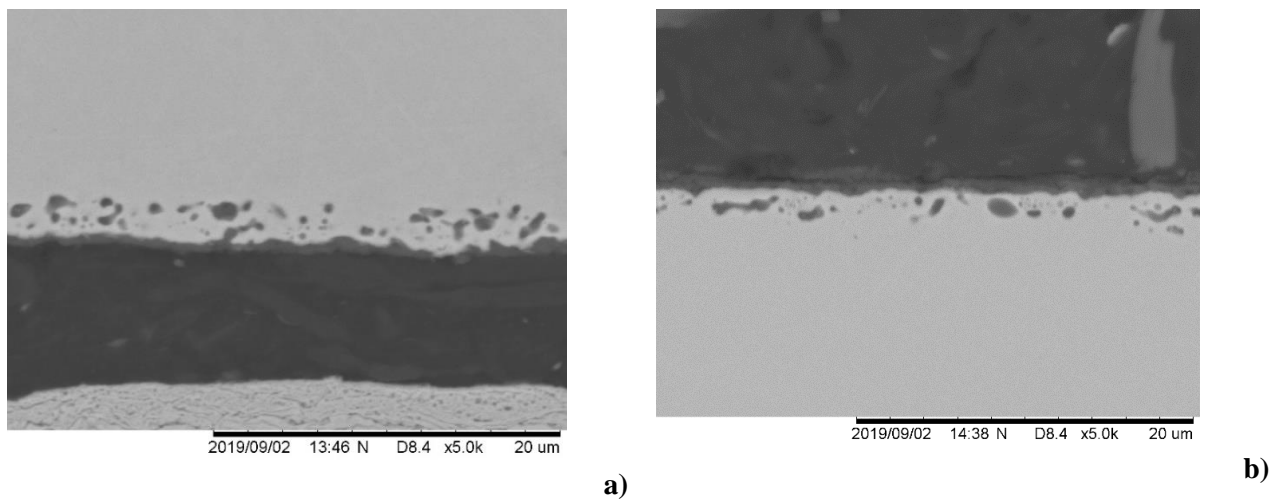
Figure 72. Morphology of the oxide, when annealed to 1050 oC and coated with MgO only (a) up-facing surface b) downwards facing surface.

Figure 73 demonstrates the oxide layer developed at 1100°C during the HTA. The development of the surface oxide appears to increase in thickness and consistency across the sample. In addition, the globular structures below the surface oxide have begun to coarsen further, and there are keying points that have begun to develop in the surface oxide.

2019/09/05 14:05 N   D8.4 x5.0k   20 um

a)

2019/09/05 14:51 N   D8.3 x5.0k   20 um

b)
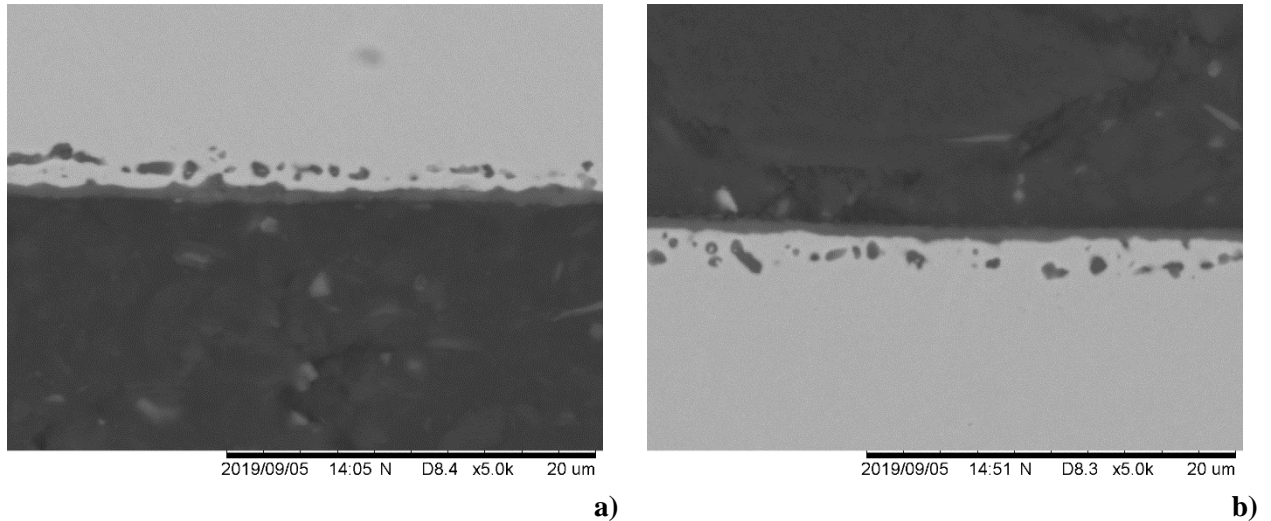
Figure 73. Morphology of oxide after annealing to 1100 °C and coated with MgO only a) up-facing surface b) downwards facing surface.

The oxide layer that has developed at 1150°C during the HTCA is shown in Figure 74. The globular structure below the surface oxide continues to coarsen, and there is no noticeable increase in oxide thickness.

2019/09/02 12:02 N   D8.3 x5.0k   20 um

a)

2019/09/02 12:13 N   D8.3 x5.0k   20 um

b)
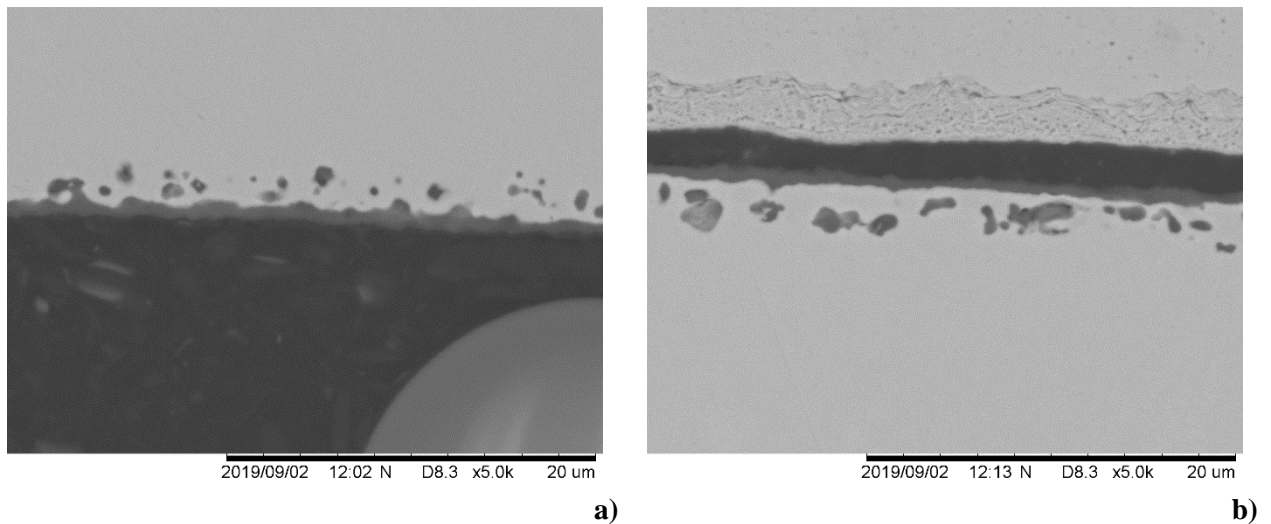
Figure 74. Morphology of the oxide after annealing to 1150°C and coated with MgO only a) up-facing surface b) downwards facing surface

The MgO coated samples begin to show changes in the surface oxide at 950°C with coarsening of the Fayalite layer, but no clear surface oxide developed. At 1050°C, a thin surface oxide layer has developed, but it is inconsistent and bare patches are present. However, a further increase (>1050°C) in temperature results in a continuous, uniform layer developed. When comparing 1100°C and 1150°C, no significant change is seen in the thickness of the surface oxide.

3.2.2   Composition Changes through the Surface Oxide using GDOES with MgO Only Coating.

The chemical composition of the surface, as measured using GDOES, of the substrate sample heated to 700°C using GDOES is illustrated in Figure 75, and further elemental plots are shown in Figure 76.

80

At 700°C, no noticeable changes have occurred throughout the surface of the substrate, and the plot is like the de-carburization plot using GDOES analysis.

Figure 75. Results change in chemical composition through the surface oxide to the substrate when coated with MgO only and heat-treated to 700°C.

On closer inspection of what is occurring at the surface in Figure 76 it illustrates that limited development in the surface oxide has occurred, but there are signs that magnesium is present at the surface. The Mg detection could be result of ineffective cleaning of the surface, especially as no other indication of change is apparent. The concentration of Al, Si and S and Mn have remained at low levels throughout the analysis. This indicates that minimal changes have occurred, and the precipitates remain effective, and the migration of such elements as silicon to the surface has not occurred.
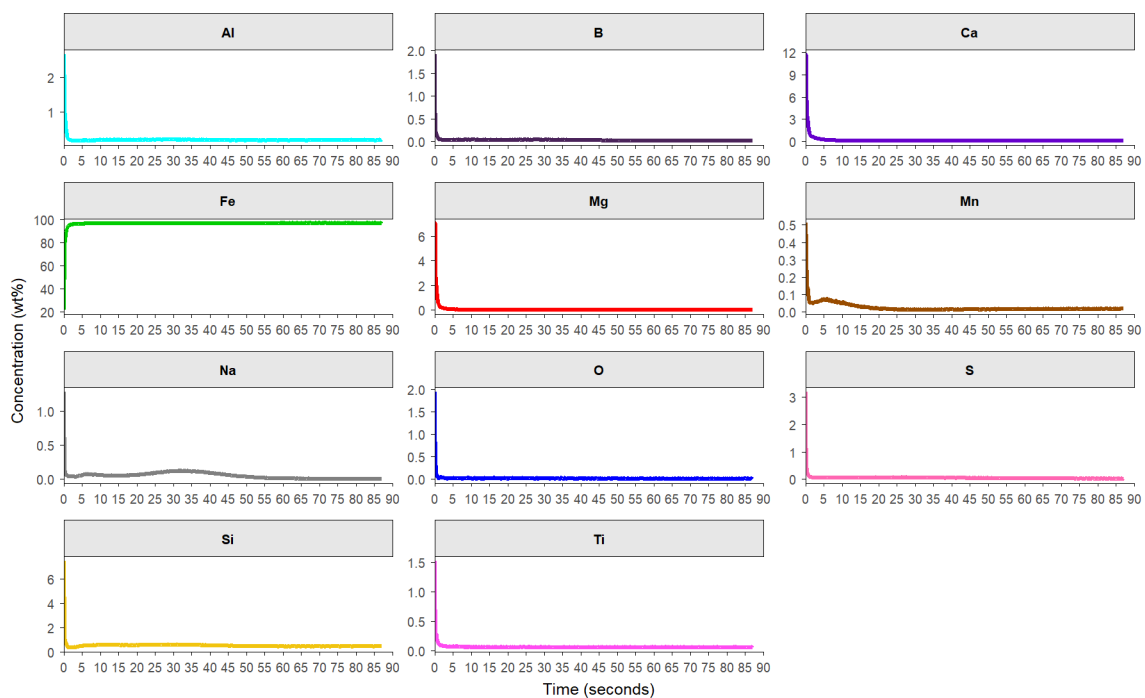
Figure 76. Individual line plots of each element that Figure 75 is composed of when a sample is coated with MgO only and heat-treated to 700°C following.

81

The surface oxide developed at 900°C is displayed in Figure 77 and Figure 78, whereby minor changes are seen in the composition at the surface. However, these changes cannot be confirmed due to variations seen in the composition of electrical steel.

Figure 77. Results change in chemical composition through the surface oxide to the substrate when coated with MgO only and heat-treated to 900°C.

As expected, the concentration Mg is highest at 0.0 second at 8.5%, and 0.5 seconds reduces to 2.0%, suggesting some diffusion of Mg into the surface has occurred at 900°C. The silicon concentration in the substrate is around 3%, though the concentration levels have increased to 7.1% at 0 seconds at the surface and begin to decrease, as Figure 76 displays immediately. Additionally, aluminum concentration has increased at the surface with a maximum of 2.9% at 0 seconds and reaches 1% at 0.5 seconds. This is an indication Al-N particle have begun to break down, and as a result, the aluminum is diffusing to the surface. This is also a sign that secondary crystallization has begun. The subtle changes are seen in the morphology (Figure 71) with coarsening of spherical oxides. Although detection of Mg has increased, there is no clear apparent layer developed at the surface, but it may be that the preparation of samples has resulted in the removal of the magnesium layer.

Figure 78. Individual line plots of each element that Figure 77 comprises when a sample is coated with MgO only and heat-treated to 900°C.

At 950°C, there is a rapid and significant change in the surface oxide that is illustrated in Figure 79. The Fe concentration drops at the surface due to several elements (Al, Si, Mg and S). However, decreased Fe is still prevalent amongst these elements.

Figure 79. Results change in chemical composition through the surface oxide to the substrate when coated with MgO only and heat-treated to 950°C.

On closer examination, the concentration of numerous elements at the surface is initially detected at high levels at the surface and then start to decrease when etching into the substrate. The magnesium reaches a maximum of 18.1% at 0.1 seconds and then decreases to 1.1% at 2.9 seconds. Further diffusion of Al to the surface has continued with a maximum concentration of 4.2% at 0.7 seconds. The silicon concentration reaches a maximum of 5.3% at 0.8 seconds.

The detection of magnesium at 2 seconds at 2.61% indicates that magnesium forms at the surface and into regions of the substrate. Similarly, the high concentration of silicon and aluminium at the surface demonstrates that these elements are migrating from the bulk of the substrate to the surface. The change in chemical composition at the surface reflects what is seen in the morphology displayed in Figure 71, where a distinct oxide layer has developed at the surface.
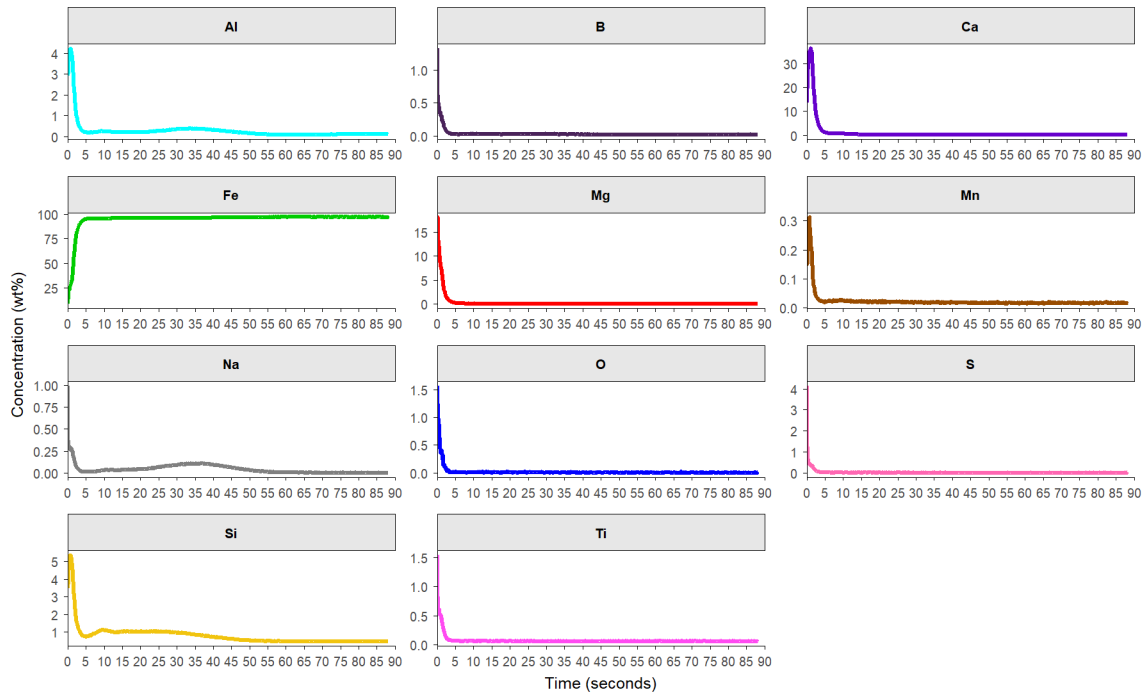
Figure 80. Individual line plots of each element that Figure 79 comprises when a sample is coated with MgO only and heat-treated to 950°C.

At 1050°C, significant changes at the surface have occurred, and the first signs of the suppression of Fe (when compared to other elements) present at the surface of the substrate are apparent. The increase in temperature has resulted in a higher concentration of detected Al and Si at the surface/subsurface oxide region, as seen in Figure 81. This increase in Al detected at the surface oxide indicates a continuation of breaking down Al-N. The presence of Na has appeared; however, the explanation of the presence of Na is not understood.

Figure 81. Results change in chemical composition through the surface oxide to the substrate when coated with MgO only and heat-treated to 1050ºC.

Figure 82 focuses on the individual elements detected in the substrate and shows Mg is suppressing the Fe concentration with the Mg_{max} reaching 22.3% at 0.2 seconds and the line of interception of Mg-Fe is at 3 seconds. The presence of Mg at the surface indicates that the coated slurry has diffused into the surface to form the oxide. The silicon concentration has also increased, reaching a maximum of 17.1% at 2.9 seconds which implies that silicon is accumulating at the surface, which is sourced from the bulk of the material. There is a presence of S at the surface with a concentration of 2.4% at 0.1 seconds and drops to 1% by 0.5 seconds. The second peak of Al is seen at 27.2 seconds with an Al_{max} of 2.6%. The increase in temperature has allowed for Mg to form at the surface of the substrate significantly and diffuse into the substrate forming an Mg oxide enriched layer, and this change is seen in the surface oxide cross-sectional image in Figure 72. The increase in temperature has resulted in a breakdown of Al-N precipitates and Mn-S, allowing Al and S to diffuse towards the surface.
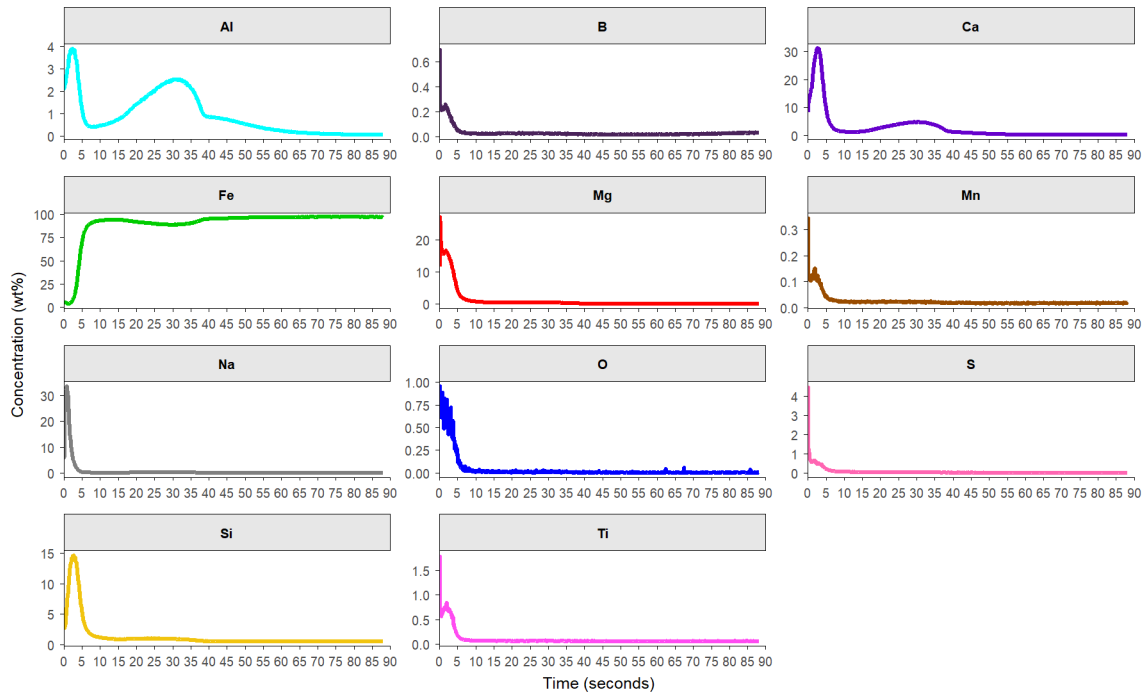
Figure 82. Individual line plots of each element that Figure 80 comprises when a sample is coated with MgO only and heat-treated to 1050ºC.

At 1100ºC has seen a continued intensification of elements diffusing into the surface of the substrate is observed, as illustrated in Figure 83. The suppression of Fe continues with the line of interception of Mg-Fe occurring at 2.5 seconds, whereby the Mg_{max} is 21.0% at 0.2 seconds.
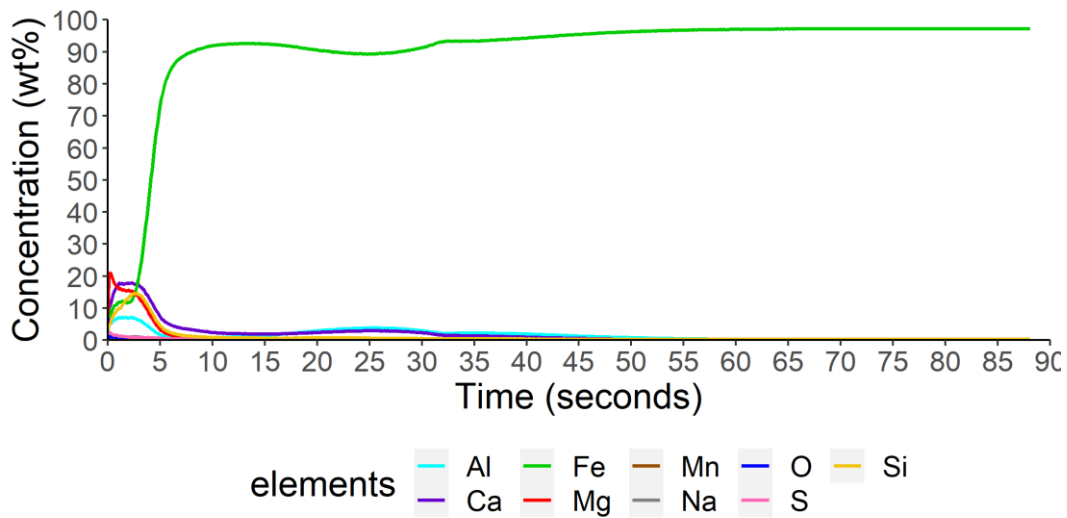
Figure 83. Results change in chemical composition through the surface oxide to the substrate when coated with MgO only and heat-treated to 1100ºC.

The movement of elements from the bulk material to the surface continues with temperatures reaching 1100ºC. Elements such as S and Al have further increased their presence at the surface with S_{max} 2.7% at 0.1 seconds and begins to decrease to 1% at 2.9 seconds. Al_{max} at the surface reaches 7.2% at 1.1 seconds, and the second peak reaches 3.9% at 24 seconds. Silicon remains consistent, with Si_{max}

86

reaching 14.6% at 2.7 seconds. The morphology of the surface oxide displayed in Figure 73 does not show apparent changes compared to the 1050°C morphology (Figure 72).
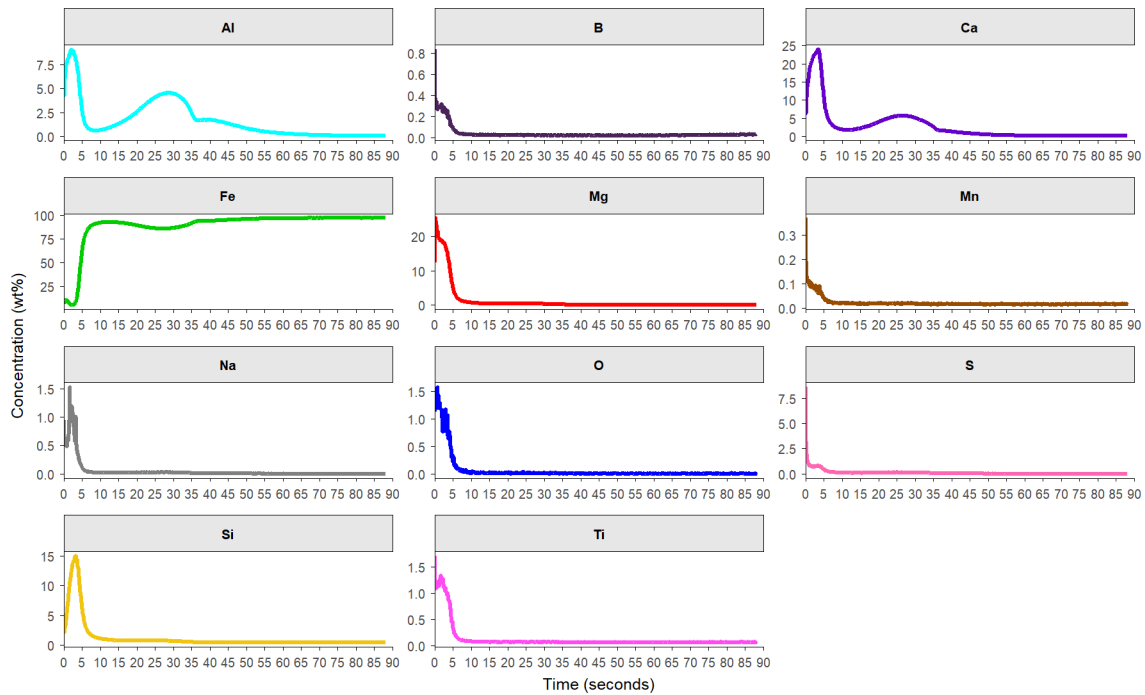
Figure 84. Individual line plots of each element that **Figure 83** comprises when a sample is coated with MgO only and heat-treated to 1100°C.

At the maximum temperature studied at 1150°C, there is a sizeable change in the second peak of Al where the Al_{max} is 7.0% at 31.8 seconds and the peak of Al reaches 14.2% at 2.2 seconds, as displayed in Figure 85. This indicates that Al is continuing to migrate from the bulk of the material towards the surface.
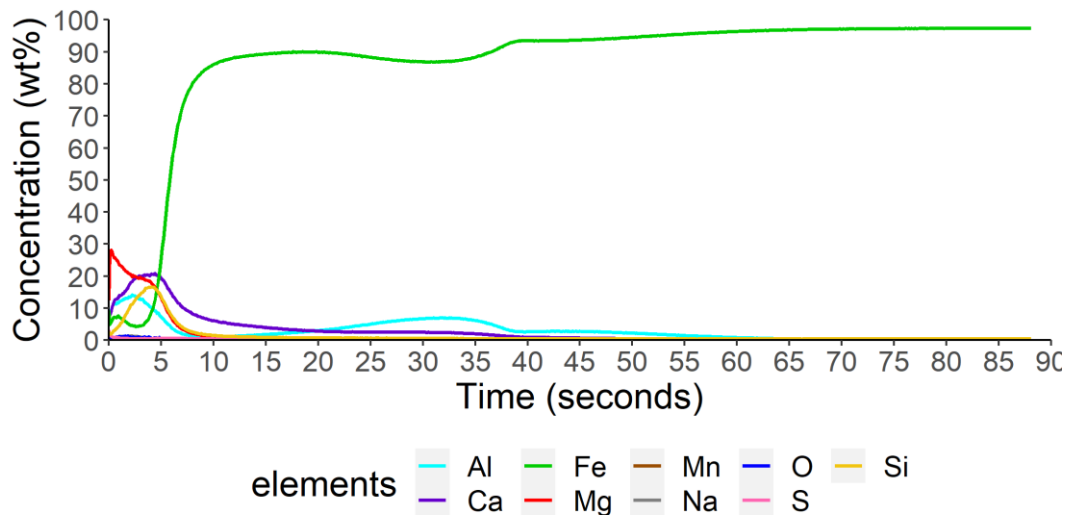
Figure 85. Results change in chemical composition through the surface oxide to the substrate when coated with MgO only and heat-treated to 1150°C using GDOES.

As seen in Figure 86, the line of interception between Mg-Fe occurs at 4.6 seconds with a Mg_{max} of 28.2% at 0.2 seconds. The S_{max} reaches 3.11% at 0 seconds and reaches 1% by 0.4 seconds. The silicon concentration reaches 16.6% at 4.1 seconds.
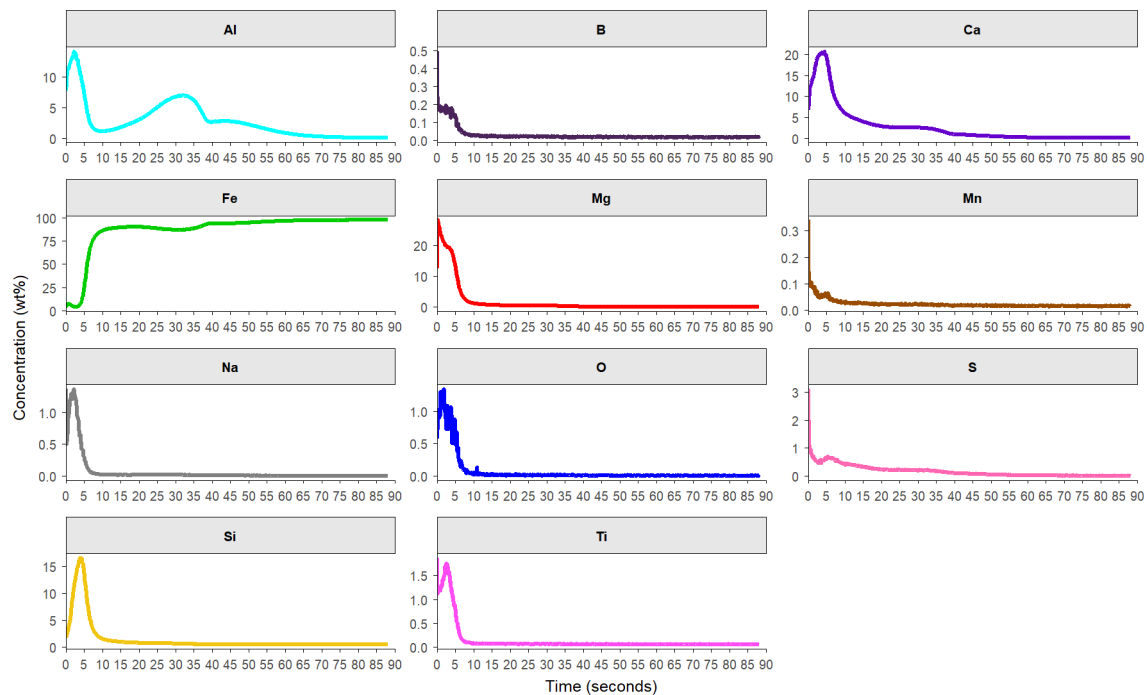
Figure 86. Individual line plots of each element that **Figure 85** is composed of when a sample is coated with MgO only and heat-treated to 1100°C following HTCA annealing profile.

The MgO coating shows signs of evolution with the development of an Mg enriched surface occurring when temperatures reach 950°C. However, the amount of Mg diffused at the surface is not enough to reduce the levels of Fe at the surface. As well as a development of an Mg enriched surface, the diffusion of Al and Si from the substrate to the surface is observed at 950°C, and this is an indication that secondary recrystallization is occurring. At 1050°C, the first signs of a dominant Mg layer appear, resulting in the reduction in the concentration of Fe and the continuation of Al and Si diffusing towards the surface, resulting in a second peak of Al detected in the subsurface area. At 1050°C, a significant Mg presence occurs at the surface where Fe is suppressed, but there are no apparent changes in the chemistry apparent with a further increase in temperature. The detection of Ca is not fully understood, however one possibility it could be result of degradation of refractory bricks resulting in contamination. The refractory bricks were placed at either end of samples to prevent welding of the sample blocks to the refectory. These bricks were initially white but after a single heat treatment turn black after an HTA.

3.2.3   Magnetic Properties with MgO Only Coating

Figure 87 illustrates the result of the magnetic testing of the substrates that have followed the HTCA profile and have been interrupted during various stages of the process. The magnetic testing used the Soken tester, as explained in Section 2.8. The increase in temperature has affected the magnetic

properties. At 1050ºC, there is a critical development in magnetic properties, whereby secondary crystallization appears to have partially occurred, agreeing with previous work showing this temperature region is secondary recrystallisation occurs [123], [124]. In addition, there is a continued reduction in magnetic losses measured on further increases in temperature (>1050ºC). This continuation of improvement of magnetic properties can be related to the continued grain growth of GOSS grains, development of the surface oxide and purification of the substrate. This correlates to the observations in the GDOES data whereby a significant increase in surface Al is seen at 1050ºC, and a further increase in temperature results in further levels of Al detected at the surface.
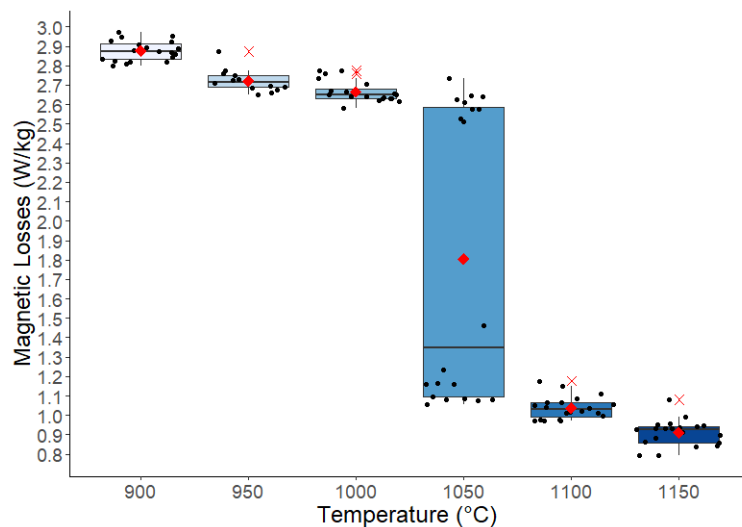
Figure 87. Magnetic properties at various temperatures following the HTCA heat cycle where the substrate has been coated with MgO only.

When comparing the magnetic losses in Figure 87 with the composition of the surface oxide in Figure 81, it displays the process of the breakdown of Al-N precipitates that prevent primary recrystallization during the early stages of the heat treatment. Once the Al-N has broken down, the Al then diffuses towards the surface of the substrate and forms as part of the surface oxide.

3.2.4 Current Detected Through Developing Oxide Layer with MgO Coated.

Figure 88 shows results from the conductivity assessment of the surface oxide using the Franklin test as explained in section 2.9, which has developed at the point of interruption of the HTCA profile. Figure 88 shows, the increase in temperature has decreased the current detected through the surface. The decrease in current detected results from an insulating layer being developed which is desired in electrical steel to prevent conductivity between laps when placed in a transformer. For this research, the data has been left as current, but resistance can be calculated.
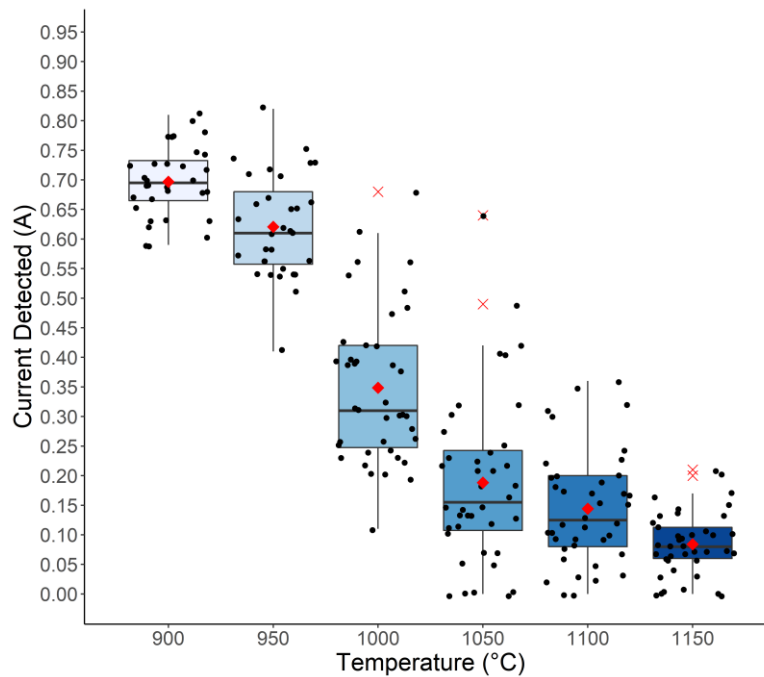
Figure 88. Magnetic losses at various stages of the heat treatment following the HTCA cycle using a soaking tester.

When comparing the results currently detected with the evaluation of the oxide development in sections 3.2.1 and 3.2.2, the development of the surface oxide has influenced the current detected by the Franklin tester. The reduction of the presence of Fe is required to be reduced at the surface to prevent a pathway for the current to travel to the surface. Therefore, a significant reduction of Fe at the surface oxide is required to get the desired resistance properties, with lower conductivity apparent as the coating becomes continuous and thicker with processing temperature.

3.2.5   Bulk Analysis of Carbon, Oxygen, Nitrogen and Sulphur

Figure 89 illustrates the nitrogen content detected in the substrate at various temperatures using TN400 Leco analysis. Figure 89 displays that an increase in temperature has resulted in a decrease in nitrogen content. This reduction in nitrogen content with increased temperate indicates that the Al-N precipitates are beginning to break down, and this will allow for secondary recrystallisation to occur and diffusion of Al to the surface of the substrate. This decrease in nitrogen content is related to the improvements in the magnetic properties displayed in Figure 87, whereby the precipitates have become ineffective and allowed secondary recrystallization to occur, enabling the desired large GOSS grains to develop.
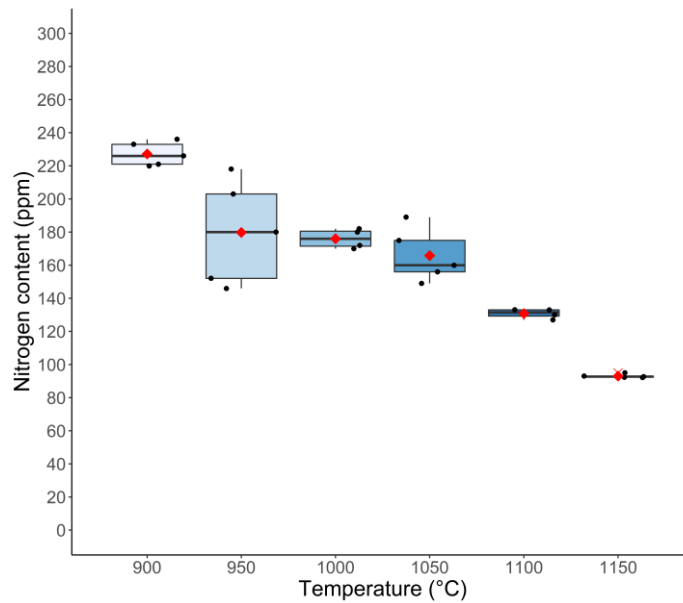
Figure 89. Nitrogen content present of the bulk substrate at various temperatures during the HTCA cycle collected by LECO TN400.

Figure 90 displays the results of sulphur content contained in the substrates using CS844 carbon Leco. As expected, the sulphur has fallen as the temperature has increased. The reduction of S implies that the Mn-S precipitates are broken down, allowing for secondary recrystallisation. Signs of sulphur migrating from the bulk of the material to the surface is seen in section 3.2.2. Additionally, the removal of sulphur impurities will improve magnetic properties by reducing domain wall pinning.
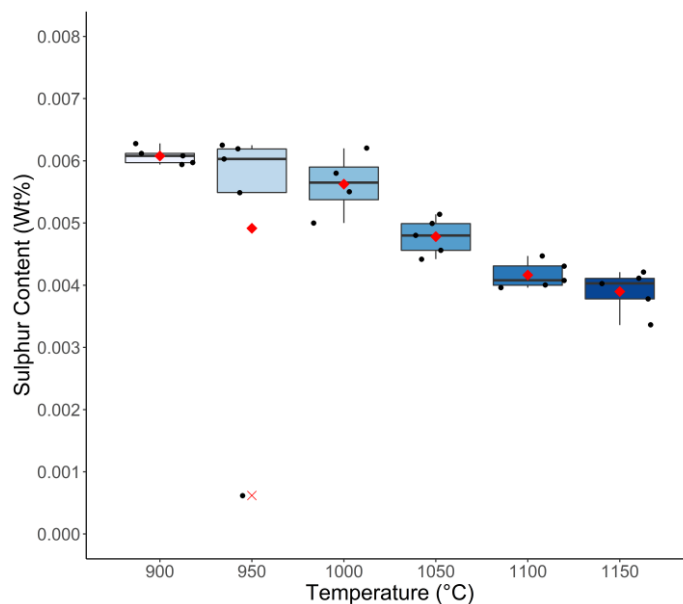
Figure 90. The sulphur content present of the bulk substrate at various temperatures during the HTCA cycle collected by LECO CS844 carbon.

Figure 91 illustrates the oxygen content detected in the substrate at identified temperatures through the HTA process using TN400 Leco analysis. As Figure 91 shows, the oxygen content increases with

91

the increase in temperature. This increase in oxygen content demonstrates that oxidation is occurring and can be linked with the development of surface oxide.
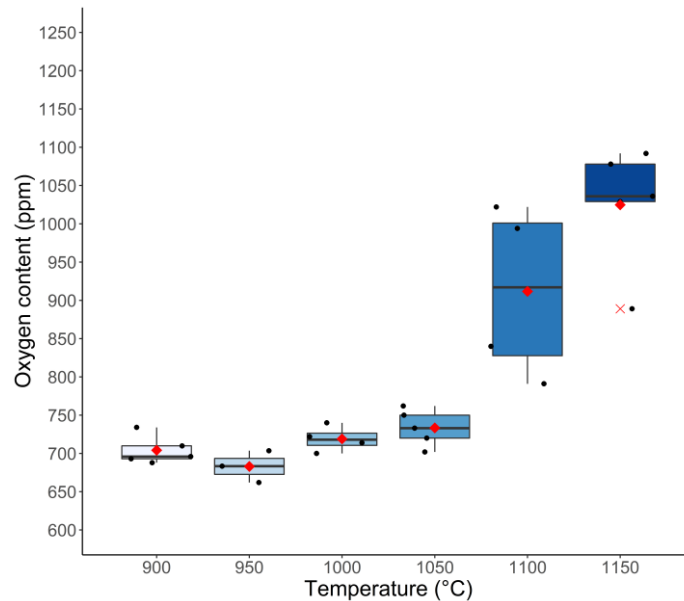
Figure 91. The oxygen content present of the bulk substrate at various temperatures during the HTCA cycle was collected by LECO TN400.

3.2.6 Discussion

As the temperature rises through the HTA, the microstructure and surface oxide experience a dramatic change in chemical composition and microstructure. At the surface, the fine lamellar and spherical "Fayalite" begins to coarsen into coarse spherical particles at 950°C and signs of magnesium diffusing into the surface can be observed. At the same time, the Ostwald ripening of Al-N and MnS begin to occur, and these migrate towards the surface, which is seen in the GDOES results in Figure 81, whereby Al and S increase at the surface.

The dissolved inhibitors allow a select few grains to have an advantage which allows faster growth than other grains. In the case of GOES, the desired grain orientation are "GOSS" grains that nucleate and grow over other orientations. This results in a decrease in the amount of energy required to create a magnetic field. This is represented in this body of work through the decrease in magnetic losses in Figure 87, whereby at 1050°C, the samples show a substantial reduction in magnetic losses. This dramatic change has been displayed in previous research whereby Electron Back Scattered Diffraction (EBSD) has shown that secondary recrystallisation occurs at 975°C, and by 1050°C, the GOSS grain is dominating the microstructure of the electrical steel[125]. This research suggests that at 1050°C, a rapid change occurs, the rapid grain growth of GOSS grains.

Upon a further increase in temperature, i.e., > 1050°C, further improvements are seen in magnetic properties, which correlates with the increase in Al, S and Si present at the surface region detected in GDOES scans the decrease in nitrogen and sulphur content in the substrate.

92

The development of the "Forsterite" has always been believed to occur at temperatures >1200ºC when observing the binary phase diagram of Fe_2SiO_4 – Mg_2SiO_4 [78], [126]. However, the development of the Forsterite layer may occur at significantly lower temperatures compared with the phase diagrams suggest. With detection of Mg by GDOES at 950ºC (Figure 79) which suggest that the Forsterite begins to develop. The detection of Mg intensifies with an increase in temperature.

The increase in Mg at the surface has caused a decrease in the current detected through the surface of the steel, suggesting that an insulation layer has been created. With the increase in Mg detected, there is an increase in O detected using Leco TN400, indicating that oxidation has occurred. Further analysis is required to identify the compound that is present in Mg enrich using X-Ray Diffraction (XRD) and/or X-Ray photoelectron spectroscopy (XPS). An increase in temperature results in an increased presence of Mg at the surface, indicating that more Forsterite is developing at the surface, but the process starts at 950 degrees.

3.3 The Development of Surface Oxide during the Heating Phase of High-Temperature Annealing with MgO+TiO₂ Only Slurry.

Titanium dioxide is one of the additions to the magnesium slurry by Orb Steelworks to enhance oxide development during the HTCA. TiO_2 is commonly stated to improve the coating thickness and consistency. However, there is limited information available as to what role TiO_2 plays and when TiO_2 influences oxide development. This section will investigate the influence TiO_2 has during the heating process of the HTCA.

3.3.1 Morphology of Surface Oxide Developed

The morphology in Figure 92 illustrates a representative oxide developed at the top and bottom surface of a heat-treated sample when heated up to 900°C during an HTCA cycle. The effect of heating the substrate to 900°C has not demonstrated any noticeable changes in the morphology compared to the Fayalite produced in the decarbonization stage.

2019/09/09   11:41 N   D8.1   x5.0k   20 um
a)

2019/09/09   11:32 A   D8.1   x5.0k   20 um
b)
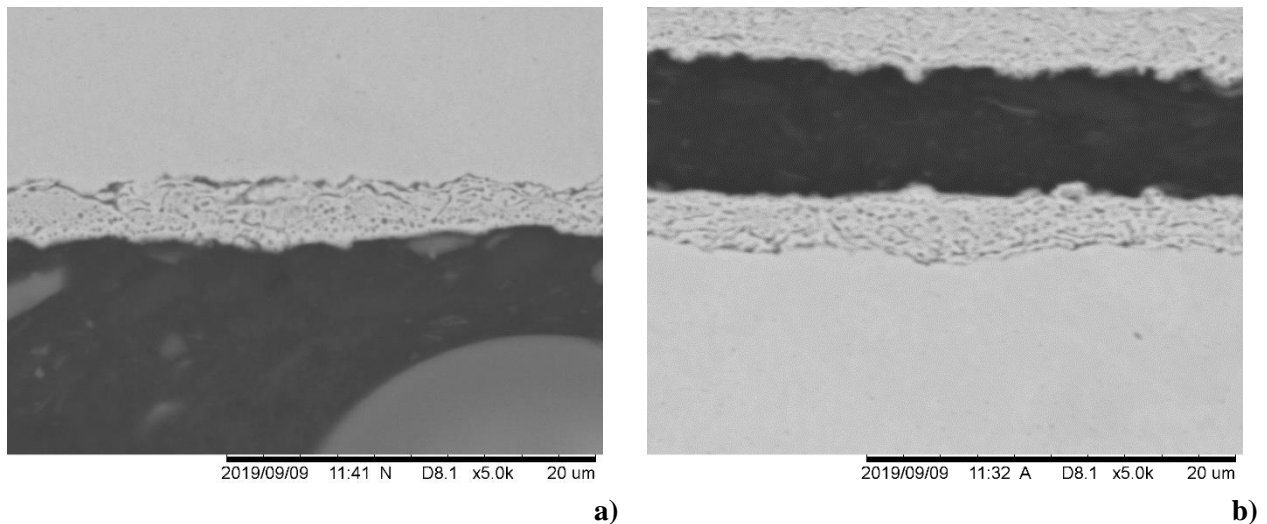
Figure 92. Morphology of the oxide annealed to 900°C and coated with MgO + TiO_2 only (a) up-facing surface (b) downfacing surface.

The morphology of the surface oxide when the HTCA is interrupted at 950°C is illustrated in Figure 93. The fine globular and lamellar structure seen at 900°C has dramatically changed to a course globular structure with a reduction in lamella structure seen in the surface oxide.
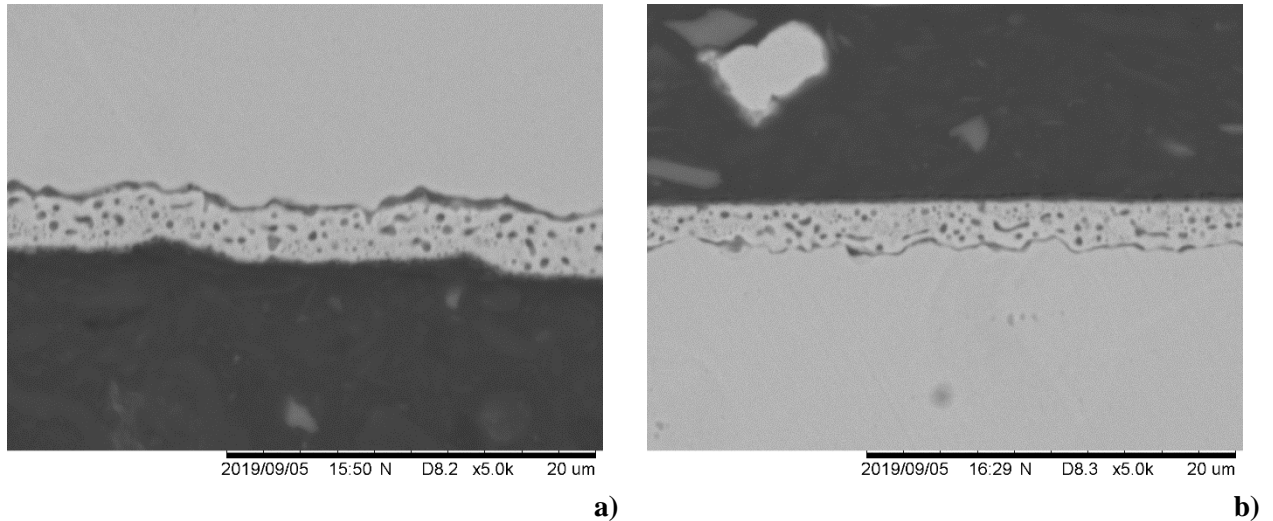
Figure 93. Morphology of the oxide annealed to 950°C and coated with MgO + TiO₂ only (a) up-facing surface (b) downfacing surface.

Figure 94 illustrates the surface oxide that has developed at 1050°C with a TiO$_2$ addition to the slurry. The first signs of a continuous oxide layer have developed at the surface, with globular subsurface oxide remaining below the surface. There are no apparent influences by the TiO$_2$ addition on morphology or thickness of the surface oxide when compared to the MgO only mixture (Figure 71).
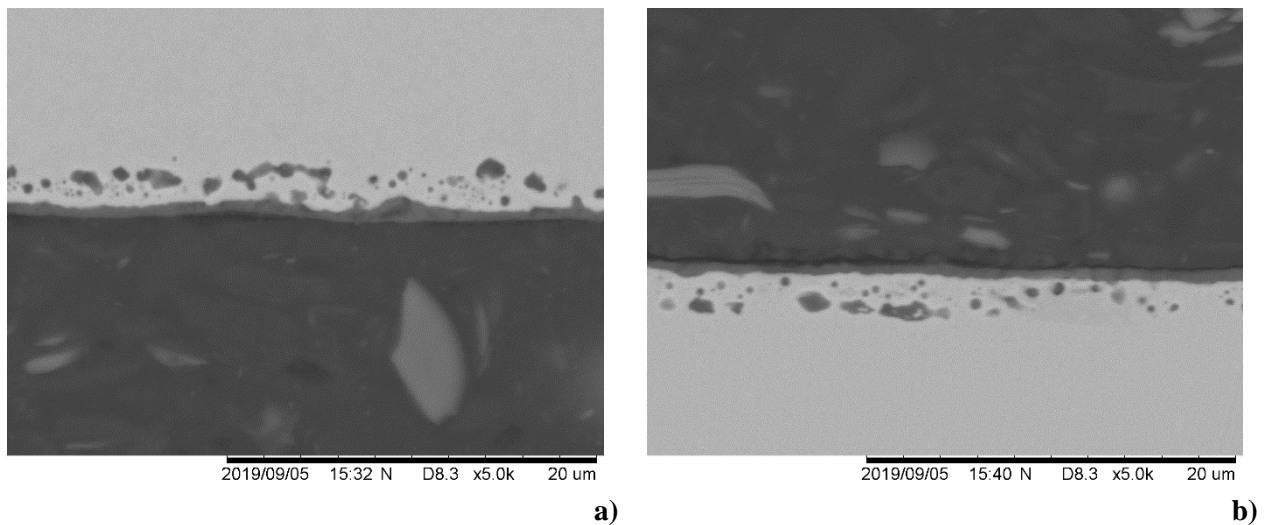
Figure 94. Morphology of the oxide annealed to 1050°C and coated with MgO + TiO$_2$ only (a) up-facing surface (b) downfacing surface.

Figure 95 illustrates the oxide layer developed with a TiO$_2$ addition to the MgO slurry at 1100°C following the HTA cycle. Again, there is no apparent increase in oxide thickness developed at the surface when compared to 1050°C (Figure 94), but it does appear that keying points have begun to develop in the bottom surface (Figure 95b).
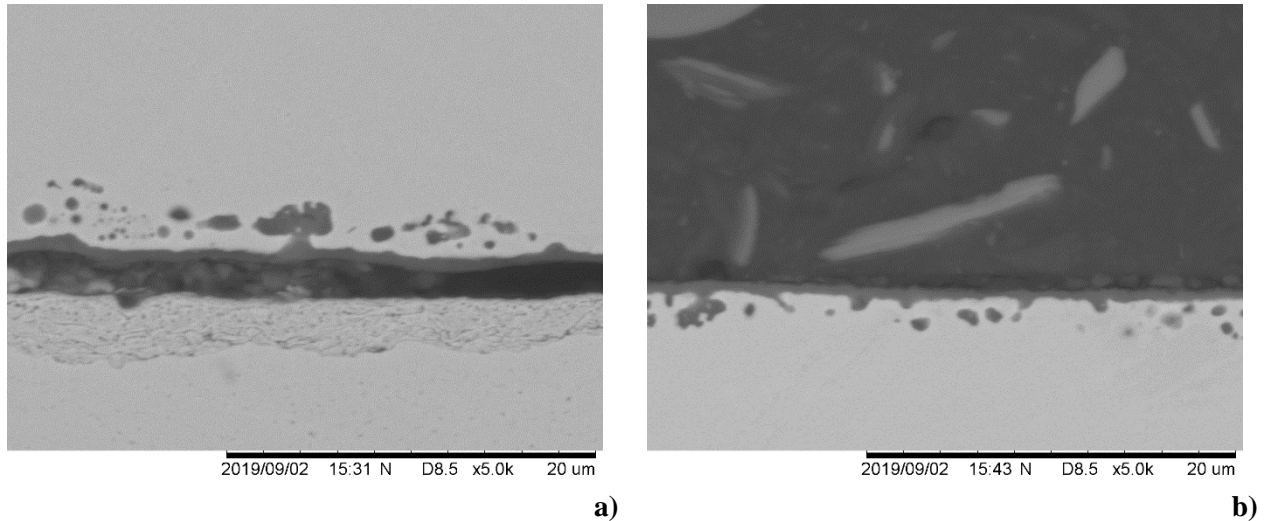
Figure 95. Morphology of the oxide annealed to $1100^{\circ}C$ and coated with $MgO + TiO_2$ only (a) up-facing surface (b) downfacing surface.

Figure 96 illustrates the oxide layer developed at $1150^{\circ}C$ with TiO_2 additions to the magnesium slurry. There is no noticeable increase in the surface oxide thickness, and there is still a significant presence of subsurface oxide. Thus, the TiO_2 has not presented an alteration of surface oxide.

a)   b)
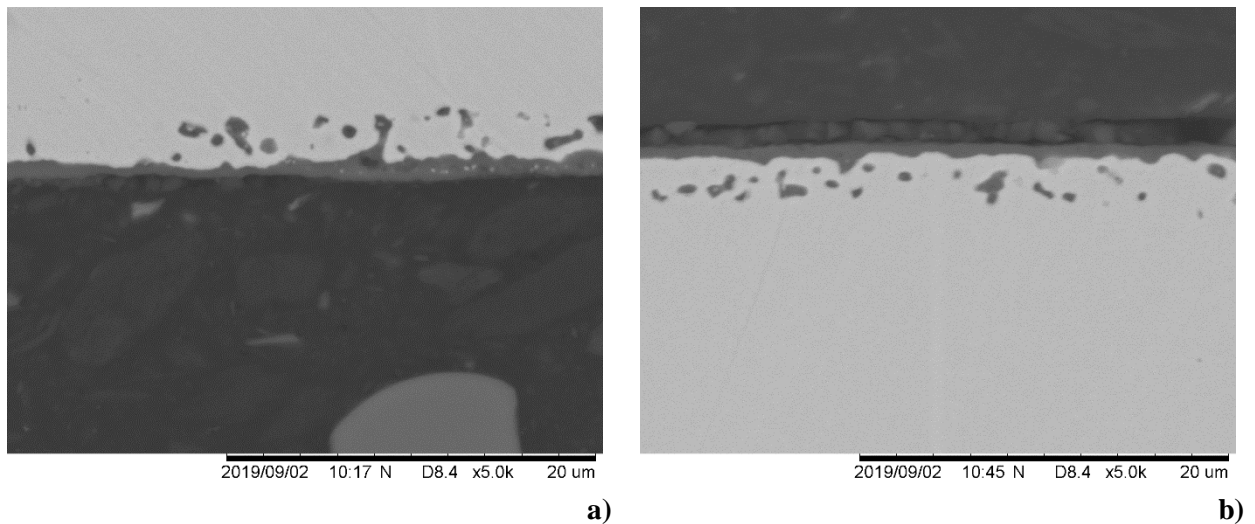
Figure 96. Morphology of the oxide annealed to $1150^{\circ}C$ and coated with $MgO + TiO_2$ only (a) up-facing surface (b) downfacing surface.

The addition of TiO_2 to the slurry has not illustrated any clear improvements in the thickness of surface oxide or the temperature at which the surface oxide develops during the heating stage of the process.

3.3.2 Composition Changes through the Surface Oxide using GDOES with Addition of TiO_2 to the MgO Slurry

The chemical composition of the oxide layer at $900^{\circ}C$ with TiO_2 added to the Mg slurry is illustrated in Figure 97 and Figure 98. The level of iron is marginally reduced at the surface by the presence of several elements. Nonetheless, after approximately 2 seconds, the GDEOS data indicates that the substrate consists of ~97% Fe with ~3% Si.
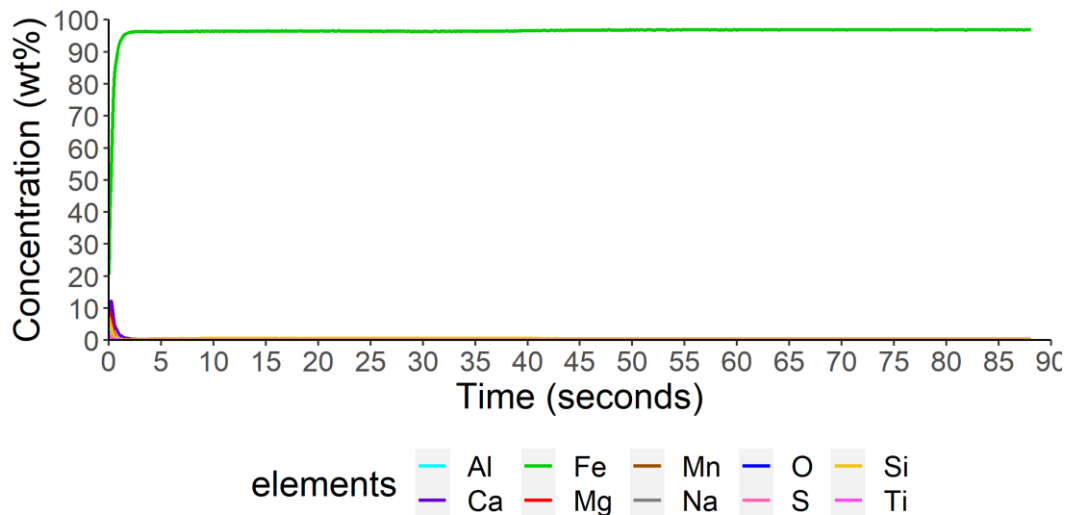
Figure 97. Changes in chemical composition through the surface oxide to the substrate when coated with MgO + TiO$_2$ only and heat-treated to 900ºC.

Figure 98 demonstrates the small amount of the Mg and Ti present at the surface of the substrate at 900ºC. The Ti$_{max}$ is 1.5% at 0 seconds and is less than 1% by 0.1 seconds, demonstrating that a detectable amount of Ti is present within the surface at 900ºC. It appears that a small amount of Mg has diffused at the surface and into the substrate with Mg$_{max}$ of 8.5% at 0.1 seconds, and the concentration becomes <1% at 0.5 seconds. There are also signs that Al and Si have diffused towards the surface with Si$_{max}$ of 7.1% at 0 seconds and Al$_{max}$ of 2.9% at 0 seconds. The aluminium concentration at the surface indicates that some Al-N has started to fail as a precipitate and diffused towards the surface. The morphology displayed in Figure 92 does not display any obvious changes, and only a slight coarsening of the lamella and spherical oxides is visible.

Figure 98. Individual line plots of each element that Figure 97 is composed of when a sample is coated with MgO + TiO$_2$ and heat-treated to 900ºC.

97

Further increasing the temperature to 950°C following the HTA heating rates has resulted in a certain change at the surface, as Figure 99 illustrates. The Mg and Ti powder at the surface has begun to significantly diffuse into the surface of the steel, forming an oxide layer. Additionally, Al and Si have begun to diffuse towards the surface of the substrate.
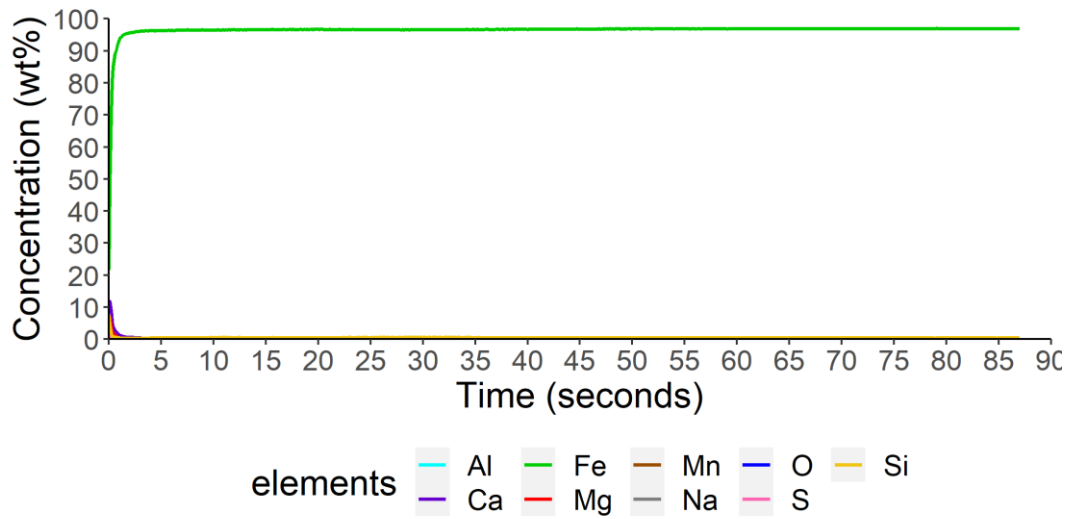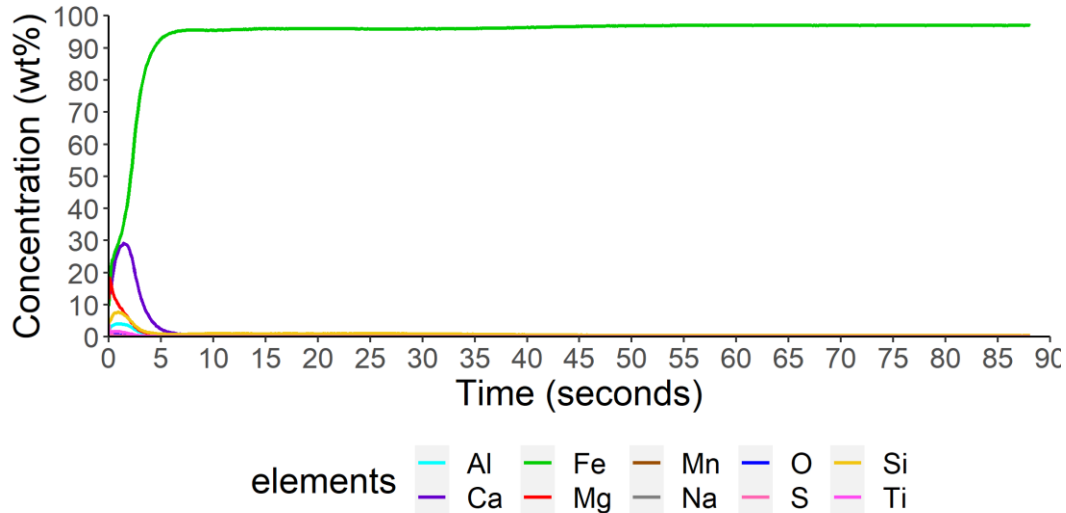

Figure 99. Changes in chemical composition through the surface oxide to the substrate when coated with MgO + TiO$_2$ only and heat-treated to 950°C.

When examining the elements present at the surface, the magnesium peaks at the surface with a Mg$_{max}$ of 18.3% at 0 seconds and begins to drop in concentration immediately. Additionally, the concentration Ti$_{max}$ is at 1.8% at 0 seconds and reaches levels of <1% after 1.9 seconds. The concentration of Si and Al have increased at the surface, whereby Al$_{max}$ of 4.1% at 0.9 seconds and Si$_{max}$ of 7.8% at 0.9 seconds. The development of a uniform layer is not clear from the cross-sectional images in Figure 93, although the coarsening of the Fayalite has occurred whereby the fine structure of lamella and spherical morphology is transformed into large spherical regions. Previous work has identified the spherical regions to be SiO$_2$ which would explain the increase in the concentration of Si at the surface[59].
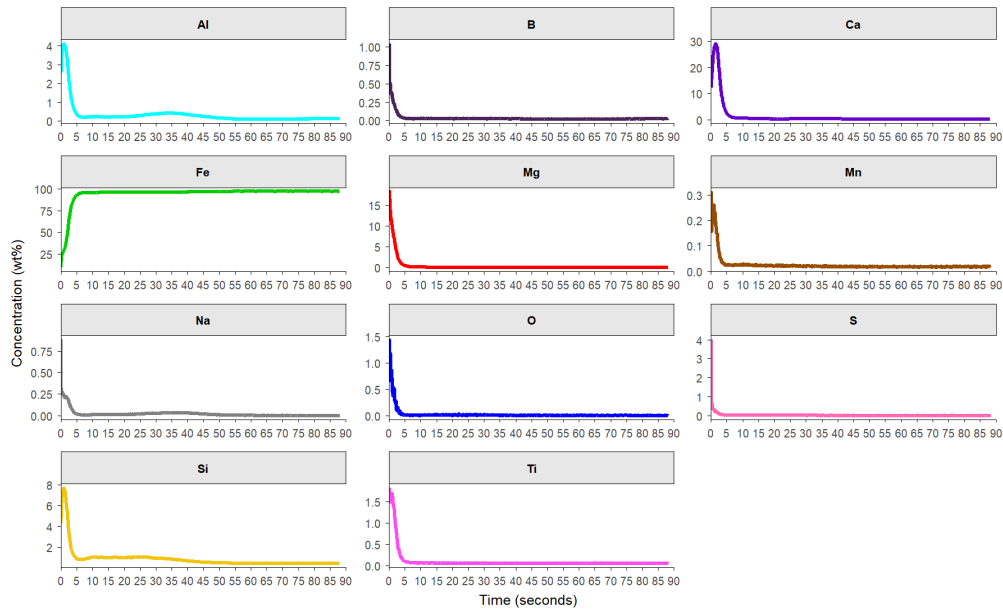
Figure 100. Individual line plots of each element that Figure 99 comprises when a sample is coated with MgO + TiO$_2$ and heat-treated to 950°C.

The chemical composition of the surface oxide at 1050°C that has been coated with Mg + TiO$_2$ is displayed in Figure 101. At 1050°C, the first signal Fe has been suppressed by Mg, with the line of interception between Mg-Fe at 3.7 seconds. There is an increase in Al concentration between 25 and 40 seconds. This indicates that significant Al-N precipitates are breaking down, and the Al is diffusing to the surface. The first peak of Al occurs at 3 seconds with a concentration of 4% and a second peak occurs at 35.8 seconds with a concentration of 2.1%.
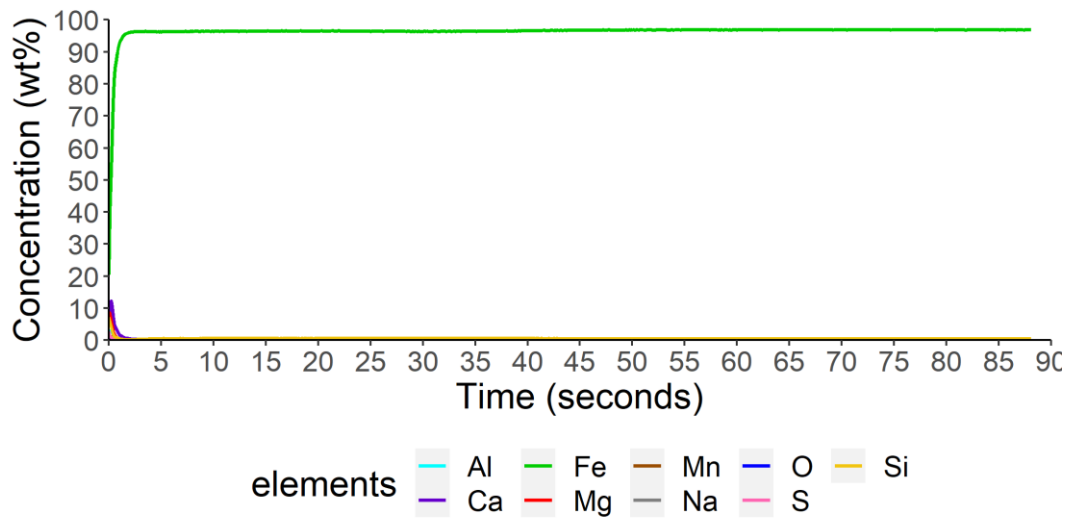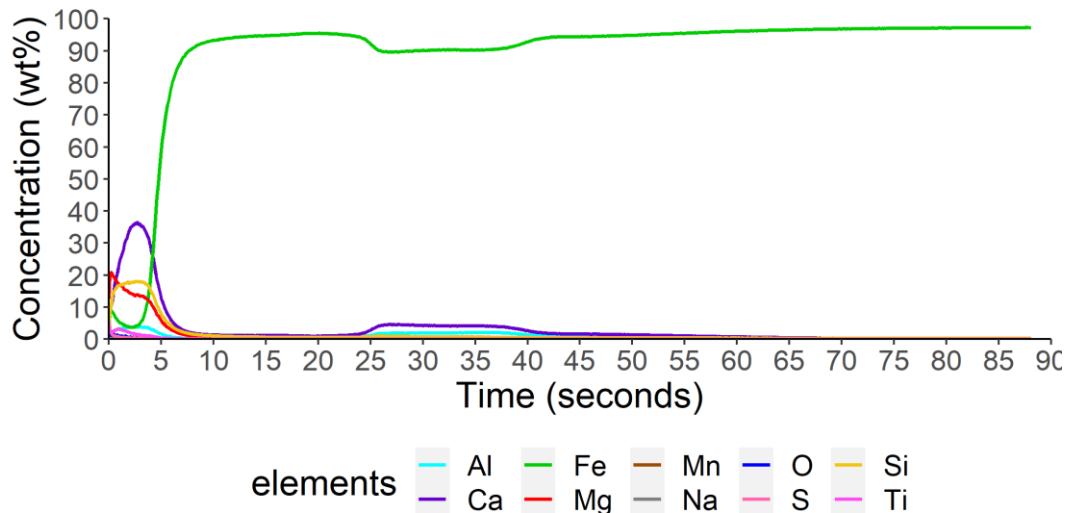

Figure 101. Changes in chemical composition through the surface oxide to the substrate when coated with MgO + TiO$_2$ only and heat-treated to 1050°C.

On closer inspection of the surface, the Mg$_{max}$ is at 20.8% at 0.2 seconds. The presence of Ti at the surface has increased where Ti$_{max}$ is 3.2% at 0.9 seconds, which suggest that Ti is diffusing into the surface layer. The silicon concentration reaches a maximum of 18.0% at 2.7 seconds which has to

increased further from 950ºC, showing that Si has continued to diffuse from the substrate interior towards the surface. Additionally, the concentration of Ti has continued to increase its presence at the surface. The change seen at 1050ºC in relationship with composition is reflective of the changes seen in the morphology as display in Figure 94, where a layer of oxide has developed at the surface, and below the surface oxide, significant spherical oxides have developed.
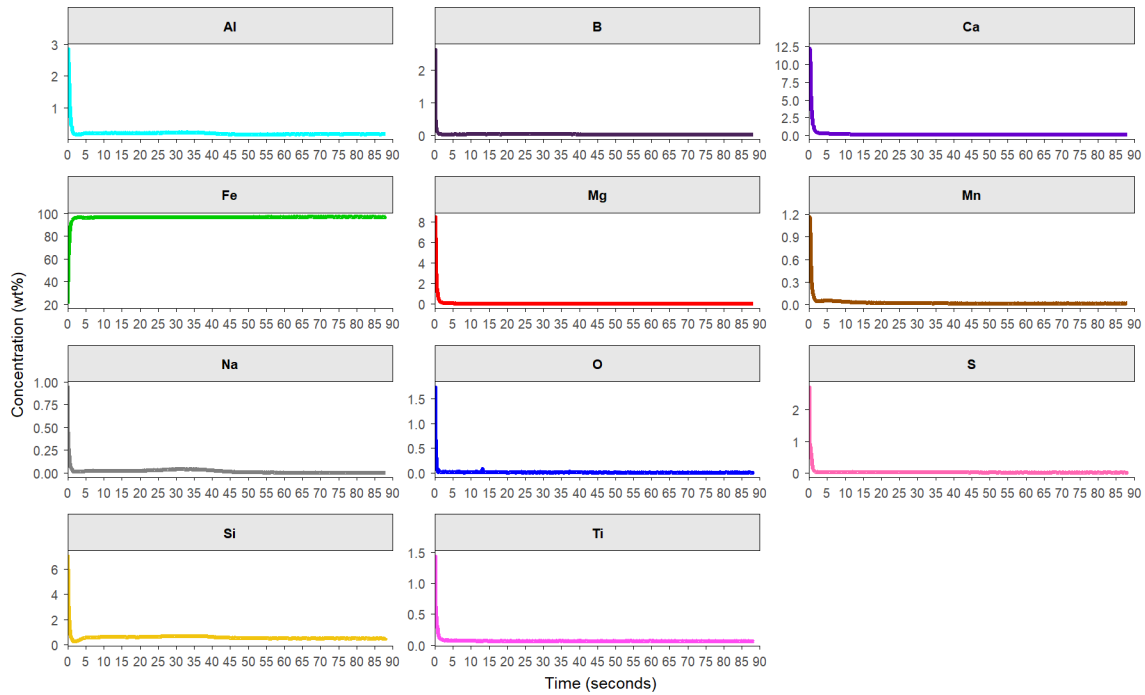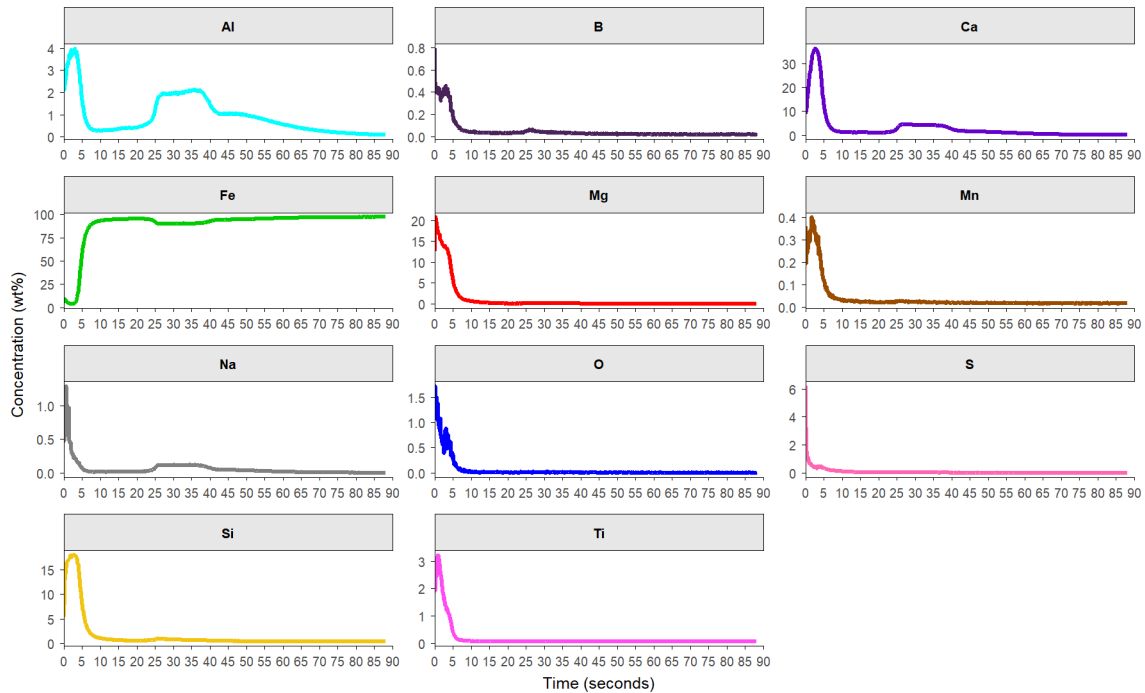

Figure 102. Individual line plots of each element that Figure 101 comprises when a sample is coated with MgO + TiO$_2$ and heat-treated to 1050ºC.

The chemical composition of the surface oxide when heated to 1100ºC is illustrated in Figure 103. The continuation of elements from the slurry diffusing into the substrate and elements within the bulk diffusing towards the surface is still occurring at 1100ºC. The iron has been suppressed by Mg, whereby the line of interception occurs at 4.2 seconds. The Mg$_{max}$ concentration detected is 21.4% at 0.1 seconds.
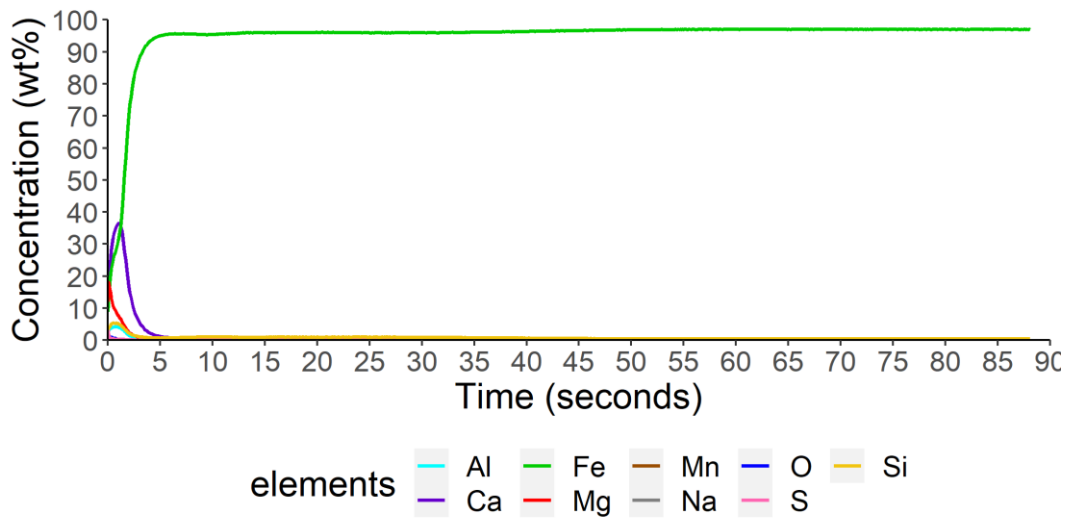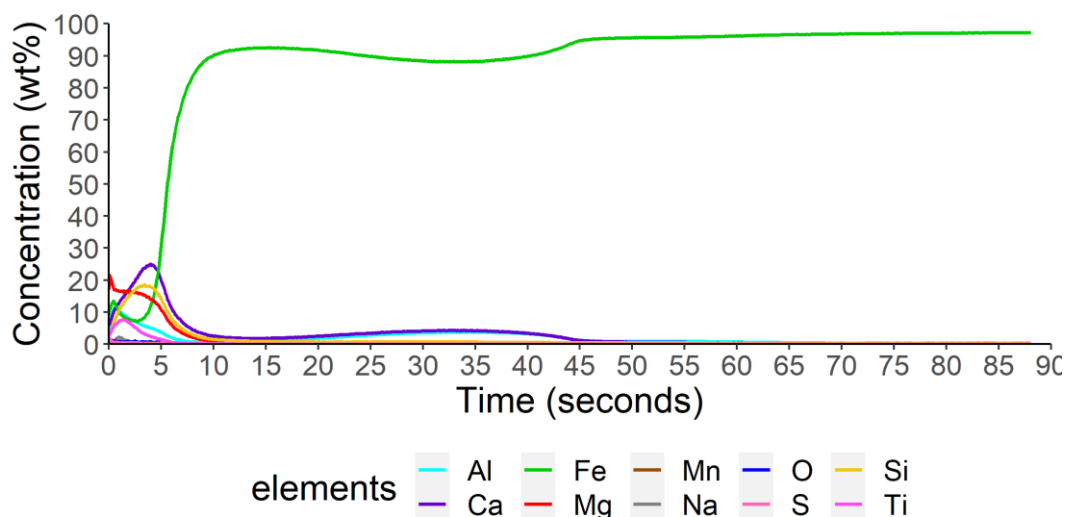
Figure 103. Changes in chemical composition through the surface oxide to the substrate when coated with MgO + TiO$_2$ only and heat-treated to 1100°C.

The detection of Ti has become prevalent, with the detection of Ti$_{max}$ at levels of 7.7%, occurring at 1.5 seconds, as seen in Figure 104. The trend of two Al peaks continues with the initial peak occurring at 0.7 seconds at a max concentration of 11.2% and a second peak at 34.1 seconds with a concentration of 3.9%. The Si$_{max}$ is 18.6% which occurs at 3.4 seconds. Increased temperature has increased Ti's presence at the surface, indicating that diffusion has not been completed, unlike Si, which appears to reach a maximum peak at ~18% with no further increase from 1050°C. The Mg enriched surface relates to the uniform thick surface layer of the surface oxide seen in Figure 95 and the grouping of fine spherical oxide to form large spherical oxide in the subsurface.
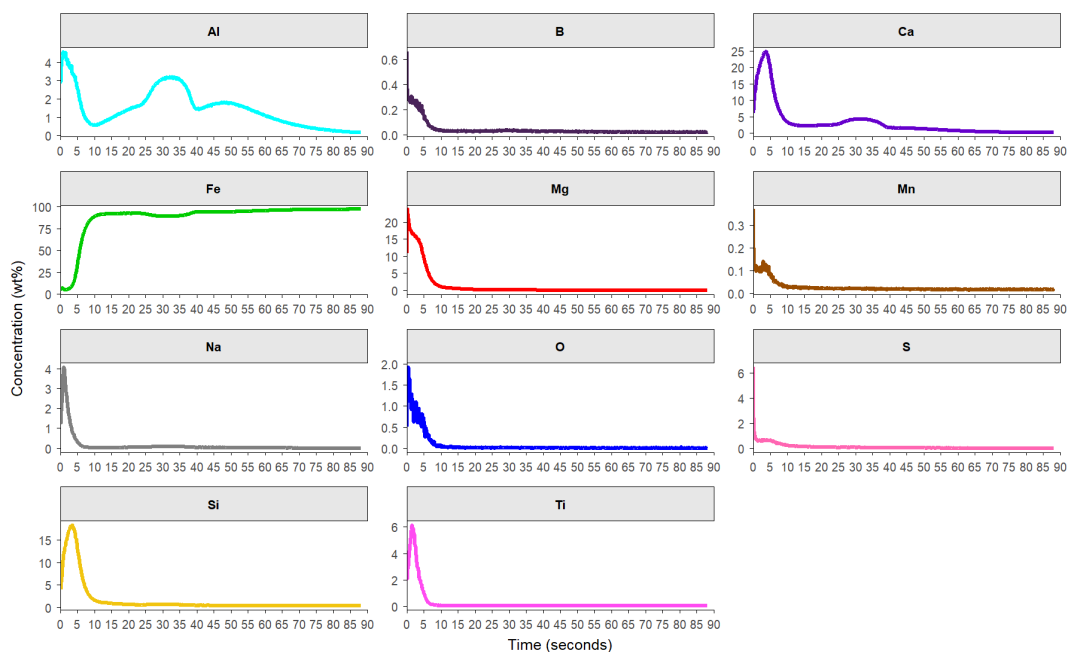
Figure 104. Individual line plots of each element that Figure 103 is composed of when a sample is coated with MgO + TiO$_2$ and heat-treated to 1100°C.

101

The composition of oxide developed with Mg+TiO$_2$ slurry at 1150°C is displayed in Figure 105. The line of interception between Mg-Fe occurs at 5.1 seconds, whereby the Mg$_{max}$ of 23.9% at 0.2 seconds.
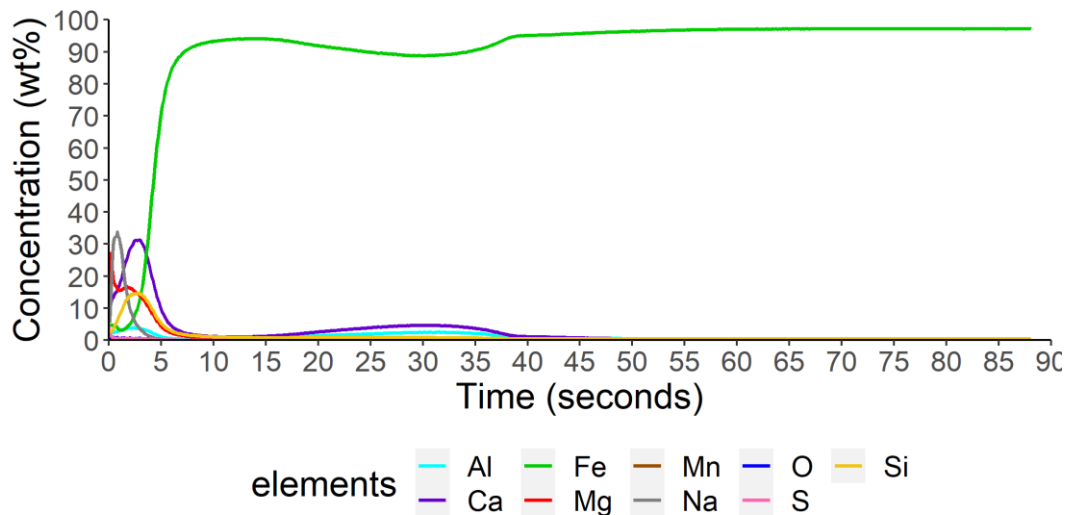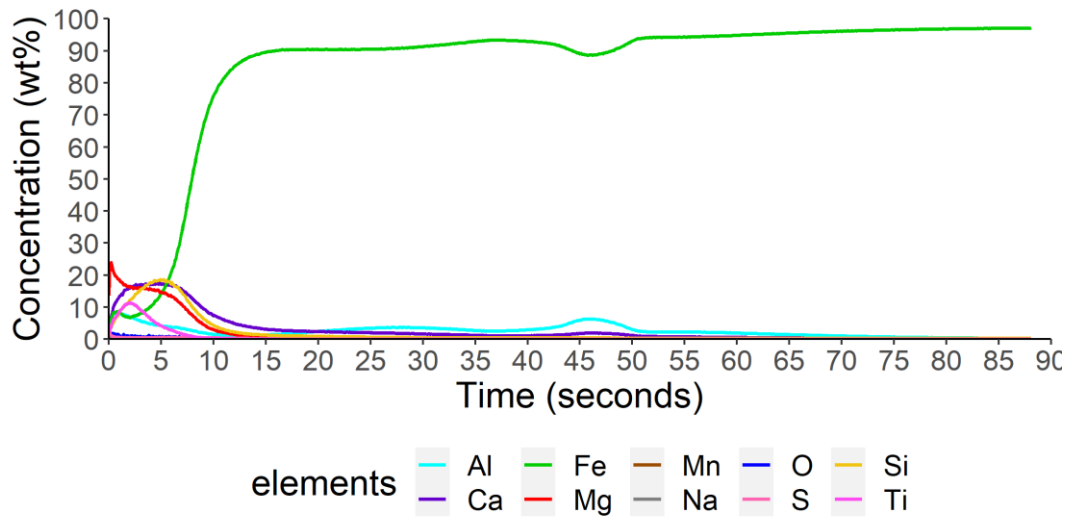

Figure 105. Changes in chemical composition through the surface oxide to the substrate when coated with MgO + TiO$_2$ only and heat-treated to 1150°C using GDOES.

Figure 106 shows that further increase in Ti$_{max}$ reaches 11.4% at 2 seconds and the Si$_{max}$ concentration of 18.6% at 5.2 seconds. The continuation of Al migrating to the surface and subsurface continues with Al$_{max}$ at the surface, reaching 8.1% at 0.5 seconds, and the second peak occurs at 46.1 seconds at 6.4%.
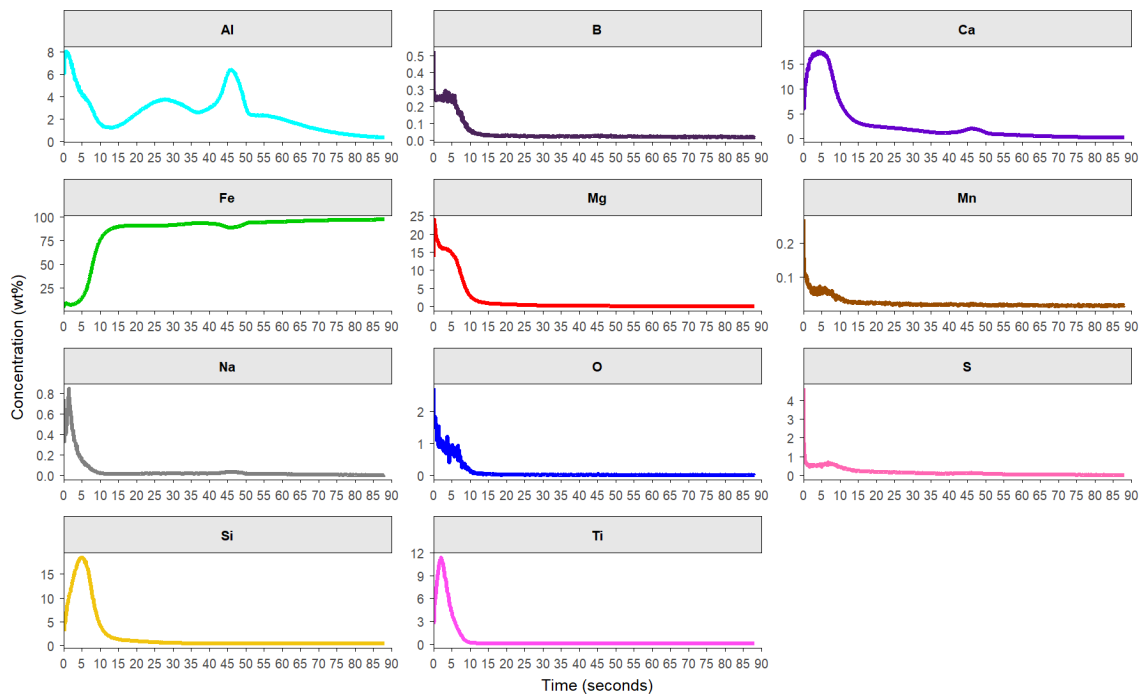
Figure 106. Individual line plots of each element that Figure 105 is composed of when a sample is coated with MgO + TiO$_2$ and heat-treated to 1150°C following HTCA annealing profile.

The addition of TiO$_2$ to the Mg slurry has resulted in the presence of Ti in the surface oxide detected by the GDOES. Where initial detection occurs at 1050ºC and the presence of Ti increase with temperature increase. The presence of Ti does not appear to affect the morphology compared to the MgO only coated samples.

3.3.3 Magnetic Properties with TiO$_2$ Addition to the Slurry

Figure 107 displays the results of magnetic losses when TiO$_2$ addition to the magnesium and the HTA cycle is interrupted at various temperatures. The magnetic properties were collected with a Soken tester as described in section 2.8. The trend that has been shown in section 3.2.3 has continued, with an increase in temperature resulting in a decrease in magnetic losses. Additionally, at 1050ºC, a critical temperature is reached where significant changes in the microstructure have occurred, resulting in a significant decrease in magnetic losses. Thus, the TiO$_2$ addition does not appear to influence the magnetic properties during the heating phase dramatically.
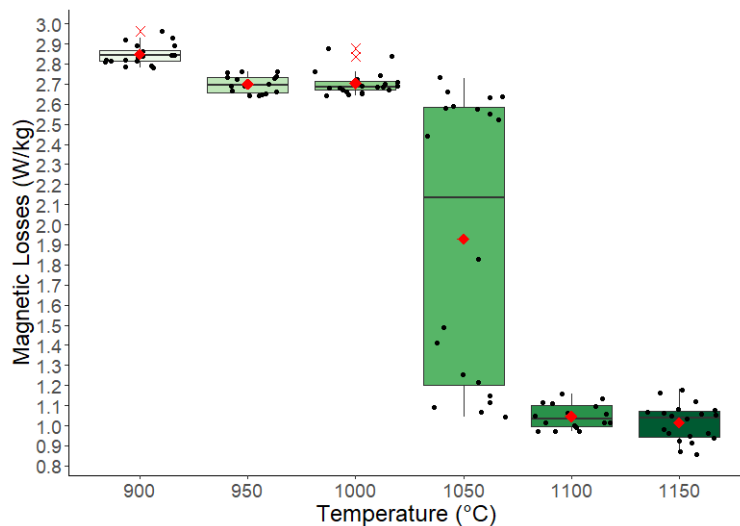
Figure 107. Magnetic properties at various temperatures following the HTA heat cycle where the substrate has been coated with MgO + TiO$_2$.

3.3.4 Current Detected Through Developing Oxide Layer with MgO + TiO$_2$ Coated.

Figure 108 illustrates the detected current of the resulting oxide layer at various temperatures with TiO$_2$ addition to the magnesium slurry. The trend that is seen in section 3.2.4 continues with an increase in temperature resulting in a decrease in current detected through the oxide layer, as the layer becomes continuous and thicker. Thus, the TiO$_2$ addition does not appear to have a dramatic improvement in performance nor a negative influence.
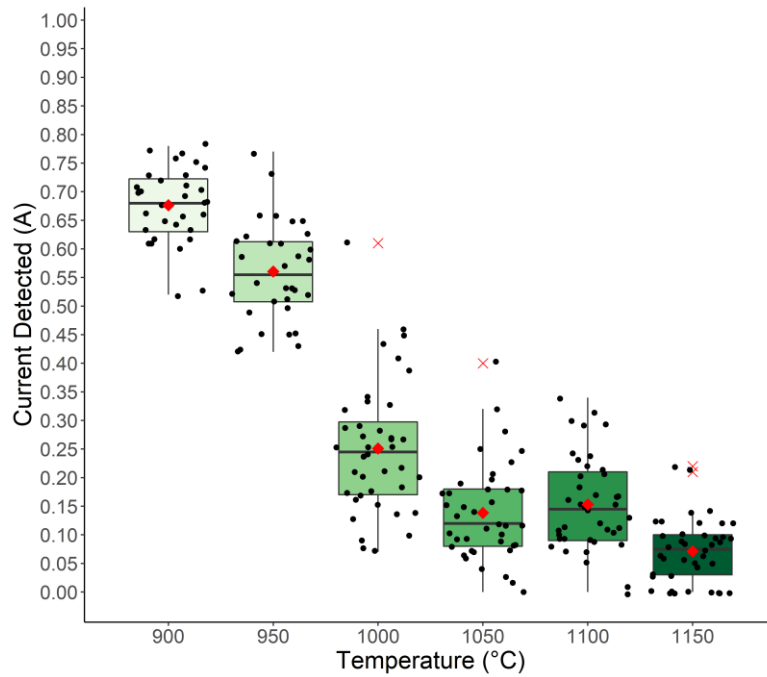
Figure 108. Current detected through the oxide layer at various stages of the heat treatment following HTCA cycle that has been coated with MgO + TiO2.

3.3.5 Bulk Analysis of Carbon, Oxygen, Nitrogen, and Sulphur when Coated with MgO + TiO2.

Figure 109 illustrates the nitrogen content of a substrate that has been coated with a MgO slurry with TiO$_2$ addition, and interrupted anneals have been conducted during the HTA process. As shown in the graph below, the reduction in nitrogen content shows a linear relationship with nitrogen content and temperature increase. Thus, the addition of TiO$_2$ has not affected the trend of the degrading of the Al-N precipitates. Although nitrogen levels have reduced to ~90 ppm at 1150ºC when compared to the samples with an extended Soak at the high temperature, the nitrogen content decreases to 30 ppm. This indicates that removing nitrogen from the substrates has not reached its maximum potential, and additional temperature and time are required to purify the substrate fully.
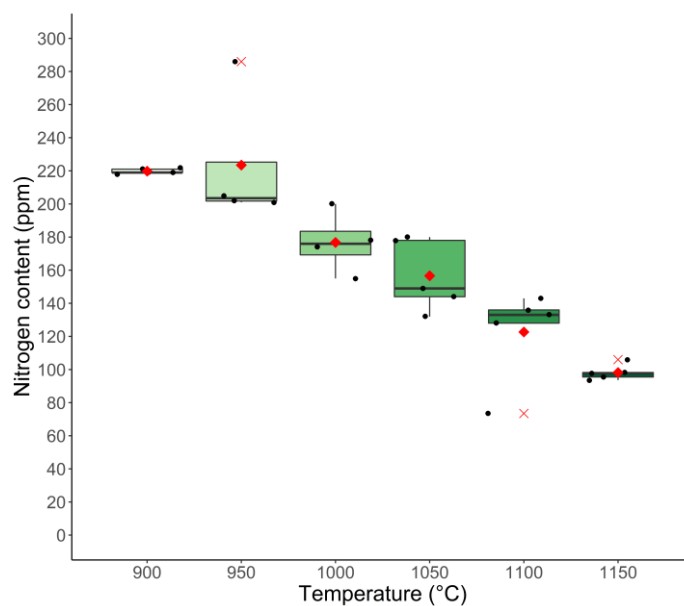
Figure 109. Nitrogen content present of the bulk substrate at various temperatures during the HTCA cycle collected by LECO TN400.

The results of sulphur content at various temperatures of the HTCA cycle with a TiO$_2$ addition to the slurry. The sulphur content does not show a noticeable change between 900ºC – 1000ºC. At 1000ºC, there is a decrease in sulphur, and this trend continues with an increase in temperature through the HTA cycle.
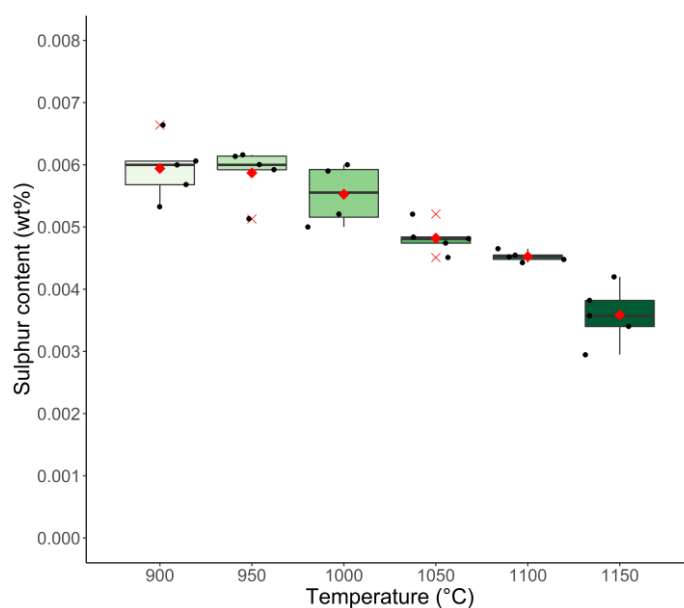
Figure 110. The sulphur content of the bulk substrate at various temperatures during the HTCA cycle was collected by LECO CS844.

The results of oxygen content detected in the substrate by TN400 Leco is displayed in Figure 111. The oxygen content does not display significant change between 900ºC to 1000ºC. The oxygen levels detected similar levels to decarburisation, typically between 650-750 ppm. On further increase in slight temperate increase in oxygen content is detected. Finally, at 1100ºC, there is a significant

increase in oxygen content. This can be explained by the increase in the surface oxide seen in the morphology changes in section 3.3.1.
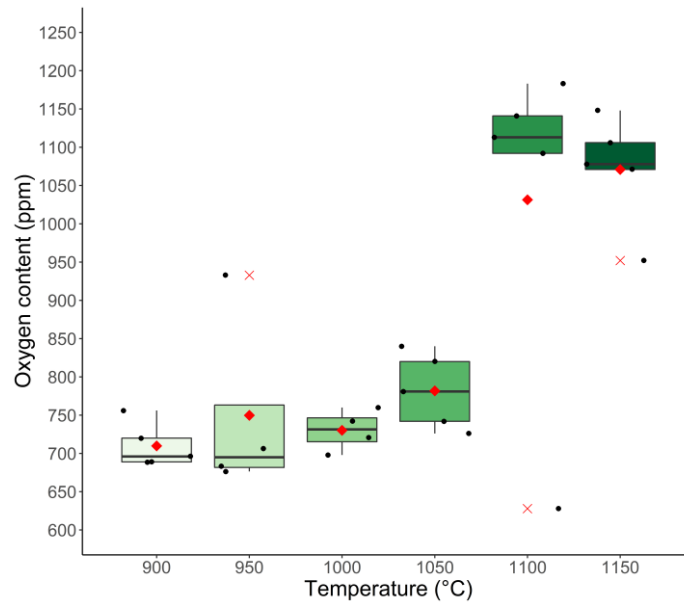
Figure 111. Oxygen content present of the bulk substrate at various temperatures during the HTCA cycle collected by LECO TN400.

3.3.6   Discussion

The trend that is seen in section 3.2 of increase in temperature results in an evolution of the magnetic properties, purification of substrate and development of a surface oxide continues with the TiO_2. There are no prominent improvements or deterioration seen in magnetic properties, purification, or resistance properties with the TiO_2 addition to the slurry. Similarly, the morphology has not changed with the TiO_2 addition. However, the composition of surface oxide through GDOES analysis has altered with the detection of TiO_2 at 900°C, and with further increase in temperature, the presence of TiO_2 becomes more prevalent in the surface oxide. The literature review did not identify any explanation of the purpose of the TiO_2 addition or the role TiO_2 has on the Forsterite film other than a statement saying TiO_2 promotes densification of the Forsterite layer. This investigation has identified that Ti forms during the heating phase of the HTCA as part of the surface oxide. It is unclear of the advantages of the use of TiO_2 during the heating phase of the annealing process due to the continuation of the evolution of the properties even at a max temperature of this segment of work, which demonstrates the requirement for a soak at high temperature. The discovery of the TiO_2 present in the surface oxide has led to the possibility of Ti compounds that may be present. Magnesium dititanate ($MgTi_2O_5$)[127]. This will be discussed further in section 4.4,The Impact of Range of Concentration TiO_2 Addition on the Formation of Oxide Layer.

3.4 The Development of Surface Oxide During High-Temperature Annealing with MgO+TiO₂+Borax Slurry.

3.4.1 Morphology of Surface Oxide Developed

The developed oxide layer that has been coated with Mg + TiO_2+ Borax and followed the HTCA cycle up to 900ºC is illustrated in Figure 112. The top and bottom surfaces have not exhibited changes in the surface oxide compared with the decarburization surface oxide developed.

a)   b)
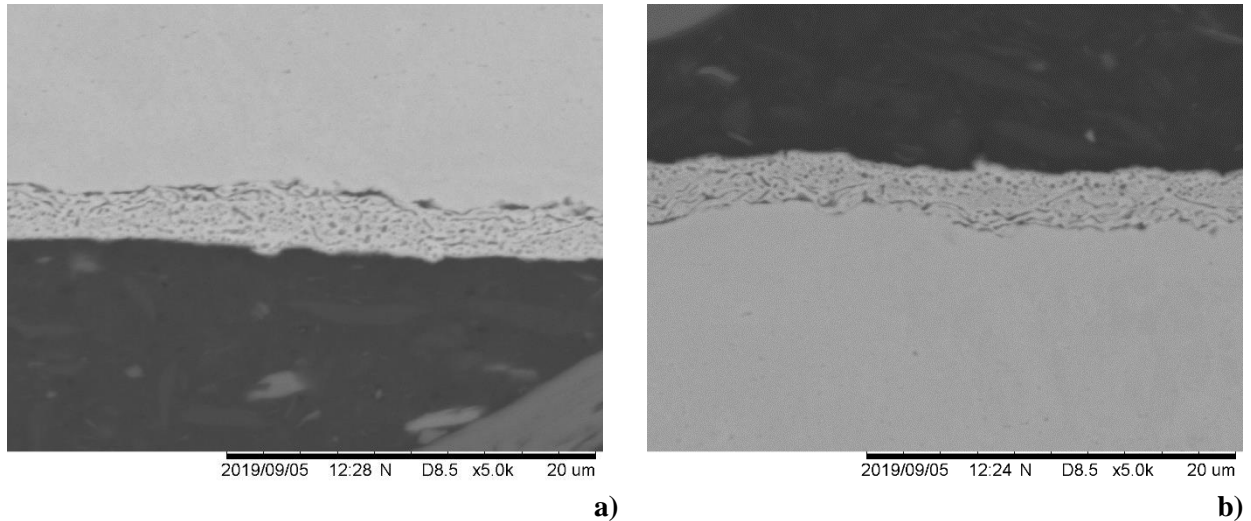
Figure 112. Morphology of the oxide annealed to 900ºC and coated with MgO + TiO_2 + $Na_2B_4O_7 \cdot 10H_2O$ (a) up-facing surface (b) downfacing surface.

When the HTCA cycle is interrupted at 950ºC when coated with Mg + TiO_2+ Borax, the Fayalite layer developed in the decarburization stage of the process has begun to transform from a fine globular and lamella structure to a large globular structure throughout the surface of the oxide. Additionally, an unknown interface layer developed between the globular structure and the iron matrix in both top and bottom surfaces (Figure 113a) and Figure 113b).

a)   b)
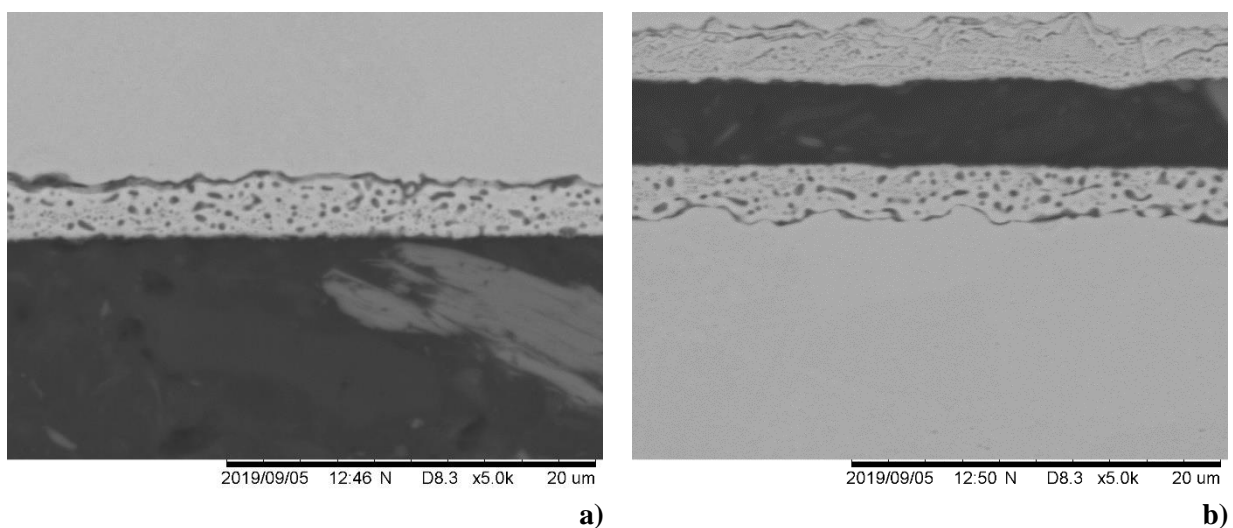
Figure 113. Morphology of the oxide annealed to 950ºC and coated with MgO + TiO_2 + $Na_2B_4O_7 \cdot 10H_2O$ (a) up-facing surface (b) downfacing surface.

At 1050°C, the oxide has developed a continuous layer at the surface of the substrate illustrated in Figure 114. As a result, the subsurface oxide has a range of globular oxides, and the fine Lamellar structures are not present.

| a) | b) |
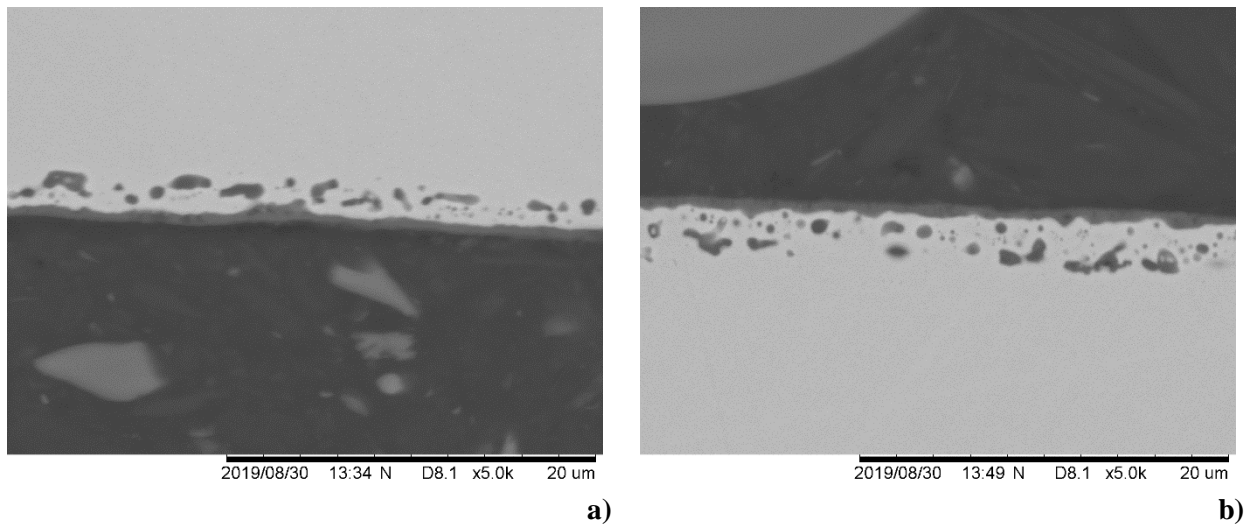
Figure 114. Morphology of the oxide annealed to 1050°C and coated with $MgO + TiO_2 + Na_2B_4O_7 \cdot 10H_2O$ (a) up-facing surface (b) downfacing surface.

Figure 115 illustrates the oxide layer that has developed at 1100°C when coated with $Mg + TiO_2 +$ Borax. The surface oxide appears thicker, and the fine globular structure seen in 1050°C SEM cross-sections have reduced and appears to form coarse spherical oxide particles in the subsurface.

| a) | b) |
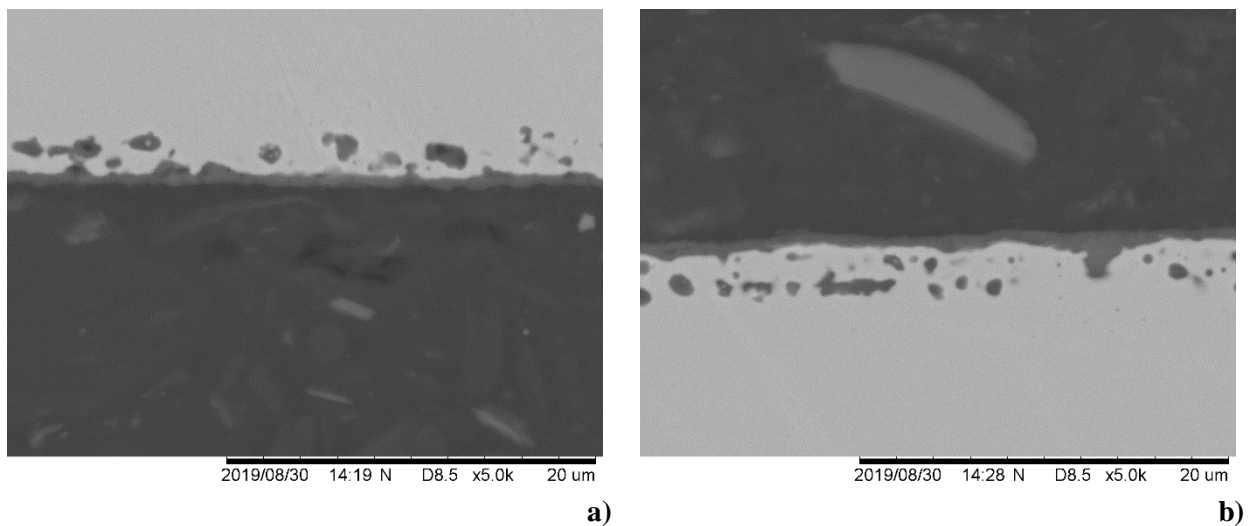
Figure 115. Morphology of the oxide annealed to 1100°C and coated with $MgO + TiO_2 + Na_2B_4O_7 \cdot 10H_2O$ (a) up-facing surface (b) downfacing surface.

The oxide layer developed at 1150°C is illustrated in Figure 116, and the surface oxide is consistent, and uniform at the surface and areas of large keying points are present.
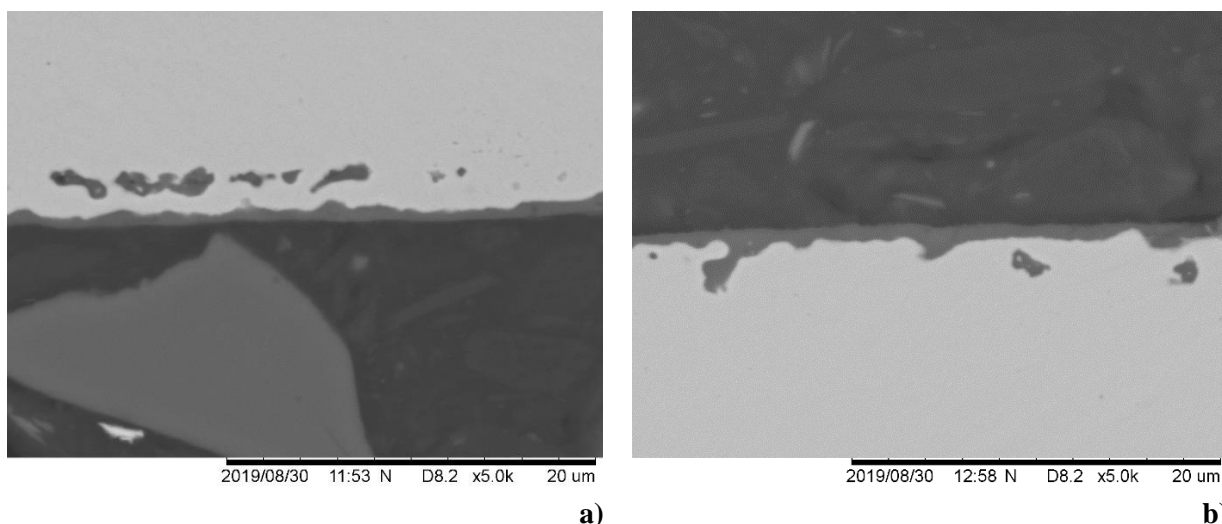
Figure 116. Morphology of the oxide annealed to 1150°C and coated with MgO + TiO$_2$ + Na$_2$B$_4$O$_7\cdot$10H$_2$O (a) up-facing surface (b) bottom surface.

3.4.2 Composition Changes Through the Surface Oxide using GDOES with the Addition of TiO$_2$ and Na$_2$B$_4$O$_7$ 10H$_2$O (Borax) Add to the MgO Slurry.

The resulting composition at the surface at 900°C are illustrated in Figure 117 and Figure 118. Again, iron is predominant throughout the 90-second scan, with minor constituents being detected. The elements that are detected at the surface at 900°C are Mg, Si, Al, Ti, S and B, and the concentration of these t elements detected at the surface has reduced to below 1% by 0.7 seconds.
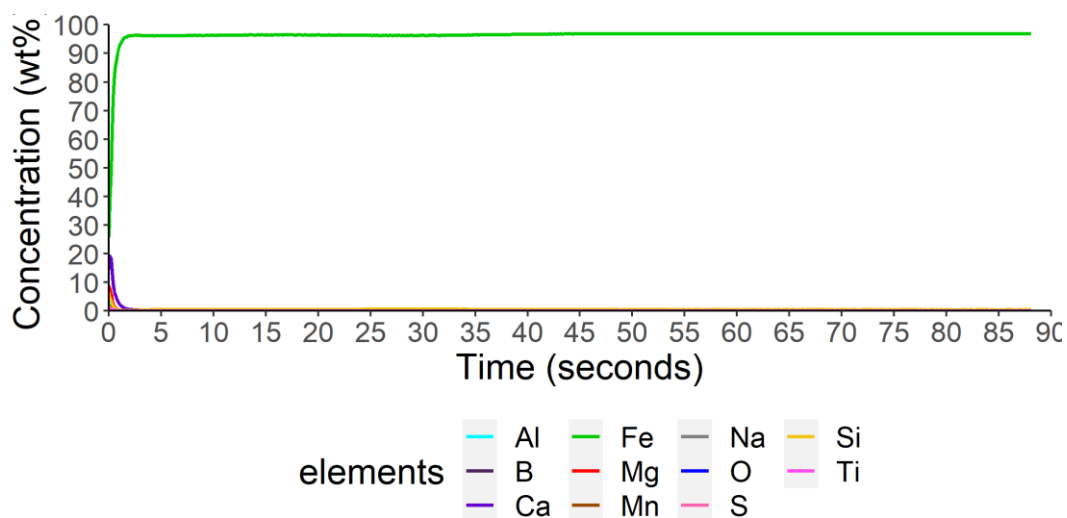
Figure 117. Changes in chemical composition through the surface oxide to the substrate when coated with MgO +TiO$_2$ + Na$_2$B$_4$O$_7\cdot$10H$_2$O (Borax) and heat-treated to 900°C.

Figure 118 illustrates the short period of the presence of the elements, and the Mg$_{max}$ is 9% at 0 seconds, and the Si$_{max}$ is 6.6% at 0 seconds. The addition of TiO$_2$ and borax is detected at the surface, where Ti$_{max}$ is 1.1% at 0 seconds, and B$_{max}$ is 1.6% at 0 seconds. However, these additives are detected at low levels and do not appear to influence the surface oxide at 950°C with no apparent development of oxide or change in the morphology of spherical oxides visible in the corresponding SEM images.

Elements have begun to diffuse from the bulk of the substrate to the surface, whereby S_{max} is 1.5% at 0 seconds, and Al_{max} is 2.9% at 0.1 seconds.
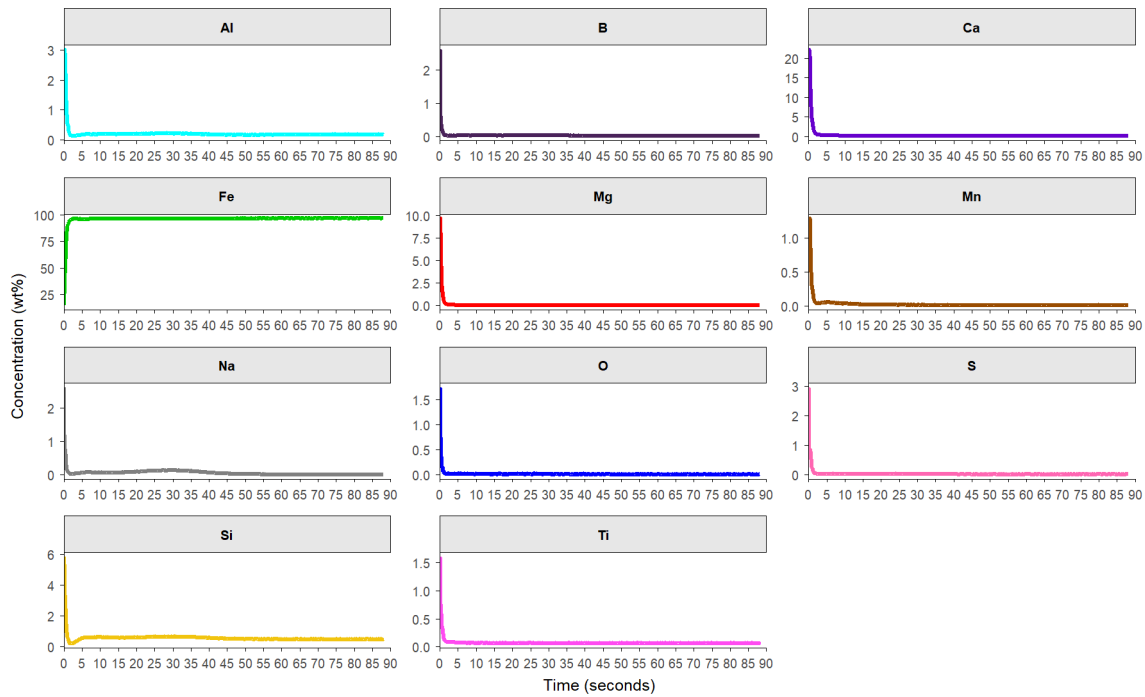
Figure 118. Individual line plots of each element that Figure 117 is composed of when a sample is coated with MgO + TiO$_2$ + Na$_2$B$_4$O$_7 \cdot$10H$_2$O (Borax) and heat-treated to 900°C.

A significant change has occurred with a further increase in temperature to 950°C when following the HTCA cycle. Mg, Si, Al, Ti, S and B are detected at the surface, and these elements are present >1% for up to 3.6 seconds. The presence of Fe is compromised at the surface due to the presence of these elements as the coating develops.
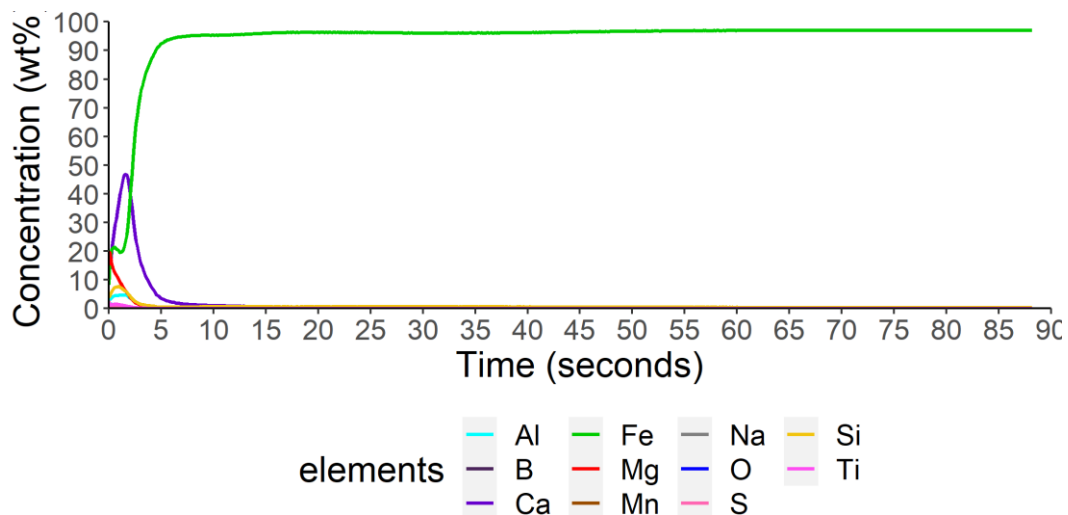
Figure 119. Changes in chemical composition through the surface oxide to the substrate when coated with MgO +TiO$_2$ + Na$_2$B$_4$O$_7 \cdot$10H$_2$O (Borax) and heat-treated to 950°C using GDOES.

On closer inspection of the surface in Figure 120, multiple elements are present, increasing concentration at this region. The MgO slurry and additives are detected in the surface oxide. The Mg_{max} is 19.6% at 0.1 seconds and small detection of Ti_{max} 1.7% at 0 seconds and B_{max} 1.5% at 0 seconds. Na is beginning to be detected at the surface with a Na_{max} of 1.5 at 0 seconds. A continuation of elements that are found in the bulk material is diffusing towards the surface with the Al_{max} 4.8% at 1.1 seconds, Si_{max} 7.8% at 0.9 seconds and S_{max} at 2.7% at 0 seconds. The composition changes at the surface are reflective of the morphology seen in Figure 113. The globular oxide structure has developed from a lamella to a spherical oxide with no obvious oxide layer developed at the surface.
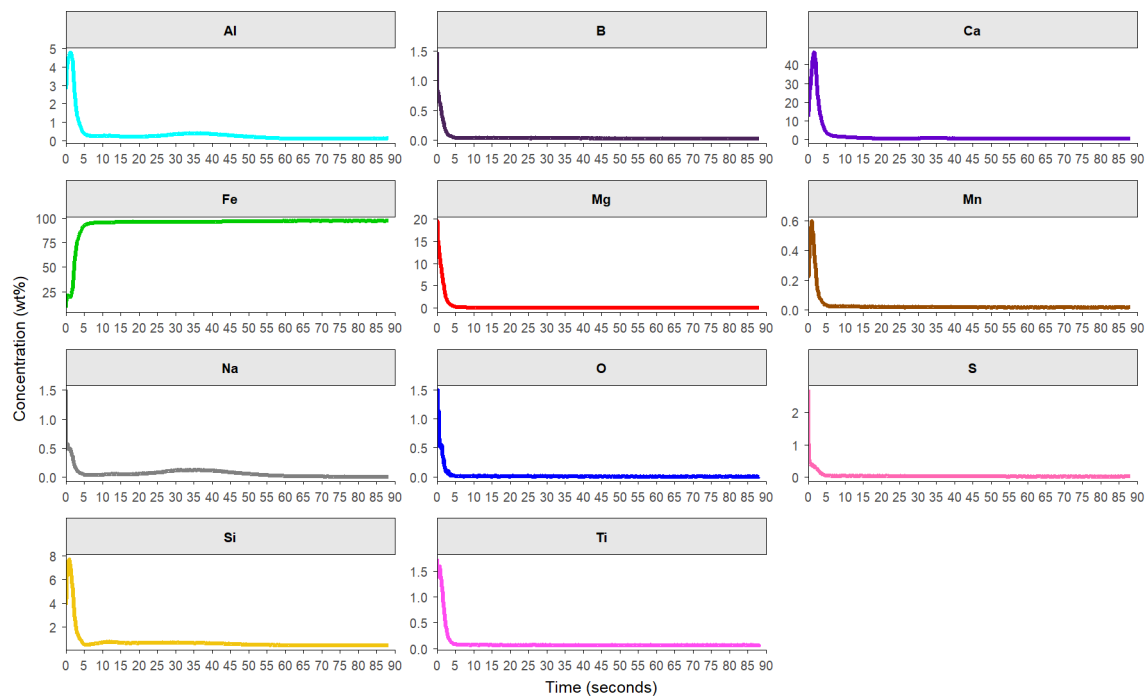
Figure 120. Individual line plots of each element that Figure 119 comprises when a sample is coated with $MgO + TiO_2 + Na_2B_4O_7 \cdot 10H_2O$ (Borax) and heat-treated to 900ºC.

When the HTCA profile is interrupted at 1050ºC, the GDOES analysis is displayed in Figure 121. The Fe presence at the surface has significantly diminished due to the presence of Mg, Na, Ti, Si, S, Al, and B. As a result of this, the Mg-Fe line of interception occurs at 4.1 seconds.
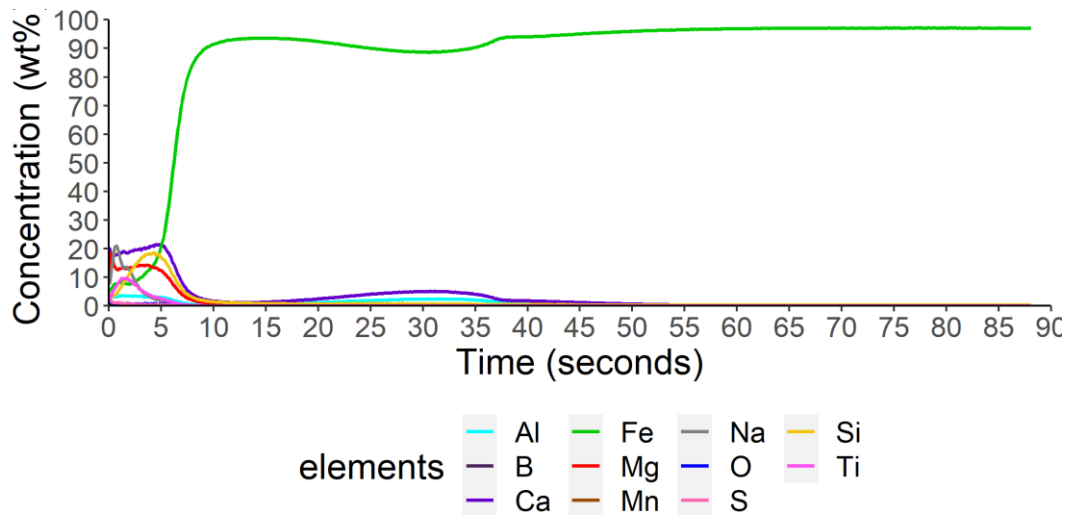
Figure 121. Changes in chemical composition through the surface oxide to the substrate when coated with MgO +TiO$_2$ + Na$_2$B$_4$O$_7 \cdot$10H$_2$O (Borax) and heat-treated to 1050°C.

Figure 121 shows the complex oxide developed at the surface at 1050°C. The elements present in the MgO dry slurry coating have diffused into the surface of the substrate. The Mg$_{max}$ is 18.4% at 0.2 seconds, and Ti$_{max}$ is 9.7 at 1.7 seconds. The B$_{max}$ is 0.5% at 0 seconds which has decreased compared to previous heat treatments. In addition, there is a significant increase in Na present, reaching a Na$_{max}$ concentration of 21% at 0.7 seconds.

The elements contained in the steel continue to diffuse to the surface of the oxide, as Figure 122. The Si$_{max}$ has reached 18.7% at 4.3 seconds, and the S$_{max}$ is 4.9% at 0 seconds. The first signs of two peaks are seen where the first is detected at the surface with an Al$_{max}$ of 3.7 at 1.3 seconds and the second peak in the subsurface region at 3.2 seconds with an Al$_{max}$ 2.5% at 30.5 seconds. As a result of changes in the chemical composition, a uniform layer has developed at the surface, which is seen in the SEM cross-section in Figure 114.

112
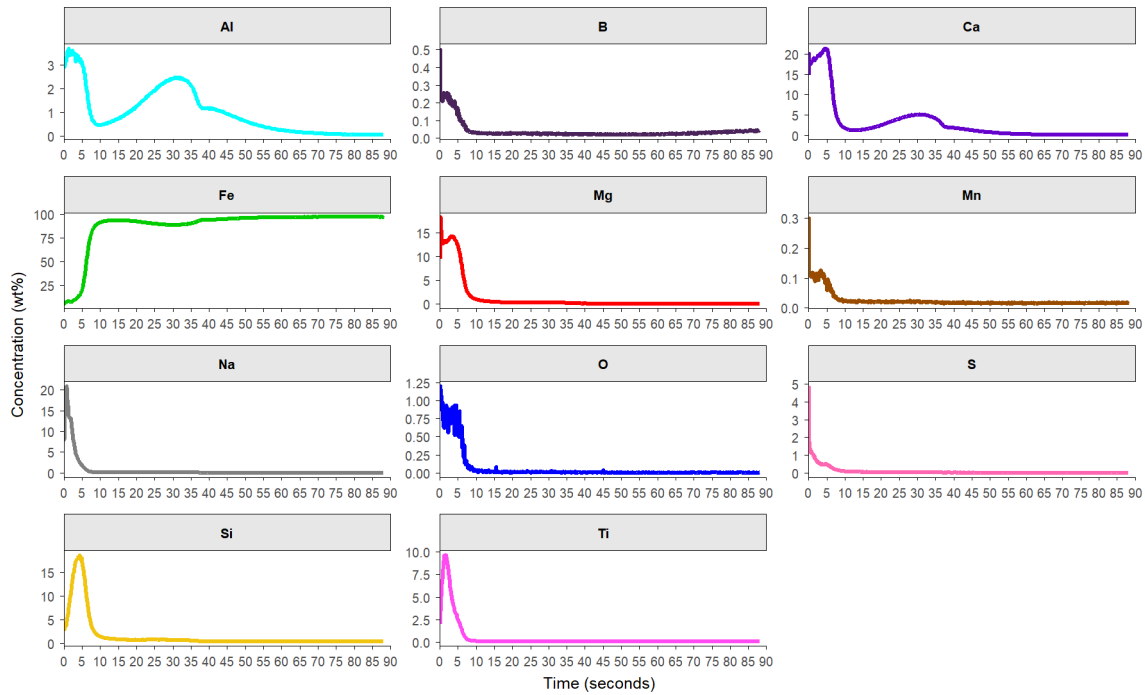
Figure 122. Individual line plots of each element that Figure 121 is composed of when a sample is coated with MgO + TiO$_2$ + Na$_2$B$_4$O$_7\cdot$10H$_2$O (Borax) and heat-treated to 1050ºC.

The resulting composition when a further increase in temperature to 1100ºC occurs when following the HTCA cycle is displayed in Figure 123. The suppression of Fe at the surface has continued; additionally, a drop in Fe is seen between 22 seconds to 42 seconds. The line of interception between Mg-Fe has occurred at 4.8 seconds.
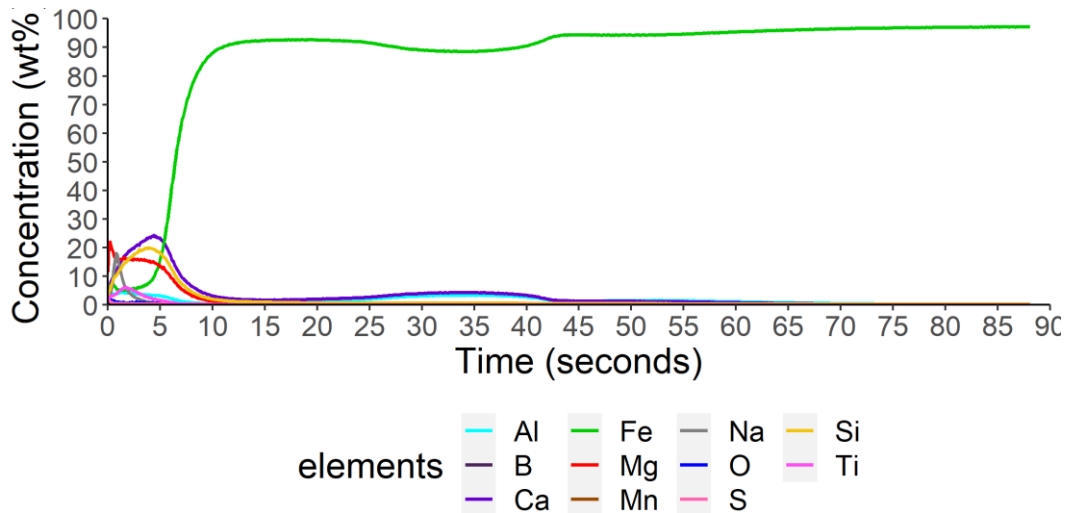
Figure 123. Changes in chemical composition through the surface oxide to the substrate when coated with MgO +TiO$_2$ + Na$_2$B$_4$O$_7\cdot$10H$_2$O (Borax) and heat-treated to 1100ºC.

On closer inspection of the surface oxide in Figure 124, the oxide layer developed consists of Mg, Na, Ti, Si, S, Al, and B. The elements present in the applied slurry have formed as part of the surface and are detected at levels of Mg$_{max}$ is 22.1% at 0.2 seconds, Ti$_{max}$ is 3.6% at 1.7 seconds and Na$_{max}$ at 18% at 0.8 seconds. B levels are detected at 0.6% at 0 seconds, suggesting that B is not prevalent in the

surface oxide. The elements present in the steel have continued to diffuse towards the surface; the Si_{max} is 20.0% at 3.9 seconds. The Al has continued to peak twice, whereby the surface peak Al_{max} is 4.4% at 1.4 seconds and the second peak located in the subsurface oxide at Al_{max} of 3.5% at 35.5 seconds. The coarsening in the subsurface oxide morphology between 1050ºC (Figure 114) and 1100ºC (Figure 115) seen in the SEM cross-sections is not represented in changes seen in the composition in Figure 124.
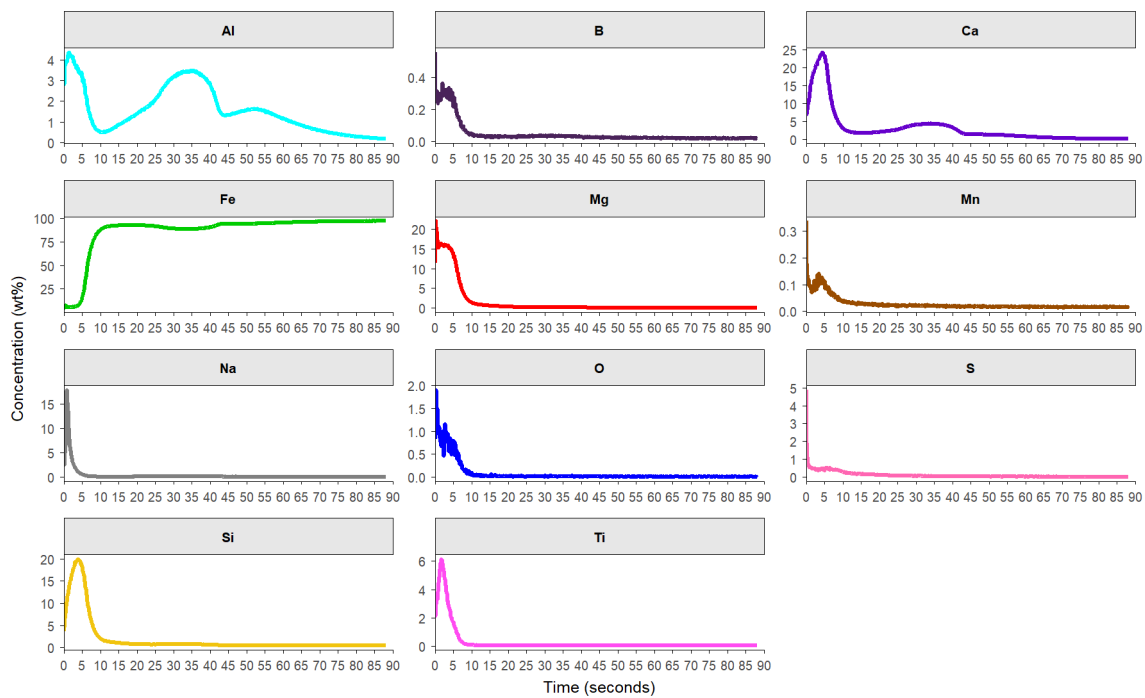
Figure 124. Individual line plots of each element that Figure 123 is composed of when a sample is coated with MgO + TiO$_2$ + Na$_2$B$_4$O$_7$·10H$_2$O (Borax) and heat-treated to 1100ºC.

The resulting composition using GDOES analysis when heated to 1150ºC following HTCA cycle in Figure 125 and Figure 126. The trend of the suppression of Fe at the surface and in the subsurface is still prevalent. The line of interception between Mg- Fe occurs at 4 seconds.

114
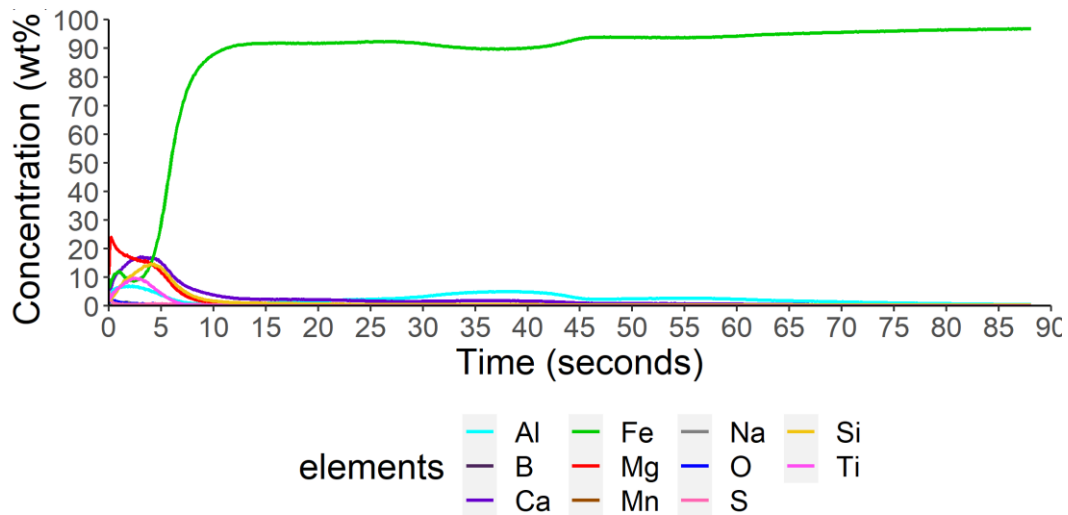
Figure 125. Changes in chemical composition through the surface oxide to the substrate when coated with MgO +TiO$_2$ + Na$_2$B$_4$O$_7$·10H$_2$O (Borax) and heat-treated to 1150ºC.

The Mg$_{max}$ concentration reaches 24% at 0.2 seconds, and Ti$_{max}$ is detected at 9.8% at 2.5 seconds. The detection of low levels of B continues with a B$_{max}$ of 0.6% at 0 seconds. The Si$_{max}$ is 14.7% at 4.1 seconds. The diffusion of Al from the substrate has continued with a surface Al$_{max}$ of 7.1% at 2.2 seconds and a subsurface Al$_{max}$ of 5.1% at 38.2 seconds. There are no significant changes in the composition through the surface oxide to the bulk material, reflected in the slight changes seen in the morphology under SEM shown in Figure 116.
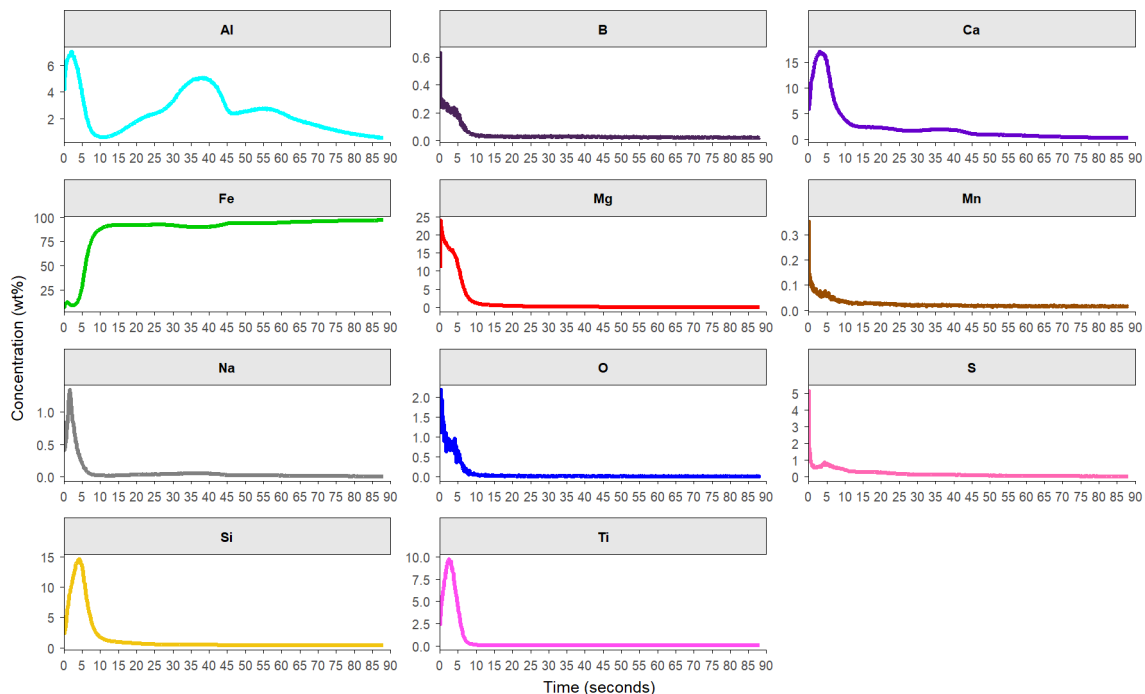
Figure 126. Each element's line plots that Figure 125 is composed of when a sample is coated with MgO + TiO$_2$ + Na$_2$B$_4$O$_7$·10H$_2$O (Borax) and heat-treated to 1150ºC.

115

3.4.3 Magnetic Properties with TiO₂ and Na₂B₄O₇·10H₂O (Borax) Addition to the Slurry

The magnetic properties of the electrical steel when coated with TiO_2 and Borax additions to the MgO slurry that have been interrupted through the HTA cycle are displayed in Figure 127. Minor improvements in magnetic properties are seen between 900°C – 1000°C. Nevertheless, at 1050°C, a dramatic change in the magnetic properties whereby a large spread in performance is observed. The reason for this dramatic change is not studied in this body of work. However, many factors affect the pinning effect, such as precipitate size, dislocation density and temperature, to state a few [93][128]. However, the literature indicates that Al-N begins to break down between 1000-1100°C, and the decrease in losses occurs because secondary recrystallisation has begun.
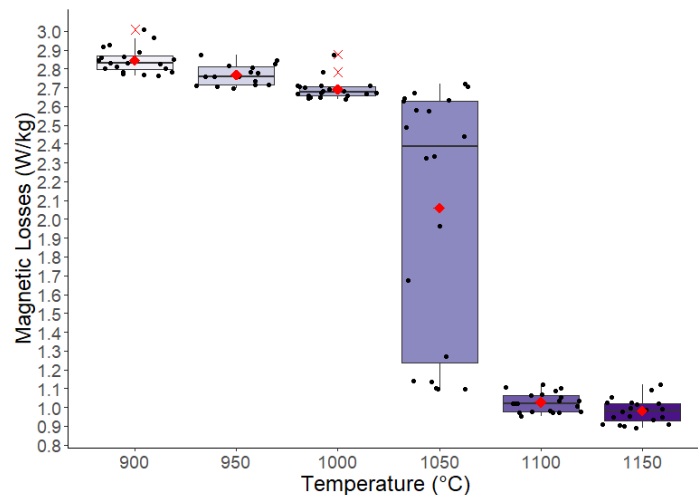
Figure 127. Magnetic properties at various temperatures following the HTA heat cycle where the substrate has been coated with MgO + TiO₂ + Na₂B₄O₇·10H₂O (Borax).

3.4.4 Current Detected Through Developing Oxide Layer with Addition of TiO₂ and Borax to the MgO Slurry

The results of the current detected through the oxide layer developed when TiO_2 and Borax were added to the MgO slurry at various points of the HTA cycle is displayed in Figure 128. The increase in temperature has resulted in a decrease in current is detected through the surface oxide layer using a Franklin tester. At 1000°C, a significant reduction in current is detected through the oxide layer and indicates that an insulation layer has developed. Further increases in temperature to 1050°C show additional improvements in reducing current detected, which correlates with developing a "uniform" Mg layer developing at the surface of the electrical steel. A continued temperature increase has resulted in a decline in current detected.
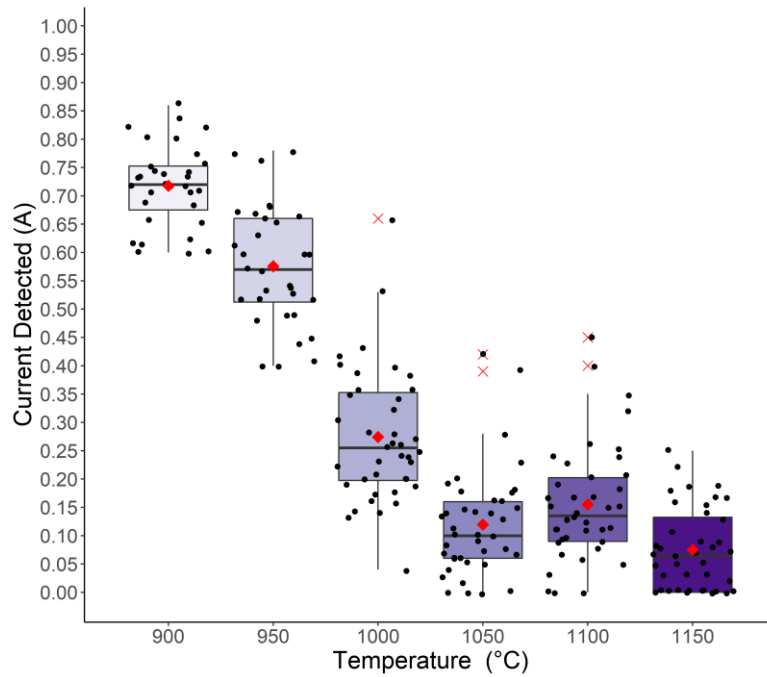
Figure 128. Current detected through the oxide layer at various stages of the heat treatment following HTCA cycle that has been coated with MgO + Na$_2$B$_4$O$_7$·10H$_2$O (Borax) using Franklin Tester.

3.4.5 Bulk Analysis of Carbon, Oxygen, Nitrogen and Sulphur

The oxygen detected in the substrate coated with a MgO slurry with TiO$_2$ and borax additions interrupted during the HTA cycle at various points is displayed in Figure 129. An increase in oxygen content is seen at 1000ºC and continues with temperature increases. The increase in oxygen content can be attributed to the development of the surface oxide seen in the SEM cross-section in section 3.4.1.
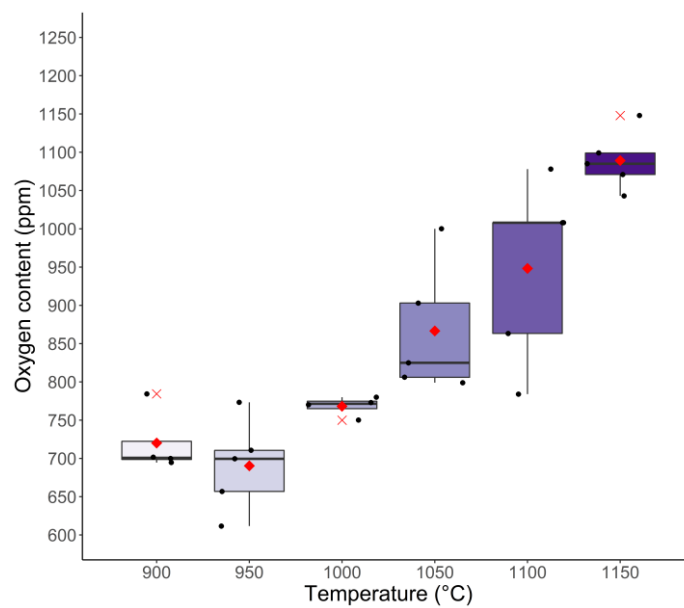
Figure 129. Magnetic properties at various temperatures following the HTA heat cycle where the substrate has been coated with MgO + TiO$_2$ + Na$_2$B$_4$O$_7$·10H$_2$O (Borax).

Figure 130 shows the nitrogen content of a substrate that has been coated with TiO_2 and Borax additions to the MgO slurry, which has then undergone an HTA cycle that has been interrupted at various stages of the cycle. As Figure 130 displays a slight reduction in nitrogen content between 900ºC and 1000ºC at 1050ºC, a sizeable reduction in the nitrogen content is detected, and this trend continues with temperature increases. Although the nitrogen content has decreased from 218 ppm to 105ppm, the complete removal of nitrogen has not reached potential minimum levels. Nitrogen levels were detected in samples of < 40ppm in samples that have been exposed to high temperatures for an extended period of time. This will be discussed further in Chapter 4.
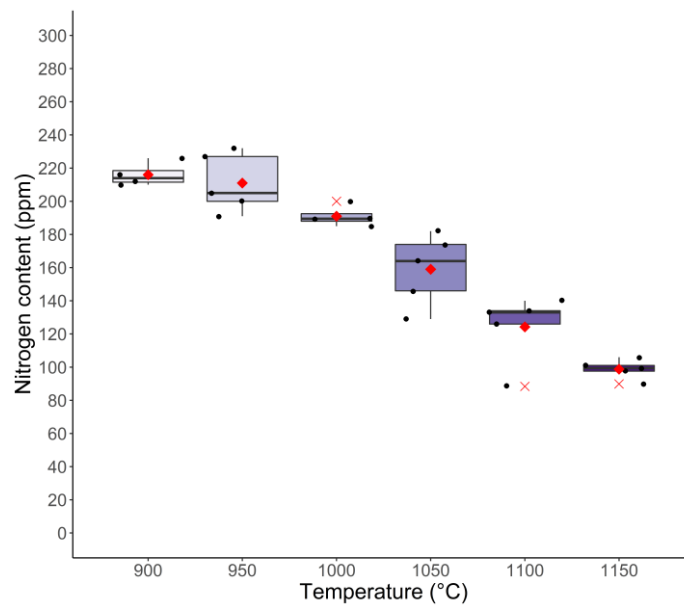
Figure 130. Nitrogen content present of the bulk substrate at the various temperature during the HTCA cycle collected by LECO TN400 when coated with MgO + $Na_2B_4O_7 \cdot 10H_2O$ (Borax)

The sulphur content follows a similar trend to the nitrogen content, whereby the sulphur content decreases at 1050ºC, which indicates the reduction of Mn-S precipitates becoming ineffective. This allows for secondary recrystallization to take place and the sulphur to be removed from the substrate by hydrogen gas by the following reaction: -

$$MnS + H_2 \rightarrow Mn + H_2S$$
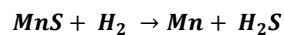
Equation 11. The chemical reaction for the reduction of manganese sulphide.
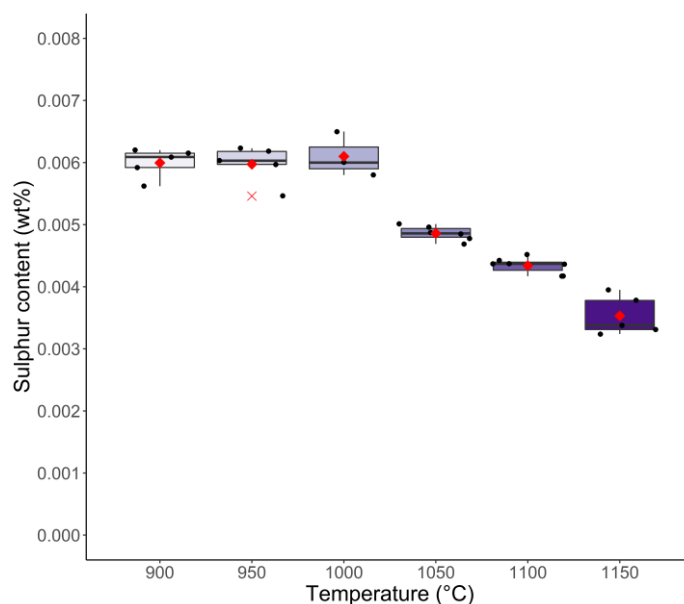
Figure 131. The sulphur content present of the bulk substrate at various temperatures during the HTCA cycle was collected by LECO CS844.

3.4.6 Discussion

The trivial amount of $Na_2B_4O_7 \cdot 10H_2O$ (Borax) added to $MgO + TiO_2$ used by Orb Steelworks has not demonstrated any impact on the magnetic or resistance properties of the steel. Furthermore, there are no significant changes in the morphology of the surface oxide through the heating stage. However, there is the detection of high levels Na from the GDOES results at >1050ºC. It is difficult to conclude that samples coated with $MgO + Na2B4O7 \cdot 10H2O$ (Borax) did not increase Na from the GDOES analysis. There would be an expectation that B would also be detected along with Na. However, only trace amounts are detected (<2%). Therefore, the role of $Na_2B_4O_7 \cdot 10H_2O$ (Borax) is inconclusive during the heating phase of the annealing process, but the removal of this addition would be recommended to remove a variable from the process and requirement of purchasing of $Na_2B_4O_7 \cdot 10H_2O$ (Borax).

3.5 Comparison of additives.

The purpose of this chapter was to identify the region in which an Mg enriched layer begins to develop due to literature indicating that the Forsterite layer develops at high temperatures i.e., >1200ºC. The work also aimed to establish whether the additions that Orb Steelworks currently use, at the concentrations used influence the development of this Mg during the heating phase of the annealing cycle.

The line of interception between Mg-Fe between all the mixes at temperatures 1050ºC, 1100ºC and 1150ºC is displayed in Table 9. It is difficult to come to any definite conclusion due to minor changes seen in the line of intercept. However, for all 3 mixes the critical temperature is 1050 ºC, at this point a consistent Mg layer at the surface has developed, with indications that higher temperatures further increase this layers consistency as indicated by the line of interception between Mg and Fe. Using

119

qualitative SEM assessment, it is difficult to determine if the coating thickness has increased, therefore in the next section image analysis has been undertaken to see if a more quantitative approach provides clearer indications.

Table 9. Displaying the time in which Mg-Fe intercept at various temperatures when coated with MgO only, MgO + TiO_2 and MgO + TiO_2+ $Na_2B_4O_7 \cdot 10H_2O$.

Mix	Mg-Fe Line of interception at 1050°C	Mg-Fe Line of interception at 1100°C	Mg-Fe Line of interception at 1150°C
MgO	3 seconds	2.5 seconds	4.6 seconds
MgO + TiO_2	3.7 seconds	4.2 seconds	5.1 seconds
MgO + TiO_2 +$Na_2B_4O_7 \cdot 10H_2O$	4.1 seconds	4.8 seconds	4 seconds

The magnetic properties that developed through at the various points of the heating phase of the HTCA when the three coatings that were applied to the substrate is displayed in Table 10. Again, all three mixes show a critical development in magnetic properties at 1050 °C, with further but less dramatic reductions in magnetic losses as the temperature is increased further. Ultimately at temperatures greater than 1100 °C the magnetic losses are comparable across all three formulations. Therefore, the addition of TiO_2 and $Na_2B_4O_7 10H_2O$ are neither beneficial nor detrimental to the magnetic properties of the material.

Table 10. Comparison of the magnetic properties developed with the three-coating applied at various temperatures during the heating phase of the HTA.

Mix	Average magnetic properties at various point of the heating phase of the HTA of samples(W/kg)					
	900°C	950°C	1000°C	1050°C	1100°C	1150°C
MgO	2.86 ± 0.45	2.74 ± 0.05	2.68 ± 0.04	1.94 ± 0.70	1.04 ± 0.05	0.94 ± 0.07
MgO + TiO_2	2.86 ± 0.05	2.71 ± 0.04	2.71 ± 0.06	1.94 ± 0.70	1.04 ± 0.05	0.97 ± 0.08
MgO + TiO_2 +$Na_2B_4O_7 \cdot 10H_2O$	2.86 ± 0.05	2.75 ± 0.05	2.70 ± 0.06	2.04 ± 0.66	1.03 ± 0.05	0.98 ± 0.06

All mixes have exhibited an improvement with an increase in temperature, and the mixes display near the same current detected at the temperature of interest. At 1000°C, there is a significant decrease in current detected and continue to improve upon further temperature increase. There is no apparent improvement or nor deterioration of the resistance with the addition of additives during the heating phase of HTA.

Table 11. Comparison of the resistance properties developed with the three-coating applied at various temperatures during the heating phase of the HTA.

Mix	Average current detected at various points of the heating phase of the HTA of samples (amps)					
	900°C	950°C	1000°C	1050°C	1100°C	1150°C
MgO	0.70 ± 0.06	0.62 ± 0.09	0.35 ± 0.13	0.19 ± 0.14	0.14 ± 0.09	0.08 ± 0.05
$MgO + TiO_2$	0.68 ± 0.06	0.56 ± 0.09	0.25 ± 0.11	0.14 ± 0.08	0.15 ± 0.08	0.07 ± 0.05
$MgO + TiO_2$ $+Na_2B_4O_7 \cdot 10H_2O$	0.72 ± 0.07	0.58 ± 0.10	0.27 ± 0.12	0.12 ± 0.09	0.16 ± 0.10	0.08 ± 0.072

3.5.1 Conclusion

This Chapter has shown the presence of an Mg enriched layer of a significant thickness to occur at 1050°C, which has not been displayed in previous work. Furthermore, the introduction of TiO_2 is not significantly beneficial, and the role which TiO_2 plays in the development of the surface oxide and previously published work have just stated that 0-30% of TiO_2 should be added to the MgO slurry without explanation. This work has also demonstrated that Ti forms as part of the surface oxide as low as 1050°C. There are no signs of influence on the magnetic properties, or the resistance of the surface oxide with all the addition of TiO_2 or $Na_2B_2O_7$ $10H_2O$ tested showed a similar result. At 1050°C, there is also a significant change in the magnetic and resistance properties of the steel, which correlates with literature that highlights that at ~1050°C, secondary recrystallisation occurs. This critical temperature remains consistent across the three formulations. The addition of $Na_2B_2O_7$ $10H_2O$ is inconclusive and does not exhibit measurable or deterioration of properties of the steel or surface oxide. However, improvement may not be exhibited due to the small sample size compared with the production scale.

3.5.2 Future Work

The Mg enriched layer developed at 1050°C and above requires identification throughout the heating phase of the HTCA to identify the compound and any changes that may be seen when increasing the temperature. This identification may be possible through XRD; however, due to the possible inconsistency in the compound and the thin layer developed, an alternative technique such as XPS may prove a more suitable technique. Similarly, the presence of the Ti in the surface oxide requires the identification of the compound.

Trials at Orb Steelworks should be conducted without the addition of $Na_2B_2O_7$ $10H_2O$ to identify noticeable changes that occur and analysed using techniques in this body of work.

Chapter 4. The Effects of Duration of the High Temperature Soak on the Development of Surface Oxide.

4.1 Introduction

As outlined in Section 1.11, one of the main obstacles of batch annealing at a large scale is the creation of large temperature gradients during the heating phase of the process. The extent of the temperature gradient created during the heating increases the minimum time required at the high-temperature soak (HTS) phase to ensure that the temperature is reached through the whole batch of coils. Several studies of the temperatures gradients have been investigated by Orb Steelworks process using measurements and computer modelling [85][129]. However, there is inadequate research on the minimum time the substrate is required to spend at high temperatures to achieve the desired purification of the substrate, magnetic properties, and oxidation. In addition, there is limited information on the potential influence of additives used by Orb Steelworks has during the HTS.

The aim of this section is to improve the understanding of changes that occur during the HTS and whether an extended time at temperature has a beneficial or detrimental effect on electrical steel performance. In addition to understanding the influence, current additives have on the properties of the steel during the HTS.

4.2 Methods

The following section outlines the details of the substrate selection, the amount of addition, coating method, heat treatment and analysis conducted on the heat-treated samples presented in this chapter. Further details on all described processes can be found in the Methods and Materials section in Chapter 2.

The substrate used for all the samples in this chapter was J15155 collected from the exit of D-line at Orb Steelworks and reduced to 350 x 100 x0.23mm coupons. The additives that were added to the magnesium slurry were TiO_2 and Borax. The quantity and combination of these additives are displayed in Table 12. The MgO and additives were added in distilled water that was chilled at 10°C and mixed for 1 hour before the coating was applied to the substrate. The viscosity and pH of the slurry were tested for each mix.

Table 12. Quantities of ingredients are used to create the various percentages of additives to create the desired slurry.

Mix	MgO	TiO_2	Borax $(Na_2B_4O_7)$	Distilled water (ml)
MgO Only	112g	-	-	800
MgO + TiO_2	112g	4.80g	-	800
MgO + TiO_2 + Borax	112g	4.80g	0.092g	800
MgO + Borax	112g	-	0.092g	800

The samples were coated at Orb Steelworks using the custom laboratory roller coater. The slurry applied to the substrates was dried in the Nabertherm furnace at 750°C until the water has been driven

122

out of the MgO slurry. The mass of each substrate was weighed before and after coating. Each sample gained approximately 0.50g after coating with the slurry and dried.

All mixtures and reference samples were placed in a stack with sacrificial samples between different mixes. The stack of samples was then placed between two steel heat treatment blocks scurried with metal banding in a cross configuration.

Heat treatment was carried out in the bespoke Carbolite GPC 1300 furnace described previously. The stack of banded samples was placed in the furnace and followed the heat treatment cycle C) carried out by Orb Steelworks, as shown in Figure 49. The average coating thickness was assessed by cross-section images of the surface and processed using Matlab as explained in section 2.7.2.

4.3 The Influence of High-Temperature Soak when using MgO Only Coating.

4.3.1 Morphology and Coating Thickness of Surface Oxide Developed

Figure 132 is a representative image of the surface oxide developed with a sample that has been coated with MgO only slurry and been heat-treated for 10 hours. Both surfaces have formed a uniform oxide at the surface with keying points across the length of the image of the surface oxide. There is a substantial quantity of subsurface oxide present below the surface oxide.

a)   b)
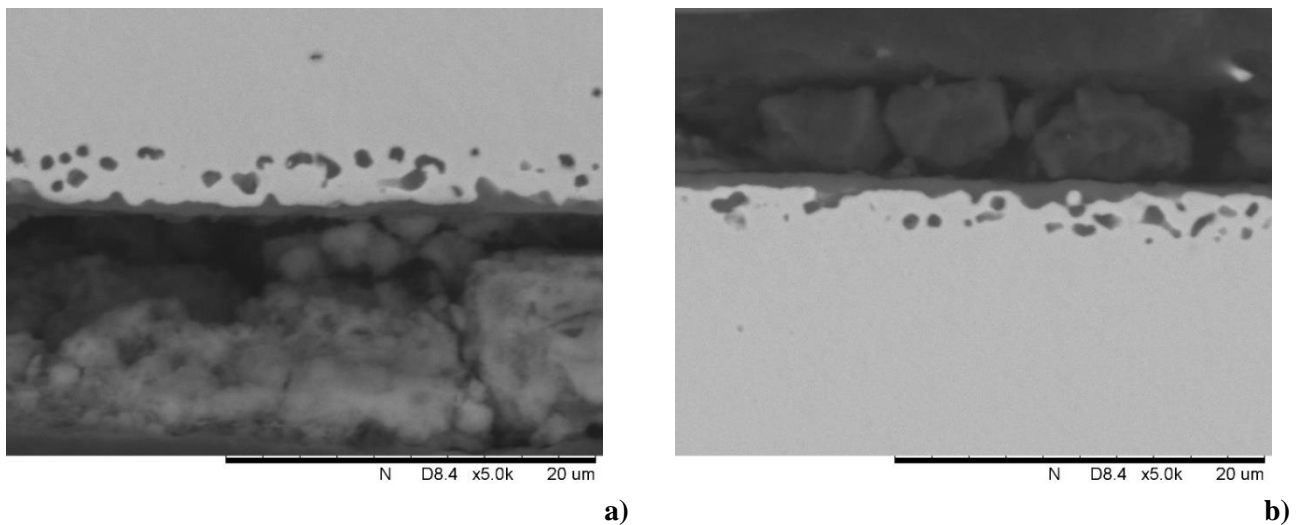
Figure 132. Morphology of the oxide after spending 10 hours at HTS and coated with MgO only (a) up-facing surface (b) down-facing surface.

Figure 133 illustrates the cross-sections of the oxide layer developed after 25 hours of soak when coated with MgO slurry. The additional time at the high-temperature soak appears to have a limited effect on the surface oxide. The surface and subsurface remained consistent across the image, and no apparent changes in thickness when compared with 10 hours. The presence of subsurface oxide appears to be reduced, but this is difficult to clarify due to the distribution of precipitates contained in these steels.
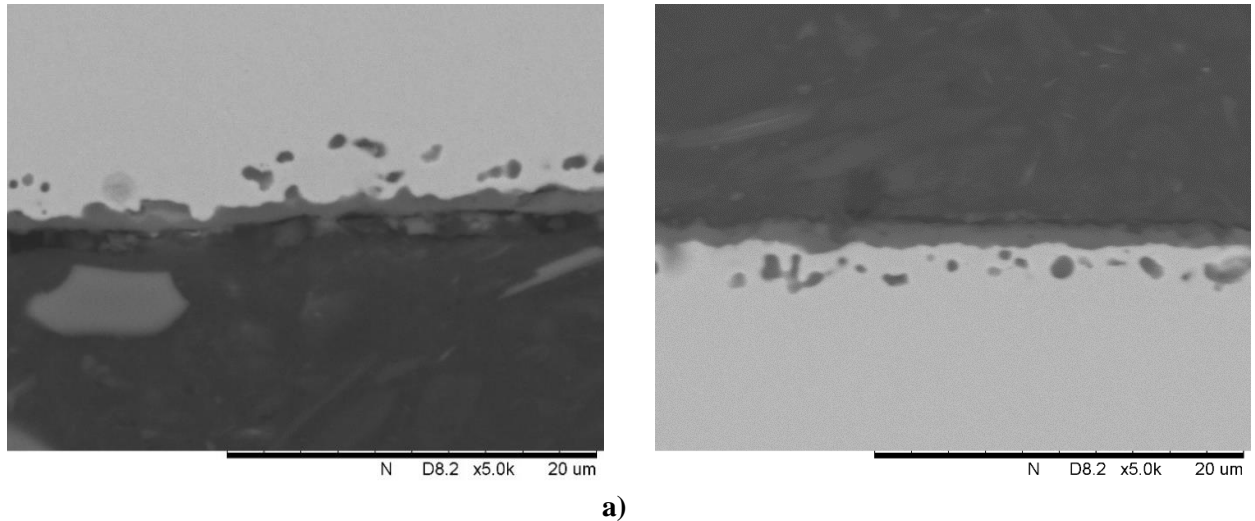
Figure 133. Morphology of the oxide after spending 25 hours at HTS and coated with MgO only (a) up-facing surface (b) down-facing surface.

Figure 134 illustrates the cross-sectional image of the surface oxide coated with MgO and soaked for 50 hours. The surface oxide has remained consistent with several keying points. Subsurface oxide is still present even with the additional time at temperature and has resulted in incomplete migration of the surface oxide to the surface.
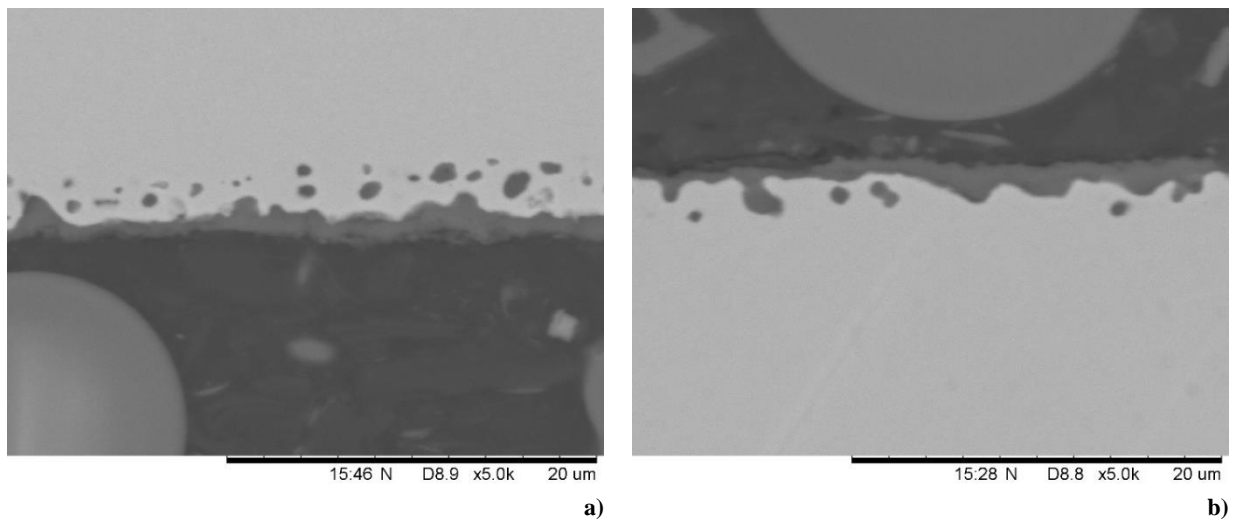
Figure 134. Morphology of the oxide after spending 50 hours at HTS and coated with MgO only (a) up-facing surface (b) down-facing surface.

The morphology of the coating does not display significant changes during the length of the HTS examined. Both surface oxide with keying points and subsurface oxides exists. However, the measurements indicated a small increase in thickness over time to a maximum of approximately to 1micron.

The measurements of the surface oxide layers of cross-sections coated with MgO and exposed to a period at HTA are displayed in Figure 135. The average thickness of the oxide layer developed at 10 hours soak is 0.79μm which is identical to the 5 hours soak, but the standard deviation has decreased from ±0.16 after 5 hours soak to ±0.11 in the 10 hours soak. Additional time at HTS (20 hours) has

resulted in the average coating thickness increasing to 0.94 µm and, when increased to 30 hours, soak an average of 1 µm. The MgO samples that were placed in the production furnace achieved an average oxide thickness of 0.96 µm. The spread of the measured coating thickness makes it a difficult to come to any clear trend and the duration of the soak does not appear to influence the thickness of measured surface oxide with MgO only coated samples.
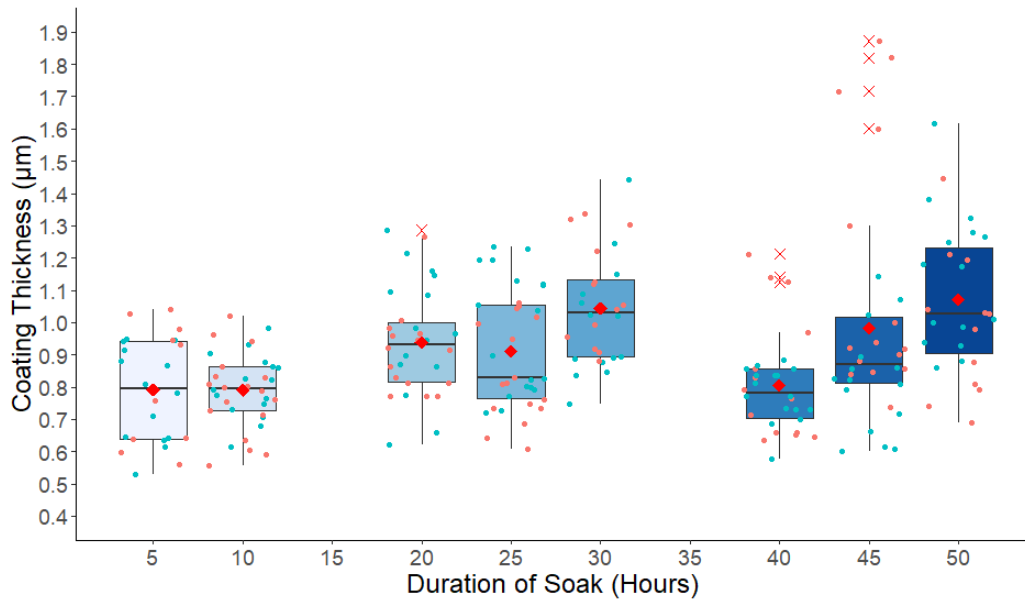
Figure 135. Measured SEM cross-sections of samples that have been coated with MgO only and heat-treated at the various duration of soak time at the HTS.

4.3.2   Composition Changes through the Surface Oxide using GDOES Analysis with Samples that have been Coated with MgO.

The composition developed after 10 hours of soak during the high-temperature annealing process with MgO is only demonstrated in Figure 136. The resulting composition has achieved an enriched Mg surface layer, suppressing the Fe content at the surfaces. The line of interception between Mg-Fe occurs at 4.5 seconds.

125
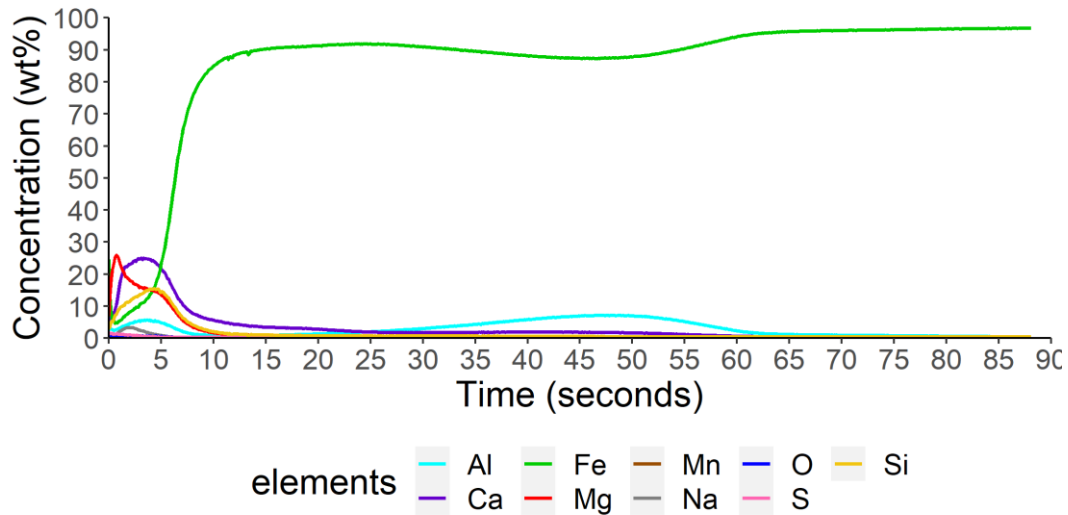
Figure 136. Changes in chemical composition which has been coated with MgO only and is held at HTS for 10 hours.

The elements detected in the surface oxide Mg, Fe, Al, Si, S and Na. The maximum concentration of Mg_{max} is 25.9% at 0.7 seconds and reaches 1% at 11 seconds. The Si_{max} is 15.4% at 4.3 seconds. The Al displays two peaks; the surface peak occurs at 3.7 seconds with an Al_{max} 5.7%, and the subsurface peak occurs at 47.6 seconds with an Al_{max} of 7.2%. The S_{max} occurs at 0.1 seconds with a concentration of 1.7%
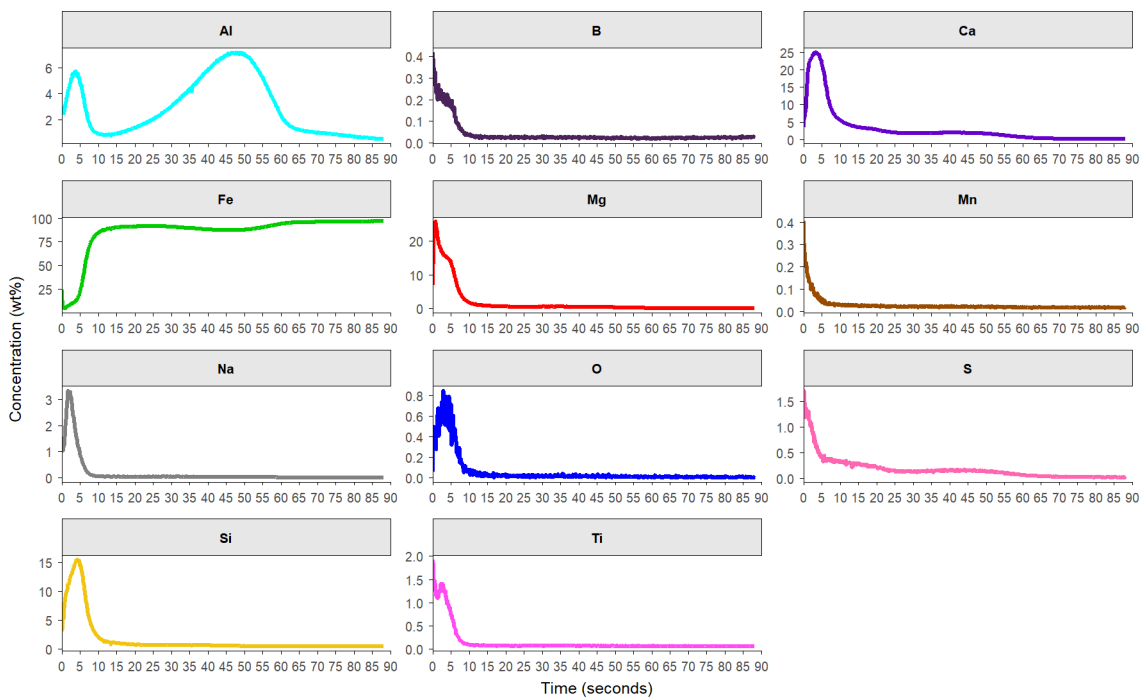
Figure 137. Individual line plots of each element that Figure 136 is composed of when a sample is coated MgO and is held at HTS for 10 hours.

The chemical composition developed after 30 hours at the HTS that is coated with MgO is displayed in Figure 138. There are no apparent changes in the chemical composition at the surface or subsurface

126

oxide with Mg, Si, Al, Fe, S and Na still detected. The line of interception between Mg-Fe occurs at 3.6 seconds.
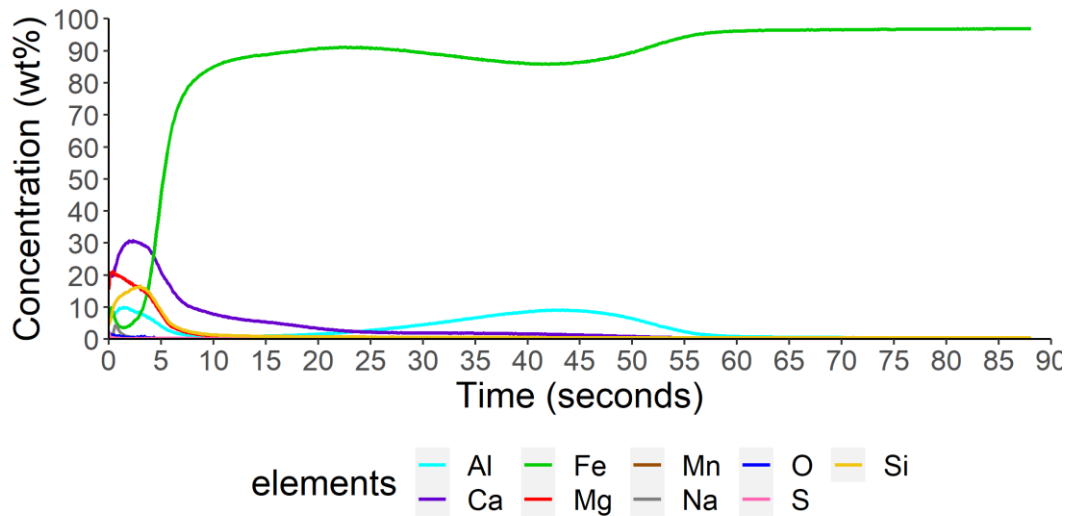
Figure 138. Changes in chemical composition through the surface oxide to the substrate, when coated with MgO, have been exposed to a Hi-B annealing cycle and held at HTS for 30 hours.

Figure 138 is focused on the surface oxide, and it shows no significant changes in the chemical composition with the additional time spent at the soak temperature. The concentration Mg_{max} reaches 21.2% at 0.4 seconds and reduces to 1% at 10.6 seconds, and the Si_{max} is 16.7% at 3 seconds. The Al surface peak reaches 10.0% at 1.4 seconds and a second peak at 9.2% at 43.3 seconds. The S concentration reaches a maximum of 2.5% at 0 seconds and rapidly drops. Na_{max} at 4.29% at 0.7 seconds and drops to 1% by 1.7 seconds.
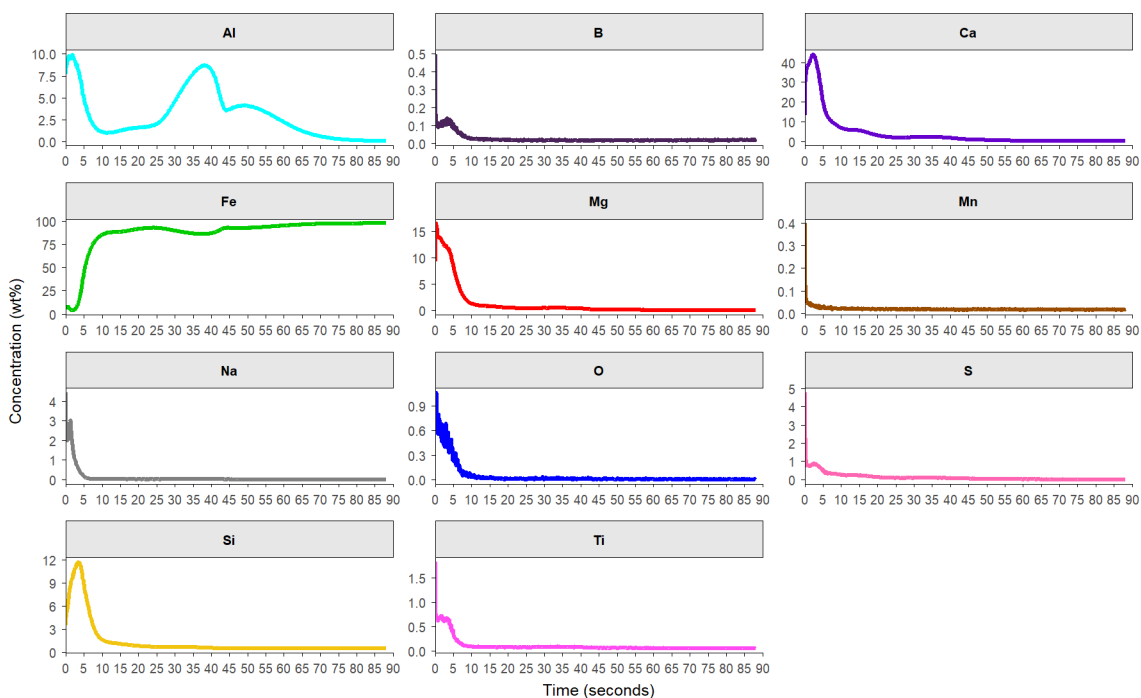
Figure 139. Individual line plots of each element that Figure 138 is composed of when a sample is coated MgO and is held at HTS for 30 hours.

127

The change in chemical composition through the surface oxide to the substrate developed after 50 hours of soak is displayed in Figure 140. There have been no additional elements detected from the 5- and 30-hours soak, and the line of interception between Mg-Fe occurs at 3.3 seconds.
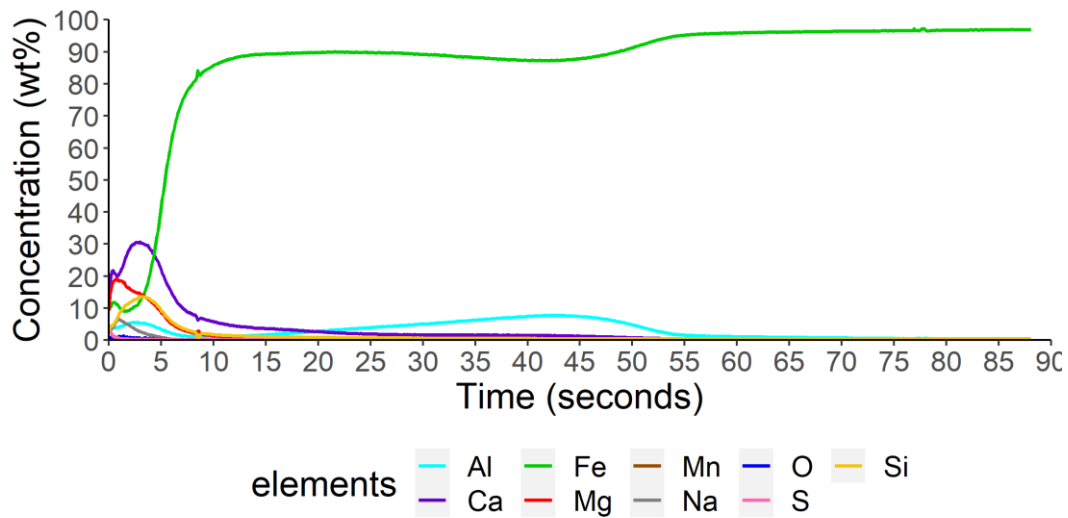
Figure 140. Changes in chemical composition through the surface oxide to the substrate, when coated with MgO, are held at HTS for 50 hours.

On closer inspection of the surface oxide in Figure 140, the Mg_{max} is 19.2% at 0.7 seconds and reduced to 1% by 12.8 seconds. The Si_{max} is 13.7% at 3.1 seconds. The Al_{max} peaks at the surface at 5.7% at 2.7 seconds the surface at 7.8% at 42.4 seconds. The S_{max} reaches 4.9% at 0 seconds and reduces to 1% at 0.6 seconds. Finally, the Na reaches a maximum of 6.6% at 1.0 seconds.
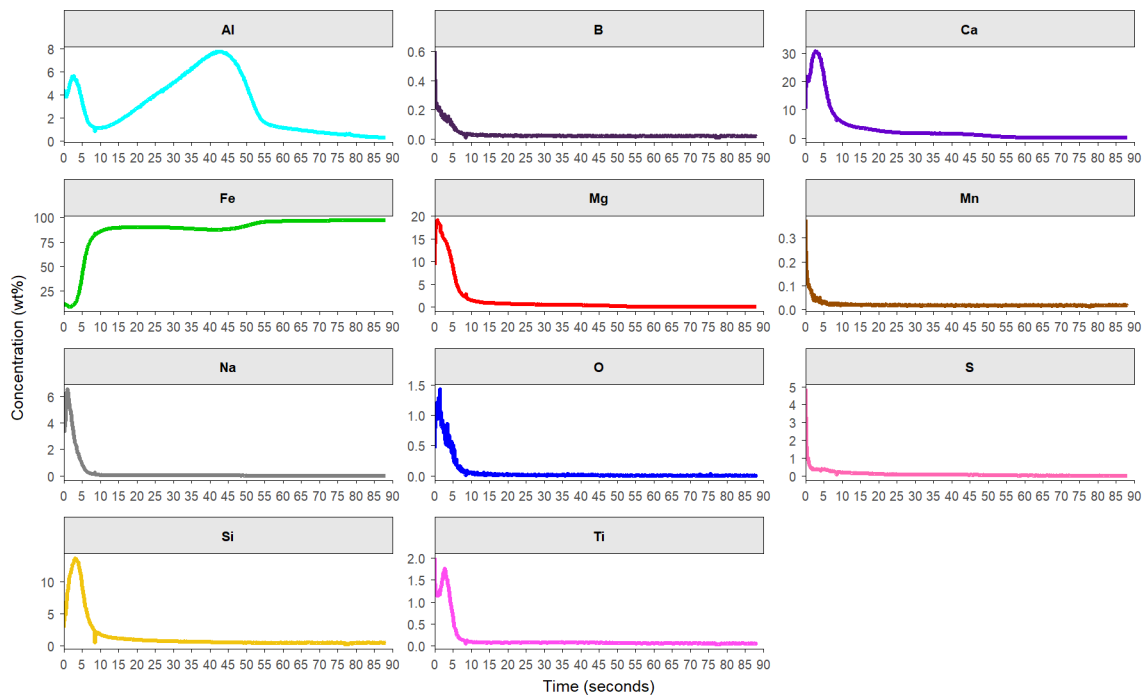
Figure 141. Individual line plots of each element that Figure 140 is composed of when a sample is coated MgO and is held at HTS for 50 hours.

128

The extended Soak time shows no evidence in influencing the chemical composition changes with the duration of the soak from GDOES analysis. There is variation observed in the concentration of elements, but the variation is typically present within a sample.

4.3.3 Magnetic Properties

The results of magnetic properties at different high-temperature soak periods when coated with a slurry containing MgO using the Soaking tester method are displayed in Figure 142. The magnetic properties achieved at 5 hours show considerably higher losses with an average loss of 0.93 W/kg compared to 10 hours soak, which has reduced to 0.85 W/kg. The higher magnetic properties detected in 5 hours and the variation in the magnetic properties suggest that the process of secondary recrystallisation has not fully occurred, and some Al-nitrides maybe still be present. However, after 5 hours, the average magnetic losses remain reasonably consistent throughout all the soaks and variations that are seen are likely due to incorrect texture developing rather than purification of the substrate due to the levels of N, C, and S detected, which are very low after 20 hours.
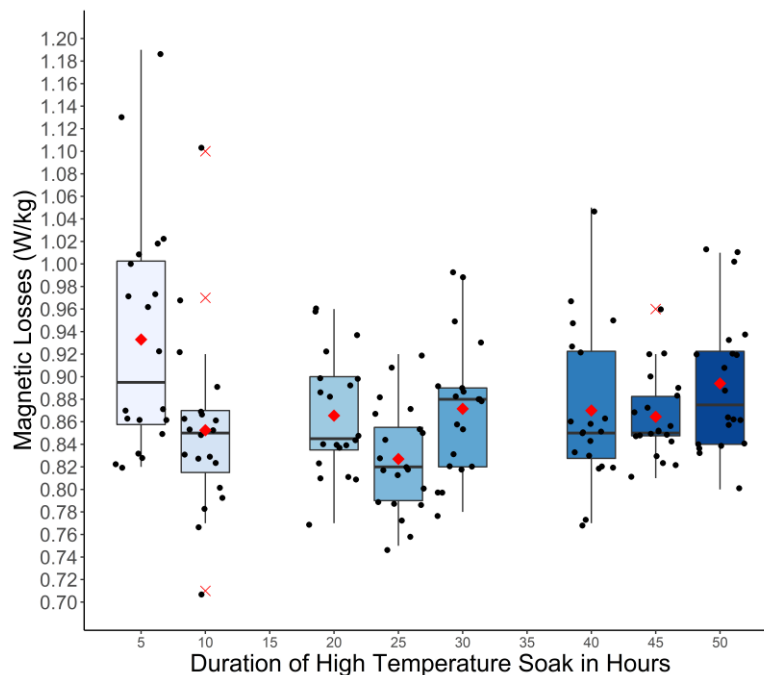
Figure 142. Magnetic properties of substrates that have been exposed to different durations at HTS when coated with MgO.

4.3.4 Bulk analysis of Carbon, Oxygen, Nitrogen and Sulphur

The oxygen content detected at the various durations of HTS coated with MgO is displayed in Figure 143. All heat treatments show oxidation has occurred with an increase in oxygen content from 700 ppm detected in the decarburisation stage to > 1000ppm. However, there is no apparent trend when increasing the duration of the soak.
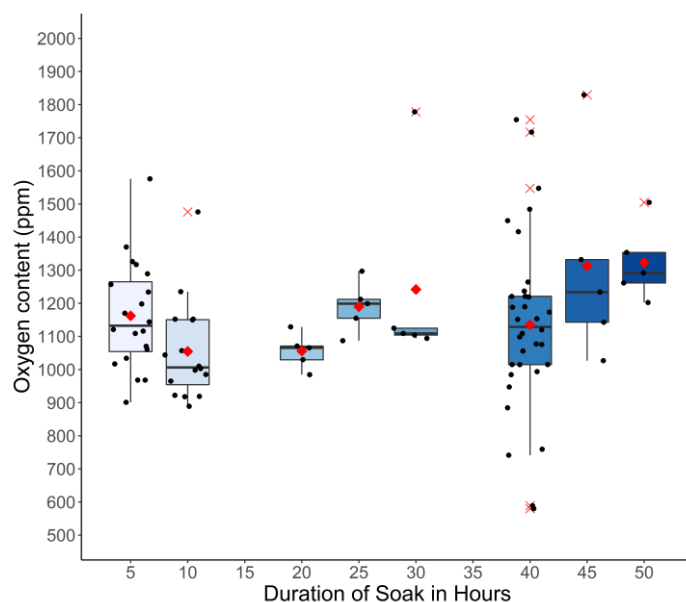
Figure 143. Oxygen content is present in the bulk substrate at the various times spent at the HTS when coated with MgO.

The nitrogen content of the substrate that has been coated with MgO slurry and been exposed to various times of high-temperature soak is shown below in Figure 144. Samples that have had 5 hours soak appear to have not had sufficient time to remove the Al-N from the substrate. This will result in areas of partial recrystallization and pinning sites which will cause an increase in magnetic losses. However, there is a reduction in nitrogen content at 10 hours soak, and the low levels of nitrogen content do not decrease further with increased time at high temperatures.
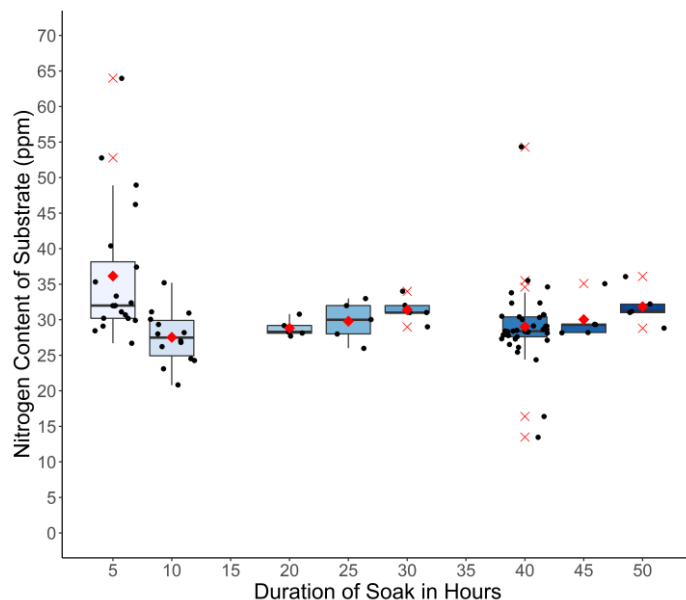
Figure 144. The Nitrogen content present of the bulk substrate at the various times spent at the HTS when coated with MgO using LECO TN400.

The sulphur content detected in substrates at various high-temperature soak duration using a Leco CS844 is displayed in Figure 145. The sulphur content shows a variation between soaks, but the variation of the sulphur is not likely a result of an extended period of time at the high-temperature soak but is likely due to the local areas of sulphur enrichment at the surface, which has been seen in

130

SEM cross-sections and GDOES analysis. It appears that an extensive soak does not show a substantial reduction in sulphur content.
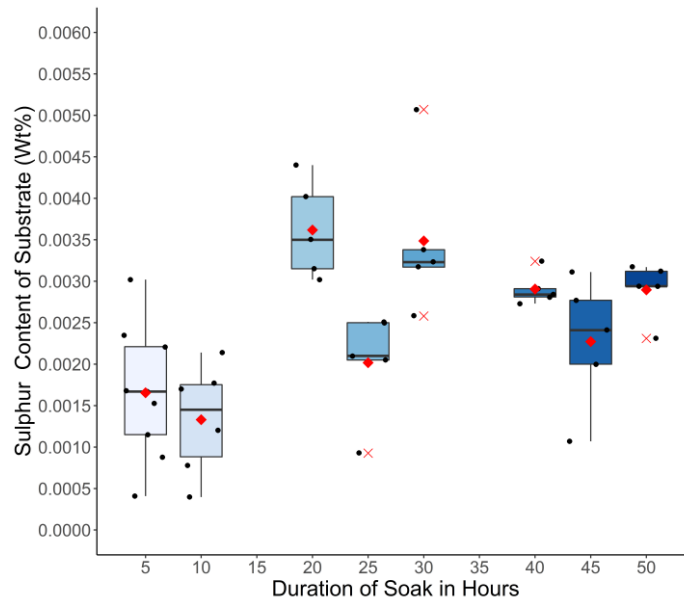
Figure 145 The sulphur content of the bulk substrate at the various times spent at the HTS when coated with MgO collected by LECO CS844.

The carbon content that is detected in the bulk of the substrate using a Leco CS844 carbon is displayed in Figure 146. The carbon concentration for most of the soaks remains below <0.5 (wt%) with the exception of the 45 and 50-hours soak. The low levels of carbon are expected due to the decarbonisation stage of the process when levels are reduced to 0.0030 wt% and the heat treatment spends a considerable amount of time in the hydrogen/nitrogen atmosphere.
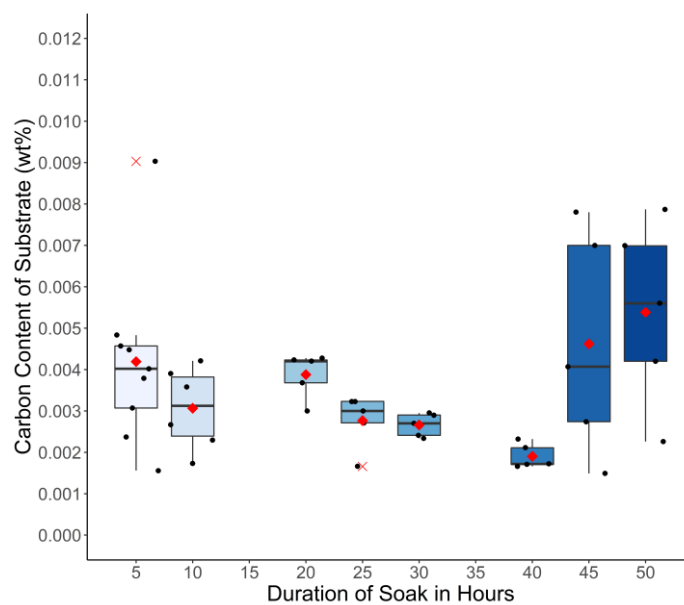
Figure 146. Carbon content is present in the bulk substrate at the various times spent at the HTS when coated with MgO collected by LECO CS844.

4.3.5 Discussion on the Effect of Duration of HTS with MgO Only Coated Substrate.

As highlighted in the introduction, the HTS is a significant proportion of the heat treatment with the high cost of maintaining the furnace for 24 hours at maximum temperature. In addition, the coils are not uniformly heated to add complications, resulting in a variety of exposure to the HTS. The HTCA conducted by Orb Steelworks is based on experience and trials conducted within a production environment. However, the minimum time required at high temperature is unknown and previous trials have highlighted that additional time is needed for the purification of the substrate to be achieved and allow for Forsterite to develop at the surface, which in turn results in an improvement in magnetic properties.

As seen in Figure 135, the duration of a soak does have a benefit on the surface oxide thickness with 0.79µm at 5 hours with additional time at HTS (20 hours) develops a 0.94µm oxide. Extending the HTS ≥30 hours shows a small improvement in the surface oxide reaching 1.07µm, but the cost of additional time at HTS does not display the benefits to justify the additional time at the high temperature. This is further confirmed by the samples placed in the production furnaces coated with MgO. These samples were subjected to "ideal" conditions and maximum HTS. The MgO samples were only capable of achieving 1.17µm surface oxide. This confirms that the MgO coating can only produce a ~1µm surface oxide with 20-30 hours soak, and <20 hours soak will result in an inferior surface oxide. This information provides Orb Steelworks with an explanation for the variations in oxide thickness within coil laps and coils in different regions of the furnace.

Furthermore, future examination of the furnaces should reduce the temperature gradients for increased productivity, improved product, and reduced production cost. The morphology of the surface oxide throughout does not demonstrate any changes in the surface/subsurface oxide. These negligible changes in morphology are reflected in the chemical composition using GDOES analysis which displays minimal changes between the various HTS periods. The magnetic properties do exhibit changes with an increase in the duration of HTS. At 5 hours, the soak is inadequate with an average of 0.93 W/kg compared with 10 hours soak, seeing a dramatic decrease in magnetic losses with an average of 0.85 W/kg. This improvement could be supported by reducing nitrogen detected from 36ppm at 5 hours to 28 ppm at 10 hours. Nitrogen content is "associated" with the precipitate Al-N, and the detection of nitrogen suggest that precipitates are present in the steel and with additional time, the remaining precipitates are removed and increase in oxide thickness.

The further time at high temperature does not display an apparent improvement with sporadic magnetic losses. For example, with 25 hours of HTS resulting in a 0.83 W/kg, an additional 5 hour soak (30 hours) has resulted in a 0.87 W/kg. It must be noted that the 45 hours and 50 hours soak do display an increase in magnetic losses, which can be explained by the unexpectedly high levels of carbon detected from the bulk analysis in Figure 146, which cannot be explained at this time. As

literature has shown, grain orientation and grain size are critical to the magnetic performance of the steel, and the surface oxide has a limited effect on the overall performance of the magnetic properties currently using an Mg enriched surface layer, i.e., "Forsterite".

4.4 The Influence of High Temperature Soaks when using MgO and TiO$_2$ Coating.

4.4.1 Morphology and Coating Thickness of Surface Oxide Developed

The resulting oxide layer developed after 10 hours at the HTS with MgO+TiO$_2$ coating applied to the substrates is displayed in Figure 147. The oxide layer is uniformed across the images, with keying regions across the oxide. There is subsurface oxide present below the surface oxide.

a)   b)
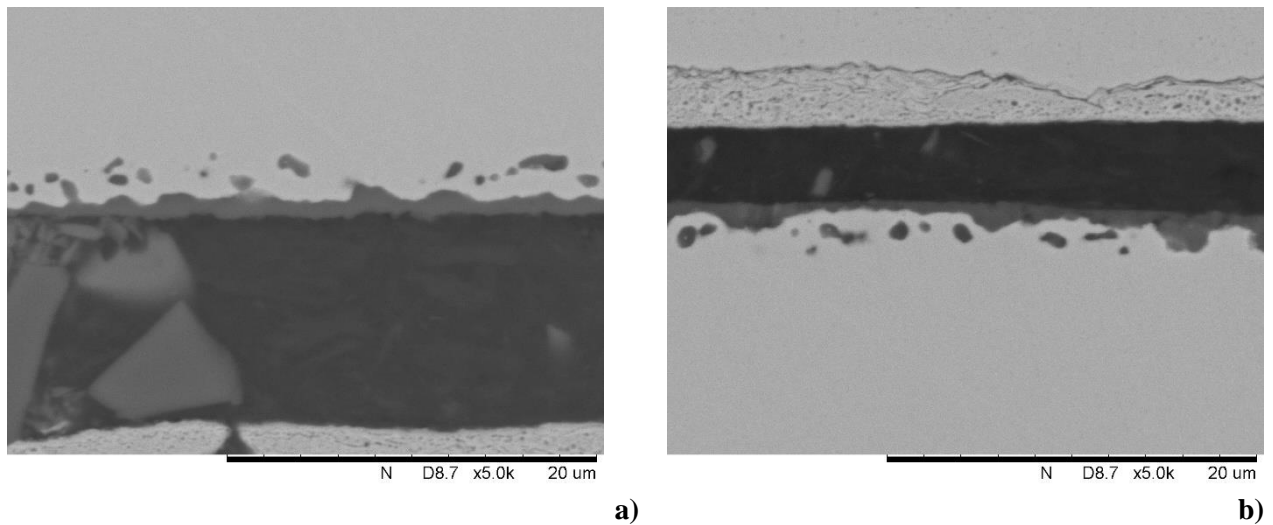
Figure 147. Morphology of the oxide after spending 10 hours at HTS and coated with MgO + TiO$_2$ (a) up-facing surface (b) down-facing surface.

The oxide layer developed after 30 hours of soak is displayed in Figure 148, and the surface oxide, indicating that no further diffusion of Mg or TiO$_2$ occurs because of the increase in time spent at high temperature.

a)   b)
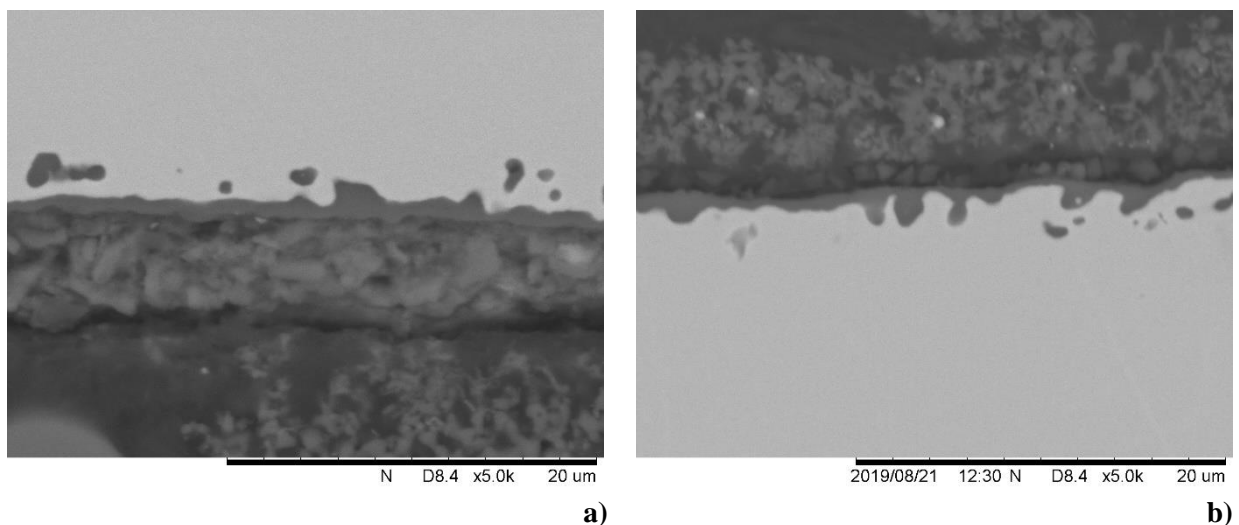
Figure 148. Morphology of the oxide after spending 30 hours at HTS and coated with MgO + TiO$_2$ (a) up-facing surface (b) down-facing surface.

On a further increase in the duration of the soak to 50 hours, as seen in Figure 149, no distinct changes in the surface oxide morphology and subsurface oxide are apparent.
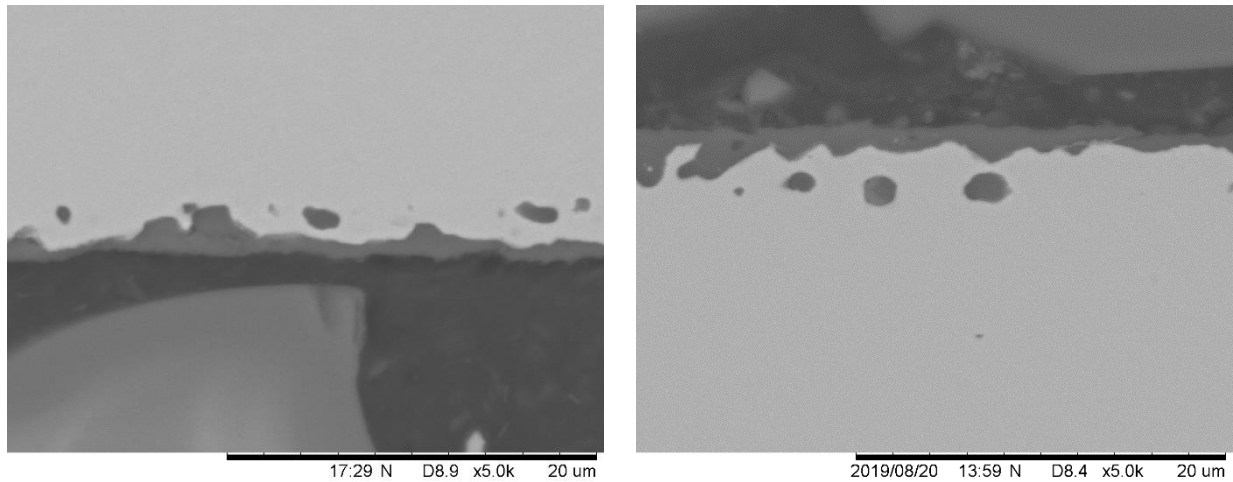
Figure 149. Morphology of the oxide after spending 50 hours at HTS and coated with MgO + TiO$_2$ (a) up-facing surface (b) down-facing surface.

TiO$_2$ to the slurry has not resulted in a noticeable change in morphology of the surface oxide under the conditions examined. Additionally, after 10 hours of soak, there is or morphology. Therefore, the morphology of the surface oxide is not improved or deteriorate with an increased duration of soak.

Figure 150 displays the measured surface oxide from cross-section SEM images. The surface oxide thickness shows a subtle increase in the average coating thickness measured when increasing the soak duration at the HTA. At 5 hours, the average coating thickness is 0.80µm; increasing the soak time to 10 hours has resulted in an average coating thickness of 0.90 µm. At the 25 and 30 hours, the oxide thickness appears to reach its maximum potential with an average oxide layer of around 1 µm, and further increase appears to fluctuate between 0.95 to 1 µm. Although under maximum soak and ideal heating when placed in HTCA, the oxide layer develops to an average of 1.2 µm, suggesting that at this point, some other mechanism is limiting the oxide thickness growth.
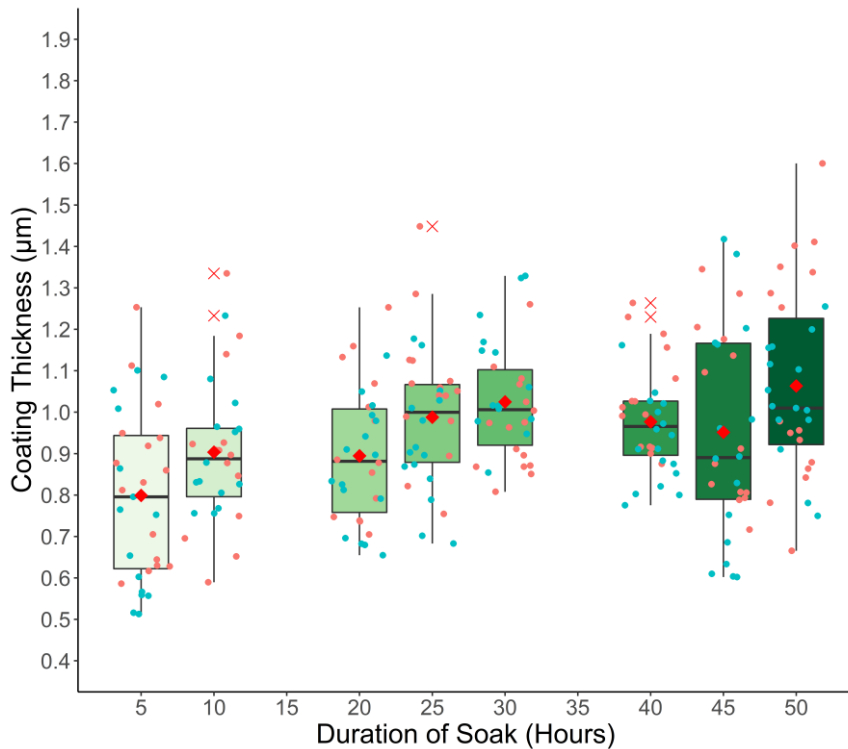
Figure 150. Measured SEM cross-sections of samples that have been coated with MgO + TiO₂ and heat-treated at the various duration of soak time at the HTS.

4.4.2 Composition Changes Through the Surface Oxide using GDOES Analysis with Samples that have been Coated with MgO and TiO₂.

The composition of the surface oxide into the substrate after samples have been coated with MgO + TiO₂ held HTS for 10 hours is illustrated in Figure 151. The typical elements detected are Mg, Si, Fe, Al, Na and S. The TiO₂ is detected at the surface of the oxide layer with Ti_{max} of 2.15% at 1.5 seconds and decrease to 1% by 3.3 seconds.
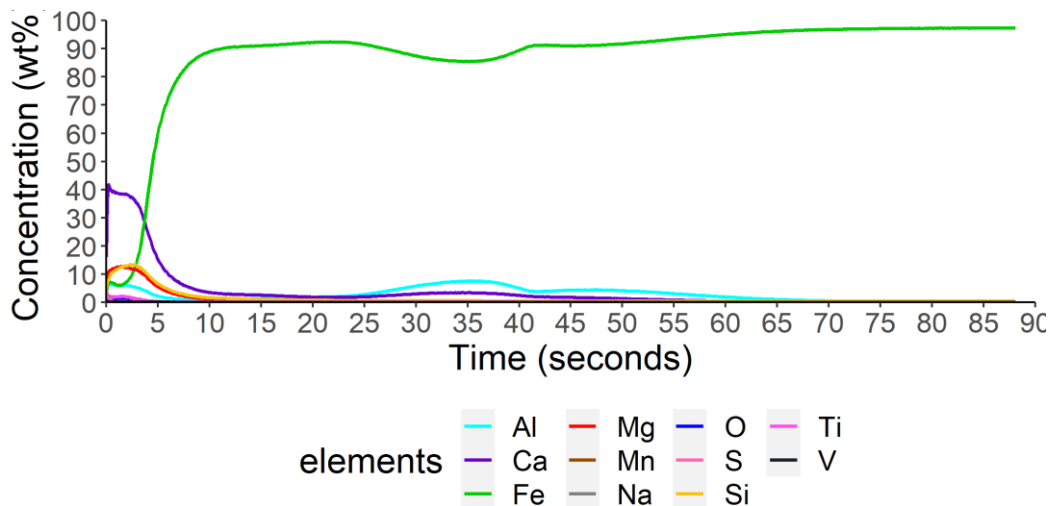
Figure 151. Changes in chemical composition from the surface to the centre of the substrate when coated with MgO + TiO₂ and is held at HTS for 10 hours.

135

On closer examination of the surface region, the line of interception between Mg – Fe occurs at 2.7 seconds. The concentration levels of Mg_{max} reaches 12.77% at 1.4 seconds and decrease to 1% at 11.5 seconds. The silicon content peaks at the surface with a Si_{max} 13.43% at 2.3 seconds, indicating that silicon is migrating from the bulk of the substrate to the surface. The S_{max} occurs at 0 seconds at 4.68%, which shows that the S has migrated to the surface, and S then reacts with Hydrogen gas that removes it from the substrate. Na was detected at a maximum concentration of 4.54% at 0 seconds which decrease to 1% by 1.7 seconds.
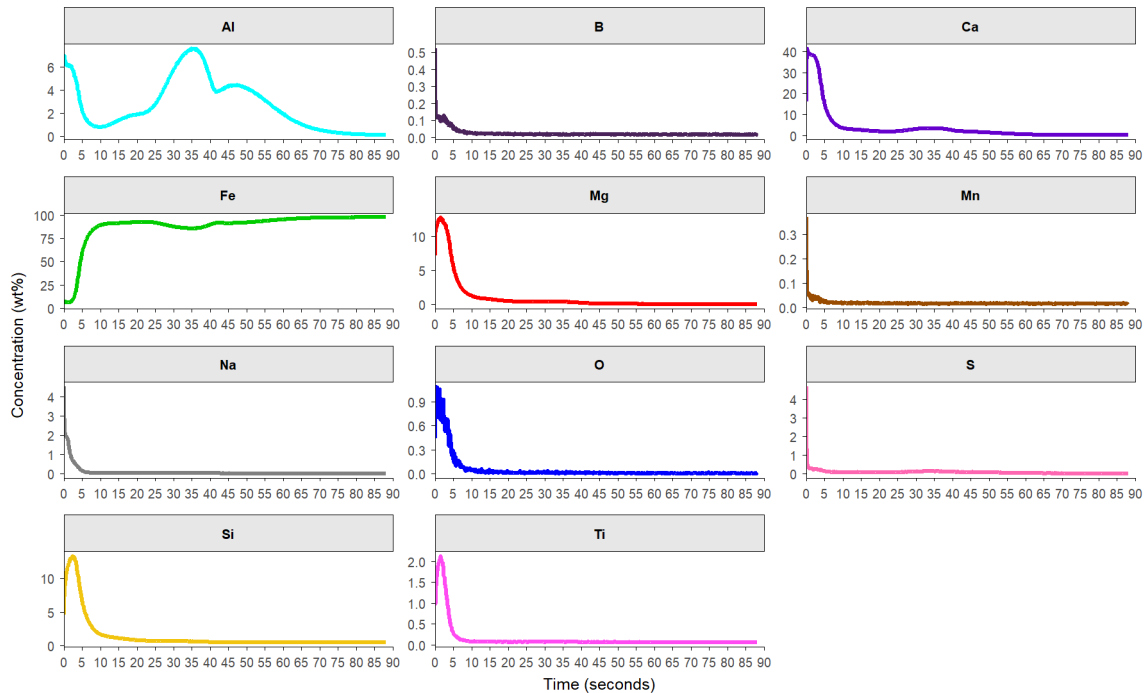
Figure 152. Individual line plots of each element that Figure 151 is composed of when a sample is coated MgO + TiO₂ and is held at HTS for 10 hours.

The composition of the coating that has developed after 30 hours with a TiO₂ addition to the MgO slurry is shown in Figure 153. The composition at the surface has not shown any significant changes with the additional time at the soak temperature. The TiO₂ is still detected at a maximum concentration of 2.95% at 0.6 seconds and reduces to <1% at 3.8 seconds. The line of interception between Mg-Fe occurs at 1.6 seconds.
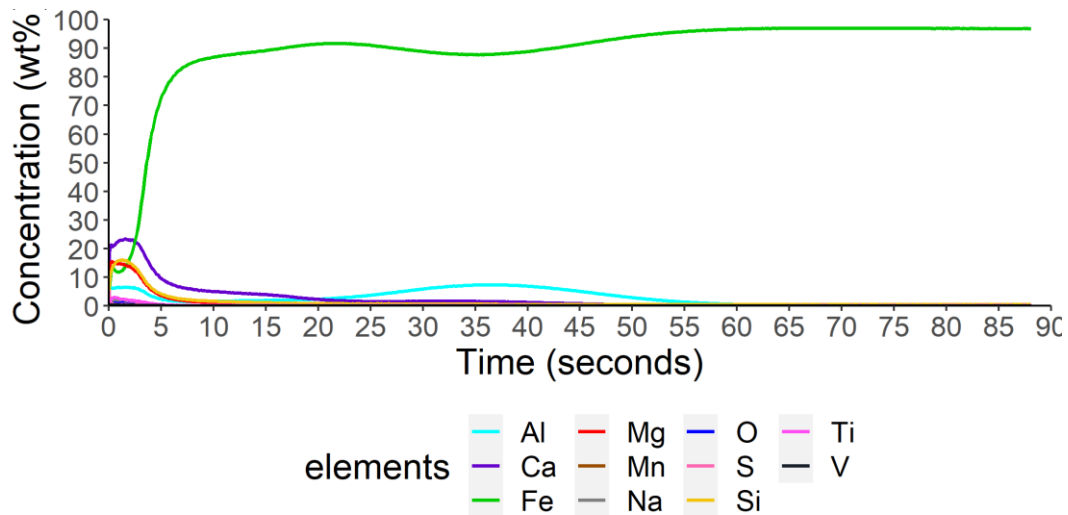
Figure 153. Changes in chemical composition from the surface to the centre of the substrate when coated with MgO + TiO₂ and is held at HTS for 30 hours.

Once again, the silicon concentration is enriched at the surface at 16.09% at 1.3 seconds. Additionally, the sulphur is enriched at the surface with a S_{max} 7.17% and decrease to <1% by 0.2 seconds. The trend of two peaks of Al occurring at the surface and subsurface with the surface concentration of Al_{max} at 6.62% at 0 seconds and the subsurface oxide max is at 7.38% at 36.6 seconds.
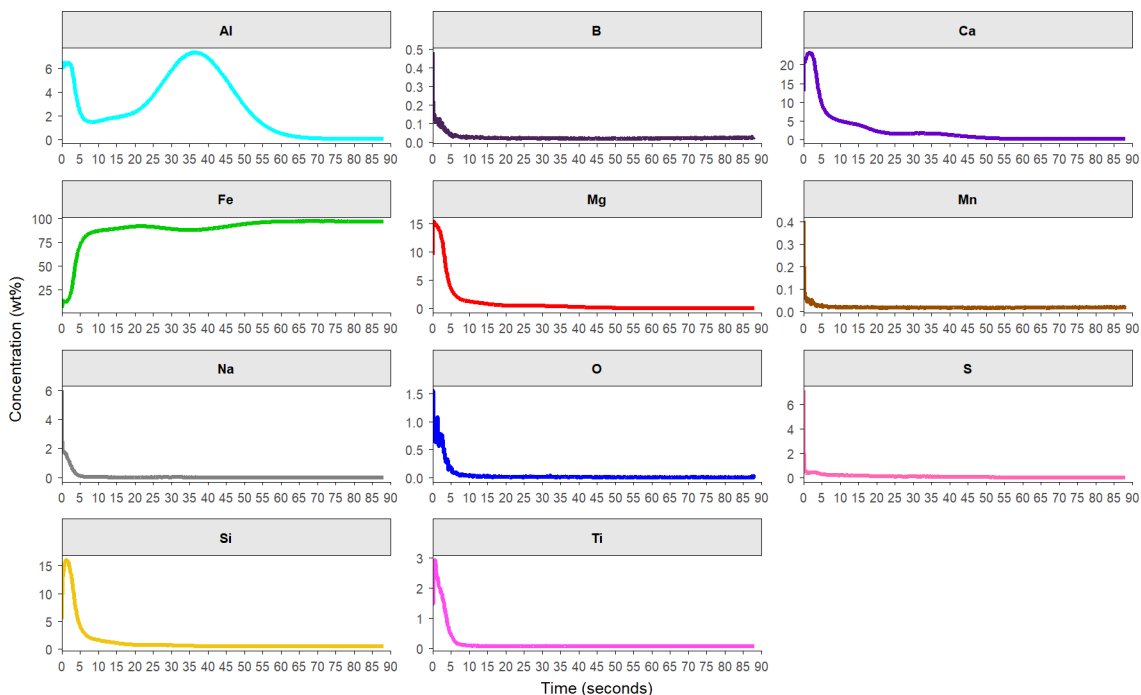
Figure 154. Individual line plots of each element that Figure 153 comprises when a sample is coated MgO + TiO₂ and is held at HTS for 30 hours.

After 50 hours of soak, the composition developed at the surface is illustrated in Figure 155. Once again, Ti is detected at the surface oxide with a Ti_{max} of 2.79% at 2 seconds and reduced to <1 by 4.4 seconds. The line of interception between Mg – Fe occurs at 3.8 seconds.

137
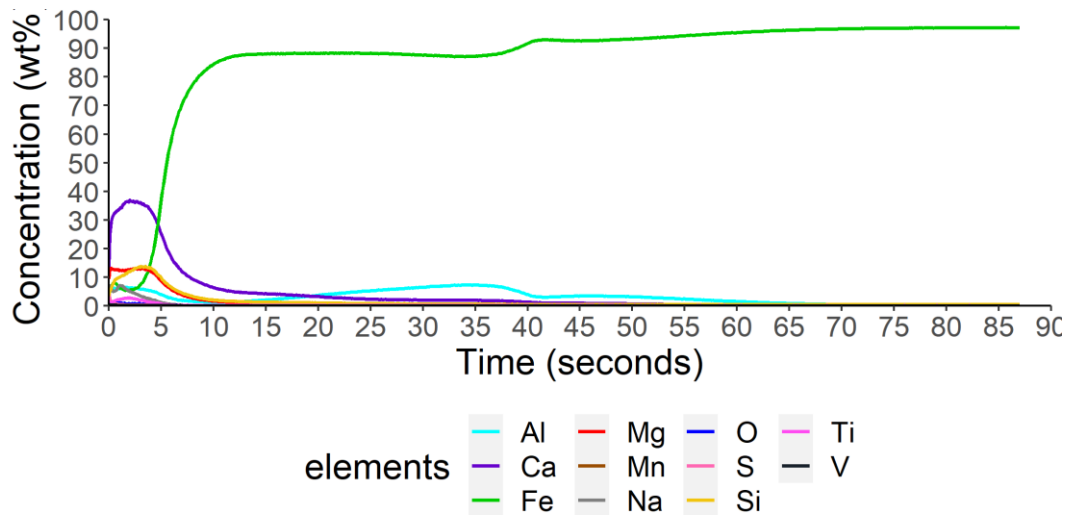
Figure 155. Changes in chemical composition from the surface to the centre of the substrate when coated with MgO + TiO₂ and is held at HTS for 50 hours.

The Mg_{max} occurs at 3.2 seconds at a concentration of 13.08% and reduces to <1% at 14.6 seconds. The elements that are sourced from the substrate have diffused toward the surface with Si_{max} of 13.86% occurring at 3.5 seconds and S_{max} of 5.22% at 0 seconds and drops to <1% by 0.5 seconds. The surface Al_{max} 6.44% at 1.6 seconds and subsurface peak at 7.30% at 33.9 seconds.
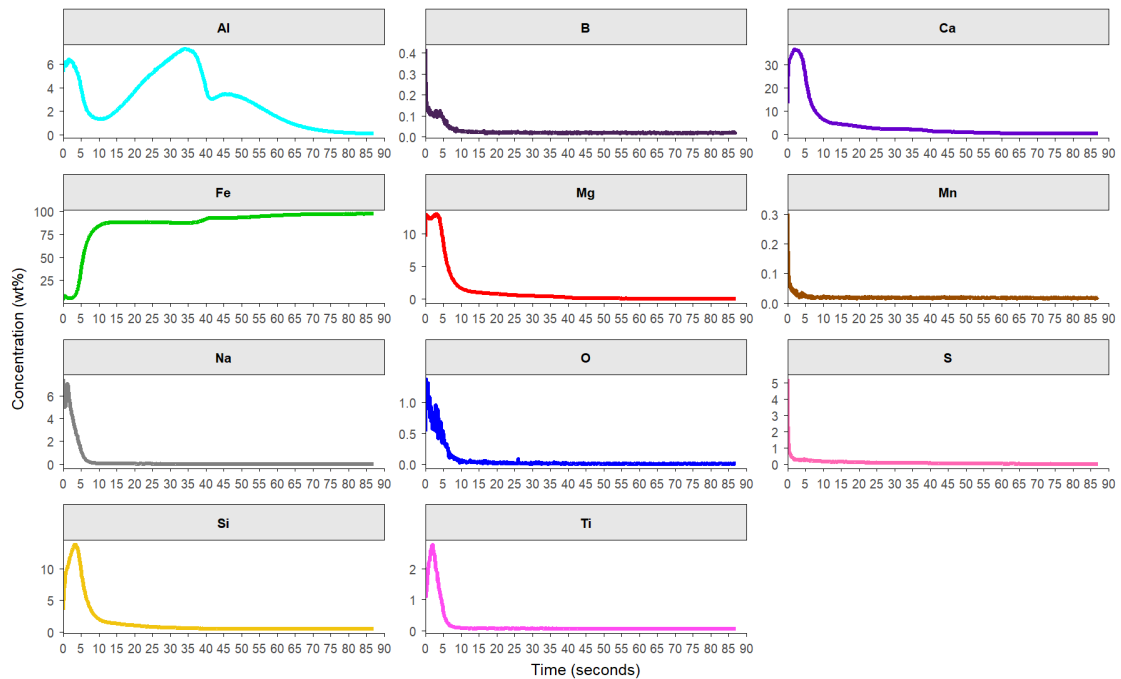
Figure 156. Individual line plots of each element that Figure 155 comprises when a sample is coated MgO + TiO₂ and is held at HTS for 50 hours.

4.4.3 Magnetic Properties

Figure 157 illustrates the magnetic properties developed when coated with MgO and TiO₂ and exposed to different duration at high temperatures soaks. The magnetic properties developed at 5 hours indicate that secondary recrystallisation has not fully occurred, which is reinforced by the

138

nitrogen content. The 10 hours soak has achieved 0.86 W/kg loss, and when the soak is increased to 30 hours, the magnetic properties achieved is 0.84 W/kg, and further heat treatment does not show further improvement.
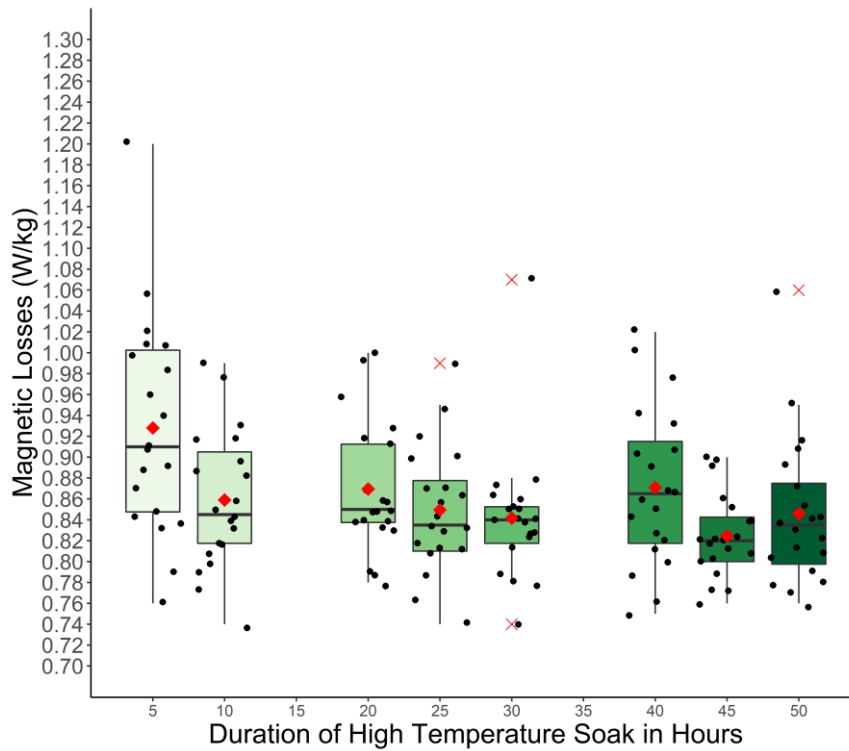
Figure 157. Magnetic properties of substrates that have been exposed to different durations at HTS when coated with MgO + TiO$_2$.

4.4.4 Oxygen Content

The oxygen content of the substrate is shown in Figure 158 when exposed to various times at HTS. Figure 158 displays an oxygen increase detected in the substrate compared with the decarburisation stage, where oxygen content is around 700ppm. The additional time at HTS does not significantly increase the oxygen content in the substrates.
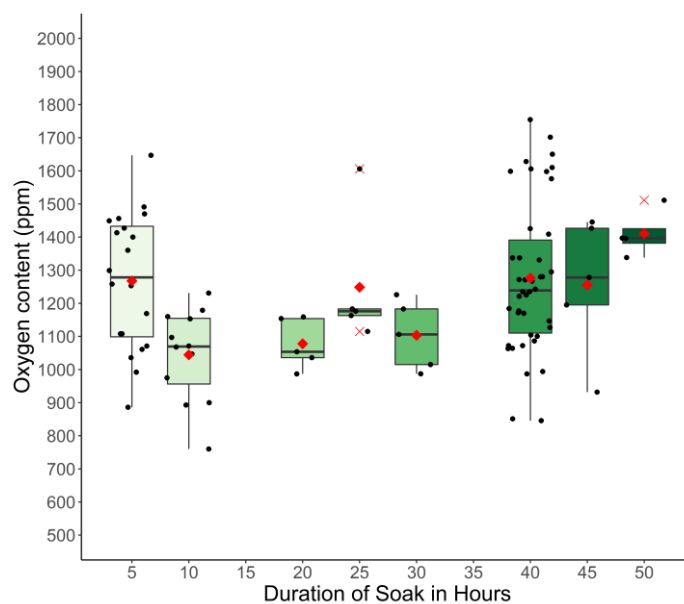
Figure 158. Oxygen content is present in the bulk substrate at the various times spent at the HTS when coated with MgO + TiO₂.

4.4.5   Bulk Analysis of Carbon, Oxygen, Nitrogen and Sulphur

The nitrogen content of samples that have been coated with MgO + TiO₂ and exposed to different durations of high-temperature soak. The trend was previously seen with a MgO only coating in section 4.3.4 continues, whereby the nitrogen levels are high compared to the 10 hours soak. This indicates that Al-N precipitates are still present, and additional heat treatment is required.

The mean amount of nitrogen that can be removed is around 30 ppm, and if nitrogen content is greater than 30 ppm, it is likely to have Al-N precipitates still present in the substrates increasing magnetic losses. Therefore, the nitrogen content provides critical information for Orb Steelworks to evaluate the purification of the substrate without additional equipment. This ideal target of 30 ppm of nitrogen can indicate whether a coil has reached its maximum performance potential from a purification aspect or does the heat cycle require adjustment to ensure sufficient time for purification to complete. Additionally, the TiO₂ addition has not affected the amount level of nitrogen content nor the speed at which it reduces.
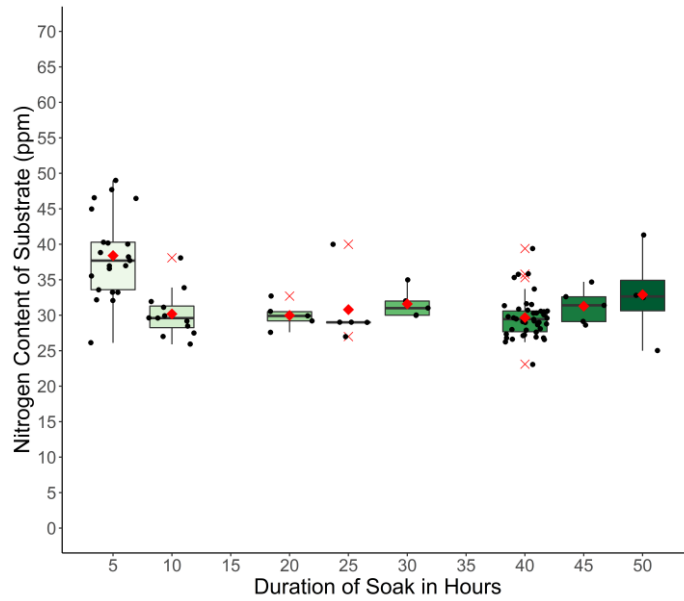
Figure 159. Nitrogen content of the bulk substrate at the various times spent at the HTS when coated with MgO + TiO$_2$.

The sulphur concentration detected is displayed in Figure 160 and shows that the TiO$_2$ and the duration of the soak do not affect the sulphur content contained in the substrate. The Sulphur content is comparable to the concentration levels observed in standard material. The variations in concentration are due to the pockets of sulphur sporadically distributed throughout the subsurface oxide.
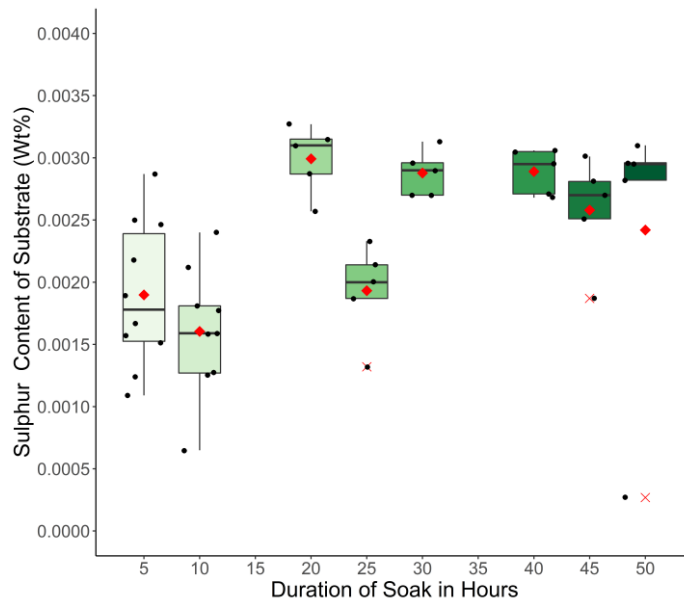
Figure 160. The sulphur content of the bulk substrate at the various times spent at the HTS was coated with MgO + TiO$_2$ collected by LECO CS844.

The carbon content seen in Figure 161 is that of the typical range seen after heat treatment, and the introduction of TiO$_2$ to the slurry has not introduced carbon to the substrate or affected the levels of carbon detected.

141
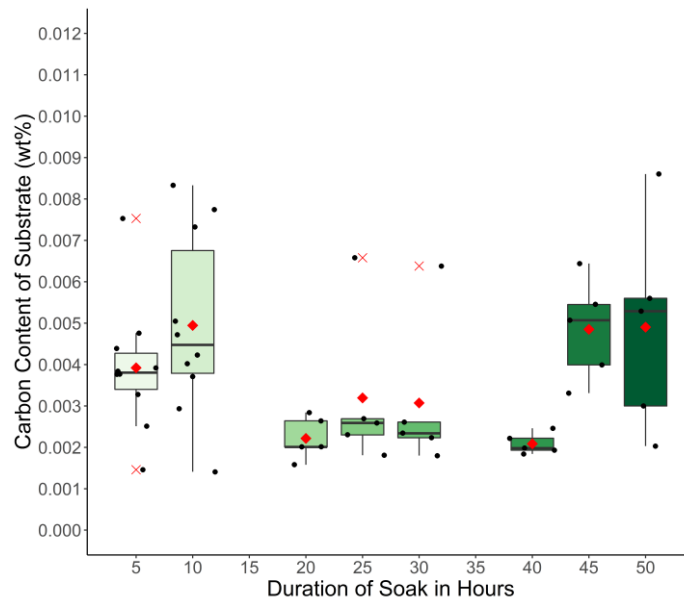
Figure 161. Carbon content is present of the bulk substrate at the various times spent at the HTS when coated with MgO + TiO$_2$ collected by LECO CS844.

4.4.6 Discussion

TiO$_2$ to the MgO slurry, when exposed to an extended time at HTS, has resulted in changes in the surface oxide thickness. At 5 hours of soak, the average oxide thickness is 0.80 µm with an additional 5 hour soak (10 hours), resulting in an increase in average coating thickness to 0.90 µm. The next step-change is at 25 hours, where the average thickness is 0.99 µm. Further duration of soak (>25 hours) does not exhibit any improvements in coating thickness. However, samples placed in the production furnaces resulted in an average coating thickness of 1.2 µm. The coating thickness achieved by the production line is unrealistic due to the control of heat treatment, and the duration of the heat treatment condition could be "ideal" with control of heating rates, soak, and atmosphere conditions. The surface oxide presented in section 4.3.1 has not exhibited any dramatic changes in the shape or thickness of the surface oxide when comparing the cross-sections at various HTS lengths.

The surface and subsurface oxide composition does not show any dramatic changes, but TiO$_2$ is detected in the surface oxide. It does not display any increase in intensity, the maximum level ranging between 2-3% detected, as the soak duration increases. The magnetic properties are influenced to some extent with the increase in soak duration with 5 hours producing an average of 0.93 W/kg, and an additional 5-hour soak (10 hours) results in a decrease in magnetic losses to produce an average of 0.86 W/kg. With additional soak duration, i.e., >10 hours, soak does not display relevant improvements with losses fluctuating between 0.85-0.87 W/kg with the exception of 45 hours that produced 0.82 W/kg. This improvement does not correlate to any changes in composition, thickness, or purity of the substrate. Therefore, the assumption is that the improvements seen by 40 hours must be due to a preferential texture developed, which could be due to many factors such as texture development during the decarburization stage, the influence of precipitates, to name a few. The

improvements seen in the 10 hours magnetic properties could be explained by the lower levels of nitrogen and sulphur content detected by the Leco bulk analysis. However, the nitrogen content detected at 10 hours or greater remains consistent.

4.5 The Effects of Duration of the High-Temperature Soak have on the Development of Surface Oxide When Coated with MgO + TiO$_2$ +Na$_2$B$_4$O$_7$·10H$_2$O.

4.5.1 Morphology and coating thickness of surface oxide developed

The surface oxide that has developed with the additions of TiO$_2$ and borax to the slurry and is held at high temperature for 10 hours is illustrated in Figure 162. Again, the uniform coating has developed with keying areas present, and the combination of additives does not appear to influence the oxide morphology. Similar, there is no significant changes seen in the subsurface oxide.

a)   b)
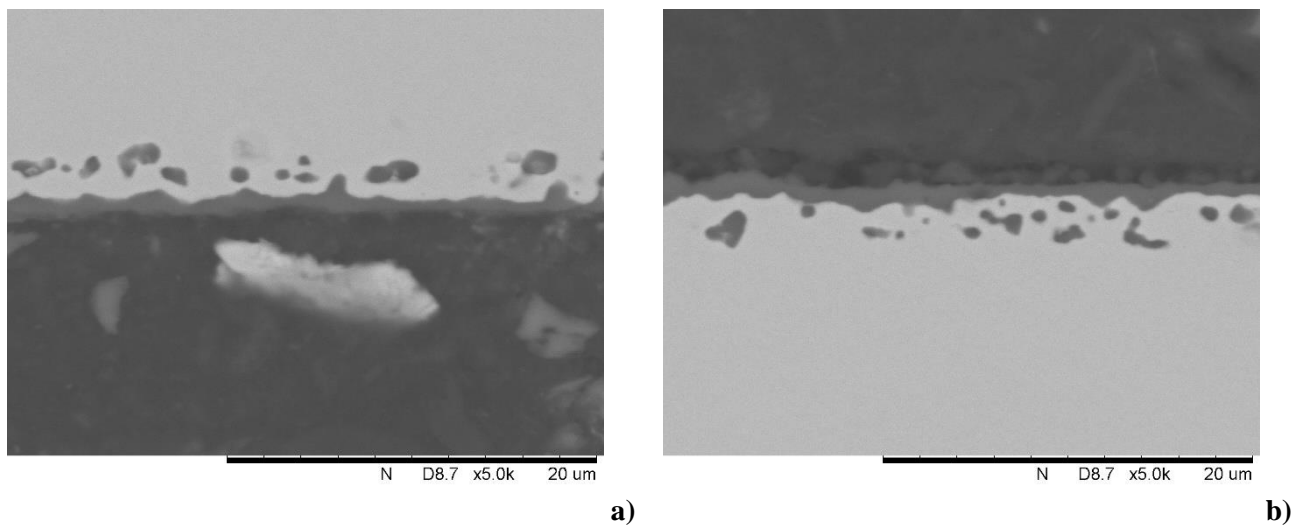
Figure 162. Morphology of the oxide after spending 10 hours at HTS and coated with MgO + TiO$_2$ +Na$_2$B$_4$O$_7$·10H$_2$O (a) up-facing surface (b) down-facing surface.

The additional time at temperature (30 hours) soak shows no noticeable improvement in the surface oxide thickness or a change in morphology. Therefore, the subsurface oxide is still present.

a)   b)
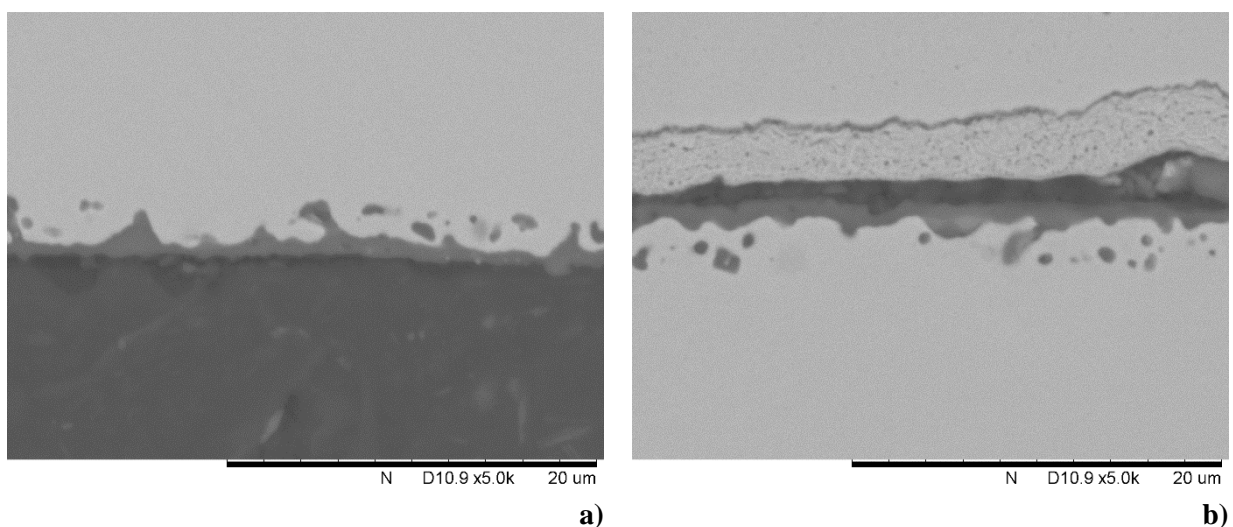
Figure 163. Morphology of the oxide after spending 30 hours at HTS and coated with MgO + TiO$_2$ +Na$_2$B$_4$O$_7$·10H$_2$O (a) up-facing surface (b) down-facing surface.

With the maximum time spent at a high temperature of 50 hours soak, there is no clear and noticeable change in the morphology of the surface oxide with keying point and subsurface oxide still present.

a)

b)
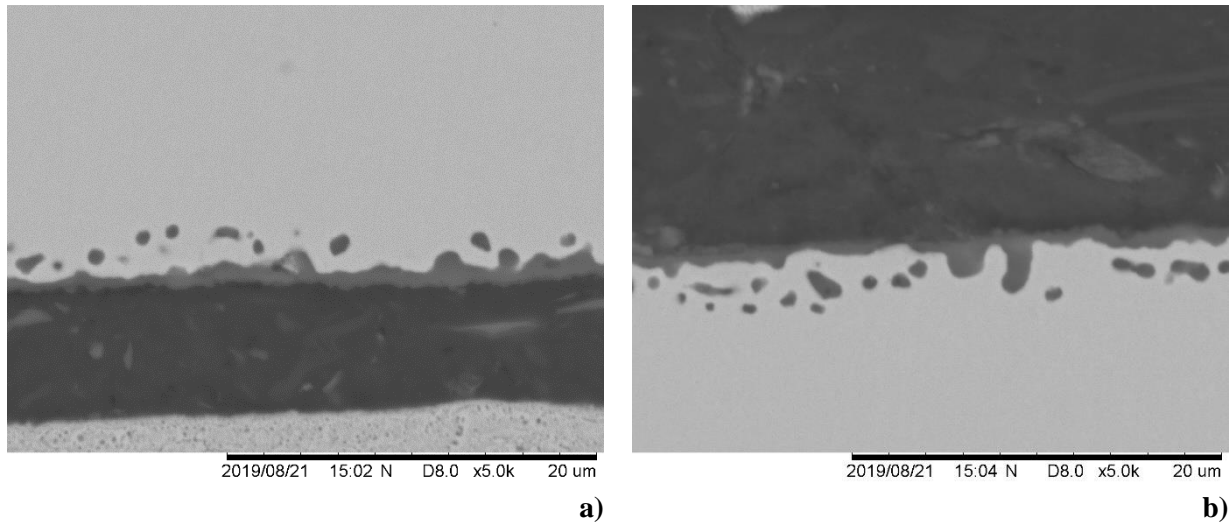
Figure 164. Morphology of the oxide after spending 50 hours at HTS and coated with MgO + TiO$_2$ +Na$_2$B$_4$O$_7$·10H$_2$O (a) up-facing surface (b) down-facing surface.

The measured coating thickness from SEM cross-sections coated with MgO + TiO$_2$ +Na$_2$B$_4$O$_7$·10H$_2$O and then exposed to various durations at HTS is shown in Figure 165. The coating thickness at 5 hours is an average of 0.78µm with additional soak (10 hours) and increases coating thickness to 0.90 µm. At 20 hours, the average coating thickness reaches 1 µm, and further increases in soak time do not see any significant increase in coating thickness ranging between 0.92-1.1 µm.
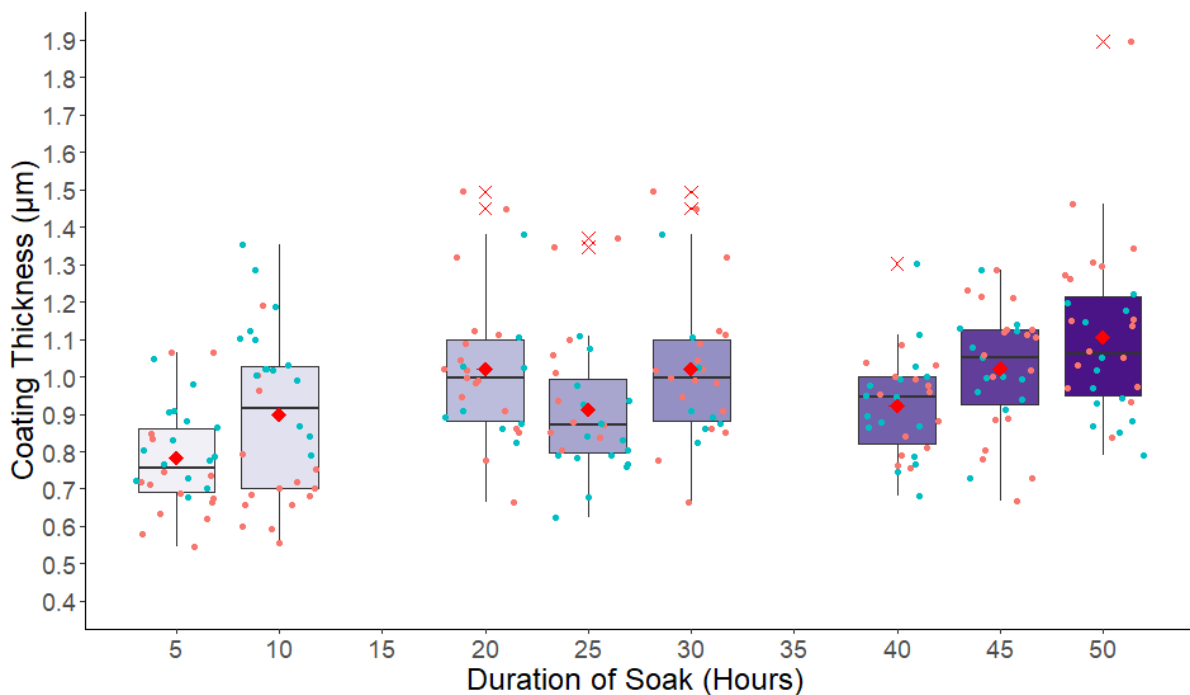
Figure 165. Measured SEM cross-sections of samples that have been coated with MgO + TiO$_2$ +Na$_2$B$_4$O$_7$·10H$_2$O and heat-treated at the various duration of soak time at the HTS.

4.5.2   Chemical Composition by GDOES Analysis

The chemical composition of a sample coated with MgO, TiO2 and Borax and exposed to HTS for 10 hours is displayed in Figure 166. The elements that have been detected during previous GDOES scans are present with the detection of Mg, Fe, Si, S, Ti, Al, Na. The desired Mg layer has developed at the surface with the addition of TiO_2 and Borax to the slurry. The line of interception between Mg-Fe occurs at 3.6 seconds with a Mg_{max} concentration of 18.52% at 0.6 seconds and drops to 1% by 11.2 seconds. The silicon concentration reaches a maximum of 21.59% at 2.3 seconds.
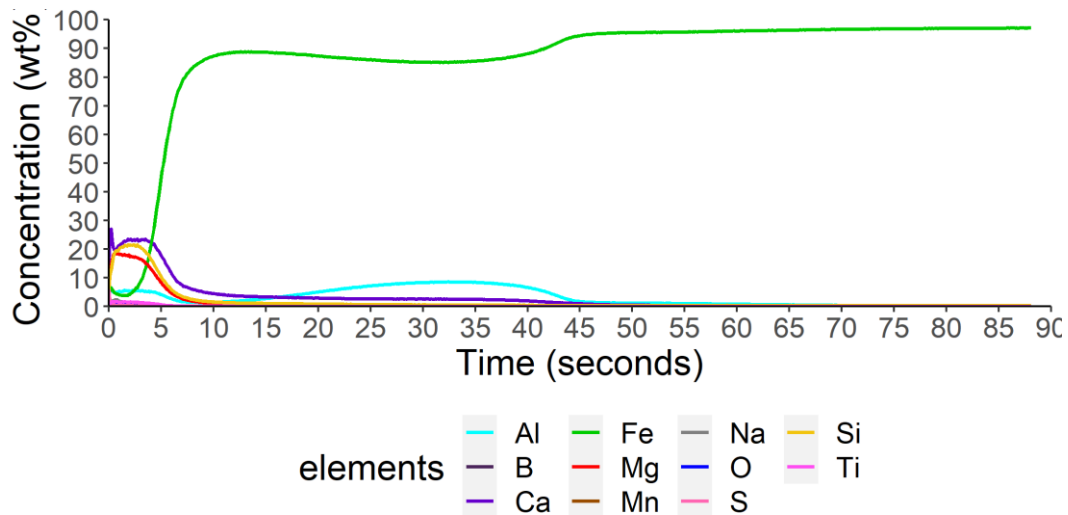
Figure 166. Changes in chemical composition from the surface to the centre of the substrate when coated with $MgO + TiO_2$ +$Na_2B_4O_7 \cdot 10H_2O$ is held at HTS for 10 hours.

On closer inspection of the surface oxide in Figure 167, the detection of Ti and Na can be seen with a concentration of 1.78% at 0.5 seconds and a decreases to <1% by 4.3 seconds. The Na peaks at 4.57% at 0 seconds and drops to <1% by 2.2 seconds. The detection of B is at very low levels at a max level of 0.59% at 0 seconds and drops rapidly. The addition of both additives has not affected the trend of Al peaking twice once, with the surface peak reaching a maximum of 6.44% and a subsurface max of 8.67% at 32.4 seconds.
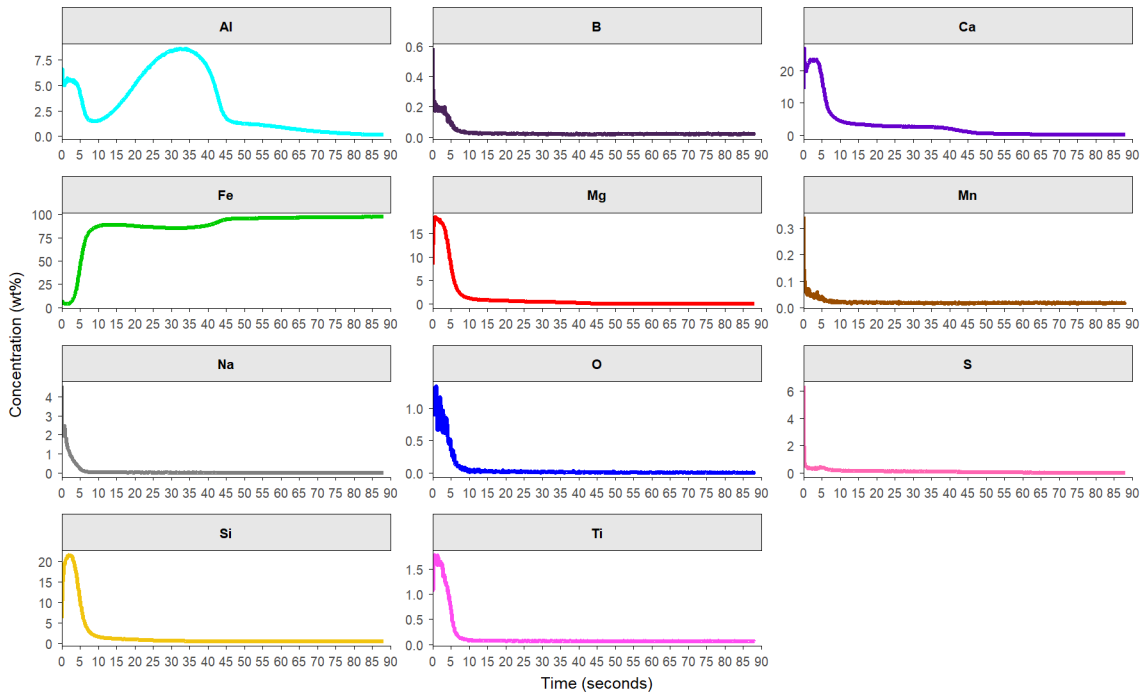
Figure 167. Individual line plots of each element that Figure 166 is composed of when a sample is coated MgO + TiO$_2$ + Na$_2$B$_4$O$_7\cdot$10H$_2$O and is held at HTS for 10 hours.

The developed surface oxide after 30 hours of a soak at high temperature is illustrated in Figure 168. The composition has changed with the presence of Al with the desired Mg. The line of interception occurs at 3 seconds with a Mg$_{max}$ of 17.30% at 0.6, which drops to <1% by 17.1 seconds. The Al intensity at the surface reaches 18.90% at 2 seconds and a second peak at 32.3 seconds at 6.34%.
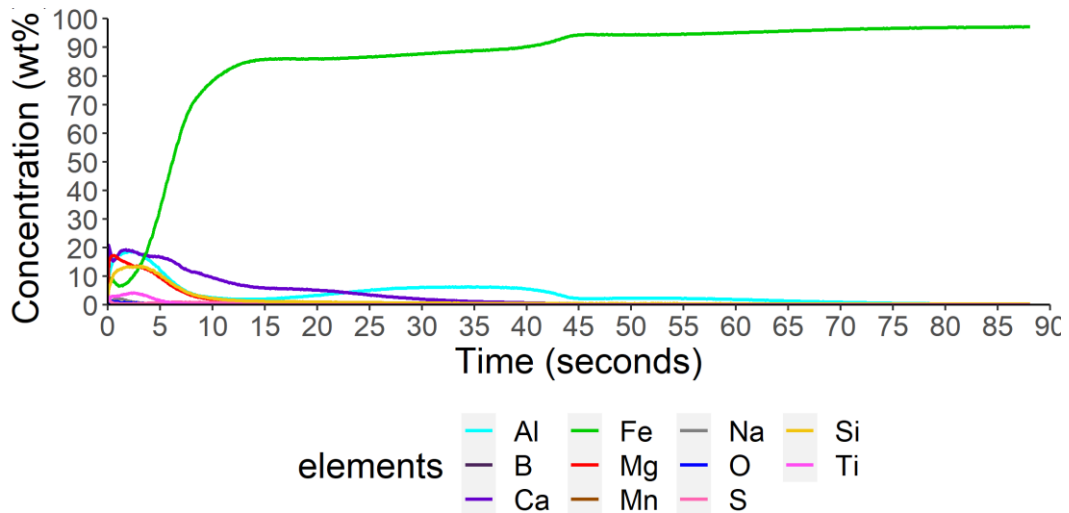
Figure 168. Changes in chemical composition from the surface to the centre of the substrate when coated with MgO + TiO$_2$ +Na$_2$B$_4$O$_7\cdot$10H$_2$O and is held at HTS for 30 hours.

Figure 169 displays the detection of Ti and Na in the surface oxide with a max concentration of 4.24% at 2.4 seconds and reduces to <1% by 5.7%. The Na peaks at 3.52% at 0 seconds and decreases to <1% by 4.4 seconds. The presence of S is also detected with a max peak of 4.54% at 0 seconds and

146

decreases to <1% by 0.3 seconds. However, an additional peak is seen at 4.7 seconds, where S is detected ~1%.
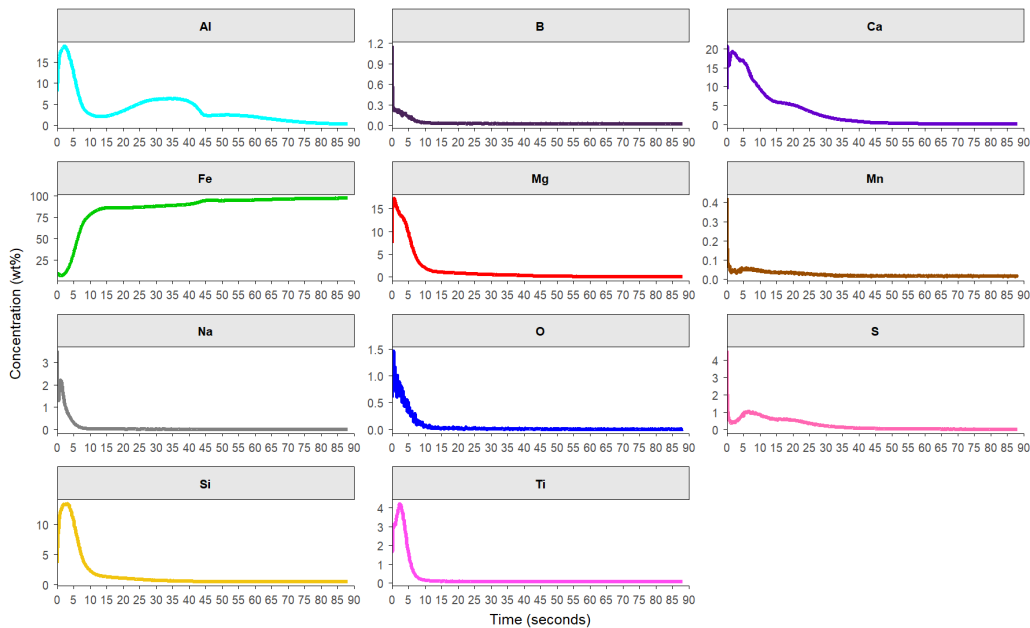
Figure 169. Individual line plots of each element that Figure 167 is composed of when a sample is coated MgO + TiO$_2$ + Na$_2$B$_4$O$_7$·10H$_2$O and is held at HTS for 10 hours.

When exposed to 50 hours soak at high temperature, the composition that is developed at the surface through to the substrate is illustrated in Figure 170. The composition is like that seen in 10 hours soak (Figure 162), with the desired Mg present at the surface with a Mg$_{max}$ concentration of 16.26% at 1.5 seconds and the line of interception between Mg-Fe occurring at 3.6 seconds.
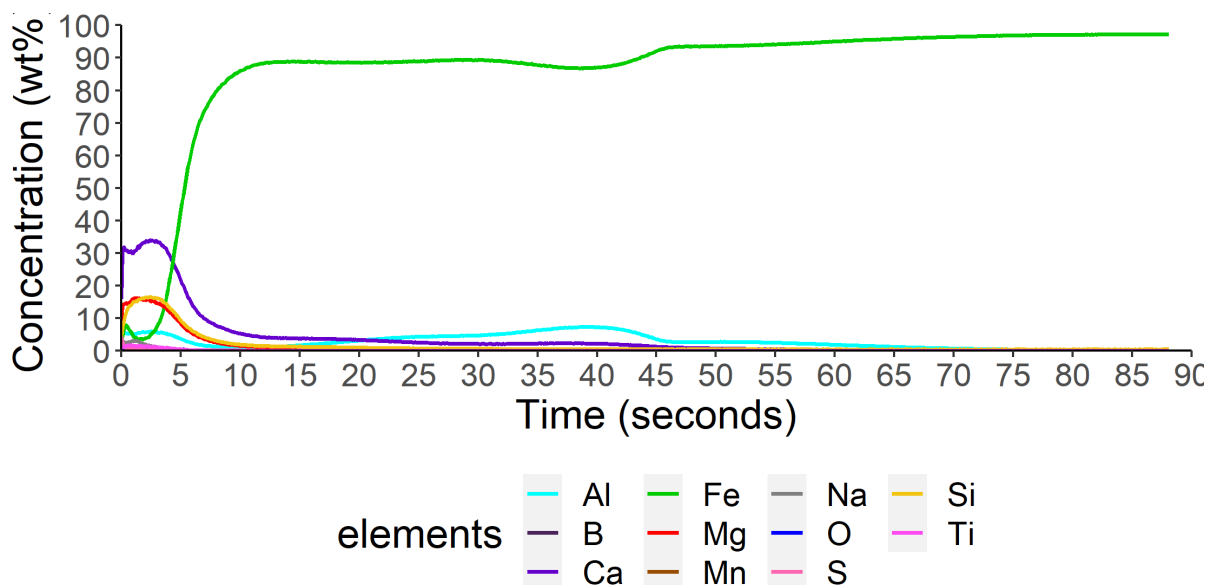
Figure 170. Changes in chemical composition from the surface to the centre of the substrate when coated with MgO + TiO$_2$ +Na$_2$B$_4$O$_7$·10H$_2$O and is held at HTS for 50 hours.

147

The detection of Ti and Na are seen in Figure 170, where the Ti_{max} concentration reaches 1.77 at 0.6 seconds and reduces to <1% by 3.8 seconds. The Na_{max} concentration reaches 4.84% at 0 seconds ad reduces to <1% by 3.5 seconds. There are significant changes in the Al trend, with the Al_{max} at the surface reaching 5.89 at 2.8 seconds and the subsurface peak reaching an Al_{max} of 7.40% at 39.5 seconds.
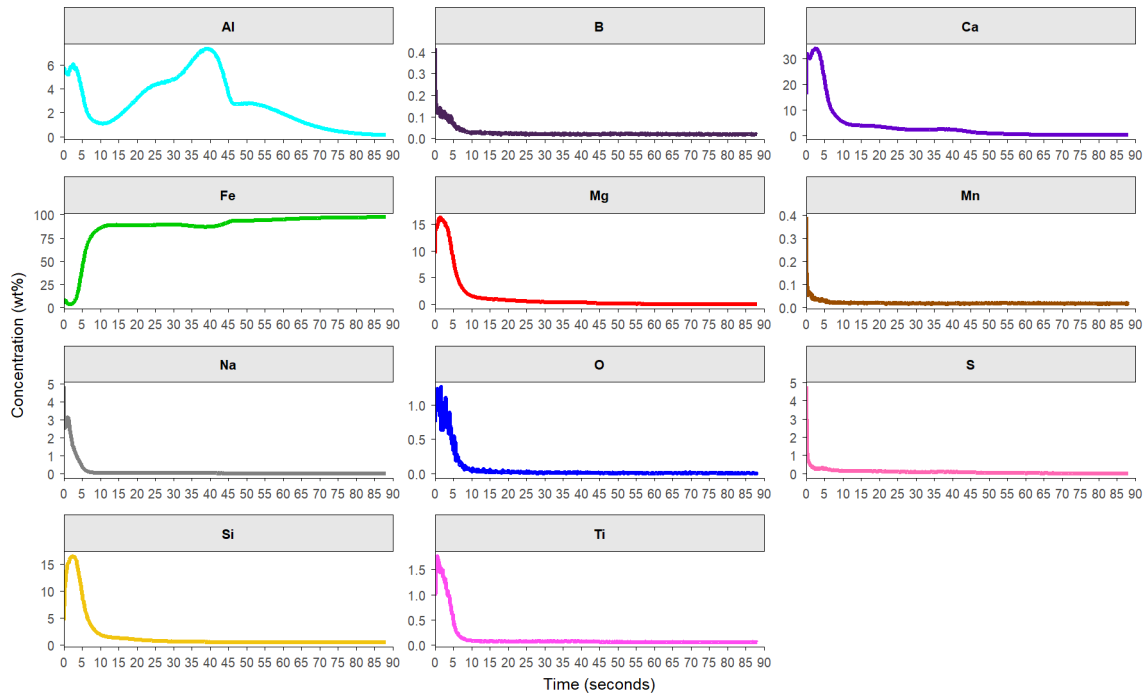
Figure 171. Individual line plots of each element that Figure 170 is composed of when a sample is coated MgO + TiO_2 + $Na_2B_4O_7 \cdot 10H_2O$ and is held at HTS for 10 hours.

4.5.3   Magnetic Properties

The magnetic properties that have developed at the various durations of high-temperature soak when coated with the additions of TiO_2 and Borax to the MgO slurry are displayed in Figure 172. The magnetic properties after a 5 hours soak have not fully developed to the maximum potential where at 5 hours, the average loss is 0.93 W/kg, and this reduces to 0.87 W/kg after a 10 hours soak is applied. The average magnetic properties remain around 0.87 W/kg± 0.01W/kg except for 25 hours and 50 hours, which achieve 0.82 W/kg. There is no apparent trend of improvements in purity of the substrate, change in thickness/ composition of surface oxide, and this improvement can be possible due to the preferential GOSS texture developed, and the correct grain size has developed.
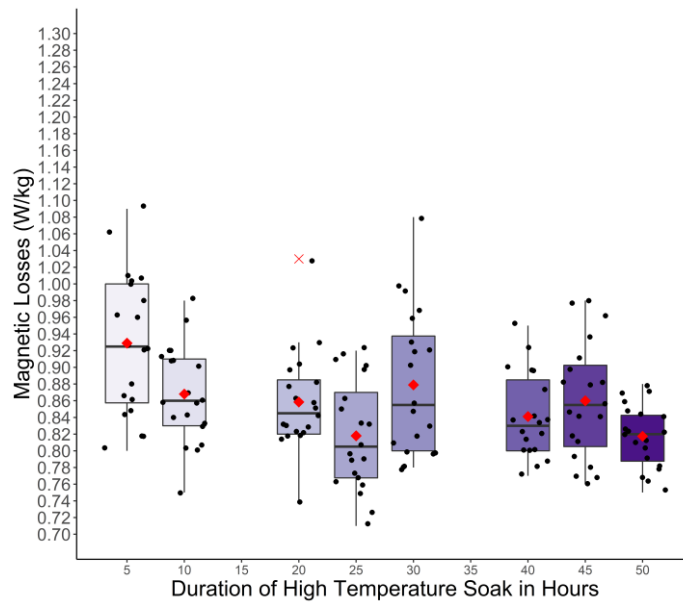
Figure 172. Magnetic properties of substrates that have been exposed to different durations time at HTS when coated with MgO + TiO_2 + $Na_2B_4O_7 \cdot 10H_2O$.

4.5.4   Bulk Analysis of Carbon, Oxygen, Nitrogen and Sulfur

The levels of sulfur detected in the bulk material when coated with addition TiO_2 and Borax additions to the MgO slurry and then held at HTS at various durations is displayed in Figure 173. The sulfur detected is sporadic with no clear trend. However, the ranges are between 0.0010-0.037 wt% and are typical ranges detected after heat treatment in production material.
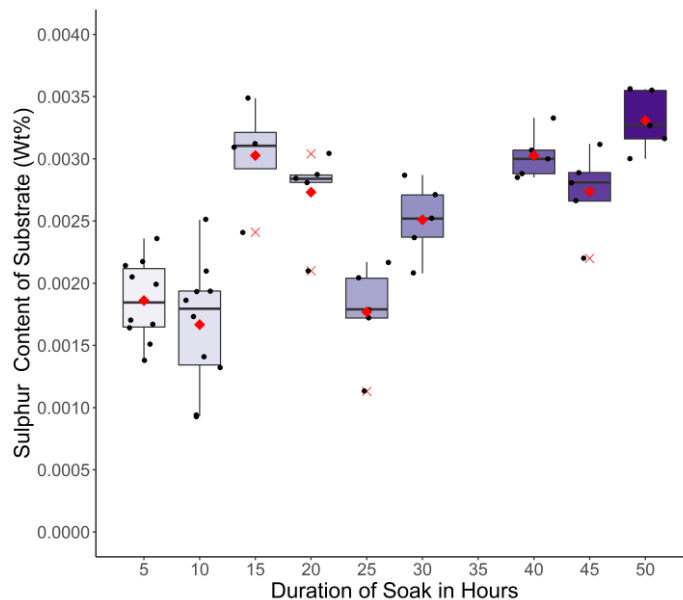
Figure 173. The sulphur content present of the bulk substrate at the various times spent at the HTS when coated with MgO + TiO_2 + $Na_2B_4O_7 \cdot 10H_2O$ collected by LECO CS844.

The nitrogen content that is detected in the bulk substrate that has been exposed to several duration of HTS applied to samples that have been coated with MgO + TiO_2 + $Na_2B_4O_7 \cdot 10H_2O$. The average nitrogen content at 5 hours is 36ppm. After that, this nitrogen content drops to 28ppm.

149
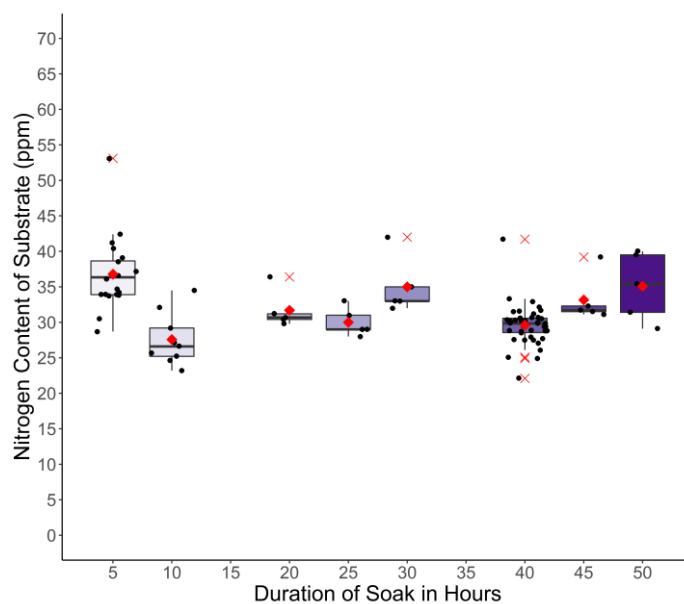
Figure 174. Nitrogen content present of the bulk substrate at the various times spent at the HTS when coated with MgO + TiO$_2$ +Na$_2$B$_4$O$_7 \cdot$10H$_2$O collected by LECO TN400.

4.6   Discussion

The MgO + TiO$_2$ +Na$_2$B$_4$O$_7 \cdot$10H$_2$O slurry mixtures is the current formulation used by Orb Steelworks. It is believed that this combination of additives to the magnesium slurry produces a superior oxide layer when compared to MgO only slurry. The coating thickness measured from the cross-section displayed that the duration of the soak has an impact on the thickness. At 5 hours of soak, the average thickness of the oxide is 0.78µm. At 10 hours of soak, the oxide thickness has increased to an average of 0.90µm. The average coating thickness increased further at 20 hours, whereby the average coating thickness is 1µm. At greater than 20 hours, no improvements in coating thickness except 50 hours, whereby the average coating average thickness is >1.1 µm. This increase in coating thickness between 5 -20 hours indicates that the development of the surface oxide is not complete <20 hours. This demonstrates that a minimum requirement of soak is 20 hours to achieve a 1µm surface oxide, and if this is not achieved, an inferior oxide layer will develop. The extension of the HTS duration has increased the oxide thickness, as shown in Figure 165, and the morphology of the surface/subsurface oxide has not changed. The surface/ subsurface oxide morphology has not altered with the small addition of Na$_2$B$_4$O$_7 \cdot$10H$_2$O. This is supported by little to no changes in the chemical composition change seen by the GDOES analysis of the samples tested. This suggests that Na$_2$B$_4$O$_7 \cdot$10H$_2$O has little or no effect on the oxide development during the HTS.

4.7   Comparison of the Performance of the Mixtures

This chapter aimed to identify any improvements that may be seen by introducing the present additives and concentrations used by Orb Steelworks and establish if these additives are functional during the HTS.

Table 14 displays the average measured coating thickness that has been coated with the various mixtures and exposed to different HTS durations. Even though TiO_2 and $Na_2B_4O_7 \cdot 10H_2O$ have limited or no improvement in the measured surface oxide when comparing the three mixtures at each Soaking interval, except 10 hours where MgO only remains 0.79µm. However, the two mixtures achieved 0.90 µm. This variation in oxide thickness could be explained by adding TiO_2 detected amongst the Mg enriched layer. The Ti could explain this increase in oxide thickness detected in composition analysis using GDOES. However, >10 hours HTS it appears that this advantage of thicker coating that is seen by $MgO + TiO_2$ and $MgO + TiO_2 + Na_2B_4O_7 \cdot 10H_2O$ is diminished with further increase in HTS and upon further increase soak does not improve the oxide layer developed.

Table 13. The average measured coating thickness over the range of HTS and mixtures.

Mix	Average coating thickness measured from SEM images after the time (microns)								
	5 Hours HTS	10 Hours HTS	20 Hours HTS	25 Hours HTS	30 Hours HTS	40 Hours HTS	45 Hours HTS	50 Hours HTS	HTCA Samples
MgO	0.79±0.16	0.79±0.11	0.94±0.16	0.91±0.18	1.04±0.17	0.80±0.15	0.98±0.34	1.07±0.22	1.17±0.15
$MgO + TiO_2$	0.80±0.20	0.90±0.17	0.89±0.16	0.99±0.16	1.02±014	0.98±0.12	0.95±0.24	1.06±0.22	1.20±0.14
$MgO + TiO_2 + Na_2B_4O_7 \cdot 10H_2O$	0.78±0.13	0.90±0.21	1.02±0.19	0.91±0.17	1.02±0.20	0.92±0.13	1.02±016	1.10±0.22	1.30±0.19

Table 14. The average measured coating thickness over the range of HTS and mixtures.

Table 15 displays the results of magnetic losses of each mix at the various durations of time at HTS. It appears all three mixtures experience a reduction in magnetic properties at 10 hours soak and a more minor reduction in losses at 25 hours. It seems that the magnetic properties are not affected by the mixtures placed upon the surface, with all three mixtures having a similar magnetic loss with one another. At this concentration of additives, it suggests that magnetic properties are not affected nor the thickness of oxide that has developed.

Table 15. The average magnetic losses of samples that have been exposed to a range of HTS time and coating mixtures.

Mix	Average magnetic properties of heat-treated samples (W/kg)							
	5 Hours HTS	10 Hours HTS	20 Hours HTS	25 Hours HTS	30 Hours HTS	40 Hours HTS	45 Hours HTS	50 Hours HTS
MgO	0.93±0.10	0.85±0.08	0.87±0.05	0.83±0.05	0.87±0.06	0.87±0.07	0.86±0.04	0.89±0.06
$MgO + TiO_2$	0.93±0.10	0.86±0.07	0.87±0.06	0.85±0.06	0.84±0.06	0.87±0.07	0.82±0.04	0.85±0.07
$MgO + TiO_2 + Na_2B_4O_7 \cdot 10H_2O$	0.93±0.08	0.87±0.06	0.86±0.06	0.82±0.06	0.88±0.09	0.98±0.06	0.86±0.07	0.82±0.04

4.7.1   Conclusion

The duration of the high temperature is critical to purify the electrical steels which is indicated by the nitrogen content detected which is correlated with Al-N inhibitors are present in the material. This research has demonstrated samples with <10 hours at the HTS have a high-level of detection of nitrogen content in all mixtures and has resulted in high magnetic losses. At 30 hours soak at the HTS accomplish an average of ~1µm oxide thickness and an extension of the soak (>30 hours) does not exhibit any further increase in oxide thickness. Therefore, HTS appears to be optimum between 10-30 hours.

The TiO_2 is incorporated into the MgO slurry, a slight improvement in the measured coating thickness in the <10 hours soak when compared with MgO. However, upon further duration of soak the improvements that is seen at <10 hours with TiO_2 addition are eliminated and MgO only coating thickness is similar thickness.

The introduction of $Na_2B_4O_7 \cdot 10H_2O$ has no noticeable impact on the magnetic properties, coating thickness or composition of the electrical steel at any soak duration. This provides evidence that if $Na_2B_4O_7 \cdot 10H_2O$ has any impact on Forsterite or magnetic properties it during the heat phase of the cycle. Therefore, the HTS should aim to have a minimum 30-hour soak and if not possible TiO_2 should be used to minimise the affect of not having sufficient soak on Forsterite development. The use $Na_2B_4O_7 \cdot 10H_2O$ should be removed form slurry due no noticeable effect on magnetic properties or Forsterite thickness.

4.7.2   Future Work

The study into the heat profile of a coil in section 1.11 shows that there is large in temperature gradient within a coil with multiple regions not achieving the desired temperature. Combined with the evidence in this chapter assessing the effect of duration of soak at the high temperature, it is recommended to detailed evaluation the performance of the current furnaces using measurements and modelling simulations. Whilst the evaluation of the current furnace is being conducted efforts should be made to work with single stacked bell furnaces manufacture to excite a trail using the single stack bell furnace and evaluate the performance of these types of furnaces. Once all the data is collected from both types of furnaces are inquired a capital investment analysis should be conducted. This will allow a inform decision on the future investments and increase yield.

Chapter 5. The Effect of Additives to the Magnesium Slurry on Oxide Layer Produced during High-Temperature Annealing.

The following chapter describes the effect of additives on the magnesium slurry during High-temperature annealing. Individual sections investigate a range of concentrations of additives added to the magnesium slurry and the effect this has on the oxide layer developed and magnetic properties of the steel.

The following additives were analysed and summarised in this chapter:

- MgO only (The reference sample)
- TiO_2
- FeO-Fe_2O_3
- V_2O_3

5.1 Methods

The following section outlines the details of the substrate selection, the amount of addition, coating method, heat treatment and analysis conducted on the heat-treated samples presented in this chapter. Further details on all described processes can be found in Methods and Materials (Chapter 2).

The substrate used throughout this chapter was J19071 collected from the exit of the D-line at Orb Steelworks and reduced to 350 x 100 x 0.23mm.

The additives that were added to the magnesium slurry were TiO_2, FeO-Fe_2O_3, V_2O_3. The quantity added to the magnesium slurry is displayed in Table 16. The MgO and additive were added in distilled water that was chilled at 10ºC and mixed for 1 hour before the coating was applied to the substrate. The viscosity and pH of the slurry were tested for each mix.

Table 16. Quantity of ingredients used to create the various percentages of additives to create the desired slurry.

Wt% of additive	MgO	The amount of additive added to slurry (g)	Distilled Water (ml)
0%	112g	0	800
0.5%	112g	0.56	800
1%	112g	1.12	800
5%	112g	5.6	800
10%	112g	11.2	800
15%	112g	16.8g	800
25%	112g	28g	800

The samples were coated at Orb Steelworks using the custom laboratory roller coater. The slurry applied to the substrate was dried in the Nabertherm furnace at ~750ºC until the water has been driven out. The samples were individually weighed before and after coating.

All mixtures and reference samples were placed in a stack with sacrificial samples between different mixes. The stack of samples was then placed between two steel heat treatment blocks and scurried with metal banding in a cross configuration.

Heat treatment was carried out at Orb Steelworks production furnaces. The stack of banded samples was placed on top of a bottom coil, and a 10-day heating cycle was used to heat treat production coils, as shown in Figure 175.
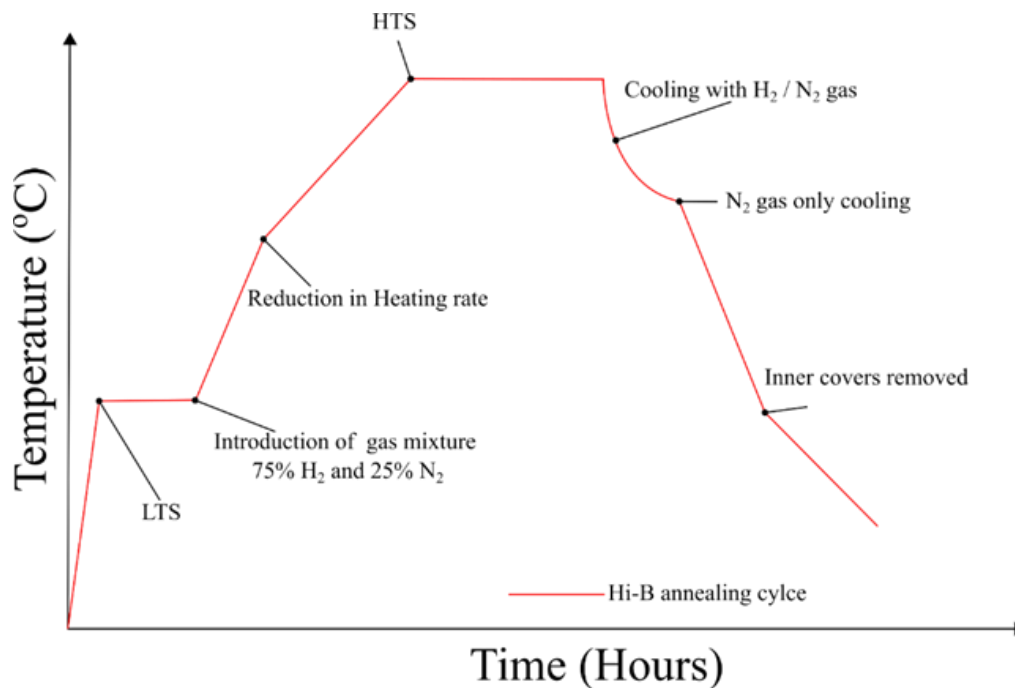
Figure 175. Heating profile of a typical heat treatment conducted on production furnaces at Orb Steelworks in which the additives samples were heat treated.

On completion of the heat treatment in the production furnaces, samples were removed from the furnaces, and the banding was removed. Excess magnesium powder was removed from the surface with distilled water and a cloth.

A minimum of 5 samples per additive was analysed. A wide range of analyses was conducted to evaluate the magnetic properties, resistance, bulk composition, coating thickness and chemical composition of developed surface oxide. The following methods were used to evaluate the samples:

- Franklin tester (Resistance)
- Soken Tester (Magnetic properties)
- SEM/EDS
- GDOES
- Bulk analysis (C, O, N and S)

The following chapter presents analyses from the samples using these techniques unless stated otherwise.

154

5.2   The Impact of MgO Only on the Formation of the Oxide Layer

MgO has been the main component in the slurry for the last 70 years; initially, it was to prevent the welding of laps during high temperatures annealing cycle. An unintentional oxide layer developed that produced an insulation layer and improved the magnetic properties of the steel. Since this discovery, there have been modifications to the characteristics of the MgO to improve the oxidation layer produced on the surface of the electrical steel. This section will investigate the current performance of the oxide developed when a MgO only slurry is applied to the substrate and heat-treated in production furnaces at Orb Steelworks. This section will reference the subsequent sections that investigate the effects of additions to the magnesium slurry.

5.2.1   Coating Thickness with MgO Only Slurry

The oxide layer thickness in reference samples coated with MgO only was measured to be an average of 0.96 µm (± 0.15 standard deviation) from SEM images.

5.2.2   Morphology at the Surface

Figure 176 shows the cross-section of the top and bottom surfaces of a heat-treated reference sample. The oxide layer developed is a thin uniform layer with the bottom surface displaying keying areas. Both top and bottom surfaces have subsurface oxides.

a)   **b)**
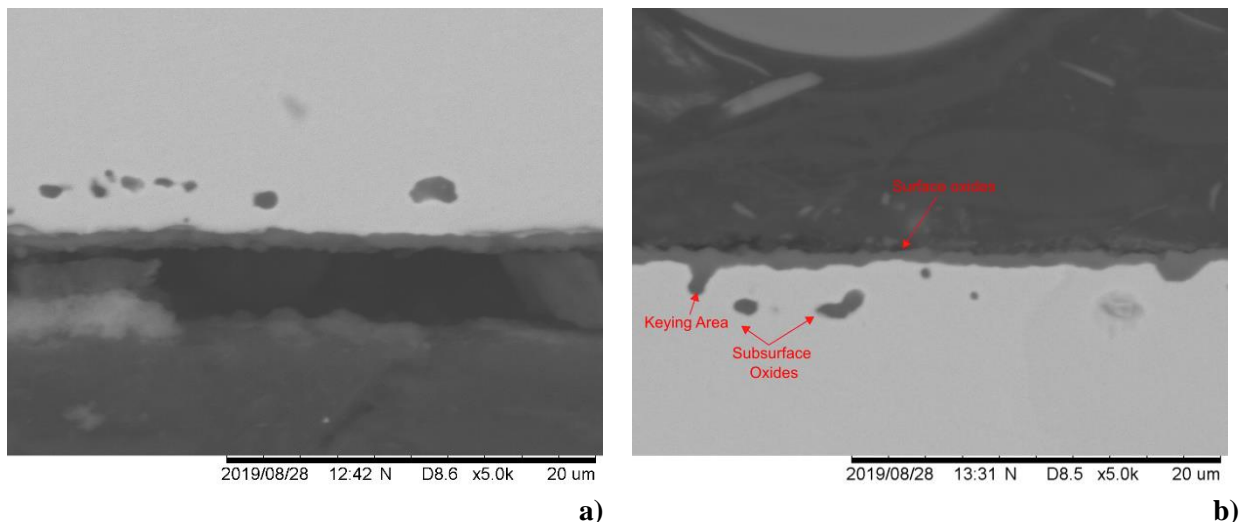
Figure 176. a) SEM cross-section of the top surface of a heat-treated reference sample, **b)** shows SEM image of the bottom surface of heat-treated MgO only coated samples.

5.2.3   EDS Analysis of MgO Only Coated Samples

Figure 177 shows a cross-section of a top surface of a reference sample. Figure 177 displays a Magnesium-silicon oxide layer developed at the surface of the substrate. The magnesium oxide surface layer has been identified in the literature as Forsterite (Mg_2SiO_4) [130]. Forsterite is an orthosilicate and is part of the olivine group, and Forsterite is isomorphous with Fayalite (Fe_2SiO_4). Both these compounds can co-exist within a range of 5-25% of Fayalite (Fe_2SiO_4) with the Forsterite [131].

Below the magnesium layer (Forsterite layer) is the iron matrix with areas of subsurface oxides developed (Figure 177b). The subsurface oxides contain regions of enriched areas of oxygen and aluminium and area of magnesium and oxygen. The regions of oxygen and aluminium have been identified as spinel's ($MgAlO_4$) in literature [132]. The source of aluminium is from the substrate in which the aluminium is purposely placed in the steel during the production of the hot band at IJmuiden steelworks, as explained in 1.2.1. As a result, the aluminium diffuses to the surface and forms subsurface oxides. Additionally, magnesium oxide is found in the subsurface oxide, whereby the magnesium has diffused from the MgO coating to enriched silicon and oxygen regions.
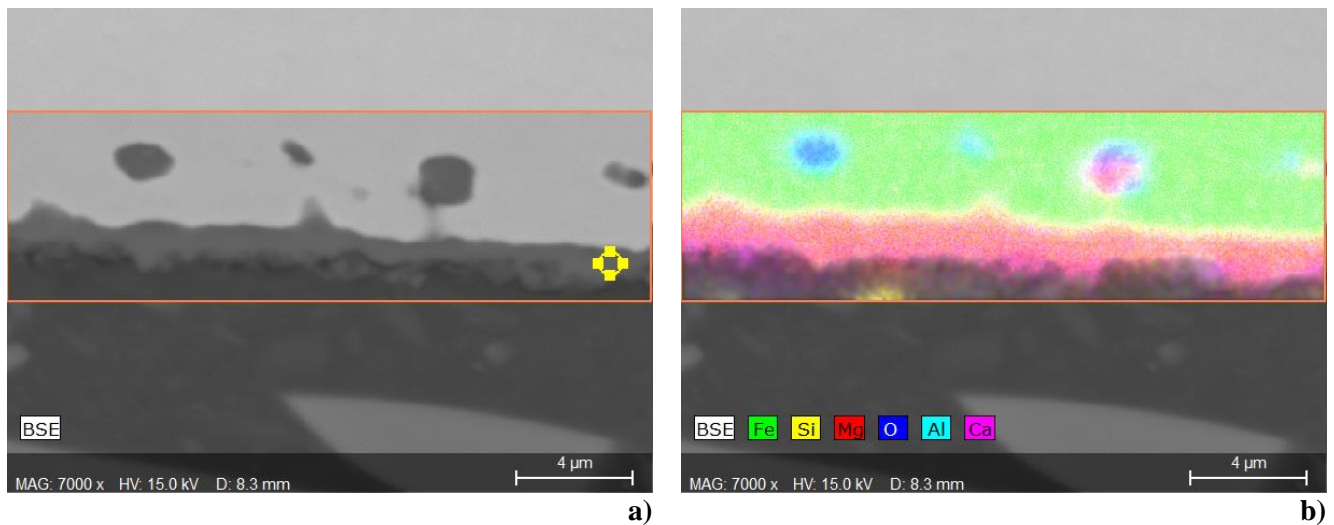
Figure 177. a.) SEM image of a top surface of a heat-treated reference sample, b.) EDS map of Figure 177a.

Figure 178 displays the spot scans using EDS on the reference sample, which has been heat-treated at the production HTCA furnaces at Orb Steelworks, to evaluate the elements present in the area. Area 1-4 are surface oxide analysis, and 5,6,8 is subsurface oxide element analysis. Area 7 is the EDS analysis of the matrix.
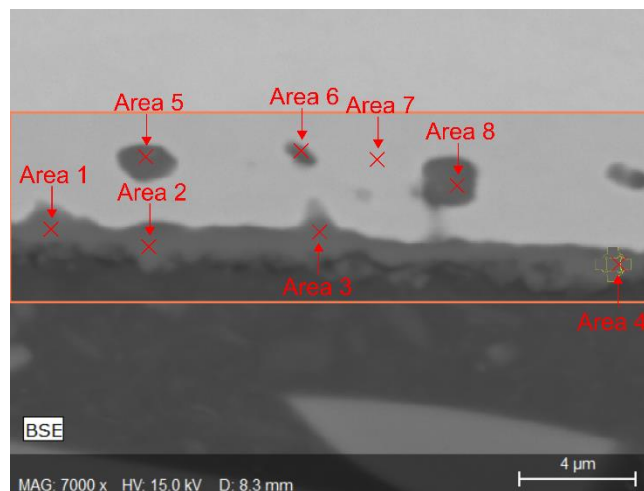
Figure 178. SEM image spot scan conducted on the substrate to give element concentration of the area of interest.

Figure 179 displays the concentration of magnesium and oxygen, with both consistently being greater than 30%. This indicates that Forsterite (Mg_2SiO_4) has developed. However, there is the presence of iron in these areas of scans that indicates the presence of Iron oxide or Fayalite. The range of iron detected ranges between 8% to 20%. Iron in the oxide layer can lead to possible resistance problems due to iron providing a conducting path to the substrate.
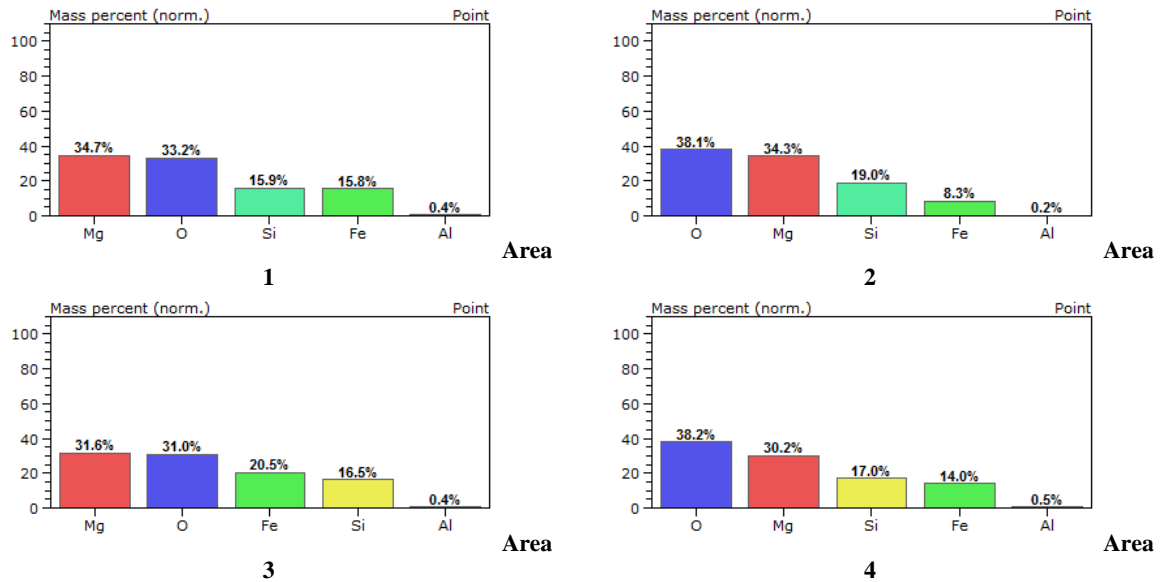
Figure 179. The results of spot scans of the EDS of surface oxide of the reference sample.

Figure 180 illustrates the concentration of elements at the subsurface and the matrix of the sample. Area 6 is a typical concentration of the bulk of the substrate, with the majority of the matrix is Iron ~97% with ~3% silicon. The elements detected in the subsurface oxides (areas 4,5,7) mainly consist of iron, aluminium, oxygen, magnesium, and silicon. As expected, Area 4 has a large percentage of iron detected in the subsurface oxide due to the iron matrix. However, the ratio of aluminium, oxygen, and magnesium shows in literature to be spinel ($MgAl_2O_4$)[133].

Similarly, area 6 displays a small quantity of spinel developed. The concentration in Area 8 shows the development of a combination of oxides are present, Forsterite (Mg_2SiO_4, Fayalite (Fe_2SiO_4) and Spinel ($MgAl_2O_4$)[132]. The source of the oxides come from two sources to form this subsurface oxide. The first is the substrate impurities and inhibitors, which have diffused from the iron matrix towards the surface. The second is the magnesium coating that is applied to the surface, diffusing from the surface of the top surface into the substrate, as discussed in previous sections. There is a level of confidence that the magnesium oxide has diffused into the substrate from GDOES analysis in section 2.15.3. Rather than cross-contamination through the preparation of samples. Where samples were etched using GDOES, and there were high concentrations of magnesium found after 60 seconds of surface etching.
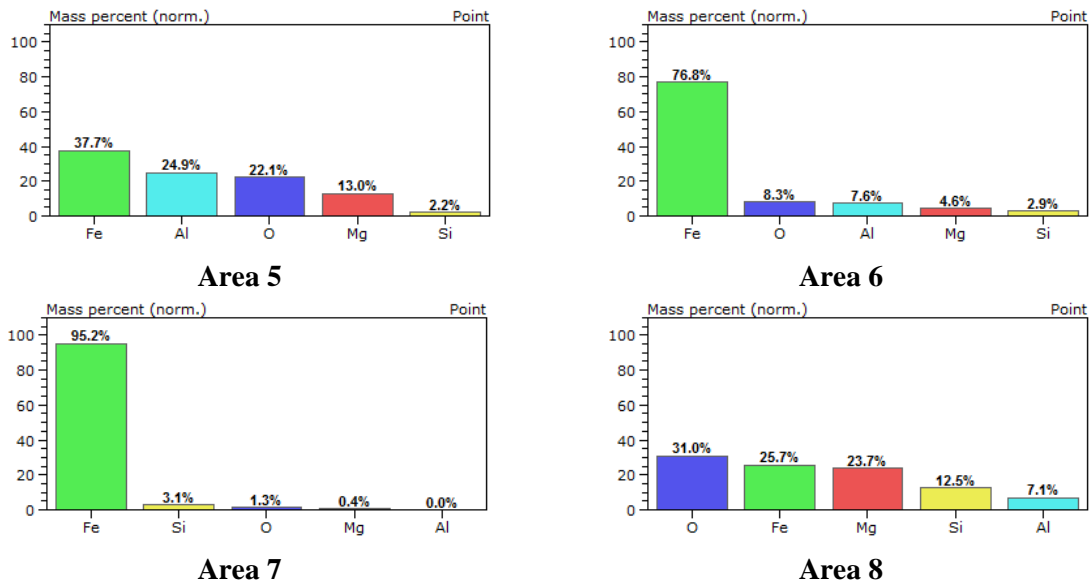
Figure 180. Displays the subsurface oxide and matrix concentrations of elements of a heat-treated reference sample.

Figure 181a.) displays areas where the line scan has taken place. Figure 181c.) and d.) illustrate the concentration of elements present through the surface of the oxide to the substrate. The coating surface is initially magnesium-rich, but the iron content increases when approaching the iron matrix, resulting in a decrease in magnesium content. Figure 181b.) The subsurface oxide displays magnesium in the subsurface oxide, indicating that some magnesium oxide has diffused into the substrate and formed Forsterite, although cohabiting with iron.
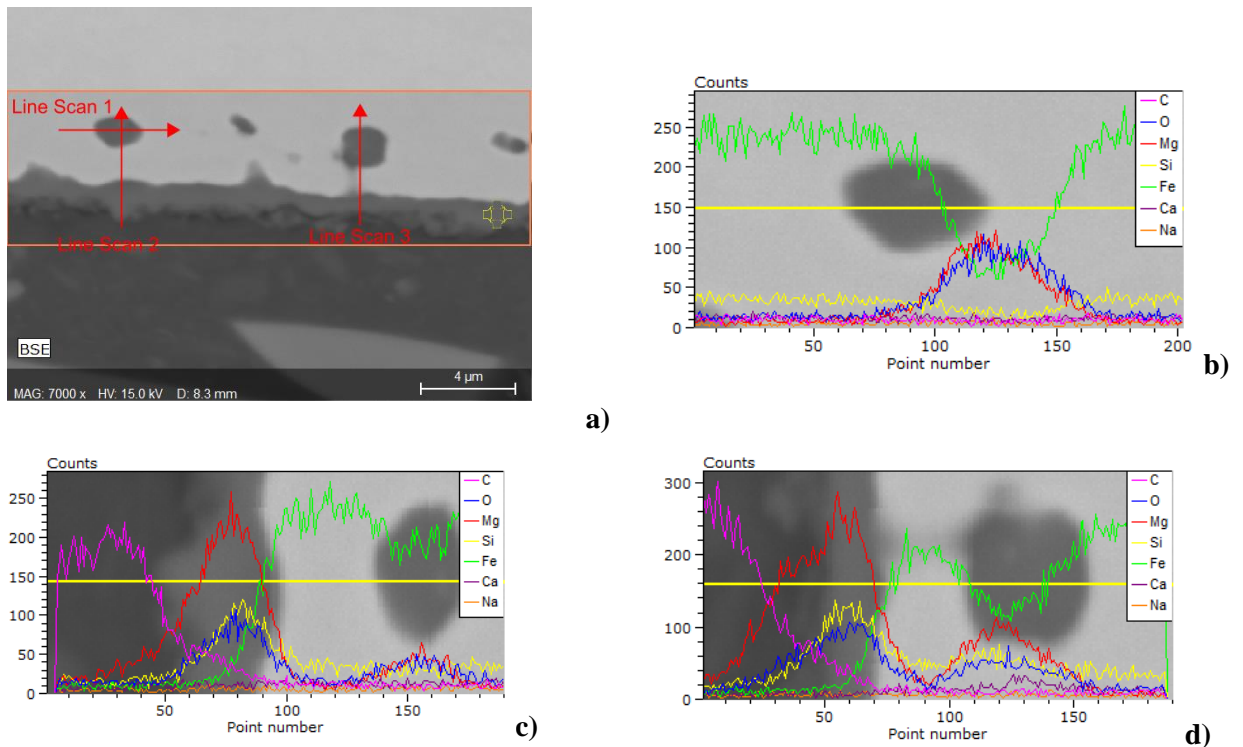
Figure 181. a) SEM cross-section of the 3 EDS line scans conducted. b) the composition changes of subsurface oxide.

5.2.4 GDOES Analysis of MgO Only Slurry

The chemical composition of the surface oxide developed in the reference sample was analysed using GDOES, as illustrated in Figure 182 and Figure 183. The concentration of elements alters through the depth of the substrate. For example, the magnesium concentration reaches a maximum of 18.3% at 2.5 seconds and decreases when moving from surface oxide to the iron matrix. The silicon reaches a maximum concentration of 12.7% at 1.6 seconds.
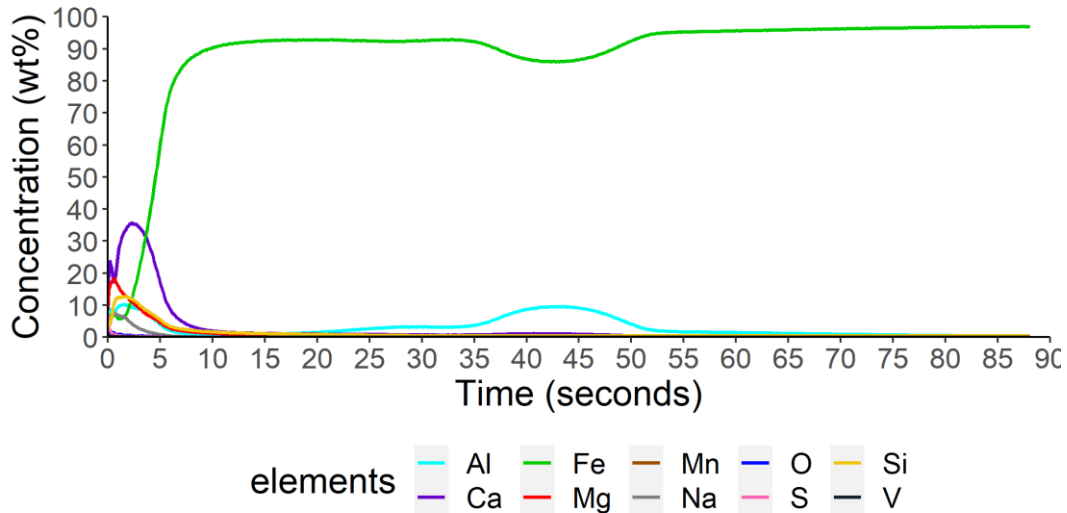
Figure 182. Illustrates the change in chemical composition with a MgO only coating applied.

Figure 183 illustrates the line of intersection between Mg and Fe occurs at 2.1 seconds. The aluminium concentration peaks twice, once at the surface of the oxide and once in the iron matrix. The peak surface at 10.3% at 1.6 seconds and again in the iron matrix 9.6% at 43.1 seconds.
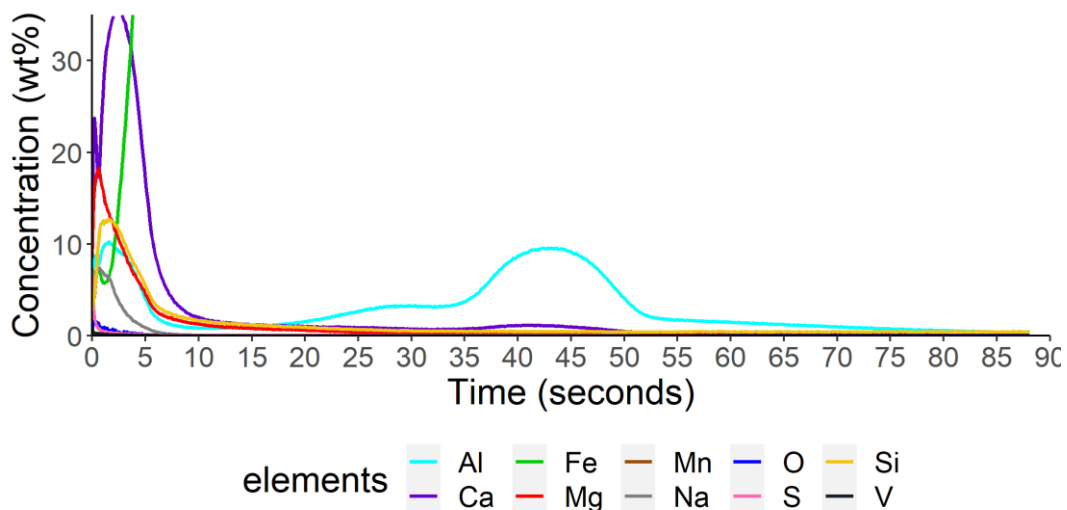
Figure 183. Illustrates a focused region the change in chemical composition with a MgO only coating applied.

5.2.5 Magnetic Properties

The magnetic losses of MgO only coated samples were measured and found to have an average of 0.85 W/kg (±0.09 standard deviation).

5.2.6 Resistance of Surface Coating

The resistance performance of the oxide layer is assessed by the amount of current detected through the oxide layer. The average current detected was 0.16 amps (± 0.10 standard deviation).

5.2.7 Bulk Analysis of Carbon, Oxygen, Nitrogen and Sulfur

The bulk chemical analysis was performed on 3 sample discs, each sample being 3mm disc in size. The oxygen content detected averaged 1415.53 ppm (± 161.95 standard deviation). The nitrogen content average is 29.34 ppm (± 0.85 standard deviation). The carbon content average was 0.0034 wt.% (±0.0002 standard deviation). The sulfur concentration average is 0.0034 wt.% (±0.0034 standard deviation).

5.3 The Impact of Range of Concentration TiO_2 Addition on the Formation of Oxide Layer

The TiO_2 is commonly added to the magnesium slurry in a range of 0-30%. It is believed that the TiO_2 addition improves the thickness of the oxide layer produced at the surface. However, there is no open-source evidence to support this theory. The analysis of this is presented in patients with little to no explanation of the measurement methods and concentration. Furthermore, the results within the patents are typically displayed in improvements in magnetic properties only, without other supporting quantitative evidence [117]. However, section 3.3 investigated the addition of TiO_2 to the MgO slurry and identified Ti in the surface oxide and showed indication of a benefit but was far from conclusive. This work seeks to expand on this and identify the impact on the oxide layer and the magnetic properties of the material produced

5.3.1 Experimental

The substrate used to coat the various concentration of TiO_2 was J19071. The samples were coated with MgO with TiO_2 addition at the concentration of TiO_2 to the slurry displayed in Table 17.

Table 17. Quantities of TiO_2 that is added to the slurry to achieve the range of addition between 0.5% to 25%.

Wt% of additive (TiO_2)	MgO	The amount of TiO_2 addition	Distilled water (ml)
0.5%	112g	0.56g	800
1%	112g	1.12g	800
5%	112g	5.6g	800
10%	112g	11.2g	800
15%	112g	16.8g	800
25%	112g	28g	800

Further details on sample preparation and experimental methods can be found in Chapter 2. In brief, samples were prepared and placed on top of the edge of the bottom coil in the production furnace.

The following analyses were conducted on the substrates:

- SEM cross-sectional thickness analysis
- EDS

- GDOES depth profiling surface oxide

- LECO bulk analysis of elements (C, O, N and S)

- Soken testing magnetic performance.

- Franklin testing resistance of oxide layer

The adhesion test results were all grade 1, and no variance was seen throughout all the samples. Pellets were then placed in a laboratory Carbolite furnace for 15 hours soak.

5.3.2 Morphology and Coating Thickness of Surface Oxide Developed with TiO_2 Additions to the Slurry.

Figure 184 shows a cross-section of the top and bottom surface of a heat-treated sample that has been coated with MgO slurry addition of 1% TiO_2 to the slurry. The oxide layer developed is an irregular layer with regions where very little oxide has developed, and there are no clear keying areas into the substrate. There is the presence of subsurface oxides which can originate from two possible sources. The first can be from the substrate, whereby inhibitors such as aluminium nitrides and manganese sulfides are rejected from the iron matrix and migrate to the surface. Alternatively, when magnesium diffuses into the substrate forming regions of oxides such as Forsterite (Mg_2SiO_4) or Spinel ($MgAlO_4$).

a)

b)
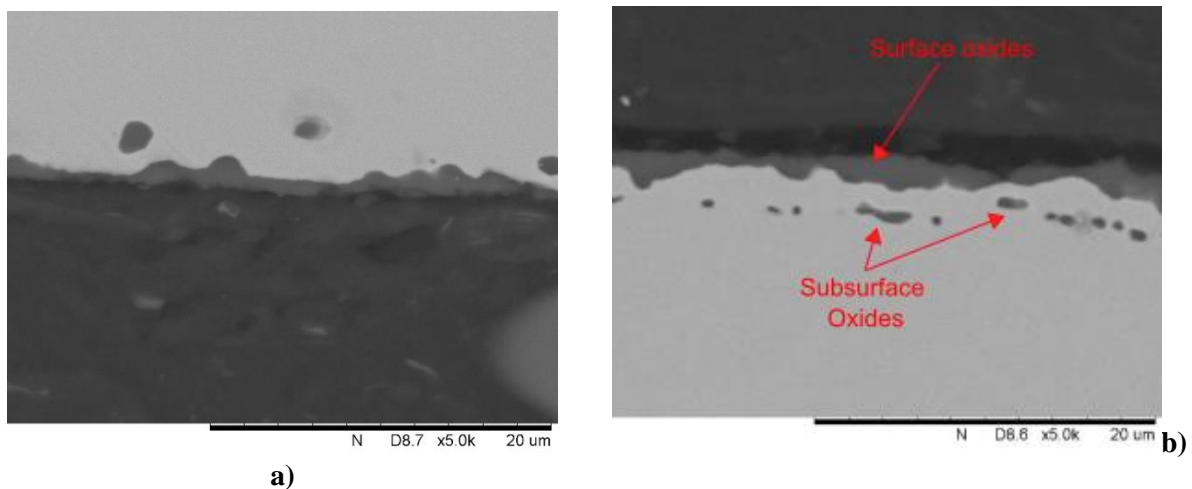
Figure 184. a.) Illustrates the SEM showing the top surface of a heat-treated sample that has been coated in MgO slurry with 1% TiO_2 addition, **b.)** shows the SEM of the image bottom surface.

Figure 185 shows a cross-section of a top and bottom surface of a heat-treated sample that has been coated in 10% addition of TiO_2 to the MgO slurry. There is an improvement in the thickness of the coating. The oxide continues to have a non-uniformity, with some regions appearing to have preferable oxide development than other regions. The oxide layer appears to enhance into the substrate surface rather than creating an oxide on the surface of the substrate.
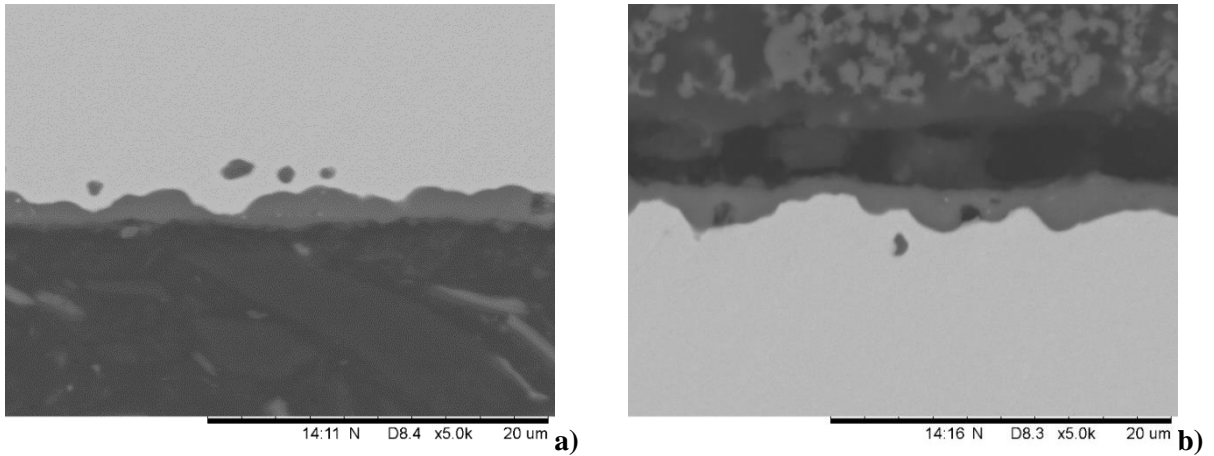
Figure 185. a) illustrates the SEM showing the top surface of the heat-treated sample that has been coated in MgO slurry with 10% TiO$_2$ addition, **b.)** shows the SEM image of the bottom surface

Figure 186 shows a cross-section of a top and bottom surface of a heat-treated sample that has been coated in 25% addition of TiO$_2$ to the MgO slurry. There is a continuation in the improvement in the thickness when comparing the 10% TiO$_2$ sample. In addition, the coating is consistent and uniform across the imaged sample. Figure 186a) is an example image of a keying area entering the substrate.
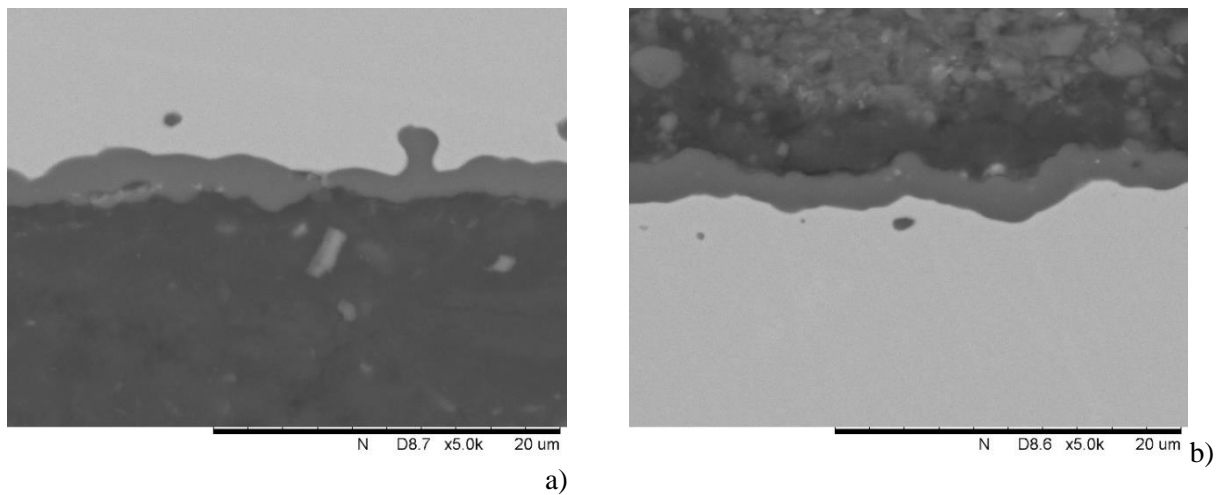
Figure 186. a) Illustrates the SEM showing the top surface of the heat-treated sample that has been coated in MgO slurry with 25% TiO$_2$ addition, **b)** shows the SEM image of the bottom surface

Figure 187 shows the calculated coating thickness from SEM images of the oxide layer developed with various amounts of TiO$_2$ addition. A reference sample has been coated in MgO only. It is noticeable that the addition of TiO$_2$ to the magnesium oxide slurry has resulted in an increase in oxide thickness developed on the surface of the substrates.
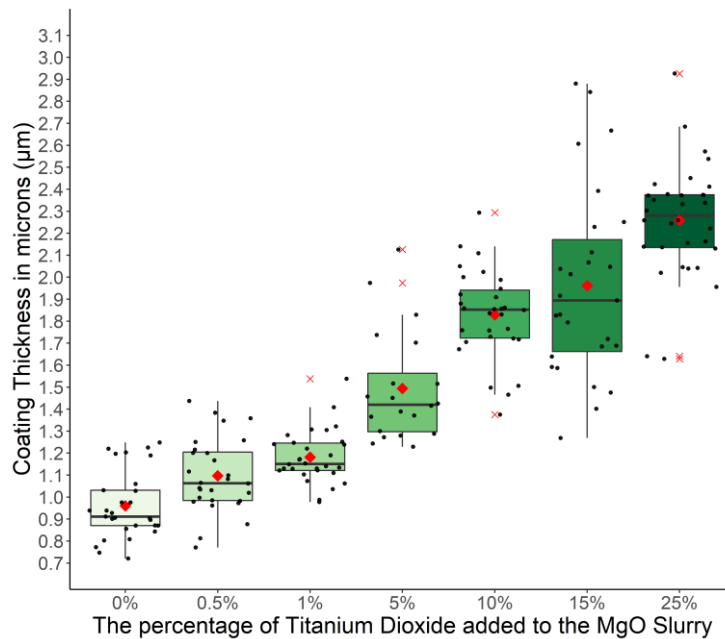
Figure 187. The effect of increasing the addition of TiO_2 to the MgO slurry on the oxide developed at the surface of the substrate.

An F-Test was conducted to establish whether the samples display a statistical difference in the variance or have dissimilar because of TiO_2 addition. The results of the F-Test and t-test are displayed in Table 18. The confidence level was set at $p=0.05$, and the null hypothesis was that an increase in the addition of TiO_2 does not affect the thickness of the coating.

Table 18. The results of the t-test and F-test to establish the variance are comparable and whether there is a significant difference between the concentration of TiO_2 added to the slurry.

	Comparing 0% to 0.5% TiO_2		Comparing 1% to 0.5% TiO_2		Comparing 5% to 1% TiO_2		Comparing 10% to 5% TiO_2		Comparing 15% to 10% TiO_2		Comparing 25% to 15% TiO_2	
P = 0.05	0% TiO_2	0.5% TiO_2	0.5% TiO_2	1% TiO_2	1% TiO_2	5% TiO_2	5% TiO_2	10% TiO_2	10% TiO_2	15% TiO_2	15% TiO_2	25% TiO_2
Mean	0.9599	1.0966	1.0966	1.1816	1.1816	1.4942	1.4942	1.8293	1.8293	1.9615	1.9615	2.2709
Variance	0.0236	0.0281	0.0281	0.0144	0.0144	0.0637	0.0637	0.0417	0.0417	0.1857	0.1857	0.0702
Observations	29.0000	28.0000	28.0000	30.0000	30.0000	20.0000	20.0000	30.0000	30.0000	27.0000	27.0000	30.0000
P(T<=t) two-tail	0.0023		0.0296		0.0000		0.0000		0.1383		0.0017	
F-Test	Un-equal Variance		Un-equal Variance		Equal variance		Un-equal Variance		Un-equal Variance		Equal variance	

To determine whether TiO_2 influences coating thickness, samples were compared to the reference sample that has been coated with MgO and was heat treated with the TiO_2 sample. A small addition of TiO_2 has an impact on the oxide layer developed at the surface of the substrate. This is evident when comparing higher concentrations to the reference sample. A slight addition increase between 0.5% to 1% addition of TiO_2 sees a significant increase in coating thickness measured. This trend of increase of thickness of the coating is displayed throughout the increasing additions of TiO_2, except when comparing the 15% to the 10% addition of TiO_2. Where there is no significant difference, the reasoning for this disparity cannot be fully explained. However, the large spread seen in the 15%

addition results suggests that uniformity of the slurry applied or distribution of TiO_2 may have been a factor. The improvements in quality of the oxide layer have also been shown in a study looking at the sinterability of dielectric properties using MgO, TiO_2 and SiO_2 powders to look at the effects on the formation of Forsterite. Increasing the TiO_2 content in the pellet has resulted in a denser formation of Forsterite [131].

5.3.3 Chemical Composition using EDS Analysis at the Surface with TiO_2 Addition to the Slurry.

The same analysis as presented above was performed on the sample with 1% TiO_2 addition to MgO slurry. Figure 188 illustrates the result from EDS mapping. The surface oxide is primarily oxygen, magnesium, silicon, and iron. The subsurface oxide mixture of elements present is Fe, Mg, Si, O, Al, S, Ca.

a)   b)
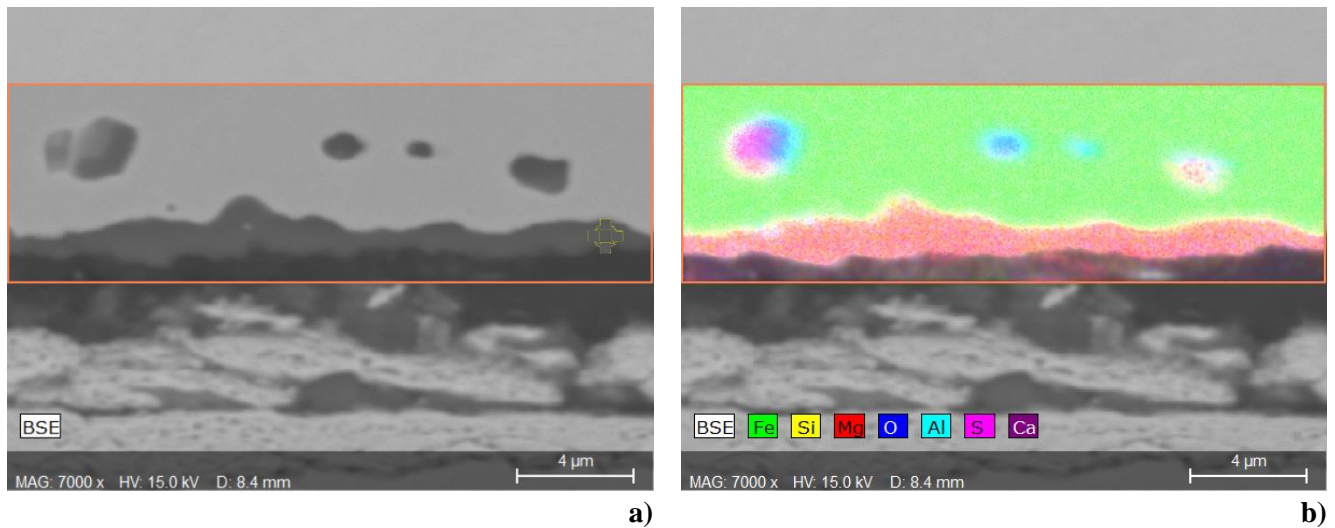
Figure 188. a) Illustrates an SEM of a cross-section of surface oxide with 1% TiO_2 addition to the slurry **b)** is an EDS mapping of the surface of the substrate.

Figure 189 illustrates the point scan areas in which EDS analyses were conducted. Area 1-4 are point scans of the surface oxide, and Area 5-7 analyses subsurface oxides.
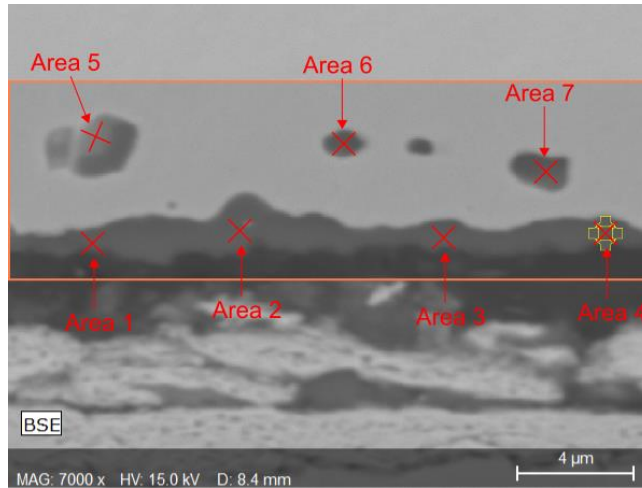
Figure 189. Illustrates the areas that point scans using EDS on surface and subsurface oxides on the heat-treated sample with 1% TiO_2 addition.

Figure 190 displays the concentration levels at each point scan. The elements present in the surface oxide are predominantly magnesium, oxygen, iron, and silicon, with a slight trace of aluminium detected. Areas 1-3 display signs of iron present in the surface which indicates Fayalite to be present. Area 1 has signs of aluminium diffusing to the surface and forming a part of the surface oxide.
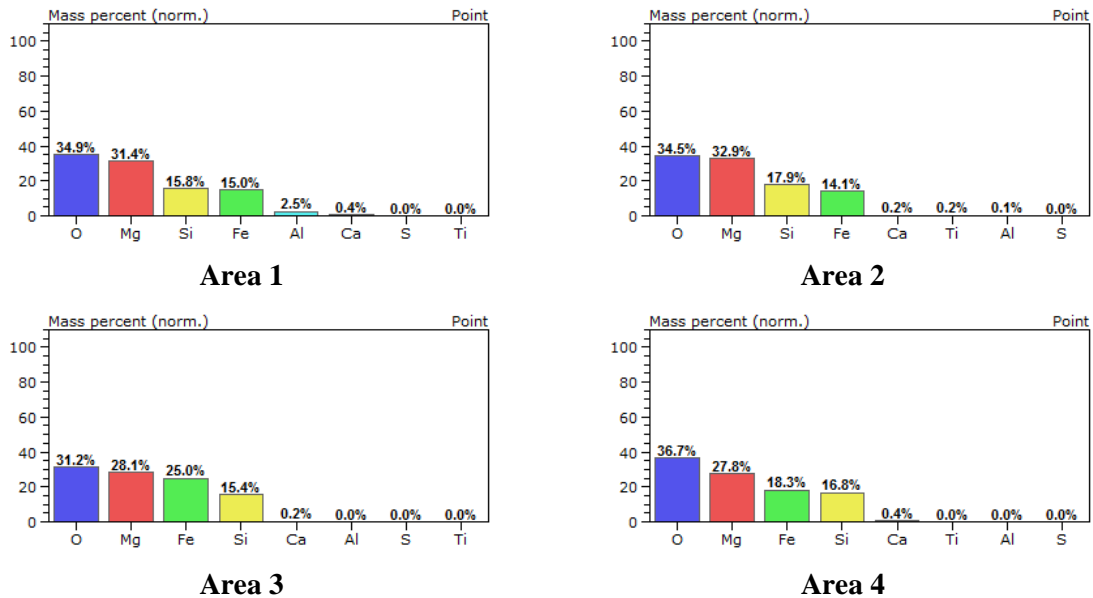
Figure 190. Displays the result of the surface oxide point scans (1-4) using EDS on the surface of the heat-treated sample with 1% TiO_2 addition to the magnesium slurry.

Figure 191 displays the subsurface oxide EDS analysis. It illustrates a mixture of oxides that have developed in the subsurface region of the substrate. Previous research identified the oxides that can develop under the correct conditions are: - spinel ($MgAl_2O_4$), Fayalite (Fe_2SiO_4), Forsterite (Mg_2SiO_4), monticellite ($CaMgSiO_4$) and kirschsteinite ($CaFeSiO_4$). Area 5 in Figure 191 displays multiple elements present in the subsurface oxide. Iron is dominant in the subsurface due to the

presence of the iron matrix. The high presence of Aluminium and sulphur indicates that aluminium sulphide (Al_2S_3) has developed at the surface. Additionally, it appears that spinel coexists with the aluminium sulphide.

Area 6 has fewer elements present in the scanned area and is iron with spinel oxide being present. Area 7 has developed a Forsterite layer in the subsurface with a small amount of spinel developed.

The addition of 1% of TiO_2 to the magnesium slurry appears not to affect the surface and subsurface oxide composition, and there is no obvious formation of an alternative oxide containing titanium.

Area 5

Area 6

Area 7
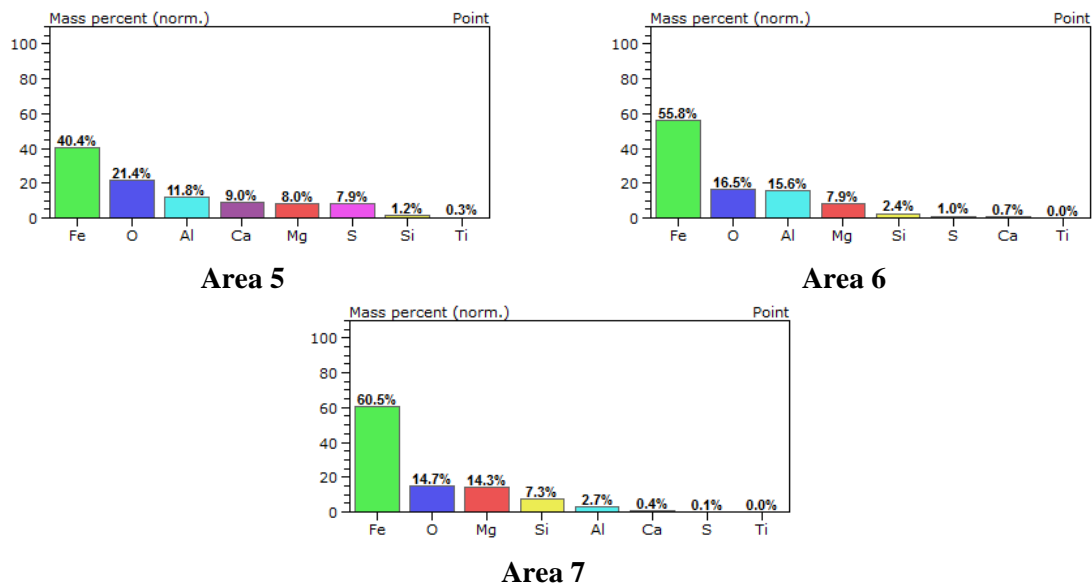
Figure 191. Displays the result of the sub-surface oxide point scans (Area5-7) using EDS on the heat-treated sample with 1% TiO_2 addition to the magnesium slurry.

The same analysis as presented above was performed on the sample with 10% TiO_2 addition to MgO slurry. Figure 192 illustrates the cross-section of a sample. The oxide that has developed is thick with no signs of thin oxide at the surface. The surface oxide is dominated by oxygen, magnesium, silicon, and iron. There are no signs of titanium present at the surface. There is no sign of subsurface oxide present but appears an oxygen-rich area at the surface oxide/ iron matrix interface.

166
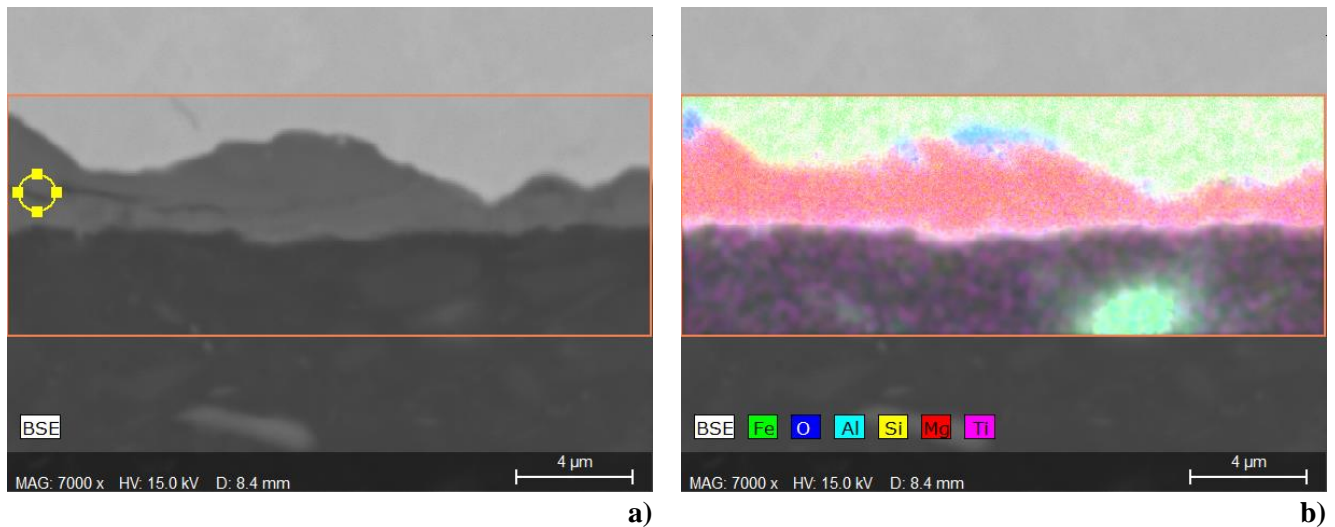
Figure 192. SEM image of a cross-section of a sample that has been coated with magnesium oxide with the addition of 10% TiO$_2$ and heat-treated at Orb steelworks HTCA production furnaces.

Figure 193 illustrates the EDS point scans. The surface oxide is represented by areas 1-4, and the matrix is represented by 5,7 and 8, with area 6 investigating the composition of the oxygen-enriched area displayed in Figure 192b.)
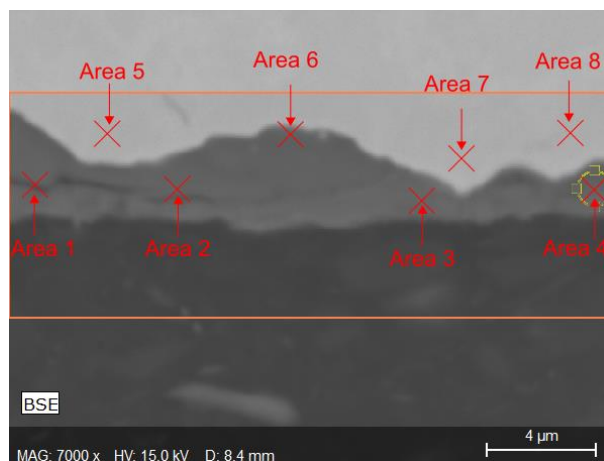
Figure 193. Illustrates the point scans using EDS at the surface and subsurface oxide of a sample that has been coated with magnesium oxide with 10% addition of TiO$_2$ to the slurry and heat-treated at Orb Steelworks HTCA production furnaces.

Figure 194 displays the results of point scans of the surface oxide. Area 1 and 2 are dominated by the main concentration of elements of oxygen, magnesium, and silicon. The ratios of the elements indicate that Forsterite has developed with a small percentage of iron (<7%) present. Area 3 and 4 shows a slight decrease in magnesium present and an increase in iron. The increase in iron indicates that Fayalite (Fe$_2$SiO$_4$) is coexisting with Forsterite (Mg$_2$SiO$_4$) in the surface oxide. Titanium is detected in the oxide layer but in small quantities (<0.2%).
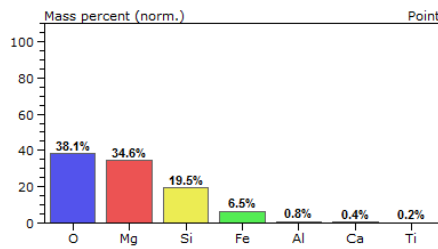
167
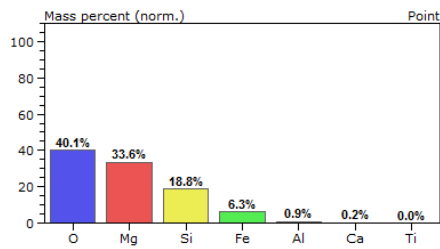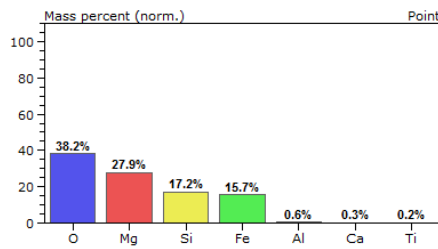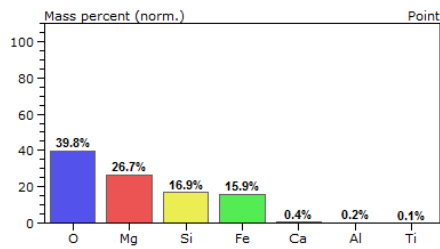
Figure 194. Displays the result of the surface oxide point scans (Area 1-4) using EDS on a heat-treated sample with 10% TiO$_2$ addition to the magnesium slurry

There is no sub-surface oxide present below the oxide layer in Figure 192. Figure 195 displays the EDS point scans conducted at the matrix (areas 5,7 and 8) and the surface oxide and matrix (area 6). The matrix is predominantly iron with ~3.5% Silicon and small oxygen, magnesium, titanium, and calcium. Area 6 represents the interface between the surface oxide iron matrix the concentration. The interface mainly consists of iron, and there is the presence of oxygen, magnesium, silicon, and aluminium. This suggests that several oxides are coexisting. In addition, a small amount of TiO$_2$ was detected in the subsurface, which is a negligible amount detected in the subsurface oxide.
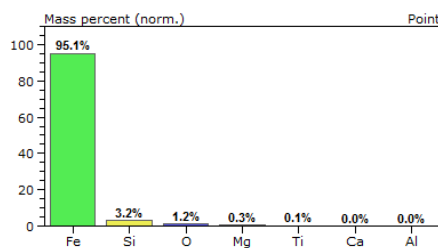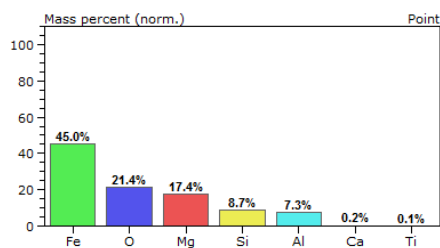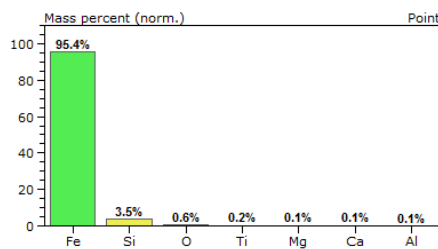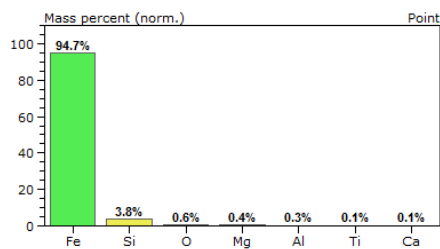
Figure 195. Displays the result of the sub-surface oxide point scans (Area 5-8) using EDS on heat-treated sample with 10% TiO$_2$ addition to the magnesium slurry.

168

The same analysis as presented above was performed on the sample with 25% TiO$_2$ addition to MgO slurry. Figure 196 illustrates the cross-section of a sample. The surface is a magnesium-enriched layer that has developed at the surface of the substrate, with no signs of interruption of the magnesium coating. The surface oxide also has titanium enriched areas present in the magnesium oxide. There is no subsurface oxide present in the scanned area.

a)   b)
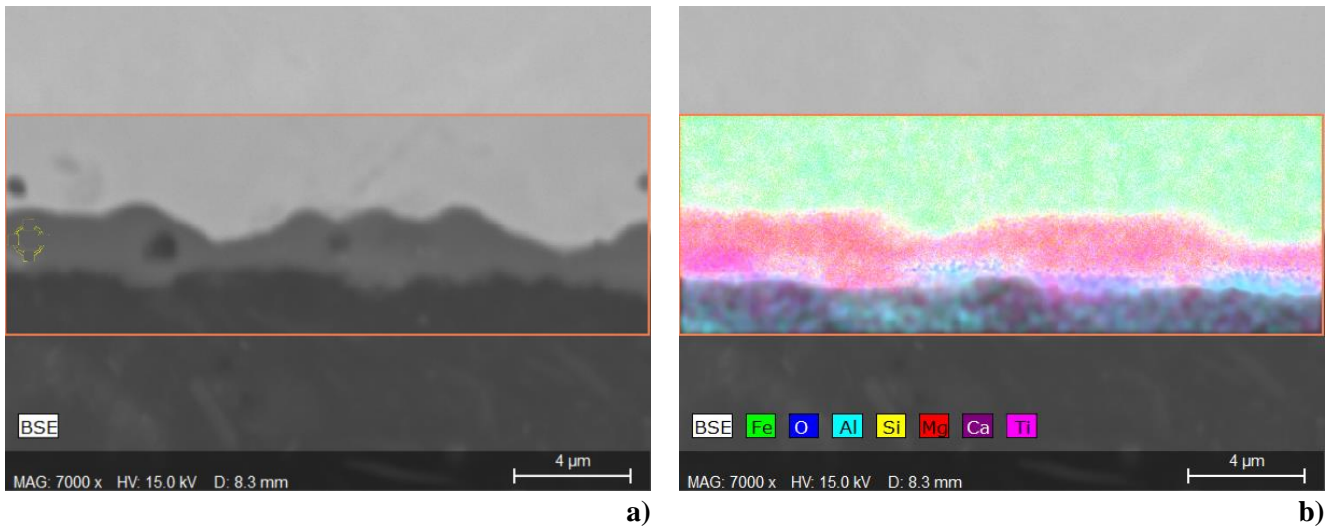
Figure 196. Illustrates an SEM image of a cross-section of a sample that has been coated with magnesium oxide with the addition of 25% TiO$_2$.

Figure 197 illustrates the point scans. The surface oxide analysis using EDS is represented by point scan 1-7, and the iron matrix is represented by 8 and 9 to investigate the concentration of elements present in the scanned area.
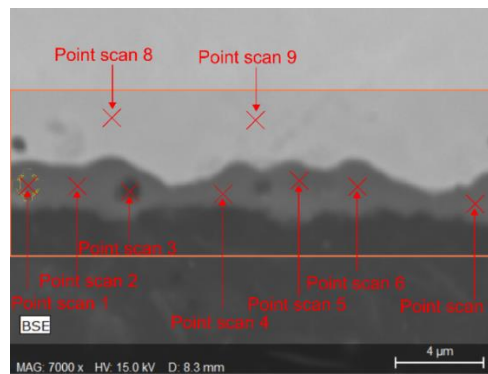
Figure 197. Demonstrates the EDS point scans across the surface oxide and matrix of a sample that has been coated with magnesium oxide with 25% addition of TiO$_2$.

The results from the point scans of the surface oxide layer are shown in Figure 198. Point scans 1-3,5,6 all demonstrate a concentration of oxygen, magnesium, and silicon. The ratio that Forsterite has developed at the surface, with a low concentration of iron present in the magnesium oxide. Point scans 4 and 7 also display ratios consistent with Forsterite development. However, there is an increase in iron concentration in the scanned areas. This suggests that Fayalite (Fe$_2$SiO$_4$) or iron oxide is coexisting with the Forsterite. The increase in Ti to the magnesium oxide slurry has seen a slight increase of titanium present within the surface oxide.

169

Point Scan 1

Point Scan 2

Point Scan 3

Point Scan 4

Point Scan 5

Point Scan 6
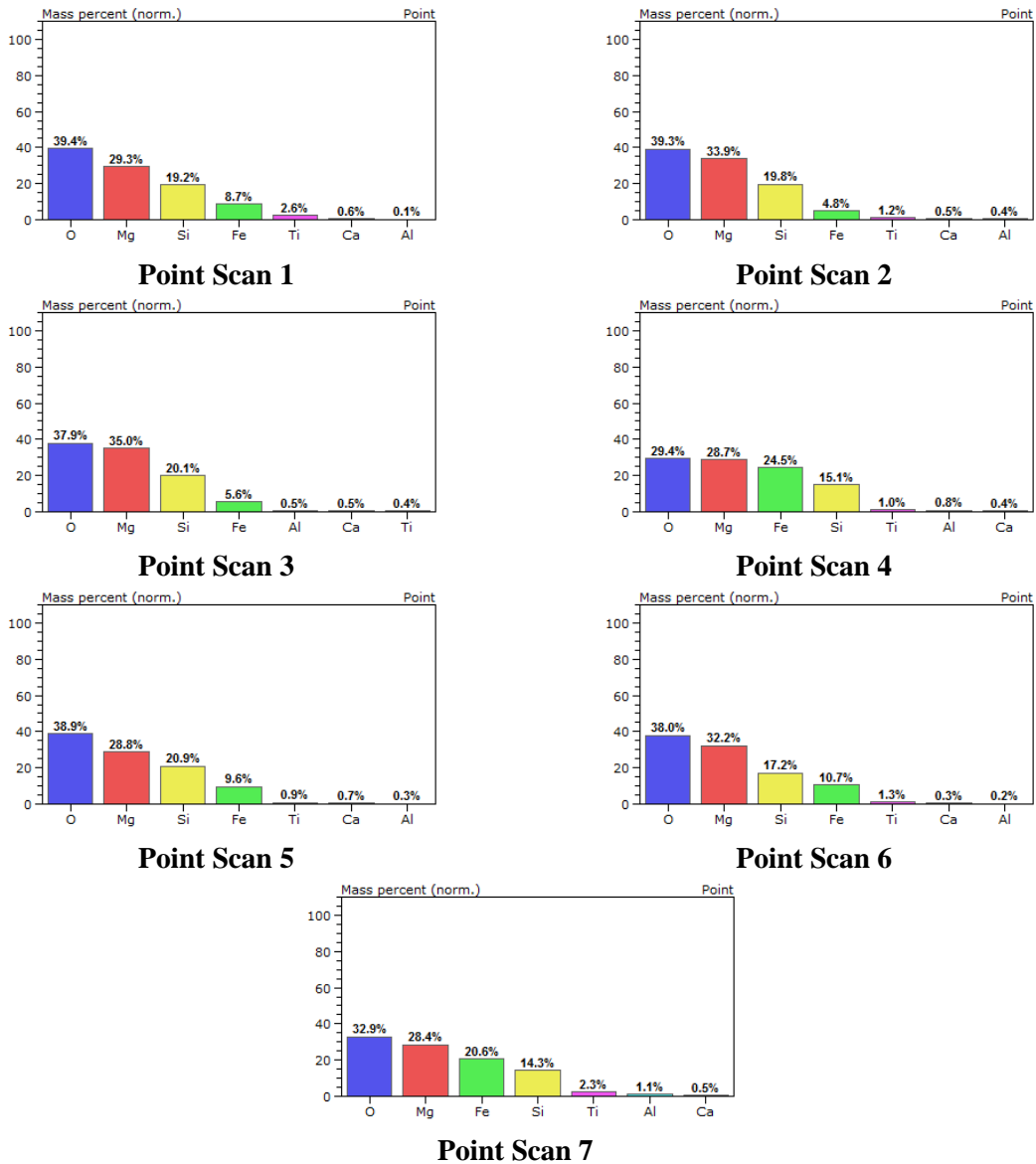
Point Scan 7

Figure 198. Displays the result of the surface oxide point scans (1-7) using EDS on a heat-treated sample with 25% TiO_2 addition to the magnesium slurry.

The results from the EDS point scan of the matrix are displayed in Figure 199. As expected, the matrix is mainly consisting of iron with silicon present. There are no signs of any oxide development or any titanium present.

Point Scan 8
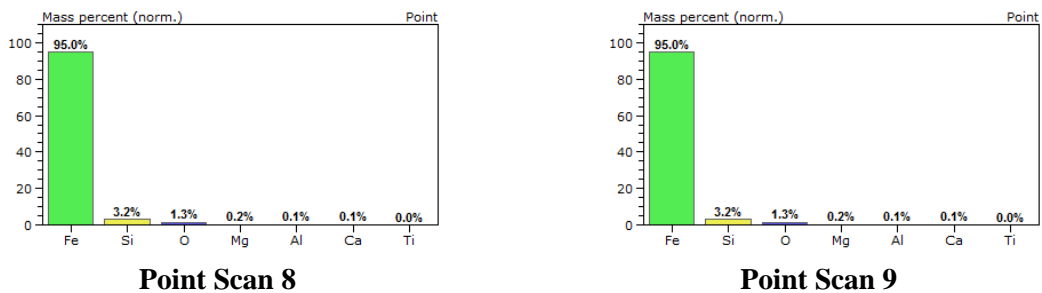
Point Scan 9

Figure 199. Displays the results of the iron matrix of point scans (8 and 9) using EDS on a heat-treated sample with 25% TiO_2 addition.

5.3.4 Chemical Composition of Samples with TiO₂ Addition to the Slurry using GDOES Analysis.

The chemical composition of the coating was determined by using Glow Discharge Optical Emission Spectroscopy (GDOES). The result obtained for 1% TiO₂ addition to the MgO slurry are displayed in Figure 200. As explained in section 2.15, the line of interception between magnesium and iron will be considered the end of a uniform oxide layer.
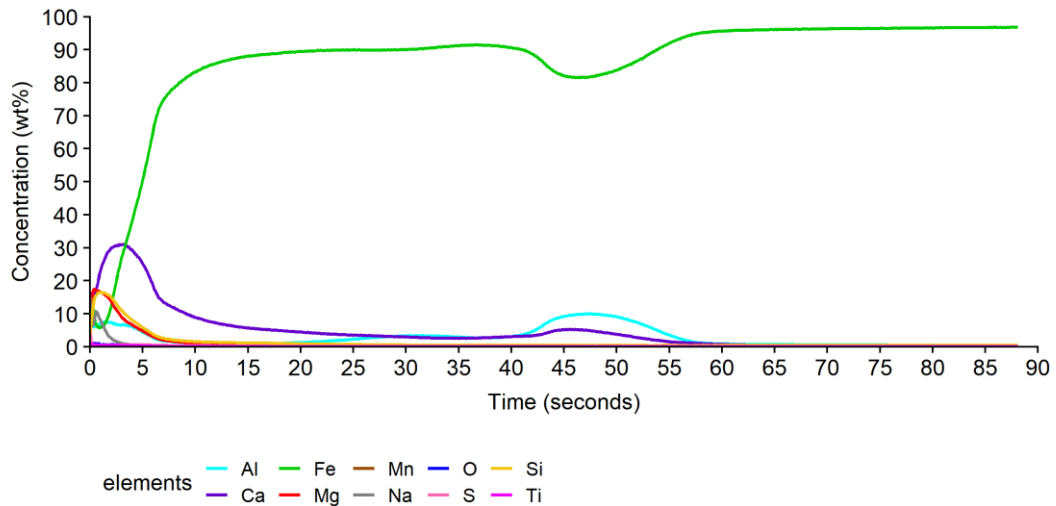
Figure 200. Chemical composition of the oxide with the addition of 1% TiO₂.

As expected, the oxide layer is a complex system where the composition of the oxide changes with depth. The elements detected through the coating thickness are explained in section 2.15. The focus in this section is the concentration of magnesium, iron, aluminium, and titanium levels. The concentration of magnesium peaks at 17% and begins to fall while iron content increases

As expected, the oxide layer is a complex system where the composition of the oxide changes with depth. The elements detected through the coating thickness are explained in section 2.15. The focus in this section is the concentration of magnesium, iron, aluminium, and titanium levels. The concentration of magnesium peaks at 17% and begins to fall while iron content increases

dramatically. This indicates that magnesium oxide's uniform coating is no longer present, and the 50/50% concentration of magnesium to iron ratio occurs at 2.5 seconds.
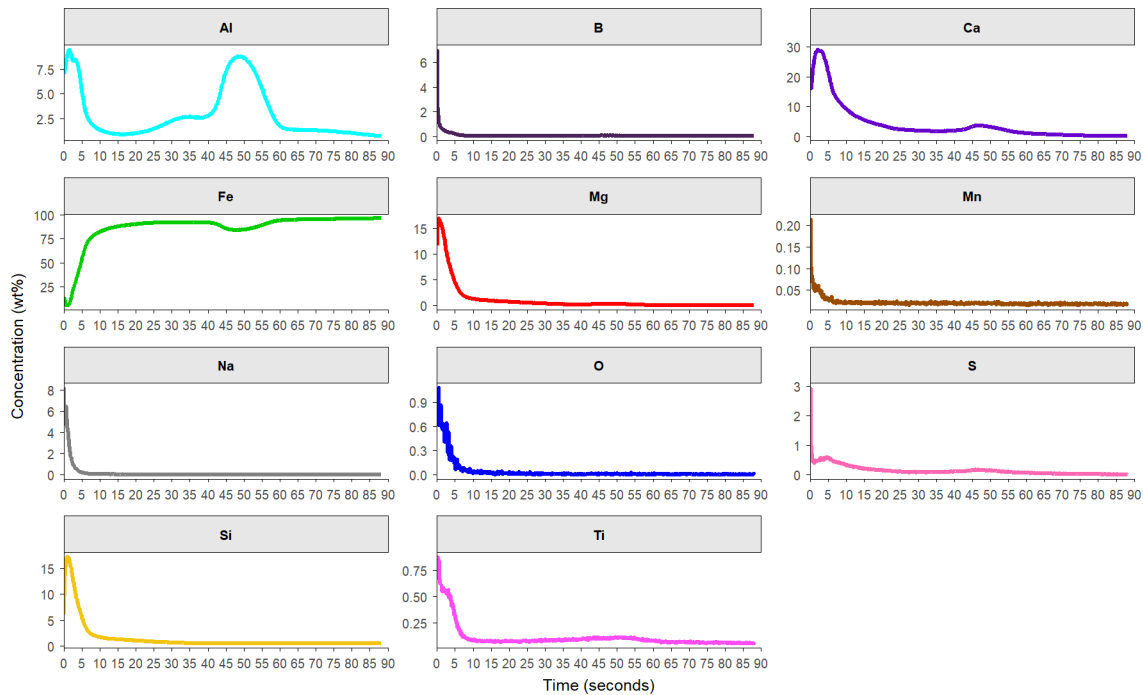
Figure 201. The individual elements of the chemical composition of the surface oxide of a sample that has been coated with 1% TiO_2 addition to MgO slurry.

The titanium levels remain insignificant throughout the analysis where the with the maximum peak in titanium detected being 0.88%. The aluminium continues trends seen in previous sections 3.2.2 and peaks twice, first at the surface of the substrate where concentrations level reach peaks 9.4% and the second peak is in the subsurface of the steel where maximum levels reach 8.2%. The aluminium nitrides cause pinning of other orientations to give GOSS grains advantageous nucleation and growth [134]. At around 800°C, the aluminium nitrides begin to break down and migrate to the surface. These form part of the subsurface oxide, as seen in the EDS section. SEM/EDS images display pockets of aluminium below the initial oxide layer, and aluminium pockets are present in the iron matrix, causing the second spike in aluminium.

172

The GDOES analysis of a substrate coated MgO slurry with 10% TiO_2 addition is displayed in Figure 202. The oxide layer has changed dramatically, with an initially prominent peak of aluminium detected with a concentration of 57%, which then begins to drop.
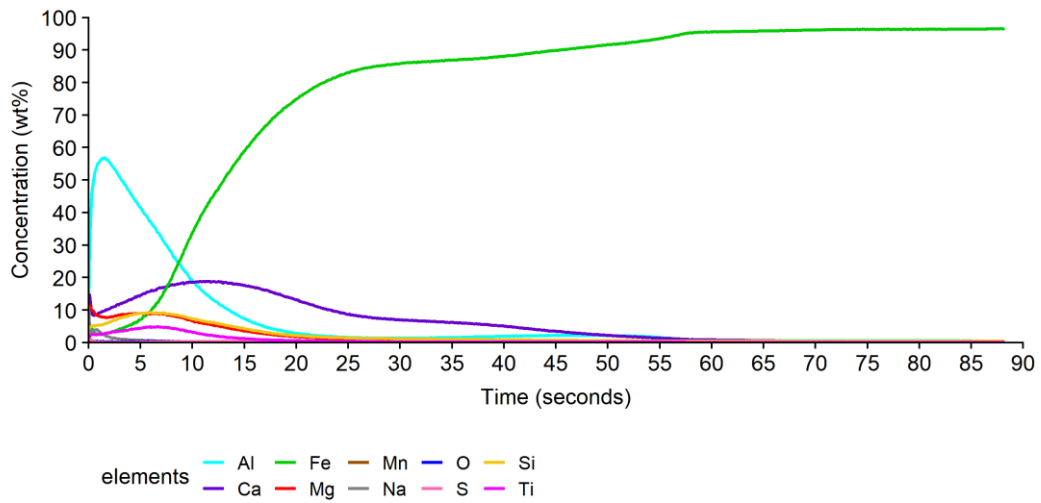
Figure 202. Chemical composition of the oxide with the addition of 10% TiO_2 to the MgO slurry using GDOES.

The second peak of aluminium concentration that has been seen previously in the 1% Ti addition has dropped down to a 2% maximum peak. The magnesium oxide levels have reduced to a maximum concentration of 11%, and the line of interception of the 50/50 magnesium and iron is at 5.6 seconds. The addition of TiO_2 appears to form a part of the oxide layer where the maximum concentration of titanium detection is 5%. Previous additions of 0.5%,1% and 5% titanium were not detected in GDOES.
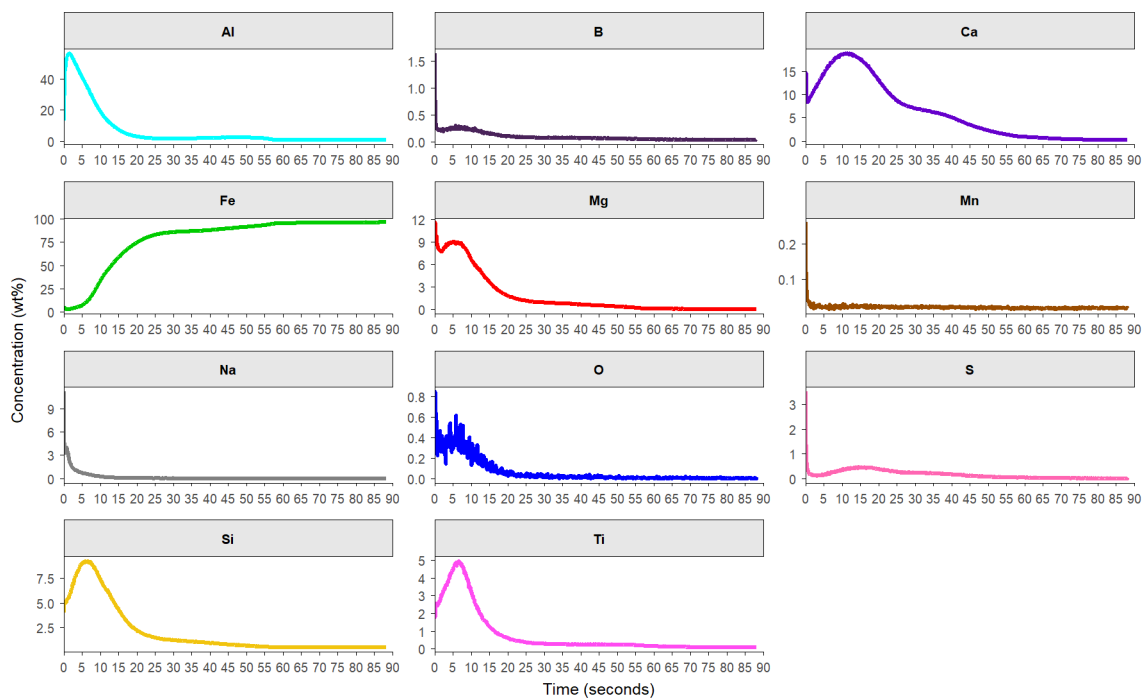
Figure 203. The individual elements of the chemical composition of the surface oxide of a sample that has been coated with 10% TiO_2 addition to MgO slurry.

The results of the GDOES analysis on the oxide developed after increasing the TiO_2 to 25% in the magnesium slurry and completing heat treatment is displayed in Figure 204. The titanium content detected in the oxide layer has a more distinct presence than in the previous analysis.
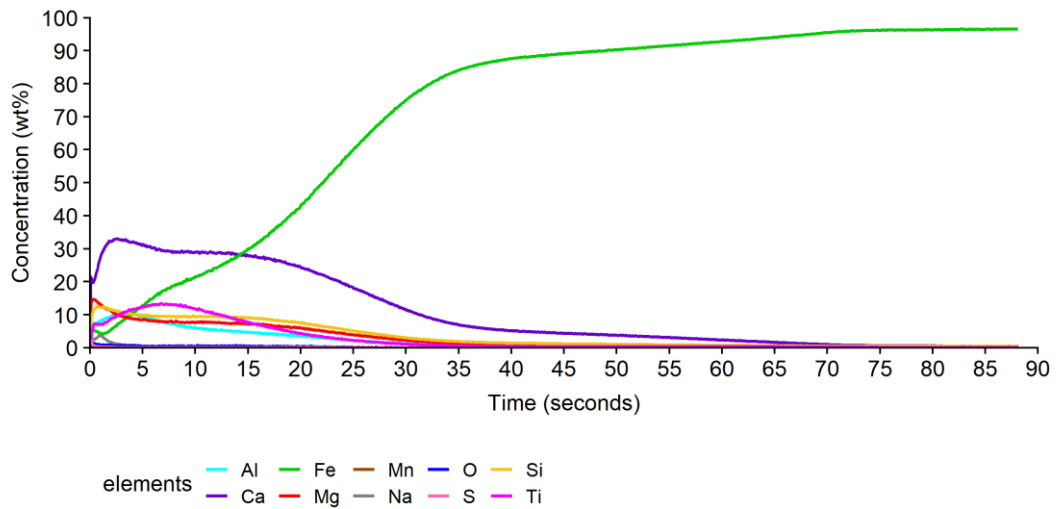
Figure 204. Chemical composition of the oxide with the addition of 25% TiO_2 to the MgO slurry.

The titanium content reaches a maximum level of 13.5%. The maximum magnesium concentration reaches 14.7% initially and then reduces. The line of interception between the iron and magnesium is at 3.5 seconds.
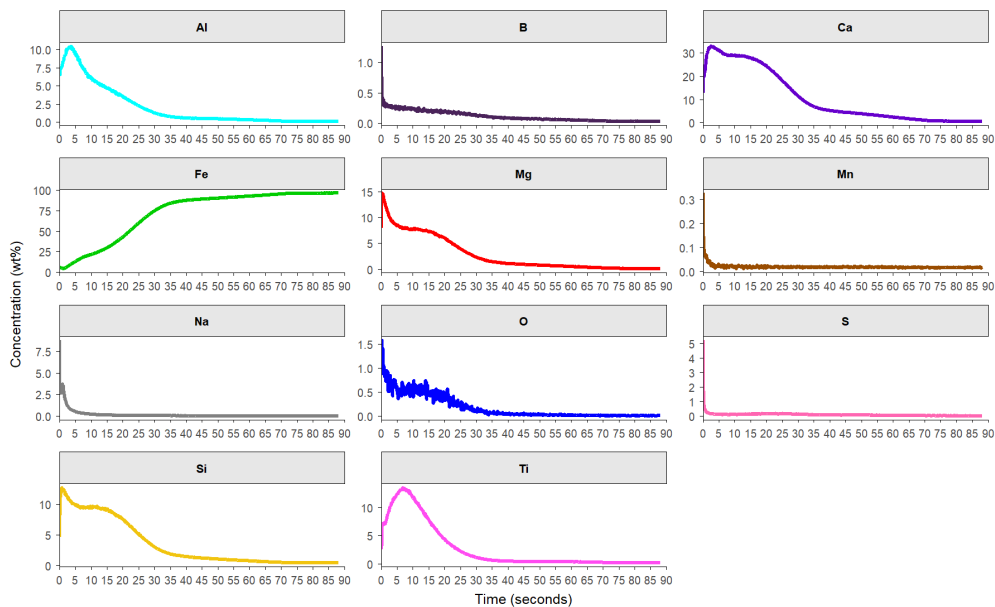
Figure 205. The individual elements of the chemical composition of the surface oxide of a sample that has been coated with 25% TiO_2 addition to MgO slurry.

When the addition of TiO_2 is >10%, the titanium has altered the composition of the oxide layer developed during the heat treatment. Thus, it appears that titanium has developed as part of the oxide layer, and detection of Ti provides evidence of the role of TiO_2 added to MgO slurry.

174

5.3.5 Magnetic Properties

Figure 206 illustrates the results obtained for magnetic properties of the different concentrations of TiO_2 added to the magnesium slurry using a Soken tester which was explained in section 2.8. Due to the significant variance F test and T-test were conducted to determine the significant difference between the concentration of TiO_2.
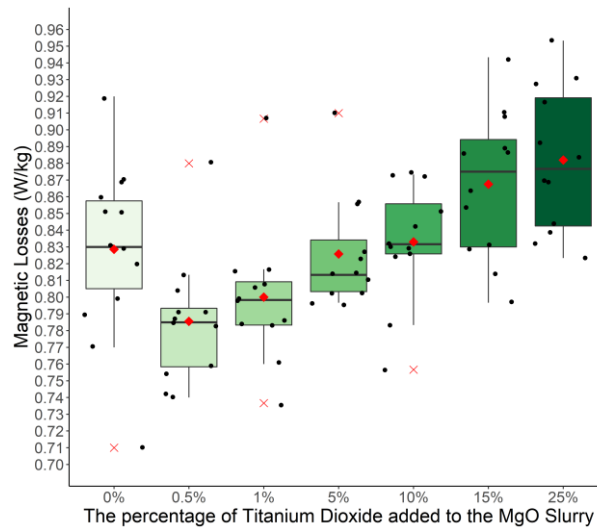
Figure 206. The effect of addition of TiO_2 to magnesium slurry on Magnetic losses using a Soken tester.

Table 19 displays the results for an F-Test and T-Test. The confidence level was set at $p=0.01$, and the null hypothesis was that an increase in the addition of TiO_2 does not affect the magnetic properties. There is a significant difference between the magnesium only coated sample compared to 0.5% TiO_2 and 1% TiO_2 addition to the magnesium. The introduction of 0.5% and 1 % has decreased the magnetic losses of the substrate. When comparing 0.5% and 1% TiO_2, there is no significant difference in reducing magnetic losses.

Further increasing the TiO_2 content to 5% to the slurry magnesium has no significant difference compared to 1% TiO_2 addition. However, the improvements in magnetic properties achieved by the 0.5% and 1% are lost, and the performance of 5% TiO_2 is the same as magnesium only slurry. Similarly, the 10% addition of TiO_2 to the slurry results in similar magnetic properties as magnesium only slurry and no significant difference compared to the 5% addition of TiO_2.

When TiO_2 is increased to 15%, the magnetic losses have increased, and performance is reduced compared to the magnesium oxide only. This trend of losses increase continues with 25% TiO_2 addition. There is no significant difference between 25% and 15%.

Table 19. The results from F-Test and T-Test on magnetic properties comparing TiO$_2$ concentrations.

P = 0.05	Comparing 1% to 0.5% TiO$_2$		Comparing 1% to 5% TiO$_2$		Comparing 5% to 10% TiO$_2$		Comparing 10% to 15% TiO$_2$		Comparing 15% to 25% TiO$_2$	
	0.5% TiO$_2$	1% TiO$_2$	1% TiO$_2$	5% TiO$_2$	5% TiO$_2$	10% TiO$_2$	10% TiO$_2$	15% TiO$_2$	15% TiO$_2$	25% TiO$_2$
Mean	0.7856	0.8000	0.8000	0.8258	0.8258	0.8331	0.8331	0.8675	0.8675	0.8819
Variance	0.0014	0.0017	0.0017	0.0011	0.0011	0.0012	0.0012	0.0019	0.0019	0.0018
Observations	12	12	12	12	12	12	12	12	12	12
P(T<=t) two-tail	0.3778		0.1048		0.6119		0.0466		0.4234	
F-Test	Un-equal Variance		Un-equal Variance		Un-equal Variance		Un-equal Variance		Un-equal Variance	

The performance of the magnetic properties is overlapping with a slight increase in the concentration of TiO$_2$ to the slurry. However, when comparing more significant variances in concertation, the significance is apparent, which is displayed in Table 20.

Table 20. The results from F-Test and T-test on magnetic properties comparing significant variations concentration in TiO$_2$.

P = 0.05	Comparing 0.5% to 5% TiO$_2$		Comparing 1% to 10% TiO$_2$		Comparing 5% to 15% TiO$_2$		Comparing 10% to 25 TiO$_2$	
	0.5% TiO$_2$	5% TiO$_2$	1% TiO$_2$	10% TiO$_2$	5% TiO$_2$	15% TiO$_2$	10% TiO$_2$	25% TiO$_2$
Mean	0.7856	0.8258	0.8000	0.8331	0.8258	0.8675	0.8331	0.8819
Variance	0.0014	0.0011	0.0017	0.0012	0.0011	0.0019	0.0012	0.0018
Observations	12	12	12	12	12	12	12	12
P(T<=t) two-tail	0.0111		0.0163		0.0163		0.0060	
F-Test	Un-equal Variance		Un-equal Variance		Un-equal Variance		Un-equal Variance	

5.3.6

5.3.7 Resistance

The resistance performance of the oxide layer developed with the various amounts of TiO$_2$ addition to the magnesium oxide slurry is displayed in Figure 207.
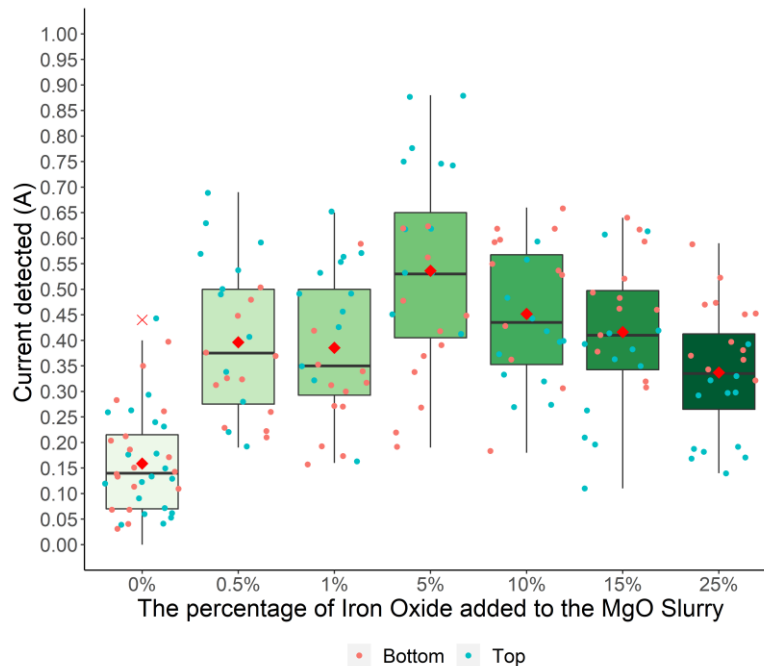
Figure 207. The resistance properties of the developed oxide layer with the addition of TiO$_2$ to the magnesium slurry.

Figure 207 illustrates the results obtained from the Franklin tester and displays the recorded current detected. An F- Test and T-test were conducted to establish whether there is a significant difference when increasing the concentration of TiO_2 to the slurry. The null hypotheses assume that there is no difference when increasing the TiO_2 to the slurry. The confidence levels were set as a P-value of 0.01. There was no significant difference between the 0.5% and 1% TiO_2 addition, which was expected. However, when increasing the content further, comparing the 1% to the 5%, there is a significant difference in the resistance. There is an increase in the current which means the resistance of the coating has depreciated. There is no significant difference between the 5% and 10%. However, there is a significant difference when comparing the 25% to the 15%. This means that a reduction in current was detected and, therefore, an improvement in the resistance of the coating.

Table 21. The results of the F-test and t-test on the current detected when franklin testing is conducted.

P = 0.05	Comparing 1% to 0.5% TiO$_2$		Comparing 1% to 5% TiO$_2$		Comparing 5% to 10% TiO$_2$		Comparing 10% to 15% TiO$_2$		Comparing 15% to 25% TiO$_2$	
	0.5% TiO$_2$	1% TiO$_2$	1% TiO$_2$	5% TiO$_2$	5% TiO$_2$	10% TiO$_2$	10% TiO$_2$	15% TiO$_2$	15% TiO$_2$	25% TiO$_2$
Mean	0.3963	0.3854	0.3854	0.5363	0.5363	0.4517	0.4517	0.4163	0.4163	0.3371
Variance	0.0213	0.0215	0.0215	0.0384	0.0384	0.0178	0.0178	0.0200	0.0200	0.0146
Observations	24	24	24	24	24	24	24	24	24	24
P(T<=t) two-tail	0.7987		0.0042		0.0873		0.3771		0.0429	
F-Test	Un-equal Variance		Equal variance		Un-equal Variance		Un-equal Variance		Equal variance	

5.3.8   Bulk Analysis of Carbon, Oxygen, Nitrogen and Sulfur

Figure 208 displays the concentration of oxygen detected in the bulk of material using a LECO TN400. The results show that initial additions between 0.5% to 5% of titanium have lower oxygen content than the magnesium only coated sample. However, at 10% addition, there is a significant increase in oxygen levels detected in the substrate, and when comparing these results with the coating thickness results discussed previously and with the results from SEM images, this can be attributed to an increase in surface oxide. Thus, the oxygen content detected by the LECO TN400 confirms that oxygen is present, and due to the limitation of detection of GDOES, oxygen is not detected.
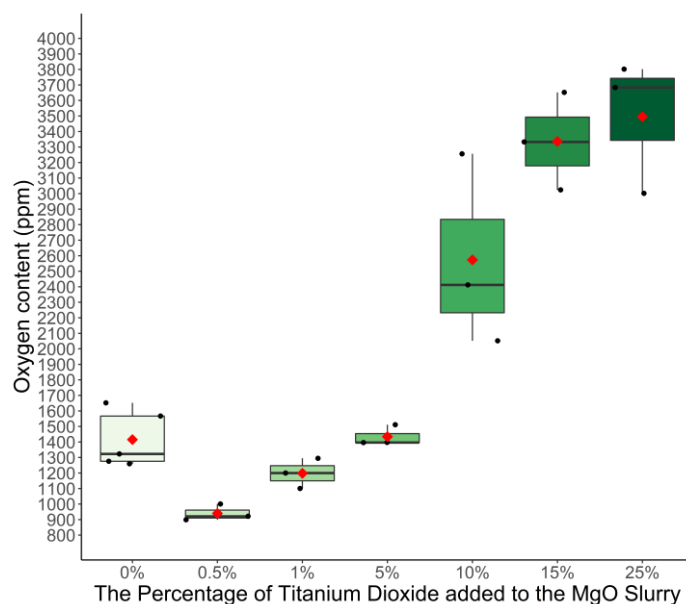
Figure 208. The oxygen content of the total substrate of the various amounts of TiO$_2$ addition to the magnesium slurry using the Leco TN400 nitrogen.

One of the roles of high-temperature annealing is to purify the substrates from impurities to ensure magnetic properties reach maximum potential. The bulk chemical analysis on key elements of carbon, sulfur and nitrogen provides information on the success of the purification of the substrate. To ensure that the addition of TiO$_2$ has not influenced the purification, Leco analysis was conducted on the substrate. The manganese sulfides and retaining them in the substrate as these levels are typically seen in production material. Similarly, the nitrogen content is similar to typical levels observed in standard material.

5.3.9   General Observations

A change in the excess coating was observed when a concentration of TiO$_2$ was added to the MgO slurry; therefore, it was decided to create pellets. This involved mixing the MgO and TiO$_2$ powders to concentrations of 0.5%, 1%, 5% ,10%, 15% and 25%. The powder was mixed for 12 hours on a tube roller. After mixing, 2 grams of the powder was pressed in a 2cm diameter XRD press at 1 tonne of pressure. The pellets created were then placed in the laboratory furnace and heat-treated following annealing cycle A with a 10-hour soak. This test aimed to establish whether this was due to the increase in TiO$_2$ or some unknown variable. Concentrations of 1%, 10% and 25% TiO$_2$ by weight percentage were mix with MgO. Once samples were mixed and pellets pressed as demonstrated in Figure 209a), they were placed on top of a steel sample and annealed in the Laboratory Carbolite furnace, where the temperature was set to 1190ºC and soaked for 15 hours.

The appearance of the pellets entering the furnace is shown in Figure 209. The addition of TiO$_2$ resulted in a change in colour after heat treatment. Further increase (10%) of concentration results in a darker appearance, and a concentration of 25%, TiO$_2$ results in a black appearance. This is significant because is due to 99% of the quality of the glass film is a visual appearance by production line

178

operators, and the introduction of TiO2 produced a "darker" shade of grey after completing the HTA. This "darker" shade of grey was presumed/perceived to be an improved "glass film," i.e., thicker oxide layer and signs of a lighter shade of grey were presumed poor "glass film". As highlighted in this research, the introduction of TiO_2 results in the presence of Ti in the surface oxide. The Ti compound has not been identified, and further work is required. The benefits of TiO_2 additions to the slurry appears to have a point of diminishing returns at around 5%, which Orb Steelworks operate at these concentrations. The change in the colour of TiO_2 indicates that a reaction is occurring, and literature has suggested the cause of this colour change is a result of the formation of H_2O by the following reaction.

$$4H + TiO_2 + 2H_2O_{(g)} + Ti \qquad \Delta G_f^o = -348kJ$$
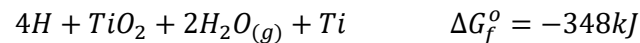
Equation 12 The Gibb Free energy for TiO_2 in hydrogen at 300ºC [108]

This colour change was seen in the excess coating off the substrate. The production of H_2O between laps will result in a change in the dew point. This change in environment can promote the formation of additional Fayalite during the heating phase, which then could transform into Forsterite, as explained in section 1.9. However, it must be noted that the laboratory furnace's operation has significantly less material placed in the furnace during the heat treatment, and a "relatively" uniform heating is occurring within the furnace. The control of the production furnaces is limited, and large thermal gradients are created within laps in a coil. If the introduction of water does occur through the reaction, as Equation 12 states, this may alter the dew point of the furnace during the formation of Forsterite and may cause an adverse effect on Forsterite formation.

a)   b)
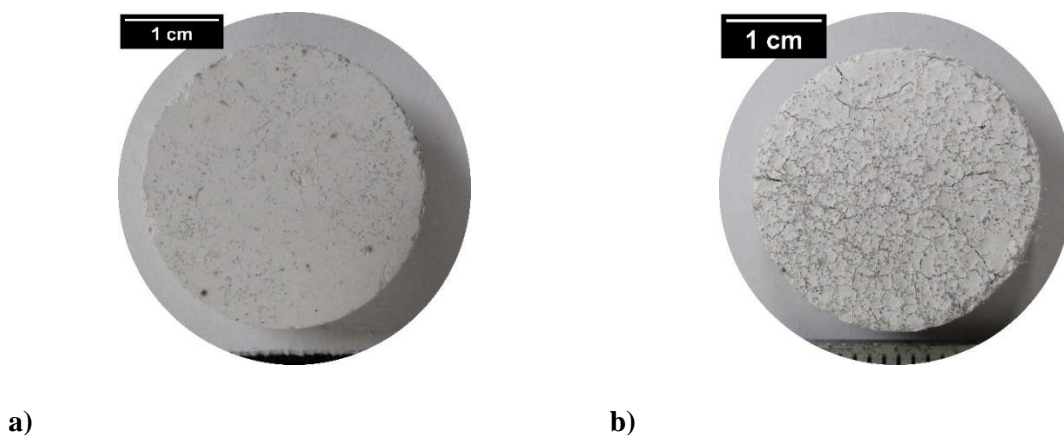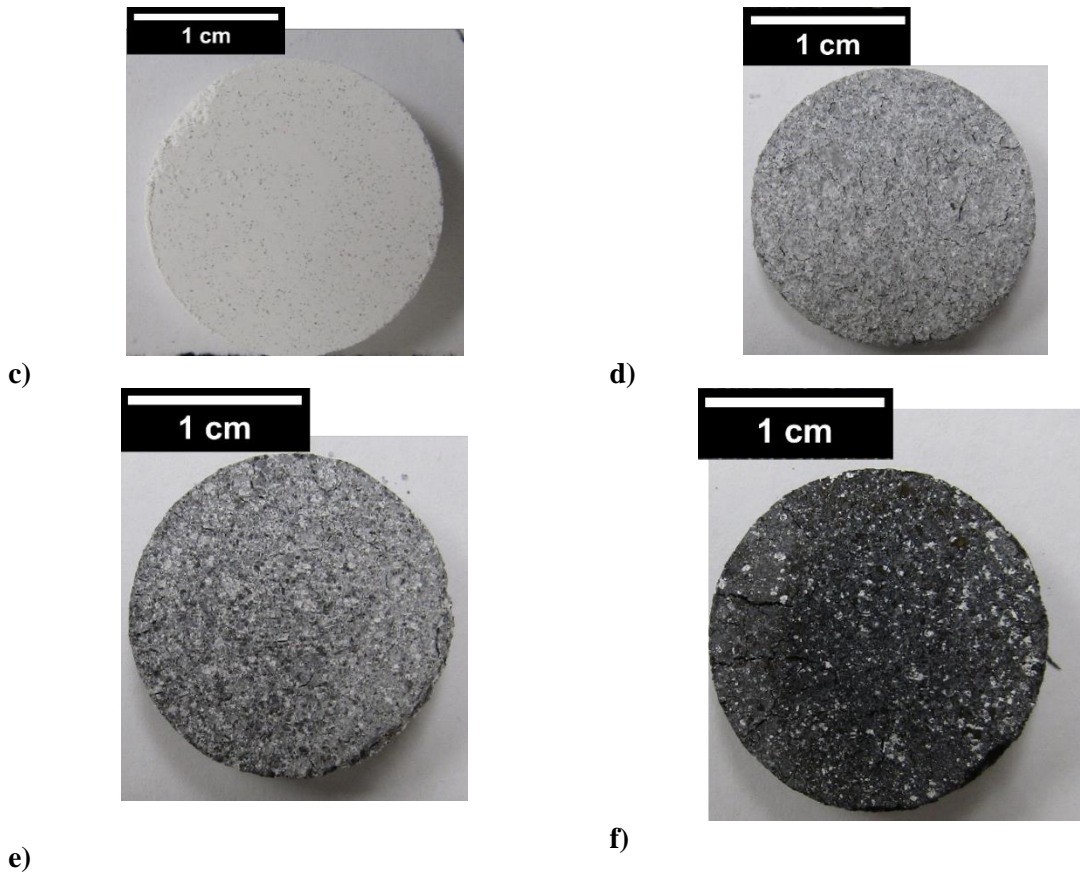
Figure 209. a) MgO only pellet before heat treatment **b)** MgO only pellet after heat treatment **c)** A MgO-10% TiO$_2$ mixture that has been pressed into a pellet before heat treatment, **s)** A heat-treated MgO- 1% TiO$_2$ mixture pressed into a pellet, **e)** A heat-treated MgO- 10% TiO$_2$ mixture pressed into a pellet, **f)** A heat-treated MgO- 25% TiO$_2$ mixture pressed into a pellet

5.3.10 Discussion

The purpose of this research was to determine the influences TiO$_2$ has on the thickness of the developed coating and what influences this, as well as any changes in magnetic and other properties as described. While it was not the aim of this research to determine the mechanism in which TiO$_2$ acts during the development of Forsterite, it will be discussed and speculate the findings of this study and the possible mechanisms that may be occurring during this process.

Adding TiO$_2$ to the magnesium slurry has had a significant effect on the development of the oxide layer, resulting in a thicker oxide layer at the surface of the steel. The measurement of the oxide layer from SEM cross-sections clearly illustrates an increase in the oxide thickness, as shown in Figure 187. The addition of a small (0.5%) quantity of TiO$_2$ has an increase in coating thickness compared to the MgO substrate. The further increase of TiO$_2$ to the slurry continues the trend of increasing the coating thickness.

The oxide layer thickness not only consists of Forsterite as literature claims [91] but also a mix of several oxides with Mg dominating the surface oxide. The EDS and GDOES analysis has demonstrated the multiple numbers of elements present that form as part of the oxide layer. The

various elements that have been detected in the surface and subsurface oxide in this study are Mg, O, Si, Al, Fe, Ca, S and Ti.

The 0.5%-25% additions of TiO$_2$ results from EDS and GDOES display signs of detection of titanium present in the surface oxide whereby enriched regions have been detected in the SEM cross section. The composition of these Ti enriched areas is not fully understood, and further investigation is required. However, upon further reading after discovering the Ti in the surface oxide and highlighted, magnesium dititanate could be developing[127]. Again, however, further investigation is needed to identify the Ti compound present in the surface oxide.

$$MgO + 2TiO_2 \rightarrow MgTi_2O_5$$
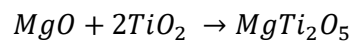
Equation 13. Is the empirical formula of magnesium dititanate at 500°C[127]

Another mechanism that could be playing a part in developing a thicker oxide could be due to the development of H$_2$O during the HTA with a hydrogen atmosphere. It is possible that water development occurs due to the reduction of TiO$_2$ when exposed to elevated temperature in a hydrogen atmosphere, as the reaction below demonstrates.

$$4H + TiO_2 \rightarrow 2H_2O_{(g)} + Ti \qquad \Delta G_f^o = -348kJ$$
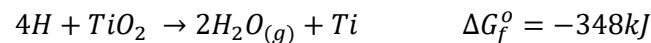
This reaction has been identified in different fields of research, such as battery and photovoltaic performance, as discussed in section 1.13.5. In addition, the introduction of water will alter the dew point between laps during the HTA, creating the possibility of a favorable environment for additional Fayalite or adverse effect on the development of the "Forsterite" oxide. The balance of dewpoint and the development of Fayalite has been modelled as Figure 210[73].
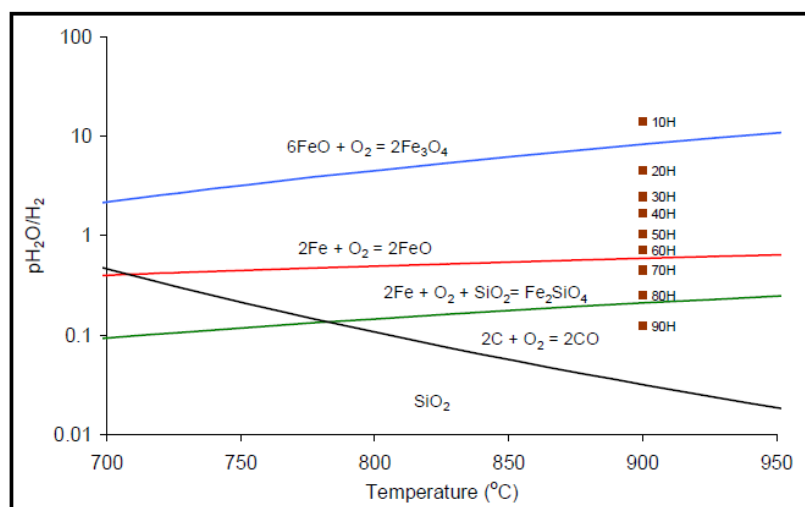
Figure 210: The equilibrium predictions of oxides developed under pH2O/H2 at various temperatures[73]**.**

This evolution of additional Fayalite (Fe_2SiO_4) will allow for substitution reactions to form Forsterite (Mg_2SiO_4).

$$Fe_2SiO_4 + MgO \rightarrow Mg_2SiO_4 + 2FeO$$
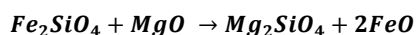
Equation 14. The chemical reaction of development from Fayalite to **Forsterite** [33]

The reduction of TiO_2 by a hydrogen atmosphere is indicated by the change in colour of the TiO_2 that was seen firstly on samples coated with different TiO_2 additions to the slurry with a change in colour from a light grey to a darker grey to a black with increasing levels of TiO_2 as discussed in 5.3.9. Unfortunately, images were not captured of the substrate. However, pellets were made with different concentrations of TiO_2 additions to the pellets and underwent significant colour changes, as seen in Figure 209. The change in the TiO_2 appearance has been seen in a study on battery and photovoltaics where hydrogen evolution is present. Conducting X-Ray Diffraction would be able to identify any shift in peaks and/or change in peaks. Unfortunately, this was out of this project's scope and due to time constraints, this was not possible to conduct at this time.

The magnetic losses between $0.5 - 5\%$ are improved or equal to that of Magnesium only slurry. These improvements in the 5% addition of TiO_2 has been seen in previous confidential documents from competitors [118]. One of the undesirable's effects of addition increasing the content to 0.5-5% of TiO_2 is an increase in current detected (Figure 207). At 5% TiO_2 to the magnesium slurry sees a significant upsurge in current detected by the Franklin test.

At 10% addition of TiO_2, there is a significant increase in titanium detected in the surface oxide in the GDOES depth analysis. This indicates a second possible mechanism that involves the development of titanium oxide in the surface oxide. The development of titanium in the surface oxide results in a thicker oxide. However, determining the chemical composition and the chemical state cannot be determined from this research, and a more focused study to identify the composition would be beneficial.

The other formation of titanium seen in the 10% addition of TiO_2 oxide layer has resulted in a thicker oxide with the presence of titanium in the surface oxide and therefore has seen less current detected through the oxide layer compared to the 5%. The trend of reducing current detected through the oxide layer is seen in the 15% and 25% TiO_2. The additional thickness of oxide developed in the 10-25% additions of TiO_2 has impacted the steel's magnetic properties, resulting in a significant detrimental effect on the magnetic losses. The decrease in magnetic losses could be caused in numerous ways. Further investigation is required, but to speculate on the possible mechanism that could take place are:-

- The development of titanium in the surface oxide may reduce the tension effect of the Forsterite developed at the surface. This results in a reduction in surface domains being refined to thin domains and has thick domains requiring additional energy to rotate.

- The opposite to the previous mechanism could be happening where tension created in the oxide layer results in domain pinning. The rotation of these domains requires significant energy to rotate.

The literature from section 1.13.4 demonstrated improvements in forsterite with the addition of TiO_2. However, limited details have been given on the type of analysis conducted on samples and as demonstrated in this body of work the addition of TiO_2 forms alternative phase than the desired Forsterite. Therefore, cross sectional measurements alone will not identify these alternative phase present.

5.3.11 Conclusion

The TiO_2 addition has had a significant influence on the oxide layer developed and the magnetic / resistance properties of the electrical steel. There is an increase in oxide thickness measured at the surface of the substrate when the TiO_2 content is increased in the magnesium oxide slurry. There is a significant improvement in the magnetic losses seen at 0.5% and 1% TiO_2. At 5% addition, the magnetic losses are equal to no addition of TiO_2. Further increase of $TiO_2 > 5\%$ sees a net detrimental effect on the magnetic properties. Between 0.5% - 5%, there are no signs of titanium detected in the oxide layer. At 10% addition, titanium is detected and appears to form unidentified titanium oxide. The current detected in the surface oxide in all additions of TiO_2 to the magnesium slurry has increased, with 5% having the highest current detected. Some recovery in reducing the current detected in the oxide layer is seen with the thicker oxide developed in the >10%. This is likely due to a combination of thicker oxide and titanium in the surface oxide. However, not to the levels seen in the MgO slurry coating.

5.3.12 Further Work

- Further investigation should be conducted on TiO_2 under high temperature and hydrogen atmosphere to understand the reaction occurring to transform the TiO_2 from a white powder to a dark black colour. This could be conducted using several methods such as TGA (Thermogravimetric Analysis), DSC (Differential Scanning Calorimetry), or simply build on taking the approach this study has used and placing TiO_2 powder in a furnace and XRD the powders before and after.
- Further investigation into the phase that Ti has in the oxide layer which possibly identified by X-Ray Photoelectron Spectroscopy (XPS).

5.4 The Impact of Vanadium (III) Oxide (V_2O_3) Addition on the Formation of Oxide Layer

5.4.1 Experimental

The substrate used to coat the various V_2O_3 was J19071, where the composition is displayed in Section 2.1. The samples were coated with MgO with V_2O_3 additions to the slurry at the concentrations displayed in Table 22.

Table 22. Displays the quantity of Vanadium (III) Oxide V_2O_3 is added to the slurry to achieve the range of additions between 0.5% to 25%

Wt% of additive (V_2O_3)	MgO	The amount of V_2O_3 addition	Distilled water (ml)
0.5%	112g	0.56g	800
1%	112g	1.12g	800
5%	112g	5.6g	800
10%	112g	11.2g	800
15%	112g	16.8g	800
25%	112g	28g	800

Further details of the coating and drying method of the magnesium slurry that was applied to the sample are discussed in section 2.3. Samples were secured between two metal plates and held in place with metal banding—further details as discussed in section 2.6.2.

Samples were placed on top of the edge of the bottom coil in the production furnace. The heat treatment conducted was Annealing cycle c) as detailed in 2.6.2.3. Annealing cycle c) involves samples being placed in the production furnace and then exposed to the production annealing cycle. Excess MgO/V_2O_3 powder was removed using a cloth and distilled water and then immediately dried.

The following analyses were conducted on the substrates:

- Thickness
- SEM cross-sectional thickness analysis
- EDS
- GDOES depth profiling surface oxide
- LECO bulk analysis of elements (C, O, N and S)
- Soken testing magnetic performance.
- Franklin testing resistance of oxide layer

The adhesion test results were all grade 1, and no variance was seen throughout all the samples.

5.4.2 Morphology and Coating Thickness of Surface Oxide Developed with V_2O_3 Addition to the Slurry.

Figure 211 shows the SEM cross-section of a standard sample that has been coated with magnesium oxide only and has been heat-treated in production furnaces, and the resulting oxide layer developed SEM image through a cross-section of the top and bottom surface is displayed below. The oxide layer

developed is a thin uniform layer in both the top surface and bottom surface. Figure 211 displays keying areas developing into the iron matrix.
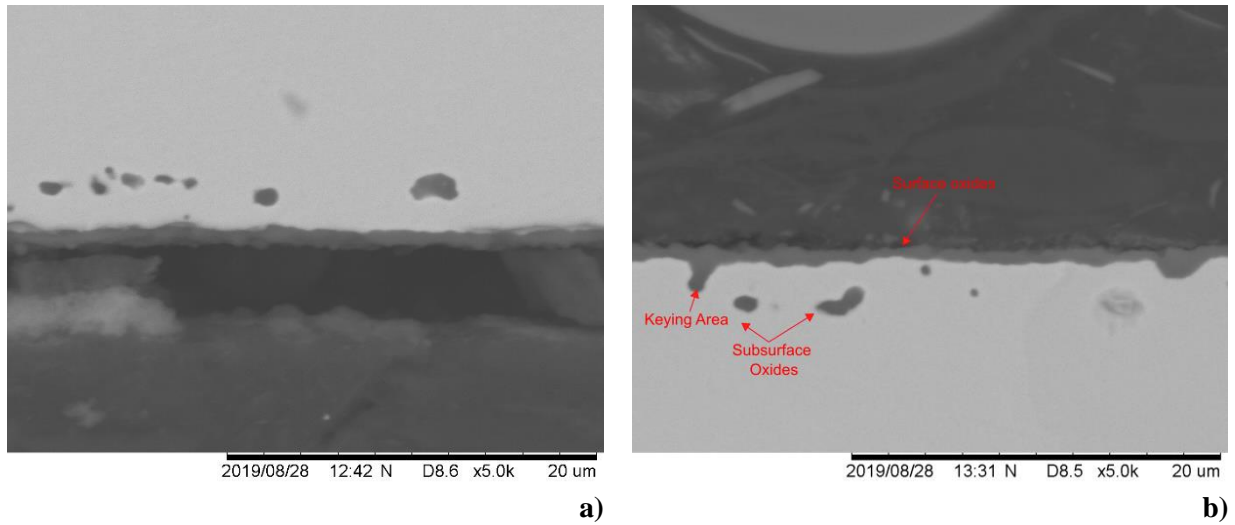
Figure 211. a) SEM cross-section of the top surface of a heat-treated sample that has been coated in magnesium only slurry, **b)** show SEM image of the bottom surface

Figure 212 demonstrates the surface oxide layer developed when introducing 1% addition of V_2O_3 is made to the magnesium slurry of the top and bottom surface of the substrate. Both top and bottom surfaces display keying areas into the substrate. The coating thickness appears to be thicker throughout the image, with only a few areas of thin oxide developed across the surface of the oxide. There are numerous subsurface oxides present below the surface oxide. The composition of these subsurface oxides is unknown and will be investigated in section 5.2.3.

a)

b)
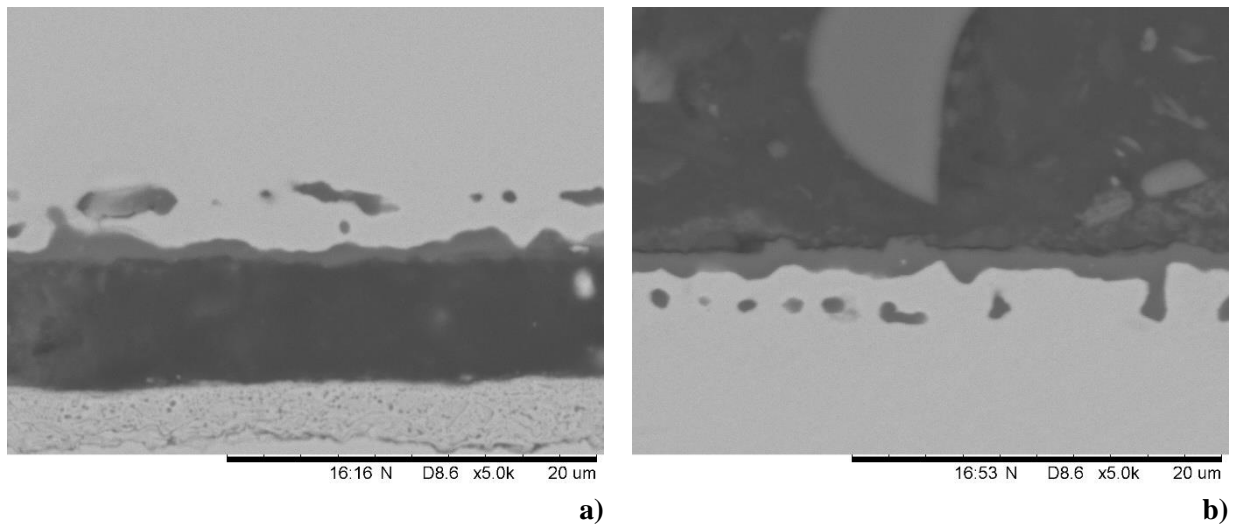
Figure 212. a) SEM cross-section of the top surface of a heat-treated sample that has been coated in magnesium slurry with 1% of Vanadium (III) Oxide, **b)** shows SEM image of the bottom surface

Figure 213 shows the resulting surface oxide with a further increase of V_2O_3 to 10% to the magnesium slurry of the substrate's top and bottom surface. The coating thickness is irregular with regions of thin oxide development and regions of thick coating. Figure 213b.) the surface oxide layer

185

appears to be more consistent and thicker than that seen in Figure 213a). Also, the surface oxide appears to have a significant keying point into the substrate.
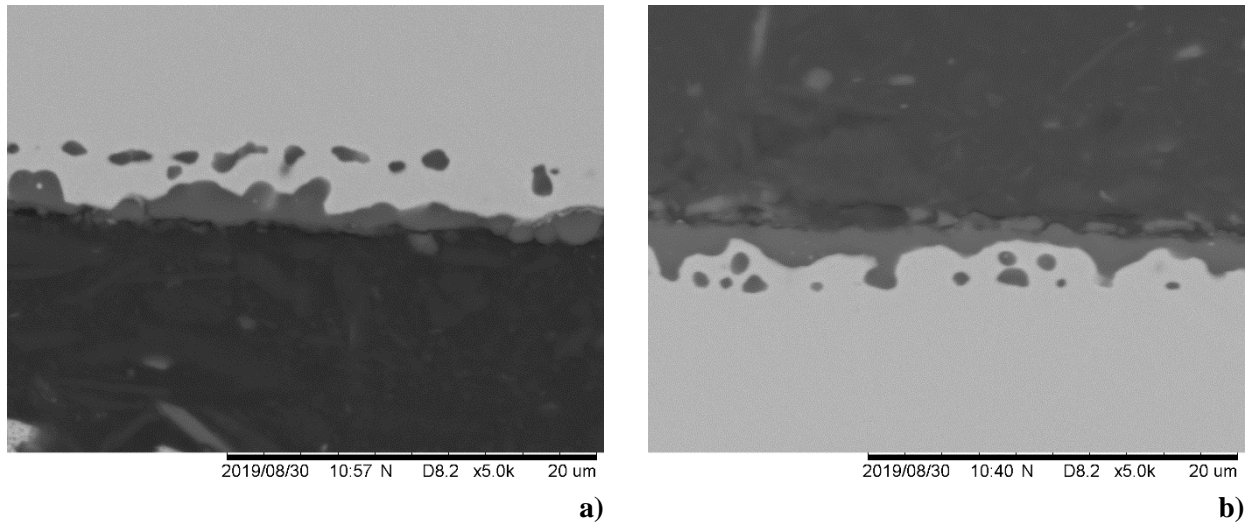
Figure 213. a) SEM cross-section of the top surface of a heat-treated sample that has been coated in magnesium slurry with 10% of Vanadium (III) oxide added to the slurry, **b)** show SEM image of the bottom surface

Figure 214 displays the resulting oxide layer developed when 25% vanadium is added to the magnesium oxide slurry. The frequency of keying points has increased in both examples displayed in Figure 214. The coatings still have regions of thin oxide development.

a)
b)
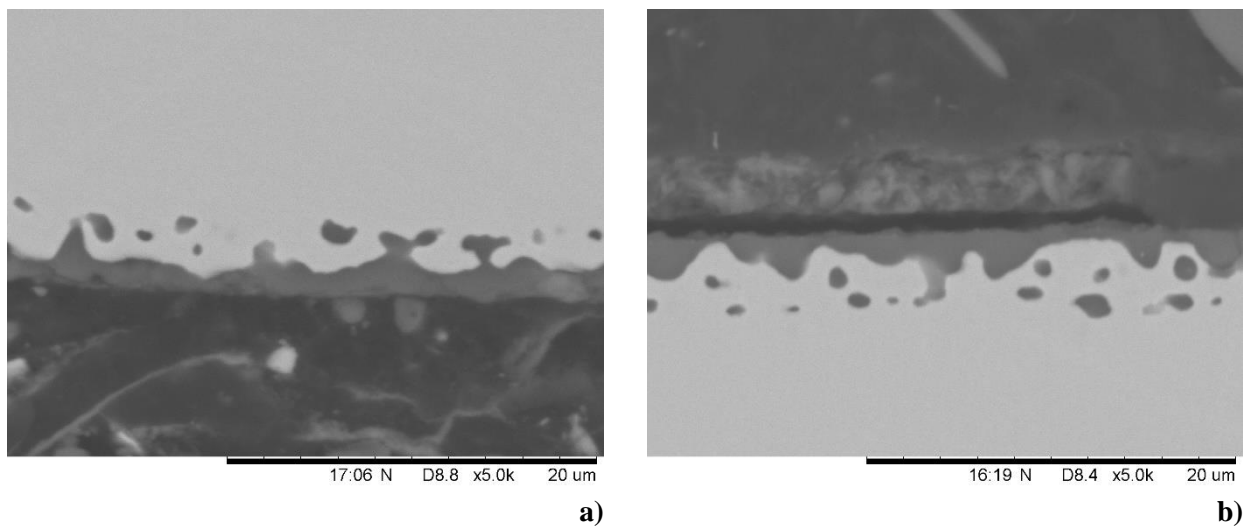
Figure 214. a) SEM image of a cross-section of the top surface of a heat-treated sample that has been coated with MgO slurry with a 25% Vanadium (III) oxide addition

The result of increasing Vanadium (III) oxide to the magnesium slurry coated onto a substrate and then heat-treated in the production furnace is displayed in Figure 215.
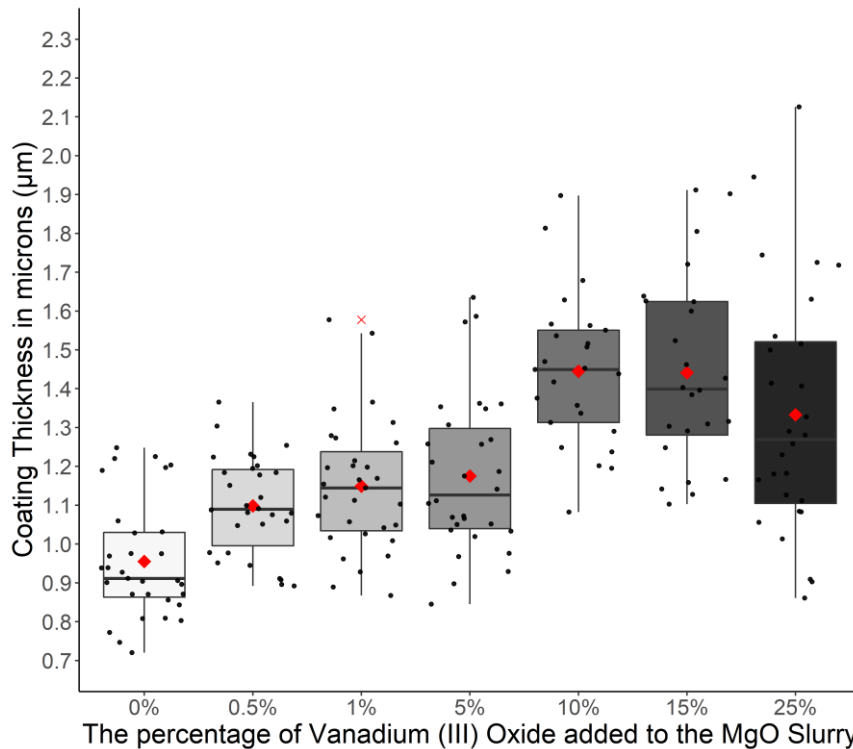
Figure 215. The resulting oxide thickness when introducing Vanadium (III) oxide to the MgO slurry and been applied and heat-treated the substrate. The mean is represented by a red square at 45°and outliers are represented by the red cross.

An F-test and T-test were conducted to establish that each condition has a statistical difference between results. The level of confidence for the T-test was set at p=0.01, and the null hypothesis was that an increase of vanadium (III) oxide does not affect the thickness of the oxide layer developed after heat treatment.

Table 23. The results of the T-test and F-test to establish the variance are comparable and whether there is a significant difference.

P = 0.01	Comparing 0% vs 0.5% V_2O_3		Comparing 0.5% to 1% V_2O_3		Comparing 1% to 5% V_2O_3		Comparing 5% to 10% V_2O_3		Comparing 10% to 15% V_2O_3		Comparing 25% to 15% V_2O_3	
	0% V_2O_3	0.5% V_2O_3	0.5% V_2O_3	1% V_2O_3	1% V_2O_3	5% V_2O_3	5% V_2O_3	10% V_2O_3	10% V_2O_3	15% V_2O_3	15% V_2O_3	25% V_2O_3
Mean	0.9599	1.0982	1.0982	1.1492	1.1492	1.1750	1.1750	1.4449	1.4449	1.4411	1.4411	1.3328
Variance	0.0236	0.0162	0.0162	0.0288	0.0288	0.0406	0.0406	0.0370	0.0370	0.0591	0.0591	0.1020
Observations	29	30	30	31	31	30	30	25	25	24	24	28
P(T<=t) two-tail	0.0004		0.1882		0.5910		5.3904E-06		0.9517		0.1722	
F-Test	Un-equal Variance		Un-equal Variance		Un-equal Variance		Un-equal Variance		Un-equal Variance		Un-equal Variance	

Table 23 displays the results were comparing conditions to establish whether the addition of vanadium (III) oxide influences oxide thickness developed during heat treatment. A small increase of 0.5% of V_2O_3 to the slurry has improved the oxide thickness developed during heat treatment. Between the ranges, 0.5%-5% shows no significant improvement with the additional V_2O_3 to the slurry. A step change is seen when increasing the V_2O_3 content to 10%, which has resulted in a thicker

oxide layer developed. With the further increase,>10%, no improvements are seen, and a small decrease in thickness is displayed in the 25% but not significant.

In summary, from Figure 215 and Table 23, there are two-step changes in improving the thickness of the surface oxide layer developed. The first significant step-change is seen between the standard slurry (MgO only) and the small addition of 0.5% V_2O_3. Between 0.5-5% addition of V_2O_3, there is an overlap of the oxide layer thickness developed at the surface resulting in no significant difference between all three samples. The second step change is seen when V_2O_3 concentration increases to 10% V2O3, with additional improvements seen in the thickness of the surface oxide, developed compared with 5%. Further increase of V_2O_3 (>10%) appears to have no improvement in surface oxide layer thickness.

5.4.3 EDS Analysis

Figure 216 shows a cross-section of a top surface of a sample that has been coated with magnesium oxide slurry with 1% addition of V_2O_3 and heat-treated in the production line HTCA furnaces. A thick oxide layer has developed at the surface of the substrate that is predominantly magnesium present at surface. The subsurface oxide varies in composition depending on the availability of elements either diffused from the matrix or the surface to form oxides.
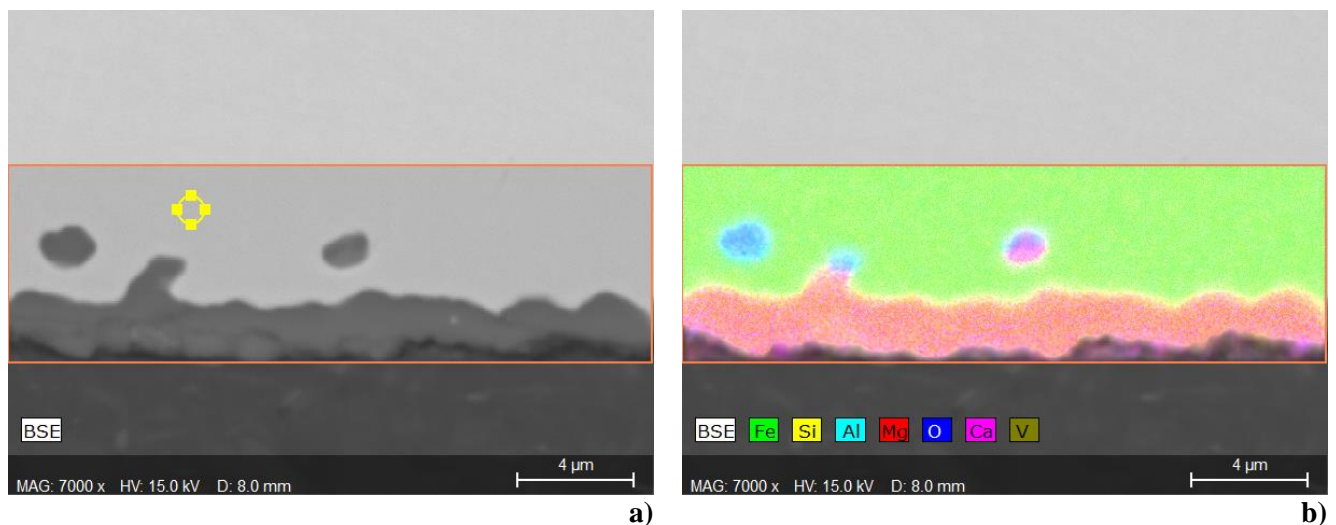
Figure 216. a) SEM cross-section of an oxide layer that has been coated in a magnesium oxide with 1% Vanadium (III) oxide and heat-treated in production furnace. **b)** is the EDS mapping of elements detected

The results of the point scan display in Figure 217 are displayed in the bar graphs in Figure 218. The surface oxide point scans (1-5) mainly consist of oxygen, magnesium, and silicon. The content of oxygen is in the range between 36-40.8% wt%. The magnesium content ranges between 29-33% wt%. The silicon content ranges 17.6%- 20% wt%. The content of the elements in the surface of the oxide layer suggests that the oxide developed is Forsterite that has been found in previous literature [102]. The content of iron detected in the oxide layer is low, ranging between 7.4-11.2% wt%. The iron

content in the surface oxide is essential because the presence of iron in the surface oxide will reduce the resistance properties of the Forsterite oxide provides.
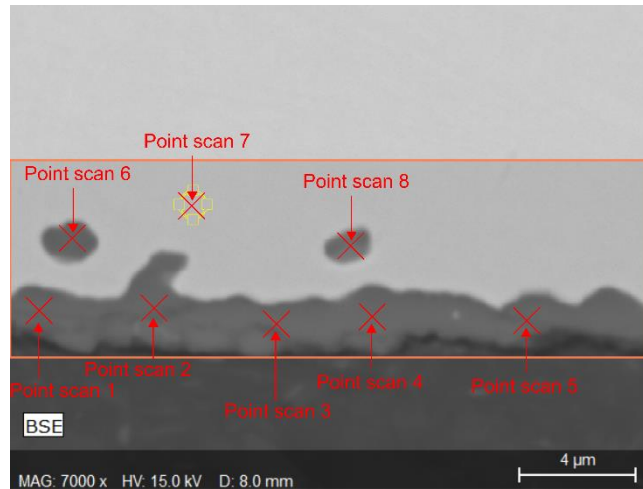
Figure 217. Displays the locations of point scans conducted on the oxide layer of a sample with 1% addition of Vanadium (III) oxide to magnesium oxide slurry.

The subsurface oxide display in Figure 217 in point scans 6 and 8. The subsurface oxides is a combination of multiple oxides. Point scan six mainly consists of iron, but substantial oxygen, aluminium, and magnesium are present. Previous research has identified these oxides as spinels $(MgAl_2O_4)$[90]. The aluminium has migrated from the substrate to the surface during the heat treatment, while the magnesium has diffused from the surface of the substrate to the subsurface oxide. The subsurface oxide that has developed at point 8 consists of several oxides. With sulphur, oxygen, calcium, and aluminium being around ~10% wt%. The origin of sulphur and aluminium can be accounted for as these are used as precipitates in preventing secondary recrystallization [21]. Once these precipitates are broken down, they diffuse out of the iron matrix to the surface of the substrate forming as a part of the subsurface or surface oxide. The origin of calcium is unaccounted for, and the exact composition is also unknown. However, it is possible that calcium inosilicate $(CaSiO_3)$ could develop [135]. The substrate (point 7) is a typical composition of the seen in electrical steel with mainly iron composition with ~3% wt% Silicon present. Although 1% vanadium (III) oxide has been added to the magnesium slurry, there is no detection of vanadium present in the surface or subsurface oxide.

189
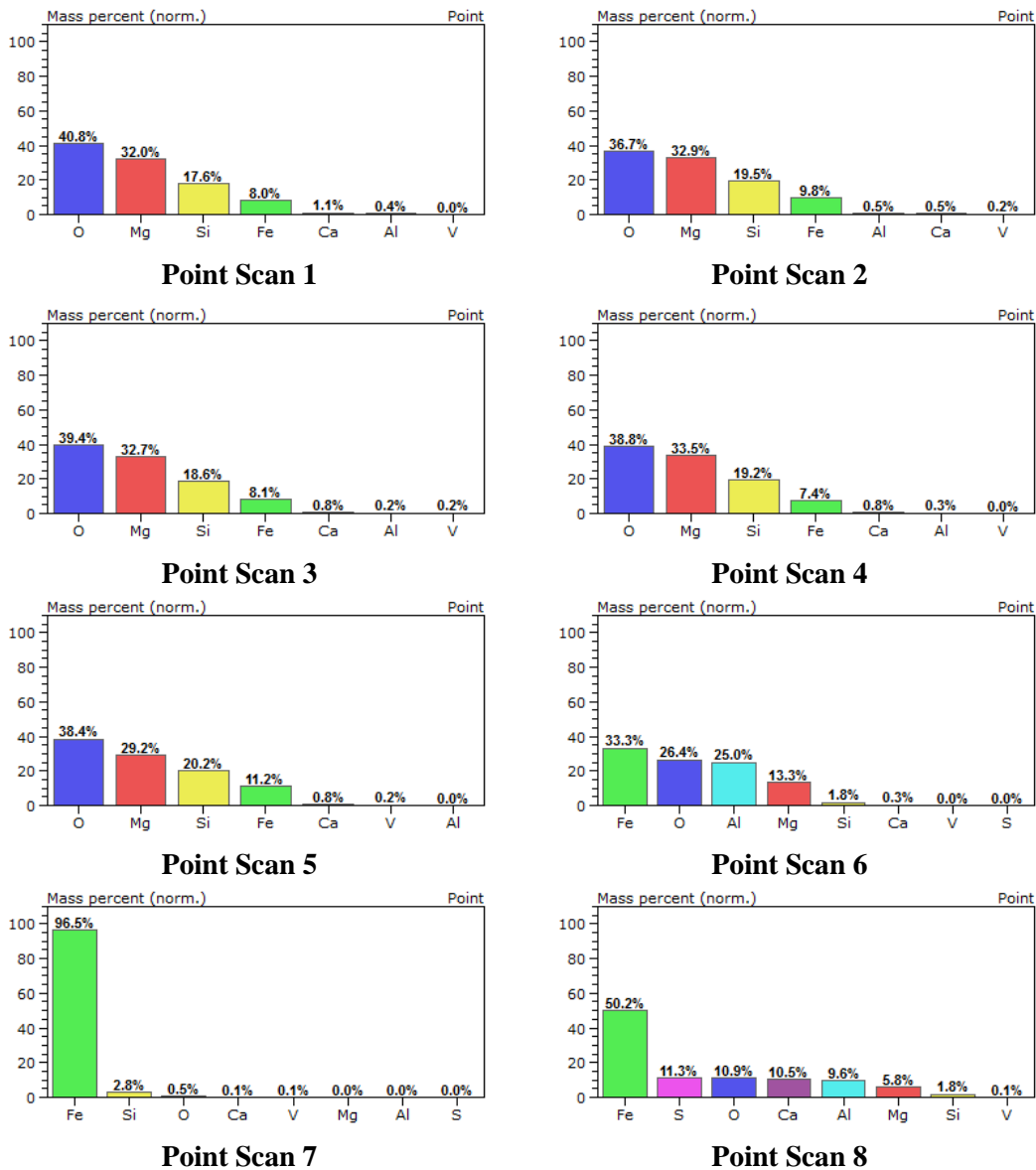
Figure 218. Displays the result of the surface oxide point scans (1-8) using EDS on the surface on a heat-treated sample with 10% V_2O_3 addition to the magnesium slurry.

Figure 219 shows an SEM/EDS cross-section of a sample that has been coated with magnesium slurry with a 10% addition to the slurry of vanadium (III) oxide and then heat-treated at Orb Steelworks HTCA furnace. The surface oxide primarily consists of magnesium oxide and the dominant surface oxide species with subsurface oxides present.
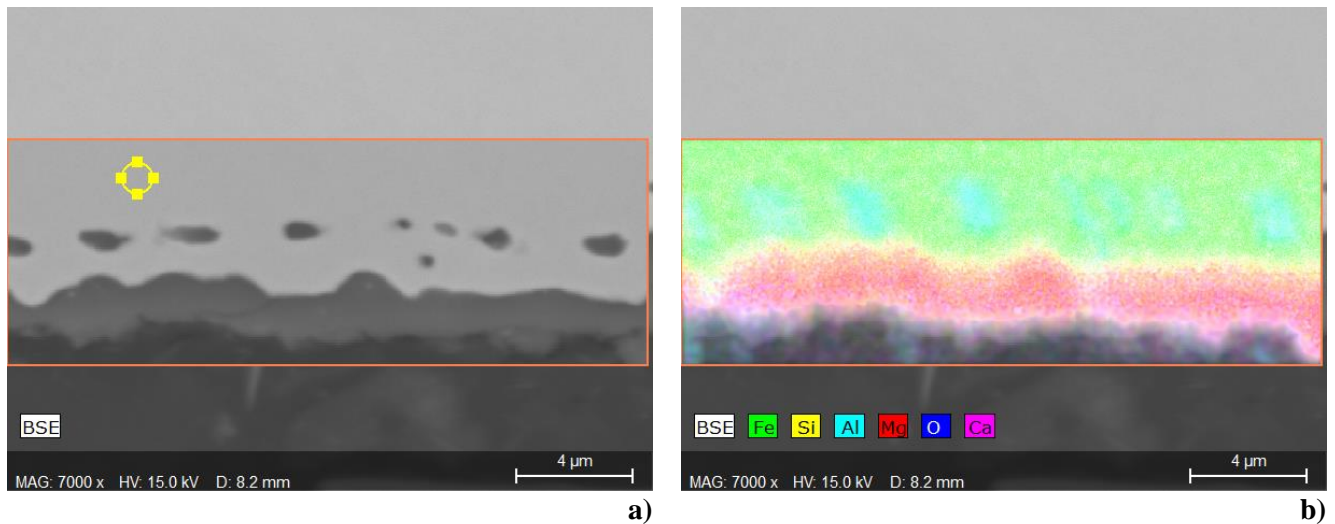
Figure 219. a) SEM cross-section of an oxide layer that has been coated in a magnesium oxide with 10% Vanadium (III) oxide and heat-treated in production furnace. **b)** is the EDS mapping of elements detected.
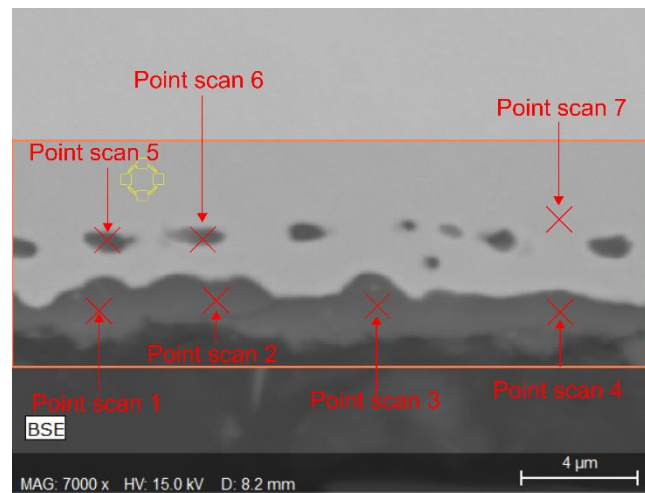
Figure 220. Illustrates the location of the point conducted on the surface and subsurface oxide**.**

The results of the point EDS scan from Figure 220 is displayed in Figure 221. The element composition of the surface oxide is displayed in areas 1 to 4. There was no vanadium detected in the surface oxide throughout all point 4 scans. This indicates that vanadium does not form as part of the oxide layer. The content of iron ranges from 19.8-44.2%, and oxygen ranges between 32%-36%. Because of a high iron concentration, magnesium detection has reduced, ranging between 13-26%. The silicon concentration ranges between 7.8% to 17%. The reduction of magnesium and silicon indicates a reduction of Forsterite development in the surface oxide layer and iron oxide.

The subsurface oxide composition displayed in areas 5 and 6 is predominantly iron, ranging from 63-71.5%. Forsterite is likely to be present with magnesium detected in the ranges between 9.2 – 14.6% and oxygen content range between 12.5 – 9.9%, and silicon content between 5.7-7.6%. A small content of aluminium is detected as well in the subsurface oxide. No vanadium was detected in the subsurface oxide.

Point Scan 1

Point Scan 2

Point Scan 3

Point Scan 4

Point Scan 5

Point Scan 6
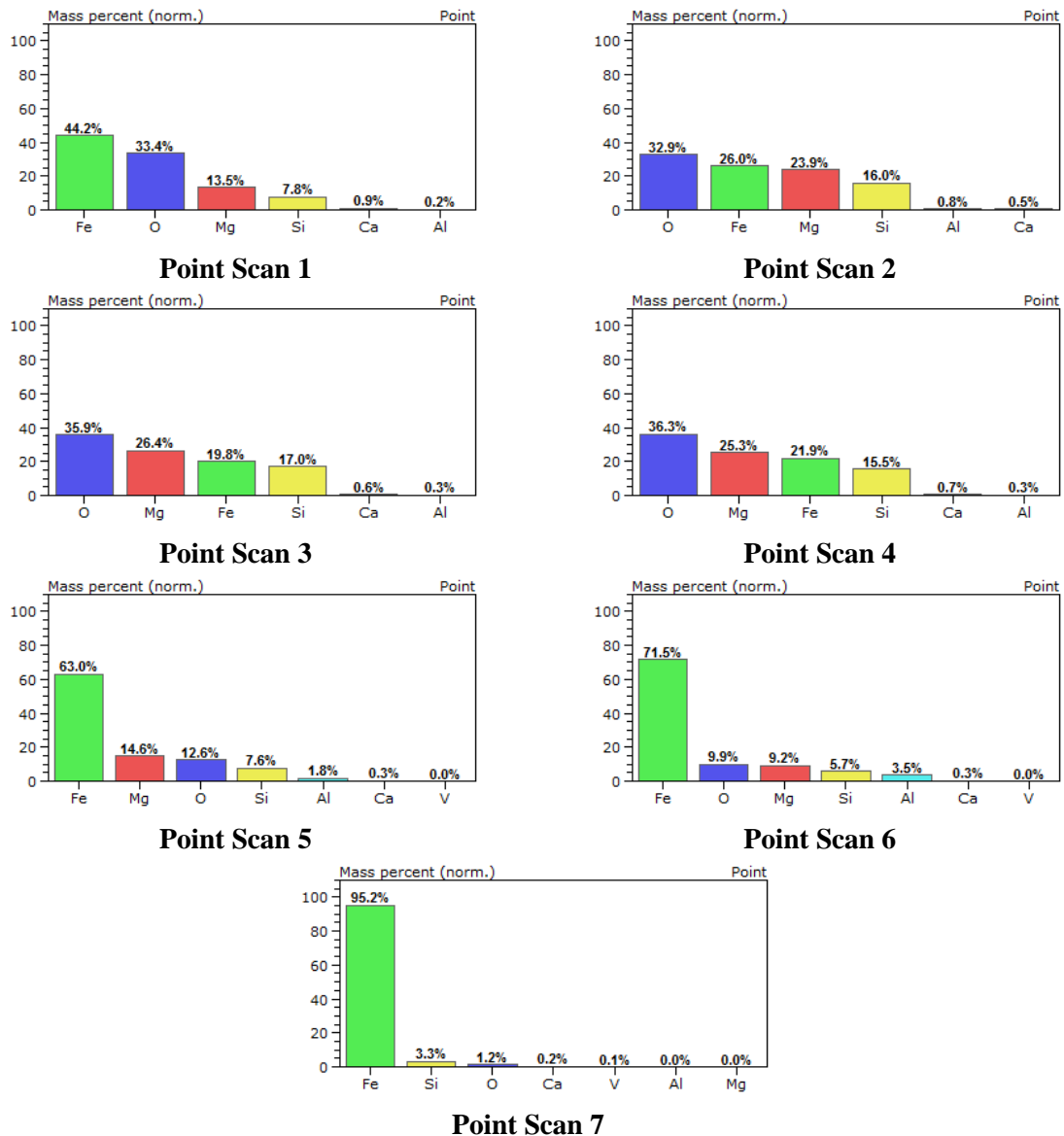
Point Scan 7

Figure 221. Displays the result of the sub-surface oxide point scans (1-7) using EDS on the surface of the heat-treated sample with 10% V_2O_3 addition to the magnesium slurry.

Figure 222 demonstrates a cross-section of a bottom surface of a 25% addition of vanadium to the magnesium slurry that has then been heated coated onto a substrate and heat-treated in the production HTCA furnaces at Orb Steelworks, as previously explained in section 2.6.2.3. The EDS image is displayed in Figure 222b.) shows a magnesium-enriched layer at the surface of the substrate with an iron matrix.
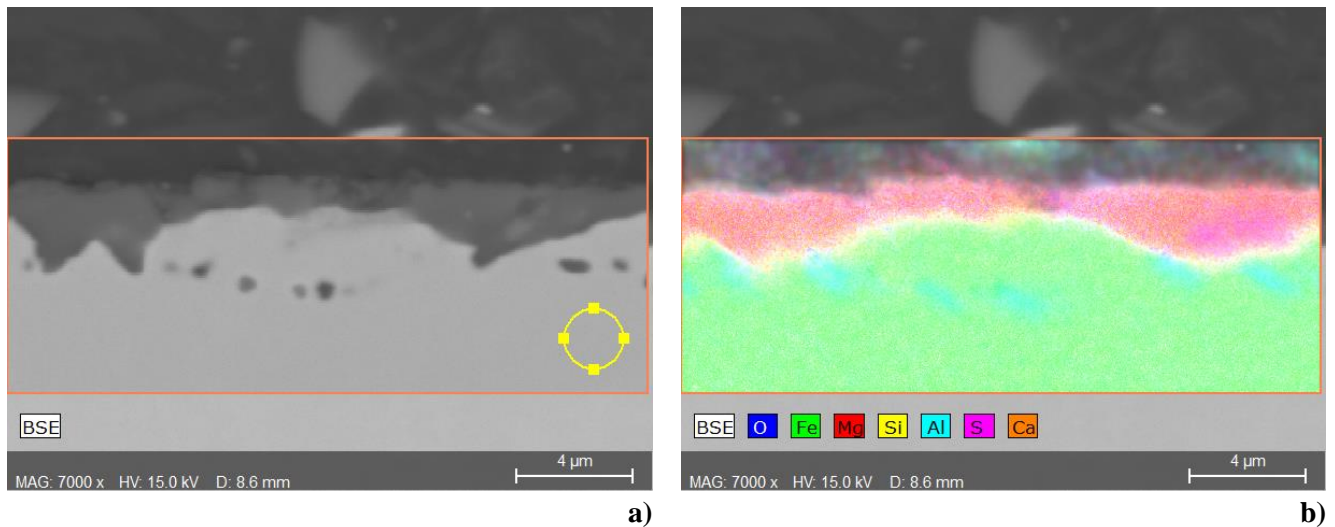
Figure 222. SEM cross-section of an oxide layer that has been coated in a magnesium oxide with 25% Vanadium (III) oxide and heat-treated in production furnace. **b)** is the EDS mapping of elements detected.

Figure 223 displays the regions where point scans were tested using EDS point scan on a sample with 25% addition to magnesium slurry. The surface oxide illustrated by areas 1-5 contain a strong concentration of oxygen (34-39%), magnesium (32% - 35%) and silicon (13% - 18%). The presence of these elements suggests that Forsterite has developed [102]. The presence of iron ranged from 8-17%. With the highest concentration of vanadium (III) oxide added to the magnesium oxide slurry, no vanadium is detected in the surface oxide.
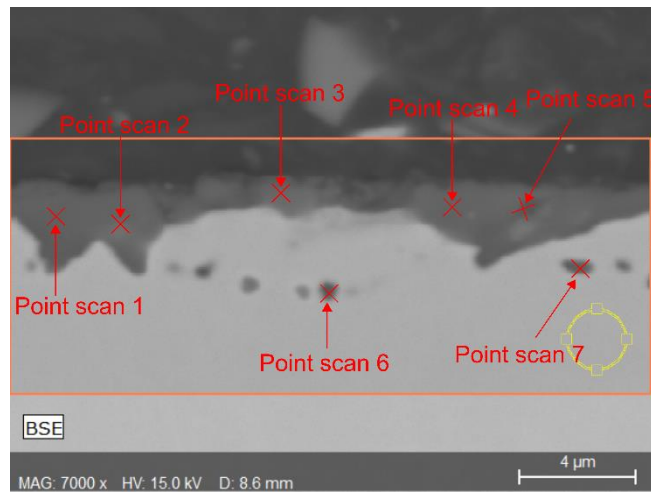
Figure 223. Illustration of point scans conducted on a sample that has 25% vanadium addition to the magnesium slurry.

Point Scan 1

Point Scan 2

Point Scan 3

Point Scan 4

Point Scan 5

Point Scan 6
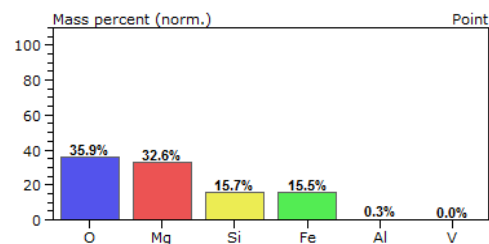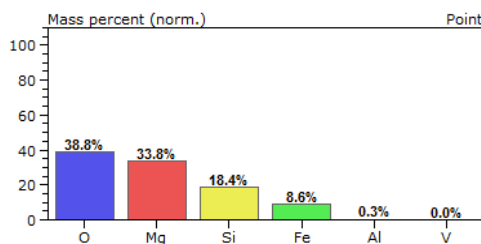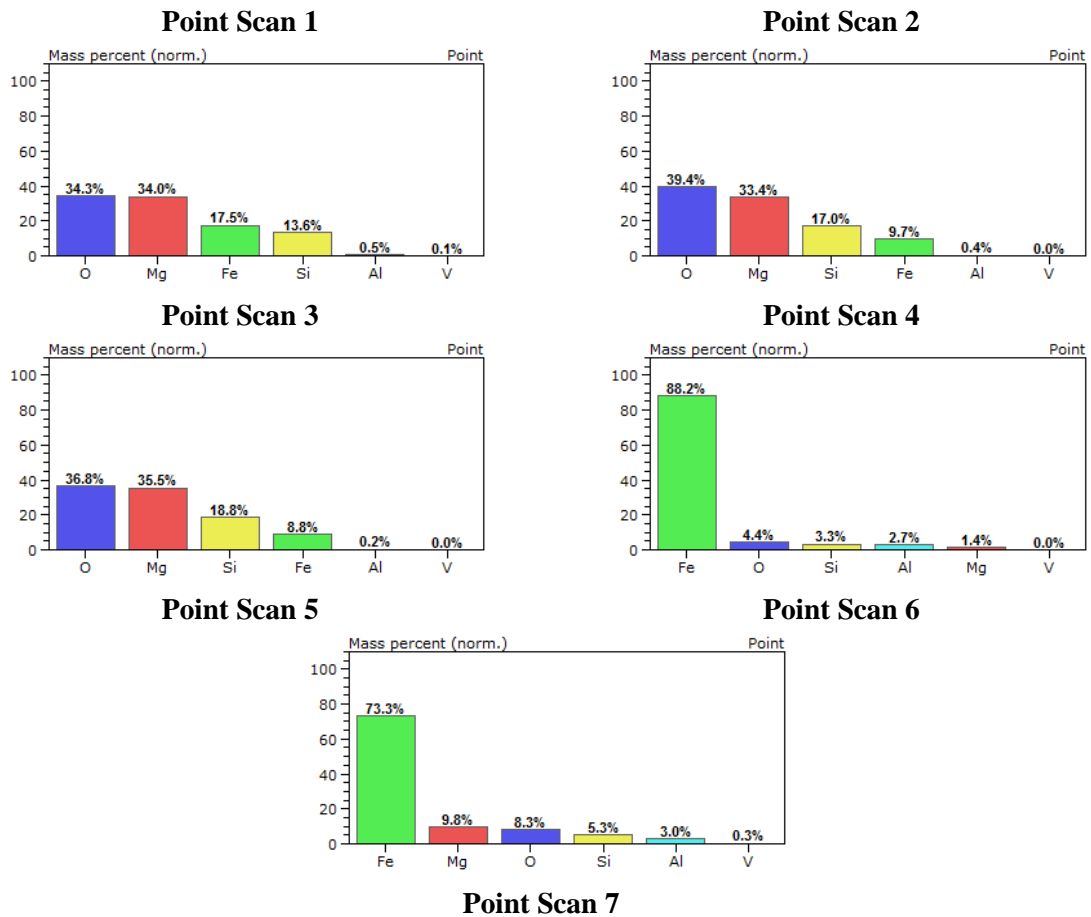
Point Scan 7

Figure 224. Displays the result of the surface oxide point scans (1-5) and subsurface (6-7) using EDS on the surface on a heat-treated sample with 25% V_2O_3 addition to the magnesium slurry.
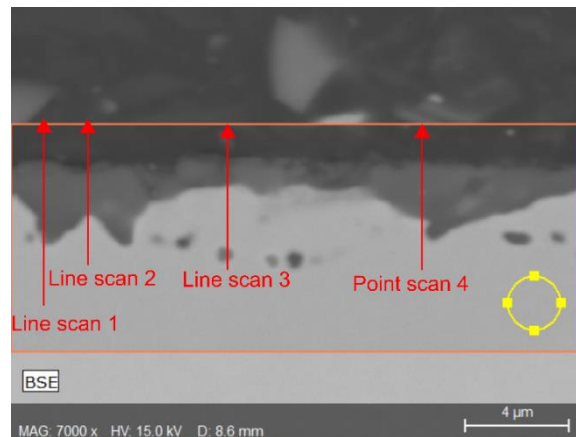
Figure 225. Illustrates a position of line scan conducted on 25% addition of Vanadium (III) oxide magnesium slurry.

All 4-line scans display similar trends whereby there is a decrease in iron concentration from the iron matrix, and an increase is observed in in magnesium, oxygen, and silicon. The intensity increases further away from the iron matrix. There is a slight increase in aluminium at the interface of the oxide layer (iron/magnesium). Vanadium is not present in any of the line scans.
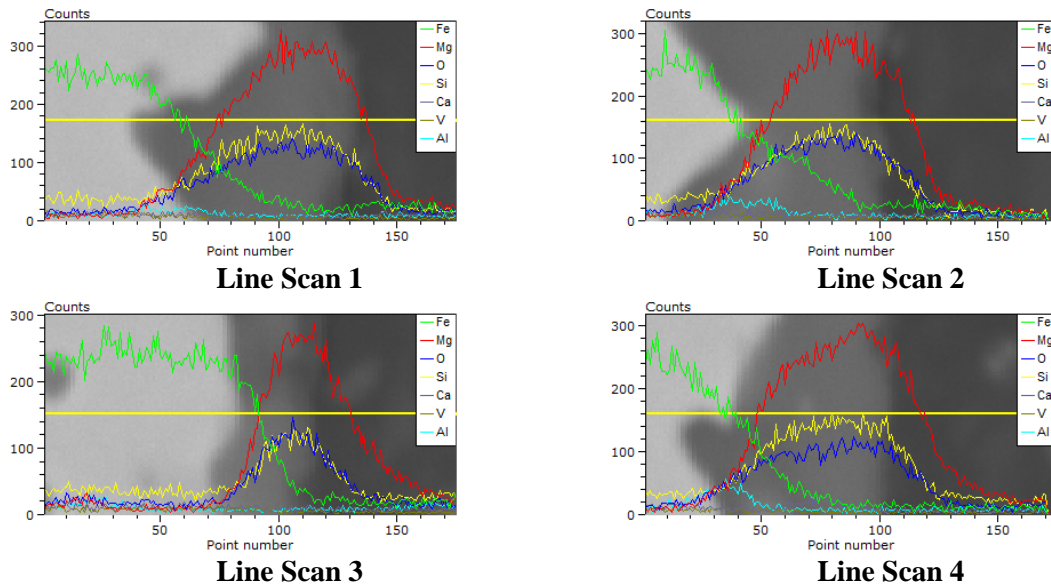
Figure 226. The composition changes at various regions of the surface oxide.

5.4.4 GDOES Analysis of Surface Oxide with V₂O₃ Addition to the Slurry

The chemical composition of the coating was determined by GDOES over a 3-diameter area etching into the surface layer of the oxide with argon, as explained in section 2.15. This section will focus on elements Fe, Mg, Si, Al, and V.

The results of the GDOES analysis through the surface and sub-surface oxide layer that has developed after heat treatment in the production furnaces with 1% addition of V_2O_3 to the slurry are displayed in Figure 227. The determination of the thickness of the oxide layer is explained in section GDOES Assumptions2.15.2.
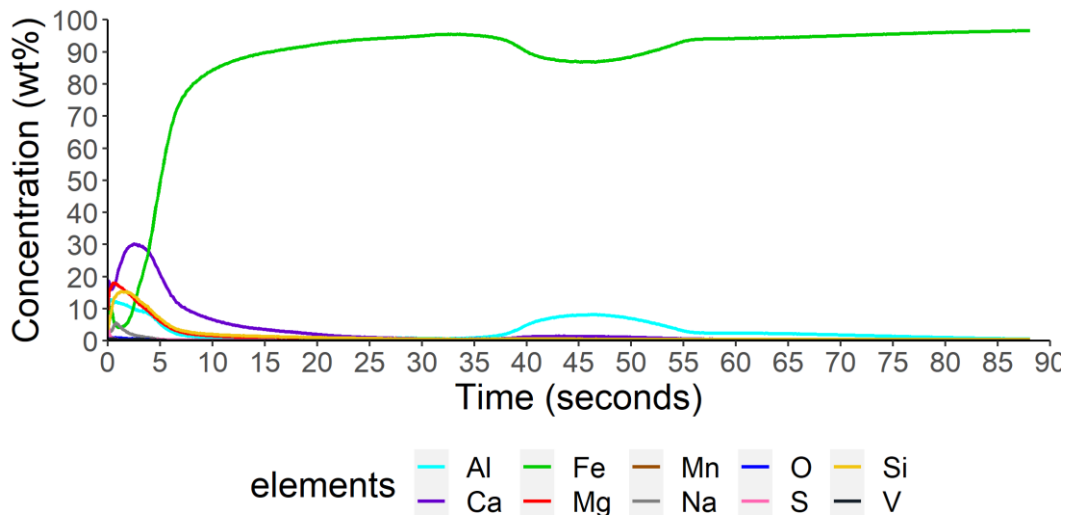
Figure 227. Is the chemical composition through the surface and subsurface oxide, when heat treated in production furnace at Orb Steelworks with 1% addition of V₂O₃ to the magnesium slurry

The oxide layer is a mixture of elements present at the surface and becomes less prevalent through the depth from the surface to the iron matrix—the concentration of the magnesium peaks at 18% at 1

195

second. The magnesium continues to decrease and reaches the line of interception of iron at 2.6 seconds. Silicon concentration peaks at 15.4% at 1.3 seconds.
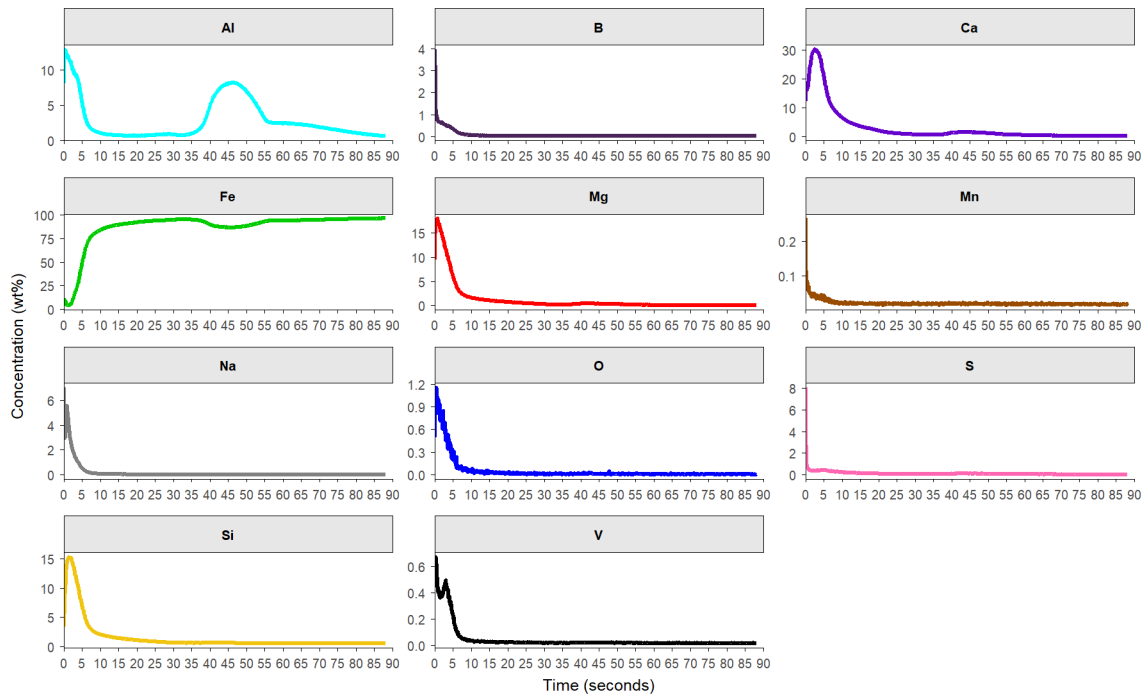
Figure 228. The individual elements of the chemical composition of the surface oxide of a sample that has been coated with 1% V_2O_3 addition to MgO slurry.

The aluminium concentration follows the same trend as seen in the previous section, where the aluminium peaks at the surface with a second peak further into the substrate. The first peak in the aluminium concentration reaches a maximum of 12.9% at 0.2 seconds and the second peak at 8.3% at 46 seconds. A small proportion of vanadium is detected at the surface with 0.67% concentration at 0.3 seconds and decreasing rapidly through the thickness of the surface oxide.

Figure 229 illustrates the change in composition through the surface oxide/matrix developed at the surface when coated with 10% addition of V_2O_3 to the magnesium slurry.
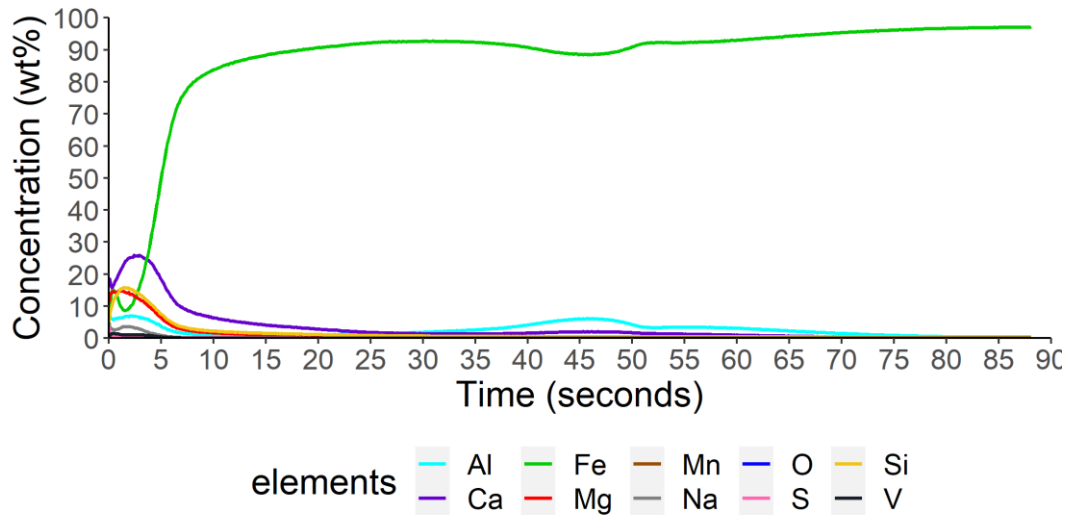
Figure 229. Displays the change of chemical composition of the developed surface oxide to the matrix of the electrical steel when coated with a magnesium slurry with 10% addition of V_2O_3 and heat-treated in Orb Steelworks.

The magnesium concentration peaks at 14.9% at 2.9 seconds and decreases further into the surface oxide and into the Fe matrix. Iron is present at the surface and intercepts the magnesium at 0.6 seconds, but the iron content decreases while magnesium increases and the second line of interception is at 2.5 seconds. The silicon concentration peaks at 15.8% at 1.5 seconds and begins to decrease.
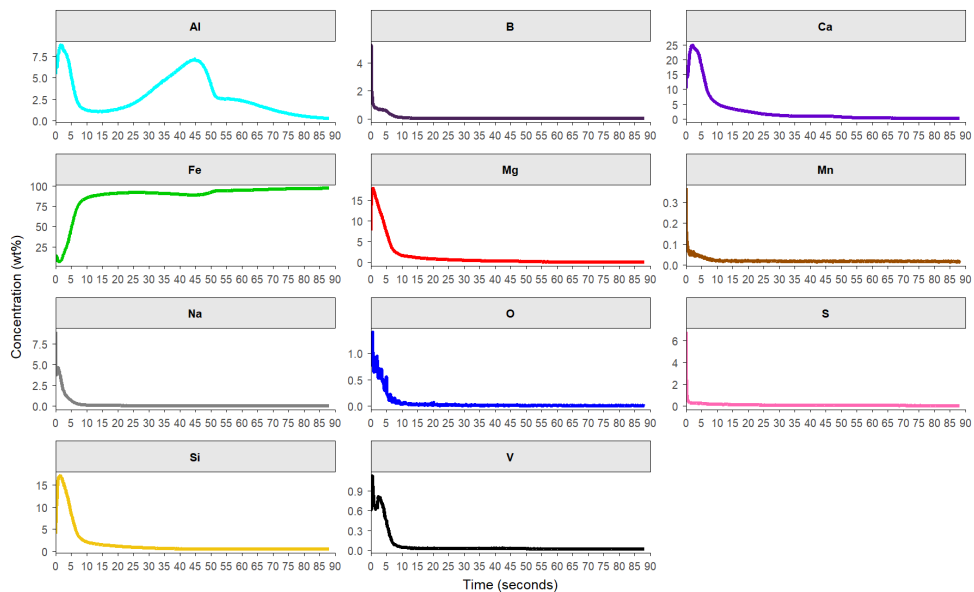
Figure 230. The individual elements of the chemical composition of the surface oxide of a sample that has been coated with 10% V_2O_3 addition to MgO slurry.

Aluminium peaks initially at 7% at 2.2 seconds and a second peak at 46 seconds at a maximum of 6.2%. Vanadium peaks at 0.4 seconds at 1.6%, the presence of vanadium >1% until 3.3 seconds. The detection of vanadium indicates that vanadium is forming a minor oxide as part of the surface oxide layer.

197
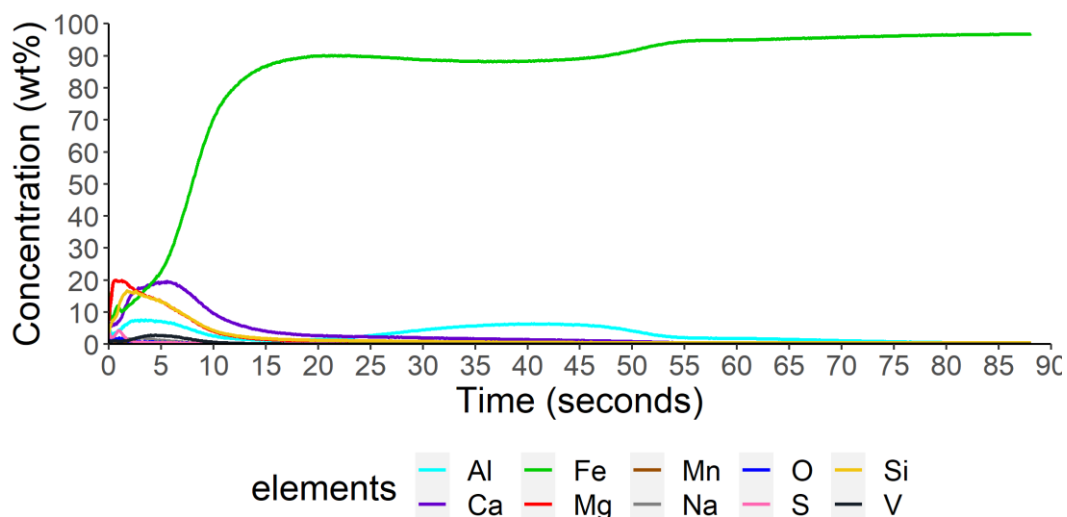
Figure 231. Changes in the chemical composition of the surface oxide with 25% V_2O_3 addition to MgO slurry.
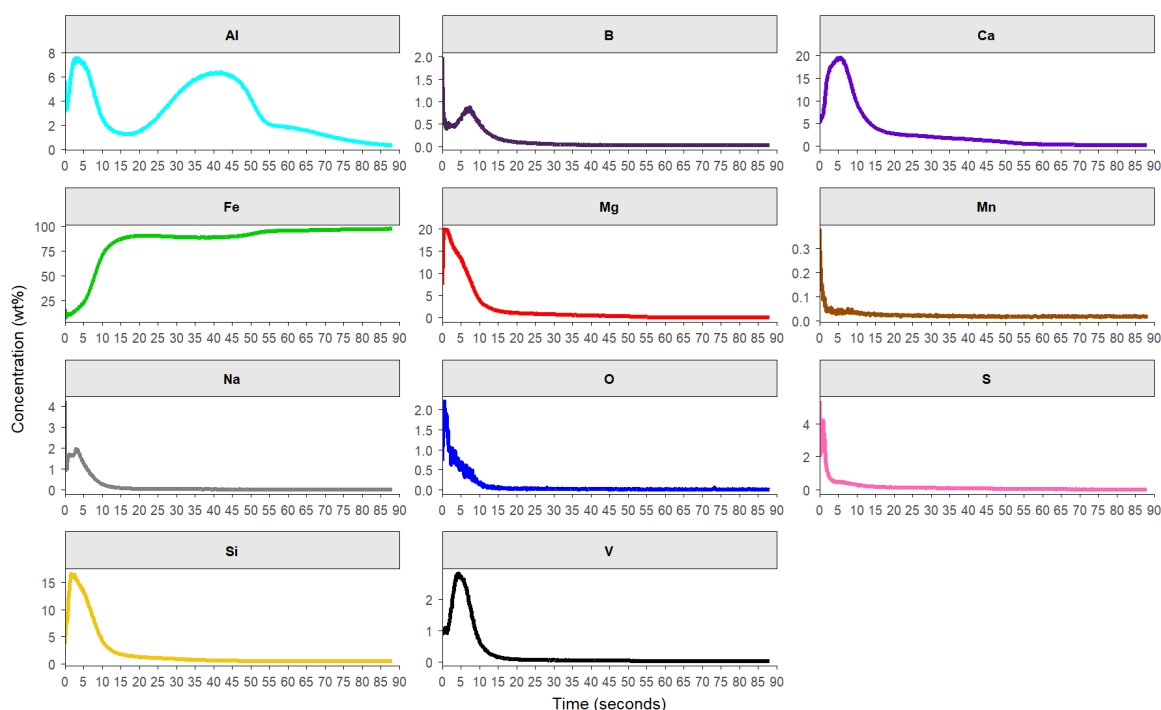
Figure 232. The individual elements of the chemical composition of the surface oxide of a sample that has been coated with 25% V_2O_3 addition to MgO slurry.

The concentration of magnesium peaks at 20% at 0.6 seconds and begins to reduce in concentration with further etching through the surface/matrix of the substrate. The line of interception with iron occurs at 3.1 seconds. The silicon detection at 16.7% at 1.7 seconds. The aluminium concentration at the first peak is lower than the previous two mixes with vanadium additions, with a peak of 7.7% at 3.1 seconds and a second peak of 6.4% at 42 seconds. Sulphur concentration has peaked at 5.3% at 1.9 seconds. The vanadium concentration has increased further by a 2.8% at 4.4 seconds.

198

5.4.5 Magnetic Properties

Figure 233 illustrates the result obtained for magnetic properties of the different concentrations of Vanadium (III) oxide added to the magnesium oxide slurry from the Soken tester. The increase in vanadium (III) oxide has no significant effect on the sample's magnetic properties when increasing the vanadium oxide content.
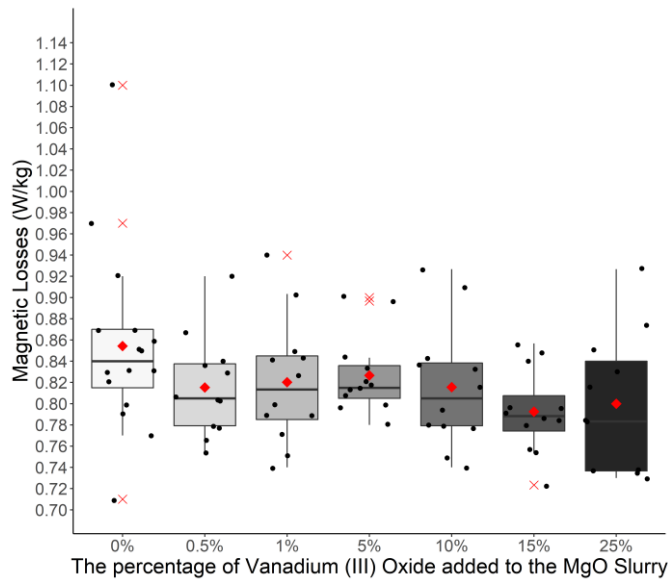
Figure 233. Magnetic properties after heat treatment with various amounts of Vanadium (III) oxide additions to the MgO slurry.

To prove statistically that the vanadium oxide has no significant difference, an F-Test was conducted to determine whether the variances are similar or not similar. The F-Tests determine the type of T-test to be conducted. The confidence level was set at p=0.01, and the null hypothesis was that the increase in vanadium (III) oxide does not affect the magnetic performance of the steel Table 24 confirms the trend seen in Figure 233 that there is no significant difference in magnetic properties when increasing the vanadium (III) oxide to the magnesium oxide.

Table 24. Illustrates the significant difference between vanadium (III) oxide concentration and magnesium slurry using the T-test method.

	Comparing 0% vs 0.5% Vanadium Oxide		Comparing 0.5% to 1% Vanadium Oxide		Comparing 1% to 5% Vanadium Oxide		Comparing 5% to 10% Vanadium Oxide		Comparing 10% to 15% Vanadium Oxide		Comparing 25% to 15% Vanadium Oxide	
P = 0.01	0% V_2O_3	0.5% V_2O_3	0.5% V_2O_3	1% V_2O_3	1% V_2O_3	5% V_2O_3	5% V_2O_3	10% V_2O_3	10% V_2O_3	15% V_2O_3	15% V_2O_3	25% V_2O_3
Mean	0.8158	0.8544	0.8158	0.8200	0.8200	0.8267	0.8267	0.8158	0.8158	0.7933	0.7933	0.7908
Variance	0.0022	0.0078	0.0022	0.0035	0.0035	0.0014	0.0014	0.0034	0.0034	0.0017	0.0017	0.0050
Observations	12	16	12	12	12	12	12	12	12	12	12	12
P(T<=t) two-tail	0.1827		0.8509		0.7455		0.596264974		0.2900		0.9166	
F-Test	Un-Equal T-Test		Un-Equal T-Test		Un-Equal T-Test		Un-Equal T-Test		Un-Equal T-Test		Un-Equal T-Test	

5.4.6

5.4.7 Resistance

Figure 234 displays the current detected by probes using a Franklin tester at Orb Steelworks. The magnesium oxide has the lowest average value of current detected out of all the samples. However, a rise in current is detected with an increase in vanadium (III) oxide introduced to the magnesium oxide slurry.
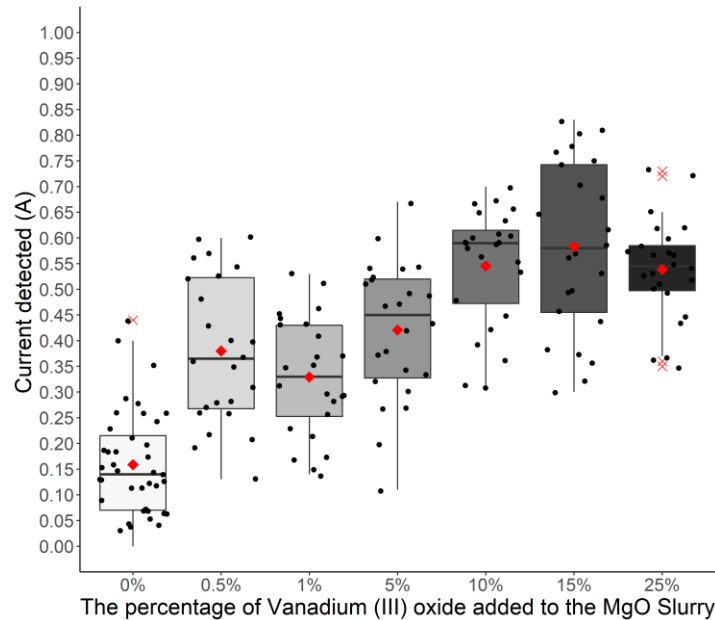
Figure 234. Current detected with an increase in V_2O_3 addition to the slurry using Franklin tester

A statistical F-Test and T-Test were conducted to establish whether there is a significant resistance when increasing vanadium (III) oxide. The confidence level was set at $p=0.01$, and the null hypothesis was that increasing the vanadium (III) content does not affect the resistance detected. The magnesium oxide slurry has the lowest average resistance out of all the mixes. There is a significant difference when comparing the MgO only and 0.5% addition of vanadium (III) oxide. There is an increase in current detected which implies that there is a decrease in insulation properties. Therefore, an increase in vanadium content to the magnesium slurry has a detrimental effect on the resistance properties. Increasing the vanadium (III) oxide from 0.5 to 1%, there is no significant difference. A further increase to 5% vanadium (III) oxide has a significant difference, and performance in resistance properties of the coating further decrease. A significant difference is seen comparing the 5% and 10% and further decreasing resistance properties. A further increase in vanadium >15% results in no significant difference in the resistance properties.

Table 25. Illustrates the result from the F and T-test comparing the significant difference in resistance between vanadium concentrations.

P = 0.01	Comparing 0% to 0.5% Vanadium Oxide		Comparing 0.5% to 1% Vanadium Oxide		Comparing 1% to 5% Vanadium Oxide		Comparing 5% to 10% Vanadium Oxide		Comparing 10% to 15% Vanadium Oxide		Comparing 25% to 15% Vanadium Oxide	
	0% Vanadium Oxide	0.5% Vanadium Oxide	0.5% Vanadium Oxide	1% Vanadium Oxide	1% Vanadium Oxide	5% Vanadium Oxide	5% Vanadium Oxide	10% Vanadium Oxide	10% Vanadium Oxide	15% Vanadium Oxide	15% Vanadium Oxide	25% Vanadium Oxide
Mean	0.1588	0.3800	0.3800	0.3292	0.3292	0.4208	0.4208	0.5454	0.5454	0.5833	0.5833	0.5388
Variance	0.0105	0.0203	0.0203	0.0131	0.0131	0.0180	0.0180	0.0132	0.0132	0.0285	0.0285	0.0098
Observations	40	24	24	24	24	24	24	24	24	24	24	24
P(T<=t) two-tail	0.0000		0.1801		0.0144		0.0012		0.3684		0.2701	
F-Test	Un-Equal T-Test		Un-Equal T-Test		Un-Equal T-Test		Un-Equal T-Test		Un-Equal T-Test		Equal T-Test	

5.4.8 Bulk Analysis of Carbon, Oxygen, Nitrogen and Sulphur

The bulk analysis was conducted using the Leco TN400 and Leco CS844 carbon, as explained in sections 2.10 and 2.11. The C, O and S did not display any changes, and variances were as expected. The nitrogen content appeared to decrease with the >1% addition V_2O_3 producing levels of nitrogen <30 ppm, which indicates that the purification of the substrate has increased, however, due to the limited amount of data points, it is difficult to come to any conclusion.
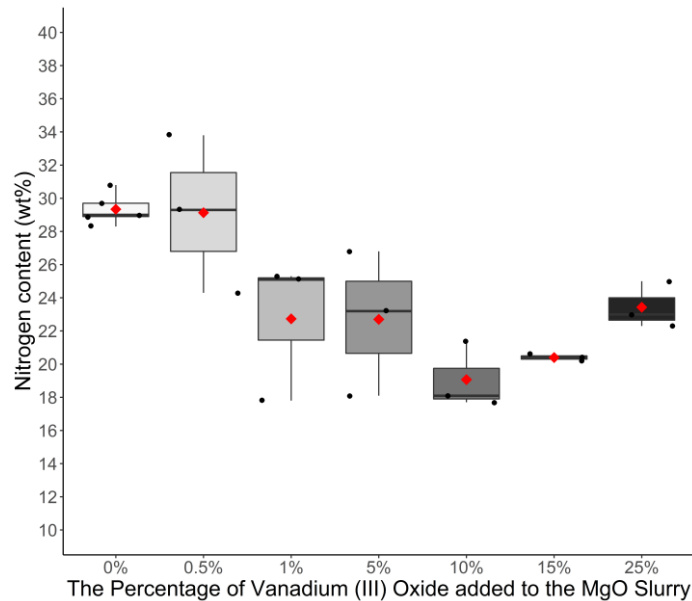
Figure 235. The nitrogen content of the bulk substrate of various concentrations of V_2O_3 was added to the MgO slurry using LECO TN400.

5.4.9 Discussion

The addition of 0.5% V_2O_3 to the slurry has resulted in an increase in thickness with further increases. No improvements are seen in the 1 and 5% additions of V_2O_3. At 10% addition, a secondary improvement is seen in the oxide thickness, but increasing additions >10% addition do not show any improvement, and at 25%, there is a reduction in coating thickness. The morphology of the oxide layer has altered when compared with magnesium only, which has has a thin uniform oxide; however,

when 0.5% of V_2O_3 has been added, the oxide layer developed becomes non-uniform, and keying points being more frequently observed in SEM images. The subsurface oxide has become more prevalent with the 0.5% V_2O_3 addition. The morphology of the surface oxide continues in 10% and 25% additions, with an irregular oxide layer and keying points, developed.

The EDS analysis identified that the surface oxide composition for all three concentrations of V_2O_3 additions was predominantly oxygen, magnesium, and silicon. This composition is typical of Forsterite that has been identified with previous research [136]. Notably, there is no significant detection of vanadium present in the local scanned areas in all three concentrations using EDS. However, GDOES has detected some small concentrations of vanadium in the 10% V_2O_3 and 25% that has been detected up to 10 seconds into the scanned surface. The GDOES analysis is a 3mm diameter circle through the surface of the substrate increases the likelihood of detecting the vanadium. The detection of vanadium could indicate that vanadium diffusion is taking place from the applied coating to the substrate has occurred or that the etching rate of vanadium is much lower than that of other elements present at the surface. Nevertheless, further testing is required to confirm this with alternative methods.

The introduction of V_2O_3 has had a negative effect on the resistance of the coating. The Franklin test has shown that a small quantity of V_2O_3 (0.5%) has increased current detected. This trend continues with an increase in concentration to the slurry of V_2O_3, seeing an increase in current detection. The reasoning for the increase in current is not clear, but vanadium's presence through the surface oxide from the GDOES analysis could provide a path for the current to travel from the surface through the coating to the substrate. Additionally, the variation of coating thickness may be seen in the morphology of the surface oxide when vanadium has been added to the slurry resulting in regions of thin surface oxide, which increase the probability of current travel through the oxide with impurities such as iron and vanadium present, despite on average the coating being thicker. Although the average thickness has increased, there are regions of thin surface oxide development. These thin regions will be more susceptible to current leakage.

The results of the Soaken test have exhibited no improvement in magnetic properties even though the measured coating thickness of the 0.5% and 10% have demonstrated an increase in oxide thickness. As well as a reduction in carbon and sulphur detected in the substrate, which indicates a reduced number of precipitates present in the substrate, which have been shown to reduce domain wall pinning and therefore improving magnetic properties of the steel. Therefore, the introduction of V_2O_3 has deteriorated the performance of the electrical steel with degradation in resistance properties even though the surface oxide has increased in thickness.

5.4.10 Conclusion

As literature has stated, the introduction of V_2O_3 to the magnesium slurry has resulted in a thicker oxide layer developed at the surface [117]. However, this has come at a price with a significant increase in current detected through the surface oxide, which is likely due to the non-uniformity of the coating morphology observed. In addition, the magnetic properties have not shown any significant improvement either. Therefore, the addition of V_2O_3 should be avoided to prevent problems with the resistance properties of the steel.

5.5 The Impact of FeO-Fe₂O₃ Addition on the Formation of the Oxide Layer

5.5.1 Introduction

Iron plays a critical role in forming an intermediate olivine/oxide known as Fayalite to create the correct condition to develop Forsterite (Mg_2SiO_4) [137]. It has been reported that an introduction of iron oxide has resulted in improvements seen in the oxidation thickness developed at the surface[117]. The information provided is limited, but through an understanding of Fayalite development and internal reports, it is possible to produce additional Fayalite and /or oxygen during the HTCA. This section will investigate the effects of the addition of the FeO-Fe₂O₃ has on the resulting oxide layer developed and properties essential to electrical steel.

5.5.2 Morphology and Coating Thickness of Surface Oxide Developed with FeO-Fe₂O₃ Addition to the Slurry.

Figure 236 illustrates the oxide development on the top and bottom surface of the substrate when 1% of FeO-Fe₂O₃ oxide is added to the magnesium slurry and subsequently coated onto the substrate and heat-treated at the production batch furnaces at Orb Steelworks. The oxide thickness varies throughout the width of the image. Where regions of thin or no oxide is present. There are subsurface oxides present, and there are no apparent keying areas where the oxide has penetrated the substrate.
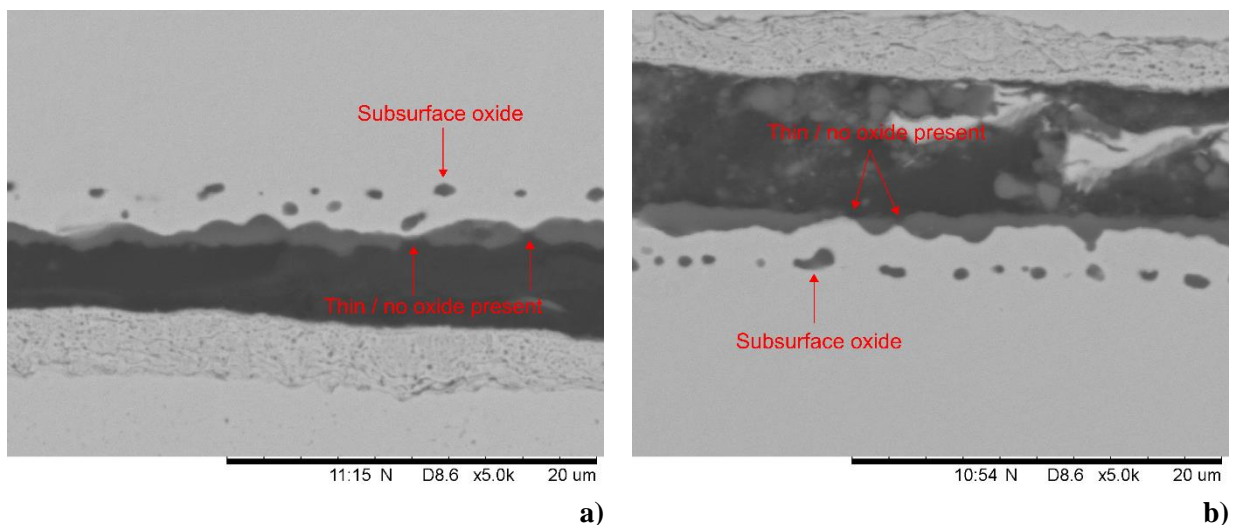
Figure 236. a) SEM cross-section of a top surface of a sample that has been coated with magnesium slurry with 1% addition of FeO-Fe₂O₃**. b)** shows the cross-section of a bottom surface

Figure 237 illustrates an oxide developed when 10% of FeO-Fe₂O₃ oxide is added to the magnesium coating and is coated and heat treated as previously outlined. The top surface oxide in Figure 237a) has developed an inconsistent layer where no coating or thin coating areas are present. The surface oxide layer has some keying areas, and there are subsurface oxides visible. The oxide layer at the bottom surface in Figure 237b.) has produced a consistent coating with several keying areas present. The subsurface oxide areas are not protruding below the keying areas reducing the pinning effect of magnetic domains.

a)   **b)**
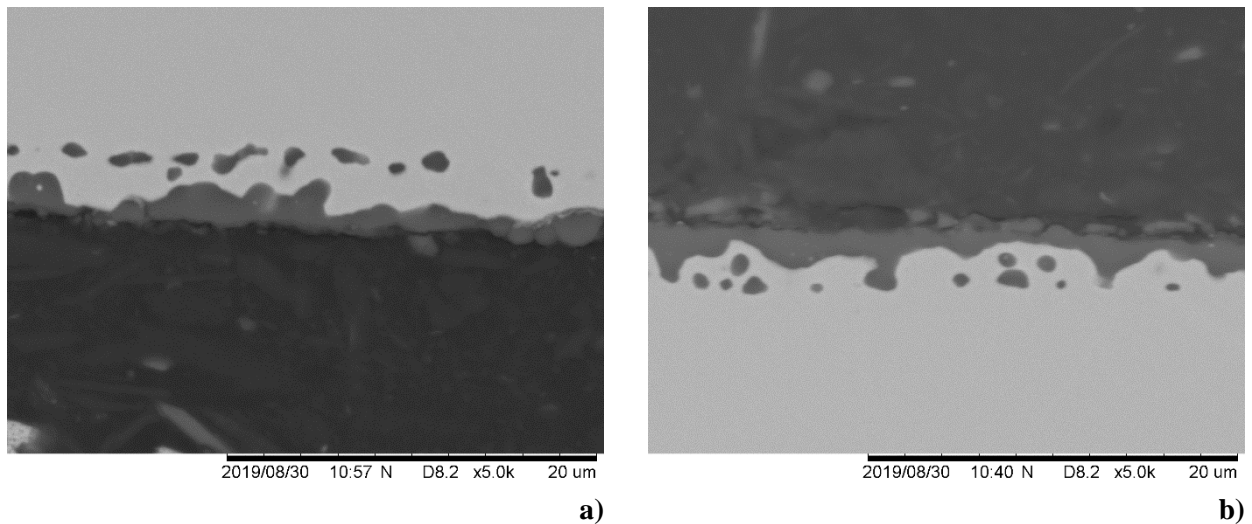
Figure 237. a) SEM cross-section of a top surface of a sample that has been coated with magnesium slurry with 10% addition of $FeO\text{-}Fe_2O_3$. **b)** shows the cross-section of a bottom surface

Figure 238 demonstrates the oxide developed when 25% $FeO\text{-}Fe_2O_3$ is introduced into the magnesium oxide slurry. Both Figure 238a, b.) have several keying points into the substrate, and the subsurface oxide does not protrude below the keying areas. However, when comparing Figure 238a, b.) there is a noticeable difference in the surface oxide, which is reflected in measurements of the surface oxide in Figure 239.

a)   **b)**
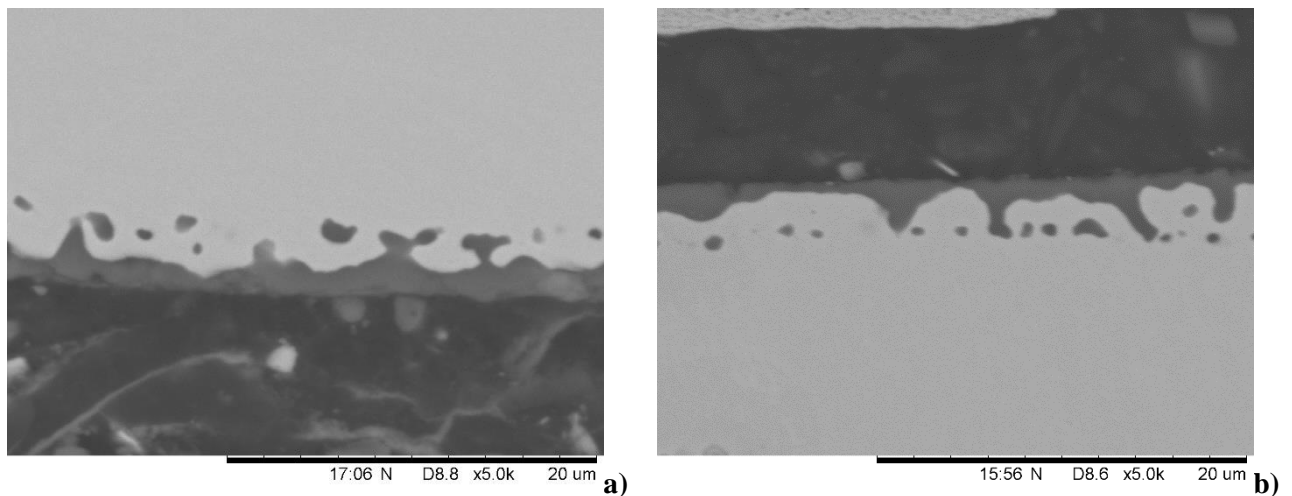
Figure 238. a) SEM cross-section of the top surface of a sample that has been coated with magnesium slurry with 25% addition of $FeO\text{-}Fe_2O_3$. **b)** shows the cross-section of a bottom surface

Figure 239 illustrates the calculated thickness of oxide developed at the surface of the substrate when introducing $FeO\text{-}Fe_2O_3$ to the magnesium slurry and subsequently coated on the substrate and heat treated. SEM images were collected and processed using Matlab as outlined in Section 2.7.2. The introduction of $FeO\text{-}Fe_2O_3$ has enhanced the oxide thickness at the substrate's surface compared to the magnesium oxide only slurry. The increase in $FeO\text{-}Fe_2O_3$ has no improvement in oxide thickness between 0.5 to 5% addition of $FeO\text{-}Fe_2O_3$. Further increase in $FeO\text{-}Fe_2O_3$ (10% and 15%) has a

negative effect on the oxide thickness and reduces the oxide thickness developed at the surface of the substrate.
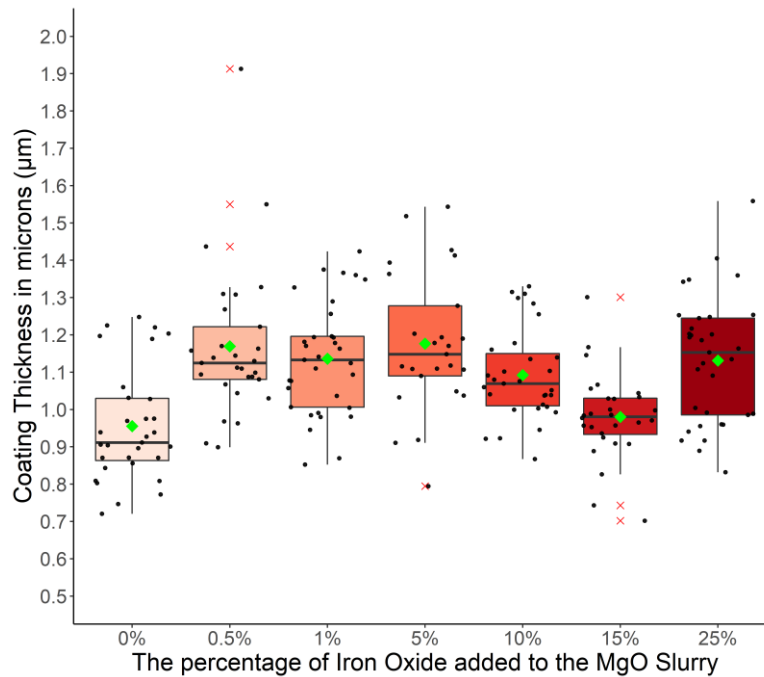
Figure 239. Illustrates the effects of iron (II, III) addition to MgO slurry ranging between (0-25%) has on the surface oxide through imaging cross-section

Table 26 displays the significant difference between concentrations of FeO-Fe$_2$O$_3$. The small addition (0.5%) of iron oxide has developed a thicker oxide at the surface. The further addition of iron oxide up to 5% has no significant effect on the oxide developed. When comparing 5% to 10%, there is a decrease in the average coating thickness, but the significant difference does not meet the P=0.01 level of confidence. When increasing the iron oxide content to 15% in the MgO, there is a significant difference. The oxide thickness has decreased to the level of MgO only thickness. At 25% iron Oxide concentration, the oxide layer produced is similar to that of 0.5% to 5%.

Table 26. The results of the T-test and F-test to establish the variance are comparable and whether there is a significant difference.

P = 0.01	Comparing 0% vs 0.5% Iron Oxide		Comparing 0.5% to 1% Iron Oxide		Comparing 1% to 5% Iron Oxide		Comparing 5% to 10% Iron Oxide		Comparing 10% to 15% Iron Oxide		Comparing 15% to 25% Iron Oxide	
	0% Iron Oxide	0.5% Iron Oxide	0.5% Iron Oxide	1% Iron Oxide	1% Iron Oxide	5% Iron Oxide	5% Iron Oxide	10% Iron Oxide	10% Iron Oxide	15% Iron Oxide	15% Iron Oxide	25% Iron Oxide
Mean	0.9553	1.1694	1.1694	1.1359	1.1359	1.1763	1.1763	1.0924	1.0924	0.9801	0.9801	1.1310
Variance	0.0228	0.0414	0.0414	0.0225	0.0225	0.0347	0.0347	0.0154	0.0154	0.0139	0.0139	0.0292
Observations	31	29	29	33	33	25	25	31	31	28	28	33
P(T<=t) two-tail	0.0000		0.4695		0.3790		0.0487		0.0007		0.0001	
F-Test	Un-equal Variance		Un-equal Variance		Un-equal Variance		Equal Variance		Un-equal Variance		Un-equal Variance	

206

5.5.3 EDS Analysis

Figure 240 illustrates a cross-section of the surface oxide developed when 1% addition of FeO-Fe$_2$O$_3$ is introduced to the MgO slurry using EDS analysis to map out the elements present in the scanned area. The surface oxide is predominantly magnesium, while the subsurface oxides are composed of several oxides containing aluminum, magnesium, and calcium.
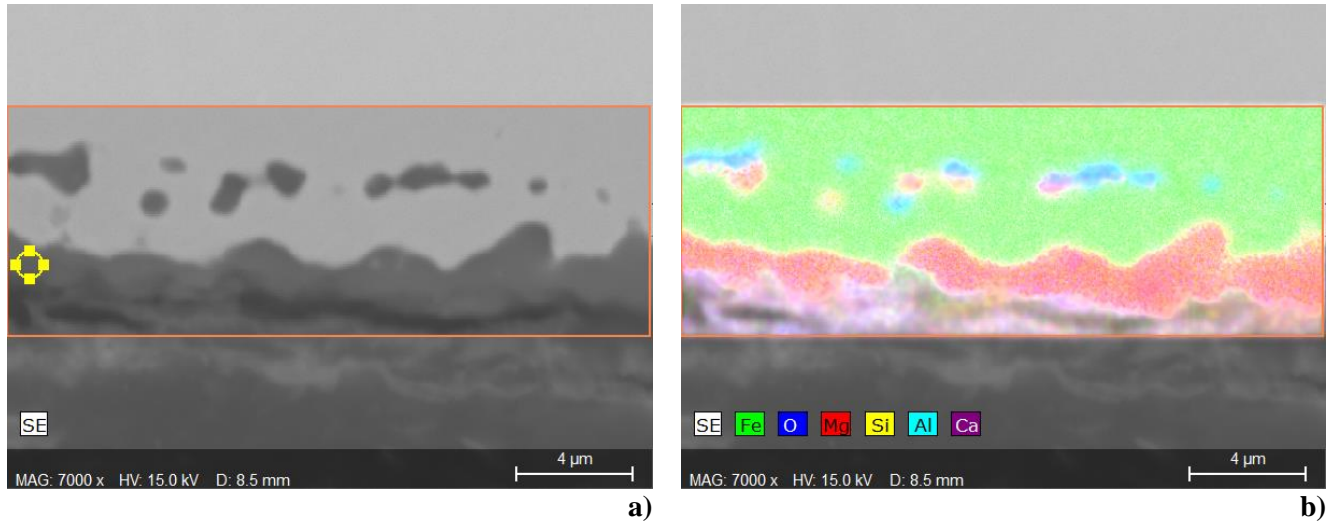
Figure 240. SEM cross-section of an oxide layer that has been coated in a magnesium oxide with 1% FeO-Fe$_2$O$_3$ addition and heat-treated in production furnace. **b)** is the EDS mapping of elements detected

Figure 241 illustrates the elemental point scans using EDS conducted on 1% iron oxide and magnesium slurry. The surface oxide results are represented by point scans 1-5 and 12. The four main elements detected at the surface oxide are oxygen, magnesium, silicon, and iron.
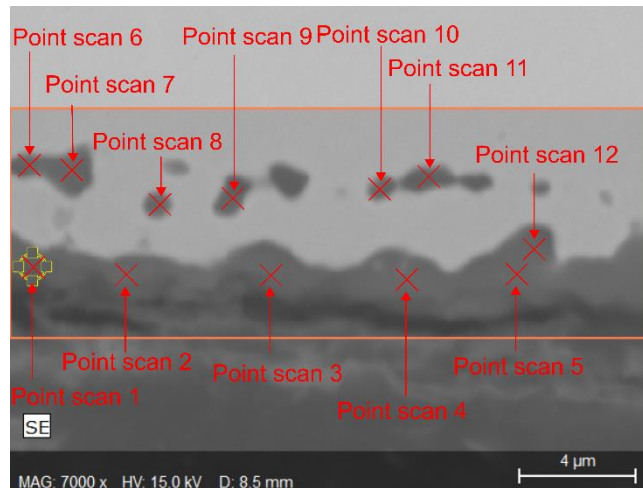
Figure 241. Displays the locations of point scans conducted on the oxide layer of a sample that has 1% addition of FeO-Fe$_2$O$_3$ to magnesium oxide slurry

The two primary elements detected in the surface oxide are oxygen and magnesium. The oxygen content within the surface oxide is consistently between 31% to 40%. The magnesium content ranges between 23%-30%, with only one exception (scan 3), magnesium is more prevalent than iron. Secondary elements detected are silicon and iron. The iron concentration varies between 11.7% to

25.6%, and silicon ranging between 13.5-17.9%. Finally, trace elements are detected, such as calcium, aluminum, and Sulfur. The concentration of aluminum and sulfur are detected <1%, and calcium being detected at a level <1.7% in the surface oxide.
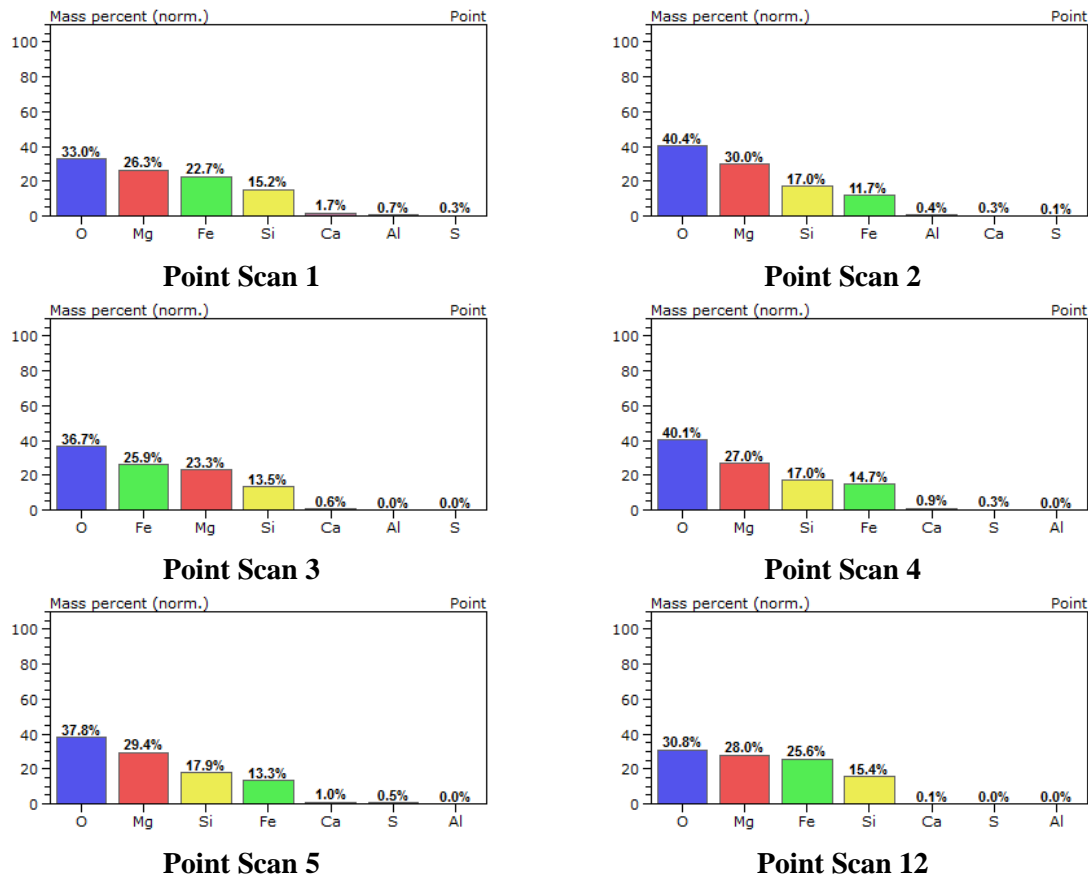
Figure 242. Displays the result of the surface oxide point scans (1-5 and 12) using EDS on the surface on a heat-treated sample with 1% FeO-Fe$_2$O$_3$ addition to the magnesium slurry.

The subsurface oxide is represented by point scans 6-11 in Figure 241. The subsurface oxides are complex, with several elements present in these regions. The primary element detected in the suboxide layer is iron ranging between 25.9-58%. This is to be expected due to the interaction volume of the technique and these regions being relatively small, isolated oxide compositions penetration into the surrounding iron matrix is to be expected. The matrix of the electrical steel after heat treatment is typically 97% Fe and 3% Si. However, in the regions scanned, the oxygen concentration ranges between 15.1- 28.2%, indicating some oxidation. The two common elements detected are aluminium and magnesium, with values between 5.9- 27.7% and 10.4- 23.8%.

Previously perception of the success of forming Forsterite was limited by the rate of diffusion of magnesium. However, the detection of magnesium in the subsurface indicates that the rate of diffusion may not be the limiting factor. Instead, it is likely to be due to incorrect conditions (i.e., insufficient Fayalite available after "initial Forsterite") to produce an increase in Forsterite thickness. Additional elements detected in the subsurface oxide are silicon, calcium and sulphur, ranging between 10.4- 4.1%, 5.1-0% and 4.8-0%, respectively.

Point Scan 6

Point Scan 7

Point Scan 8

Point Scan 10
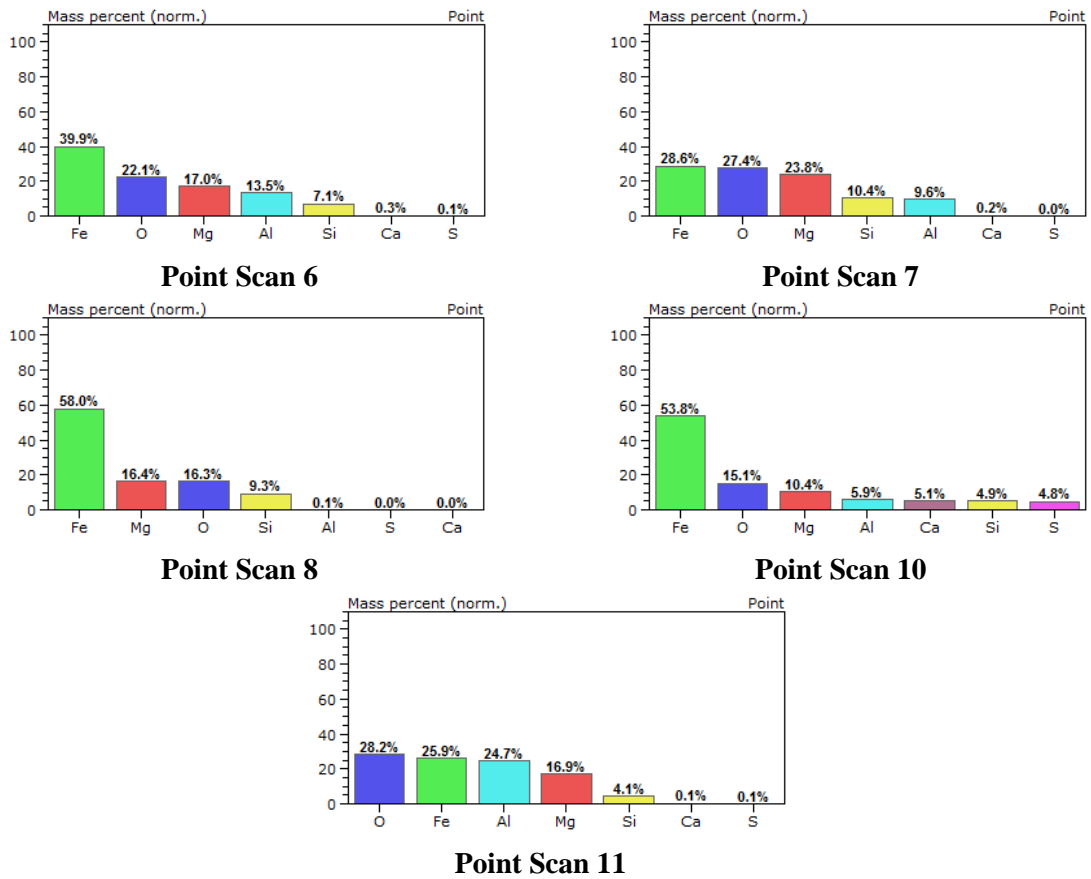
Point Scan 11

Figure 243. Displays the result of the sub-surface oxide point scans (6-8, 10 and 11) using EDS on a surface on the heat-treated sample with FeO-Fe$_2$O$_3$ addition to the magnesium slurry.

Figure 244 displays the cross-section of the oxide layer developed when 10% FeO- Fe$_2$O$_3$ oxide is added to the magnesium slurry, which has been mapped of elements using EDS. The surface oxide layer is a continuous magnesium layer developed with an area of subsurface oxide below the magnesium oxide surface.

a)

b)
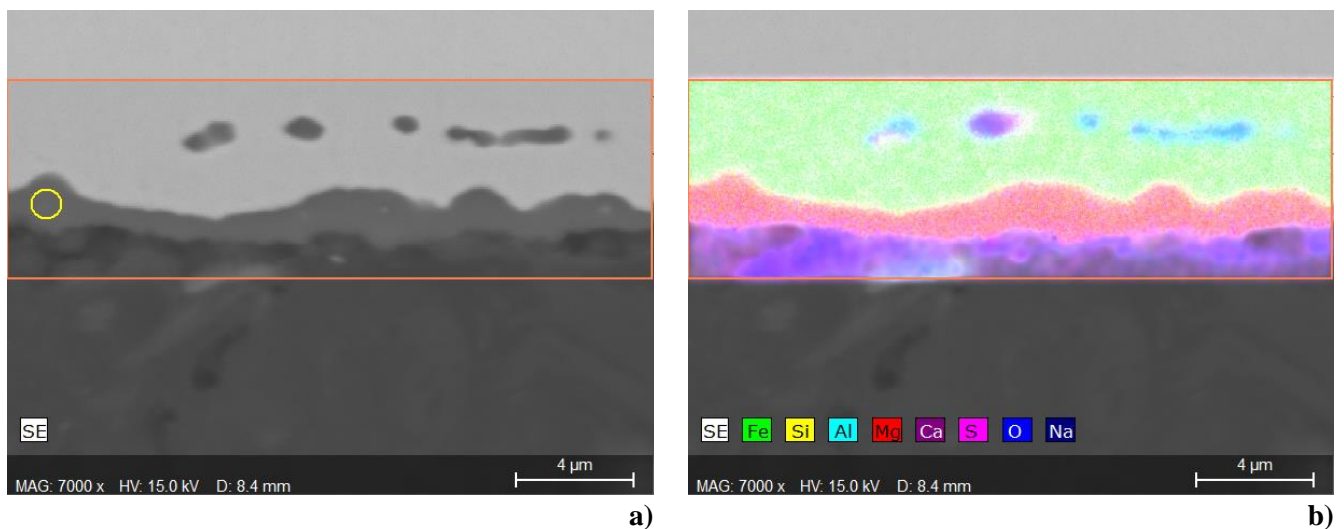
Figure 244. SEM cross-section of an oxide layer that has been coated in a magnesium oxide with 10% FeO-Fe$_2$O$_3$ addition and heat-treated in production furnace. **b)** is the EDS mapping of elements detected.
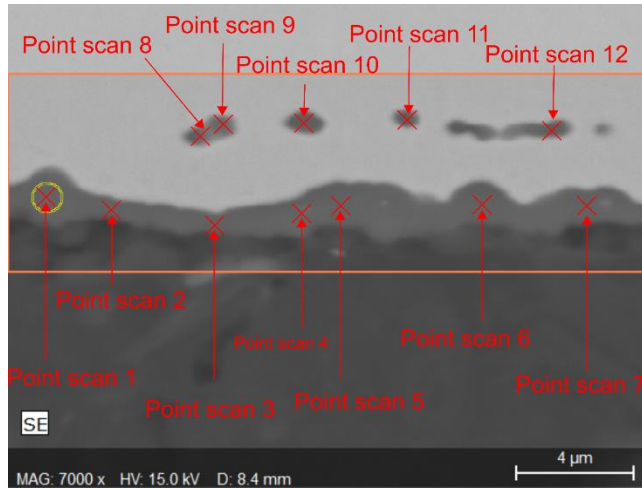
Figure 245. Displays the locations of point scans conducted on the oxide layer with 10% addition of FeO-Fe$_2$O$_3$ to magnesium oxide slurry.

Figure 245 illustrates the point scans conducted on the surface oxide and subsurface oxide. The surface oxide point scans are represented by 1-7 in Figure 245. The results for the point scans are displayed in Figure 248. With an increase of iron (II, III) oxide present, the expectation would be to increase iron concentration in the surface oxide. However, the iron content remains relatively moderate, ranging between 5.9%-11.4%. Oxygen and magnesium are prevalent in the surface oxide ranging from 36.6-40.1 and 30.7-33.2%, respectively. In addition, there is an increase in sodium detected between 0.8- 3.5%. The source of this sodium is unknown. Small traces of aluminium and calcium in the surface oxide range 0.3-0.7% and 0.4-1.6%, respectively.
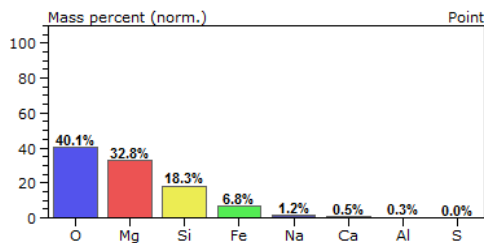
Point Scan 1
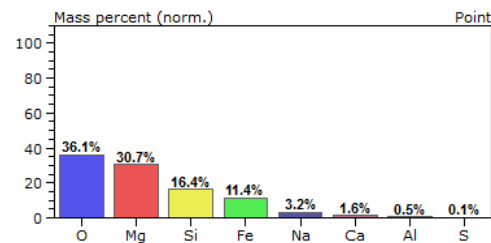
Point Scan 2
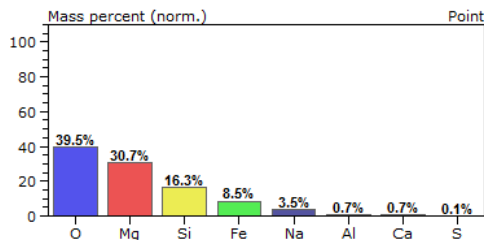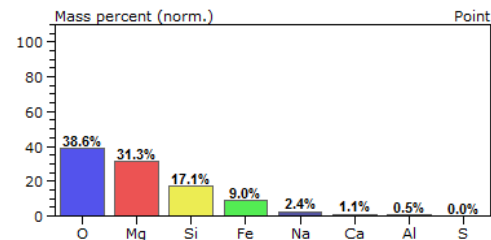
Point Scan 3
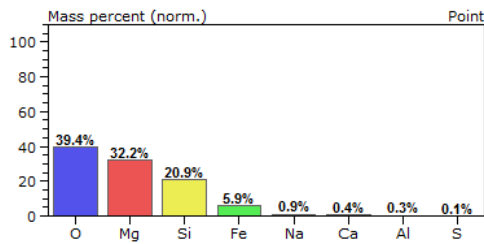
Point Scan 4
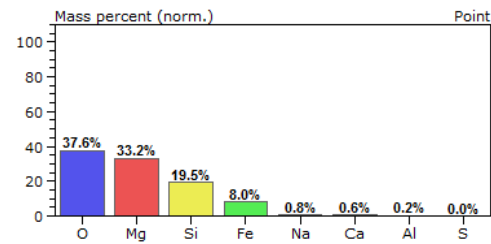
Point Scan 5
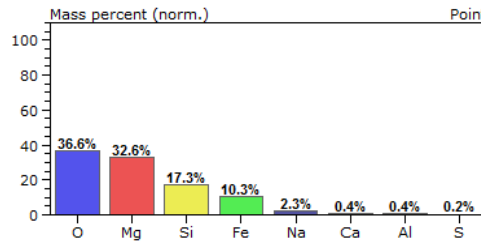
Point Scan 6

Point Scan 7

Figure 246. Displays the result of the surface oxide point scans (1-7) using EDS on the surface with 10% FeO-Fe$_2$O$_3$ addition to the magnesium slurry.

The subsurface oxide is a mixture of elements present; iron is the most abundant element present ranging between (39.3%-64.1%). The secondary elements present are oxygen (14.1%-24.9%), magnesium (7.3% -12%) and aluminium (3.6%- 19.9%). There are traces of calcium, sulphur, and sodium present in the subsurface oxide.
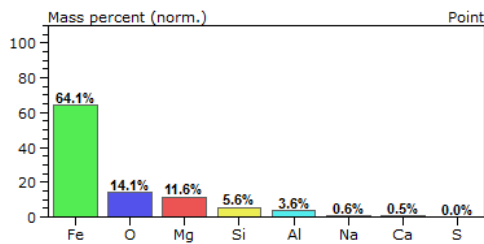
Point Scan 8
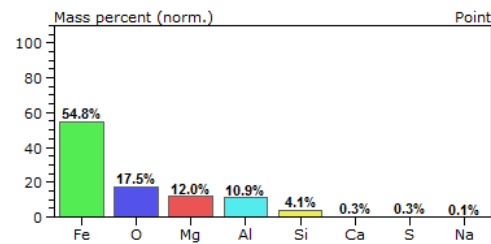
Point Scan 9
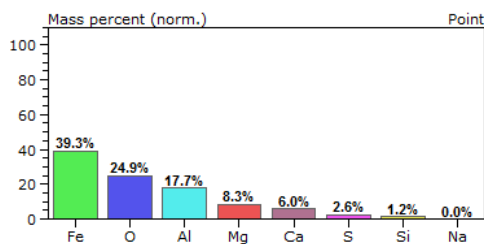
Point Scan 10
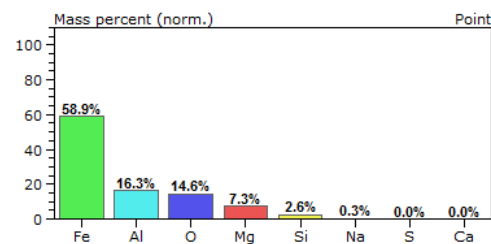
Point Scan 11
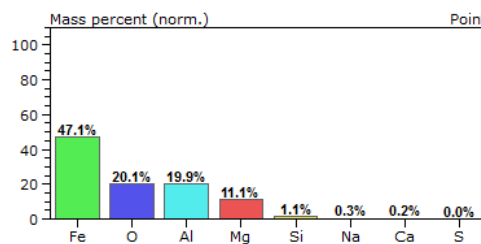
Point Scan 12

Figure 247. Displays the result of the sub-surface oxide point scans (6-12) using EDS with FeO-Fe$_2$O$_3$ addition to the magnesium slurry.

Figure 248a) illustrates the SEM image of the mapped area of the EDS mapping shown in Figure 248b). The sample in Figure 248 has been coated with a magnesium oxide slurry with 25% addition of iron (II, III) oxide. The surface oxide is a continuous layer across the surface, with the main element present being magnesium. The subsurface oxide again illustrates several additional elements, such as magnesium, oxygen, aluminium, and sulfur.

a)   b)
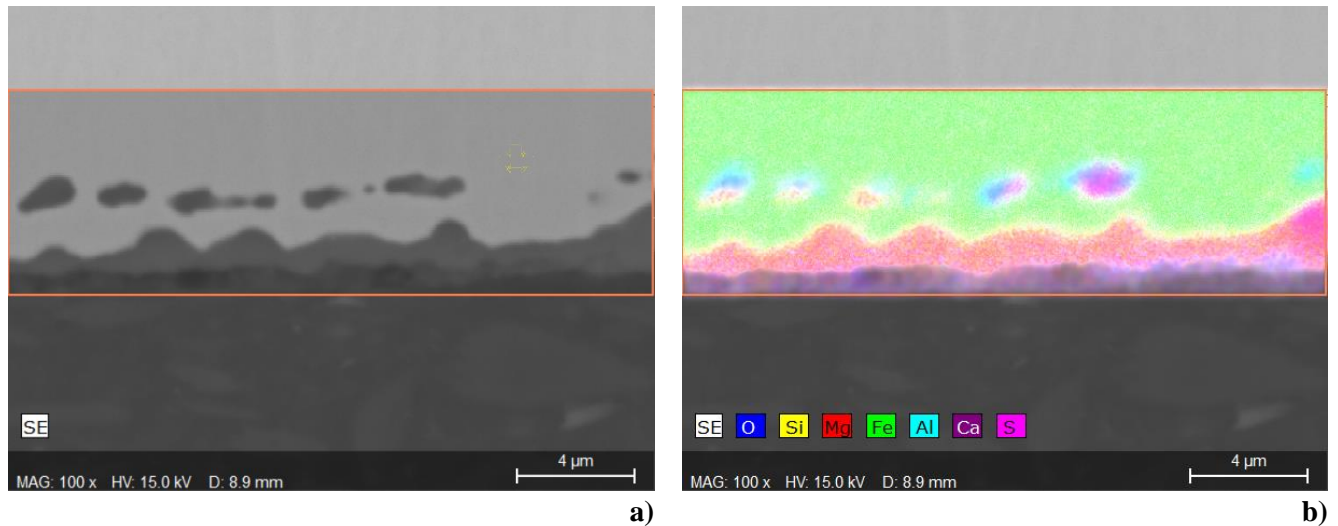
Figure 248. SEM cross-section of an oxide layer that has been coated in a magnesium oxide with 25% $FeO-Fe_2O_3$ addition to the slurry. **b)** is the EDS mapping of elements detected.

Figure 249 displays the point scans conducted on the sample with 25% iron oxide and magnesium slurry. Point scans 1 -6 are elemental analyses of the surface oxide that has developed. Point scans 7 – 12 are elemental analyses using EDS of the subsurface oxides.
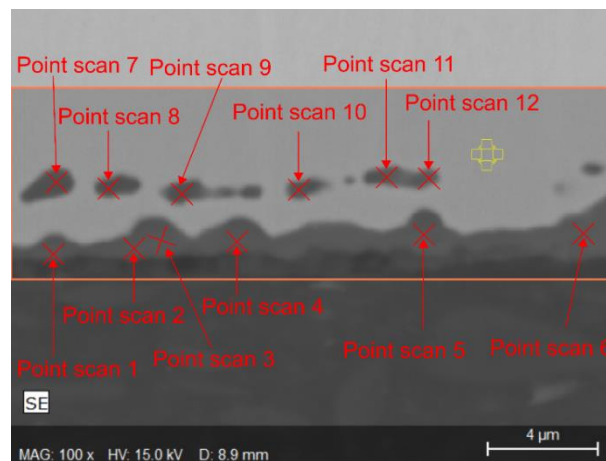
Figure 249. Displays the locations of point scans conducted on the oxide layer with 25% addition of $FeO-Fe_2O_3$ to magnesium oxide slurry.

The main elements present in the surface oxide are oxygen (37.4- 39.9%), magnesium (27.7-31.1%), silicon (15.7-18.4) and iron (9.4-16.9%). Secondary elements that are present are aluminum (0.8-1.6%) and sulfur (0-2.4%).
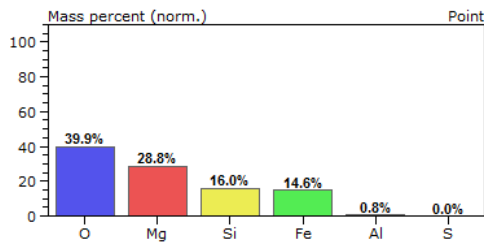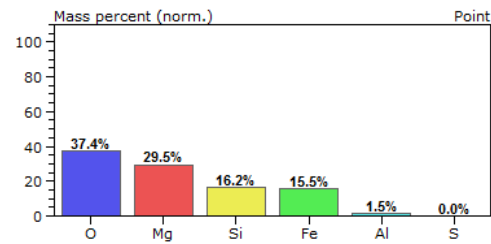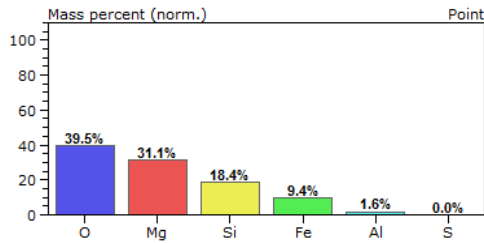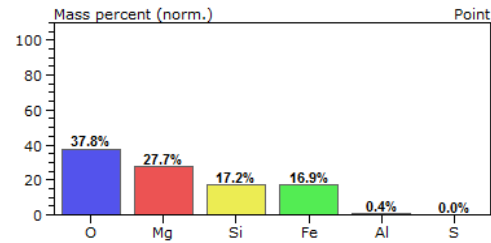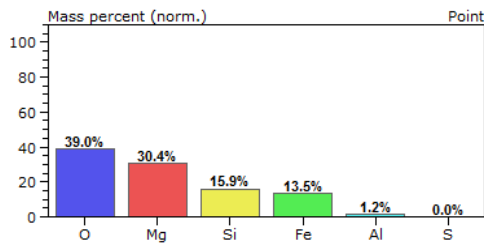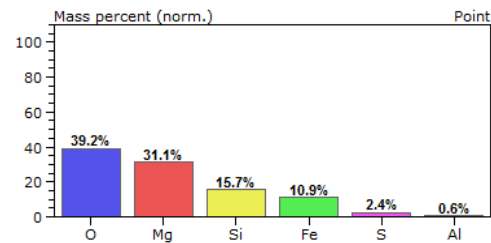
Figure 250. Displays the result of the surface oxide point scans (1-6) using EDS on the surface with 25% FeO-Fe$_2$O$_3$ addition to the magnesium slurry.

The subsurface oxide has a range of elements that vary in concentration. When evaluating the result, a consideration of the interaction volume must be factored in. The large variation seen in iron (9.4-57.3%) can be explained by the interaction volume. Other elements detected in the subsurface oxides are oxygen (13.6-39.5%), magnesium (8.2-31.1%), silicon (3.1-18.4%), aluminum (0.3-11.1%), sulfur (0.0-4.2%)
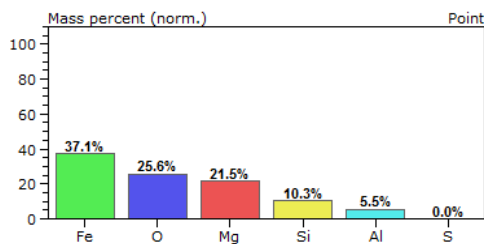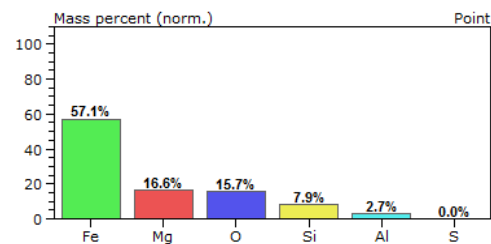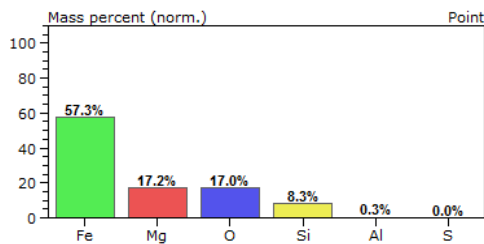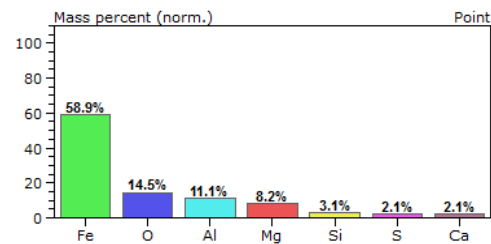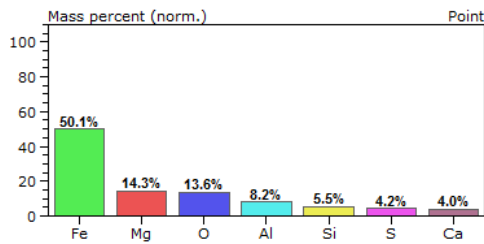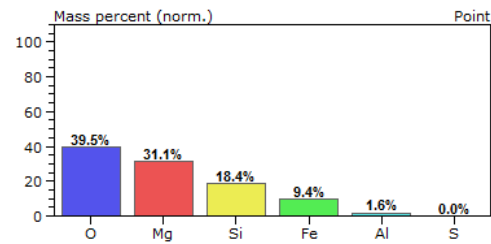
Point scan 11　　　　　　　　**Point Scan 12**

Figure 251. Displays the result of the sub-surface oxide point scans (7-12) using EDS with 25% FeO-Fe$_2$O$_3$ addition to the magnesium slurry.

The analysis conducted on the substrate to evaluate the composition change of the oxide developed when increasing the content FeO-Fe$_2$O$_3$ by EDS has shown no apparent changes to the overall composition of the oxide developed at the surface and subsurface. Additionally, there appears to be no significant increase of iron detected in the surface oxide, even though there is a significant increase of iron present in the applied MgO-FeO-Fe$_2$O$_3$ slurry. However, some care is needed in examining quantitative EDS information due to the interaction volume potentially being larger than the particles of interest, and this data has been used primarily to identify elemental presence rather than quantity.

The point scans have given confidence that the measured oxide layers in Section 5.5 are magnesium-based oxides which are likely to be Forsterite, and the increase in FeO-Fe$_2$O$_3$ has resulted in a change in morphology of the surface oxide with an increase in keying points.

5.5.4   GDOES Analysis of Surface Oxide with FeO-Fe$_2$O$_3$ Addition to the Slurry.

Figure 252 shows the change in concentration of elements through the surface oxide to the iron matrix of a sample that has been coated with MgO slurry with 1% addition of Fe$_2$O$_3$. The magnesium concentration peaks at 19.5% at 0.3 seconds and decreases when etching towards the iron matrix. The line of interception with Mg-Fe occurs at 2.7 seconds.
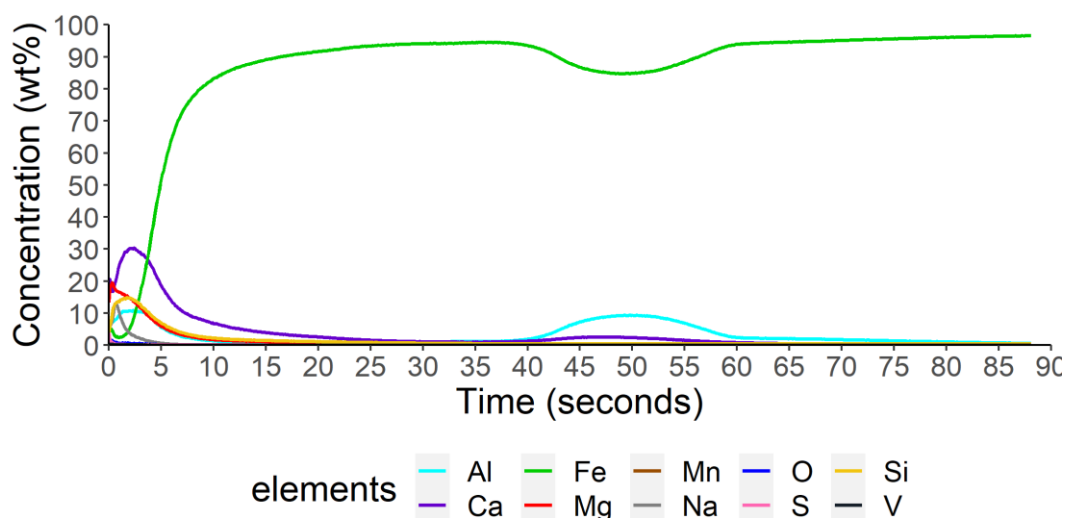
Figure 252. Changes in the chemical composition through the surface and subsurface oxide with 1% addition of Fe$_2$O$_3$ to the magnesium slurry.

214

Silicon reaches a maximum of 14.9% at 1.7 seconds. Aluminum continues the trend of two peaks occurring, and the first peak reaches 10.9% at 2.3 seconds and the second peak at 9.4% at 49.8 seconds.
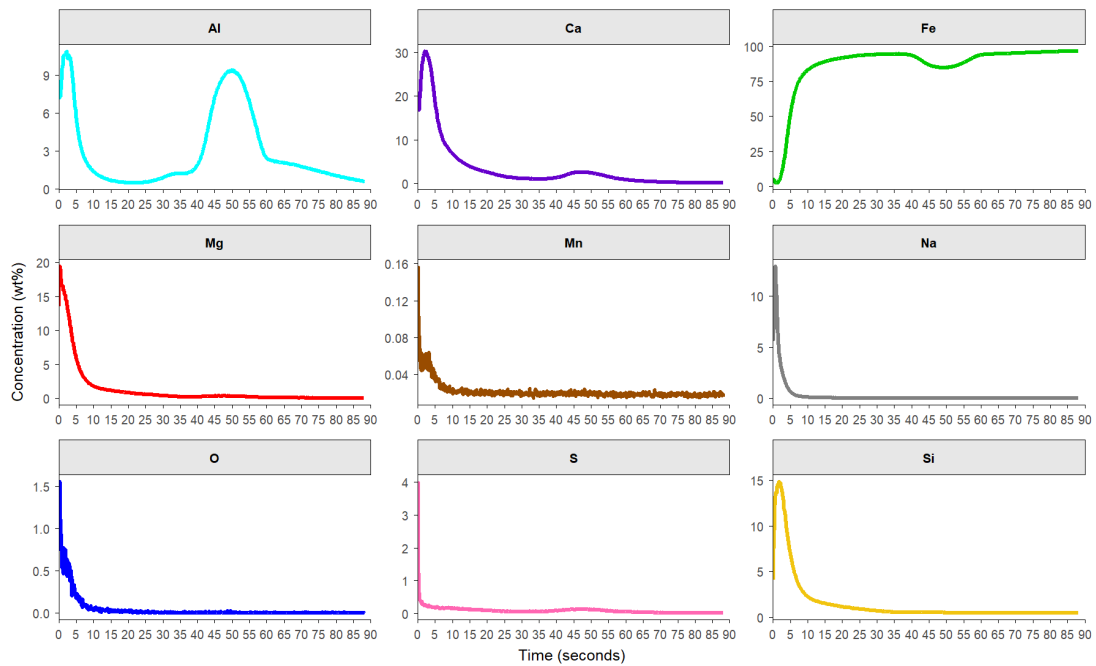
Figure 253. The individual elements of the chemical composition of the surface oxide of a sample that has been coated with 1% Fe₂O₃ addition to MgO slurry.

Figure 254 illustrates the change in concentration of elements through the surface oxide to the iron matrix using GDOES. The magnesium reaches a maximum of 17.0 at 0.4 seconds and intercepts iron at 2.6 seconds. Silicon concentration reaches a maximum of 12.4% at 1.9 seconds.
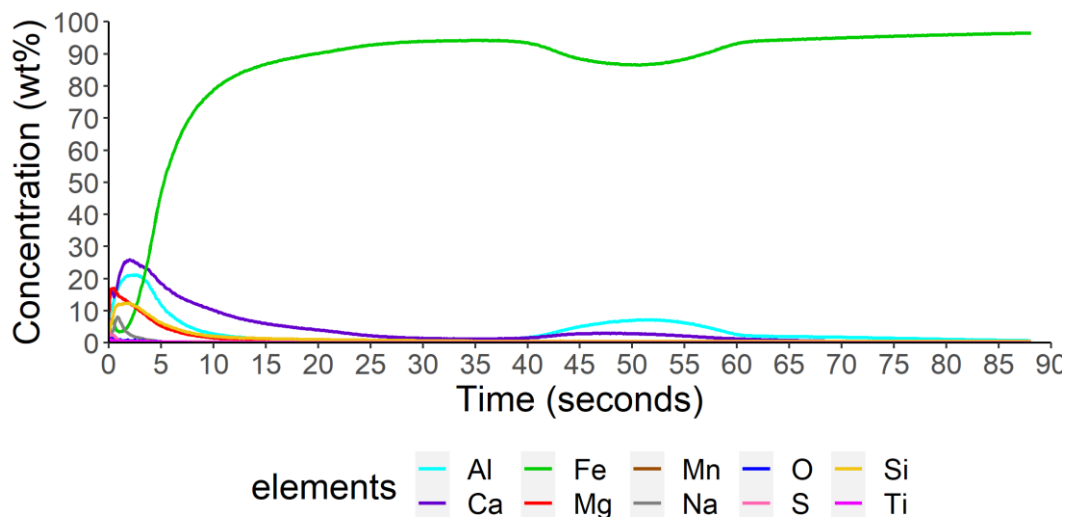
Figure 254. Is the chemical composition through the surface and subsurface oxide, when heat treated in production furnace at Orb Steelworks with 10% addition of Fe₂O₃ to the magnesium slurry Aluminium initially reaches a maximum of 20.9% at 1.9 seconds. A smaller peak occurs at 51 seconds with a concentration of 7.2%.
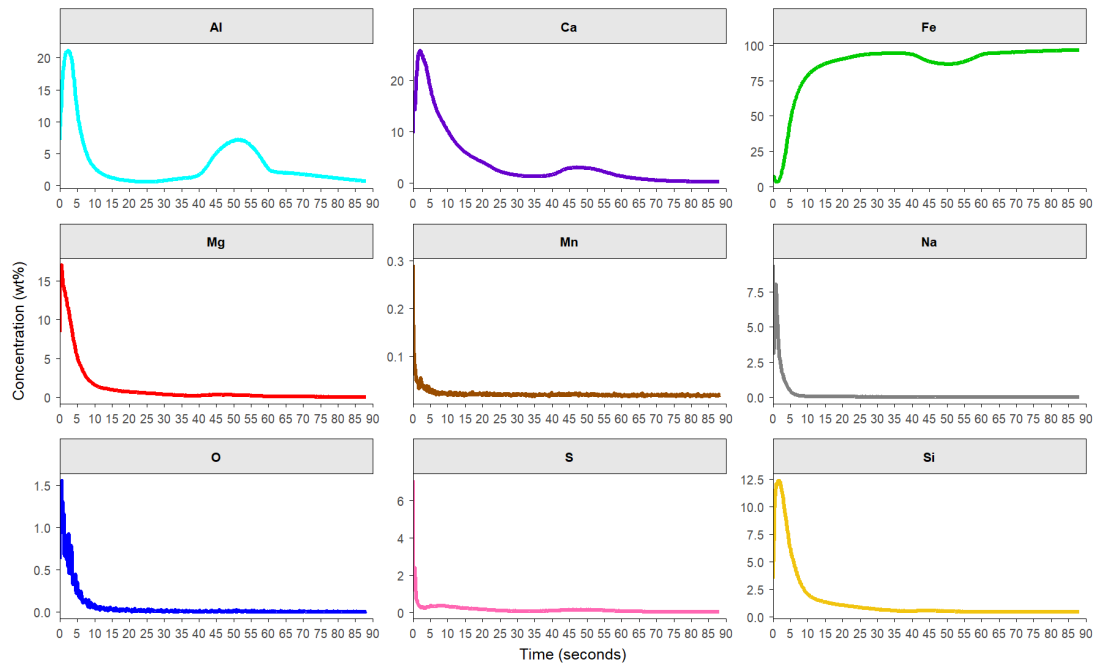
Figure 255. The individual elements of the chemical composition of the surface oxide of a sample that has been coated with 10% Fe_2O_3 addition to MgO slurry.

Figure 256 illustrates the change of chemical composition through the surface oxide to the iron matrix. The magnesium peaks at 19.2 at 0.7 seconds, and the line of interception with iron is at 2.7 seconds.
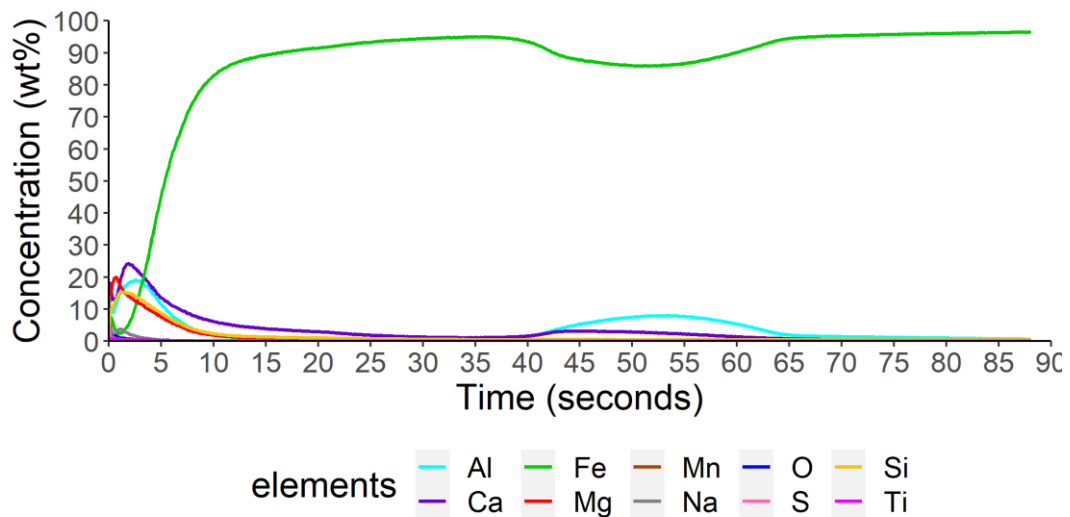
Figure 256. Is the chemical composition through the surface and subsurface oxide with 25% addition of FeO-Fe_2O_3 to the magnesium slurry.

The silicon reaches a maximum of 15.4% at 1.2 seconds. The initial aluminium peak reaches 19.2% at 2.6 seconds and a second peak at 8.0% at 54 seconds.
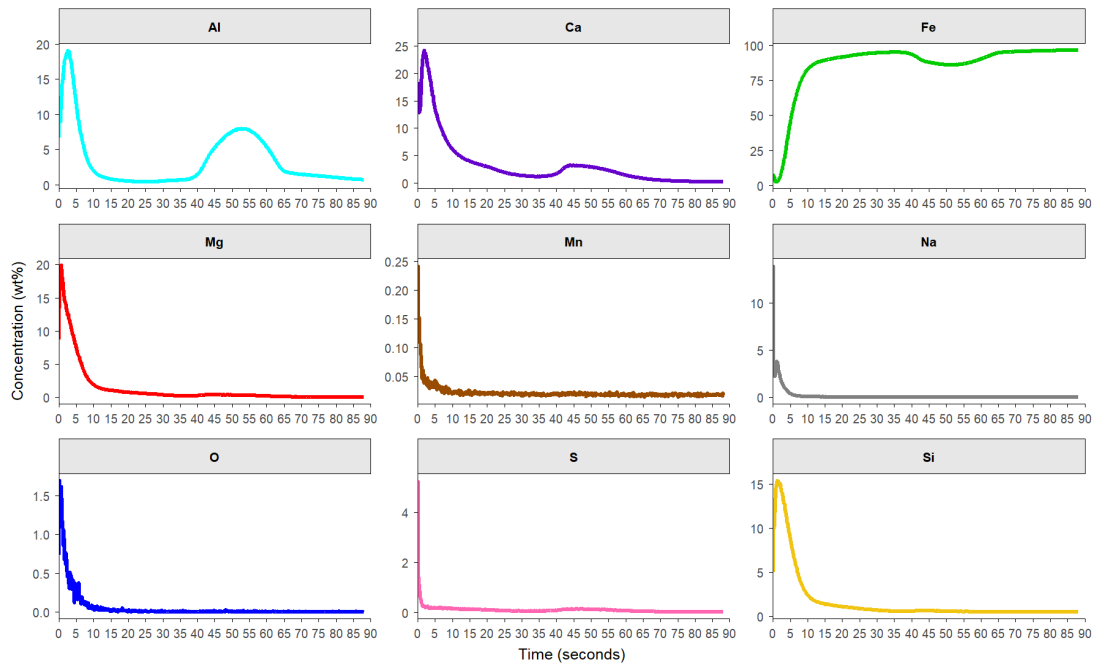
Figure 257. The individual elements of the chemical composition of the surface oxide of a sample that has been coated with 25% Fe_2O_3 addition to MgO slurry.

5.5.5   Magnetic Properties

Figure 258 displays the magnetic properties with the introduction of iron (III) oxide to the magnesium oxide slurry, as explained in 2.8. The increase in iron oxide to the slurry shows no effect on the magnetic properties, with the variance of all the mixes overlapping one another. The results from an F and T-test are displayed in Table 27. The confidence level was set as a P-value of 0.01.
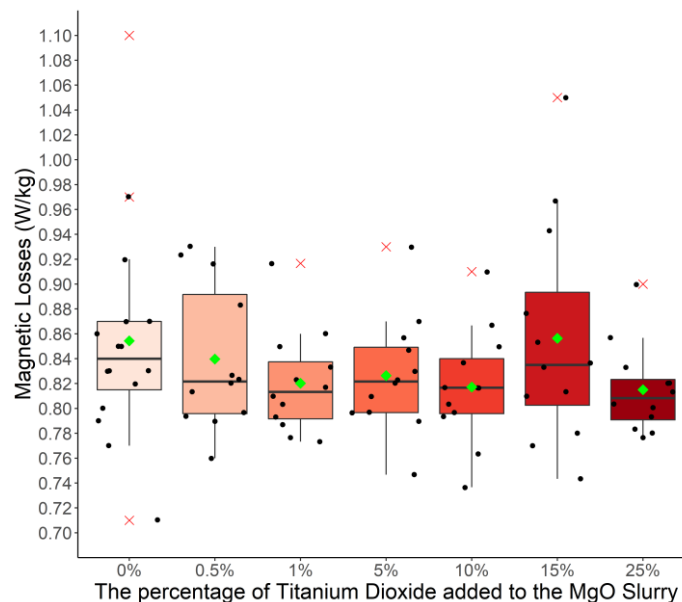
Figure 258. Magnetic properties after heat treatment with various amounts of FeO-Fe_2O_3 additions to the MgO slurry.

Table 27 shows no significant difference in magnetic properties when comparing iron concentrations (II, III) oxide. The average magnetic losses of combined concentration are 0.83 W/kg with a standard

deviation of 0.06. Thus, the introduction of iron oxide to the magnesium oxide slurry does not influence the magnetic properties.

Table 27. Illustrates the significant difference between the different concentrations of FeO-Fe$_2$O$_3$ added to the magnesium slurry using the T-test method.

P = 0.01	Comparing 0% vs 0.5% Iron oxide		Comparing 0.5% to 1% Iron oxide		Comparing 1% to 5% Iron oxide		Comparing 5% to 10% Iron oxide		Comparing 10% to 15% Iron oxide		Comparing 25% to 15% Iron oxide	
	0% Iron Oxide	0.5% Iron Oxide	0.5% Iron Oxide	1% Iron Oxide	1% Iron Oxide	5% Iron Oxide	5% Iron Oxide	10% Iron Oxide	10% Iron Oxide	15% Iron Oxide	15% Iron Oxide	25% Iron Oxide
Mean	0.8544	0.8392	0.8392	0.8200	0.8200	0.8275	0.8275	0.8183	0.8183	0.8558	0.8558	0.8142
Variance	0.0078	0.0034	0.0034	0.0017	0.0017	0.0021	0.0021	0.0021	0.0021	0.0082	0.0082	0.0013
Observations	16	12	12	12	12	12	12	12	12	12	12	12
P(T<=t) two-tail	0.5879		0.3644		0.6790		0.631165056		0.219493475		0.15260263	
F-Test	Un-equal Variance		Un-equal Variance		Un-equal Variance		Un-equal Variance		Un-equal Variance		Un-equal Variance	

5.5.6 Current Detected Through Surface Oxide with FeO-Fe$_2$O3 Addition to the Slurry.

Figure 259 displays the current detected through the surface oxide developed with the addition of FeO-Fe$_2$O$_3$ to the MgO slurry at various concentrations. It is clear to see that just a small 0.5% addition of FeO-Fe$_2$O$_3$ has increased the current detected. However, further increase of concentration of FeO-Fe$_2$O$_3$ does not appear to be further increases in the current detected.
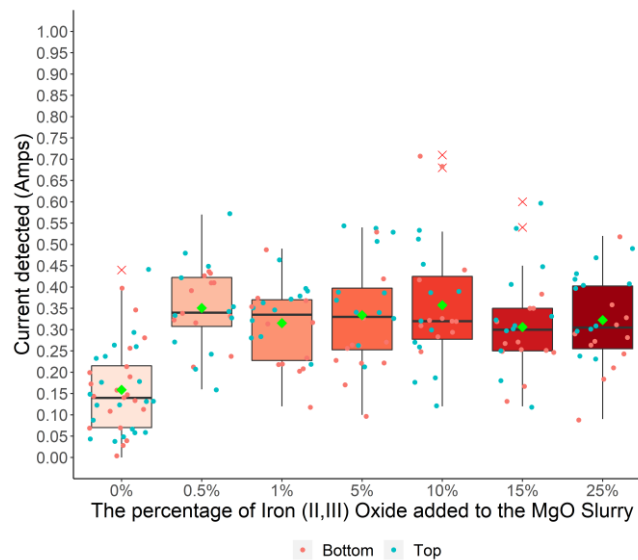
Figure 259. The results of current detected with an increase in FeO-Fe$_2$O$_3$ addition to the slurry using Franklin tester

Figure 259 displays an increase in current detected when 0.5% of iron oxide is introduced to the magnesium slurry. However, further increase of iron oxide does not increase the current detected and, therefore, no further depletion in resistance properties of the oxide layer. This is confirmed when an F and T-test is conducted, confirming no significant difference in performance between the

concentrations of iron oxide and the magnesium oxide slurry. There is a significant difference between the magnesium oxide only slurry and 0.5% iron oxide addition.

Table 28. Illustrates the F and T-test results comparing the significant difference in resistance between FeO-Fe$_2$O$_3$ concentrations added to the slurry.

P = 0.01	Comparing 0% vs 0.5% Iron Oxide		Comparing 0.5% to 1% Iron Oxide		Comparing 1% to 5% Iron Oxide		Comparing 5% to 10% Iron Oxide		Comparing 10% to 15% Iron Oxide		Comparing 15% to 25% Iron Oxide	
	0% Iron Oxide	0.5% Iron Oxide	0.5% Iron Oxide	1% Iron Oxide	1% Iron Oxide	5% Iron Oxide	5% Iron Oxide	10% Iron Oxide	10% Iron Oxide	15% Iron Oxide	15% Iron Oxide	25% Iron Oxide
Mean	0.1588	0.3508	0.3508	0.3154	0.3154	0.3342	0.3342	0.3575	0.3575	0.3063	0.3063	0.3225
Variance	0.0105	0.0095	0.0095	0.0079	0.0079	0.0160	0.0160	0.0204	0.0204	0.0131	0.0131	0.0109
Observations	40	24	24	24	24	24	24	24	24	24	24	24
P(T<=t) two-tail	1.06177E-09		0.195668358		0.555836938		0.552136187		0.177289788		0.609935702	
F-Test	Un-equal Variance		Un-equal Variance		Un-equal Variance		Un-equal Variance		Un-equal Variance		Un-equal Variance	

5.5.7 Bulk Analysis of Carbon, Oxygen, Nitrogen and Sulphur

The carbon concentration has increased with the addition of FeO-Fe$_2$O$_3$ to the magnesium slurry, as shown in Figure 260. The increase in carbon content is likely to be introduced through the FeO-Fe$_2$O$_3$ powder—the presence of carbon in electrical steel results in two phenomenon; domain wall pinning and magnetic ageing. Domain wall pinning introduces resistance of movement of domain rotation resulting in additional magnetic energy to rotate the domains where carbon is present, increasing the hysteresis losses. Magnetic ageing affects the performance of the steel over its lifetime, causing an increase in hysteresis losses, and it has been shown that less than 25ppm of carbon does not worsen the magnetic properties during accelerated ageing experiments [137].
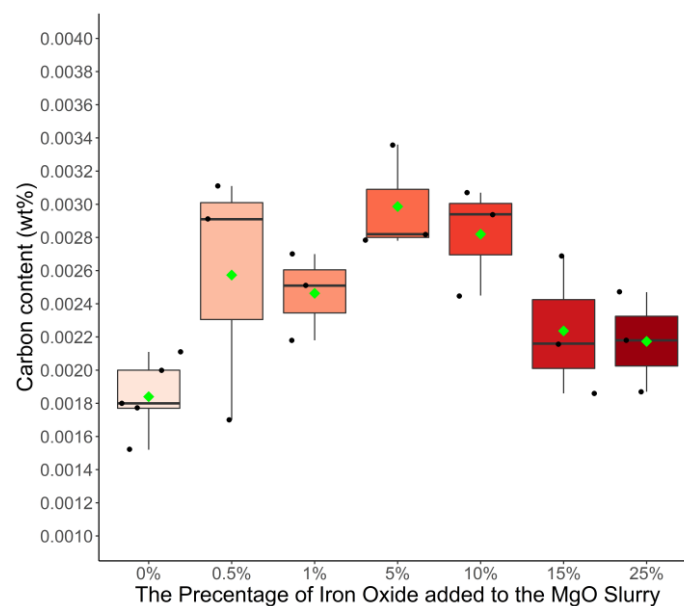
Figure 260. The carbon content present of the bulk substrate at the various times spent at the HTS when coated with FeO-Fe$_2$O$_3$ collected by LECO CS844.

The total nitrogen content (Figure 261)of the substrate tested. The nitrogen content does not change significantly between the magnesium, only a sample and 0.5% - 5% addition of FeO-Fe_2O_3. However, at 10%, there is a significant increase in the nitrogen detected in the bulk of the material. This suggests that some retained nitrogen in the substrate because of the influence of the further increase of FeO-Fe_2O_3.
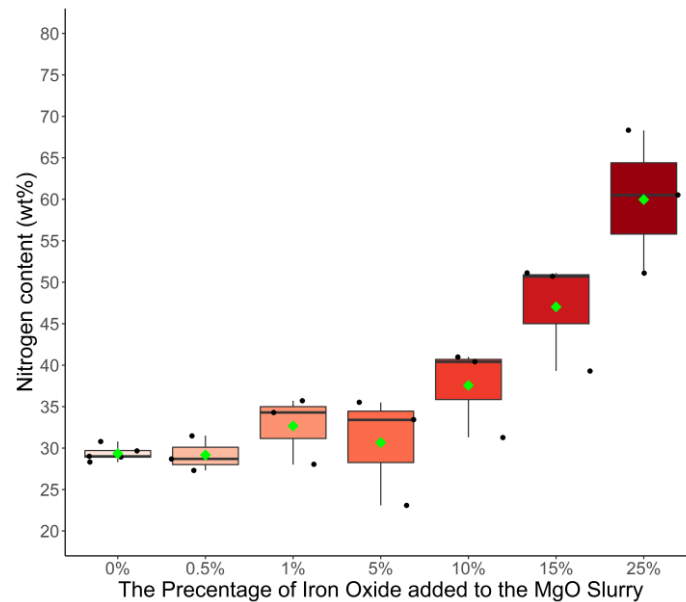
Figure 261. The nitrogen content of the bulk substrate of various concentrations of FeO-Fe_2O_3 was added to the MgO slurry using LECO TN400.

5.5.8 Discussion

The purpose of this research was to determine the influence FeO-Fe_2SiO_4 additions have has on the thickness of the developed oxide and what influence this, as well as any changes in magnetic properties as described. It is not the aim to determine the mechanism in which FeO-Fe_2O_3 acts during the development of the Forsterite. However, it is possible to discuss the findings of this study and examine possible mechanisms that may be occurring during this process.

The addition of FeO-Fe_2O_3 has seen an increase in the thickness of the oxide layer developed. The measured oxide thickness in Figure 239 illustrates that the thickness of the oxide has increased when a 0.5% addition of FeO-Fe_2O_3 was used. Further increase of FeO-Fe_2SiO_4 appears to have no significant improvement, with 15% FeO-Fe_2SiO_4 being the exception with a decrease in oxide thickness compared to other concentrations. The GDOES agrees with the increase in the oxide layer as estimated using the line of intercept of the Mg and Fe. This increases from 2.0 seconds with MgO only and 2.7 seconds in the 1% addition of Fe_2O_3. With further increase of FeO-Fe_2O_3, no improvement is seen in the line of interception between Fe-Mg.

Literature has demonstrated that a reduction in eddy current losses are seen with increased tension, and the effectiveness is dependent on the magnitude of the tension, whereby a low tension applied

reduces the domain size and high-tension levels cause rotation of the magnetization toward the rolling direction, which is believed to cause a reduction of the in-plane eddy current losses[136]. This is relevant because the "Forsterite" oxide layer applies the tension through the difference in thermal coefficient between the Forsterite and the steel substrate and therefore, an assumption that a thicker oxide layer developed would increase tension. Although 0.5 to 10% have developed a thicker oxide layer, there is no apparent improvement in magnetic losses. This lack of improvement may be due to several reasons, the increase in both C and Al content that causes domain wall pinning (immediate impact) and magnetic ageing during its lifetime (delayed impact). In addition, nitrogen detection indicates the possibility of aluminium nitrates still being present because of insufficient substrate purification. If this is the case, the aluminium nitrides will result in domain wall pinning. Nevertheless, additional samples would be needed to give this confidence in this theory.

The second hypothesis is that the levels of Al detected in the GDOES analysis has increased in the 10% and 25% addition to ~20%. This may form alternative oxides such as spinel ($MgAl_2O_4$), which may not have the same thermal coefficient as the desired Forsterite, which would lead to not as effective tension applied to the substrate. However, identifying the exact oxide developed in these Al enriched regions is needed to establish this hypothesis or a direct measure of the tension induced within the coating.

The addition of FeO-Fe_2O_3 has increased the current detected through the surface coating and, therefore, reduced the surface oxide's resistance properties. However, the expectation would be that an increase in FeO-Fe_2O_3 content in the slurry would see a further increase in current detected. This does not hold true. A significant increase in current is detected through the oxide layer when comparing the 0% and 0.5% FeO-Fe_2O_3. With further increase (>0.5%) in the concentration of FeO-Fe_2O_3 has no significant effect on the current detected through the oxide layer developed. The plateau in current detected reflects the oxide thickness with no significant change in thickness between the 0.5% addition to the 25% addition of FeO-Fe_2O_3. Even though large quantities of FeO-Fe_2O_3 does not increase the current detected, it is significant that a small quantity of FeO-Fe_2O_3 has a sizable increase in current detected through the Forsterite oxide layer.

This is significant for the production lines at Orb Steelworks, and care should be taken to minimize contamination of iron particles during the mixing, circulation, and application of MgO slurry with such measures as routine checks on the mixing tanks piping and holding tank. Any signs of possible contamination or signs of corrosion the mix should be disposed of to prevent any resistance issues later in the process.

The concentration of nitrogen detected within the heat-treated samples has significantly increased with an increase in the concentration of FeO-Fe_2O_3. This suggests that the purification of the substrate is not being achieved. It is unclear why or where the nitrogen is being retained within the substrate or

the surface oxide. However, the additional reduction of the FeO-Fe$_2$O$_3$ that has been introduced to the MgO slurry and, therefore, the surface of the substrate may have resulted in a decrease of penetration of the hydrogen into the substrate. Previous studies have shown the importance of gas penetration through the magnesium coating applied to the surface to facilitate purification [136].

The increase in intensity in Mg$_2$SiO$_4$ peak seen in pellets contain Fe compounds in section 1.14 has demonstrate improvements on the surface oxide thickness on test samples. However, the implications on nitrogen content and resistance is detrimental to the overall performance of the electrical steel.

While the addition of FeO-Fe$_2$SiO$_4$ has had a small beneficial effect on the resulting oxide thickness, their opposing influences on the performance of the electrical steel that outweighs the benefits, with a significant reduction in insulation performance and an increase in impurities detected and a null effect on improvements in the magnetic performance.

5.5.9 Conclusion

The FeO-Fe$_2$O$_3$ addition has resulted in a small improvement in oxide layer thickness. However, the improvements expected with a thicker oxide layer is not reflected in the performance of the electrical steel tested. The introduction of FeO-Fe$_2$O$_3$ has resulted in a decrease in resistance and an increase in impurities contained in the substrate resulting in a null effect on magnetic performance. Any signs of contamination of iron particles or an introduction of iron during the coating process of the magnesium slurry should be disposed of to ensure the quality of the Forsterite and prevent any resistivity problems during the quality certification at the end of the process.

Chapter 6.   Overall Conclusion and Future Work

6.1   Overall Conclusion

The objective of this thesis was to enhance the understanding of the development of the Forsterite film throughout the high-temperature annealing process and clarify the influence of additives to the magnesium slurry have on the resulting Forsterite film.

Monitoring the changes at the surface using various analytical techniques has shown the dramatic changes occurring during the high-temperature annealing process. Chapter 3 demonstrated that the first signs of a magnesium-enriched layer develop during the heating phase between 1050°C and 1150°C. The first signs of a distinct magnesium-enriched layer have developed, resulting in the suppression of iron at the surface at 1050°C. Further increases in lead to temperature result in suppression of the iron detected at the surface which indicate a growing magnesium coating, and consequently, there is less detection of current through the magnesium-enriched surface. Simultaneously elements such as silicon and aluminium are diffusing towards the surface. The interrupted annealing during the heating phase of the annealing cycle has demonstrated the breaking down of Al-N through bulk analysis of nitrogen content, and GDOES scans have demonstrated the diffusion of Al towards the surface and forming a part of the surface oxide and subsurface oxide.

Investigation the effects of HTS on surface oxides demonstrated that the minimum soak time required to produce the maximum potential of both magnetic properties and Forsterite film is 10 hours, whereby all three mixes showed a significant reduction in nitrogen content which is an indication of breaking down of Al-N. Because of the decrease in nitrogen content, the magnetic properties have significantly improved. Also, extensive heat treatment does not appear to diminish the performance of the electrical steel, nor the thickness of the Forsterite layer developed. Therefore, Orb Steelworks should aim to get a minimum of 10 hours to soak at the high temperature at the coldest region of the furnace to ensure quality throughout the coils in the furnace. Using this minimum processing requirement and further studies on furnace design and performance, it should be possible to optimise the process, enhance throughput, and reduce costs.

Chapters 3 and 4 also evaluated the recent additions to MgO used by Orb Steelworks, TiO_2 and $Na_2B_4O_7 \cdot 10H_2O$ throughout the annealing process. No significant difference was seen with the introduction of $Na_2B_4O_7 \cdot 10H_2O$ in the magnetic properties or the measured surface oxide. The addition of TiO_2 resulted in detection of it amongst the Mg surface oxide at 1050°C but resulted in little improvement in the magnetic properties and Forsterite development at the high-temperature soak.

Additives on HTA studied the effects of adding TiO_2, V_2O_3 and $FeO\text{-}Fe_2O_3$ at various concentrations, and all demonstrated an improved coating thickness, with mixtures containing TiO_2 and V_2O_3 displaying a thicker surface oxide developing with increasing concentration. The addition of TiO_2

demonstrated improved magnetic properties with less than 5% addition. However, this came at a cost with an increase in current detected through the surface. Upon addition of greater concentrations (>5%), the balance of increased oxide layer thickness was outweighed by a detrimental effect on the current detected through the surface oxide but decreased magnetic performance. This may be explained by the increase in detection of TiO_2 with an increase in the concentration of TiO_2 in the slurry.

The addition of V_2O_3 displayed a small improvement in magnetic properties, and the oxide layer thickness increased. Although the thickness had increased, it came at the expense of uniformity of the surface oxide, where thin or no surface oxide regions developed. It is likely due to thin or no surface oxide resulting in significant current detection even though the coating thickness increases with an increase in the concentration of V_2O_3 regions of thin or no still present in the surface oxide.

The addition of Fe_2O_3 showed a small improvement in measured oxide thickness, however little improvement in the magnetic properties and an increase in current were detected through the surface oxide. An increase in the concentration of Fe_2O_3 displayed a null improvement or slight diminishing in the properties compared with 1% addition of Fe_2O_3.

6.2   Future Work

As with any research of this magnitude, a further question arises from the study. The following briefly introduces several future directions of further investigation.

- Due to the thin oxide development during the heating phase of the annealing process, it was not possible to identify the magnesium oxide as Forsterite. Therefore, a quantitative method such as XPS should be conducted to establish the state of oxidation and whether the oxidation state changes through the depth of the Mg oxide and whether the oxidation state changes with increasing temperature during the heating phase.

- Similarly, other regions of enrichment such as Ti, Al, and S require quantification, and XPS should be conducted on these regions to establish the oxidation states of these enriched areas.

- Further experiments are required at concentrations lesser than 5% TiO_2 to establish the optimum quantity for the balance of improved magnetic properties and resistance.

- For future analysis on Grain Oriented electrical steel for Orb Steelworks using GDOES is recommended, calculating the etching rates, and creating specific standards for the coating of interest would be critical to providing reliability, repeatability, and further quantification of results. This would then allow for Orb Steelworks or another Grain Oriented electrical producer to calculate the thickness of the coatings. This body of work has shown the benefits of using GDOES, which offers a rapid analysis of the surface coating, allowing Orb Steelworks to remove wet chemistry methods to evaluate coating thickness, such as the "Forsterite", which takes a considerable time to prepare and requires Mg free glassware.

- Extensive characterisation of as received raw material and after mixing and drying of MgO and TiO_2 using Thermo Gravimetric Analysis and differential scanning calorimetry (DSC) could provide information about the hydration of the powders and the release of water molecules.

Chapter 7. The Development of Surface oxide During Heating phase of the High-Temperature Annealing Process Interrupted with the addition of Borax to MgO slurry

As the literature has highlighted that the addition of Borax to the MgO slurry has demonstrated improvements in the development of the Forsterite layer Orb Steelworks has added a small quantity of Borax to the MgO slurry for the past 30 years. However, the small quantity added (~0.5% wt%) to the slurry and the uncertain mechanism in which Borax improves the forsterite makes the suggested improvements debatable. This section will investigate the influence of borax during the heating phase of the High Temperature Coil Annealing and what effect it may have on the properties of electrical steel.

7.1 Method

The detail of the method is described in section 3.1.2 and the slurry composition is displayed in Table 29.

Table 29. Illustrates the quantity of ingredients used to create the various percentages of additives to create the desired slurry.

Mix	MgO	TiO$_2$	Na$_2$B$_4$O$_7$10H$_2$O (Borax)	Distilled water (ml)
MgO Only	112g	-	-	800
MgO + Borax	112g	-	0.092g	800

7.2 Scanning Electron Microscope

The cross-sectional SEM images of the developing Forsterite at 950ºC, 1050ºC, 1100ºC and 1150ºC are displayed in **Figure 262**. The fine lamella-spherical structure developed in the decarbonization stage has coarsened at 950ºC. An increase in temperature to 1050ºC displays the first signs of the formation of a thin uniform surface oxide with the presence of subsurface fine and coarse spherical oxide below the surface. Upon a further increase in temperature to 1100ºC minimum change is seen in the surface oxide morphology. At 1150ºC further coarsening of the subsurface continues with a consistent unform surface oxide layer has developed.
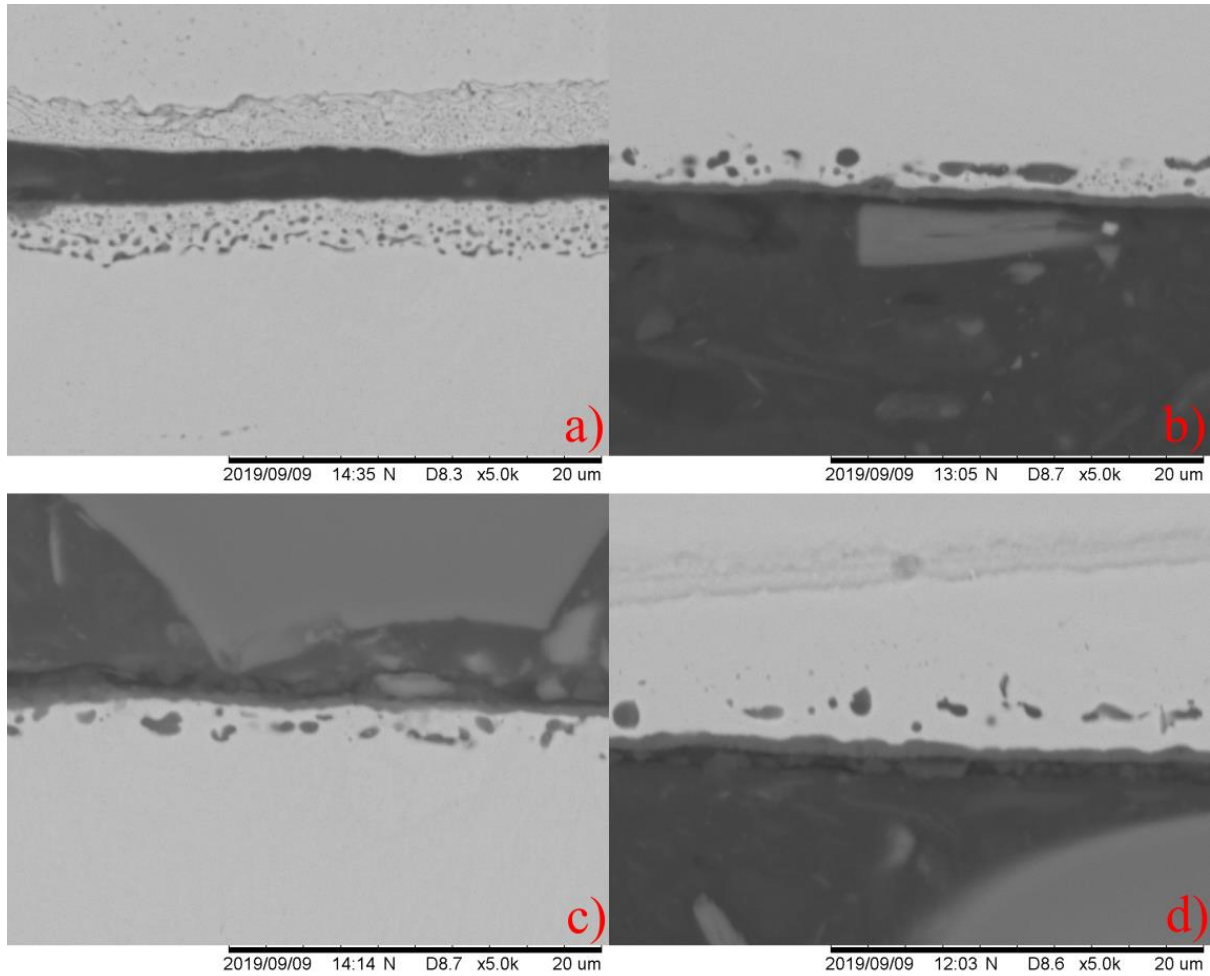
Figure 262. Morphology of the surface oxide at 950°C b) 1050 °C c) 1100°C d) 1150°C through the heating phase of the high temperature coil annealing, that have been coated with MgO + $Na_2B_4O_7 10H_2O$ (Borax).

7.3 Composition Changes through the Surface Oxide using GDOES with Addition of $Na_2B_4O_7 10H_2O$ (Borax) to the MgO Slurry

The chemical composition changes through the substrate during the heating phase from 900°C to 1150°C as observed using GDOES are displayed in **Figure 263** to **Figure 268**. At 900°C signs of Mg are present in the surface at a maximum of 9.9% at 0.1 seconds which immediately decreases. As a of this rapid decrease in concentration of magnesium it is never greater than the iron concentration. Indications of silicon and aluminium diffusing towards the surface are present with an increase in detection of silicon of 5.2% at 0 seconds and aluminium 3.2% at 0.2 seconds.
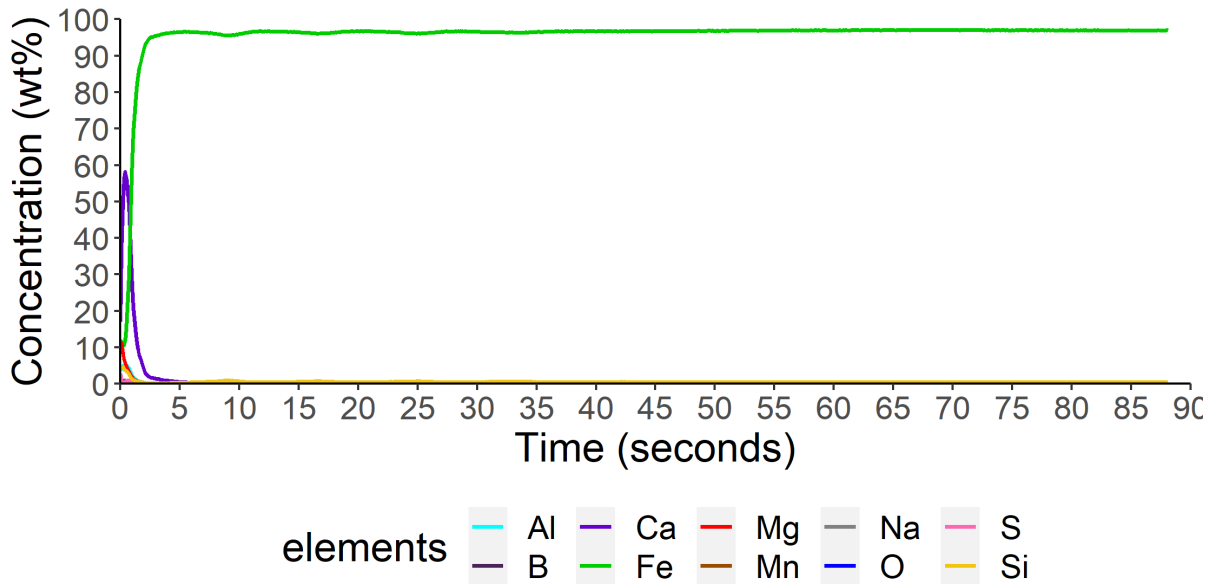
Figure 263. Chemical composition through the surface with borax addition at 900°C.

On close examination of **Figure 263** there is a small presence of sodium at the surface of 2.7% at 0 seconds and immediately reduces to a trace level detected. Equally boron is detected at a concentration of 3.1% at 0 seconds and reduces to <1% detected after 0.1 seconds.
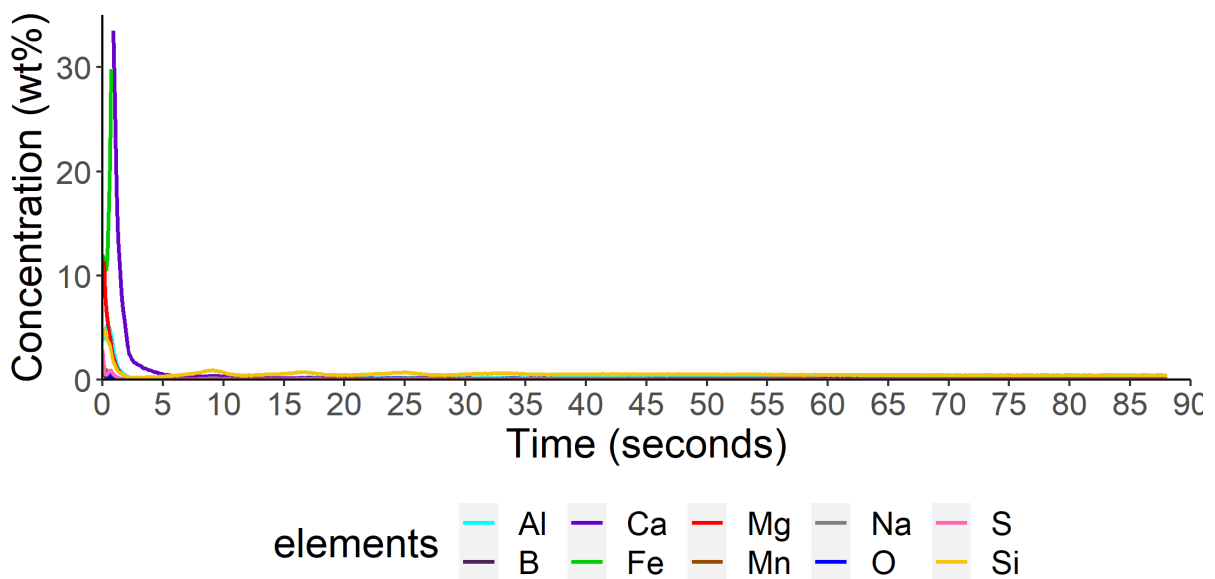
Figure 264. Enhanced plot of chemical composition through the surface with a borax addition at 900°C.

At 1050°C there is an increase in the concentration of magnesium detected at the surface with the maximum of 30.2% at 0.2 seconds. This has resulted in the line of interception occurring between Mg-Fe at 4.2 seconds, indicating a uniform magnesium layer has developed at the surface. The

presence of silicon and aluminium at the surface has also increased with a silicon content of 17.6% at 3.5 seconds and an aluminium content of 5.0% at 1.9 seconds.
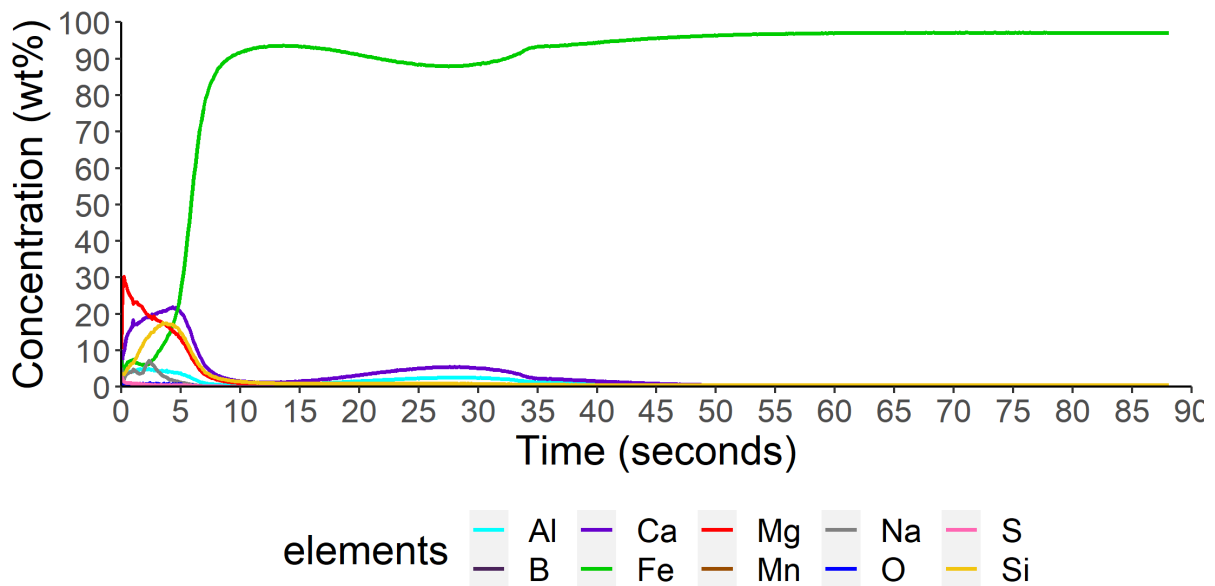
Figure 265. Chemical composition through the surface with borax addition at 1050°C.

Figure 266 shows the detection of elevated levels sodium reaching 7.2% at 2.3 seconds. However, the boron levels detected are low with a maximum concentration detected of 0.65% at 0 seconds.
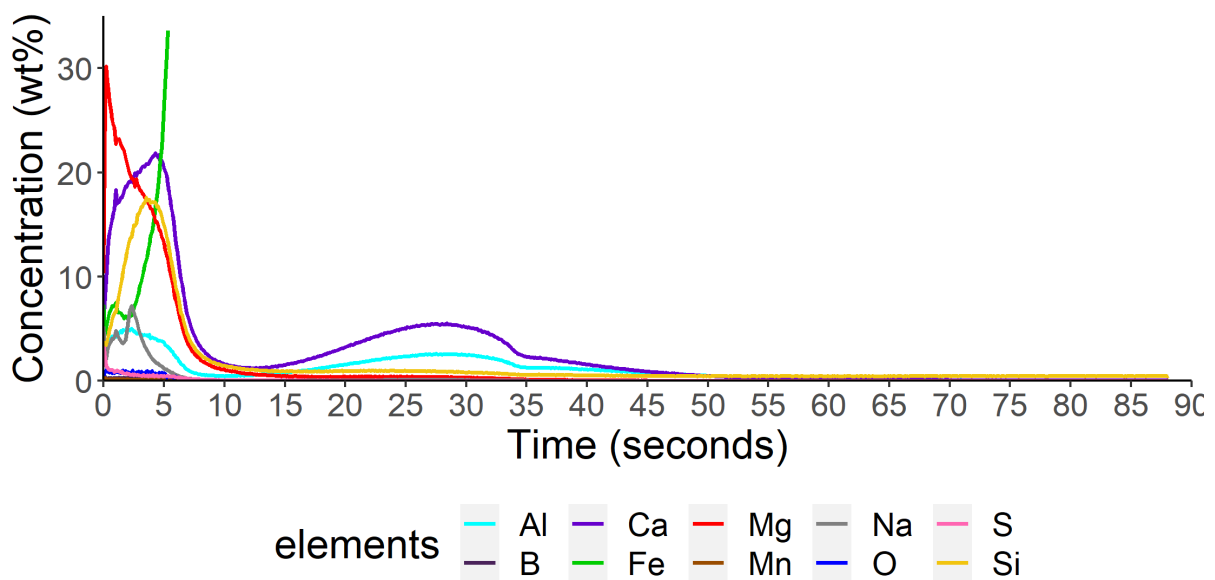
Figure 266. Enhance plot of Chemical composition through the surface with borax addition at 1050°C.

The chemical composition that has formed at 1150°C with borax addition to the MgO slurry is displayed in **Figure 267**. The increase in temperature has delayed the line of interception of Mg-Fe to 5.6 seconds, which indicates a thicker magnesium layer having developed. The presence of

aluminium and silicon continues to increase at the surface with maximum aluminium detected of 29.5% at 5.3 seconds and silicon of 12.3% at 4.3 seconds.
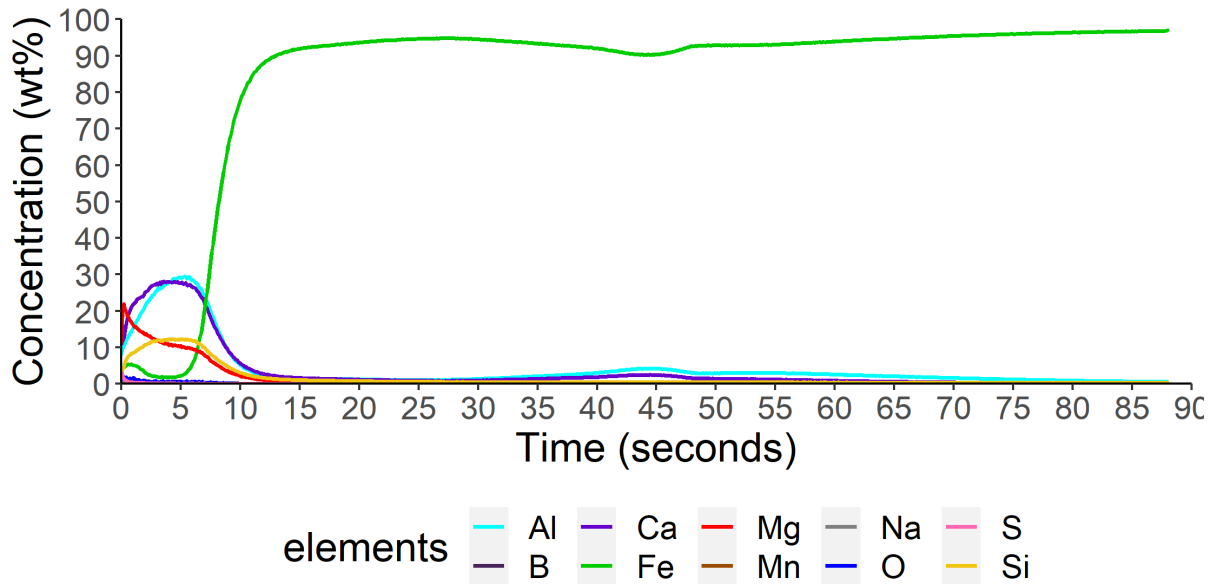
Figure 267. Chemical composition through the surface with borax addition at 1150°C.

The presence of sodium and boron are detected at low levels with boron detected at a maximum of 0.96% and sodium at 1.1%, both at 0 seconds. With no further detection of boron at increased time intervals indicating no borax is present at the region of analysis taken place.
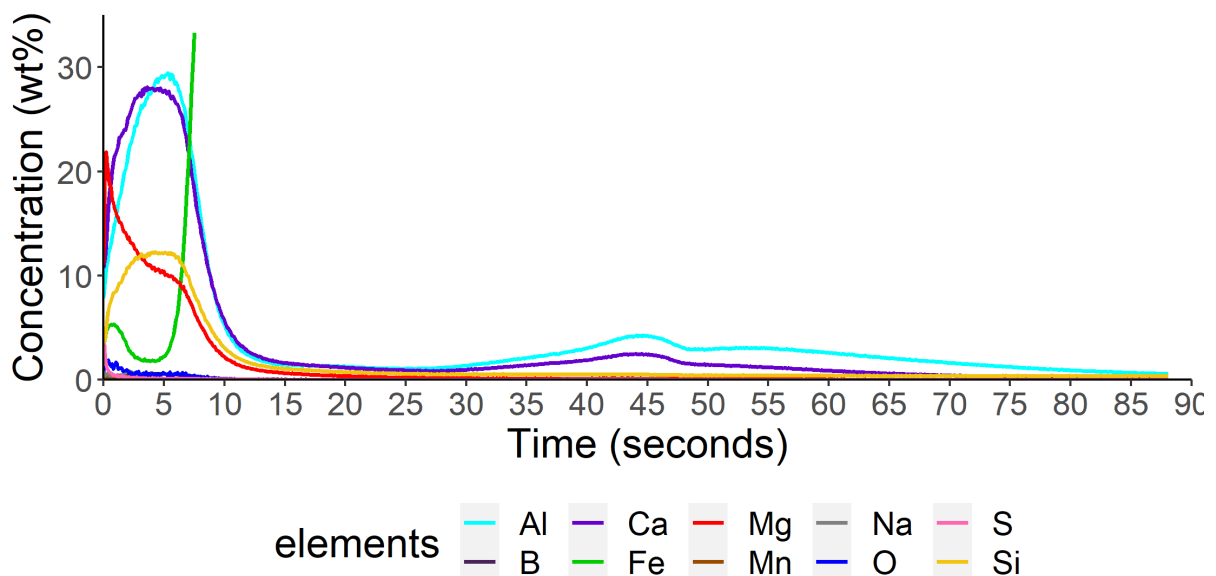
Figure 268. Enhance plot of Chemical composition through the surface with borax addition at 1150°C

7.4 Magnetic Properties

The measured magnetic properties are displayed in **Table 30** of MgO only and MgO + Borax. As previously outlined in Chapter 3 as the temperature increases through the heating phase the magnetic losses begin to decrease which indicates that secondary recrystallization is occurring. The addition of borax to the slurry does not appear to have a significant influence on the magnetic properties during the heating phase with both sets of results being within the error margin for the experiment.

Table 30. Magnetic properties at various temperatures following the HTA heat cycle where the substrate has been coated with MgO + $Na_2B_4O_710H_2O$ (Borax).

Mix	Average magnetic properties detected at various point of the heating phase of the HTA of samples (W/kg)					
	900°C	950°C	1000°C	1050°C	1100°C	1150°C
MgO only	2.88 ± 0.05	2.72 ± 0.05	2.67 ± 0.05	1.81 ± 0.07	1.03 ± 0.06	0.91 ± 0.07
MgO + Borax	2.87 ± 0.05	2.77 ± 0.07	2.75 ± 0.058	1.82 ± 0.07	1.02 ± 0.06	0.90 ± 0.08

7.5 Resistance of surface coating

The increase in temperature has resulted in a decrease in current detected at the surface indicating an insulation layer is developed. When comparing MgO only slurry and borax it does not appear to have any significant improvements on the resistance properties, with the comparative measurements at each temperature being within the margin of error for the measurement.

Table 31. Resistance properties at various temperatures following the HTA heat cycle where the substrate has been coated with MgO + $Na_2B_4O_710H_2O$ (Borax).

Mix	Average current detected at various point of the heating phase of the HTA of samples (amps)					
	900°C	950°C	1000°C	1050°C	1100°C	1150°C
MgO only	0.70 ± 0.06	0.61 ± 0.10	0.31 ± 0.13	0.15 ± 0.10	0.15 ± 0.10	0.08 ± 0.06
MgO + Borax	0.70 ± 0.06	0.62 ± 0.10	0.30 ± 0.13	0.16 ± 0.01	0.16 ± 0.09	0.08 ± 0.06

7.5.1 Bulk Chemical analysis

The level of oxygen and nitrogen content in the samples through the heating phase of the annealing process which have been coated in MgO + Borax is displayed in **Table 32**. The oxygen content after decarburization stage is typically around 700ppm. Between 900°C and 1000ºC the MgO + Borax coated samples display typical oxygen content detected after decarburization stage. At 1050°C there is an increase in oxygen content which continues to increase with increase temperature. When comparing with the MgO only and MgO + Borax slurry there appears no apparent difference in

oxygen content. There are slight differences at 1000°C and 1050°C with MgO only and MgO + Borax slurry but does not amount to statistically significant difference due to the spread.

The trend of decreasing nitrogen content through the heating phase observed in section 3.2.5 is repeated in the MgO + Borax coated samples. With a typical nitrogen content of 250ppm after the decarburization stage at 1000°C. the nitrogen content decreases with increased temperature, at a similar rate to that of the comparison of MgO only.

Table 32. The average nitrogen and oxygen content through various points of the heating phase when coated with MgO only and MgO + Borax.

	Mix	900°C	950°C	1000°C	1050°C	1100°C	1150°C
Oxygen Content (ppm)	MgO only	671.90 ± 21.09	704.2 ±16.59	635.05 ±84.38	725.2 ±17.92	911.75 ±98.30	1024.8 ±72.01
	MgO + Borax	720.19 ±37.16	690.41 ±54.19	814.6 ±93.23	866.60 ±76.28	933.33 ±105.59	1089.20 ± 34.75
Nitrogen Content (ppm)	MgO only	237.2 ±4.35	227.2 ±6.37	179.8 ±27.97	172.0 ±9.21	130.75 ±2.49	93.02 ±1.04
	MgO + Borax	216.0 ±6.2	211.0 ±15.8	182 ± 18.7	159.0 ±19.2	131.0± 3.6	98.8 ± 5.3

The level of carbon and sulphur content in the samples through the heating phase of the annealing process which have been coated in MgO + Borax is displayed in **Table 33**. The carbon remains consistently low, and no change is seen with the addition of borax to the slurry throughout the heating phase of the anneal. The sulphur content does show signs gradually decrease when temperatures are elevated >1050°C. However, due to the limited amount of test conducted a significant difference could not be determined. The addition of borax has not affected the content detected in the substrate when compared with the MgO coated samples through the temperature range tested.

Table 33. The average carbon content and sulphur content through various points of the heating phase when coated with MgO only and MgO + Borax slurry.

	Mix	900°C	950°C	1000°C	1050°C	1100°C	1150°C
Carbon Content (ppm)	MgO only	0.0009 ±0.0000	0.0010 ±0.0002	0.0009 ±0.0001	0.0011 ±0.0002	0.0013 ±0.0001	0.0012 ±0.0003
	MgO + Borax	0.0012 ±0.0002	0.0009 ±0.0001	0.0013 ±0.0001	0.0015 ± .0002	0.0013 ±0.0002	0.0013 ±0.0001
Sulphur Content (wt%)	MgO only	0.0060 ±0.0003	0.0060 ±0.0001	0.0049 ±0.0022	0.0055 ±0.0005	0.0042 ±0.0002	0.0039 ±0.0003
	MgO + Borax	0.0060 ±0.0002	0.0060 ± .0003	0.0058 ±0.0006	0.0049 ±0.0000	0.0043 ±0.0011	0.0035 ±0.00028

7.6   Discussion

The purpose of this research was to clarify the claims of $Na_2B_4O_7 10H_2O$ (Borax) in patents of improving the glass film as shown in the literature review and the apparent improvements seen at Orb

Steelworks production material. After conducting a series of tests, the improvements claimed by Orb Steelwork and patients of the small addition (0.5 wt%) $Na_2B_4O_7 10H_2O$ (Borax) is not apparent during the heating phase of the HTCA.

The addition of $Na_2B_4O_7 10H_2O$ (Borax) to the slurry does not appear to change the surface morphology through the heating phase as seen in **Figure 262**, when compared with the MgO only slurry in section 4.3. The melting point of $Na_2B_4O_7 10H_2O$ is 743°C and would expect the influence of $Na_2B_4O_7 10H_2O$ to be throughout the heating phase and affect the morphology of the surface oxide. The minimal changes observed in the morphology is reflected in the surface analysis using GDOES, with the presence of sodium and boron at low levels throughout all the scan with the maximum sodium detect of 7% and primarily at the surface. This indicates that the $Na_2B_4O_7 10H_2O$ (Borax) is not developing alternative surface oxide as seen in with TiO_2 section 5.3. Additionally, there is no statistical changes in the carbon, oxygen, nitrogen, and sulphur content when compared with the MgO only coated samples.

The trend seen section 3.2.3 of improving magnetic properties and decreasing current detected when increase temperate through the heating phase of HTCA continues with the addition of $Na_2B_4O_7 10H_2O$. Notably there is no signs of improvements when compared with MgO only coated samples which is contrary to claims of significant improvements by patients and Orb Steelworks. Due to the small sample number when compared with the production quantity it is possible that $Na_2B_4O_7 10H_2O$ does have an improvement effect on consistency of the glass film and magnetic properties but is only evident in larger data plot, but at the sample sizes examined in this work the results are not statistically different.

7.7 Conclusion

The claims that literature and Orb Steelworks that a small addition of $Na_2B_4O_7 10H_2O$ (borax) have a significant improvement on glass film and magnetic properties have not been demonstrated in this study. The addition of $Na_2B_4O_7 10H_2O$ is inconclusive and does not exhibit a measurable improvement or deterioration of properties of the steel or surface oxide.

Chapter 8. The Influence of High Temperature Soaks when using MgO and Na₂B₄O₇10H₂O Coating

8.1 Introduction

As outlined in section 1.14 $Na_2B_4O_7 10H_2O$ (Borax) is a common additive stated in patients and a small quantity of $Na_2B_4O_7 10H_2O$ (Borax) is added to Orb Steelwork slurry. The small addition of $Na_2B_4O_7 10H_2O$ (Borax) has been claimed to improve glass film formation and improve magnetic properties. However, details on the mechanism and temperature that $Na_2B_4O_7 10H_2O$ (Borax) is not known. This section is investigating what effect the addition of $Na_2B_4O_7 10H_2O$ (Borax) to the slurry has during an extended period at high temperature.

8.2 Method

The detail of the method is described in section 4.2 and the slurry composition is displayed in Table 29.

Table 34. Illustrates the quantity of ingredients used to create the various percentages of additives to create the desired slurry.

Mix	MgO	TiO₂	Na₂B₄O₇10H₂O (Borax)	Distilled water (ml)
MgO Only	112g	-	-	800
MgO + Borax	112g	-	0.092g	800

8.3 Coating thickness with MgO + Borax slurry

The measurements of the surface oxide layers of cross-sections coated with MgO + $Na_2B_4O_7 10H_2O$ (Borax) and exposed to a period of HTA are displayed in Table 35. The extended soak time at the HTA with the addition of $Na_2B_4O_7 10H_2O$ has had limited or no effect on the measured coating thickness. Similarly, when comparing with the MgO only samples throughout the various duration soaks there is no significant difference between the MgO only slurry and the MgO + $Na_2B_4O_7 10H_2O$ slurry coated samples.

Table 35. The average measured SEM cross-section of samples that have been coated with MgO + Na₂B₄O₇10H₂O and heat-treated at various duration of soak at the HTS.

Mix	Average measured surface oxide thickness (µm)							
	5 hours	10 hours	20 hours	25 hours	30 hours	40 hours	45 hours	50 hours
MgO only	0.79 ± 0.16	0.79 ± 0.11	0.94 ± 0.16	0.91 ± 0.18	1.04 ± 0.17	0.80 ± 0.15	0.98 ± 0.34	1.07 ± 0.22
MgO + Borax	0.70 ± 0.08	0.92 ± 0.17	0.85 ± 0.19	0.82 ± 0.15	0.95 ± 0.12	0.87 ± 0.18	0.82 ± 0.14	0.88 ± 0.18

8.4 Scanning Electron Microscope

The cross-section SEM images of the resulting forsterite when exposed for a) 5 hours b) 25 hours c) 40 hours and 50 hours soak at the high temperature anneal are shown in **Figure 269**. All four heat treatments display a uniform oxide layer developed at the surface of the substrate and coarse spherical

oxide below the surface oxide. The addition of $Na_2B_4O_7 \cdot 10H_2O$ (Borax) does not have any clear influence in the morphology of the surface oxide nor the subsurface oxide. The insignificant statistical differences displayed in Table 29 is reflected in the SEM images in Figure 1, with no obvious increase in thickness. Comparing the MgO slurry and MgO + $Na_2B_4O_7 \cdot 10H_2O$ (Borax) there is no significant difference throughout the extended soaks, indicating that the addition of $Na_2B_4O_7 \cdot 10H_2O$ to slurry has had a limited effect.
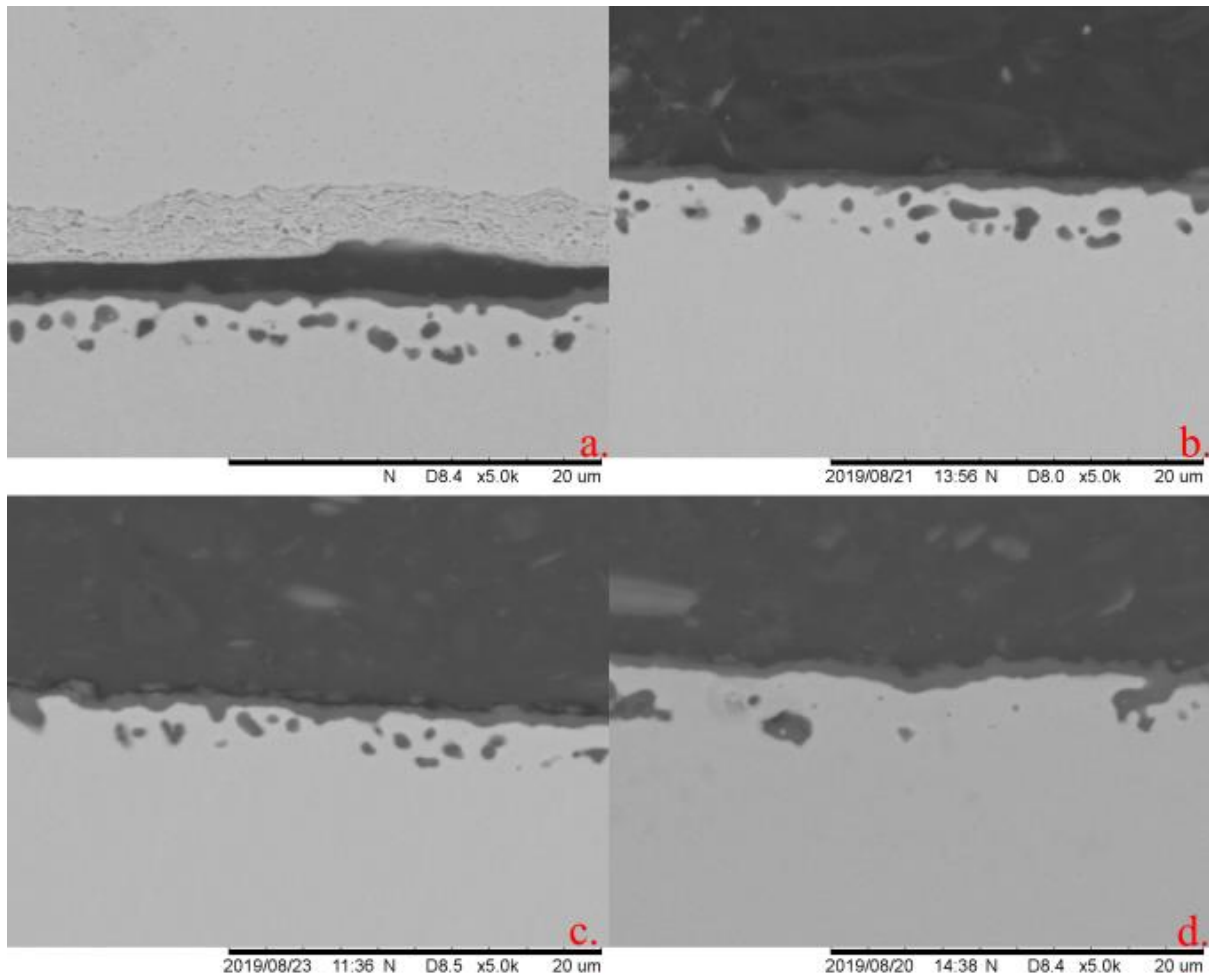
Figure 269. Morphology of the surface oxide exposed to a) 5 hours b) 25 hours c) 40 hours d) 50 hours high temperature soak that have been coated MgO + $Na_2B_4O_7 \cdot 10H_2O$ (Borax).

8.5 Glow Discharge Optical Emission Spectroscopy (GDOES)

The chemical composition changes through the substrate when exposed to an extended soak at 5, 25 and 50 hours is displayed in Figure 270 through Figure 275 using GDOES analysis. The sample that has been exposed to 5 hours soak have developed a Mg enriched layer at the surface that suppresses the iron concentration where the Mg-Fe line of interception occurs at 5.1 seconds and the Mg concentration reaches a maximum of 13.5% at 4.3 seconds. During the suppression of Fe two major

elements are present Al and Si, whereby Al reaches a maximum of 32.8% at 2 seconds and Si at 16.6% at 4.5 seconds.
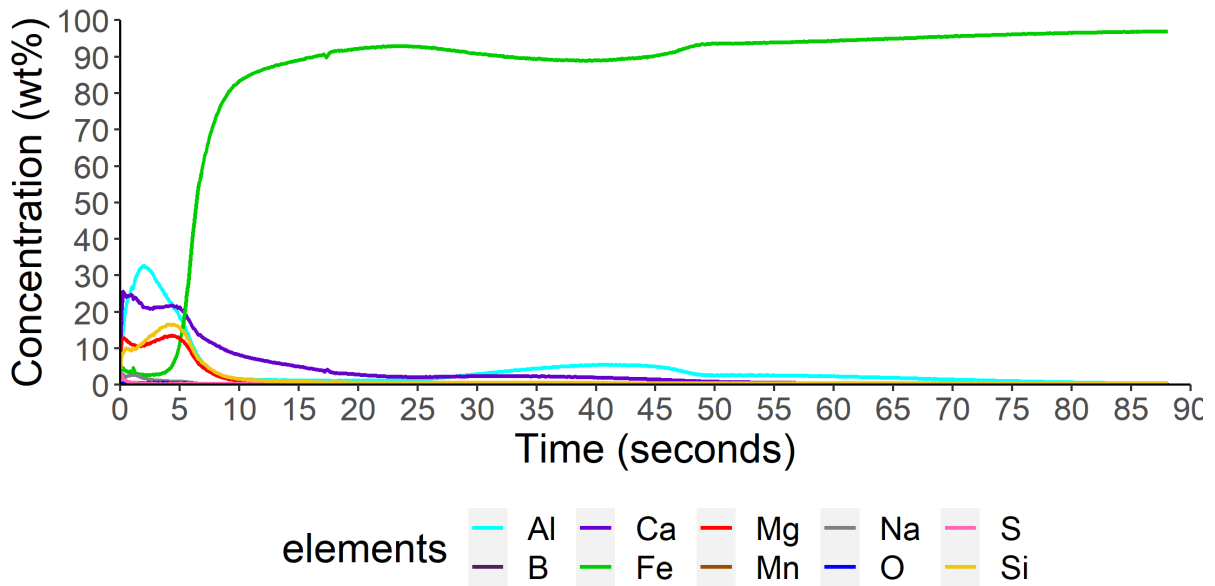
Figure 270. Chemical composition through the surface with borax addition after 5 hours at HTS.

On close examination of Figure 270 there is detection of Na at 1.9 seconds at a concentration of 3.3% and only a 0.55% at 0 seconds detection of B. A secondary Al peak is detected at 40 seconds where the concentration reaches a maximum of 5.57%.
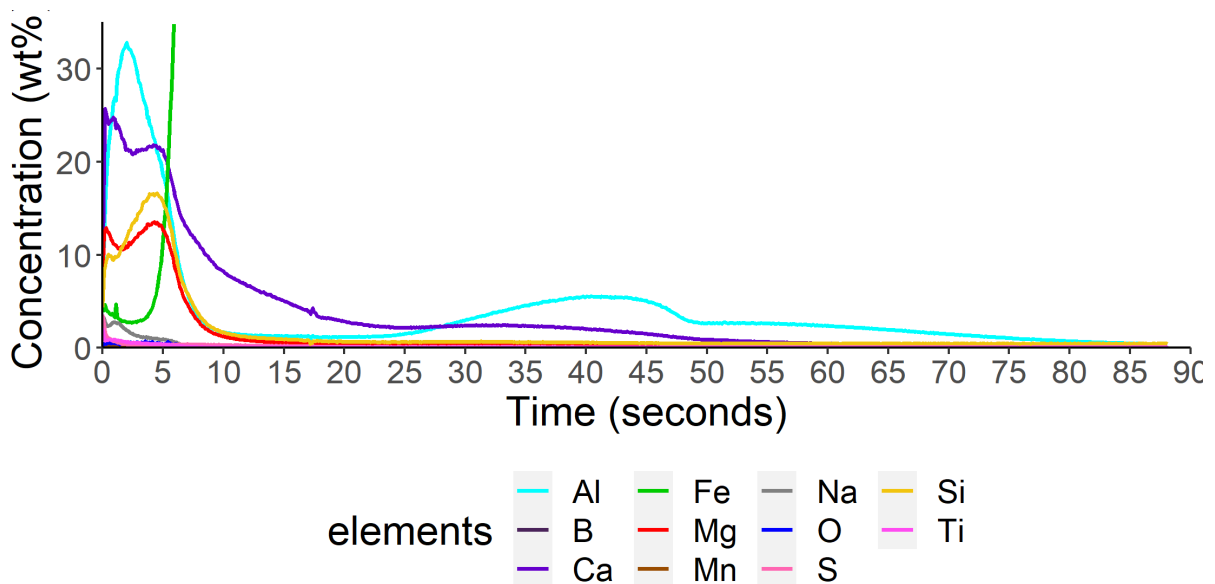
Figure 271. Enhance plot of Chemical composition through the surface after 5 hours at HTS.

The composition of samples that have been coated with $MgO + Na_2B_4O_710H_2O$ and exposed to a 25 hours HTA is displayed in Figure 4. The line of interception of Mg-Fe occurs at 3.8 seconds, where

the Mg$_{max}$ is 15.9 at 3.2 seconds. The presence of aluminium and silicon is detected at the surface with detection of maximum aluminium of 7.4% at 1.5 seconds and silicon of 17.7% at 5 seconds.
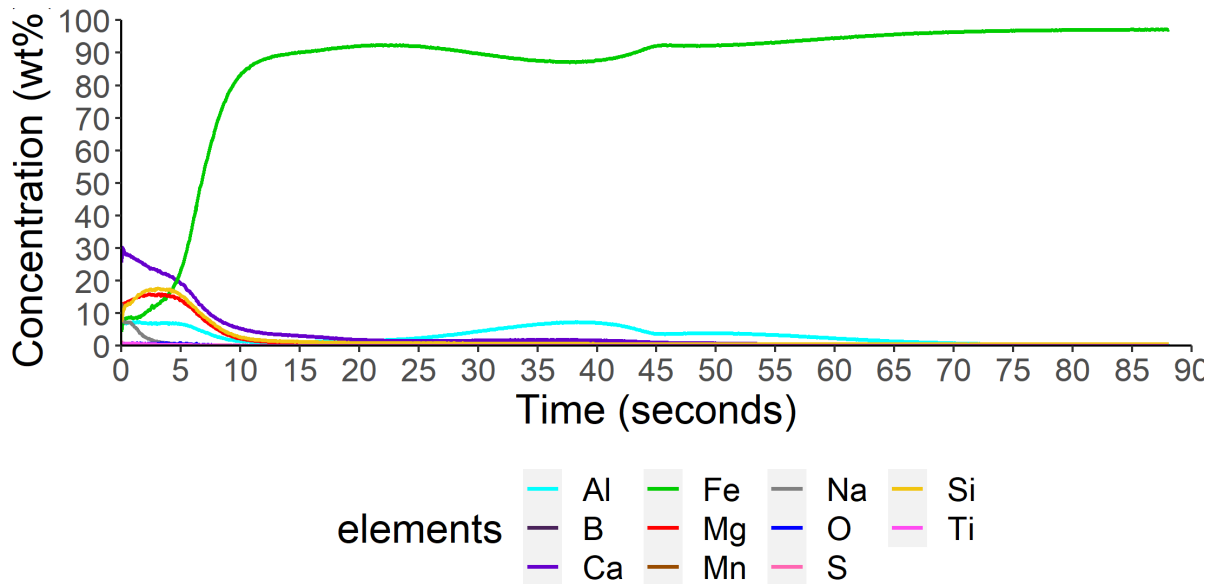
Figure 272. Chemical composition through the surface with borax addition after 25 hours at HTS.

Boron is present at a trace level with a maximum of 0.2% at 0 seconds and Sodium is detected at 12% at 0 seconds and becomes <1% by 3.5 seconds.
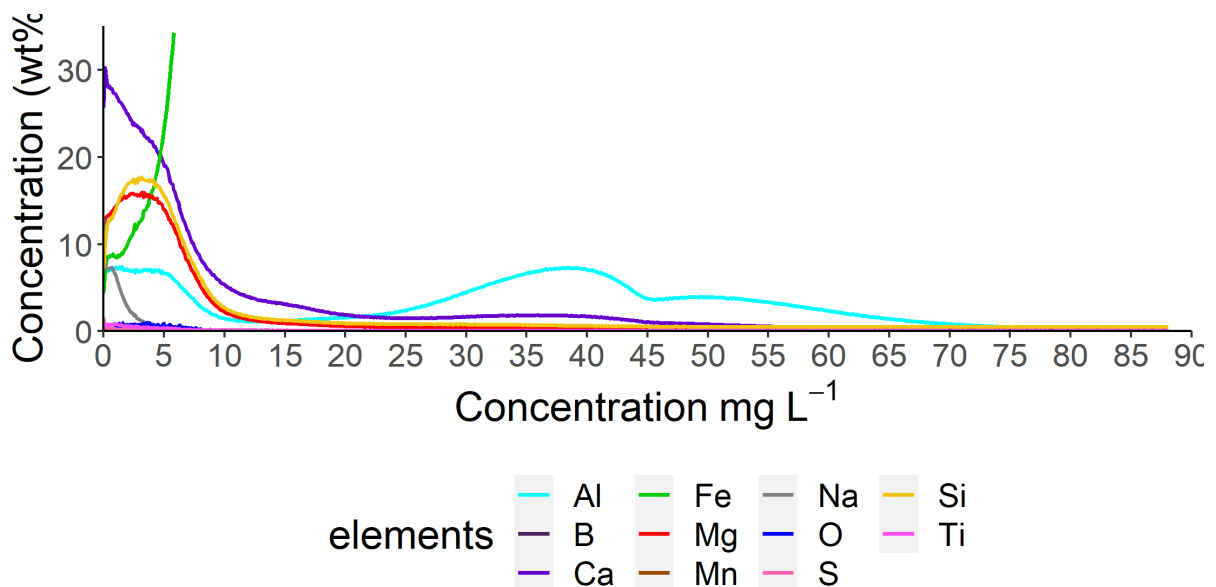
Figure 273. Enhance plot of Chemical composition through the surface after 25 hours at HTS.

At the maximum duration of the soak of 50 hours the Mg-Fe line of interception occurs at 2.7 seconds, whereby by the maximum Mg content detect is 15.7 at 0.6 seconds. The consistent levels of Si and Al detected maximum concentration of Al of 23.2% at 2.6 seconds and Si at 12.3% at 1.8 seconds.
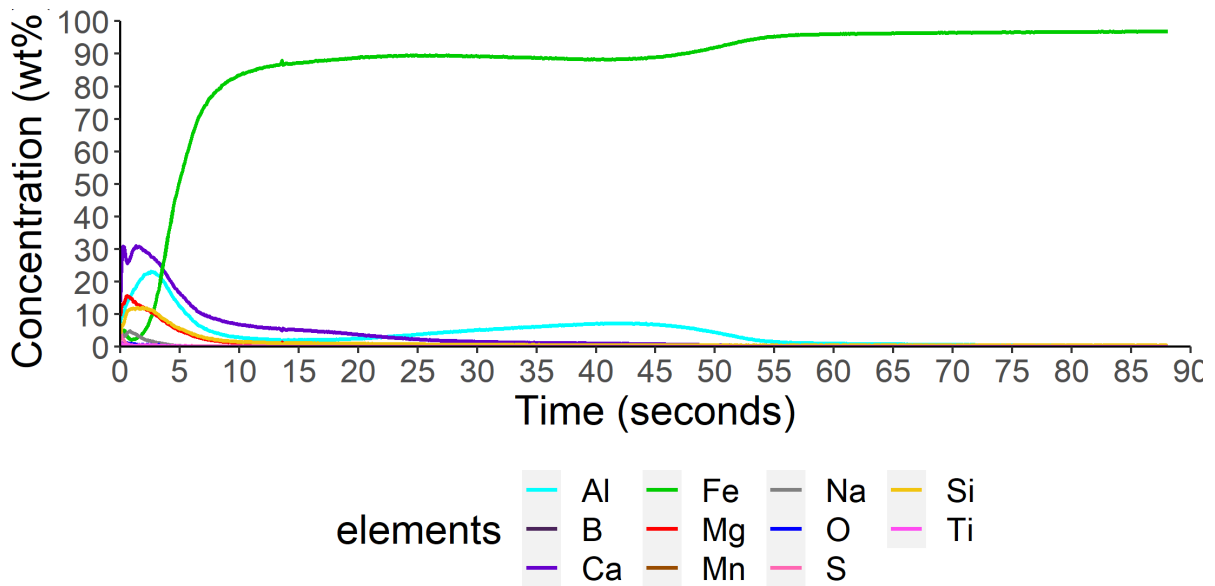
Figure 274. Chemical composition through the surface with borax addition after 50 hours at HTS.

The presence of sodium is detected at high levels of 6.1% at 0 seconds and drops to <1% by 3.5 seconds. Trace levels of B is detected at a maximum 0.5% at 0 seconds.
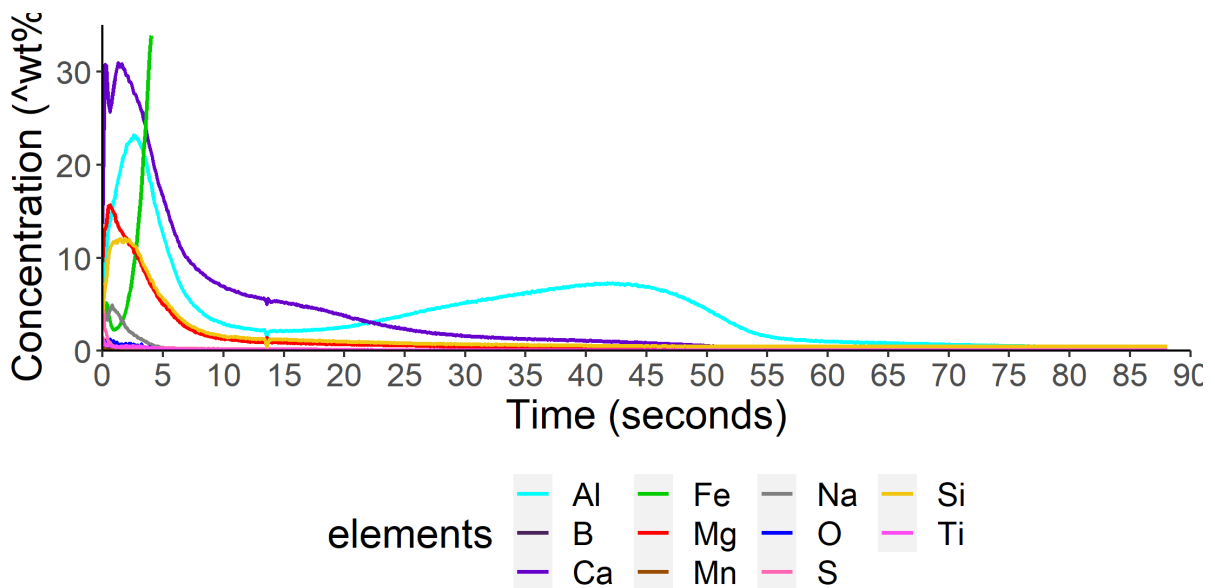
Figure 275. Enhance plot of Chemical composition through the surface after 50 hours at HTS.

The chemical analysis of the depth profile using GDOES shows that both Boron and Sodium are detected at trace levels at the surface of the samples, but that this quickly reduces through the analysis, indicating that the borax is not incorporated into the coating, but is simply present at the surface. This is consistent across the soak durations of interest. There is no significant difference in the coating chemical make up as detected by GDOES when borax is added to the slurry when compared to a slurry with no borax additions.

8.6 Magnetic Properties

The magnetic properties of samples that were coated with MgO + $Na_2B_4O_7 10H_2O$ slurry and then exposed to various duration at the HTA is displayed in Table 36. The samples that are coated with MgO + $Na_2B_4O_7 10H_2O$ do not display any significant changes with an increase in temperature and therefore display no benefit in magnetic properties when borax additions are made. Similarly, the addition of $Na_2B_4O_7 10H_2O$ has not affected magnetic properties when compared with the MgO slurry.

Table 36. Magnetic properties after an extended periods at HTA where the substrate has been coated with MgO + $Na_2B_4O_7 10H_2O$ (Borax).

Mix	Average magnetic properties detected at various point of the heating phase of the HTA of samples (W/kg)							
	5 hours	10 hours	20 hours	25 hours	30 hours	40 hours	45 hours	50 hours
MgO only	0.93 ±0.10	0.85 ±0.08	0.86 ±0.05	0.83 ±0.05	0.87 ±0.06	0.87 ±0.07	0.86 ±0.04	0.89 ± 0.06
MgO + Borax	0.87 ±0.07	0.85 ±0.07	0.84 ±0.06	0.82 ± 0.05	0.84 ±0.05	0.85 ±0.09	0.86 ±0.07	0.83 ± 0.05

8.7 Bulk Chemical analysis

The carbon and sulphur content of samples that are coated with MgO + $Na_2B_4O_7 10H_2O$ and exposed to an extended period at HTS are displayed in Table 37. The samples coated with MgO + $Na_2B_4O_7 10H_2O$ do not display any significant changes in carbon content or sulphur content when exposed for increasing time at high temperature. Additionally, the introduction of $Na_2B_4O_7 10H_2O$ has not affected the carbon or sulphur content when comparing with the MgO only slurry.

Table 37. The average carbon content and sulphur content of samples that have been coated with MgO + $Na_2B_4O_7 10H_2O$ and heat-treated at various duration of soak at the HTS.

	Mix	5 hours	10 hours	20 hours	25 hours	30 hours	40 hours	45 hours	50 hours
Carbon Content (ppm)	MgO only	0.0042 ± 0.0052	0.0034 ± 0.0053	0.0054 ± 0.0054	0.0028 ± 0.0006	0.0027 ± 0.0002	0.0019 ± 0.0003	0.0046 ± 0.0024	0.0054 ± 0.0020
	MgO + Borax	0.0042± 0.0009	0.0082± 0.0072	0.0059 0.0002	0.0050± 0.0045	0.0024 ± 0.0004	0.0017 ± 0.0009	0.0076 ± 0.0048	0.0016± 0.00127
Sulphur Content (wt%)	MgO only	0.0017 ± 0.0008	0.0022 ±0.0012	0.0024 ± 0.0008	0.0020 ± 0.0006	0.0035 ± 0.0008	0.0029 ± 0.0002	0.0023 ± 0.0007	0.0029 ± 0.0003
	MgO + Borax	0.0019± 0.0004	0.0016 ± 0.0003	0.0030 ± 0.0007	0.0020± 0.0003	0.0031± 0.0003	0.0030 ± 0.0001	0.0027 ± 0.0005	0.0031 ± 0.0003

The oxygen and nitrogen content of samples that are coated with MgO + $Na_2B_4O_7 10H_2O$ and exposed to an extended period at HTS are displayed in Table 38. The extended period of at high temperature has not demonstrated any significant changes in the oxygen content and nitrogen content. The addition of $Na_2B_4O_7 10H_2O$ to the slurry significantly alter the oxygen and nitrogen content when compared with samples that have been coated with MgO only.

Table 38. The average oxygen content and nitrogen content of samples that have been coated with MgO + Na$_2$B$_4$O$_7$10H$_2$O and heat-treated at various duration of soak at the HTS.

	Mix	5 Hours	10 hours	20 hours	25 hours	30 hours	40 hours	45 hours	50 hours
Oxygen Content (ppm)	MgO only	1162.3 ± 158.7	1055.0 ± 129.6	1195.0 ± 229.4	1190.0 ± 69.1	1242.0 ± 268.2	1111.6 ± 292.5	1312.9 ± 277.2	1322.8 ± 200.5
	MgO + Borax	1206.0 ±208.2	1042.5 ±152.1	1099 ±290.3	1179.6 ±49.0	1131.4 ±44.5	1166.6 ±286.9	1417.593 ±192.4	1435.9 ±250.0
Nitrogen Content (ppm)	MgO only	36.15 ±9.42	27.87 ±3.18	31.02 ±5.32	29.80 ±2.56	31.4 ±1.62	29.02 ±5.78	30.04 ±2.58	31.86 ±2.39
	MgO + Borax	35.90 ±5.08	28.78 ±9.96	29.03 ±7.19	29.80 ±1.17	30.60 ±2.94	28.16 ±2.57	31.96 ±1.25	29.7 ±10.75

8.8   Discussion

The purpose of this research was to determine if the addition of Na$_2$B$_4$O$_7$10H$_2$O (Borax) to the slurry is affected extended period at HTS and what influences this may have in magnetic and other properties.

The extended duration at the high temperature on samples that have coated with MgO + Na$_2$B$_4$O$_7$10H$_2$O has had no measurable significant difference on all testing conducted in this chapter. The measured oxide thickness from SEM images displayed in Table 29, where there is a significant difference between 5 hours and 10 hours. Further increase in the duration of the high temperature soak has no significant difference which is reflective in the SEM images of the cross section in Figure 269 and GDOES analysis in section 8.5, where there no clear changes in morphology or chemical composition with and extend time at high temperature. Similarly, there is no significant changes in CONS through out the increase in time spent at the HTS. Critically the magnetic properties have not altered with the increased duration of the soak. There is detection of Na in the GDOES which, indicates that there may be the presence of Na$_2$B$_4$O$_7$10H$_2$O (Borax) present amongst the surface oxide developed. However, Na$_2$B$_4$O$_7$10H$_2$O (Borax) is detected at the surface and decrease rapidly, so this may be present just at the surface. The addition Na$_2$B$_4$O$_7$10H$_2$O (Borax) to the slurry when compared with MgO only slurry demonstrated no measurable changes in magnetic properties or changes in surface oxide. The undetectable influence of Na$_2$B$_4$O$_7$10H$_2$O could be possibly due to the small sample number and a larger sample size would provide enough data to show the subtle influence that Na$_2$B$_4$O$_7$10H$_2$O that has been seen on production.

8.9   Conclusion

This research has demonstrated that the duration of the soak with the small addition of Na$_2$B$_4$O$_7$10H$_2$O displays no benefit to glass film improvements and magnetic properties of the steel, neither in the rate of the coating formation nor in the final composition or morphology.

The addition of Na$_2$B$_4$O$_7$10H$_2$O does not appear to be active during the HTS duration of the HTS. This indicates that the unknown influence and unknown mechanism in which Na$_2$B$_4$O$_7$10H$_2$O must be

occurring during the heating phase of the anneal. However, Chapter Chapter 7 has also demonstrated no significant difference in glass film thickness nor magnetic properties of the steel.

References

[1] "Electrical Steel Market by Type (Grain-oriented and Non Grain-oriented), Application (Transformers, Motors, Inductors), End-Use Industry (Energy, Automobile, Manufacturing, Household Appliances), and Region - Global Forecast to 2021," 2017. doi: 4196138.

[2] G.-D. W. Hai-Tao Liu, Hua-Long Li , Hui Wang , Yi Liu , Fei Gao , Ling-Zi An , Shi-Qi Zhao , Zhen-Yu Liu, "Effects of initial microstructure and texture on microstructure, texture evolution and magnetic properties of non-oriented electrical steel," *J. Magn. Magn. Mater.*, vol. 406, pp. 149–158, 2016, doi: 10.1016/j.jmmm.2016.01.018.

[3] N.-M. H. Hyung-Seok Shim a, Tae-Wook Na , Jin-Seok Chung , Soo-Bin Kwon , Kyehwan Gil , Jong-Tae Park, "Synchrotron X-ray microdiffraction of Fe-3 wt% Si steel focusing on sub-boundaries within Goss grains," *Scr. Mater.*, vol. 116, pp. 71–75, 2016, doi: 10.1016/j.scriptamat.2016.01.026.

[4] Y. Takada, M. Abe, S. Masuda, and J. Inagaki, "Commercial scale production of Fe-6.5 wt. % Si sheet and its magnetic properties," *J. Appl. Phys.*, vol. 64, no. 10, p. 5367, 1988, doi: 10.1063/1.342373.

[5] D. R. Patrick and S. W. Fardo, *Electrical distribution systems*. Fairmont Press, 2009.

[6] P. Darling and M. Society for Mining, *SME mining engineering handbook*. Society for Mining, Metallurgy, and Exploration, 2011.

[7] A. Goldman, "Handbook of Modern Ferromagnetic Materials," in *Basic of Magnetism Source of magnetic Effect*, First Edit., Boston, MA: Springer US, 1999, pp. 31–50.

[8] J. Svoboda, "Magnetic Techniques for the Treatment of Materials," in *Principles of Material Treatment by Magnetic Means*, Dordrecht: Kluwer Academic Publishers, 2004, pp. 1–25.

[9] S. A. Campbell, *Fabrication engineering at the micro and nanoscale*. Oxford University Press, 2008.

[10] J. A. Kilner, *Functional materials for sustainable energy applications*. Woodhead Pub, 2012.

[11] S. Birosca, *Introduction to Electrical Steel : Chemical Composition and Properties*. Swansea University.

[12] "Process Diagram | Grain Oriented Electrical Steel | Products | Cogent power." http://cogent-power.com/products/grain-oriented-electrical-steel/process-diagram (accessed Mar. 18, 2016).

[13] A. Abel, "Dislocation-associated elastic energy storage in mechanical deformations," in

Fundamental Aspects of Dislocation Interactions, G. KOSTORZ, H. A. CALDERON, and J. L. MARTIN, Eds. Elsevier, 1993, pp. 220–225.

[14]   P. Rauscher, J. Hauptmann, and E. Beyer, "Laser scribing of grain oriented electrical steel under the aspect of industrial utilization using high power laser beam sources," *Phys. Procedia*, vol. 41, pp. 312–318, 2013, doi: 10.1016/j.phpro.2013.03.083.

[15]   H. T. Liu *et al.*, "Evolution of microstructure, texture and inhibitor along the processing route for grain-oriented electrical steels using strip casting," *Mater. Charact.*, vol. 106, pp. 273–282, 2015, doi: 10.1016/j.matchar.2015.06.010.

[16]   E. J. . F. Lanesboro, "METHOD OF DECARBURZING SILICON STEEL IN A WET INERT GAS ATMOSPHERE (US 2,8 75,113)," 2875113, 1959.

[17]   L. V Mironov, K. F. Losev, L. P. Kamysheva, Y. N. Yaroshenko, and V. M. Petlyakov, "Magnetic aging of low-carbon electric sheet," *Met. Sci. Heat Treat.*, vol. 15, no. 8, pp. 677–680, 1973, doi: 10.1007/BF00654764.

[18]   C. H. Han and S. J. Kwon, "Effect of nitrogen on the size and distribution of AlN precipitates in 3% silicon steel," *Scr. Mater.*, vol. 34, no. 4, pp. 543–549, 1996, doi: 10.1016/1359-6462(95)00558-7.

[19]   D. Kalisz and S. Rzadkosz, "Modeling of the Formation of AlN Precipitates During Solidification of Steel," *Arch. Foundry Eng.*, vol. 13, no. 1, pp. 63–68, 2013, doi: 10.2478/afe-2013-0012.

[20]   D. Kalisz, P. L. Żak, J. Lelito, M. Szucki, J. S. Suchy, and B. Gracz, "MODELING OF MnS PRECIPITATION DURING THE CRYSTALLIZATION OF GRAIN ORIENTED SILICON STEEL," *Metal. Metabk*, vol. 54, no. 541, pp. 139–142, 2015.

[21]   N. Bernier, C. Xhoffer, T. Van De Putte, M. Galceran, and S. Godet, "Structure analysis of aluminium silicon manganese nitride precipitates formed in grain-oriented electrical steels," *Mater. Charact.*, vol. 86, no. September 2013, pp. 116–126, 2013, doi: 10.1016/j.matchar.2013.09.014.

[22]   A. . Etter, T. Baudin, and R. Penelle, "Influence of the Goss grain environment during secondary recrystallisation of conventional grain oriented Fe–3%Si steels," *Scr. Mater.*, vol. 47, no. 11, pp. 725–730, Dec. 2002, doi: 10.1016/S1359-6462(02)00189-6.

[23]   H. Wang, C. Li, T. Zhu, B. Cai, G. Huo, and N. Mohamed, "Effect of ball scribing on magnetic barkhausen noise of grain-oriented electrical steel," *J. Mater. Sci. Technol.*, vol. 29, no. 7, pp. 440–445, 2013, doi: 10.1016/j.jmst.2013.03.018.

[24] F.Campbell, "Elements of metallurgy and engineering alloys," in *Physical Properties of Metals*, ASM International, 2008, pp. 300–322.

[25] J.M.D.Coey, "Magnetism and Magnetic Materials," in *Magnetostatic*, Cambridge: Cambridge University Press, 2010, pp. 50–60.

[26] J. Erjavec, "Hybrid, electric and fuel-cell vehicles," in *Motor and Generator Basics*, Delmar Cengage Learning, 2013, pp. 35–41.

[27] D. Bhattacharyya and S. Fakirov, *Synthetic polymer-polymer composites*. Hanser, 2012.

[28] W. P. Mohan, Ned Undeland, Tore M. Robbins, "Power Electronics," in *Eddy Currents*, Design (3rd Edition)., John Wiley & Sons, 2003, pp. 771–777.

[29] W. a Pluta, "Core loss models in electrical steel sheets with different orientation," no. 9, pp. 37–42, 2011.

[30] K. H. J. Buschow, *Encyclopedia of materials : science and technology*. Elsevier, 2001.

[31] B. S. Guru and H. R. Hiziroglu, "Electric Machinery and Transformers," in *Oxford university press*, 2001, pp. 100–129.

[32] H. Y. Song, H. T. Liu, Y. P. Wang, and G. D. Wang, "Microstructure and texture evolution of ultra-thin grain-oriented silicon steel sheet fabricated using strip casting and three-stage cold rolling method," *J. Magn. Magn. Mater.*, vol. 426, no. October 2016, pp. 32–39, 2017, doi: 10.1016/j.jmmm.2016.11.038.

[33] Michiro Komatsubara; Yasuyuki Hayakawa; Katsuo Iwamoto; Makoto Watanabe, "Decarburized Steel Sheet for Thin Oriented Silicon Steel Sheet having Improved Coating / Magnetic Characteristics and Method of Producing," 5,571,342, 1996.

[34] F. Hiroaki Masui, Kitakyushu; Morio Shiozaki, Himeji; Nobuyuki Takahashi, Kitakyushu; Hisashi Kabayashi, Kawasaki; Takeo Nagashima, Futtsu; Shuichi Yamazaki, Futtsu; Hiroyasu Fujii, "Grain Oriented Silicon Steel Sheet having Excellent Primary Film Properties," 5,565,272, 1996.

[35] J. M. D. Coey, "Magnetism and Magnetic Materials," in *applications of soft magnets*, Cambridge University Press, 2009, pp. 440–465.

[36] C. Jekeli, "Potential Theory and Static Gravity Field of the Earth," in *Treatise on Geophysics*, vol. 4, Elsevier, 2007, pp. 278–291.

[37] D. K. Bhattacharya and P. Tandon, "Engineering physics," in *ferromagnetism—Domain theory*, Oxford, 2015, pp. 549–571.

[38]   S. W. F. Dale R. Patrick, "Understanding DC Circuits," in *Proceedings of the National Academy of Sciences*, vol. 1, no. 1, 1989, p. 181.

[39]   F. Fernandez-Alonso and D. L. Price, "Neutron scattering -- magnetic and quantum phenomena," in *Neutron Scattering in Nanomagnetism*, 2015, pp. 394–395.

[40]   D. D. Tang and Y.-J. Lee, "Magnetic Memory: Fundamentals and Technology," Cambridge University Press, 2010, pp. 55–63.

[41]   M. Gallaugher, N. Brodusch, R. Gauvin, and R. R. Chromik, "Magnetic domain structure and crystallographic orientation of electrical steels revealed by a forescatter detector and electron backscatter diffraction," *Ultramicroscopy*, vol. 142, pp. 40–49, 2014, doi: 10.1016/j.ultramic.2014.03.013.

[42]   H. Cao *et al.*, "The influence of punching process on residual stress and magnetic domain structure of non-oriented silicon steel," *J. Magn. Magn. Mater.*, vol. 406, pp. 42–47, 2016, doi: 10.1016/j.jmmm.2015.12.098.

[43]   W. T. McLyman and C. W. M. T. Mclyman, "Transformer and inductor design handbook," in *Magnetic Materials and Their Characteristics*, 2004, pp. 2.3-2.4.

[44]   J. J. Winders, "Transformers Principles and Applications," in *Basic Transformer Theory*, First Edit., Marcel Dekker, 2002, pp. 12–14.

[45]   C. W. T. McLyman, "High Reliability Magnetic Devices: Design & Fabrication," First Edit., New York: Marcel Dekker.INC, 2002, pp. 1.23-25 2.23–4.

[46]   J. J. W. SHILLING AND G. L. HOUZE, "Magnetic Properties and Domain Structure in Grain - Oriented 3% Si-Fe," *IEEE Trans. Magn.*, vol. Mag, no. 2, pp. 195–223, 1974.

[47]   S. Turner, A. Moses, J. Hall, and K. Jenkins, "The effect of precipitate size on magnetic domain behavior in grain-oriented electrical steels," *J. Appl. Phys.*, vol. 107, no. 9, 2010, doi: 10.1063/1.3334201.

[48]   D. S. Schmool, *Solid State Physics - From the Material Properties of Solids to Nanotechnologies - Knovel*. Mercury Learning and Information, 2017.

[49]   Hubert Alex and R. Schafer, "Magnetic Domains The Analysis of Magnetic Mircrostructures," in *Magnetic Domains*, 1998, p. 105.

[50]   N. P. Goss, "Electrical sheet and method and apparatus for its manufacture and test," U.S Patent 1965559, 1934.

[51]   N. Bernier, C. Xhoffer, T. Van De Putte, M. Galceran, and S. Godet, "Structure analysis of

aluminium silicon manganese nitride precipitates formed in grain-oriented electrical steels," *Mater. Charact.*, vol. 86, pp. 116–126, Dec. 2013, doi: 10.1016/j.matchar.2013.09.014.

[52]   Y. Hayakawa, "Mechanism of secondary recrystallization of Goss grains in grain-oriented electrical steel," *Sci. Technol. Adv. Mater.*, vol. 18, no. 1, pp. 480–497, Dec. 2017, doi: 10.1080/14686996.2017.1341277.

[53]   R. Shimizu and J. Harase, "Coincidence grain boundary and texture evolution in Fe-3%Si," *Acta Metall.*, vol. 37, no. 4, pp. 1241–1249, Apr. 1989, doi: 10.1016/0001-6160(89)90118-1.

[54]   H.-Y. Song *et al.*, "Fabrication of grain-oriented silicon steel by a novel way: Strip casting process," *Mater. Lett.*, vol. 137, pp. 475–478, Dec. 2014, doi: 10.1016/J.MATLET.2014.09.075.

[55]   Y. Li, W. Mao, and P. Yang, "Inhomogeneous Distribution of Second Phase Particles in Grain Oriented Electrical Steels," *J. Mater. Sci. Technol.*, vol. 27, pp. 1120–1124, 2011, doi: 10.1016/S1005-0302(12)60006-1.

[56]   I. L. Dillamore, C. J. E. Smith, and T. W. Watson, "Oriented Nucleation in the Formation of Annealing Textures in Iron," *Met. Sci. J.*, vol. 1, no. 1, pp. 49–54, Jan. 1967, doi: 10.1179/msc.1967.1.1.49.

[57]   C. E. Gifford, "A separator for silicon steel sheets during annealing," 1,842,162, 1932.

[58]   G. Si-fe, W. G. Morris, J. W. Shilling, D. R. Fecich, and F. Prakash, "Effect of Forsterite Coatings on the Domain Structure," *IEEE Trans. Magn.*, vol. 14, no. 1, pp. 14–17, 1978.

[59]   S. Jung, M. S. Kwon, S. Bin Kim, and K. S. Shin, "Characterization of chemical information and morphology for in-depth oxide layers in decarburized electrical steel with glow discharge sputtering," *Surf. Interface Anal.*, vol. 45, no. 7, pp. 1119–1128, 2013, doi: 10.1002/sia.5237.

[60]   P. Hans A. Steinherz, "PHOSPHATE COATING FOR ELECTRICAL STEEL," U.S. Patent 2,743,203, 1956.

[61]   K. Jenkins and M. Lindenmo, "Precipitates in electrical steels," *J. Magn. Magn. Mater.*, vol. 320, no. 20, pp. 2423–2429, 2008, doi: https://doi.org/10.1016/j.jmmm.2008.03.062.

[62]   G. M. Michal and J. A. Slane, "The kinetics of carbide precipitation in silicon-aluminum steels," *Metall. Trans. A*, vol. 17, no. 8, pp. 1287–1294, 1986, doi: 10.1007/BF02650109.

[63]   S. Jung, J. Park, M. Han, and S. Bin Kim, "Rapid quantitative analysis of fayalite and silica formed during decarburization of electrical steel," *Surf. Interface Anal.*, vol. 44, no. 3, pp. 270–275, 2012, doi: 10.1002/sia.3791.

[64]   M. das G. M. . Cesar and M. J. Mantel, "Effect of the temperature and dew point of the decarburization process on the oxide subscale of a 3% silicon steel," *J. Magn. Magn. Mater.*, vol. 254–255, pp. 337–339, Jan. 2003, doi: 10.1016/S0304-8853(02)00836-3.

[65]   M. L. Lobanov, A. I. Gomzikov, S. V. Akulov, and A. I. Pyatygin, "Decarburizing annealing of technical alloy Fe - 3% Si," *Met. Sci. Heat Treat.*, vol. 47, no. 9–10, pp. 478–483, 2005, doi: 10.1007/s11041-006-0015-0.

[66]   P. Wen, H. Luo, G. Zeng, J. Li, and J. Huang, "ScienceDirect In-situ measurement and numerical simulation of nitriding kinetics of grain-oriented silicon steel," *Int. J. Hydrogen Energy*, pp. 1–10, 2017, doi: 10.1016/j.ijhydene.2017.02.200.

[67]   Suzuki, "Thermodynamic analysis of selective oxidation behavior of Si and Mn added steel during recrystallization annealing," *ISIJ Int.*, vol. 49, no. 4, pp. 564–573, 2010, [Online]. Available: file://ce/rd_organisation/PTA-MAD/Common/10 Literature/2010/Suzuki (2010) # Thermodynamic analysis of selective oxidation behavior of Si and Mn-added steel during recrystallization annealing .pdf.

[68]   S. Jung, M. S. Kwon, J. Park, S. Bin Kim, and Y. Huh, "A TEM Study of Oxide Layers Formed during Decarburization Annealing of Electrical Steel," *ISIJ Int.*, vol. 51, no. 7, pp. 1163–1168, 2011, doi: 10.2355/isijinternational.51.1163.

[69]   H. Toda, K. Sato, and M. Komatsubara, "Characterization of Internal Oxide Layers in 3 % Si Grain-Oriented Steel by Electrochemical Methods," vol. 6, no. December, pp. 722–727, 1997.

[70]   P. Griesbach, W. Meisel, and P. Gütlich, "Layer formation on silicon steel by processing in H2/H2O at elevated temperatures," *Hyperfine Interact.*, vol. 69, no. 1, pp. 811–814, 1992, doi: 10.1007/BF02401950.

[71]   S. Jung, J. Park, M. Han, and S. Bin Kim, "Rapid quantitative analysis of fayalite and silica formed during decarburization of electrical steel," *Surf. Interface Anal.*, vol. 44, no. 3, pp. 270–275, Mar. 2012, doi: 10.1002/sia.3791.

[72]   C. C. Silveira, M. A. Da Cunha, and V. T. L. Buono, "The influence of internal oxidation during decarburization of a grain oriented silicon steel on the morphology of the glass film formed at high temperature annealing," *J. Magn. Magn. Mater.*, vol. 358–359, pp. 65–69, 2014, doi: 10.1016/j.jmmm.2014.01.019.

[73]   V. Hoek, "Study of the influence of decarburising furnace atmosphere on the oxide formation occurring during processing of electrical steels," *Tata Intern. Doc.*, pp. 1–4.

[74]   C. Guan, J. Li, N. Tan, Y. He, and S. Zhang, "ScienceDirect Reduction of oxide scale on hot-

rolled steel by hydrogen at low temperature," *Int. J. Hydrogen Energy*, vol. 39, no. 27, pp. 15116–15124, 2014, doi: 10.1016/j.ijhydene.2014.07.024.

[75]   R. Torkaman, S. Darvishi, M. Jokar, M. Kharaziha, and M. Karbasi, "Electrochemical and in vitro bioactivity of nanocomposite gelatin-forsterite coatings on AISI 316 L stainless steel," *Prog. Org. Coatings*, vol. 103, pp. 40–47, 2017, doi: 10.1016/j.porgcoat.2016.11.029.

[76]   A. E. Ringwood and A. Major, "The system Mg2SiO4 Fe2SiO4 at high pressures and temperatures," *Phys. Earth Planet. Inter.*, vol. 3, pp. 89–108, Jan. 1970, doi: 10.1016/0031-9201(70)90046-4.

[77]   L. Chen *et al.*, "The influence of ZnO in fayalite slag on the degradation of magnesia-chromite refractories during secondary Cu smelting," *J. Eur. Ceram. Soc.*, vol. 35, no. 9, pp. 2641–2650, 2015, doi: 10.1016/j.jeurceramsoc.2015.03.013.

[78]   P. Ctibor, K. Neufuss, Z. Pala, J. Kotlan, and J. Soumar, "Dielectric and mechanical properties of plasma-sprayed olivine," *Rom. Reports Phys.*, vol. 67, pp. 600–616, 2015.

[79]   M. A. Cunha and M. G. M. M. Cesar, "Forsterite Film Formation and Grain Growth in 3% Si Steel," *IEEE Transactions on Magnetics*, vol. 30, no. 6. pp. 4890–4892, 1994, doi: 10.1109/20.334256.

[80]   I. Transactions and O. N. Magnetics, "Evidence for the Effectiveness of Stress Coating in Altering Magnetic Properties of Commercially Produced Grain-Oriented 3% Silicon- Iron," *IEEE Trans. Magn.*, vol. 15, no. 6, pp. 1580–1585, 1979.

[81]   H. Fujii, S. Yamazaki, T. Nagashima, H. Kobayashi, H. Masui, and M. Shiozaki, "Glass film structure of grain-oriented silicon steel using aluminum nitride as an inhibitor," *J. Mater. Eng. Perform.*, vol. 3, no. 2, pp. 214–217, Apr. 1994, doi: 10.1007/BF02645845.

[82]   H. Shimanaka, T. Ichida, S. Kobayashi, and T. Funahashi, "Effect of several stress inducing coatings on magnetostriction property of a high induction 3% silicon steel," *IEEE Trans. Magn.*, vol. 15, no. 6, pp. 1595–1597, Nov. 1979, doi: 10.1109/TMAG.1979.1060473.

[83]   A. Braginski and D. Buck, "Polycrystalline ferrite films for microwave applications," *IEEE Trans. Magn.*, vol. 5, no. 4, pp. 924–928, Dec. 1969, doi: 10.1109/TMAG.1969.1066658.

[84]   K. Yasuyuki Hayakawa; Ujihiro Nishiike; Bunjiro Fukuda, all of Chiba; Masataka Yamada, Kobe; Tetsuya Oishi, Kurashiki; Shigeru Yoshida, Kurashiki; Yoh Shimizu, "Method of Manufacturing Grain Oriented Silicon Steel Sheets," U.S. Patent 5318639, 1994.

[85]   A. Buckley, A. J. Moses, and L. Trollope, "Study and redesign of high temperature batch annealing furnace for production of grain oriented electrical steel," *Ironmak. Steelmak.*, vol.

26, no. 6, pp. 477–482, Dec. 1999, doi: 10.1179/030192399677338.

[86] G. Duan, X. Yang, J. Chen, G. Huang, L. Lu, and X. Wang, "The catalytic effect of nanosized MgO on the decomposition of ammonium perchlorate," *Powder Technol.*, vol. 172, no. 1, pp. 27–29, 2007, doi: 10.1016/j.powtec.2006.10.038.

[87] Y. Inokuti, "Grain oriented silicon steel sheet with a ceramic film characterized by ultra-low iron loss," *Vacuum*, vol. 47, no. 6–8, pp. 857–862, Jun. 1996, doi: 10.1016/0042-207X(96)00082-6.

[88] Osamu Tanaka; Hiroshi Sato, "Process for Producing Grain-Oriented Electrical Steel Sheet having Improved Magnetic Properties," U.S. Patent 4775430, 1982.

[89] M. G. M. M. Cesar, D. C. L. Vasconcelos, and W. L. Vasconcelos, "Microstructural characterization of magnesias derived from different sources and their influence on the structure of ceramic films formed on a 3% silicon steel surface," *J. Mater. Sci.*, vol. 37, no. 11, pp. 2323–2329, doi: 10.1023/A:1015333719998.

[90] Y. FU, Q. JIANG, B. WANG, P. YANG, and W. JIN, "Morphologies and Influential Factors of Forsterite Film in Grain-Oriented Silicon Steel," *J. Iron Steel Res. Int.*, vol. 20, no. 11, pp. 105–110, Nov. 2013, doi: 10.1016/S1006-706X(13)60204-6.

[91] T. I. M. Komatsnbnra, "Forsterite Insulating Films formed on Surface of A Grain-Oriented Silicon Steel Sheet having A High Magnetic Induction and a Method of Forming," U.S. Patent 4127429, 1978.

[92] H. Fujii, S. Yamazaki, T. Nagashima, H. Kobayashi, H. Masui, and M. Shiozaki, "Glass film structure of grain-oriented silicon steel using aluminum nitride as an inhibitor," *J. Mater. Eng. Perform.*, vol. 3, no. 2, pp. 214–217, 1994, doi: 10.1007/BF02645845.

[93] D. C. Pleydell-Pearce, "Introduction to Electrical steel Lecture Notes," *Introd. to Electr. steel Lect. Notes*, vol. 2, 2013.

[94] H. Y. N. K. N. HAJIME, "MgO - Based Annealing separator for grain oriented silicon steel strips," U.K. Patent 2041343 (A), 1979.

[95] K. YAKASHIRO, Kenichi , HONMA, Hotaka, ISHIBASHI, Maremizu, SAKAIDA, Akira, KUMANO, Tomoji, YAMASAKI, "Process for Producing Directional Electrical Sheet Excellent in Glass Coating and Magnetic Properties," European Patent 0789093 A1, 1997.

[96] F. C. Samuel W. Sopp and S. S. F. ghalqgael w' H. Leonard S. Lee, "Magnesium Oxide Composition for Coating Silicon Steel," U.S. Patent 4443425, 1989.

[97] C. A. Strydom, E. M. van der Merwe, and M. E. Aphane, "The effect of calcining conditions

on the rehydration of dead burnt magnesium oxide using magnesium acetate as a hydrating agent," *J. Therm. Anal. Calorim.*, vol. 80, no. 3, pp. 659–662, 2005, doi: 10.1007/s10973-005-0710-x.

[98]   C. C. Silveira, "Effect of Magnesia Blending on the Magnetic Properties of Grain Oriented Silicon Steel," *J Chem Chem Eng*, vol. 8, pp. 191–194, 2014.

[99]   J. J. Thomas, S. Musso, and I. Prestini, "Kinetics and Activation Energy of Magnesium Oxide Hydration," *J. Am. Ceram. Soc.*, vol. 97, no. 1, pp. 275–282, Jan. 2014, doi: 10.1111/jace.12661.

[100]   M. E. Aphane, E. M. Van Der Merwe, and C. A. Strydom, "Influence of hydration time on the hydration of MgO in water and in a magnesium acetate solution," *J. Therm. Anal. Calorim.*, vol. 96, no. 3, pp. 987–992, 2009, doi: 10.1007/s10973-008-9095-y.

[101]   E. M. van der Merwe, C. Strydom, and A. Botha, "Hydration of medium reactive industrial magnesium oxide with magnesium acetate," *J. Therm. Anal. Calorim.*, vol. 77, no. 1, pp. 49–56, 2004, doi: 10.1023/B:JTAN.0000033187.61971.1d.

[102]   D. C. Leite, G. M. M. Cesar, M. Antônio, and W. L. Vasconcelos, "Influence of MgO Containing Strontium on the Structure of Ceramic Film Formed on Grain Oriented Silicon Steel Surface," vol. 2, no. 3, pp. 159–164, 1999.

[103]   Osamu Tanaka; Shozaburo Nakashima; Takashi Nagano; Tomoji Kumano; Yoshitaka Hiromae, "Process for Producing Grain Oriented Electrical Steel Sheet Having Both Improved Magnetic Properties and Properties of Glass Film," U.S. Patent 4543134, 1985.

[104]   V. H. S. Klaus Gunther, "Process for the Coating of Electrical Steel Strips with an Annealing Separator," U.S. Patent 6423156 B1, 2002.

[105]   T. Y. K. A. O. Tanaka, "Method of forming Electric Insulating Films on Oriented Silicon Steel," U.S. Patent 3627594, 1956.

[106]   V. Gayathri *et al.*, "Influence of La on nano titanium dioxide (TiO2) based solar cell," *Mater. Today Proc.*, no. xxxx, pp. 2–5, 2019, doi: 10.1016/j.matpr.2019.05.299.

[107]   D. Spreitzer and J. Schenk, "Reduction of Iron Oxides with Hydrogen—A Review," *Steel Res. Int.*, vol. 90, no. 10, 2019, doi: 10.1002/srin.201900108.

[108]   A. Roine, "HSC - SOFTWARE VER. 3.0 FOR THERMODYNAMIC CALCULATIONS," in *Proceedings of the International Symposium on Computer Software in Chemical and Extractive Metallurgy*, 1989.

[109]   W. Zhang, D. R. Sadedin, M. A. Reuter, and J. C. McCallum, "The de-oxidation of partially

oxidized titanium by hydrogen plasma," *Mater. Forum*, vol. 31, pp. 76–83, 2007.

[110] X. Chen, L. Liu, and F. Huang, " Correction: Black titanium dioxide (TiO 2) nanomaterials ," *Chem. Soc. Rev.*, vol. 44, no. 7, pp. 2019–2019, 2015, doi: 10.1039/c5cs90019k.

[111] H. Sekimoto, R. Shioi, T. Uda, and Y. Awakura, "Reduction of Titanium Oxide to Titanium Alloy by Hydrogen Titanium alloy Reduction of titanium oxide to Ti-Pt alloy Reduction of titanium oxide to Ti-Ni alloy Summary," 2007.

[112] C. Y. Wu, K. J. Tu, J. P. Deng, Y. S. Lo, and C. H. Wu, "Markedly enhanced surface hydroxyl groups of TiO2 nanoparticles with Superior water-dispersibility for photocatalysis," *Materials (Basel).*, vol. 10, no. 5, 2017, doi: 10.3390/ma10050566.

[113] R. Zhang, D. Liu, G. Fan, H. Sun, and J. Dang, "Thermodynamic and experimental study on the reduction and carbonization of TiO2 through gas-solid reaction," *Int. J. Energy Res.*, vol. 43, no. 9, pp. 4253–4263, 2019, doi: 10.1002/er.4551.

[114] T. Y. and S. K. Takao SEKIYA, "Annealing of Anatase Titanium Dioxide under Hydrogen Atmosphere," *Soc. Ceram.*, vol. 675, pp. 672–675, 2001.

[115] A. Naldoni *et al.*, "Photocatalysis with reduced TiO 2 : From Black TiO 2 to cocatalyst-free hydrogen production," *ACS Catal.*, vol. 9, no. 1, pp. 345–364, 2019, doi: 10.1021/acscatal.8b04068.

[116] T. Nozawa, T. Yamamoto, Y. Matsuo, and Y. Owya, "Effect of Scratching on Losses in 3% Si-Fe Single Crystals with Oriented near (110)[001]," *IEEE Trans. Magn.*, vol. 15, no. 2, pp. 972–981, 1979.

[117] K. (JP) Hiroaki Toda, Kunihiro Senda, Mitsumasa Kurosawa, Makoto Watanabe, and O. Atsuhito Honda, "GRAIN-ORIENTED SILICON STEEL SHEET AND PROCESS FOR PRODUCTION US 6,475,304 B2," 2002.

[118] D. Dorner, S. Zaefferer, L. Lahn, and D. Raabe, "Overview of Microstructure and Microtexture Development in Grain-oriented Silicon Steel," *J. Magn. Magn. Mater.*, vol. 304, no. 2, pp. 183–186, 2006, doi: 10.1016/j.jmmm.2006.02.116.

[119] D. C. Mills, "The Glow Discharge Optical Emission Spectrometer (GDOES)," in *GDOES techinque*, 2019, p. 6.

[120] N. Jayaraman, "Reactions during decarburization annealing of electrical steel," vol. 2, no. January, pp. 22–27, 1986.

[121] E. J. Song, D. W. Suh, and H. K. D. H. Bhadeshia, "Oxidation of silicon containing steel," *Ironmak. Steelmak.*, vol. 39, no. 8, pp. 599–604, 2012, doi:

10.1179/1743281212Y.0000000007.

[122] C. C. Silveira, M. A. da Cunha, and V. T. L. Buono, "The influence of internal oxidation during decarburization of a grain oriented silicon steel on the morphology of the glass film formed at high temperature annealing," *J. Magn. Magn. Mater.*, vol. 358–359, pp. 65–69, May 2014, doi: 10.1016/j.jmmm.2014.01.019.

[123] X. Lu *et al.*, "Microstructure, texture and precipitate of grain-oriented 4.5 wt% Si steel by strip casting," *J. Magn. Magn. Mater.*, vol. 404, pp. 230–237, 2016, doi: 10.1016/j.jmmm.2015.12.043.

[124] I. L. Dillamore, C. J. E. Smith, and T. W. Watson, "Oriented Nucleation in the Formation of Annealing Textures in Iron," *Met. Sci. J.*, vol. 1, no. 1, pp. 49–54, 1967, doi: 10.1179/msc.1967.1.1.49.

[125] H. Y. Song, H. T. Liu, Y. P. Wang, and G. D. Wang, "Secondary recrystallization behavior in a twin-roll cast grain-oriented electrical steel," *J. Magn. Magn. Mater.*, vol. 428, no. November 2016, pp. 325–332, 2017, doi: 10.1016/j.jmmm.2016.12.109.

[126] J. & S. Ctibor, Pavel & Neufuss, K & Pala, Zdenek & Kotlan, "Dielectric and mechanical properties of plasma-sprayed olivine." Romanian Reports in Physics, pp. 600–616, doi: Jan. (2015).

[127] Y. Suzuki and Y. Shinoda, "Magnesium dititanate (MgTi2O5) with pseudobrookite structure: A review," *Sci. Technol. Adv. Mater.*, vol. 12, no. 3, 2011, doi: 10.1088/1468-6996/12/3/034301.

[128] H. Afer, N. Rouag, and R. Penelle, "Influence of Textured Clusters on the Goss Grains Growth in Silicon Steels Consideration of Energy and Mobility," pp. 62–65, 2007.

[129] O. M. H. Fatla, A. Valera-Medina, F. Robinson, M. Cichuta, and N. Beynon, "Development of convection in high temperature coil annealing furnaces using rotating cylinder technique," *Appl. Therm. Eng.*, vol. 129, pp. 1392–1402, Jan. 2018, doi: 10.1016/j.applthermaleng.2017.10.136.

[130] S. Duncan Clark, Surrey (GB); Nicholas Morant, "Patent Application Publication (10) Pub . No .: US 2011 / 0104761 A1," vol. 1, no. 39, 2011.

[131] T. Tsunooka, M. Androu, Y. Higashida, H. Sugiura, and H. Ohsato, "Effects of TiO2 on sinterability and dielectric properties of high-Q forsterite ceramics," *J. Eur. Ceram. Soc.*, vol. 23, no. 14, pp. 2573–2578, 2003, doi: 10.1016/S0955-2219(03)00177-8.

[132] Y. jun Fu, Q. wu Jiang, B. chuan Wang, P. Yang, and W. xu Jin, "Morphologies and

Influential Factors of Forsterite Film in Grain-Oriented Silicon Steel," *J. Iron Steel Res. Int.*, vol. 20, no. 11, pp. 105–110, 2013, doi: 10.1016/S1006-706X(13)60204-6.

[133] H. Fujii, S. Yamazaki, H. Masui, M. Shiozaki, T. Nagashima, and H. Kobayashi, "Structure and formation process of the glass film on grain-oriented silicon steel using aluminum nitride as an inhibitor," *J. Appl. Phys.* , vol. 85, no. 8 II B, pp. 6016–6018, 1999, [Online]. Available: http://www.scopus.com/inward/record.url?eid=2-s2.0-4143143315&partnerID=40&md5=80b0be5465b079f18430be86e14829bf.

[134] Y. Hayakawa and J. A. Szpunar, "A new model of Goss texture development during secondary recrystallization of electrical steel," *Acta Mater.*, vol. 45, no. 11, pp. 4713–4720, Nov. 1997, doi: 10.1016/S1359-6454(97)00111-0.

[135] P. Siriphannon, Y. Kameshima, A. Yasumori, K. Okada, and S. Hayashi, "Formation of hydroxyapatite on CaSiO3 powders in simulated body fluid," *J. Eur. Ceram. Soc.*, vol. 22, no. 4, pp. 511–520, 2002, doi: 10.1016/S0955-2219(01)00301-6.

[136] U. Nishiike, T. Kan, and A. Honda, "Influence of Surface Properties on the Stress Magnetization Properties of Grain-oriented Silicon Steel," *IEEE Transl. J. Magn. Japan*, vol. 8, no. 11, pp. 777–782, 1993, doi: 10.1109/TJMJ.1993.4565744.

[137] C. C. Silveira, M. A. Da Cunha, and V. T. L. Buono, "The influence of internal oxidation during decarburization of a grain oriented silicon steel on the morphology of the glass film formed at high temperature annealing," *J. Magn. Magn. Mater.*, vol. 358–359, pp. 65–69, 2014, doi: 10.1016/j.jmmm.2014.01.019.

Mags